

AD-A 211107 AGARD-AG-315

# AGARD

ADVISORY GROUP FOR AEROSPACE RESEARCH & DEVELOPMENT

7 RUE ANCELLE 92200 NEUILLY SUR SEINE FRANCE

AGARDograph No. 315

## A Survey of Measurements and Measuring Techniques in Rapidly Distorted Compressible Turbulent Boundary Layers

DTIC

ELECTE  
AUG 0 1989

CS D

DISTRIBUTION STATEMENT A

Approved for public release  
Distribution Unlimited

NORTH ATLANTIC TREATY ORGANIZATION



DISTRIBUTION AND AVAILABILITY  
ON BACK COVER

88 8 21 886

NORTH ATLANTIC TREATY ORGANIZATION  
 ADVISORY GROUP FOR AEROSPACE RESEARCH AND DEVELOPMENT  
 (ORGANISATION DU TRAITE DE L'ATLANTIQUE NORD)

AGARDograph No.315

**A SURVEY OF MEASUREMENTS AND MEASURING TECHNIQUES IN RAPIDLY  
 DISTORTED COMPRESSIBLE TURBULENT BOUNDARY LAYERS**

by

H.H.Fernholz  
 Herman Föttinger Institut für  
 Thermo und Fluidodynamik  
 Technische Universität Berlin  
 Strasse des 17 Juni 135  
 D-1000 Berlin 12  
 Federal Republic of Germany

J.P.Dussauge  
 Institut de Mécanique Statistique  
 de la Turbulence  
 12 Avenue du Général Leclerc  
 13003 Marseille  
 France

P.J.Finley  
 Department of Aeronautics  
 Imperial College of Science and Technology  
 Prince Consort Road  
 London SW7 2BY  
 United Kingdom

A.J.Smits  
 Princeton University  
 School of Engineering and Applied Science  
 Department of Mechanical & Aerospace  
 Engineering  
 The Engineering Quadrangle  
 Princeton, New Jersey 08544  
 United States

Edited by

E.Reshotko  
 Dept. of Aerospace Mech. Engineering  
 Case Western Reserve University  
 University Circle  
 Cleveland, Ohio 44106  
 United States

Accession For	
NTIS	<input checked="" type="checkbox"/>
CRA&I	<input type="checkbox"/>
DTIC	<input type="checkbox"/>
TAB	<input type="checkbox"/>
Unannounced	<input type="checkbox"/>
Justification	
By	
Distribution	
Availability Codes	
Dist	Available for Special
A-1	

This AGARDograph has been produced at the request of the Fluid Dynamics Panel of AGARD.

## THE MISSION OF AGARD

According to its Charter, the mission of AGARD is to bring together the leading personalities of the NATO nations in the fields of science and technology relating to aerospace for the following purposes:

- Recommending effective ways for the member nations to use their research and development capabilities for the common benefit of the NATO community;
- Providing scientific and technical advice and assistance to the Military Committee in the field of aerospace research and development (with particular regard to its military application);
- Continuously stimulating advances in the aerospace sciences relevant to strengthening the common defence posture;
- Improving the co-operation among member nations in aerospace research and development;
- Exchange of scientific and technical information;
- Providing assistance to member nations for the purpose of increasing their scientific and technical potential;
- Rendering scientific and technical assistance, as requested, to other NATO bodies and to member nations in connection with research and development problems in the aerospace field.

The highest authority within AGARD is the National Delegates Board consisting of officially appointed senior representatives from each member nation. The mission of AGARD is carried out through the Panels which are composed of experts appointed by the National Delegates, the Consultant and Exchange Programme and the Aerospace Applications Studies Programme. The results of AGARD work are reported to the member nations and the NATO Authorities through the AGARD series of publications of which this is one.

Participation in AGARD activities is by invitation only and is normally limited to citizens of the NATO nations.

The content of this publication has been reproduced  
directly from material supplied by AGARD or the authors.

Published May 1989

Copyright © AGARD 1989  
All Rights Reserved

ISBN 92-835-0506-9



Printed by Specialised Printing Services Limited  
40 Chigwell Lane, Loughton, Essex IG10 3TZ

## PREFACE

A large body of data for incompressible turbulent boundary layers has been accumulated over many years by many investigators. These measurements have revealed elements of the structure of this complex flow. Three-dimensional multiple scale phenomena have been observed, and there is the beginning of an understanding of the details of the structure and physics. This will lead to more realistic models and physical understanding, which will be primary inputs into concepts of control of these turbulent boundary layers and will provide a framework to validate computations.

At high speed, where compressibility is important, there is a paucity of data. The measurements are difficult to obtain and are not easily analysed. At the same time, there appear to be some possibilities for simplification inherent in "rapid distortion theory" where the turbulent structure may be "frozen" if the disturbance is of short duration. There is a critical need for data to evaluate this concept, to provide a base for models of turbulence in compressible flows to compare with incompressible flows, to provide a more substantial base for our physical understanding, and to provide a framework for the evaluation of the extensive computations which are currently underway.

The present AGARDograph is an important start on this key problem of high speed fluid mechanics. This initial work is of limited range and primarily two-dimensional but it will provide a solid base for extensions, in the future, to wider range and three-dimensional flows. It should also provide a solid base for the modeller and the computer to evaluate their efforts.

Seymour M. Bogdonoff  
Gasdynamics Laboratory  
Mechanical and Aerospace Engineering Department  
Princeton University



## PREFACE

Un volume de données considérable relatif aux couches limites tourbillonnaires incompressibles a été accumulé au fil des années par différents chercheurs.

Les mesures effectuées ont permis d'apprécier certains éléments de la structure de cet écoulement complexe. Des phénomènes tridimensionnels multi-échelle ont été observés et ceux qui travaillent dans ce domaine commencent à comprendre le détail de la structure et les lois physiques qui régissent ce type d'écoulement. Ces activités devraient déboucher sur des modèles plus représentatifs ainsi que sur la compréhension des phénomènes physiques, éléments qui sont d'une importance capitale pour l'élaboration des concepts de contrôle de ces couches limites tourbillonnaires, et qui devraient servir de base pour la validation des calculs.

Très peu de données sont disponibles concernant les phénomènes observés à grande vitesse, où la compressibilité joue un rôle important. Les mesures sont difficiles à faire et l'analyse des résultats pose des problèmes. Cela étant, il semblerait qu'il existe des possibilités de simplification qui soient propres à la notion de "la théorie de la déformation rapide" selon laquelle la structure tourbillonnaire peut être "gelée" si la perturbation est de courte durée.

Aujourd'hui, il faut recueillir les données permettant d'évaluer ce concept, constituer une base pour la modélisation de la turbulence dans les écoulements incompressibles, créer une base plus étoffée pour la compréhension des phénomènes physiques, et établir les paramètres qui permettront d'évaluer les grands travaux de calcul qui sont entrepris à l'heure actuelle.

Cette AGARDographie est une première approche intéressante à ce problème clé de la mécanique des fluides à grande vitesse. Ce travail préliminaire est d'une étendue limitée et, pour la plupart, bi-dimensionnel, mais il servira de base solide pour de futurs travaux, de plus grande envergure, comprenant les écoulements tridimensionnels. Il devrait également servir de base pour les concepteurs de modèle et les informaticiens désirant évaluer leurs propres travaux dans ce domaine.

Seymour M. Bogdonoff.

# CONTENTS

	Page
PREFACE	iii
	Reference
INTRODUCTION by H.H.Fernholz and A.J.Smits	1
RAPIDLY DISTORTED COMPRESSIBLE BOUNDARY-LAYERS by J.P.Dussauge, J.F.Debieue and A.J.Smits	2
LARGE SCALE MOTIONS IN SUPERSONIC TURBULENT BOUNDARY LAYERS by A.J.Smits and J.H.Watmuff	3
SKIN-FRICTION MEASUREMENTS BY LASER INTERFEROMETRY by K.-S.Kim and G.S.Settles	4
HOT-WIRE ANEMOMETRY IN SUPERSONIC FLOW by A.J.Smits and J.P.Dussauge	5
LASER DOPPLER ANEMOMETRY by D.A.Johnson	6
LASER DOPPLER ANEMOMETRY IN SUPERSONIC FLOWS: PROBLEMS OF SEEDING AND ANGULAR BIAS by M.Elena	7
FLUCTUATING WALL-PRESSURE MEASUREMENTS by D.S.Dolling and J.P.Dussauge	8
GENERAL COMMENTS ON THE INTERPRETATION OF DATA by P.J.Finley and H.H.Fernholz	9
REVIEW OF MEAN FLOW DATA by H.H.Fernholz and P.J.Finley	10
REVIEW OF TURBULENCE DATA by H.H.Fernholz and P.J.Finley	11
THE ENTRIES by H.H.Fernholz and P.J.Finley	12
REFERENCES FOR CHAPTERS 1 AND 9 TO 12 by H.H.Fernholz	13

## Chapter 1

### INTRODUCTION

by

H.H. Fernholz\*) and A.J. Smits\*\*)

\*) Hermann-Föttinger-Institut, Technische Universität Berlin

\*\*) Gasdynamics Laboratory, Dept. Mechanical & Aerospace Engineering  
Princeton University

This volume presents a wide range of recent work on compressible turbulent boundary layers, and it includes a listing of flow field data from recent experiments, with an emphasis on turbulence data. It may be seen as an extension of the work by Fernholz and Finley who in 1981 brought to an end the efforts of the EUROVISC working group to collect and to discuss all compressible turbulent boundary-layer data available at that time. For that purpose data were presented in a standard format and the data collection contained a total of 77 experimental studies edited in two volumes (AGARDographs 223 (1980) and 263 (1981))\*). Twenty-eight of the experiments reported turbulence measurements, although the data were rather limited in extent, and in some cases of doubtful accuracy. A third volume (AGARDograph 253 (1980)) provided a commentary on the mean flow data, together with pertinent remarks on the theoretical background including the effects of normal pressure gradients and boundary-layer length scales. A discussion of the turbulence data is provided in AG 263 (1981) together with remarks on experimental design and technique (for example, Hot-wire Anemometry by V. Mikulla). To avoid extensive repetition we have assumed readers have access to these three earlier volumes, and we will make frequent reference to them in this fourth volume.

Since 1981, there has been renewed interest in the behaviour of high-speed compressible flows with particular attention being devoted to the understanding of shock-wave boundary layer interactions. There exist three review articles which deal with different aspects of this problem. After the first experimental paper on the subject by Ackeret, Feldmann & Rott as early as 1946, it was Green (1971) who presented the first review paper. This paper included both a discussion of the physics and of an integral calculation method and can even today be regarded as an excellent introduction to the field. A review of both theoretical and experimental investigations by Hankey & Holden (1975) laid emphasis mainly on hypersonic flows up to Mach 14. The extensive numerical work performed since that survey has been reviewed recently by Déleré & Marvin (1986), though the latter of these AGARDographs concentrates on the supersonic range with  $M_0 < 4$ .

More recent experimental and numerical work may be found in the Proceedings of an IUTAM Symposium (Déleré 1986) while AIAA, ASME and APS conferences have seen a rapidly expanding number of contributions in this area. New turbulence data describing the development of the turbulence field across the shock/boundary-layer interaction have become available and they make up a sufficient number to prompt the issue of Chapters 9 to 13. This would not have been sufficient material for an AGARDograph but in planning this particular volume it soon became clear that it would be desirable to augment the compilation and discussion of data in the mean flow and turbulence field with some other aspects of compressible boundary layers. The choice of topics was shaped on the one hand by a desire to fill gaps which had been left open by the previous surveys and on the other hand by a perception of what the important but perhaps more specialized topics were. Only one topic, computational aspects of high-speed flows, was specifically excluded, on the grounds that the review of Déleré & Marvin (1986) made additional efforts on our part unnecessary. In all other respects the items selected represent an unavoidably biased choice of subjects, mitigated perhaps by the fact that the individual authors have based their work on direct experience. The subsequent chapters are not meant to be a review of their particular areas; rather, they were meant to introduce the reader to a new area with sufficient background material.

The primary attention is focussed on flows which have been disturbed by strong perturbations, over a relatively short streamwise distance. The choice of these "rapidly distorted" flows as the subject of this volume was natural in that most of the recent data belong to this area. We use the term "rapidly distorted" rather loosely without necessarily implying that they can

\*) References are given in Chapter 13.

be described using "Rapid Distortion Theory" (RDT). In fact the next chapter, Chapter 2, attempts to specify under what conditions it is possible to apply RDT to compressible flow, and to describe the recent work in this area. In more general terms, many of the flows presented in the data compilation of Chapter 12 and some in AG 263 were subject to the effects of "extra rates of strain" in the sense used by Bradshaw (1973). In particular, the effect of bulk compression or dilatation is of interest in that it appears to influence the turbulence directly (Bradshaw 1974). Some recent evidence for the effect of bulk compression is discussed in Chapter 3. This chapter provides the first review of large-scale motions in turbulent compressible boundary layers.

Chapters 4 to 8 are all concerned with experimental techniques. Accurate measurements of the wall shear stress in compressible flows with pressure gradients are very difficult, since floating-element balances cannot be applied easily and since the problem of determining a calibration curve for Preston tubes in compressible boundary layers - as addressed by Peake et al. (1971) - has never been properly resolved. Furthermore, Fernholz & Finley (1980, 1981 and 1983) have shown that the transformed logarithmic law of the wall does not hold in highly perturbed flows of the type encountered in this volume and that it takes a rather long distance downstream of reattachment before a Preston tube can be applied again. In Chapter 4, a new technique based on the time rate of thinning of an oil film is discussed, and it promises to be a useful technique for strongly perturbed and possibly three-dimensional compressible boundary layers. Techniques for measuring the fluctuating mass-flux, velocity, temperature and wall pressure are discussed in Chapters 5 to 8. The primary emphasis of these contributions is to identify the strength and limitations of these experimental tools. For example, in Chapter 5, constant current and constant temperature hot-wire anemometry are compared, some general guidelines for correct operating procedures are developed, and the accuracy of each system is assessed. In Chapters 6 and 7, laser-Doppler anemometry for compressible flows is discussed, with particular emphasis on the most popular counter-processing techniques, together with some warnings on the sources of ambiguity and error. Another common experimental tool, the wall-pressure transducer, is considered in Chapter 8, where some strong conclusions are drawn regarding the overall accuracy of the currently available instruments.

The data are presented and discussed in Chapters 9 to 12. General comments on the interpretation of the data and of the measurements, on the boundary-layer edge state and the influence of pressure gradients, especially on the determination of the wall shear stress, are given in Chapter 9. Issues which deal with the physical interpretation of the data and the influence of pressure gradients and shocks on the development of the boundary layer are deferred to Chapters 10 and 11. Chapter 10 deals with a general assessment of the mean-flow data, and Chapter 11 deals with the turbulence data. Finally, the data themselves are presented in Chapter 12 in a format similar to that used in AGARDographs 223 and 263. The experiments are described in ENTRIES of which 59 will be found in the first volume, AG 223, 18 in the third volume, AG 263, and 12 in this volume. These are referred to all four volumes by a reference number such as CAT 7201. In AG 263 the 18 studies are distinguished by a final S, and in this volume the CAT number is followed by the letter T. AGARDograph 223, also contains introductory material designed to assist users of the collection which should be consulted by anyone proposing to use chapter 12 in this volume. It has not been possible to print all the profile data in "hard copy" form, so the ENTRIES contain only a selection. The full profile listings are on floppy disks which are available upon request (see next page).

No microfiche listings are supplied with this volume, since past experience has shown that it was not very useful.

It is our hope that this AGARDograph will help to stimulate experimenters to add to the data so urgently required in this area, and to encourage numerical workers to test their codes against the data presented here. We especially hope that the turbulence data, though still scarce, will be used to improve existing turbulence models.

#### Acknowledgements:

As always we must first give our thanks to all these who have provided us with data. Theirs is the hard work, often over a period of years, which we presume to criticise, in the belief that we are competent to assess it. In the preparation of this volume we owe a particular debt to E.U. Schade, who has resuscitated our geriatric data-handling programs and continues to provide intensive care as needed. We thank Frau L. Lindemann and Frau I. Gereke, of the Hermann-Föttinger-Institut, for preparing, respectively, the written text and the very large number of figures. The AGARD executive in Paris, M.C. Fischer, has been a constant support, and we have benefitted throughout from the active interest of Eli Reshotko as AGARD editor.

Finally we thank D.C. Damant Esq. of the Garrick Club, London, who has again provided the motto for this fourth volume: "Although this may seem a paradox, all exact science is dominated by the idea of approximation. When a man tells you that he knows the exact truth about anything, you are safe in inferring that he is an inexact man." (Bertrand Russell).

## PROCEDURE FOR OBTAINING THE FULL PROFILE DATA LISTINGS FOR AG 315

The full profile data listings which have been compiled and discussed in this AGARDograph are available on 5 floppy discs on file at various National Centers as listed below. These floppies are 5.25 inch size and are formatted 1.2 MB. They are written to by using an IBM compatible AT personal computer with MS-DOS 3.20. Specific details, costs and procedures for obtaining a copy of the floppy disc set varies from one center to the other, so interested parties must contact the appropriate location within their country or a center most geographically convenient.

## Etat-Major de la Force Aerienne

(VSL/AGARD)

Rue d'Evere

B-1140 Bruxelles

BELGIUM

Person to contact: Major N. July

Tel: 32(2)243-4923-Telex 21339 BE-PHQ-

Telefax 011-32-2-243-5703

## Dept. of Fluid Mechanics

Technical University of Denmark

Building 404

DK 2800 Lyngby

DENMARK

Person to contact: Dr. P.S. Larsen

Tel: 02-882222 ext: 4732

Telex 375290THD/ADK

Telefax 02-882239

## Fachinformationszentrum Karlsruhe

D-7514 Eggenstein-Leopoldshafen 2

FEDERAL REPUBLIC OF GERMANY

Person to contact: Gerd Tittlbach

Tel: (49)7247/82-4991-Telex 17724710

Telefax (49)7247/2968

## O.N.E.R.A. - DED

B.P. 72

92322 Chatillon Cedex

FRANCE

Person to contact: Mme F. Lhullier

Tel: 46-57-11-60-Ext. 29-24

## Scientific Library: Air War College

Dekelia Air Force Base

Dekelia Attiki

GREECE

Person to contact: Major

Papadimitriou Sotirios

Tel: 2466461

## Aeronautica Militare

Ufficio del Delegato Nazionale all'AGARD

Piazzale K. Adenauer, 3

00144 Roma/EUR

ITALY

Person to contact: Colonel P. Marconi

## National Aerospace Laboratory

Attn: Library

P.O. Box 153

od00 AD Emmeloord

NETHERLANDS

Person to contact: Mr. C.W. de Jong

Tel: 05274-2828-Telex 42134 nlrbb nl

## Norwegian Defence Research

Establishment (NDRE) Library

P.O. Box 25

N.2007 Kjeller

NORWAY

Person to contact: Per Ekern

Tel: (47-6)807129-Telex 21682

Telefax 06-807212

## Aeronautical Engineering Department

Middle East Technical University

P.K. 06531

Ankara

TURKEY

Person to contact: Prof. Dr. Ing. C. Ciray

Tel: 2237100/2471:2472:2431

Telex: 42761 ODTK TR

Telefax: 2233054

## Defence Research Information Centre

Kentigern House

65 Brown Street

Glasgow, G2 8EX

UNITED KINGDOM

Person to contact: Dr. H.M. Morgan

Tel: 041-228-2435-Telex: 779699

Telefax: 041-228-2146 or 2119

## NASA Scientific &amp; Technical

Information Facility

P.O. Box 8757

Baltimore Washington International

Airport

Maryland 21240

U.S.A.

Person to contact: Joseph Gignac

Tel: 301-621-0204

Telefax: 301-621-0134

## CHAPTER 2

## RAPIDLY DISTORTED COMPRESSIBLE BOUNDARY-LAYERS

by

J.P. Dussauge\*, J.F. Debiève\*, A.J. Smits\*\*

\* I.M.S.T., U.M. Université-CNRS N°380033  
Université d'Aix-Marseille II, Marseille, France\*\* Gas Dynamics Laboratory, Princeton University,  
Princeton, New-Jersey 08544, USA.

## 1. INTRODUCTION

In studying the response of suddenly perturbed boundary layers, two extreme forms of perturbation can be identified :

(1) Perturbations where the effects diffuse slowly through the boundary layer, with a time scale comparable to the response time of the large eddies. Typically, the mean field changes slowly, and the self-preserving part of the layer is confined to an internal layer.

(2) Perturbations which change the mean and turbulent fields immediately at all points in the layer. The sudden application of a pressure gradient, for example, can cause a perturbation of either form, depending on the strength of the pressure gradient. When the pressure gradient is relatively weak, the turbulence in the outer part of the flow is at first unaffected, and the changes are confined to a thin region near the wall. This internal layer grows slowly until eventually the whole of the boundary layer is affected by the perturbation (Townsend, 1976, Smits and Wood, 1985). In contrast, when the pressure gradient is very strong, the changes in the mean field can immediately affect the turbulence at all points in the layer.

Rapid Distortion Theory (RDT) was developed to predict the evolution of turbulence following this latter form of perturbation. The distortion is "rapid" if it acts on the turbulence during a time short compared to the characteristic time scale of the turbulent eddies. Furthermore, if the turbulence is "weak", so that the turbulence interacts *strongly with the mean flow but only weakly with itself*, the the evolution of turbulence is governed by a linear set of equations. Here, we will not discuss distortions where small departures from an unchanged non-linear state occur. For reasons of practical interest we consider only "strong" distortion where linear processes dominate.

The basic theory was developed by Ribner and Tucker (1952) and Batchelor and Proudman (1954) for homogeneous, isotropic turbulence in an irrotational mean flow. The theory was later extended to shear flows (see, for example, Moffatt (1967) and Townsend (1970)) and subsequent developments led to a wide variety of applications. The papers by Hunt (1977), Townsend (1980), Cambon (1982), and the recent review by Savill (1987) provide a comprehensive picture of the current status of RDT. What seems particularly encouraging is the observation that *despite the strict limits on the applicability of RDT, the theory often gives qualitatively useful results outside these bounds, as well as providing useful guidelines for distorted structure modelling* (Savill, 1987).

Most of the work in RDT has been confined to incompressible flows. Yet, compressible flows are potentially very attractive for the application of RDT. Changes in the mean field can occur over very short distances, much shorter than is possible in subsonic flows, and the limits of RDT can often be more easily satisfied. For example, when a boundary layer passes through a Prandtl-Meyer fan or a short region of compression, including the case where the layer interacts with a shock-wave, the perturbation can occur over a distance comparable to the boundary layer thickness. Typically, the pressure gradients are much stronger than the other stress gradients outside the viscous sublayer, and it is to be expected that RDT methods are useful in the analysis of these flows.

Recently, there has been considerable new interest in applying RDT to supersonic flows. The case of an irrotational mean flow and an initially isotropic turbulent field passing through a Prandtl-Meyer expansion was considered by Goldstein (1978). Later work by Goldstein (1979), Anyiwo and Bushnell (1982), Zang et al. (1984), Debiève (1983) and Dussauge and Gaviglio (1987) has notably extended this area.

Before proceeding, one should make a distinction between RDT (Rapid Distortion Theory) and RDA (Rapid Distortion Approximations). In RDT, the equations are obtained by linearizing the momentum equation, taking the Fourier transform and calculating the three-dimensional spectra related to the Reynolds stress. After integration in wave number space, the turbulent kinetic energy or the shear stresses are deduced. With such a method, the initial three-dimensional spectra must be specified. Unfortunately, this is not generally known when the upstream flow is a shear flow. Moreover, the limits of experimental work in supersonic flow make it more attractive to consider the Reynolds stress evolution, rather than the associated spectra. The simplifications of second-order closure needed for rapid distortion approximations to the Reynolds stress equations are not straightforward, as pointed out by Hunt (1977), mainly because terms involving pressure fluctuations must be modelled. Hence the solutions are not exact. This latter approach, where the scaling arguments and limiting processes employed in RDT are used to approximate the Reynolds stress equations is what we term RDA.

Thus the theoretical work in rapidly distorted compressible flows can be classed into three distinct groups: analyses based on formal linearisations of the equations of motion (RDT), analyses based on the Rankine-Hugoniot jump relations to study shock/turbulence interactions (RDT and RDA), and approximations to the Reynolds stress transport equations to obtain second-order closure (RDA). These three groups are considered in Sections 2, 3 and 4 respectively. An attempt is made in Section 5 to classify the currently available analyses in terms of the restrictions placed on the mean and fluctuating fields, and on the boundary conditions. Finally, in Section 6, the application of rapid distortion methods to supersonic flows is considered, and the limits of applicability are discussed.

## 2. THE LINEARIZATION OF THE EQUATIONS OF MOTION

Clearly the equations of motion can only be linearized when the non-linear terms are small compared to the linear terms. These considerations lead to a number of inequalities which define the limits of applicability of RDT and RDA techniques. These inequalities are derived below.

In the distortion of an incompressible turbulent flow, several mechanisms can alter the velocity fluctuations: viscous damping, the effect of the non-linear acceleration terms, and the effect of the remaining linear terms.

The viscous damping is important only for the smallest scales. For the energy-containing structures, which have a large scale and high Reynolds number, the effect of viscosity may be neglected as long as the non-linear process of energy transfer to the smaller scales can be neglected. This "energy-cascade" takes some time, which defines a characteristic time scale of turbulence  $T_t$ , where  $T_t$  is a function of the Reynolds number (see Section 6 for a further discussion). For small Reynolds numbers, the energy-containing range and the dissipating range have a large overlap, the energy transfer is rapid, and  $T_t$  is small. In high Reynolds number flows the time scale is large, and if the distortion is applied during a time  $T_d$  small compared to  $T_t$ , then the rate of energy dissipation remain constant during the distortion (as long as  $T_t$  is not altered significantly by the distortion as discussed in Section 6). The time scale of the large eddies can be expressed as  $T_t = \Lambda/q'$ , where  $\Lambda$  is an integral length scale and  $q'$  a fluctuating velocity scale, for example,  $q'^2 = (1/2)\overline{u_i' u_i'}$ . If the eddies have a convection velocity  $U$ , and the distortion is of length  $L$ , then  $T_d = L/U$ . The condition  $T_d \ll T_t$  becomes :

$$\frac{q'}{U} \frac{L}{\Lambda} \ll 1 \quad (1)$$

The effects of the non-linear terms may be estimated by considering the components of the fluctuating acceleration  $a_i'$ , that is ,

$$a_i' = \frac{\partial u_i'}{\partial t} + U_j \frac{\partial u_i'}{\partial x_j} + u_j' \frac{\partial u_i'}{\partial x_j} + u_j' \frac{\partial u_i'}{\partial x_j}$$

It will be assumed that the time derivative is of the same order as the other terms. To obtain a linear equation of motion, the non-linear acceleration term needs to be small compared to any one linear term. If the time derivative is dominant, we require :

$$\frac{L}{\Lambda} \ll 1$$

where  $\tau$  is the appropriate Eulerian time scale. For flows where  $T = \Lambda/U$  this inequality becomes

$$q'/U \ll 1 \quad (2)$$

If the second term is dominant, the same requirement as above results, that is,  $q'/U \ll 1$ . If the third linear term dominates, the requirement is expressed as the ratio of the turbulent and mean velocity space derivatives. Since we are particularly interested in strong accelerations and decelerations, we use  $\Delta U/L$  as a representative mean velocity gradient. For example, if it is assumed that a reasonable estimate for the turbulent velocity gradient is given by its upstream value  $q'/\Lambda$ , then:

$$\frac{q' L}{\Delta U \Lambda} \ll 1 \quad (3)$$

Alternatively, if the turbulent velocity gradient is given by  $\Delta q'/L$ , the resulting requirement is:

$$\frac{\Delta q'}{\Delta U} \ll 1$$

There are many other ways to interpret and derive relationships (1) and (3). For example, condition (3) can be shown to be equivalent to the assumption that the turbulence production within the interaction is much larger than the initial dissipation rate. As for condition (1), if the turbulent time scale is taken to be the ratio of the turbulent kinetic energy to its rate of dissipation (Townsend, 1976), then:

$$T'_t = q'^2 \Lambda_\epsilon / (q'^3)^{1/2}$$

where  $\Lambda_\epsilon$  is the dissipation length scale. Hence  $T'_t = \Lambda_\epsilon / q'$ , similar to the form for  $T_\epsilon$  used above. As pointed out by Bradshaw (1973),  $T'_t$  is the time scale of the decay of turbulence in the absence of production. Alternatively, it can be shown that condition (1) implies that during time  $T'_t$  the relative decrease of kinetic energy due to dissipation is very small. If the loss of kinetic energy due to viscous dissipation is estimated from:

$$(D/Dt)(q'^2) = -\epsilon = (q'^3)^{1/2} / \Lambda_\epsilon$$

and  $\Lambda_\epsilon$  is assumed constant, then integration from initial to final state gives, to first order,

$$\frac{\Delta q'}{q'} = \frac{q' L}{U \Lambda_\epsilon}$$

and we see that condition (1) implies that:

$$\frac{\Delta q'}{q'} \ll 1 \quad \text{in order to apply RDT.}$$

Similarly, an estimate for the total (integral) change in  $q'$  due to the non-linear acceleration term is given by the estimate for its initial value ( $= q'^2/\Lambda$ ) multiplied by its time of flight ( $= L/U$ ). When combined with condition (1), this implies  $\Delta q'/q' \ll 1$ , as above.

In incompressible flows, when conditions (1) and (2), or (1) and (3) are satisfied, the equations of motions can be linearized, and the distortion is called "rapid" (note that the "rapidity" of the distortion will depend on the scale of motion considered). The solution of the linearized equations may be split into a kinematic part and a part coming from the pressure term. The expression for the pressure-derived term contains an integral operator (required to satisfy the incompressibility condition) which demonstrates the non-local properties of the solution. When the mean field is irrotational, the kinematic transport part can be integrated and the solution depends only on the initial and final states, that is, it is independent of the integration path. However, for rotational mean fields, this procedure is not possible; supplementary source terms appear which depend on the path of integration, and the distortion of the turbulence is no longer determined solely by the initial and final states of the mean flow (see Cambon, 1982 for further details).

The analysis can be extended to compressible flows as follows. Firstly, the continuity equation becomes linear when:

$$\rho'/\rho \ll 1 \quad (4)$$

Secondly, the momentum equation can be linearized if conditions (1) to (3) are satisfied. In particular, a new term  $\rho'(\bar{a}_i + a'_i)$  appears, which can be linearized using condition (4).

The linearization of the transport terms in the entropy equation requires that the velocity fluctuations are small, whereas the linearization of the source terms requires that the fluctuations in the viscous dissipation rate  $\epsilon'/\bar{\epsilon}$ , the fluctuations in the dissipation of temperature variance  $\epsilon'_\theta/\bar{\epsilon}_\theta$ , and the fluctuations in temperature  $\theta'/\bar{\theta}$  are all small compared to unity.

The general solution of these linearized equations is beyond the scope of the present chapter (a detailed study of the solutions and their functional properties can be found in Leyland, 1984). Particular solutions may be found by imposing restrictions on the mean or fluctuating fields. In particular, it is possible to develop a simplified formulation which is general enough to describe a number of particular cases (Debieve,



1986). The general solution contains a part composed of kinematic and thermodynamic contributions, and another part which acts as a source term. When the mean entropy gradient is perpendicular to the mean vorticity, important simplifications are possible. For perfect fluids, such flows were called "oligotropic" by Casal (1966), and they represent a generalization for compressible flows of irrotational incompressible motion. In our case, for simplicity, we continue to use the term.

Many flows can be described as oligotropic, including steady and unsteady plane flows, and steady three-dimensional iso-energetic flows. Here, the first part of the solution can be integrated by defining transport operators related to the order of tensors that appear. Furthermore, this formulation permits a convenient classification of the previous rapid distortion work in supersonic flows. Only an outline of some useful results will be given, and the reader is referred to Debieve (1986) for further details.

As a first step, the Euler equation can be written with a gradient for the source terms, thus keeping the properties analogous to barotropy :

$$\partial_\delta (\dot{V} + s \text{ grad } \beta) = - \text{grad} (h - \theta s - \frac{v^2}{2}), \text{ with } (d/dt)s = 0 \quad (5)$$

where  $\partial_\delta$  is the convective derivative of a transposed vector. That is, for the vector represented by the column  $J$  :

$$\partial_\delta J = \frac{d}{dt} J + J \frac{\partial V}{\partial x}$$

where the superscript \* indicates matrix transposition,

$d/dt$  is the usual derivative along the motion,

$\partial V/\partial x$  is the velocity derivative,  $s$  the entropy,

$\theta$  the temperature,  $h$  the enthalpy and  $\beta$  is such that  $(d/dt)\beta = \theta$ .

The interesting feature of equation (5) is that a Lagrangian integral of the convective derivative can be written, and that the right hand side is of potential form.

In the general case, the linearized form of equation (5) is as complicated as the linearized Euler equations. But, when the mean flow is oligotropic the complexity of equation (5) reduces considerably. Hence, for all cases where the mean flow is two-dimensional, the linearized form of equation (5) reduces to :

$$\partial_\delta w' = \frac{D}{Dt} w' + w' \frac{\partial V}{\partial x} = - \text{grad} \left( \frac{p'}{\rho_0} \right) \quad (6)$$

with  $w' = v' + s' \text{ grad } \beta_0 - \beta' \text{ grad } s_0$ . The subscript  $( )_0$  denotes the mean field.

Equation (6) has the same form as equation (5) : for oligotropic mean fields the linearization introduces no new terms and the source terms have a potential form. Hence,  $w'$  is formally similar to the velocity fluctuation in incompressible irrotational flows. By taking the curl of (6), the solution can be obtained as a Cauchy integral for the pseudo vorticity  $\text{rot } w'$  ;  $\text{rot } w'/\rho_0$  is transported by the mean motion between two states, the quantity  $(\text{rot } w' \cdot \text{grad } s_0)/\rho_0$  being constant along the mean motion.

It should be noted that one of the difficulties to obtain a Cauchy integral for the vorticity  $w$  in compressible flow comes from the supplementary terms which are obtained by linearizing the equation for vorticity:

$$\frac{d}{dt} w + w \text{ div } V - \text{grad } V \cdot w = \frac{R\theta}{C_p} \text{ grad}(\ln \rho) \times \text{grad } s$$

To avoid this difficulty, two types of simplifications are generally made. On the one hand, if density and entropy fluctuations are considered, mean gradients of density and entropy should be zero. We obtain then the evolution between two states, but the solution holds for only a small number of mean velocity fields. On the other hand, we can consider more general mean velocity fields, but the conditions  $\rho'=0$ ,  $s'=0$  have to be imposed.

However, it is not necessary to take the curl of equation (6) to find the solution : this can be done by defining a transported part and a part related to pressure. For example, equation (6) can be integrated, as in Goldstein (1978) and has a solution of the form :

$$w' = w'_I \frac{\partial X}{\partial x} + \text{grad } \psi$$

The first term of the right hand side represents the part transported by the mean field; the second one is

the irrotational part associated with pressure. The subscript  $( )_I$  denotes the initial state and  $\partial x / \partial X$  is the linear tangent application related to the mean field.  $\Psi$  is determined from the continuity and entropy equations, which lead to the relation :

$$\begin{aligned} \frac{D}{Dt} \left[ \frac{1}{C_o^2} \frac{D}{Dt} \Psi \right] - p_o^{-1/\gamma} \text{div} (p_o^{1/\gamma} \text{grad}^* \Psi) &= S \\ &= p_o^{-1/\gamma} \text{div} \left[ p_o^{1/\gamma} (\beta' \text{grad}^* s_o - s' \text{grad}^* \beta_o + \frac{\partial X}{\partial x} w'_I) \right] \end{aligned} \quad (7)$$

This general solution is rather complicated. With some supplementary assumptions, it is possible to find simpler solutions, as follows.

a) Firstly, with the condition  $\text{grad} s_o = 0$  on the mean field, we obtain the case of the irrotational mean flows. With this assumption the right hand side  $S$  of equation (7) depends only on the initial conditions and on the mean flow

$$s'(x,t) = s'_I(X,t)$$

$$S = p_o^{-1/\gamma} \text{div} \left[ p_o^{1/\gamma} (-s'_I \text{grad}^* \beta_o + \frac{\partial X}{\partial x} w'_I) \right]$$

The resulting velocity is given by :

$$v'_I = w'_I \frac{\partial X}{\partial x} - s'_I \text{grad} \beta_o + \text{grad} \Psi$$

where three contributions can be identified : a transported part, a thermodynamic part and an irrotational part related to pressure. Note that this result is valid for unsteady mean flows.

b) If we add the condition of mean flow steadiness, we obtain iso-energetic flows where  $\text{grad} \beta_o$  can be related to the other variables by the Crocco relationship. We obtain the following equation for  $\Psi$  :

$$\frac{D}{Dt} \left( \frac{1}{C_o^2} \frac{D}{Dt} \Psi \right) - \frac{1}{\rho_o} \text{div} (\rho_o \text{grad} \Psi) = S \quad \text{with} \quad S = \frac{1}{\rho_o} \text{div} \left[ \rho_o (s'_I \frac{v_o}{2C_p} + \frac{\partial X}{\partial x} w'_I) \right]$$

and  $w'_I = v'_I - s'_I \frac{v_o I}{2C_p}$ . This solution was proposed by Goldstein (1978).

c) The following conditions can be added : Either  $\text{div} \rho_o v' = 0 \iff \frac{D}{Dt} \frac{\rho'}{\rho_o} = 0$

or, the sound speed is taken to be infinity. Each of these assumptions cancels the propagation term in the equation for  $\Psi$ , and we obtain :

$$\text{div} (\rho_o \text{grad} \Psi) = -\text{div} \rho_o (s'_I \frac{v_o}{2C_p} + \frac{\partial X}{\partial x} w'_I) \quad \text{with} \quad w'_I = v'_I - s'_I \frac{v_o I}{2C_p}$$

In this case, the distributions of  $\rho_o$  and  $s'$  can be inhomogeneous.

d) Finally, a limiting case is obtained with the following assumptions :

- irrotational mean flow  $\Omega_o = 0$
- Homentropy  $\text{grad} s_o = 0$
- Uniform mean density  $\text{grad} \rho_o = 0$
- Unsteady mean flow
- $\text{div} u' = 0$

The density is uniform in space but it is time-dependent.  $s'$  and  $\rho'$  can be non-zero, but satisfy the relations :  $(D/Dt)s' = 0$  and  $\delta(s' \text{grad} \beta_o) = 0$

The equation for  $\Psi$  simplifies to the expression :

$$\Delta \Psi = -\text{div} \left( \frac{\partial X}{\partial x} v'_I \right) \quad \text{with} \quad v'_I = \frac{\partial X}{\partial x} v'_I + \text{grad} \Psi$$

This is similar to the cases studied by Ribner and Tucker (1952) and by Hunt (1977), using a different solution technique. Hunt used it to model the practical case of the compression cycle of an internal combustion engine.

### 3. SHOCK/TURBULENCE INTERACTION METHODS

The results quoted in Section 2 belong to a class of studies where the solution of a linear set of partial derivatives is calculated. Another class of linear methods is used to study shock-turbulence interactions where the shock relations are applied to turbulent fluctuations of small amplitude using Fourier representation. The first example of this second class was developed by Ribner (1953). An exhaustive review of this approach can be found in Anyiwo and Bushnell (1982). These authors also present probably the most complete calculation of the linear amplification and generation of turbulence through a shock wave. Acoustic waves, entropy waves and vorticity waves were examined. The amplitude jump relations obtained as in McKenzie

and Westphal (1968) were deduced from the linearized Rankine-Hugoniot relations, and for the dispersion jump relations the frequency and the tangential component of the wave number vector were assumed to be continuous through the shock. In addition, the "rippling" of the shock due to harmonic incident perturbations was taken into account. The results showed that the linear mechanisms can contribute significantly to the amplification of incident velocity fluctuations, to the generation of turbulence by interaction between the shock wave and the upstream entropy fluctuations, and by externally induced shock oscillations.

All the methods described in this Section, and in Section 2, have used linearized equations and Fourier representations, and therefore belong to the domain of RDT. As indicated earlier, there also exists a class of methods where rapid distortion is used to obtain second-order closure of the Reynolds stress equations. These RDA methods were applied to shock/turbulence interactions by Debieve (1983).

Debieve defined a transport invariant relative to the Reynolds stresses, and developed "shock formulas" for the stress evolution through a steady shock wave. Turbulent source terms that modify the transport invariant could be taken into account if they were continuous through the shock, or if they varied like a Heaviside function. No explicit hypothesis on the nature of the mean field and of the velocity fluctuations was required. However, a better description of the source terms would probably require Dirac functions source terms. This work uses some of the hypothesis required by RDT. In particular, it is argued that as the distortion is very rapid through the shock, the dissipation rate and the inertial transfer are unchanged and then do not contribute to the evolution of the Reynolds stresses. This analysis leads to a particularly simple expression for the amplification of turbulence by a shock wave. The result depends on the orientation and strength of the shock wave, and it is given by :

$$T_2 = K T_1 K$$

with  $K = I - [\tilde{U}] N^* / U_{2N}$ , where  $T_1$  and  $T_2$  are the upstream and downstream Reynolds stress tensors,  $\tilde{U}_N$  is the velocity normal to the shock,  $[\tilde{U}]$  is the jump in velocity across the shock,  $N$  is the unit vector normal to the shock, and  $N^*$  is its transposition. An illustration of this formula is given in figure 1, which gives a polar representation of the Reynolds stress upstream and downstream of the shock. The vector  $\vec{OM}$  has a magnitude equal to the variance of the velocity fluctuation and a direction given by the unit vector  $\vec{m}$ . Note that  $\vec{OM} = (\vec{u}^i \cdot \vec{m})^2 \vec{m}$ , and  $\vec{u}^i \vec{v}^i = OP - OQ$ . The initial state correspond to an isotropic tensor and is represented by a circle. The diagram shows that the amplification through the shock is a maximum in the direction normal to the shock.

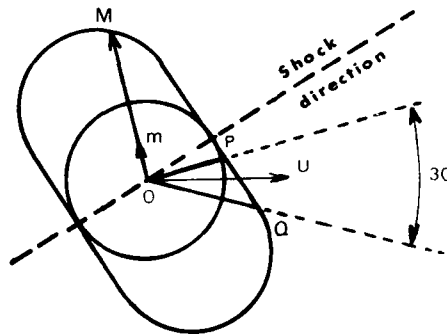


Figure 1: Evolution of the Reynolds stress tensor in a 6° compression ramp flow.

#### 4. SECOND-ORDER CLOSURE FOR SHOCK-FREE FLOWS

In many distortions of supersonic boundary layers, the turbulent fluxes can vary significantly over very short distances. Since the anisotropy of the turbulent stresses can radically alter, simple closure hypotheses are no longer adequate. The approximations used in RDT for second-order closure then become very attractive as a means for describing the Reynolds stress evolution. As emphasized by Hunt (1977), the effects of a rapid distortion are mainly observed in the fluctuating pressure terms, that is, the rapid part of the

pressure-strain terms and the pressure-transport terms.

The influence of a rapid distortion on the pressure transport has not been explored in great detail for second-order closures. Some examples were given by Oh (1974), Brown and Roshko (1974) and Vandromme (1983) where most of the attention was directed towards the effect of mean compressibility on the rapid part of the pressure-strain terms. In particular, the effect of a compressible mean field on incompressible turbulence was examined by Dussauge, Caviglio (1987) and Jayaram, Dussauge and Smits (1985) who applied RDA to the Reynolds stress equation to predict the evolution of the turbulent stress tensor in rapid expansions and compressions. They assumed that the turbulent field was essentially solenoidal, that is,  $\text{div } u' = 0$ . In this case, the rapid part of the pressure strain can simply be adapted from low speed formulations by replacing the mean velocity gradient by its deviatoric. The results of the calculation were in reasonable agreement with the experimental results.

It is rather difficult to specify the conditions under which the hypothesis  $\text{div } u' = 0$  can be used. An attempt can be made for zero pressure gradient supersonic boundary layers. In these flows, the temperature fluctuation level  $(\overline{\theta'^2})^{1/2}/\bar{\theta}$  is generally much larger than the wall pressure fluctuation level  $(\overline{p_w'^2})^{1/2}/\bar{p}_w$ . If it is supposed that this is true in the whole flow, and if the Lagrangian time scales of temperature and pressure are of the same order,  $\text{div } u'$  is only produced by the heating due to viscous dissipation and heat conduction. This result assumes that there is no significant contribution to the fluctuations by shocklets in the turbulent motion. For small fluctuations in the energetic range, a simple expression can be found :

$$\text{div } u' = - \frac{\bar{\epsilon}}{C_p \bar{\theta}} \frac{\theta'}{\bar{\theta}} - \frac{2\bar{\epsilon}_\theta}{\gamma \bar{\theta}^2} \frac{\theta'}{\bar{\theta}}$$

(see, for example, Dussauge, 1986). By assuming that  $\bar{\epsilon}$  and  $\bar{\epsilon}_\theta$  are linked as in low speed flows, and by considering adiabatic flows in which the Strong Reynolds Analogy relationship applies,  $(\theta'/\bar{\theta}) \sim (\gamma-1)M^2(u'/U)$ , the order of magnitude of the ratio  $\text{div } u'/(u'/\Lambda)$  can be given as follows :

$$O\left(\frac{\text{div } u'}{u'/\Lambda}\right) \sim (\gamma-1)^3 m^3 M \left[1 + \frac{2}{R} \frac{\overline{u'^2}}{q^{1/2}} (\gamma-1)M^2\right]$$

where  $m$  is a Mach number related to velocity fluctuations, that is,  $m = (\overline{u'^2})^{1/2}/a$ , and  $R$  is a constant of proportionality in the expression relating  $\bar{\epsilon}_\theta$  to  $\bar{\epsilon}$ , i.e.  $R \sim 0.4$ . The previous expression indicates that in most practical situations  $\text{div } u'$  is probably small in supersonic (but not hypersonic) zero-pressure gradient boundary layers, and then low-speed models can be used. On the other hand, in compressions where shocklets can appear the usual second order closures are probably not applicable. Finally, it should be emphasized that there exists no complete model taking in account these "direct" compressibility effects.

## 5. SUMMARY OF PREVIOUS WORK

The rapid distortion work in compressible flows is summarized in Table 1. In each case, the limits of applicability are given. For Anyiwo and Bushnell's study (1982), where a plane shock wave with an upstream uniform mean flow was considered, the mean flow is irrotational and homentropic on both sides of the shock wave. In Dussauge (1987) and Debieve (1983), no particular hypothesis was required for the mean field, although the application they considered had a two-dimensional oligotropic mean field. In addition, no further hypothesis was required in their analysis to deal with the entropy fluctuations.

In Table 1, the experiments presented in Chapter 12 are indicated by the shaded areas. All the mean flows are two-dimensional. The properties of the fluctuating field, however, are not clearly defined. If the flow is not hypersonic, it is likely that the condition of incompressible turbulence is a reasonable approximation for zero pressure gradient flows (see Section 4) and isentropic expansions and compressions (Dussauge and Caviglio 1987, Jayaram, Dussauge and Smits 1985). This assumption is probably not reasonable in interactions with a strong shock. In a similar way, it is difficult to define the nature of the entropy fluctuations in these experiments. Since the time of flight is small in a rapid distortion, it seems that the specific entropy should not change significantly, except through the action of a shock.

		HUNT 1977	RIBNER & TUCKER 1952	GOLDSTEIN 1978 1979	ANYIWO & BUSHNELL 1982	DUSSAUGE 1981	DEBIEVE 1983
MEAN FIELD	$\Omega = 0$	X	X	X	piecewise	no	no
	steady			X	X	hypothesis	hypothesis
	homotropic	X	X	X	piecewise	on the	on the
	$\Omega \cdot \text{grad } s = 0$					mean field	mean field
FLUCTUATING FIELD	$\text{div } u' = 0$	X	X			X	unspecified
	$\text{div } u' \neq 0$			X	X		
	$s' = 0$	X	X				
	$Ds'/Dt = 0$			X			
	$Ds'/Dt \neq 0$					X	
INITIAL CONDITIONS	isotropic	X	X	X	X		
	anisotropic					X	X

Table 1 : Some contributions to rapid distortion problems in compressible flows.

In summary, Goldstein's work gives the more elaborate solutions of the compressible linear problem, whereas Anyiwo and Bushnell's results underline the basic physical problems to be examined in a shock / turbulence interaction. The details of the analyses of Dussauge and of Debieve are less exact, but they provide formulations more easily applied to practical situations or to laboratory experiments.

## 6. DISCUSSION

Here, we discuss to what extent the flows presented in Chapter 12 can be described by rapid distortion considerations. Some answers can be given by the conditions defined in §2. It should be noted immediately that we are dealing with boundary-layers, i.e. flows with a viscous sublayer where the Reynolds number is low. Clearly, RDT cannot be applied in this zone. A second consideration is the existence of a region very near the wall (at about  $y^+ \approx 15$ , say), where the turbulence intensity can be very large, so that the small fluctuation hypothesis fails. Hence, only the evolution of the outer part of the layer can be considered by rapid distortion concepts. The time of distortion is often very small. In the case of an expanded boundary layer (Dussauge and Gaviglio, 1987) the ratio  $q'L/UA$  was about 0.2 for  $y/\delta = 0.3$ . Similar values can be found in compression ramp flows: in the flow sketched in Figure 2, the time of flight through the leading shock is very short. In the case when the flow is separated however, a continuous compression fan follows the leading shock. In this case, the interaction length is increased, and the distortion becomes slower. A typical value for  $y/\delta_0 = 0.4$  in the  $24^\circ$  compression corner studied by Selig et al. (1987) is  $q'L / UA \sim 0.4$  for  $y/\delta = 0.4$ .

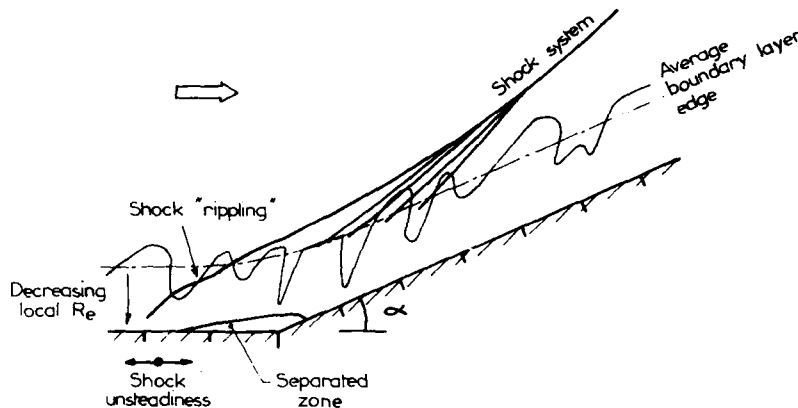


Figure 2 : Sketch of a typical interaction

These estimates are questionable, because they use the upstream values of the turbulent scales. Yet, the rate of dissipation and the rate of energy transfer can be modified by the distortion. In expanded flows, the effect of mean compressibility is to shift the energetic range to the low wave numbers, i.e. to the large wave lengths. In contrast, in a compression, the wave numbers become larger and the energy containing range is brought closer to the dissipative range. Therefore, the energy transfer in compressions can produce non linear effects and limit the range of validity of the RDT.

This point however is probably not critical: if condition (3) is fulfilled, the production of turbulence (or of Reynolds stress) is much larger than the initial energy transfer rate. If this rate changes slightly in the distortion the analysis will still hold, if the order of magnitude argument remains unchanged.

The main danger of an extensive use of the criteria defined in §2 is that they postulate that any transfer of energy takes a long time when the Reynolds number is large. An interesting peculiarity of the supersonic flows is that in a short time small scale turbulence can be created. An example can be found in Hussaini, Collier and Bushnell (1985) who calculated the interaction of an entropy spot with a shock-wave. After the interaction, two small structures replace the initial one. Another possibility is the generation of turbulence by shock corrugations produced by the fluctuations. Hence it is necessary to check if the linear approximations still hold. This was attempted by Zang, Hussaini, Bushnell (1984) who made numerical simulations of two-dimensional fluctuations passing through a shock, by solving the full Navier-Stokes equations. They compared this solution to the results of the linear analysis given by Anyiwo and Bushnell (1982). They found that the linear solution was very robust, and that in many cases the non-linear effects could be neglected, except for oblique waves near critical angles.

As to the comparison between analyses and measurement, Dussauge (1981), Jayaram, Dussauge and Smits (1985) and Debieve (1983) presented results for several different flows. The comparisons were very favourable, except in the near wall region of the flow calculated by Jayaram et al. However, this good agreement does not prove much, for the increase or decrease of the Reynolds stresses was rather weak and the comparisons were made for only one turbulent stress component. Other considerations were developed mainly by Jayaram, Taylor and Smits (1987) to interpret experimental results obtained in several configurations. It was argued that, if the linear mechanisms dominate, the results should depend mainly on the initial and final states, and not on the way the distortion is applied. In different 8° compression flows at Mach 3, it was found that the downstream turbulence profiles were practically identical, whatever the way the compression was produced. For larger compression angles, some departures in the results were observed (Smits and Muck, 1987). A difference

in the flow is that the shock and all the flow downstream both become unsteady. Part of the difference can probably be explained by the turbulence generated by the mechanism of an "externally driven" shock-wave. However, it is not clear that in separated flow the shock motion can be considered independently of the excitation due to turbulence.

Finally, some results were obtained by visualization and high speed films of the 24° compression ramp flow. It appears that downstream of the leading shock, in the zone where the compression is more progressive, "shocklets" are produced from time to time. This observation is confirmed by turbulence measurements which show a highly intermittent signal across the whole thickness of the layer. As these phenomena occur over a distance of several boundary layer thicknesses, and as the focusing of Mach waves is a non linear phenomenon, it seems obvious that the turbulence in this complicated flow cannot be described by a linear analysis.

## 7. REFERENCES

- Anyiwo J.C., Bushnell D.M. 1982 Turbulence amplification in shock-wave amplification AIAA J. 20, 893-899.
- Batchelor G.K., Proudman I. 1954 The effect of rapid distortion of a fluid in turbulent motion, Q. J. Mech. Appl. Maths, 7, 83.
- Bradshaw P. 1973 Streamline curvature effect in turbulent flow AGARDograph 169.
- Brown G.L., Roshko A. 1974 On density effects and large structure in turbulent mixing layers, J. Fluid Mech. 64, 775-816.
- Cambon C. 1982 Etude spectrale d'un champ turbulent incompressible soumis à des effets couplés de déformation et de rotation. Thèse de Doctorat d'Etat, Université Claude Bernard, Lyon.
- Casal P., 1966 Principes variationnels en fluide compressible et en magnétodynamique des fluides. J. Mécanique 5, N°2, 149-161.
- Debieve J.F. 1983 Etude d'une interaction turbulence - onde de choc. Thèse d'Etat, Université Aix-Marseille II.
- Debieve J.F. 1986 Problèmes de distortion rapide en écoulement compressible, Proceedings du Colloque ONERA-DRET "Ecoulements turbulents compressibles", Poitiers Mars 1986.
- Dussauge J.P. 1986 Rapport Convention ONERA/IMST 20.352/SAT/2CDC.
- Dussauge J.P., GAVIGLIO J. 1987 The rapid expansion of a supersonic turbulent flow: role of bulk dilatation. J. Fluid Mech. 174, 81-112.
- Goldstein M.E. 1978 Unsteady vortical and entropic distortions of potential flows round arbitrary obstacles. J. Fluid Mech. 89, 433-468.
- Goldstein M.E. 1979 Turbulence generated by the interaction of entropy fluctuations with non-uniform mean flows. J. Fluid Mech. 93, 209-224.
- Gouin H. 1978 Contribution à une étude géométrique et variationnelle des milieux continus. Thèse de Doctorat d'Etat, Université d'Aix-Marseille I.
- Hunt J.C.R. 1977 A review of the theory of rapidly distorted turbulent flows and its applications. Fluid Dynamics Transaction, Vol. 9, Thirteenth Biennial Fluid Dynamics Symposium, Warsaw, Poland, 121-152.
- Hussaini M.Y., Collier F., Bushnell D.M. 1985 Turbulence alteration due to shock motion. Turbulent shear layer/shock wave interactions IUTAM Symposium Proceedings Ed. J. Delery, Springer Verlag.
- Jayaram M., Dussauge J.P., Smits A.J. 1985 Analysis of a rapidly distorted, supersonic, turbulent boundary layer. Proc. 5th Symp. on Turbulent Shear Flows, Cornell University, Ithaca, N.Y.
- Jayaram M., Taylor M.W., Smits A.J. 1987 The response of a compressible turbulent boundary layer to short regions of concave surface curvature. J. Fluid Mech. 175, 343-362.
- Leyland P. 1984 Transport et propagation d'une perturbation compressible dans un écoulement. Thèse de Doctorat ès Sciences, Université d'Aix-Marseille I.
- McKenzie J.F., Westphal K.O. 1968 Interaction of linear waves with oblique shock waves. Phys. Fluids 11, 2350-2362.

- Moffatt H.K. 1968 The interaction of turbulence with a strong wind shear, Int. Coll. on atmospheric turbulence and radio wave propagation, Moscow 1965, Ed. Yaglom and Tatarsky, Nauka, 139-150.
- Oh Y.H. 1974 Analysis of two-dimensional free turbulent mixing AIAA Paper 74-594.
- Ribner H.S. 1953 Convection of a pattern of vorticity through a shock wave NACA T.N. 2864, Washington.
- Ribner H.S. and Tucker M. 1952 Spectrum of turbulence in a contracting stream NACA T.N. 2606, Washington.
- Savill M. 1987 Recent developments in rapid distortion theory, Ann. Rev. Fluid Mech. 19, 531-575.
- Selig M.S., Andreopoulos J., Muck K.C., Dussauge J.P., Smits A.J. 1987 Simultaneous wall pressure and mass-flux measurements downstream of a shock wave / turbulent boundary layer interaction AIAA Paper 87-0550.
- Smits A.J., Wood D.H. 1985 The response of turbulent boundary layer to sudden perturbations, Ann. Rev. Fluid Mech. 17, 321-358.
- Townsend A.A. 1970 Entrainment and the structure of turbulent flow, J. Fluid Mech. 41, 17-46.
- Townsend A.A. 1976 The structure of turbulent shear flow, Cambridge, Cambridge Univ. Press, 2nd Ed.
- Townsend A.A. 1980 The response of sheared turbulence to additional distortion, J. Fluid Mech. 98, 171-191.
- Vandromme D. 1983 Contribution à la modélisation et la prédiction d'écoulements turbulents à masse volumique variable. Thèse de Doctorat ès Sciences, Université des Sciences et des Techniques de Lille.
- Zang T.A., Hussaini M.Y., Bushnell D.M. 1984 Numerical computations of turbulence amplification in shock-wave interactions AIAA J. 22, 13-21.



## CHAPTER 3

## LARGE SCALE MOTIONS IN SUPERSONIC TURBULENT BOUNDARY LAYERS

by

A. J. Smits and J. H. Watmuff  
 Gasdynamics Laboratory, Dept. Mechanical & Aerospace Engineering  
 Princeton University

## 1. INTRODUCTION

Chapter 12 lists a number of experiments performed at the Gasdynamics Laboratory of Princeton University, encompassing zero pressure gradient and adverse pressure gradient flat plate boundary layers, flows over concavely curved walls, and shock-wave/boundary layer interactions. The Reynolds-averaged turbulent stresses, and the corresponding mean-flow data are listed, with a brief description of the experimental conditions. In addition to obtaining time-averaged results, a large number of other measurements were taken in an attempt to describe the time-dependent behavior of the turbulent field. These data do not easily lend themselves to the kind of presentation given in Chapter 12, yet they can provide the kind of fundamental insight into the structure of the turbulent field which is so necessary if we are to improve our understanding.

In this chapter, we summarize these results, in the hope that our remarks will provide useful information for the modelling of supersonic turbulent boundary layer behavior. In some ways, the data base is rather limited. For example, the undisturbed boundary layer is the same in each case, with an approximately adiabatic wall, a freestream Mach number of 2.9, and a momentum thickness Reynolds number of about 80,000. On the other hand, a wide range of perturbations in pressure gradient and wall curvature were investigated. Apart from anything else, only Owen and Horstman (1981), and Robinson (1986) have presented similar results, and therefore the Princeton results become interesting simply because of their scarcity.

Earlier flow visualization evidence gave a strong indication that large-scale motions exist in supersonic boundary layers. As early as 1958, James presented some astonishing shadowgraphs of transition on bodies of revolution over a wide range of Mach numbers, Reynolds numbers and heat transfer rates. Two examples are given in Fig. 1. Note that these axisymmetric flows minimize the spatial integration of the shadowgraph technique, and the images give an approximate view of a flow cross-section. The first example clearly shows intermittent transition to turbulence similar to the turbulent spots observed in subsonic flows. The second example shows the development of an axisymmetric boundary

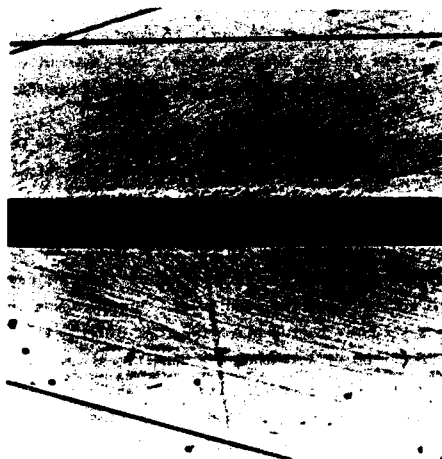


Figure 1(a). Shadowgraph of pencil model in free flight;  $M_\infty = 3.9$ ;  $U_\infty/\nu = 2.2 \times 10^6/\text{in.}$ ; wind tunnel "air-off"; conical light field (from James 1958).



Figure 1(b). Straight tube;  $M_\infty = 3.1$ ;  $U_\infty/\nu = 3.1 \times 10^6/\text{in.}$ ; wind tunnel "air-off"; conical light field (from James 1958).

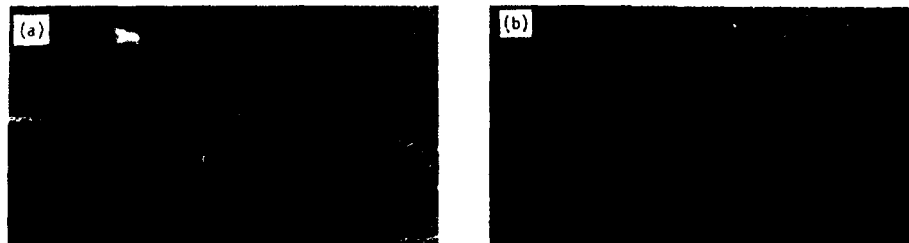


Figure 2. Structure inclined at approximately  $45^\circ$  can be seen in these shadowgraphs of boundary layers over axisymmetric bodies-of-revolution (details from photographs taken by A. C. Charters-Van Dyke, 1981).  
(a)  $M_\infty = 1.8$ ; (b)  $M_\infty = 2.5$ .

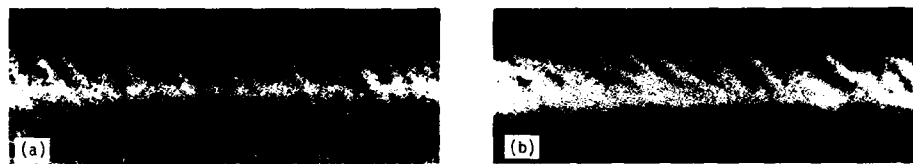


Figure 3. Enlarged schlieren photographs of flow (a) on the floor of the duct and (b) on a flat plate (from Deckker 1980).

layer, and a coarse "layered" structure is evident in the turbulent part. Further shadowgraphs of boundary layers on bodies of revolution are shown in Fig. 2. In Fig. 3 boundary layers developing after the passage of a shock are made visible using a focussed schlieren technique. In all cases, quite marked and regular striations are visible near the wall. The characteristic angles seem to lie between  $40^\circ$  and  $60^\circ$  to the wall.

These photographs prompted the quantitative work described below. We were curious to determine the nature of these striated structures, and to try to relate them to similar observations in subsonic flow (as given, for example, by Head and Bandyopadhyay 1981). We were also interested in the behavior of these structures in flows with pressure gradient and wall curvature, to extend the general understanding of large scale motions in boundary layers, and to determine the universality of these motions.

Of course, these investigations are still in progress, and it is far too early to make any sweeping conclusions. Some of the research discussed in this chapter has not yet been published, and some of our results are still ambiguous. Nevertheless, our observations have been intriguing, and it is perhaps useful to present them here, despite their premature nature.

In Section 2, we begin with a discussion of the zero pressure gradient case, corresponding to CAT 8603. This case has been investigated the most extensively, and many of the measurement and analysis techniques used in the later work were first introduced here. The second flow is the flat plate boundary layer with an externally imposed pressure gradient corresponding to CAT 8601. We continue Section 2 with a discussion of two examples of a boundary layer on a concavely curved wall. In the first case, the wall was shaped to have the same wall pressure variation as the flat plate flow adverse pressure gradient case (this flow corresponds to CAT 8501 Model II), and in the second case the radius of curvature was decreased and the turning angle was increased to produce a stronger perturbation (see CAT 8702). In the early stages of these investigations, we made extensive use of the VITA method of conditional sampling. As our experience grew, so did our misgivings regarding the way we were using the technique. These considerations prompted an evaluation of suitable conditional sampling methods, and some of these thoughts are given in Section 3. A general discussion of the results is presented in Section 4.

This chapter represents a summary of the work performed by Eric Spina, Emerick Fernando, John Donovan, Mike Smith, Michael Selig, and Amy Alving. If there is any credit to be had, it properly belongs to them. Our appreciation is also expressed for the support given by our sponsors: AFOSR Grant 85-0126 monitored by J. McMichael, and NASA Langley Grant NAG-1 545 monitored by W. Sawyer and D. Haynes.

## 2. OBSERVATIONS ON LARGE-SCALE STRUCTURES

The upstream boundary layer is described briefly in Chapter 12 (CAT 8603), and further details were given by Spina and Smits (1986, 1987). The flow had a freestream Mach number of  $2.87 (\pm 0.01)$  with a unit Reynolds number of  $6.5 \times 10^7/m$  ( $\pm 4\%$ ). The walls were approximately adiabatic and the freestream turbulence level was 1 to 1.5%. The test boundary layer developed on the tunnel floor, and the measurements were centered around a point 2210 mm downstream of the throat. The boundary layer thickness  $\delta$  at that point was 28 mm, where  $\delta$  is defined as the point where the total pressure reaches 98% of its freestream value.

The experimental techniques for all turbulent structure measurements were similar. Briefly, turbulent fluctuations were recorded at several locations simultaneously, providing spatial and temporal information about the structures. Constant-temperature hot-wire anemometry was used at high overheat ratios to obtain an output approximately proportional to fluctuations in mass flux (Smits et al. 1983), and since the correlation between density and velocity fluctuations is about 0.8 (Dussauge and Gaviglio, 1981) we have often used the assumption that the mass-flux signal is approximately proportional to either density or streamwise velocity fluctuations.

For multi-wire runs, a special hot-wire support was designed to hold four normal wires in two pairs, one pair above the other, and the two pairs of wires could be moved relative to each other vertically (see Fig. 4). No data were actually taken using all four wires; however, runs were made using both two and three hot wires simultaneously.

Where possible, measurements of the wall pressure fluctuations were made using four identical miniature differential pressure transducers. The transducers were mounted in-line in a cylindrical plug (see Fig. 4), which was then fitted in the test section floor. The plug could be rotated through  $360^\circ$ , yawing the transducers relative to the flow.

By combining the use of wall-pressure transducers and hot-wires, simultaneous measurements of the instantaneous wall pressure and instantaneous mass flux were made. The hot wires were placed at

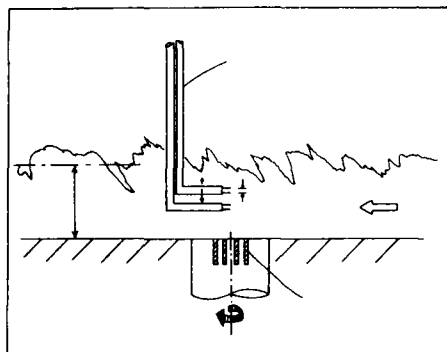


Figure 4. Arrangement of hot wire probes and wall pressure transducers.

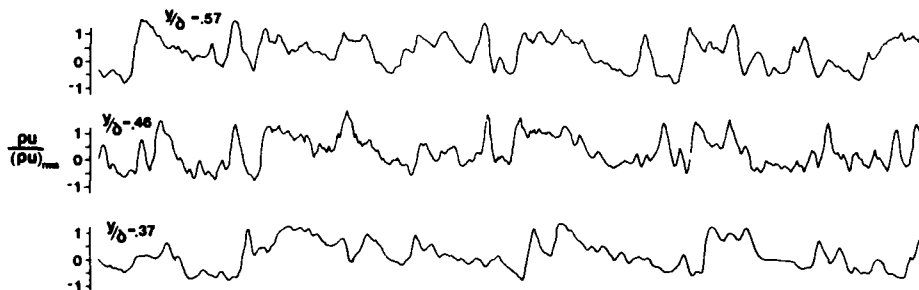


Figure 5. Fluctuating mass-flux signals from 3-wire probe.

different points in the flow (relative to the wall-pressure transducers) to obtain a wide spatial resolution of the flow field. Conditional sampling and time series analysis were then used to deduce both the mean and instantaneous behavior of the large scale structure.

To begin the discussion of the results, consider the time records of  $(pu)'$  obtained in the zero pressure gradient boundary layer from three hot wires (Fig. 5). The signals exhibit a very similar character, indicating the passage of organized motions of a scale larger than the separation distance between the top and bottom wires.

The space-time correlations for the signals from two wires are shown in Fig. 6. The peak values of the correlations are quite high, reaching a maximum of 0.65 near the middle of the boundary layer. More importantly, the dimensionless delay time  $(\tau^* = \tau U_m / \delta)$  corresponding to the peak of the space-time correlation,  $\tau_{max}$ , decreases from 0.4 ( $\tau = 20 \pm 0.5 \mu s$ ) at the floor to nearly zero at the edge of the boundary layer.

The high peak level of the correlation and the non-zero value of the time delay imply that both wires are detecting the same "disturbance", and that one wire is detecting it before the other. Since the time shift was applied to the upper wire, the peak at negative  $\tau^*$  means that the upper wire detects the disturbance first, that is, the disturbance leans downstream. Accordingly, an angle  $\theta$  can be defined for this "front" by using the value of  $\tau_{max}$  along with the wire separation distance,  $\Delta$ , and the local mean velocity. That is,

$$\theta = \arctan \frac{\Delta}{U \tau_{max}}$$

Strictly speaking, the local streamwise convection velocity should be used to determine this angle (Robinson 1986, Brown and Thomas 1977), but the convection velocity has not been determined for this flow. However, the difference in the mean structure angle owing to small variations in the convection velocity is small, and therefore the average velocity was used here.

The angle  $\theta$  may be called an "average structure angle," in that it is associated with an average large-scale motion. The results from three different traverses can be seen in Fig. 7 as a function of position in the boundary layer (at the midpoint of the boundary layer the resolution of the time shift corresponds to an angular uncertainty of  $\pm 3^\circ$ ). The angle is small near the floor, increases quickly to about  $45^\circ$ , and it remains constant at this value throughout 70% of the boundary layer. Finally, the angle shows a rapid increase at the edge of the boundary layer. Note that the distribution of the structure angle seems to be independent of the two different separation distances chosen. The distribution of  $\theta$  is in accordance with Head and Bandyopadhyay's (1981) observations in a subsonic boundary layer at lower Reynolds numbers. They observed hairpin loops which displayed small angles near the floor and  $45^\circ$  through the central portion of the boundary layer, followed by a slight increase near the edge.

While the present study traverses two "detection probes" through the boundary layer at a fixed separation distance (small compared to  $\delta$ ), most other measurements of this kind have used one detection probe fixed at the wall (a hot wire, a shear stress gauge, or some similar device) and another probe which was traversed through the boundary layer, thereby varying the separation distance. The fixed separation method used here results in a typical mean structure angle of  $45^\circ$ , while the variable separation method seems to give a lower characteristic value: in supersonic flow Robinson (1986) found  $30^\circ$  and in incompressible flows Brown and Thomas (1977) found  $18^\circ$ , whereas Rajagopalan and Antonia (1979) found  $12.5^\circ$ , and Robinson (1985) found  $16^\circ$ . The advantage of the present method is that the slope of the structure is determined locally, instead of being inferred from a large-scale measurement. This difference is reinforced by recent measurements taken by Alving (private communication) in incompressible flow, using the fixed separation technique described here. The results, shown in Figure 8, were taken in a flow with  $Re_\delta = 5000$ ,  $\delta = 21 \text{ mm}$ , and  $U_m = 31 \text{ m/s}$ . The separation distance between the hot wires was  $0.13 \delta$ . Clearly, these incompressible results are similar to the compressible results, and both sets of results give higher structure angles than those found by previous researchers using the variable separation method.

Using the same upstream flow conditions used by Spina and Smits for the zero pressure gradient layer discussed above, Donovan and Smits (1987) investigated the mean structure angle distribution following a short region of concave surface curvature using two different flow models: one which turns the flow through  $8^\circ$  with a radius of curvature of  $1270 \text{ mm}$  ( $\delta/R = .022$ ), and the other turns the flow  $16^\circ$  with  $\delta/R = .08$ . Fernando and Smits (1987) made similar measurements on a flat plate following a short region of adverse pressure gradient. In that case, the pressure gradient was generated by a contoured plate,

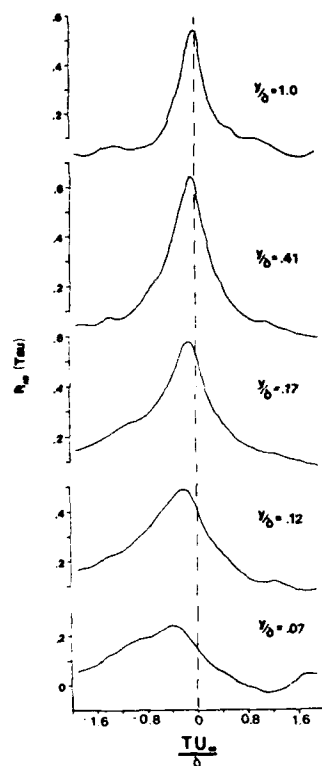


Figure 6. The space-time correlation of mass-flow fluctuations throughout the boundary layer. Hot-wire separation is 0.1 $\delta$  (from Spina and Smits 1987).

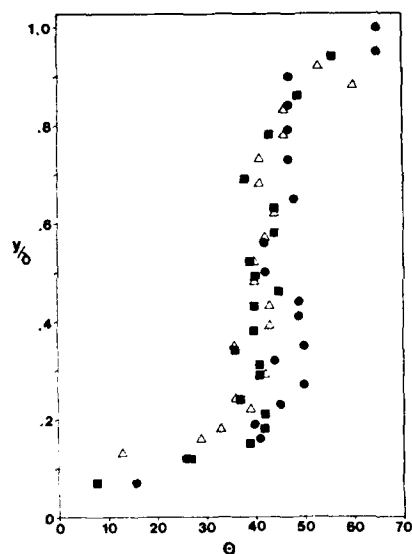


Figure 7. Structure angle for different wire separations.  $\bullet$ ,  $\Delta/b = 0.08$ ,  $\blacksquare$ ,  $\Delta/b = 0.09$ ,  $\triangle$ ,  $\Delta/b = 0.21$  (Spina and Smits, 1987).

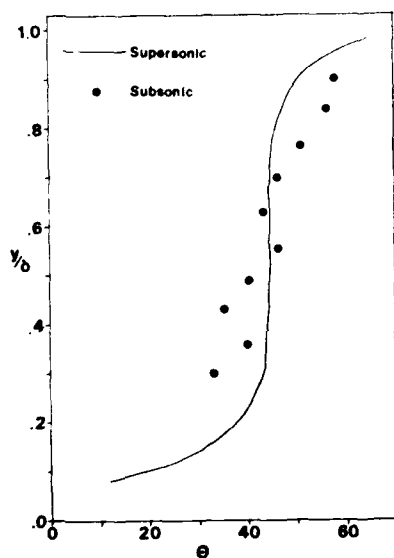


Figure 8. Large-scale structure angle through the boundary layer as measured in subsonic flow by Alving. The supersonic distribution is a faired curve from Fig. 7.

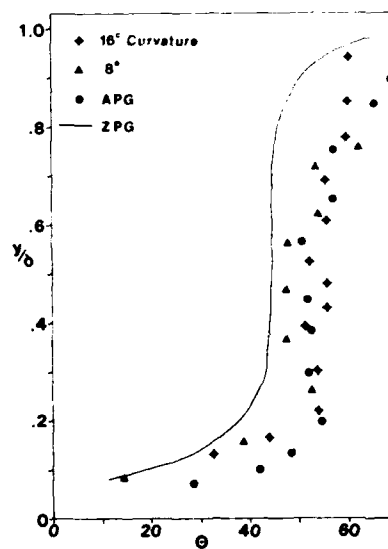


Figure 9. Large-scale structure angle through the boundary layer as measured in perturbed supersonic boundary layers by Fernando and Smits (1987) and Donovan and Smits (1987).

designed so that the pressure distribution matched that of the  $8^\circ$  model using by Donovan and Smits. The distribution of the structure angle for all three flows is seen in Figure 9, along with the zero pressure gradient case. The general shape of the distribution remains the same as in the zero pressure gradient case. However, there appears to be a small increase in the structure angle after each of the three perturbations. Furthermore, the structure angle after the stronger curvature is slightly higher than after the weaker curvature. Donovan and Smits suggested that the perturbation rate was too rapid in the stronger curvature model to allow readjustment of the large-scale motions, and thus the angle of inclination is affected. It appears that the same preliminary conclusion can be drawn for all three of the flow perturbations, since they all exhibit the same trend.

The average structure measurements reported here and elsewhere are very useful in establishing the existence of large-scale structures. However, the key to a physical comprehension of these structures lies with understanding the behavior of individual structures, that is, their instantaneous characteristics.

Conditionally sampled mass-flux results were reported recently by Spina and Smits (1987). Events were detected using the VITA method introduced by Blackwelder and Kaplan (1976). By computing the VITA ensemble average of events from three different hot wires, structure angles were computed which were nearly identical to those found from space-time correlations. Thus, it appears that VITA can detect events which make the dominant contribution to the time-average structure angle.

This result has been used by Smith at Princeton (private communication), to interpret schlieren images of the boundary layer structure. Smith used a real-time analog of VITA to condition on the mass-flux fluctuations from a hot-wire probe to detect strong, large-scale motions. Upon detection of an individual structure, a light source was flashed to record a microsecond-exposure schlieren image. The use of a hot wire as a detection probe counters some of the spatial integration effects present in schlieren images. A typical image is reproduced in Fig. 10 along with the hot-wire output and the detection signal. Structures extend the full height of the boundary layer, as indicated earlier in Figs. 1 to 3, and they display considerable variation in their characteristic angle. Similar results can be

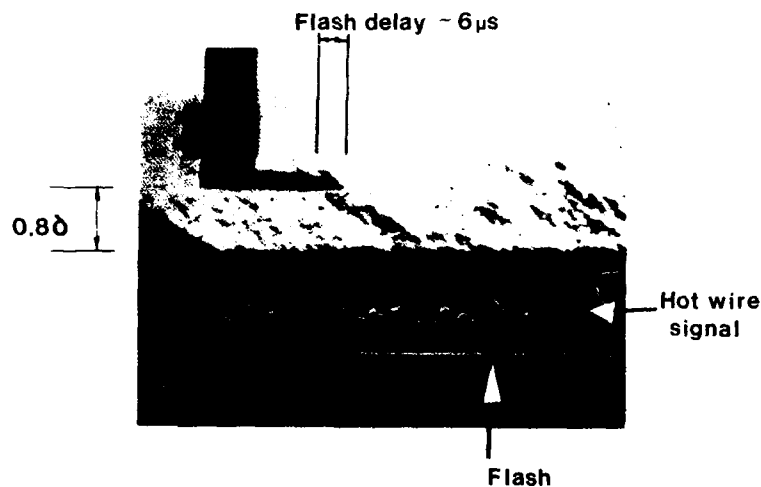
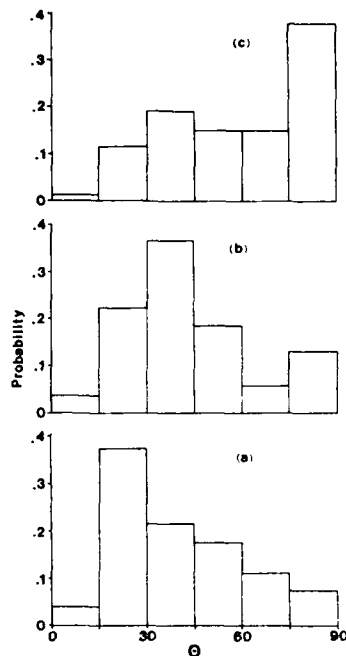


Figure 10. Microsecond schlieren video image of zero pressure gradient supersonic boundary layer taken by Smith and Smits (1986). The hot wire probe at left is located at  $y/\delta = 0.8$ , and its corresponding signal is shown at the bottom of the picture along with the detection signal. The time scale corresponds approximately to the length of the picture, and the flow is from right to left.



Figure 11. Microsecond schlieren video image by Donovan of a supersonic boundary layer in an adverse pressure gradient generated by a concavely curved wall ( $\delta/R = 0.08$ , turning angle  $16^\circ$ ). The dark shadow outside the boundary layer indicates the presence of a strong compression fan.

Figure 12. Probability distribution of individual structure angles:  
 a)  $y/\delta \approx 0.1$ , 115 events  
 b)  $y/\delta \approx 0.3$ , 306 events  
 c)  $y/\delta \approx 0.9$ , 75 events  
 (from Spina and Smits 1987).



deduced from Fig. 11, which shows the flow over the concavely curved wall used by Donovan and Smits (the second curved wall, with  $16^\circ$  turning). The average angle appears to increase, in agreement with the results given in Fig. 9, but there exists a wide dispersion. Therefore, an analytical technique was devised to determine the individual structure angles from the fluctuating signals of the double hot-wire probe (wire separation of  $0.09\delta$ ). The algorithm was described in detail by Spina and Smits (1987). In summary, the technique searches for highly correlated, highly energetic events occurring in both signals "near-simultaneously", and deduces an instantaneous structure angle from their separation time. VITA was used to detect the events but it should be noted that this method is not dependent on the VITA technique, *per se*; any conditional sampling technique can be used to find the energetic portions of each signal.

To achieve a sufficient number of realizations of the instantaneous angles, data records four times as long as usual were analyzed (i.e., 98304 data points instead of 24576). The number of accepted pairs was approximately 60% of the number of VITA events which implies that 60% of the events were large enough to span both wires. The first point of note is that the average value of the instantaneous angle matched the mean structure angle very well. The values at the wall were slightly higher than those shown in Fig. 7, but the distribution through the rest of the boundary layer was virtually identical. The standard deviation of the instantaneous angles was computed to be about  $20^\circ$  throughout most of the boundary layer, indicating a large spread in the inclination of the structures. A histogram was computed and it is shown in Fig. 12 for three points in the boundary layer. Near the floor, the majority of the structures have an angle below  $45^\circ$ , with the most populated state being  $15-30^\circ$ , and very few structures with an angle of  $90^\circ$ . Away from the wall ( $y/\delta = 0.3$ ), the structures shift towards  $45^\circ$  with an increased population at  $90^\circ$ . At the edge of the boundary layer ( $y/\delta = 0.9$ ) the population between  $75-90^\circ$  has increased dramatically, and it becomes dominant.

These trends can be interpreted in terms of the hairpin model of turbulence. In this model, the characteristic structures in the boundary layer are hairpin loops, and hairpins of all sizes populate the boundary layer (see, in particular, Perry and Chong 1982). A typical hairpin vortex (see, for example, Smith 1984) consists of elongated legs at the floor, a central portion inclined at  $45^\circ$ , and an upturned head at about  $90^\circ$ . If the instantaneous angle distribution was measured in this artificial boundary layer, the range of structure angles near the wall would vary from  $0$  to  $90^\circ$ , with the lower angles

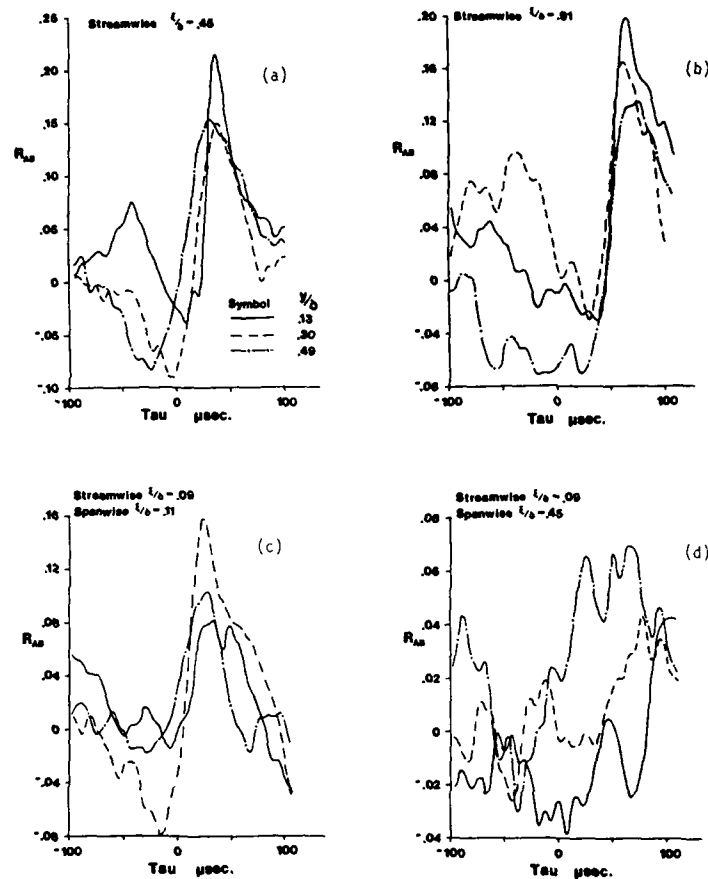


Figure 13. Space-time correlation between a wall-pressure signal and a hot-wire mass-flux signal (from Spina and Smits 1987).

dominating since the mid- to large-scale structures would not display high angles near the wall. Away from the wall, the angle of the central portion would dominate, with a slightly higher population near  $90^\circ$  due to the upturned heads of the structures of that size. Finally, near the edge of the boundary layer, the dominant angle would be close to  $90^\circ$ , since nearly all structures extending to that height would have upturned heads at that point. The distributions described for this idealized case of a "forest" of hairpin loops are similar to those seen in Fig. 12, suggesting that the large-scale structures found in this compressible flow are consistent with the hairpin structure interpretation.

Further support for the hairpin-structure hypothesis comes from the cross-correlations between pressure fluctuations at the wall and mass-flow fluctuations measured at various points within the boundary layer. Figure 13a shows the correlations with the hot wire located at  $0.45\delta$  downstream of the pressure transducer, while Fig. 13b shows them for a streamwise separation of  $0.91\delta$ .

The first point of interest is the rather low level of correlation, with a maximum peak of 0.22. This low level was observed for even the smallest transducer separations and can be ascribed to the differences in the frequency content of the pressure and mass-flow signals. Secondly, doubling the separation of the transducers did not change the level of the correlation significantly. Furthermore, the general shape of the correlation was retained (the small peak at a negative value of  $\tau$ , followed by



a sharp rise to the major peak). Hence, the structures appear to retain their shape and coherence as they are convected downstream. Figures 13c and 13d show correlations for spanwise separations between the transducers of 0.11 $\delta$  and 0.45 $\delta$  respectively (both also have a streamwise separation of 0.09 $\delta$ ). We see that the results in Fig. 13c show a slight decrease in correlation level when compared to the previous results which had no spanwise separation. In addition, in Fig. 13d, we observe that with an increased spanwise displacement, the correlation has decreased to half its original value, suggesting that the structures have a very limited spanwise extent.

The spanwise wall-pressure correlations were complemented by spanwise mass-flux correlations for the flat plate adverse pressure gradient case investigated by Fernando and Smits (1987). Peak mass-flux cross-correlation coefficients obtained from different wire spacings and orientations are plotted in Fig. 14 for stations upstream and downstream of the interaction. There appears to be little change in the relatively-high correlation coefficients through the interaction. The structures maintain their non-dimensional spanwise and vertical extent. Furthermore, the peak correlation coefficients for the spanwise separated wires are only slightly lower than for the vertically separated wires. There is significant correlation in the spanwise direction over distances of 0.2 $\delta$ . This is contrary to Spina and Smits' conclusion based on wall pressure mass-flux correlations, as given above, that these motions are of limited spanwise extent, of the order of 0.1 $\delta$ . This apparent contradiction may be resolved by the following two arguments. It is seen in Fig. 14 that the correlation coefficient between the spanwise separated wires decreases as the wall is approached. This implies that the structure is of smaller spanwise extent near the wall, as suggested by Moin and Kim (1985) based on their Large Eddy Simulation data. Hence wall pressure mass-flux correlations must drop off faster than mass-flux cross-correlations between hot-wires. The second argument relies on the lower peak cross-correlation between the two vertically separated wires closer to the wall. This indicates that the structure becomes less coherent closer to the wall again explaining why wall pressure hot-wire mass-flux correlations must drop off faster than mass-flux cross-correlations between hot-wires.

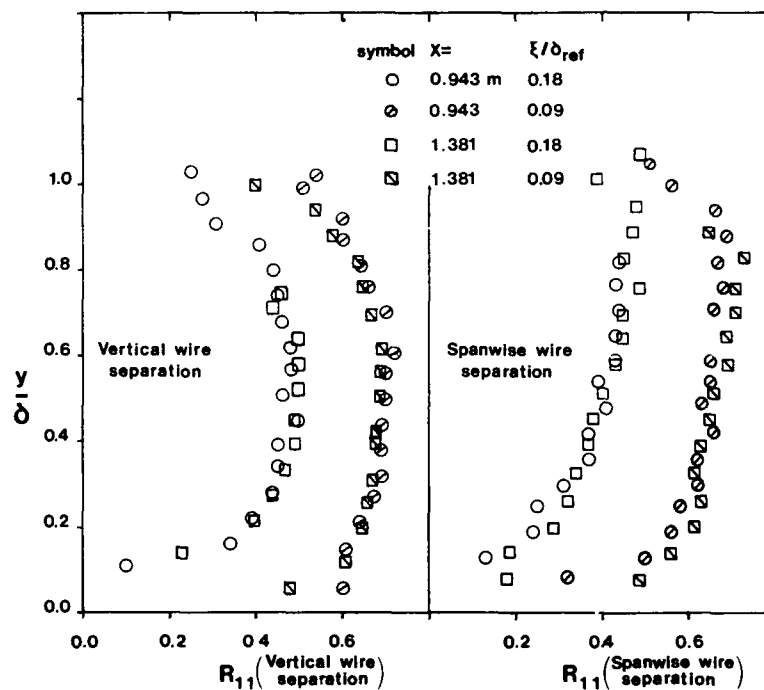


Figure 14. Peak hot-wire mass-flux cross-correlations coefficients within the boundary layer (from Fernando and Smits 1987).

### 3. CONDITIONAL SAMPLING TECHNIQUES

In the work described above, the primary basis for conditional sampling was the VITA technique, and it was applied to signals obtained from a normal wire, that is, to the time varying  $u'$  signal as derived from the  $(\rho u)'$  signal using the Strong Reynolds Analogy. The results obtained in zero pressure-gradient high-Reynolds number supersonic flows agreed well with similar results from subsonic, low Reynolds number flows (Spina and Smits 1987). However, it is not all clear how these "VITA events" can be interpreted physically. The interpretation is limited by the fact that VITA is a single point criterion, applied to measurements of a single component of the turbulent fluctuations. Our current emphasis, therefore, is to improve the detection technique to the point where the detected events can be given a more complete physical interpretation.

We first found that the VITA technique could give a distorted picture of the flow structure when we began to use a crossed wire probe to examine the instantaneous values of  $u'$ ,  $v'$  and  $u'v'$  (Fernando et al., 1987). The shear stress signal  $u'v'$  is highly intermittent, with sharp excursions from the background level, and it is extremely suitable for conditional sampling. A simple threshold criterion was used to detect the events which make the greatest contribution to the shear stress. (We used a threshold  $= 2 u'v'$ ). These events are obviously of great practical interest. The  $u$  and  $v$  events were then clarified into four quadrants: quadrant I ( $u+$ ,  $v+$ ), quadrant II ( $u-$ ,  $v+$ ), quadrant III ( $u-$ ,  $v-$ ), and quadrant IV ( $u+$ ,  $v-$ ).

The results are very revealing. Typically, the ensemble-averaged events are strong, and rather simple in shape (see Fig. 15). In particular, it should be noted that the  $u'$  event is single-sided, that is, it is either positive or negative. In contrast, when VITA is applied to the  $u'$  signal (instead of thresholding on  $u'v'$ ), the event is doubled-sided, as shown in Fig. 16. These results suggest that VITA detection is subject to ambiguity, probably caused by the superposition of two types of events which can only be separately identified by using quadrant analysis.

To explain the concept, consider two individual  $u'$  events detected by the shear stress criterion, one lying in quadrant I and the other in quadrant IV of the  $u-v$  plane. Both are single sided events. If VITA detects both these events as positive by checking the slope at their centers, the ensemble average

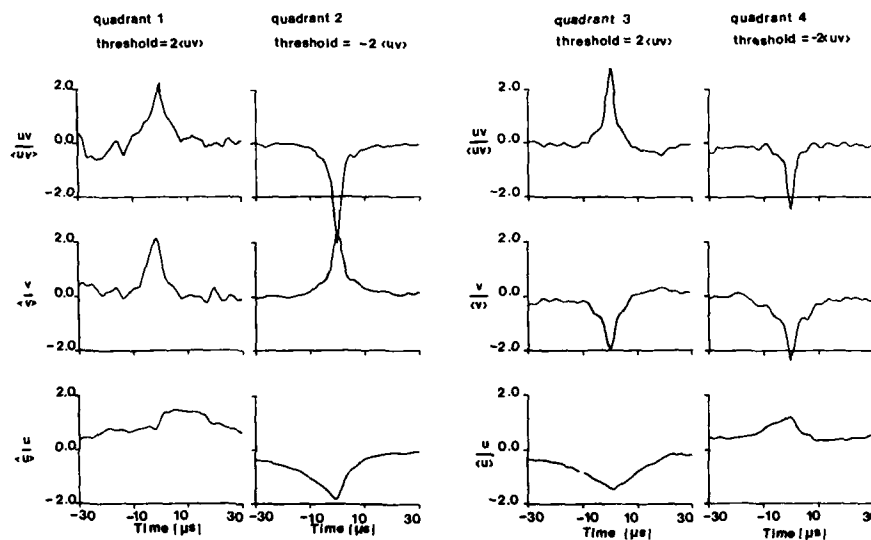


Figure 15. Ensemble-averaged events based on threshold detection applied to  $u'v'$  signal at  $y/\delta = 0.65$ : Quadrants I ( $u+$ ,  $v+$ ); II ( $u-$ ,  $v+$ ); III ( $u-$ ,  $v-$ ); IV ( $u+$ ,  $v-$ ). (Fernando et al. 1987)

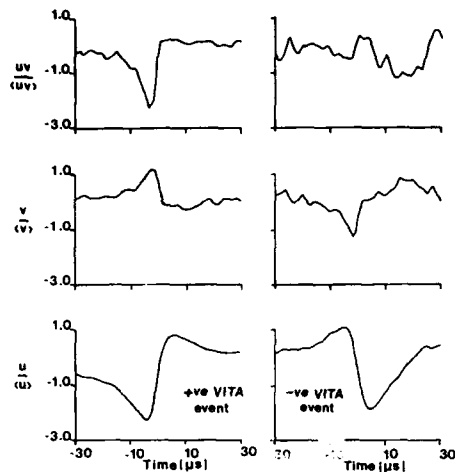


Figure 16. Ensemble-averaged events based on VITA at  $y/\delta = 0.65$  (from Fernando et al. 1987).

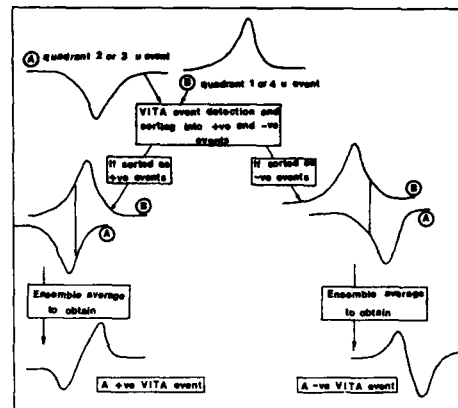


Figure 17. A possible explanation as to the difference between ensemble averages obtained by the VITA technique and by threshold criteria applied to the shear stress (from Fernando et al. 1987).

of these two events would be a two sided event. Figure 17 clarifies the concept. Depending on exactly where the VITA technique checks the slope, these events could have been picked up as negative events, giving a two sided negative event. This may explain why positive and negative VITA events are nearly mirror reflections of each other, about the velocity axis.

It can be argued that the quadrant method is a more physically realistic method to use as a detection criterion, since the detected events are associated with high levels of shear stress, whereas this is not necessarily true for the ensemble averages derived from the VITA technique. It seems better, therefore, to conditionally sample directly on the  $u'v'$  signal rather than on the  $u'$  signal, as with the VITA technique. In particular, 1) the detected events then contain a large fraction of the shear stress; 2) similar patterns of  $uv$  are grouped together, unlike VITA, and therefore stronger, more clearly defined ensemble averages result; 3) the events are consistent with simple boundary layer hairpin vortex models; and 4) the detection criterion has no preset bias towards any particular frequency, unlike the VITA detection function.

#### 4. DISCUSSION

For the zero pressure gradient case, the experiments showed that large-scale structures, inclined at about  $45^\circ$  to the wall, appear to fill the major extent of the boundary layer. As they convect downstream, these structures retain much of their shape and character, and preserve their identity for at least  $1.5\delta$ . However, the spanwise extent of the structures is rather limited. The average and the instantaneous behavior of these structures was found to be consistent with a distribution of hairpin vortex loops. Furthermore, the effect of compressibility on the large-scale organized structures in an undisturbed turbulent boundary layer appears to be small. For example, the deduced structure angles from this investigation are consistent with Head and Bandyopadhyay's [1981] observations and Alving's recent measurements in incompressible flow. The eddy angle is low near the floor, increases quickly to  $45^\circ$  (where it remains throughout 70% of the boundary layer), and increases again near the edge of the boundary layer. For the flows with adverse pressure gradients, the structures appear to have a higher characteristic angle, although the measurements and flow visualization suggest that a strong pressure gradient is required to make a noticeable difference.

The measurements in fully developed turbulent water-channel flows by Johansson and Alfredsson [1982] using VITA conditional sampling show a strong similarity to the VITA conditional results presented by Spina & Smits (1987). Furthermore, the ensemble-averaged positive VITA events detected in incompressible flows by Thomas and Bull [1983] were found to be strikingly similar to the mass flow events observed in

the zero pressure gradient case. However, although VITA conditional sampling is a very useful technique, it does have limitations. When this technique was applied to a  $u'v'$  signal obtained from a crossed-wire in an undisturbed supersonic boundary layer, the conditionally sampled signal consisted only of negative and positive spikes. Yet, the resultant positive ensemble average event contained a combination of positive and negative excursions about the mean. Thus, these ensemble averages are not representative of the signal shapes in the original signal. Conditional sampling techniques based on the quadrant method appear to be less ambiguous and more physically meaningful. The drawback of the quadrant method is that  $u'$  and  $v'$  information is required, and unfortunately crossed-wires are difficult to use in supersonic flows. Wire breakages are very common, strain-gaging is often a problem, and spatial resolution is usually rather limited (Fernando et al. 1987). Nevertheless, it seems essential to develop the crossed-wire technique for future investigations.

Refined flow visualization techniques are also essential. At present, we are developing a method of conditionally sampling schlieren images of boundary layer structure in supersonic flow. This technique is based on that described in Section 2. A hot-wire probe is used to detect the presence of strong, large-scale motions by using a real-time analog of the VITA detection method. Upon detection, a light source is flashed to record a microsecond exposure schlieren image on video tape. The hot-wire output is recorded simultaneously on the same video frame, and a typical image is shown in Fig. 10. The image was recorded using a CCD camera with linear gain so that the intensity can be linearly related to density gradient, and images can be added to obtain an ensemble-averaged picture. The conditionally sampled nature of the images means that we record only large events which are in the plane of the wire. We hope this method will remove the spatial integration effect of schlieren images. The preliminary results presented by Smith and Smits (1986) look encouraging.

Smith has also recently made high speed (40K frames/sec) laser schlieren movies of a supersonic boundary layer which clearly show the presence of strong large-scale motions convecting within the layer. Figure 18 is a typical sequence of alternate frames taken from one of these movies. (The camera exposes frames alternately on either side of the film). Although it is possible to "threshold" the schlieren images so that only the very strongest structures are detected, the spatial integration inherent in the schlieren technique makes it difficult to produce convincing images of individual structures. One way around this problem may be to photograph laser sheet cross-sections through smoke or some other light scattering medium introduced at some strategic point in the flow. Unfortunately, it is difficult to provide sufficient light intensity to record the images on movie film or still photographs. Further work is in progress.

#### REFERENCES

- Blackwelder, R. F. and Kaplan, R. E. [1976], On the wall structure of the turbulent boundary layer, Journal of Fluid Mechanics, Vol. 76, p. 89.
- Brown, G. L. and Thomas, A. S. W., [1977], Large structure in a turbulent boundary layer, Physics of Fluids, Vol. 20(10), p. 243.
- Deckker, B. E. L. [1980], Boundary layer on a shock tube wall and at a leading edge using schlieren, Second International Symposium on Flow Visualization, Ruhr-Universität Bochum, West Germany. Ed. W. Merzkirch, Hemisphere, p. 413.
- Deckker, B. E. L. and Weekes, M. E. [1976], The unsteady boundary layer in a shock tube, Proc. I. Mech. Eng., Vol. 190, p. 287.
- Dussauge, J. P. and Gaviglio, J. [1981], Bulk dilatation effects on Reynolds stress in the rapid expansion of a turbulent boundary layer at supersonic speed, Proc. Third Symposium on Turbulent Shear Flows, Univ. Cal., Davis.
- Donovan, J. F. and Smits, A. J. [1987], A preliminary investigation of large-scale organized motions in a supersonic turbulent boundary layer on a curved surface, AIAA Paper 87-1285.
- Fernando, E. M. and Smits, A. J. [1987], The effects of an adverse pressure gradient on the behavior of a supersonic turbulent boundary layer, AIAA Paper 87-1286.
- Fernando, E. M., Spina, E. F., Donovan, J. F. and Smits, A. J. [1987], Detection of large-scale organized motions in a turbulent boundary layer, Sixth Symposium on Turbulent Shear Flows, Toulouse, France.
- Head, M. R. and Bandyopadhyay, P. [1981], New aspects of turbulent boundary-layer structure, Journal of Fluid Mechanics, Vol. 107, p. 297.

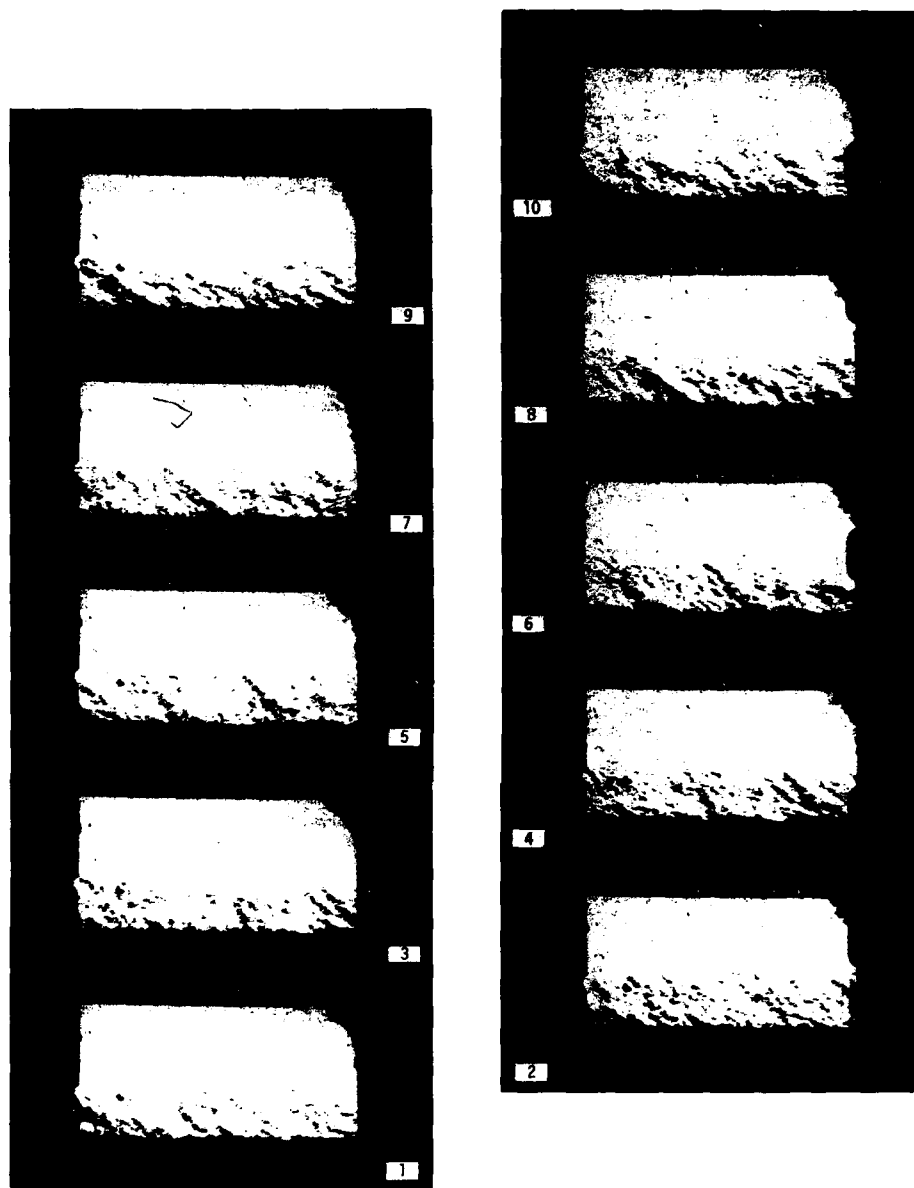


Figure 18. Consecutive frames from M. Smith's laser schlieren movie of a supersonic turbulent boundary layer. Note convection of large-scale motions from right-to-left. Time between consecutive frames is  $27\mu\text{sec}$ .

- James, C. S. (1958), Observations of turbulent-burst geometry and growth in supersonic flow, NASA TN 4235.
- Johansson, A. V. and Alfredson, P. H. [1982], On the structure of turbulent channel flow, Journal of Fluid Mechanics, Vol. 122, p. 295.
- Moin, P. and Kim, J. [1985], The structure of the vorticity field in turbulent channel flow. Part I - analysis of instantaneous fields and statistical correlations, Journal of Fluid Mechanics, Vol. 155, p. 441.
- Owen, F. K. and Horstman, C. C. [1981], Turbulent measurements in an equilibrium hypersonic boundary layer, AIAA Paper 74-93.
- Perry, A. E. and Chong, M. S. [1982], On the mechanism of wall turbulence. Journal of Fluid Mechanics, Vol. 119, pp. 173-217.
- Rajagopalan, S. and Antonia, R. A. [1979], Some properties of the large structure in a fully developed turbulent duct flow, Physics of Fluids, Vol. 22(4), p. 614.
- Robinson, S. K. [1985], Instantaneous velocity profile measurements in a turbulent boundary layer, Chem. Eng. Communications, Vol. 43, p. 347.
- Robinson, S. K. [1986], Space-time correlation measurements in a compressible turbulent boundary layer, AIAA Paper 86-1130.
- Smith, M. and Smits, A. J., [1986], Conditionally-averaged schlieren video images of large-scale motions in supersonic turbulent boundary layers, Presented at the 39th Annual meeting, Division of Fluid Dynamics, American Physical Society, Columbus, Ohio.
- Smith, C. R. [1984], A synthesized model of near-wall behavior in turbulent boundary layers, Proceedings of Eighth Symposium on Turbulence, (Ed. G. K. Patterson and J. L. Zakin), Department of Chemical Engineering, University of Missouri-Rolla).
- Smits, A. J. and Muck, K. C. [1986], Experimental study of three shock wave/turbulent boundary layer interactions. Journal of Fluid Mechanics, Vol. 182.
- Smits, A. J., Hayakawa, K. and Muck, K. C. [1983], "Constant-temperature hot-wire anemometer practice in supersonic flows. Part I - The normal wire, Experiments in Fluids, Springer-Verlag.
- Spina, E. F. and Smits, A. J., 1986 Organized structures in a supersonic turbulent boundary layer, Princeton University, Dept. of Mechanical and Aerospace Engineering, Report #1736.
- Spina, E. F. and Smits, A. J., 1987 Organized structures in a compressible turbulent boundary layer, Journal of Fluid Mechanics, Vol. 182.
- Thomas, A. S. W. and Bull, M. K. [1983], On the role of wall-pressure fluctuations in deterministic motions in the turbulent boundary layer, Journal of Fluid Mechanics, Vol. 128, p. 283.
- Van Dyke, M. [1982], An Album of Fluid Motion, The Parabolic Press, Stanford, CA.

## SKIN-FRICTION MEASUREMENTS BY LASER INTERFEROMETRY

by

K.-S. Kim and G. S. Settles  
 Mechanical Engineering Department,  
 Penn State University, University Park, Pennsylvania 16802 USA

## SUMMARY

The measurement of skin friction in rapidly distorted compressible flows is difficult, and very few reliable techniques are available. A recent development, the Laser Interferometer Skin Friction meter (LISF), promises to be useful for this purpose. This technique interferometrically measures the time rate of thinning of an oil film applied to an aerodynamic surface. Under proper conditions the wall shear stress may thus be found directly, without reference to flow properties. In the present work, the applicability of the LISF meter to supersonic boundary layers is examined experimentally. Its accuracy and repeatability are assessed, and conditions required for its successful application are considered.

## 1. INTRODUCTION

The traditional methods for the measurement of skin friction in compressible flows have been reviewed previously, eg by Winter (1977). Recent developments were also surveyed by Settles (1986). Briefly, other than the direct measurement of wall shear stress by a balance, most of the available techniques infer skin friction from some other measured quantity (such as heat transfer or pitot pressure). The validity of such inferential methods is questionable in such complex flows as rapidly distorted turbulent boundary layers. Further, floating-element balances themselves have serious problems in rapidly distorted flows, especially due to pressure gradients. Thus, for the class of flows in question, reliable measurement techniques are almost nonexistent.

A recent development, the Laser Interferometer Skin Friction meter (LISF), may help solve this problem. The LISF meter was invented by Tanner and Blows (1976), and subsequently refined by Tanner (1981), Monson and Higuchi (1981), Monson, Driver and Szodruch (1981), Monson (1983 and 1984), and most recently by Westphal, Bachalo, and Houser (1986). It interferometrically senses the time rate of thinning of an oil film on a polished surface subjected to aerodynamic shear. In two-dimensional flows without pressure gradients, oil lubrication theory then gives the wall shear stress,  $\tau_w$ , directly without any reference to the properties of the overlying boundary layer. While some corrections are required in three-dimensional, pressure-gradient, and shear-gradient flows, the instrument nonetheless delivers what may be considered a "quasi-direct" measurement of skin friction. Since the idea is new, apparently only four LISF instruments have been built to date: Tanner's, Monson's, Westphal's, and the Penn State instrument intended for compressible flow measurements and described below.

Monson, Driver, and Szodruch (1981) were the first to attempt LISF measurements in supersonic flows. Although the technique ignores, in principle, the speed of the flow, difficulties were experienced nonetheless. For example, Mateer (1984) was unable to obtain LISF interference fringes in high-Reynolds-number transonic flow due to the presence of surface waves on the oil film. Murphy and Westphal (1985) have since studied the surface wave problem theoretically, and various improvements have been made in the experimental apparatus (Westphal et al, 1986).

The cited previous work demonstrates that the LISF meter is an elegant experimental technique for low-speed, continuous-running test facilities. Though it loses some of its elegance in compressible flows, it still appears to be practical and useful. Since the theoretical background and description of the LISF meter are readily available in the cited literature, most of that information will not be repeated here. Instead, this chapter considers the applicability, repeatability, and accuracy of the technique for use in compressible flows as determined by an experimental calibration over a range of Mach numbers.

## 2. FACILITY AND INSTRUMENT DESCRIPTION

The wind tunnel used in this study is an intermittent blowdown facility with a 15x17 cm test section. An asymmetric sliding-block nozzle permits testing over the range  $1.5 < M < 4.0$ . Test times vary from a few seconds to about two minutes at stagnation pressures from 3 to 15 atm and near-ambient stagnation temperatures. A polished stainless steel flat plate spans the test section, with optical glass windows on either side. All results discussed here were obtained with near-adiabatic wall conditions on the flat plate.

Fig. 1 is a diagram of the LISF meter setup currently used for testing in this wind tunnel facility. The instrument consists of a pedestal-mounted optical breadboard, 0.9m x 1.2m in size, upon which are mounted the optical sending and receiving elements of the interferometer. In the sending apparatus, the beam from a 5 milliwatt linearly-polarized helium-neon laser is divided by a beamsplitter, yielding about 50% reflected and 50% transmitted power. The reflected beam from the front surface of the beamsplitter is focused by a lens to form a spot of about 300  $\mu\text{m}$  diameter at an appropriate point on the flat plate in the wind tunnel. The reflected beam from the back surface of the beam-

splitter is blocked. The beam transmitted by the beamsplitter is aimed by an adjustable first-surface mirror and is also focused on the flat plate with the same spot size and incidence angle as the first beam. These two incident beams are positioned to form spots about 1 mm apart on the flat plate.

During experiments, a thin film of oil applied to a local region of the flat plate is sheared by  $T_w$ . Each incident laser beam is reflected by both the surface of the oil film and the polished plate beneath it. This produces two pairs of interfering laser beams directed out of the wind tunnel through a window. These beams are intercepted by two first-surface aiming mirrors, whence each pair is directed onto a separate photodiode through a 6328 Angstrom filter. Each photodiode senses a time-dependent light intensity due to the interference of light reflected from the oil film and test surface. The two photodiode outputs are amplified, low-pass filtered to remove high-frequency noise, and recorded. Direct digitization and storage of these data is accomplished by a micro-computer equipped with an A/D-converter board. For present purposes a 20Hz data rate was chosen, yielding at least 20 points per fringe. The photodiode output is also monitored on a stripchart recorder during experiments.

Fig. 2 shows a typical digitized fringe record from the present data set. Upon startup of the wind tunnel the oil film is initially too thick, resulting in surface waves which scatter the laser beams and cause an abrupt reduction in signal intensity. After a few seconds the thinning of the film begins to suppress the surface waves and visible fringes appear. However, these initial fringes (appearing as sine waves in Fig. 2) are still affected by surface waves. Following the disappearance of surface waves, typically 5 to 9 usable fringes are obtained before the end of a test. Toward the end, the fringe period grows such that less than 1/2 fringe is gained by extending the tunnel run time. Further, as the oil film thins to approach the scale of the surface roughness on the flat plate, additional distortions occur.

### 3. DATA REDUCTION PROCEDURE

Primarily due to the limited fringe count available in a given LISF test in supersonic flow, the data reduction procedure is necessarily somewhat different from that reported by other investigators for incompressible flows. Given only 5-9 fringes, it becomes necessary to determine  $T_w$  based on the entire signal within the usable fringe record. Merely determining the time interval required for a given number of fringes, as is done in incompressible flow, does not yield sufficient accuracy here.

Thus, the first issue is to define that part of the fringe record which is usable. As noted earlier, the initial fringes suffer from surface-wave distortion, rendering them unusable. From experience, we have determined that initial data lying outside the fringe "envelope," shown by dashed lines in Fig. 2, are unusable. A more rigorous criterion is applied later in the data reduction procedure as described below.

The next step in the data reduction procedure is to smooth the raw fringe data. Smoothing is required to eliminate any noise, which would confuse the automated determination of the fringe peaks. Any reasonable smoothing algorithm can be used. A simple adjacent-point averaging technique has been used for the results presented here.

The main equation for LISF data reduction, assuming constant wall shear stress, is given (eq by Monson and Higuchi, 1981) as:

$$x = [T_w \lambda N' t'] / [2n\rho \nu \cos(r)] \quad (1)$$

where  $x$  = distance from oil film leading edge to laser beam spot,  $N'$  = effective fringe number,  $t'$  = effective oil-flow time,  $n$  = oil refractive index,  $\rho$  = oil density,  $\nu$  = oil viscosity,  $\lambda$  = laser wavelength, and  $r$  = oil refraction angle. The use of this equation for compressible LISF data reduction is somewhat complicated by the fact that wall temperature changes affect the oil viscosity directly. For the present experiments, the flat plate wall temperature,  $T_w$ , decreases gradually with time, requiring the following second-order polynomial curvefit:

$$T_w(t) = a_1 + a_2 t + a_3 t^2 \quad (2)$$

The oil viscosity as a function of time can then be expressed, in terms of a reference viscosity  $\nu_r$  at reference temperature  $T_r$ , as:

$$\nu(t) = \nu_r \exp[-s(a_1 + a_2 t + a_3 t^2 - T_r)] \quad (3)$$

where  $s$  = the oil temperature-viscosity coefficient, determined by an independent testing laboratory, of the Dow-Corning "200" silicone oil used in the present experiments.

Using Eqns. 2 and 3, the data points of the fringe signal at each corresponding time,  $t_i$ , are corrected to constant effective  $T_w$  conditions over the length of a wind tunnel test, yielding the following expression for the corrected time interval  $\Delta t_i'$ :

$$\Delta t_i' = (\Delta t + (s a_2 / 2)(t_i^2 - t_s^2) + (s/3)(a_3 + s a_2^2 / 2)(t_i^3 - t_s^3) + (s^2 a_2 a_3 / 4)(t_i^4 - t_s^4) + (s^3 a_2^2 a_3 / 10)(t_i^5 - t_s^5)) \exp[s(a_1 - T_r)] \quad (4)$$

where  $t_s$  is the starting time at which usable fringes begin. The smoothed, temperature-corrected fringe data may now be used to find  $N'$  and  $t'$  for each fringe peak.



Oil lubrication theory dictates that the product  $N't'$  in Eqn. 1, when evaluated at the laser beam spot location where  $x$  is fixed, must also be constant:

$$N't' = (N' + \Delta N_1)(t' + \Delta t_1') = (N' + \Delta N_2)(t' + \Delta t_2') = \text{constant} \quad (5)$$

(Here,  $\Delta N_i$  is the incremental change in fringe number.) Thus, the effective fringe number,  $N'$ , and the effective oil-flow time,  $t'$ , for any fringe peak can be calculated using any other two fringe peaks according to:

$$N' = - [\Delta N_2 (\Delta t_2' / \Delta t_1' - 1)] / [\Delta t_2' / \Delta t_1' - \Delta N_2 / \Delta N_1] \quad (6)$$

$$t' = - \Delta t_1' (N' / \Delta N_1 + 1) \quad (7)$$

In order to minimize the effect of random errors in the fringe data, we have computed  $N', t'$  for each peak using all possible combinations of the other peaks in the signal, then averaged the results.

These results are next compared with oil lubrication theory in the  $N', t'$  plane, as shown by example in Fig. 3. Each triangle shown represents the  $N'$  value of a given fringe peak in the LISF signal. A least-squares curvefit of the data to the lubrication theory is performed, followed by a computation of the reduced chi-squared deviation of the data from the fitted curve. Then, the first fringe peak is eliminated and the fit is repeated. This process is continued up to  $\Delta N = -2$  (the fifth fringe peak from the last peak of the fringe signal). The starting point which results in a minimum reduced chi-squared for the fit defines our rigorous criterion for the best answer. Since lubrication theory is the basis for the LISF meter, those early fringes which are contaminated by surface wave distortions to the extent that they do not fit the theory must be discarded. In the example of Fig. 3 (corresponding to the raw data shown previously in Fig. 2), seven usable fringe peaks remain after this process has been completed. The result of this optimized curvefit is an accurate value of the product  $N't'$ , based on the total usable signal, for use in determining  $T_w$  from Eqn. 1.

Of the remaining parameters in Eqn. 1,  $n$  is known from the oil manufacturer's data. The oil refraction angle,  $r$ , is calculated from the measured incident laser beam angle and Snell's law. Oil viscosity,  $\nu$ , and density,  $\rho$ , are determined based on the constant effective wall temperature of the experiment as discussed earlier. The distance,  $x$ , from the oil film leading edge to the laser beam spot, is measured prior to the experiment by means of a cathetometer with a least count of 0.025 mm. The repeatability of this measurement has been established at  $\pm 2\%$ , using an auxiliary white light reflected from the oil film to aid visibility. In previous work the dual laser spots of the instrument were used to eliminate the measurement of  $x$ . In the present case, however,  $x$  is measured for both spots and the two fringe signals are independently reduced to provide redundancy of the measurement.

#### 4. ISSUES REGARDING COMPRESSIBLE-FLOW LISF MEASUREMENTS

In addition to the data reduction modifications discussed above, several other factors need to be considered in LISF setup and operation in compressible flows:

##### 4.1 Beam polarization and orientation.

For maximum beam reflection intensity with the optics arranged as shown in Fig. 1, the polarization vectors of the incident light beams should be perpendicular to the test surface (S-polarization). This is achieved by rotating the laser in its mount until maximum transmission occurs through a polarizing filter with its axis perpendicular to the test surface. Further, a maximum fringe count is obtained when the beam incidence angle with the test surface approaches 90 deg, which becomes highly desirable for compressible-flow measurements. (This was prevented by window locations in the present experiments. Instead, a 51 deg incidence angle was required as illustrated in Fig. 1.)

##### 4.2 Surface wave phenomena.

As mentioned previously, surface wave phenomena on the oil film appear to impose the most serious limitation on LISF meter usefulness in high-speed flows. Monson, Driver, and Szodrach (1981) found that these waves are promoted by the high shear levels typical of supersonic flows. Murphy and Westphal (1985) found that, as the oil film thins sufficiently, the waves move downstream and LISF data may be obtained near the film leading edge. However, at this point in our high-speed flow tests the film has already become quite thin.

Fig. 4 shows the wave-free oil film thickness as a function of Mach number and oil viscosity from the present experiments. Since  $Re_\theta$  is relatively constant at about 12,000 to 14,000 for all the data shown, the situation tends to improve somewhat as  $M$  increases and  $T_w$  decreases. However, in no case was a usable oil film thickness greater than 2.6  $\mu\text{m}$  obtained.

Thus the surface wave phenomena have a direct impact on the number of usable interference fringes obtainable in a given test, and thus on the accuracy of the results. By carefully analyzing these few obtainable fringes, we have made successful LISF measurements with shear levels up to 205  $\text{N/m}^2$ . However, it seems possible that there is an upper wall shear stress limit on the success of the instrument, and that this places the most serious limitations on the use of the LISF meter in transonic flows at high Reynolds numbers.

#### 4.3 Maximum number of usable fringes.

In view of the above, it is desirable to optimize all test parameters in order to obtain the maximum number of usable fringes,  $N_{max}$ , that can be obtained for given test conditions in high-speed flow. Present results indicate that  $N_{max}$ , for a given test geometry, is a function of  $T_w$ , oil viscosity, and leading-edge distance  $x$ . The effect of Mach number and oil viscosity on  $N_{max}$  is shown in Fig. 5. The highest usable fringe count (9) was obtained at  $M = 3.92$ , where  $T_w = 122 \text{ N/m}^2$ . At  $M = 2.43$ , with  $T_w = 205 \text{ N/m}^2$ , at most 5 fringes were obtained. The effect of oil viscosity over the range of 50 to 1000 centistokes is noticeable, with a value of 500 centistokes yielding the largest number of usable fringes for present flow conditions. The optimum distance,  $x$ , from the oil-film leading edge to the laser beam spot is found to equal the length of wave-free oil film downstream of the film leading edge at the time when supersonic flow is first established (a few seconds after the airflow begins). For present conditions, using 500 centistokes oil, the optimum  $x = 2, 3, 4$ , and 5 mm for  $M = 2.43, 2.95, 3.51$ , and 3.92, respectively.

#### 4.4 Preparation of oil film.

About  $0.03 \text{ cm}^3$  or more of oil is necessary to produce an oil film of sufficient coverage on the test surface. The oil is "pre-thinned" into an initial film by squeezing it with a small flat glass plate prior to the test, thus reducing the lost run time before the surface waves migrate downstream. While a very thin initial film is desirable to minimize surface waves, it is not possible to pre-thin the film to such small dimensions as those shown in Fig. 4. Thus, no attempt is made to rigidly control the initial film thickness. Variations in initial thickness then show up only as variations in the test duration before usable fringes begin to occur. These variations are minimized when the optimum leading edge distance,  $x$ , is maintained as described above.

The oil film leading edge should be straight and normal to the flow direction. After an oil drop is applied to the test surface and pre-thinned, a sharp leading edge is created by cutting the film with the edge of an index card. The region upstream of this leading edge is then cleared of oil by wiping it with lens tissue.

#### 4.5 Preparation of test surface.

The LISF meter has the advantage that it does not require any equipment installation in the surface of a model to be tested. However, it is necessary that the test surface be highly and uniformly polished so that it produces specular light reflection. Given a suitable surface material, such a polish with average irregularity down to  $0.05 \text{ } \mu\text{m}$  can be obtained using a polishing powder such as aluminum. Aluminum surfaces themselves, however, have not performed well in our experience, being too soft to hold the necessary polish during extended testing. While abrasion from particles in the airstream will spoil any surface for LISF work, stainless steel has shown the best polish and durability characteristics during the present experiments.

#### 4.6 Effect of particles in the airstream.

Any particles entrained in the flow tend to disturb the oil film and distort the resulting LISF fringe records. This problem is especially noticeable for test surfaces inclined toward the oncoming airstream, where particle impacts tend to damage the highly-polished surface. Potential LISF users are cautioned that the technique is not likely to succeed in a "dirty" test environment.

#### 4.7 Wind tunnel vibration.

Most interferometric methods are vibration-sensitive, and the LISF meter is no exception. Fortunately, the fringe frequency is well below that of turbulence-generated flow noise, so that effective low-pass signal filtering can be accomplished. Nonetheless, precautions should be taken to isolate the instrument from low-frequency vibrations. The optics should be rigidly mounted to a common frame and kept free of dust. Further, long-focal-length lenses are preferred for laser beam focusing on the test surface in order to minimize vibration-induced changes in beam spot diameter. Finally, both the test surface and any intervening glass windows must be cleaned thoroughly between wind tunnel runs to remove moisture and residual oil.

#### 4.8 Oil film heating by laser beam.

Previous investigators have attenuated their laser beams to avoid the possibility of heating the oil film, thus changing its viscosity. In the present case, the surface temperature beneath the beam spot was monitored for more than one hour with the beam at full power (2.5 mW); no appreciable heating was observed. It is thus recommended that no attenuation be used for helium-neon lasers in the milliwatt range.

#### 4.9 Oil film evaporation.

While evaporation errors appear negligible in low-speed flows, they may be significant in high-speed testing where  $T_w$  is high and static pressure is low. Unfortunately, it appears not possible to make a straightforward calculation of the evaporation rate, since the diffusion coefficients or effective gas constants of polymer oils are unknown. It is known, however, that the vapor pressure of Dow-Corning "200" silicone oil (500 centistokes viscosity) at 10 deg C is a few millionths of an atmosphere, which is far below the minimum tunnel static pressure (0.09 atmosphere) of the present experiments. Further,

the calibration test results presented below show no evidence of a systematic positive error with increasing Mach number, which would result if oil evaporation were significant.

#### 5. CALIBRATION EXPERIMENTS

Given the constraints described above, tests have been carried out to determine the repeatability and accuracy of the LISF meter in a controlled compressible-flow environment. The turbulent boundary layer on the near-adiabatic flat plate described earlier was used for this purpose. For calibration standards, a finite-difference, eddy-viscosity code (EDDYBL), the Van Driest II theory (Van Driest, 1956), and the results of curvefits of the wall-wake similarity law (Settles, 1986) to measured boundary layer profiles have been used. Sixteen LISF tests each were conducted at Mach numbers of 2.43, 3.51, and 3.92, while 19 such tests were conducted at Mach 2.98.  $Re_\theta$  was held relatively constant (between 12,000 and 14,000) for all these data, but several different values of oil viscosity were used.

The calibration results are shown in Fig. 6, where  $c_f/C_{fi}$  is plotted vs. Mach number ( $C_{fi}$  is the equivalent incompressible skin friction coefficient). Error bars on both the LISF and the wall-wake data illustrate the ranges of the values obtained. For comparison, a typical error band from earlier incompressible LISF tests in our laboratory is also shown at  $M = 0$  in Fig. 6.

The overall repeatability of the compressible LISF data is within  $\pm 4\%$ , which is the standard deviation about the mean. The wall-wake curvefit data have similar repeatability, though fewer samples were involved in their determination.

The accuracy of the LISF results may be assessed by the comparison with wall-wake, Van Driest II, and EDDYBL results shown in Fig. 6. At worst, the mean LISF value falls 8% below the mean of the 3 calibration standards at  $M = 2.43$ . This error improves to -3% at  $M = 3.92$ , presumably due in part to the improvement in LISF fringe count as  $M$  increases. The viscosity uncertainty of the silicone oil itself (which contributes an uncertainty of equal magnitude to  $c_f$ ) is within  $\pm 1\%$  as determined by an independent testing lab. Finally, experience indicates that no known skin friction technique has a trusted accuracy better than about  $\pm 3\%$ .

#### 6. CONCLUSIONS

The present LISF meter results in compressible flow demonstrate that the instrument is potentially very useful. It will not replace simpler methods such as the Preston tube or wall-wake fit for flows simple enough to admit the latter. It is also least accurate in cases of extremely high wall shear stress. Nonetheless, the LISF meter has the potential to deliver quasi-direct  $c_f$  measurements in a wide range of compressible flows including rapidly distorted flows, hypersonic flows, and three-dimensional flows. Such measurements are sorely needed, for example, to aid in the validation of computational flow predictions, especially as regards turbulence modeling. The success of the LISF meter in these cases calls for proper data reduction and an awareness of the constraints of the instrument, as discussed above.

A suggested improvement to the instrument is the use of a shorter laser light wavelength, which should increase the fringe count by as much as 20%. Otherwise, more experience with the instrument in complex flows is needed. The present authors have recently carried out three-dimensional LISF measurements in a Mach 3 swept shock wave/boundary layer interaction successfully (Kim and Settles, 1988), which has further demonstrated the utility of the instrument despite flow complexity and very high shear levels.

#### 7. REFERENCES

- Yim, K.-S., and Settles, G. S., 1988, "Skin Friction Measurements by Laser Interferometry in Swept Shock Wave/Turbulent Boundary Layer Interactions," AIAA Paper 88-0497.
- Mateer, G., 1984, private communication.
- Monson, D. J., and Higuchi, H., 1981, "Skin Friction Measurements by a Dual-Laser-Beam Interferometer Technique," *AIAA Journal*, Vol. 19, No. 6, pp. 739-744.
- Monson, D. J., Driver, D. M., and Szodrach, J., 1981, "Application of a Laser Interferometer Skin-Friction Meter in Complex Flows," *Proceedings of the International Congress on Instrumentation in Aerospace Simulation Facilities*, pp. 232-243 (IEEE Publication 81CH1712-9).
- Monson, D. J., 1983, "A Nonintrusive Laser Interferometer Method for Measurement of Skin Friction," *Experiments in Fluids*, Vol. 1, No. 1, pp. 15-22.
- Monson, D. J., 1984, "A Laser Interferometer for Measuring Skin Friction in Three-Dimensional Flows," *AIAA Journal*, Vol. 22, No. 4, pp. 557-559.
- Murphy, J. D., and Westphal, R. V., 1985, "The Laser-Interferometer Skin-Friction Meter - A Numerical and Experimental Study," *Proceedings of the Third Symposium on Numerical and Physical Aspects of Aerodynamic Flows*, Long Beach, CA, Paper 7-1.
- Settles, G. S., 1986, "Recent Skin Friction Techniques for Compressible Flows," AIAA Paper 86-1099.

Tanner, L. H., and Blows, L. G., 1976, "A Study of the Motion of Oil Films on Surfaces in Air Flow, with Application to the Measurement of Skin Friction," Journal of Physics E: Scientific Instruments, Vol. 9, No. 3, pp. 194-202.

Tanner, L. H., 1981, "The Application of Fizeau Interferometry of Oil Films to the Study of Surface Flow Phenomena," Optics and Lasers in Engineering, Vol. 2, pp. 105-118.

Van Driest, E. R., 1956, "The Problem of Aerodynamic Heating," Aeronautical Engineering Review, Vol. 15, No. 10, pp. 26-41.

Westphal, R. V., Bachalo, W. D., and Houser, M. H., 1986, "Improved Skin Friction Interferometer," NASA TM 88216.

Winter, K. G., 1977, "An Outline of the Techniques Available for the Measurement of Skin Friction in Turbulent Boundary Layers," Progress in the Aerospace Sciences, Vol. 18, pp. 1-57.

#### 8. ACKNOWLEDGEMENT

This research was supported by NASA-Lewis Research Center Grant NAG 3-527, monitored by W. R. Hingst. The authors gratefully acknowledge the assistance of F. K. Lu and P. J. Barnhart with the experiments, and useful discussions with D. J. Monson and R. V. Westphal of the NASA-Ames Research Center.

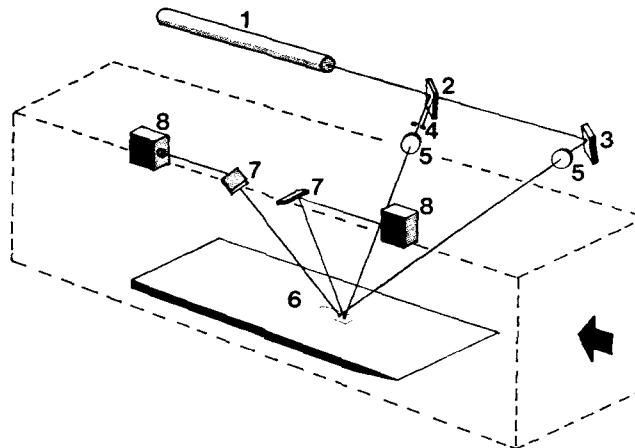


Fig. 1 Diagram of LIFS meter: 1 - He-Ne laser, 2 - 50/50 beamsplitter, 3 - planar mirror, 4 - stop, 5 - focusing lens, 6 - flat plate, 7 - planar mirror, 8 - housing for 6328 Angstrom filter, photodiode, and amplifier.

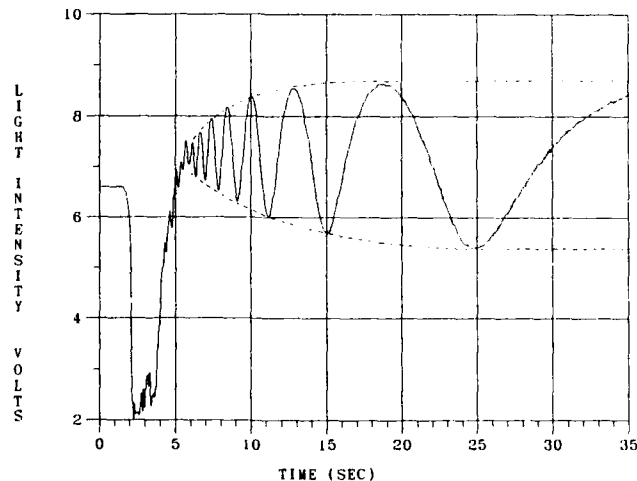


Fig. 2 Typical LIFS fringe record ( $M = 2.98$ ,  $\nu = 500$  centistokes).

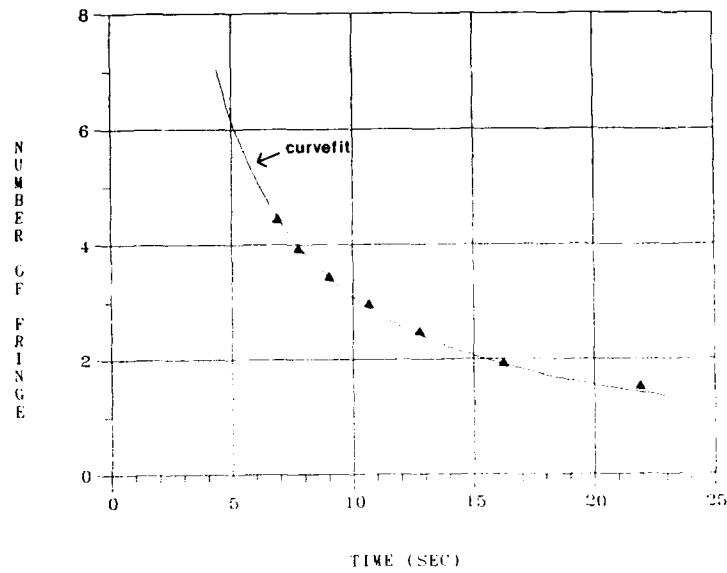


Fig. 3 Typical  $N', t'$  curve ( $M = 2.98$ ,  $\nu = 500$  centistokes,  $\tau_w = 160 \text{ N/m}^2$ ).

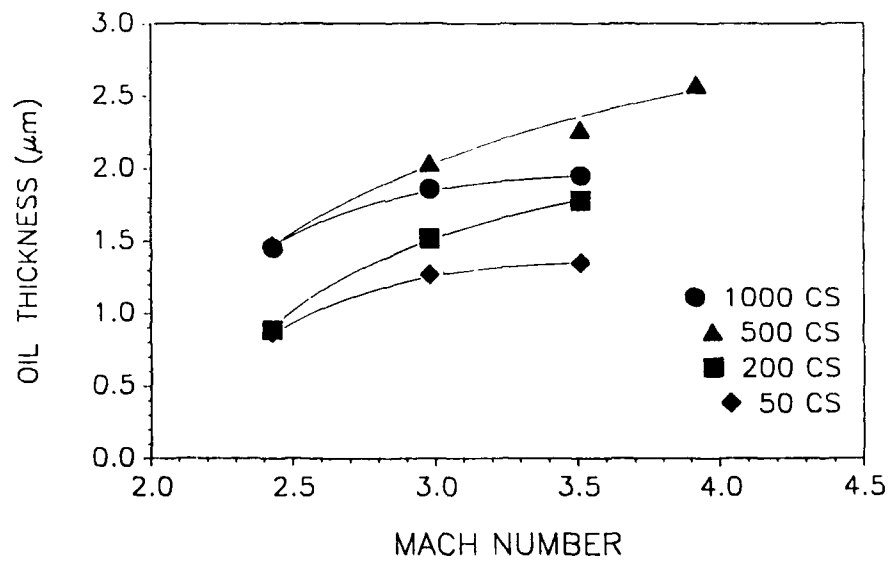


Fig. 4 Wave-free oil film thickness vs. Mach number for various oil viscosities.

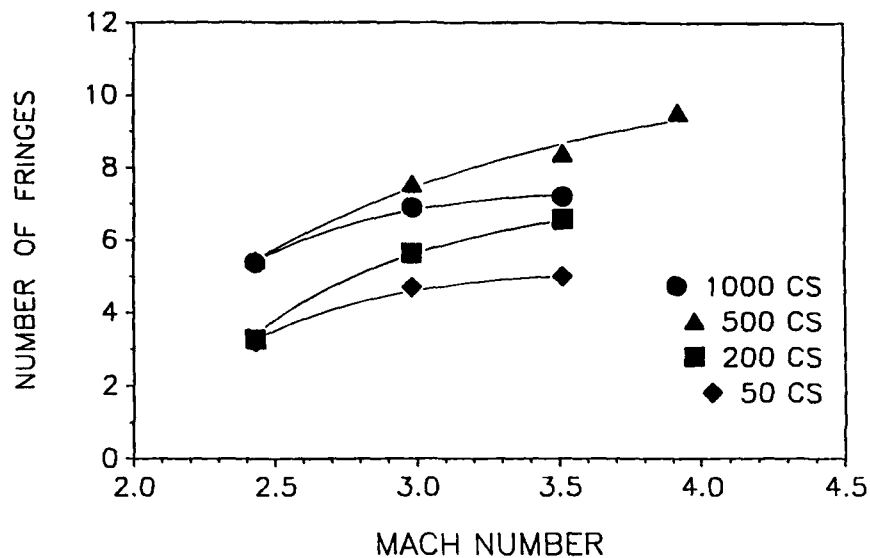


Fig. 5 Maximum number of usable fringes,  $N_{\max}$ , vs.  $M$  for various oil viscosities.

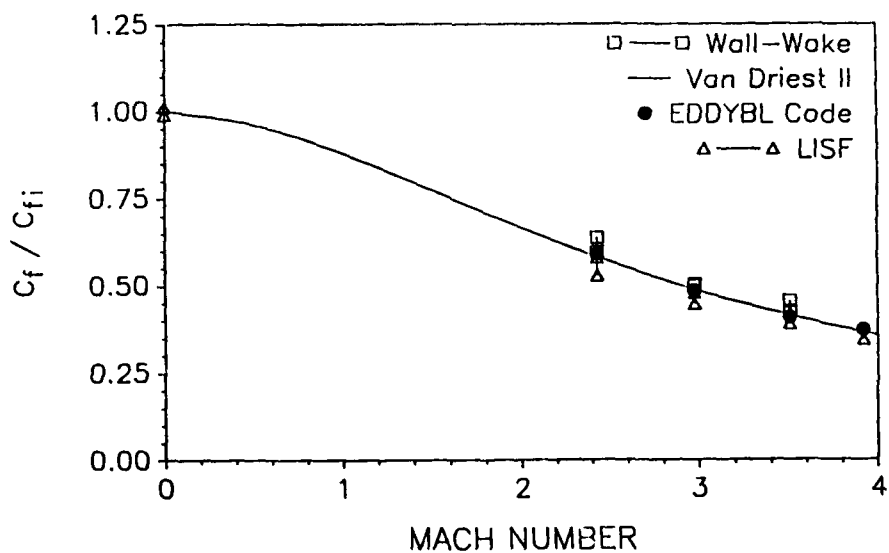


Fig. 6 LISF calibration plot of  $c_f/c_{fi}$  vs. Mach number.

## CHAPTER 5

## HOT-WIRE ANEMOMETRY IN SUPERSONIC FLOW

by

A. J. Smits\* and J.-P. Dussauge\*

\*Department of Mechanical and Aerospace Engineering,  
Princeton University, Princeton, New Jersey 08544, U.S.A.

\*Institut de Mecanique Statistique de la Turbulence, U. M. C. N. R. S. N° 33,  
12 Avenue General Leclerc, 13003 Marseille, France

## 1. INTRODUCTION

Hot-wire anemometers were first used in 1888, according to the extensive bibliography prepared by Freymuth (1978), and the application of hot-wire anemometry to subsonic flows has been systematically researched since that time. Hot-wire anemometry in supersonic flows is more recent, and the earliest work is probably that due to Kovaszny (1950) and Lowell (1950). Further work by Kovaszny (1953, 1954), Morkovin (1956, 1962), Laufer & McLellan (1956), and Kistler (1959) advanced the development of supersonic hot-wire anemometry, and by the early sixties the technique was widely used.

The instrument in general use at that time was of the constant current type. The wire filament was heated using a constant current source, and variations in heat transfer produced fluctuations in wire resistance. There was no feedback loop, and the frequency response was extended beyond the limits of the wire thermal inertia by using a compensating network (see Fig. 1). With the development of stable, integrated-circuit operational amplifiers, it became relatively straightforward to operate the anemometer in a constant-temperature mode. In this mode of operation, a feedback loop is used to keep the wire temperature (and resistance) constant, and variations in heat transfer produce fluctuations in wire current. The main advantage of the constant temperature system is that the feedback loop automatically compensates the frequency response for the thermal lag of the wire filament (see Fig. 2).

In subsonic flows, the constant current mode is still preferred for measuring temperature fluctuations but it has been largely superseded by the constant temperature mode for measuring velocity fluctuations. In supersonic flows, both instruments are still in use, for two major reasons. Firstly, the output of the anemometer is sensitive to fluctuations in mass-flux  $(\rho u)'$  and total temperature  $T_o'$ . To identify the individual contributions due to  $(\rho u)'$  and  $T_o'$ , it is necessary to operate the wire at a number of different wire temperatures or overheat ratios (see Section 3). Since the constant temperature system is not suitable for use at low overheat ratios (Smits et al. 1983), the constant current system must be used. However, at high overheats it is sometimes possible to neglect the contribution to the output due to  $T_o'$ , and then it is possible to use a constant temperature anemometer to measure  $(\rho u)'$  directly.

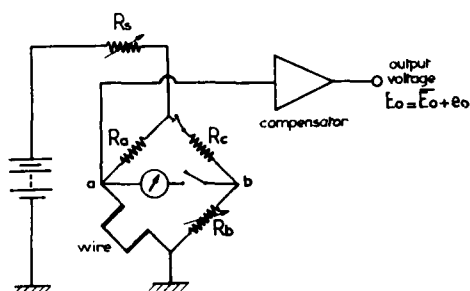


Figure 1. Constant current circuit.

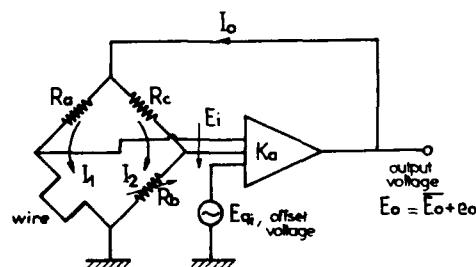


Figure 2. Constant temperature circuit.

The second major reason is that in supersonic flows, the frequency content of the signal is generally very broad. In the past, only the constant current system with its open loop response offered a sufficiently wide dynamic range. In the last ten years, however, constant temperature systems with balanced bridges have become commercially available, and an upper frequency response of 300 to 400 kHz is possible with careful adjustment.

In the present chapter, we summarize the theory and practice of both types of anemometer, and we discuss the advantages and disadvantages of each system. We begin in Section 2 by considering probe designs suitable for supersonic flow. Next, the behavior of a single wire placed normal to the flow direction is examined, including its quasi-static response (Section 3), and its dynamic response (Section 4). The behavior of inclined and crossed-wire probes is discussed in Section 5, and the effects of low Mach and Reynolds numbers are considered in Section 6. The Chapter concludes with two examples chosen to illustrate the uncertainties in the measurement (Section 7).

## 2. PROBE DESIGN

The probes used in supersonic flow differ somewhat from those used in subsonic flow for reasons of aerodynamic design and strength. It is important, for example, to taper the prongs and use a wedge-shaped body to minimize aerodynamic interference, and the prongs are usually kept short to reduce vibrations and deflections under load (Fig. 3). For crossed wires (Fig. 4), shocks emanating from one wire and its supports may interfere with the other wire, and the probe must be designed to avoid this interference at all Mach numbers. Recent work suggests that commercially available probes can be used when the prongs are shortened and wedge-shaped fillets are added (Donovan, Dussauge, Horstman, private communications, Bonnet & Knani 1986).

The filament can be soldered or welded to the prongs, using tungsten, gold-plated tungsten, or platinum-plated tungsten as the filament material (platinum, or platinum-rhodium is not recommended unless the aerodynamic loading is extremely low). It also seems possible to attach the filament by glueing (Doughman 1972) but the authors have had no experience with this technique. In the soldered design (Fig. 3a), the filament material is first coated with copper to a diameter 5 to 10 times the filament diameter. The coated wire is soldered to the prongs and the central portion of the coating is etched away using a dilute acid to expose the active portion of the wire. By this procedure, the aerodynamic interference caused by the relatively bulky prongs is reduced, and the active length is well

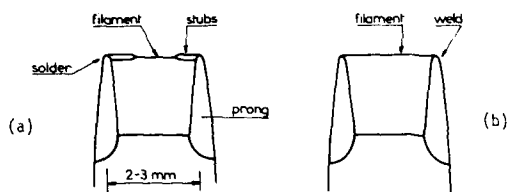


Figure 3. Hot-wire probes: (a) normal wire, "etched" design; (b) normal wire, "welded" design.

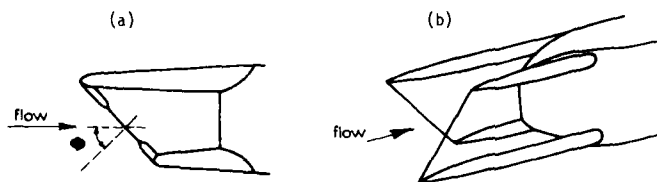


Figure 4. Hot-wire probes: (a) single-inclined wire probe; (b) crossed wire probe.



defined. In the welded design (Fig. 3b), the uncoated wire filament is attached to the prongs directly by welding. Care must be taken to use finely tapered prongs to minimize aerodynamic interference.

The length of the active filament  $l$  is usually between 0.5 mm and 2 mm, and the diameter  $d$  ranges from 1  $\mu$ m to 5  $\mu$ m. If the wire is too long, the spatial resolution deteriorates. If the  $l/d$  ratio is too small, the temperature distribution along the wire is highly non-uniform, and heat conduction to the stubs and prongs can be significant (see Section 4.2). If the  $l/d$  ratio is too long, wire breakages are more common. Choosing the optimum length and diameter is always a compromise, and further recommendations regarding filament size will be given in subsequent sections.

### 3. STATIC RESPONSE OF A NORMAL WIRE

#### 3.1 Sensitivity of the Wire

We begin by considering the quasi-static response of a wire oriented at right angles to the direction of a supersonic flow. A detached bow shock forms, and the front face of the wire is exposed to subsonic flow downstream of this nearly normal shock. Since the major part of the heat transfer occurs by convection over the front surface area of the filament, it is a good approximation for reasonable Reynolds numbers ( $Re > 20$ ) to neglect the sensitivity of the heat transfer to Mach number outside the transonic regime (that is, outside the range  $0.8 < Ma < 1.2$ ) (see Section 6). When Mach number effects and low Reynolds number effects can be neglected, the wire voltage fluctuation produced by small, slow perturbations in flow parameters may be written as

$$e' = \frac{\partial E}{\partial (\rho U)} (\rho U)' + \frac{\partial E}{\partial T_o} T_o' \quad (1)$$

$$\text{That is,} \quad \frac{e'}{E} = F \frac{(\rho U)'}{\rho U} + G \frac{T_o'}{T_o} \quad (2)$$

where  $e'$  is the wire voltage perturbation due to variations in  $(\rho U)'$  and  $T_o'$ , and where it has been assumed that there are no fluctuations in wire resistance (for constant temperature operation) or current (for constant current operation). The overbars denote time averaged quantities, and

$$F = \partial \ln E / \partial \ln \rho U \quad (3a)$$

$$G = \partial \ln E / \partial \ln T_o \quad (3b)$$

Equation 2 follows directly from the assumed functional dependence of the heat transfer, and it does not depend on any particular heat transfer law. All calibration procedures described in this chapter are also independent of any such heat transfer law, although sometimes an empirical heat transfer relationship will be assumed to illustrate a point.

In this simple static analysis, the anemometer output voltage  $e_o'$  is directly proportional to the wire voltage  $e'$  for both the constant current and the constant temperature system. The evaluation of  $F$  and  $G$ , however, depends strongly on the mode of operation.

Equations 1 and 2 indicate that the response is sensitive to fluctuations in stagnation temperature and mass-flux. It can be shown that the relative sensitivity  $F/G$  depends strongly on  $A_w$ , where  $A_w = (\partial \ln R_w / \partial \ln I) / 2$  and  $A_w$  is only a function of the overheat ratio  $a_w \equiv (R_w - R_e) / R_e$  (Bestion et al. 1983). Here,  $R_w$  is the wire resistance at the operating temperature, and  $R_e$  is the wire resistance at the recovery or equilibrium temperature  $T_e$ . Figure 5 shows the variation of  $F/G$  with overheat ratio for a typical wire. The curve is independent of the mode of operation of the anemometer (at the same Reynolds number, when the Reynolds number is low). At low overheats, the output is primarily sensitive to  $T_o'$ , and if the overheat is low enough the sensitivity to  $(\rho U)'$  can be neglected. At high overheats, the output is primarily sensitive to fluctuations in mass-flux, but it is not possible to increase  $a_w$  to the point where the output is sensitive only to  $(\rho U)'$  because there is an upper limit on the overheat set by material property limitations. At high overheats, therefore, the anemometer always operates with a degree of mixed-mode sensitivity.

For time-averaged measurements, we have

$$\frac{\overline{e'^2}}{\overline{E}^2} = F^2 \frac{(\overline{\rho u})'^2}{\overline{\rho u}^2} + 2 FG \frac{(\overline{\rho u})' \overline{T_o'}}{\overline{\rho u} \overline{T_o}} + G^2 \frac{\overline{T_o'^2}}{\overline{T_o}^2} \quad (4)$$

and in principle it is possible to determine  $\overline{(\rho u)'^2}$ ,  $\overline{(\rho u)' T_o'}$  and  $\overline{T_o'^2}$  by operating at three different overheats. In practice, at least 15 different overheats must be used, and the results are analyzed using the fluctuation diagram method first suggested by Kovaszny (1953). If the pressure fluctuations are small,  $\overline{u'^2}$ ,  $\overline{T'^2}$  and  $\overline{u'T'}$  may be found by using the definition of the total temperature and the equation of state. By using the same procedure within fixed frequency bands, it is possible to obtain the spectral distribution of velocity and temperature (see, for example, Bestion 1982).

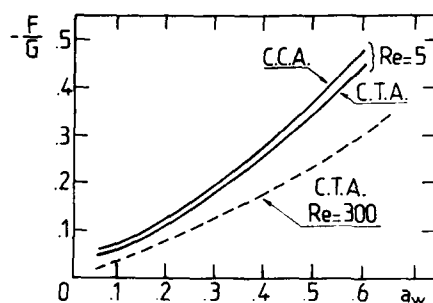


Figure 5. Variation of the sensitivity ratio with overhear ratio and Reynolds number (from Bestion et al. 1983).

The fluctuation diagram method is usually carried out over the range  $0.02 < a_w < 0.5$ . Unfortunately, the constant temperature system is difficult to use at low overhear ratios because small fluctuations in  $T_o$  cause large relative changes in  $a_w$  and serious non-linearities occur (Smits et al. 1983). Moreover, the sensitivity to  $T_o'$  tends rapidly to zero as  $a_w$  decreases. The fluctuation diagram technique can therefore be recommended only for use with a constant current system. However, if  $T_o'$  is small, the constant temperature system can be used at high overhear to measure  $(\rho u)'$  directly. Alternatively, it may be possible to use a constant current anemometer at a very low overhear to measure  $T_o'$  directly, and simultaneously use a constant temperature anemometer at high overhear to measure the output due to both  $(\rho u)'$  and  $T_o'$ . By recording the signals,  $u'$  and  $T'$  may be found as a function of time, as long as pressure fluctuations can be neglected.

For adiabatic flows,  $T'$  and  $u'$  can often be found by assuming the Strong Reynolds Analogy (Morkovin, 1962). That is,

$$\frac{\sqrt{\overline{T'^2}}}{\overline{T}} = (\gamma - 1) Ma^2 \frac{\sqrt{\overline{u'^2}}}{\overline{u}} \quad (5)$$

When  $p'$  is small,

$$\frac{\overline{u'^2}}{\overline{u}^2} = \frac{(\overline{\rho u})'^2}{(\overline{\rho u})^2} \left[ 1 - 2 R_{Tu} (\gamma - 1) Ma^2 + (\gamma - 1)^2 Ma^4 \right]^{-1} \quad (6)$$

(see also Debieve 1976). The correlation coefficient  $R_{Tu}$  has been measured in a variety of undistorted and distorted boundary layers without heat sources, and it appears to be virtually constant across the layer and equal to 0.8 (Dussauge & Gaviglio 1981). Relationships 5 and 6 are particularly useful for deducing  $u'$  and  $p'$  from measurements of  $(\rho u)'$  by a constant temperature anemometer.

### 3.2 Calibration

Calibration depends on the mode of operation. For a constant temperature system at high overheat, it is necessary to record the mean output voltage  $E_0$  while varying the mass-flux over a range slightly larger than that encountered in the experiment (for details see Gaviglio 1971). This gives a plot of  $E_0$  versus  $\rho U$  (or  $Nu$  versus  $Re$ , if preferred). What is required, however, is the logarithmic slope of this curve  $\partial \ln E_0 / \partial \ln \rho U$ . To avoid differentiating discrete data, the calibration points are usually fitted by some polynomial and the sensitivity coefficients are derived analytically. Curve fitting experimental data to obtain derivatives is also a difficult procedure and great care must be taken to obtain accurate results. When acquiring the experimental data digitally, it is possible to avoid the use of sensitivity coefficients by inverting the calibration data for each point. For a constant temperature system at high overheat ratio,  $F$  appears to be almost independent of Reynolds number and overheat ratio (see Fig. 6). This result could be anticipated from the heat transfer law suggested by Kovaszny (1954), which gives  $F \approx n/2$ , where  $n$  is the exponent on the Reynolds number in the  $Nu(Re)$  relationship. At low Reynolds numbers,  $F$  is no longer constant at low overheat but since the constant temperature system should only be used at high overheats ( $a_w > 0.4$ ) this effect can usually be ignored.

For a constant current system, the calibration is more complex because two sensitivities  $F$  and  $G$  must be found at each overheat ratio. In the usual procedure, the output current  $I_0$  is measured while varying  $a_w$  at constant mass-flux and total temperature. The mass-flux is then changed, and the procedure is repeated until the required mass-flux range has been covered. The calibration is obtained as curves of  $I_0$  versus  $a_w$  at different mass-flux values. A combination of curve fitting and interpolation is used to find the sensitivity  $F$  at any particular operating point, and since  $F$  is almost independent of  $T_0$  (see below), this procedure gives  $F$  under all operating conditions.

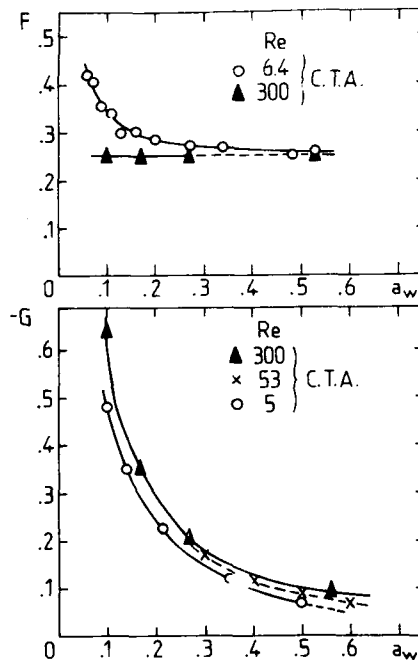


Figure 6. Sensitivity coefficients of CTA to mass flux ( $F$ ) and stagnation temperature fluctuations ( $G$ ) as a function of overheat ratio and Reynolds number (from Bestion et al. 1983).

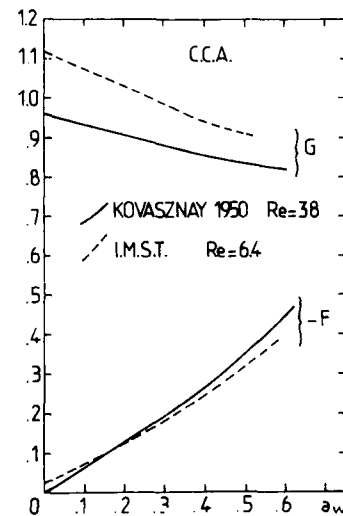


Figure 7. Sensitivity coefficients of CCA to mass-flow ( $F$ ) and to stagnation temperature fluctuations ( $G$ ) as a function of overheat ratio. Solid lines, results from Kovaszny (1950); dotted lines, results obtained at IMST (Institut de Mecanique Statistique de la Turbulence, Marseille). From Bestion et al. 1983.

where  $K = \partial \ln R_w / \partial \ln T_w$ , and where it has been assumed that the fluid thermal conductivity and viscosity vary according to

$$G = K + A_w (K - 1 - a) - bF \quad (7)$$

To find  $G (= \partial \ln E_0 / \partial \ln T_0)$ , we could vary  $T_0$  while keeping the mass-flow rate constant. This is difficult to achieve in practice, and we make use of the fact that for high enough Reynolds number,  $G$  may be written as

$$\frac{k}{k_e} = \left( \frac{T}{T_e} \right)^a \quad \text{and} \quad \frac{\mu}{\mu_e} = \left( \frac{T}{T_e} \right)^b$$

In Equation 7,  $F$  is known from the mass-flux calibration, and  $K$  can be found by placing the unheated wire in a variable temperature oven. The parameter  $A_w$  may be derived from the mass-flux calibration (for a constant current system  $A_w = 2 (\partial \ln Nu / \partial \ln Re)^{-1}$ ), or it can be found directly during the experiment by measuring the changes in  $I_0$  and  $R_w$  as the overheat is varied at a fixed mass-flux. The constants  $a$  and  $b$  are available from the literature but some uncertainty exists. Kovaszny (1950) uses  $a = b = 0.768$ , Morkovin (1956) suggests  $a = 0.885$ ,  $b = 0.765$ , and Grant & Kronauer (1962) use  $a = 0.86$ ,  $b = 0.71$ . The effect on typical boundary layer measurements seems to be rather small (see Section 7).

The behavior of  $F$  and  $G$  for typical constant current wires is shown in Fig. 7. The sensitivity  $F$  is almost a linear function of  $a_w$ , a result which may be expected from the heat transfer law given by Kovaszny (1954) which can be used to show that  $F \approx n a_w$  at high Reynolds number. A weak Reynolds number dependence is observed, mainly because the recovery ratio  $r = T_e/T_0$  depends on Reynolds number for  $Re < 20$  (Laufer & McLellan 1956). The sensitivity  $G$  varies with overheat ratio but it is almost independent of Reynolds number, according to equation 7 ( $K$  is a material property,  $A_w$  varies approximately as  $a_w$ ,  $a$  and  $b$  are fluid properties). The differences shown in Fig. 7 are probably due to differences in material properties since the dominant term in the expression for  $G$  at high Reynolds number is usually the parameter  $K$ .

Finally, we need to consider how  $F$  and  $G$  vary with changes in mean stagnation temperature. When  $T_0$  changes during calibration or measurement, corrections may be required to allow for changes in  $F$  and  $G$ . In fact, for the constant temperature system,  $F$  is almost independent of  $T_0$  for high Reynolds numbers and overheat ratios, and temperature corrections are only necessary if the absolute value of  $(\bar{u})'$  is required and  $\bar{u}$  is deduced from the mean hot wire output. However, the hot wire is not a very suitable instrument for measuring mean flow quantities, and this practice should be avoided. If  $\bar{u}$  is available from additional measurements, temperature corrections are not required at any stage and  $(\bar{u})'$  can be found directly.

For the constant current system,  $F$  is virtually a unique function of overheat ratio when the Reynolds number is high. The sensitivity  $G$  is a function of  $a_w$  and  $T_e$ , and  $Re$  is usually found during measurement by extrapolating the graph of  $R_w$  versus  $R_w I^2$  to zero current. Hence, temperature corrections due to changes in  $T_0$  can be accommodated by correcting the overheat ratio and the equilibrium temperature appropriately.

In summary, the calibration of hot wires in supersonic flow appears to be remarkably well-conditioned procedure. For a constant temperature system at high overheat ratio, the sensitivity to fluctuations in mass-flux is almost completely independent of Mach number, Reynolds number and overheat ratio. (Since the constant temperature system should not be operated at low overheats, the behavior of  $F$  at low overheats and  $G$  at any overheat is not of interest.) For a constant current system, the variation of  $F$  and  $G$  with Reynolds and Mach number appears to be negligible for  $Re > 20$ , but  $F$  and  $G$  both depend on overheat ratio.

These observations are not meant to suggest that calibrations are not important. Different wires can display significantly different behaviors, and each wire must be calibrated before and after each experiment to ensure accurate measurements (see also Section 7).

#### 4. DYNAMIC RESPONSE OF A NORMAL WIRE

##### 4.1 Compensation For Thermal Inertia

The wire filament has a thermal inertia determined by its volume, specific heat capacity, and the rate of heat transfer. A wire without end conduction behaves as a simple pole with a time constant  $T_w$ , and a typical value for  $1/(2\pi T_w)$  is 400 Hz. The frequency content of the turbulent fluctuations is very much higher, and the response must be compensated electronically to resolve the entire frequency content. For example, to measure  $u'^2$  in a boundary layer to within 10% accuracy, Kistler (1959) suggested that the upper frequency response of the system  $f_R$  must exceed  $5U_\infty/\delta$ , where  $U_\infty$  is the freestream velocity and  $\delta$  is the boundary layer thickness. For a typical application (Example 2 in Table 1), we find  $5U_\infty/\delta = 240$  kHz. This criterion ignores the Reynolds number and Mach number dependence of the frequency content, as well as the variation with distance from the wall, and in the wall region a better criterion is perhaps given by  $f_R > U_\infty/y$ . Even if this frequency response is achieved, it is a criterion based on rms measurements, and the shape of the high frequency end of the spectrum will still be distorted. Furthermore, the bandwidth required for the measurement of the transverse velocity fluctuation  $v'$  is even greater because the  $v'$  spectrum is broader than the  $u'$  spectrum (see Section 5.2, and Gaviglio et al. 1981).

In the constant temperature system, the compensation for thermal lag is achieved automatically by the use of feedback. For maximum frequency response, a symmetrical bridge must be used, and careful tuning is required. Bridge inductance and capacitance, cable length, and feedback amplifier characteristics all need to be adjusted carefully using the method of square wave injection (see Perry 1982, Watmuff 1987). The results of the square wave test agree well with those obtained by direct heating of the wire for  $\alpha_w < 0.1$  (Bonnet & Alziary de Roquefort 1980), and it appears to be a reliable technique for setting the frequency response. The optimum value of  $f_R$  varies approximately as  $\alpha_w^{1/3}$  (Smits et al. 1983) and the best response is achieved at the highest overheat.

In the constant current system, the compensation is achieved using a network which approximates a simple zero with time constant  $T_c$ . The time constant  $T_c$  is adjusted until it matches the wire time constant  $T_w$ . This adjustment requires great precision because a small mismatch causes a step in the frequency response of magnitude  $(1 - T_w/T_c)$ , at a frequency near  $1/T_w$ . The adjustment is usually performed at each operating point by injecting a square wave current perturbation across the bridge. Several factors limit the accuracy of this process. Firstly, end conduction effects are important (see Section 4.2). To minimize these effects, the frequency of current injection should be much greater than  $1/T_w$ . Secondly, current perturbations are not equivalent to velocity and temperature perturbations. Differences can occur if the bridge is not perfectly balanced, or if stray bridge inductances are present (Smits 1974, Perry 1982). Thirdly, the current perturbation must be small enough to avoid non-linearities yet large enough to make the signal clearly visible over the background turbulence. Phase averaging and autocorrelations could be used to overcome this difficulty. Without these refinements, repeatability tests show that the mismatch between  $T_w$  and  $T_c$  is typically less than 5% (representing 10% error in  $e^{-x^2}$ ).

As mentioned above, the transfer function of the compensating network is not quite a simple zero, and it has an additional pole at a frequency of about  $100/T_w$  which limits the maximum bandwidth of the system (Gaviglio & Dussauge 1977, Gaviglio 1978). Decreasing  $T_w$  will increase this cut-off frequency, with the additional benefit of reducing high frequency noise. It may be shown that for a given wire material  $T_w$  varies approximately as  $(1 + \alpha_w)d^2/Re^n$ , for high Reynolds numbers (Hinze 1959). Since  $n \approx 0.5$ , it is advantageous to use wires of small diameter. The lower limit on  $d$  is given by the Knudsen number, where  $Kn = Ma/Re$ , and for low Reynolds numbers, the continuum hypothesis may break down. Decreasing the wire diameter also decreases its mechanical strength, and in practice the diameter tends to fall in the range  $2 \mu m < d < 5 \mu m$ .

Since the compensation is unlikely to be adequate even under ideal conditions, it may be necessary to correct the output. Two methods have been proposed. In the first method, the system transfer function is determined by a preliminary calibration and the signal spectrum is corrected accordingly (Laderman & Demetriades, 1974). In the second method, the variance of the measured signal is related to the variance of the ideal signal using the experimental autocorrelation (Gaviglio & Dussauge 1977, Gaviglio 1978). Debieve (private communication) found the accuracy of the two methods to be comparable. It should be noted that the compensations for amplitude and phase are different, and the phase compensation is limited to lower frequencies than the amplitude compensation (Owen & Fiore 1986).

#### 4.2 End-conduction effects

Thus far, it has been implicitly assumed that the temperature of the filament was constant along its length, that is, the filament was infinitely long. For a wire of finite length there is heat conduction to the supports, and the temperature distribution is no longer uniform. Furthermore, heat conduction along the wire and through the prongs modifies the frequency response of the sensor. Steps in the amplitude Bode diagram can occur, similar to those arising from inaccurate compensation, and they can cause errors in measuring variances, spectra, and correlations. End conduction effects can also introduce phase differences between sensors, and the effect on space-time correlations can be particularly significant. These effects depend strongly on the geometry of the probe and the boundary conditions on the wire, and probes of the soldered design will behave differently from those of the welded design. End-conduction effects also depend on the mode of operation and the overheat ratio.

For the constant-temperature system, end-conduction effects have only been studied for probes of the soldered design operating in an incompressible flow (Perry et al. 1979). The analysis indicates that these effects are small at high overheats, provided the temperature distribution along the wire is symmetrical. With asymmetrical temperature profiles, caused by wire property variations, surface contamination, and wire bowing, significant end conduction effects can occur. Heat waves can travel along the wire and change its effective time constant. A single, distributed step in the frequency response occurs, in the range 20 Hz to 1 kHz, and experimental results suggest that the resulting error in rms turbulence level can be as high as 10%. These effects are difficult to predict but they do not appear to be systematic. Thus, repeating the same measurement using different probes can help to establish the error band. It is not clear that these results apply to a supersonic flow. Nevertheless, it seems reasonable to suppose that similar effects can occur, and caution is required.

For constant current operation, the phenomenon has been studied in subsonic and supersonic flow (Smits 1974, Smits et al. 1978, Moughangola, 1986). The results are qualitatively in mutual agreement. The responses to  $\langle \rho u \rangle'$  and  $T_0'$  are affected differently, in amplitude and phase, and they depend critically on the boundary conditions applied at the point where the filament joins the support. The boundary conditions for a soldered wire are given by the properties of the stub, which has a time constant  $T_s$  and a non-dimensional heat transfer coefficient  $K_s$ . Similarly, a welded wire is connected to a prong characterized by  $T_p$  and  $K_p$ . Typical values for the parameters are  $T_s = 0.01$  sec,  $T_p = 0.5$  sec, and  $K_s \ll K_p$  (Perry 1982). Note that  $K = \infty$  corresponds to infinitely conducting supports, and  $K = 0$  implies perfectly insulating supports.

The response to temperature fluctuations (at low overheat ratios) displays two steps in the amplitude Bode diagram. The first step is down, at a frequency close to  $1/T_p$  (or  $1/T_s$ ), and the second step is up, at a frequency near  $1/T_w$ . For both types of support, the steps are equal in magnitude, and since the frequencies of interest in supersonic flow are always greater than  $1/T_w$ , it appears that end conduction effects can be ignored in the measurement of  $T_0'$ . To avoid errors in setting the compensator, the frequency of current injection should either be much greater than  $1/T_w$ , or it should cover a wide range of frequencies.

The response to fluctuations in mass-flux (at high overheat ratios) also displays two steps. Again, the first step is down, at a frequency close to  $1/T_p$  (or  $1/T_s$ ), and the second step is up, at a frequency near  $1/T_w$ . However, the two steps are not of equal magnitude. The first step has a magnitude approximately equal to  $(K + 4\beta)/(K + 2\beta)^2$ , and the second step is approximately equal to  $1/2\beta$ , where

$$\beta = \frac{\ell}{d} \left( \frac{Nu}{(1+a_w)} \frac{k_f}{k_w} \right)^{1/2} \quad (8)$$

$k_f/k_w$  is the ratio of heat conductivities for fluid and wire at the mean film temperature. Since  $K$  is generally large, the first step is usually small but for typical values of  $\beta$  (2 to 10), the second step is not. Note that for  $K = 1.24$  the two steps are of equal magnitude, and end conduction effects can be neglected for high frequencies. This would be difficult to achieve in practice. A more successful approach to reducing end conduction effects would be to make both steps small by making  $K$  and  $\beta$  large. It is particularly important to make  $\beta$  large, and this is most easily achieved by increasing the  $\ell/d$  ratio. Remember that limits on  $\ell/d$  are set by spatial resolution (Section 4.3), mechanical strength and Knudsen number (Section 4.1).

End-conduction effects are particularly difficult to control, and they may represent the largest source of error in measuring  $(\rho u)'$ . Further work is required, and it is suggested here that a direct experimental comparison between a constant temperature and a constant current system may lead to a better understanding of the phenomenon.

#### 4.3 Spatial Filtering

The smallest scales of motion in a turbulent flow will have a length scale given by the Kolmogorov length scale  $\eta_k$ . In a flow where  $\eta_k \ll \ell$ , the hot wire attenuates the small scale contributions to the turbulent signal and distorts the high frequency end of the spectrum. Although this problem is a familiar one, there is no special theory for supersonic flow. In supersonic flows which are approximately self-preserving, however, the turbulence characteristics are similar to those observed in subsonic flow (Morkovin 1962, Spina & Smits 1987) and it should be possible to estimate the effects of spatial integration in supersonic flows by using the results obtained in subsonic flows. For instance, Wyngaard (1968) suggests that when  $\eta_k/\ell \rightarrow 0$ , the measured one-dimensional spectrum falls to one-half its true value at a wave number of  $2.1/\ell$ . For the second example in Table 1, the corresponding frequency  $f_s$  is about 200 kHz. For the motions in the outer flow, the appropriate length scale is  $\delta$ , and  $f_s \delta/U \approx 5$ . Near the wall, however, the length scales decrease, and the effects of spatial integration become more serious. The effects can be reduced by decreasing  $\ell$  but there is an obvious limit on  $\ell$  if a reasonable  $\ell/d$  ratio is required at the same time.

#### 4.4 Strain-Gaging

The term "strain-gaging" describes a type of high frequency noise with very limited bandwidth that sometimes appears on the signal spectrum as shown in Fig. 8. Traditionally, this phenomenon has been ascribed to the fluctuations in mechanical tension produced by high frequency changes in aerodynamic loading. Hence the term "strain-gaging". It is often suggested in the literature that to avoid strain-gaging the wire tension should be reduced by deliberately slackening the wire. In the authors' experience, there is no strong correlation between wire slack and strain-gaging. The phenomenon appears to be extremely complex, and it may depend on the electronic characteristics of the anemometer, as well as wire and fluid properties (see Watmuff, 1987). Since strain-gaging is so poorly understood, no specific recommendation can be made to avoid its effects, except the traditional slackening of the wire.

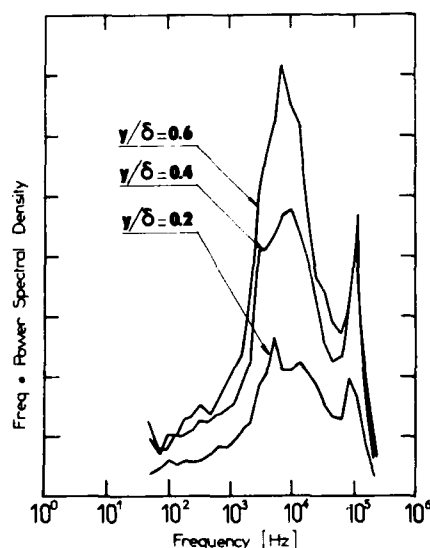


Figure 8. Spectra of  $(\rho u)'$  measured at three positions in a zero pressure gradient boundary layer showing peak at 100 kHz due to "strain-gaging".

## 5. INCLINED WIRES

### 5.1 Static Response

When the wire is inclined to the mean flow direction, the output is sensitive to  $(\rho u)'$ ,  $T_o'$  and  $v'$ . For small, slow fluctuations

$$\frac{e}{E} = F \frac{(\rho u)'}{\rho U} + G \frac{T_o'}{T_o} + H \frac{\bar{\rho} v'}{\rho U} \quad (9)$$

where

$$H = \partial \ln E / \partial \Psi \quad (10)$$

The sensitivities  $F$  and  $G$  were given by Equation 3, and they can be determined by a calibration similar to that described for a normal wire (Section 3.2). The parameter  $H$  can be found by yawing the wire through a small angle, typically  $\pm 10^\circ$ .

If it is assumed that the wire heat transfer depends on an "effective" mass-flux which is geometrically related to the longitudinal mass-flux, it follows that the ratio  $\xi = H/F$  is only a function of wire angle. The analysis by Reshotko & Beckwith (1958) for an infinitely long wire supports this hypothesis as long as the Mach number in the direction normal to the wire is outside the transonic range. The analysis also indicates that  $\xi$  increases by a factor of about 2 as the Mach number increases from about 0.8 to 1.2, and the experiments by Smits & Muck (1983) using wires of the soldered design confirmed this result.

In contrast, Anguillet (1980), Bestion (1982) and Bonnet & Knani (1986) found that for wires of the welded design  $\xi$  depended strongly on overheat ratio. Also, Bonnet & Knani reported that for some short wires  $\xi$  was similar to that observed in subsonic flows, whereas for other wires  $\xi$  was about twice the subsonic value, as predicted by Reshotko & Beckwith. They suggested that small differences in aerodynamic interference may have been responsible. In any case, if the angular sensitivity is calibrated over the range of conditions experienced in the experiment no assumptions about the heat transfer law are required. Note that for constant current operation, since  $\xi$  is a function of  $a_w$  (Bonnet & Knani 1986),  $\xi$  should be calibrated at each overheat.

When a single inclined wire is used in the measurement, two traverses are made. If the wire is first oriented as shown in Fig. 4, (subscript 1) and then rotated  $180^\circ$  about the probe axis (subscript 2), we obtain

$$\frac{e_1^2}{E_1^4} - \frac{e_2^2}{E_2^4} = 4H \left[ F \frac{\bar{\rho} (\rho u)' v'}{\rho U^3} + G \frac{\bar{\rho} v' T_o'}{\rho U T_o} \right] \quad (11)$$

and

$$\frac{e_1^2}{E_1^4} + \frac{e_2^2}{E_2^4} = 2 \left[ F^2 \frac{(\rho u)^2}{\rho U^2} + G^2 \frac{T_o'^2}{T_o^2} + H^2 \frac{\bar{\rho} v'^2}{\rho U^2} + 2FG \frac{(\rho u)' T_o'}{\rho U T_o} \right] \quad (12)$$

In principle, the six unknowns in equations 11 and 12 can be found by operating the wire at three different overheats in each orientation. In practice, this approach is usually limited to constant current operation (see Section 3.1), and it is necessary to use up to 10 values of  $a_w$ . Even then, the terms in Equation 12 suffer from an accumulation of errors, and it is difficult to obtain accurate results. The mode diagram for Equation 11 has the advantage of being linear but it is formed by finding the difference between two large quantities, and the procedure is inaccurate at low overheat ratios. At high overheat ratios, small differences can occur in the compensation for thermal inertia between orientations 1 and 2 (caused by a shift in wire temperature distribution due to changes in the flow field around the probe), and large errors can occur. Hence, the use of inclined wires in the constant current mode is usually limited to overheat ratios where  $0.3 < a_w < 0.5$  (Anguillet, 1980).

It is possible to use constant temperature operation when the overheat ratio is large and the fluctuations in stagnation temperature are small. Then

$$\frac{e_1^2}{E_1^4} - \frac{e_2^2}{E_2^4} = 4HF \frac{\bar{\rho} (\rho u)' v'}{\rho U^3} \quad (13)$$

and it is possible to find  $(\rho u)' v'$  directly (see Smits & Muck 1984). If the pressure fluctuations are also small,  $u' v'$  can be found using the Strong Reynolds Analogy (see Section 3.1).



It is important to avoid errors in the alignment of the probe and in the 180° rotation. For a small misalignment  $\delta_m$  we have  $\delta_m = (1/H_1) - (1/H_2)$ , and significant errors are avoided when  $\delta_m < 1^\circ$  (Smits & Muck 1984).

A single inclined wire can only be used to measure time averaged quantities. To measure the instantaneous fluctuations in  $(\rho u)'$ ,  $v'$  and  $(\rho u)' v'$ , a crossed wire must be used. When total temperature fluctuations are negligible, the instantaneous outputs from the two wires are

$$\frac{e_1}{E_1} = F_1 \frac{(\rho u)'}{\rho U} + H_1 \frac{\overline{\rho v'}}{\rho U} \quad (14a)$$

$$\frac{e_2}{E_2} = F_2 \frac{(\rho u)'}{\rho U} - H_2 \frac{\overline{\rho v'}}{\rho U} \quad (14b)$$

Therefore  $(\rho u)'$  and  $v'$  can be determined from the fluctuating voltages once  $F_1$ ,  $F_2$ ,  $\overline{\rho v'}$ , and  $\overline{\rho v'}$  have been found by calibration.

Crossed-wire probes need careful design to avoid aerodynamic interference. The effect of placing the wires too close to each other is seen in the angular sensitivity calibration shown in Fig. 9. As the wires are yawed relative to the mean flow direction, a point can occur where the shock system originating from one wire and its supports cuts across the active length of the other wire, leading to discontinuities in the calibration. To minimize these effects, it is probably best to use a soldered design where the active lengths are isolated from the relatively bulky prongs by thin stubs. Using such a design, Fernando et al. (1987) found that at Mach 3 these interference effects were not observed when the planes containing the two wires were greater than 1 mm apart. Such probes are acceptable as long as the flow field measured by the two wires is not significantly different, that is, there are no serious spatial resolution problems (see also Section 4.3).

### 5.2 Dynamic Response

The high frequency content of  $v'$  is considerably higher than that of  $(\rho u)'$ , as pointed out by Gaviglio et al. (1981). Their work suggested that  $(\rho u)' v'$  is underestimated by more than 5% if  $f_R < 10 U_\infty / \delta$  Hz, and the error exceeds 10% if  $f_R < 5 U_\infty / \delta$  Hz. Some examples of  $(\rho u)'$  and  $v'$  spectra are given in Fig. 10. These results were taken with a constant temperature anemometer using a symmetrical bridge, with a frequency response exceeding 250 kHz ( $= 12.5 U_\infty / \delta$ ). The  $v'$  spectra extends to frequencies which are about twice the maximum frequencies observed in the  $(\rho u)'$  spectra.

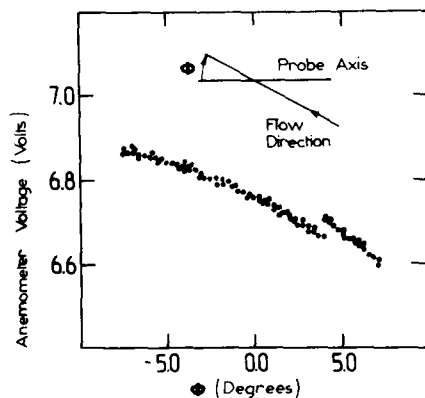


Figure 9. Calibration curve for one wire of a crossed-wire array. Note the discontinuity caused by shock-wave interference originating from the other wire.

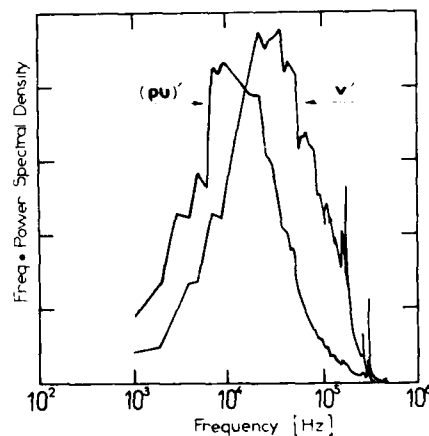


Figure 10. Spectra of  $(\rho u)'$ ,  $v'$  and  $(\rho u)' v'$  taken at  $y/\delta = 0.45$  using a crossed wire probe.

The spatial filter is determined by the largest dimension of the wire array, and the effects are similar to those described in Section 4.3 for normal wires. In the case of crossed wires, however, the effects are aggravated because the spatial scales associated with  $v$  are typically smaller than those associated with  $(\rho u)^2$ .

#### 6. THE EFFECT OF LOW MACH AND REYNOLDS NUMBERS

It was shown in Section 3 that at high Reynolds number the calibration of a single normal wire in supersonic flow is a relatively robust procedure, and careful calibration should give accurate measurements. When the Reynolds number is small, or when the Mach number is in the transonic regime, however, the sensitivities to fluctuations in density and velocity ( $F_{\rho}$  and  $F_u$ ) differ from the sensitivity to fluctuations in mass-flux ( $F_{\rho u}$ ), and additional calibrations are required (Morkovin 1956). Horstman & Rose (1975) calculated the ratio  $F_u/F_{\rho}$  as a function of Mach number, Reynolds number, and overheat ratio, and showed that for  $aw < 0.5$  and  $Re < 20$ ,  $F_{\rho} \neq F_u \neq F_{\rho u}$ . However, for  $aw > 0.5$  and  $Re > 20$ ,  $F_{\rho} = F_u = F_{\rho u}$  independent of Mach number, sensor material and  $\Delta T/d$  ratio. The measurements by Rong et al. (1985) were in agreement with these conclusions.

The effects of Mach number on inclined wires at high Reynolds number were discussed in Section 5.1. It seems likely that the combination of low Mach number and low Reynolds number will have similar effects to those observed with normal wires. Unfortunately, no analytic or experimental results for this regime are currently available.

#### 7. CONCLUDING REMARKS: MEASUREMENT ACCURACY

The accuracy of hot-wire measurements in supersonic flow depends on the limits set by the instrument itself, and on the care exercised by the operator. The effect of an uncalibrated operator on the measurements is unknown, of course, but some recommendations can be made to reduce operator bias. Probably the single best method to determine the confidence limits on the measurements is to repeat the measurements. For example, to check on drift, a measurement at a given point in the flow should be repeated at a different time. If at all possible, calibrations should be performed before and after each profile, and the wire performance should be checked against a known flow (for example, a zero pressure gradient turbulent boundary layer). Furthermore, the entire set of results should be repeated using a different wire, anemometer, and operator.

Given that operator bias has been removed, the remaining uncertainties associated with the limitations on the instrument can be determined with reasonable precision. Consider the following two examples for measurements in an adiabatic, zero pressure gradient boundary layer. The operating conditions for both examples are given in Table 1.

	EXAMPLE 1 Blowdown tunnel	EXAMPLE 2 Return-circuit tunnel
$p_0$ (Nt/m <sup>2</sup> )	$6.8 \times 10^5$	$4.05 \times 10^4$
$T_0$ (°K)	$265 \pm 5$	$296 \pm 1$
$M_e$	$2.84 \pm 0.04$	$1.76 \pm 0.02$
$U_e$ (m/s)	$575 \pm 20$	$477 \pm 7$
$(\rho U)_e$ (kg/m <sup>2</sup> s)	$500 \pm 30$	$68.1 \pm 3.4$
$Re_w/\mu$	$6.5 \times 10^7 \pm 0.5 \times 10^7$	$5.6 \times 10^6 \pm 0.3 \times 10^6$
$\delta_0$ (mm)	$26 \pm 1.5$	$10 \pm 1$
$C_f$	$.001 \pm .0001$	$.0022 \pm 0.0002$
$f_n$ (kHz)	250	320
$l$ (mm)	0.8	0.9
$l/d$	160	36
$aw$	1.0	$0.02 < aw < 0.5$

Table 1. Two examples of flat plate, zero pressure gradient, adiabatic wall, turbulent boundary layers (Example 1: Fernando, et al. 1987; Example 2: Dussauge & Gaviglio 1981)

In the first example, constant temperature anemometry was used, at a single overheat ratio, to measure  $(\rho u)^2$  with a normal wire, and  $(\rho u)^2$ ,  $v^2$  and  $(\rho u)v$  with a pair of crossed wires. The kinematic Reynolds stresses  $u^2$  and  $u^2v^2$  were deduced using the Strong Reynolds analogy with  $R_p = -Rr_u = 0.8$ . The measurements were subject to random and systematic errors. Random errors are introduced by the uncertainties in the calibration and measurement procedures, the possibility of drift in the calibration constants and the presence of end-conduction effects. Systematic errors included neglecting the total temperature fluctuations and the effects of the limited spatial and temporal resolution. These errors vary through the flowfield, but at  $y/\delta = 0.4$ , the error in  $\sqrt{(\rho u)^2}/\rho U$  using a normal wire was estimated to lie between +9% and -5%. For the crossed wire the error estimates were as follows:  $\sqrt{(\rho u)^2}/\rho U$ ,  $\pm 7.5\%$ ;  $\sqrt{v^2}/U$ ,  $\pm 7\%$  to  $-15\%$ ;  $-\rho(\rho u)v^2/(\rho U)^2$ ,  $+11\%$  to  $-27\%$ . When the Strong Reynolds Analogy was used to derive the kinematic turbulent stresses, the error estimates became:  $\sqrt{u^2}/U$ ,  $-7\%$  to  $-25\%$  (normal wire) and  $-9\%$  to  $-27\%$  (crossed wire);  $-\rho u^2v^2/U^2$ ,  $-14\%$  to  $24\%$ . Note that the measurement of  $-\rho(\rho u)v^2/(\rho U)^2$  tends to be lower than the true value, whereas the Strong Reynolds Analogy tends to make the estimate of  $-\rho u^2v^2/U^2$  higher than the true value.

In the second example, constant current anemometry was used at 14 overheat ratios to measure  $(\rho u)^2$ ,  $(\rho u)T_0$  and  $T_0^2$ . The error estimates were as follows:  $\sqrt{(\rho u)^2}/\rho U$ ,  $0\%$  to  $+16\%$ ;  $(\rho u)T_0/(\rho U T_0)$ ,  $-17\%$  to  $+13\%$ ;  $\sqrt{T_0^2}/T_0$ ,  $-3\%$  to  $-17\%$ . For the velocity and temperature fluctuations the estimates were:  $\sqrt{u^2}/U$ ,  $3\%$  to  $+17\%$ ;  $\sqrt{T^2}/T$ ,  $20\%$ ;  $\sqrt{T^2}/T$ ,  $2\%$  to  $+15\%$ . The uncertainty in the fluid property variations with temperature (already discussed in connection with Equation 7) has a rather small effect, and for the different values of  $a$  and  $b$  given in Section 3.2 the resulting uncertainty in any rms quantity is less than  $\pm 1.3\%$ .

Note that the measurements of  $\sqrt{(\rho u)^2}/\rho U$  using a constant current system overestimate the true value, in contrast to the results obtained using a constant temperature system where the systematic errors cancel (at least in this example). The differences between the two systems are primarily due to differences in end-conduction effects. Furthermore, the error analysis indicates that the true value of  $\sqrt{u^2}/U$  lies between the value obtained by the two systems.

#### ACKNOWLEDGEMENTS

The chapter was written while the first author was Chercheur Associe at I. M. S. T., with support from C. N. R. S. The useful comments given by J. F. Debieve and J. Gaviglio are also acknowledged with thanks.

#### REFERENCES

- Anguillet, J. P. (1980), Sur les mesures de flux de quantite de mouvement et de chaleur au moyen de l'anemometre a fil chaud, en ecoulements turbulents. These de Doctorat de Troisieme Cycle, Marseille, France.
- Bestion, D. (1982), Methodes anemometriques par fil chaud: Application a l'etude d'interaction turbulence-gradient de pression eleve en couches limites a vitesses supersoniques. These de Docteur Ingenieur, Marseille, France.
- Bestion, D., Gaviglio, J. and Bonnet, J. P. (1983), Comparison between constant-current and constant-temperature hot-wire anemometers in high-speed flows. *Rev. Sci. Instr.* 54: 1513-1524.
- Bonnet, J. P. and Alziary de Roquefort, T. (1980), Determination and optimization of frequency response of constant temperature hot-wire anemometers in supersonic flows. *Rev. Sci. Instr.* 51: 234-239.
- Bonnet, J. P. and Knani, M. A. (1981), Mesures par anemometrie a fil chaud incline dans un sillage turbulent supersonique. Colloque DRET-ONERA Ecoulements Turbulents Compressibles, Poitiers, France.
- Debieve, J. F. (1976), Contribution a l'etude du comportement d'un ecoulement compressible turbulent ( $M = 2.3$ ) soumis a des gradients eleves de vitesse et de pression. These de Doctorat de Specialite, Universite Aix-Marseille II, France.
- Doughman, E. L. (1972), Development of a hot-wire anemometer for hypersonic turbulent flows. *Rev. Sci. Instr.* 43: 1200-1202.
- Dussauge, J. P. and Gaviglio, J. (1981), Bulk dilatation effects on Reynolds stresses in the rapid expansion of a turbulent boundary layer at supersonic speed. *Proc. Third Symp. on Turbulent Shear Flows*, Univ. of Calif., Davis, p. 2.33.
- Fernando, E. M., Donovan, J. F. and Smits, A. J. (1987), The calibration and operation of a constant-temperature crossed-wire probe in supersonic flow. *ASME Symp. on Thermal Anemometry*, Cincinnati, Ohio, June 1987.
- Freytmuth, P. (1978), A bibliography of thermal anemometry. TSI Inc, St. Paul, Minnesota.

- Gaviglio, J. (1971), C. R. Acad. Sci., Paris, t.273, Serie A., p. 634.
- Gaviglio, J. and Dussauge, J. P. (1977), On reduction of errors arising in hot-wire anemometry of thin turbulent shear layers. Symp. on Flow in Open Channels and Closed Conduits, Gaithersburg, Maryland (NBS Special Publ. 484).
- Gaviglio, J. (1978), Quelques aspects de l'anemometrie par fil chaud dans les ecoulements turbulents de gaz presentant de forts gradients de temperature. Proc. Dynamic Flow Conf., Baltimore, Maryland (available from P.O. Box 121, DK-2740, Sjakovlund, Denmark, and I.M.S.T., Marseille).
- Gaviglio, J., Dussauge, J. P., Debieve, J. F. and Favre, A. (1977), Behavior of a turbulent flow, strongly out of equilibrium, at supersonic speeds. Phys. Fluids, 20: S197.
- Gaviglio, J., Anguillet, J. P. and Elena, M. (1981), On the application of hot-wire anemometry to the solution of problems arising in variable temperature turbulent flows. Rech. Aerosp. 1: 59-66.
- Grant, H. P. and Kronaver, R. E (1962), Fundamentals of hot-wire anemometry. ASME Symp. on Measurements in Unsteady Flow, Worcester, Massachusetts.
- Hinze, J. O. (1959), Turbulence. McGraw-Hill, New York, 586p.
- Horstman, C. C. and Rose, W. C. (1975), Hot-wire anemometry in transonic flow. NASA TM X-62, 495.
- Kistler, A. L. (1959), Fluctuation measurements in a supersonic turbulent boundary layer. Phys. Fluids 2: 290-296.
- Kovaszny, L. S. G. (1950), The hot-wire anemometer in supersonic flow. J. Aero. Sci., 17: 565-584.
- Kovaszny, L. S. G. (1953), Turbulence in supersonic flow. J. Aerodyn. Sci. 20: 657-682.
- Kovaszny, L. S. G. (1954), Hot wire method. High Speed Aerodynamics and Jet Propulsion, 9: 219-285.
- Laderman, A. J., Demetriades, A. (1974), Mean and fluctuating measurements in the hypersonic boundary layer over a cooled wall. J. Fluid Mech. 63: 121-144.
- Laufer, J. and McLellan, R. (1956), Measurements of heat transfer from fine wires in supersonic flows. J. Fluid Mech. 1: 276-289.
- Lowell, H. H. (1950), Design and application of hot-wire anemometers for steady-state measurements at transonic and supersonic air speeds. NACA TN2117.
- Morkovin, M. V. (1956), Fluctuations and hot-wire anemometry in compressible flows. AGARDograph 24.
- Morkovin, M. V. (1962), The effects of compressibility on turbulent flows. Mecanique de la Turbulence, Favre, A. (Ed.) CNRS, Paris, pp. 367-380.
- Mougnat, H. (1986), Influence de la conduction thermique sur la response en frequence de l'anemometre a fil chaud en ecoulement supersonique. These Docteur de l'Universite d'Aix-Marseille II, France.
- Owen, F. K. and Fiore, A. W. (1986), Turbulent boundary layer measurement techniques. Flight Dynamics Lab., Air Force Wright Aero. Lab. Tech. Rept. 86-3031.
- Perry, A. E. (1982), Hot wire anemometry. Oxford: Oxford University Press, 184pp.
- Perry, A. E., Smits, A. J. and Chong, M. S. (1979), The effects of certain low frequency phenomena on the calibration of hot-wire. J. Fluid Mech. 90:415-431.
- Reshotko, E. and Beckwith, I. E. (1958), Compressible laminar boundary layers over a yawed infinite cylinder with heat transfer and arbitrary Prandtl number. NACA Rept. 1379.
- Rong, B. S., Tan, D. K. M. and Smits, A. J., (1985), The calibration of the constant temperature normal hot-wire anemometer in transonic flow. Dept. Mech. and Aerosp. Engin. Rept. 1696, Princeton University, Princeton, New Jersey.
- Smits, A. J. (1974), Further development of hot-wire and laser methods in fluid mechanics. Ph.D. Thesis, University of Melbourne, Melbourne, Australia.
- Smits, A. J. (1984), The static response of a bowed inclined hot wire. Expts. in Fluids 2.
- Smits, A. J., Perry, A. E. and Hoffmann, P.H. (1978), The response to temperature fluctuations of a constant-current hot-wire anemometer. J. Phys. E: Sci. Instr. 11: 909-914.
- Smits, A. J., Hayakawa, K. and Muck, K. C. (1983), Constant temperature hot-wire anemometer practice in supersonic flows. Part 1: The normal wire. Expts. in Fluids 1: 89-92.
- Smits, A. J., and Muck, K. C. (1984), Constant temperature hot-wire anemometer practice in supersonic flows. Part 2: The inclined wire. Expts. in Fluids 2: 33-41.
- Wetmuff, J. H. (1987), Higher order effects in the frequency response of the constant temperature hot-wire anemometer. To be presented ASME Symp. on Thermal Anemometry, Cincinnati, Ohio, June 1987.
- Wyngaard, J. C. (1968), Measurements of small-scale turbulence structure with hot-wires. J. Phys. E: Sci. Instr. 1: 1105-1108.

## CHAPTER 6

## LASER DOPPLER ANEMOMETRY

by

Dennis A. Johnson

NASA Ames Research Center  
Moffett Field, CA 94035, U.S.A

## 1. INTRODUCTION

Laser Doppler anemometry (LDA) in compressible flows offers the advantages of unambiguous signal interpretation (the laser Doppler anemometer senses velocity only) and nonintrusiveness. Another strength of the LDA is its ability to accurately measure the normal or vertical velocity fluctuations in regions close to a solid surface. This measurement even for zero-pressure-gradient boundary layers is extremely difficult for hot-wire anemometry. Also, LDA is not limited to attached flows with moderate turbulence levels as is hot-wire anemometry.

The primary disadvantage of the technique is that the velocities of micron-size particles are measured rather than the velocity of the fluid itself. In most applications, this requires the introduction of seed particles into the flow (see also Chapter 7). Measurement errors can arise if the particles are not sufficiently small to follow the fluid motions or if they are not uniformly distributed in the flow. Errors also can occur if the signal quality of the photodetector output, which depends on the intensities of the particle-scattered light, is not sufficiently high. Measurements are made difficult because of the rapid fall off in scattered-light intensities with particle diameter. In the particle size range of interest, the intensities decrease nearly with the sixth power of the diameter. Given the current state of the art in lasers and signal processing electronics, the minimum size particles from which measurements can be made at compressible speeds are marginally adequate from a standpoint of trackability.

Another disadvantage of LDA is that it is not well suited for spectra or correlation measurements because of the discontinuous nature of the signal output which is governed by Poisson statistics.

Most LDA compressible boundary-layer measurements have relied on the "dual-beam" (or "fringe") optical arrangement with forward-scatter light collection and burst-counter signal processing. In transonic and supersonic wind tunnels, it is extremely difficult to achieve high particle concentration levels. The dual-beam, burst-counter approach is well suited to applications such as these where the particles are sparsely distributed. There are a vast number of papers in the literature describing various aspects of LDA, numerous technical meetings have been dedicated just to LDA and several books have been written on the subject. The intent of this chapter is to discuss some of the more relevant aspects of applying LDA (specifically, the dual-beam, burst-counter approach) to compressible flows.

## 2. BASIS OF DUAL-BEAM, BURST-COUNTER LDA SYSTEMS

A simplified dual-beam arrangement for single-component velocity measurements is shown in Fig. 1. In this configuration, the collecting lens is positioned to collect only particle-scattered light from the two incident laser beams. In earlier LDA systems, the Doppler signal was obtained by heterodyning non-scattered light from one of the incident beams with particle-scattered light from the other beam. This approach had the disadvantages of being sensitive to mechanical vibrations and of requiring small light-collection solid angles. The dual-beam arrangement does not have these disadvantages. Early analyses of the dual-beam optical arrangement were performed by Rudd (1969), and Mazumder and Wankum (1970).

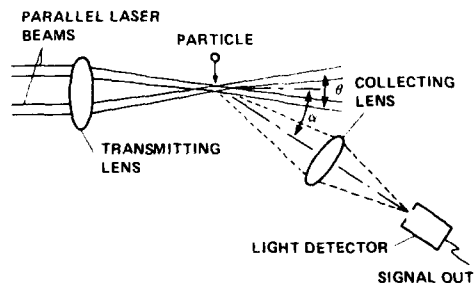


Figure 1. Simplified "dual-beam" laser Doppler anemometer.

With the availability of the argon-ion laser in the early 1970s high-speed LDA measurements became realizable. It provided the additional laser power (more than two orders of magnitude over the standard helium-neon laser) needed to detect individual submicron particles traveling at the speed of sound or higher with the dual-beam optical arrangement. From the oscilloscope traces of signal bursts produced from individual particles, came the idea of using high-speed counters to measure the velocity of individual particles crossing the sensing volume. The earliest work on the burst counter approach was performed by a research group at AEDC, Arnold Air Force Station, Tenn. (Lennert, et al., 1970).

An alternative approach to using burst counters is that of photon correlation (Abbiss, 1976) which is capable of working with much lower scattered light levels. Another, is the digitization of the signal bursts followed by signal analysis via a digital computer (Peterson and Maurer, 1975). By Fourier transforming the digitized signals, measurements by this approach can be obtained from signals too noisy to be processed by a burst counter. However, neither approach has attained the same level of popularity in compressible flow applications as the burst counter. One reason for this has been the lower signal frequency limits of these approaches compared to those for burst counters. Also, both techniques require substantial computer postprocessing.

The dual beam arrangement is often referred to as the fringe arrangement because of the fringe pattern which is formed by the mutual interference of the two (ideally of equal intensity) incident laser beams. This fringe pattern is depicted in Fig. 2. These fringes are parallel to the bisector of the two incident beams and perpendicular to the plane formed by the two incident beams. The spacing of the fringes  $x_f$  is given by  $x_f = \lambda/2 \sin \theta/2$  where  $\theta$  is the angle between the two incident beams and  $\lambda$  is the wavelength of the laser light. The electrical signal,  $e(t)$  produced at the photodetector by an individual particle crossing these fringes has the form:

$$e(t) = \frac{1}{2} e^{-gt^2} \left( 1 + \cos \frac{2\pi u_1}{x_f} t \right) \quad (1)$$

where the envelope function  $g$  depends on the trajectory of the particle passing through the sensing volume,  $u_1$  is the velocity component perpendicular to the interference fringes, and  $t$  is time in Eq. 1. Passing this signal through a high-pass filter produces a signal given by

$$e(t) = \frac{1}{2} e^{-gt^2} \cos \frac{2\pi u_1}{x_f} t \quad (2)$$

that is symmetric with respect to zero and which crosses zero at fixed time intervals of  $\tau_0 = (1/2) x_f/u_1$ .

In compressible flow applications,  $\theta$  is made relatively small (1 to 2°) so the signal frequencies do not exceed the capabilities of the photodetector or the signal processing electronics. If the laser is not operated in single mode, then high-frequency noise from the laser also becomes a consideration in limiting the maximum signal frequency (Dopheida and Durst, 1979). Typical fringe spacings are in the 10 to 30  $\mu\text{m}$  range in compressible flow studies.

Because  $\theta$  and the light collection angle,  $\alpha$  (Fig. 1) are both relatively small in compressible flow applications, the sensing volume is highly elongated in the direction of the optical axis (i.e., the bisector of the two incident laser beams). Its shape is ellipsoidal with a Gaussian cross-sectional intensity distribution. The aspect ratio of the ellipsoid can be as large as 50 but likely never less than 10. The effective diameter, which is determined by the diameter of the laser beams ahead of the transmitting lens and the transmitting lens focal length, is typically between 200 and 400  $\mu\text{m}$ . The upper frequency limit of the signal processing electronics restricts how small the sensing volume can be.

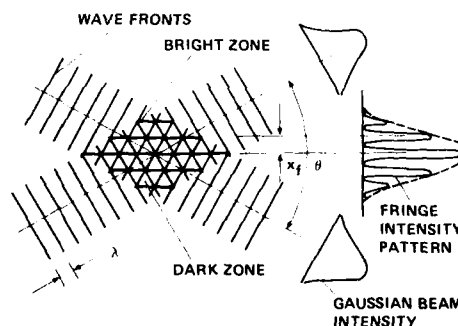


Figure 2. Depiction of fringe formation at beam crossover.

Forward-scatter light collection refers to the case where  $\alpha$  in Fig. 1 is small while in back-scatter configuration,  $\alpha$ , is near  $180^\circ$ . In wind tunnel applications, the forward-scatter configuration generally requires that the light-collection optics be placed on the opposite side of the tunnel test section from that of the transmitting optics. Although this makes for mechanical inconveniences, experience has shown that the gain of about two orders of magnitude in light scattered intensities over that for back scatter is essential in the transonic and supersonic regimes when burst counters are used for signal processing.

The burst counter is designed to filter out the low-frequency component in Eq. 1 and then measure the average period of a given number of cycles of the signal (eight cycles is the most common). Pulses from a high-frequency clock (up to 1 GHz) are counted to determine the average period. The number of cycles used is a compromise between resolution and frequency limitations.

In the study of compressible boundary-layer flows, the two-velocity component systems which use the two strong lines (4880 and 5145 Å) of the argon-ion laser are the most popular. These two laser lines are sufficiently apart that signal separation at the detectors can be accomplished by optical filtering. With this system, four laser beams (two with  $\lambda = 4880$  Å and two with  $\lambda = 5145$  Å) are brought to a common focus with a single transmitting lens. The results are overlapping sensing volumes whose fringes are orthogonal. Usually a shift in frequency,  $f_B$ , is introduced into each pair of beams which causes the fringes to move at a constant velocity,  $v_f = x_f f_B$ . With this fringe motion, forward and reverse velocities can be distinguished.

While frequency shifting is obviously important in the measurement of separated flows, it can be important even in moderately high turbulent flows when burst counters are used. Depending on the turbulence level, the number of fringes in the sensing volume, and the minimum number of fringe crossings required by the burst counter, there is the possibility that certain particles will not cross a sufficient number of fringes to be measured. In which case, measurement errors can occur. The use of frequency shifting, if properly applied, can prevent this possibility. The observed fall-off of the near-wall Reynolds shear stresses in early studies (Johnson and Rose, 1975; Yanta and Lee, 1974; and Dimotakis et al., 1979) of zero-pressure-gradient compressible boundary layers appears to have been at least partly the result of not using frequency shifting (Schairer, 1980; and Robinson et al., 1983).

### 3. SIGNAL PROCESSING ASPECTS

The major difficulty in the application of LDA is that the signals from the photodetector are relatively noisy even under ideal situations. This is further complicated in high-speed applications because of the need for smaller light scatterers for particle tracking and the reduced residence time of the particles in the sensing volume. The signal-to-noise ratio (SNR) for an LDA signal, defined as the ratio of signal power to noise power, is approximately given by the following expression:

$$\text{SNR} = \frac{\eta}{h\nu} \cdot \frac{P_S}{(1 + P_B/P_S)\Delta f} \quad (3)$$

where  $\eta$  is the quantum efficiency of the photodetector,  $h\nu$  is the energy of a single photon,  $P_S$  is the particle-scattered light power,  $P_B$  is the background light power, and  $\Delta f$  is the instrument bandwidth. This expression assumes there are many photoelectrons-per-filter resolving interval; i.e., the signals are sufficiently strong as not to be photon resolvable.

The particle-scattered light power depends on the incident laser intensity, the Mie scattering function of the particle, and the location and F number of the collection lens. In general,  $P_S$  drops dramatically with particle size as will be discussed in the next section. The penalty paid by the burst counter's ability to measure the frequency of individual scatters in a highly turbulent flow is its wide bandwidth (large  $\Delta f$ ) which increases the noise in signal. The required instrument bandwidth for turbulent flow measurements depends on the highest expected measurement speed and the fringe spacing. Hence, the need for smaller particles reduces  $P_S$  while the greater speeds demands an increase in  $\Delta f$ , both of which result in reduced SNRs. The variable  $P_B$  represents the total of all undesired laser light which enters the detector. This generally will be laser light which is scattered from optical components, wind tunnel windows and model surfaces. Well designed LDA systems using low-loss optics attempt to minimize the collection of this stray light but it cannot be completely eliminated. The deterioration in SNR caused by stray light can be acute when measurements are attempted close to model surfaces. In compressible flow applications, an SNR of 100 (20 dB) would be considered quite respectable.

Burst counters have been designed to have some noise rejection capabilities; however, the signals must be relatively clean or erroneous measurements can occur. All of the commercially available burst counters have a threshold level which determines the minimum level signal the counter will attempt to process. The threshold level is normally set well above the switching level of the Schmidt trigger which converts the signal into a series of square waves. Either the threshold level is directly adjustable or indirectly via a variable gain control on the preamplifier. Without this threshold level capability, measurements are virtually impossible.

Other noise rejection techniques commonly used include 1) a comparison of the average period of four or five signal cycles to that for eight cycles (other variations on this four/eight or five/eight comparison are now available), and 2) a three-level comparison which requires that the signal passes a + level, 0 level and - level in the proper sequence. Of these two methods of noise discrimination, it has been the writer's experience that the three-level comparison is more effective in eliminating noisy signals than the four/eight or five/eight cycle comparison. As a rule however, any burst counter will give erroneous output if it is required to process signals which are sufficiently noisy. For example, a burst counter can generate output from just the shot noise of the detector--the laser does not even have to be on to obtain data.

In practice, an attempt is made to set the threshold level sufficiently high so all the signal bursts satisfy the signal quality requirements of the counter, and yet sufficiently low that an acceptable data rate is achieved. Generally the SNRs of the signal bursts are not measured in an experiment (this can be done by digitizing and then Fourier transforming the signal bursts). Usually, measurements in the free-stream of the flow of interest (where the turbulence levels are known to be low) are made to test whether the signal qualities are sufficiently good for reliable measurements. In practice, the minimum recordable rms with an LDA is almost without exception governed by signal quality (i.e., SNR) and not the clock rate of the burst counter. Although there are too many variables to extract an exact relationship between SNR and measurement uncertainty, it is reasonable to expect the minimum measurable rms to depend inversely on the square root of the SNR (Mayo, 1979; and Binder et al., 1986). The lowest free-stream root mean square (rms) observed by this writer in compressible experiments has been 1% (the actual turbulence levels were considerably less). These were cases where the frequency bandwidth was large since the flows of interest were highly turbulent.

Care must be taken when measurements closer to a solid surface are attempted since the SNRs will generally be lower because of an increase in  $p_b$ . When the background light level increases, a common practice is to raise the threshold level so that only the strongest signals are processed. Often a real-time observation of the output in histogram form is used to help detect bad readings and to set the threshold of the counters.

Because of the noise-in-signal effects, the LDA is not well suited for measuring very low turbulence levels. The measured rms can be reduced to some extent by using two counters to measure the same signal or even better, signals from two different photodetectors and then cross correlating their outputs as suggested by Lau et al. (1981). The accuracy of mean-velocity measurements can be significantly better than the minimum measurable rms if the noise effects produce a Gaussian probability density function (pdf). This theoretically will be the case if the SNRs are reasonably high (Cobb, 1965).

#### 4. PARTICLE LIGHT SCATTERING AND TRACKING

For the realization of accurate LDA measurements, particle lag effects must be negligibly small (see also Chapter 7). To the accuracy of Stokes's drag law, the time constant (i.e., the  $1/e$  point) for a particle subjected to a discontinuous change in gas velocity is given by

$$\tau_c = \frac{\rho_p d_p^2}{18\mu_g} \quad (4)$$

where  $\rho_p$  and  $d_p$  are the particle density and diameter, respectively and  $\mu_g$  is the viscosity of the gas. For fixed fluid properties and particle density, the particle response is proportional to the square of the particle diameter. Analogous to the 3-dB frequency response quoted for hot-wire anemometry, but in the moving reference frame of the particle, the particle response is given by  $f_{3dB} = 1/2\pi\tau_c$ . If we assume the step change in velocity to be small, the response distance  $x_c$  can be expressed as  $x_c = u_g\tau_c$  where  $u_g$  is the speed of the flow.

Values of  $f_{3dB}$  and  $x_c$  are given in Table 1 for different sizes of particles with a specific gravity of unity in a Mach 3 flow with a 293 K stagnation temperature. For lower Mach numbers, these values improve because of the decrease in  $u_g$  and the increase in  $\mu_g$  (e.g.,  $\mu_g$  is 2.5 times larger at ambient

Table 1. Particle response based on Stokes's drag law for  $M_\infty = 3$ ,  $T_t = 293^\circ \text{K}$  and particles with a specific gravity of 1.

$d_p$ ( $\mu\text{m}$ )	$f_{3dB}$ (kHz)	$x_c$ (mm)
5.0	0.9	110
2.0	5.4	18
1.0	22	4.4
0.5	86	1.1
0.3	239	0.4



temperature conditions). For low-density flows as encountered in hypersonics, a correction for mean-free path relative to particle diameter must be made (Becker et al., 1967) in which case the time constant is given by

$$\tau_c = \frac{\rho_p d_p^2}{18\mu_g} \left( 1 + k \frac{L}{d_p} \right)$$

where  $L$  is the mean free path and  $k$  is the Cunningham correction;  $k = 1.8$  for air. When the Knudsen number is large, the particle response goes as the particle diameter rather than the particle diameter squared. Because of this, Owen and Calarese (1987) suggest that an optimum seeding particle in some hypersonic flows may be one that is nominally larger than normally used in LDA, but which has a much lower specific gravity.

Since the particles are convected in the Lagrangian frame, it is difficult to assess how large the particles can be, and still have negligibly small particle lag relative to the turbulent fluctuations. Mean convective speeds of the turbulent eddies in a zero-pressure-gradient turbulent boundary layer are all within 20% of the local mean velocity. This suggests that for a zero-pressure-gradient boundary layer the relevant frequency response could be a factor of five larger than those given in Table 1. Supporting evidence that the frequency responses given in Table 1 are overly conservative comes from the study of Yanta and Lee. In that study, reasonably accurate mean velocities and Reynolds stresses were obtained in a supersonic turbulent boundary layer using  $5 \mu\text{m}$  seed particles. Obviously, the effective response of these  $5 \mu\text{m}$  particles must have been better than the 0.9 kHz quoted in Table 1.

Rapid spatial changes (such as that caused by shocks) or sustained strong streamwise curvature are of more concern than the response to convected turbulence fluctuations. Although locally the particle speeds may be very close to that of the surrounding fluid in the situation of sustained streamwise curvature, substantial particle concentration gradients can result which in turn can produce a biased sample of the flow statistics. (The author is not aware of any studies which have addressed this potential problem.)

To illustrate the advantages of forward scatter over back scatter and the rapid fall off in scattered-light intensities with particle diameter, results (taken from van de Hulst, 1957; and Gumprecht et al., 1952) based on Mie scattering calculations are shown in Fig. 3. Light scattering intensities,  $i$ , for water droplets (index of refraction,  $n = 1.33$ ) exposed to  $0.5 \mu\text{m}$  wavelength light for forward scatter

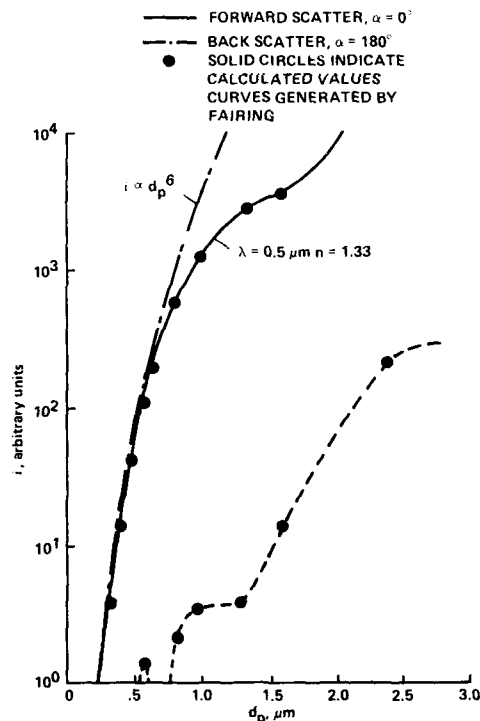


Figure 3. Calculated light scattering intensities for water droplets ( $n = 1.33$ ) and  $0.5 \mu\text{m}$  laser light. Calculated intensities taken from van de Hulst (1957) and Gumprecht et al. (1952).

( $\alpha = 0^\circ$ ) and back scatter ( $\alpha = 180^\circ$ ) are plotted as a function of particle diameter. Up to  $d = 0.5 \mu\text{m}$  it is seen that the forward scatter intensity varies very nearly as the sixth power of the particle diameter as predicted by Rayleigh-scattering theory. This is somewhat surprising since Rayleigh scattering is theoretically only valid for  $d \ll \lambda$ . A common seed particle in LDA are polystyrene spheres ( $n = 1.55$ ), and these particles show a similar behavior. The water droplet results are shown because more extensive Mie scattering calculations were available. For a given size particle, Fig. 3 shows that the scattering intensities in forward scatter are approximately two orders of magnitude larger than those in back scatter. This is significant since Eq. 3 states that this results in two orders of magnitude difference in SNR ( $P_S$  is determined by integrating 1 over the solid angle of light collection). On the other hand, if the minimum acceptable intensity for accurate velocity measurements were, for example,  $I = 60$  then a  $0.5 \mu\text{m}$  particle could be measured in forward scatter according to Fig. 3, while in back scatter measurements would be limited to  $2 \mu\text{m}$  or larger particles. If the system sensitivity were considerably less, say  $I = 600$ , then particles as small as  $0.8 \mu\text{m}$  could still be sensed in forward scatter, but in back scatter, the particles would have to be  $6 \mu\text{m}$  or larger (this is based on calculations which are off the scale of Fig. 3). Clearly, substantial gains in sensitivity result from using forward scatter.

Because the intensities fall so rapidly for  $d_p < 1 \mu\text{m}$ , it is difficult to effect any significant improvements in the minimum size particle that can be measured. Below  $d_p = 0.5 \mu\text{m}$  for example, an order of magnitude increase in incident laser power would only result in a 33% reduction in diameter of the smallest detectable particle.

The problem is compounded by the fact that it is nearly impossible to generate an aerosol which does not contain some particles which are larger than desired. Since these larger particles will scatter more light, they will have a higher probability of being measured than a smaller particle. The recent Mach 3 compression corner study of Kuntz et al. (1987) exemplifies the difficulty of generating sufficiently small particles for trackability yet large enough for detection. Measurements across an oblique shock at Mach 3 showed that the effective diameters of the oil droplets used for light scattering in that study were between  $1.5$  and  $2 \mu\text{m}$ . These particles have to be considered definitely borderline in the study of supersonic shock-wave/boundary-layer interaction flows. In the Mach 3 shock-induced separation study of Modarress and Johnson (1979), aerodynamic diameters of  $0.5 \mu\text{m}$  were confirmed from shock-wave response measurements. Realistically, this is about as small a particle that can be used in supersonic measurements when burst counters are used to process the signals.

##### 5. DATA REDUCTION AND SAMPLING BIAS

Most commonly, the flow statistics are calculated from the burst counter output based on the assumption that the sampling is random. Thus, the possibility of a sampling bias toward higher velocity particles as first discussed by McLaughlin and Tiederman (1973) is generally ignored. This bias is argued to occur when particle concentrations are low because more fluid is swept through the sensing volume during periods of high velocity than periods of low velocity which thus enhances the possibility of high-velocity samples over that for low-velocity samples. Although this bias has been verified in numerous low-speed studies (Stevenson et al., 1982; Johnson et al., 1984; and Binder et al., 1986) and evidence of its existence in high-speed flows has been presented (Petrie et al., 1985), there has been a reluctance to correct results for this bias. Fortunately, the effect of this sampling bias when present is negligibly small at moderate turbulence levels (say less than 20%). The reluctance to correct for sampling bias stems from the conflicting results that have been reported in the literature. Also, there is the possibility of compensating errors because of inadequate photodetector response (Dunao et al., 1980). This effect, though, should be minimal when frequency shifting is used.

One way to avoid the effects of sampling bias is to heavily seed the flow such that particle interarrival times are much less than the turbulence time scale and then restrict the sampling of the counter to much longer, fixed sample times (Stevenson et al., and Edwards and Jensen, 1983). However, this is not practical in high-speed applications. Edwards and Meyers (1984) proposed that the degree of sampling bias be determined by measuring the mean sample rate as a function of the velocity over periods short relative to the turbulence time scales. With this information available corrections to the uncorrected pdf's can be made. This again requires data rates beyond that which can be obtained in compressible flows. Moreover, there is an additional problem with this proposal because of the relatively long sensing volumes of most LDA systems. If the sensing volume is long relative to the turbulence scales, then even if sampling bias was present little correlation between sample rate and velocity would be apparent. Chen and Lightman (1985) using this approach, observed a very strong correlation between velocity and mean sample rate for a low-speed centerbody flow. But in that study, the flow was dominated by very large vortical structures (their scales were large even compared to the 5-mm length of the sensing volume).

Theoretically, if the sensing volume is cylindrical in shape and of a high aspect ratio (this is a good approximation to the actual ellipsoidal sensing volumes), the mean and rms velocities based on  $N$  samples should be calculated using the following formulas (for brevity, only the expressions for the streamwise velocity component  $u$  are given):

$$\bar{u} = \frac{1}{N} \sum_{i=1}^N \omega_i u_i \quad \sum_{i=1}^N \omega_i \quad (6)$$

and

$$\langle u' \rangle = \frac{\sum_{i=1}^N \omega_i (u_i - \bar{u})^2}{\sum_{i=1}^N \omega_i}^{1/2} \quad (7)$$

where  $\omega$  is a weighting factor given by

$$\omega_i = \left[ \frac{1}{\rho} \left( u_i^2 + v_i^2 \right)^{1/2} + \frac{\pi}{4} \cdot \frac{d}{\ell} \cdot w_i \right] \quad (8)$$

In this expression,  $\rho$  is the fluid density; and  $v$  and  $w$  are the normal and cross stream velocity components, respectively; and  $d$  and  $\ell$  are the diameter and length of the cylindrical sensing volume. Under the assumption of no sampling bias  $\omega = 1$ .

Although density fluctuations can theoretically affect the sampling bias as seen from Eq. 8, they are ignored when corrections are made for sampling bias. For high Mach number flows, their effect could become important. Also, since the cross stream velocity component  $w_i$  is not usually measured, the last term in Eq. 8 is either ignored or estimated (Nakayama, 1985) in terms of  $\langle u' \rangle$  and  $\langle v' \rangle$ . Because  $d/\ell$  is usually quite small, this term is normally small compared to the other two terms.

The possible measurement errors due to sampling bias increase with turbulence intensity. Shown in Fig. 4 are results for a transonic, shock-wave/turbulent-boundary-layer interaction on an axisymmetric bump obtained using  $\omega_i$  given by Eq. 8 (with  $w$  neglected) and using  $\omega_i = 1$ . Except in the separated

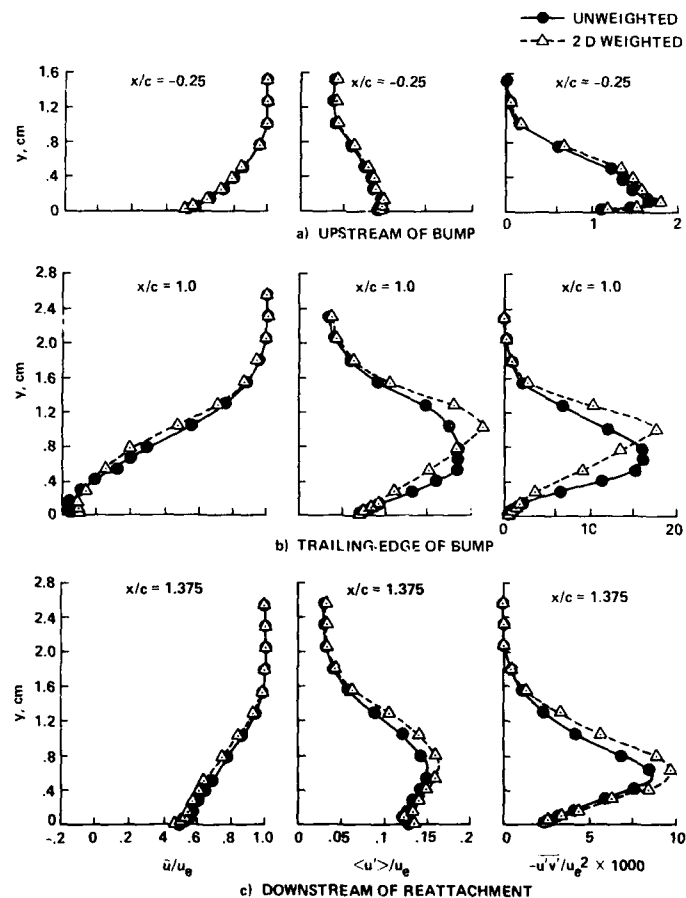


Figure 4. Uncorrected and bias-corrected results; axisymmetric bump model ( $M_\infty = 0.875$ ).

flow region (maximum separation occurred at the bump trailing edge), the differences are probably within the accuracy of the measurements. And even there, the maximum difference in mean velocity is only 1% with respect to the edge velocity. The largest differences were observed in the  $\overline{u'v'}$  measurements. Similar trends to those shown in Fig. 4 were observed by Petrie et al. (1985) for a supersonic base flow.

The issue of sampling bias has yet to be resolved within the LDA scientific community. At the present time, the two approaches given previously must be thought of as a bound on the data. This suggests that the data be reduced in both ways to check the possible effects sampling bias could have on the results. Given that both  $u$  and  $v$  are measured simultaneously, which is the most accurate way of determining the shear stress  $\overline{u'v'}$ , little additional effort is needed to reduce the data using both formats. At very high Mach numbers, the potential effect of density fluctuations on the sampling bias adds another level of uncertainty.

## 6. THREE-DIMENSIONAL MEASUREMENTS

The measurement of the third velocity component,  $w$ , in a three-dimensional turbulent boundary layer with an LDA is extremely difficult. As discussed earlier, with the "dual beam" optical arrangement the measured velocity component is perpendicular to the bisector of the two incident beams. Since in most wind tunnels, optical access is from the sides of the test section the measurement of  $u$  and  $v$  are straightforward. Such is not the case for the measurement of  $w$ .

In boundary-layer studies, it is best to have the laser beams come in at a grazing incidence to the surface of interest to reduce background scattered light. The most common procedure in three-dimensional applications has been to have a third pair of beams (of either a third color, a different polarization or frequency shifted) which lie in the same plane as the pair of beams used to measure  $u$ , but which make a substantial angle  $\psi$  with respect to these beams (Fig. 5). The velocity component sensed, in this case, is  $w = u \cos \psi + v \sin \psi$ . In wind tunnel applications, the angle  $\psi$  is normally restricted because of limitations in optical access. This limits the resolvability of  $w$ . To improve resolution, electronic mixing of the signal dependent only on  $u$  with the signal dependent on  $u$  and  $w$  was performed by Asherman and Yanta (1984). In this procedure, the fringe spacings are adjusted so that the difference frequency of the two signals depends only on  $w$ . Besides the added complexity of this approach, it has the disadvantage that the SNR of the mixed signal is considerably reduced from that of the original two signals which causes other measurement uncertainties. It also does not circumvent the basic problem of reduced sensitivity to  $w$  caused by  $\psi$  being small.

An additional complication in three-dimensional measurements arises because of the small overlap region of the third velocity component beams relative to the original sensing volume for  $u$  and  $v$  (Fig. 5). Even when coincidence between all three components is required to affect a measurement, there is a relatively high likelihood that the measurement will be from two particles (one or both of which are not in the overlap region) if the overlap region is small relative to the individual sensing volumes. In which case, in addition to the desired velocity component pairs ( $u_i, v_j : i = j$ ) obtained from the same particle, velocity component pairs ( $u_i, v_j : i \neq j$ ) generated by two particles are measured. Boutier et al. (1985) refer to these latter velocity component pairs as "virtual" particles and show that they can produce significant overestimations in  $\overline{w'w'}$ . Driver and Hebbart (1987) in a low-speed boundary layer study found this virtual particle problem for  $\psi$  equal to  $60^\circ$  to result in an underestimation of  $\overline{w'v'}$  by 20%. This represents a serious problem which will need to be addressed in future high-speed, three-dimensional boundary-layer studies.

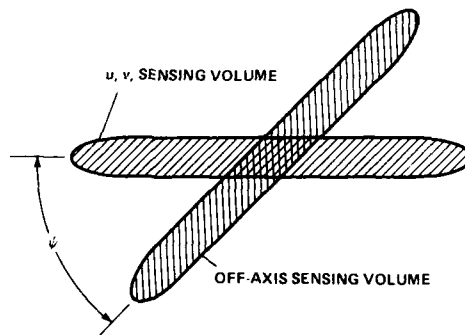


Figure 5. Overlapping sensing volumes for three-dimensional velocity measurements.

## 7. CONCLUDING REMARKS

Much has been accomplished with LDA in compressible flows despite the difficulties posed by the high speeds and additionally by the rapid spatial changes in speed or flow direction in some cases. The successful application of the technique is difficult because the SNRs are fairly low even under the best of

conditions and highly variable because of variations in particle size and particle location within the sensing volume. And, the available signal processing is not very effective in discarding signals that are too noisy to provide an accurate velocity measurement. The temptation is to work with particles which are too large to adequately follow the flow but which provide cleaner signals due to increased scattering intensities. For the data to have credibility, some check on the particle response must be made for a given facility and LDA system. The capability, if developed, of being able to determine the size of each particle upon which a measurement is based and the SNR of the corresponding signal burst would be extremely valuable in reducing much of the uncertainty now present in LDA compressible flow measurements.

## B. REFERENCES

- Abbiss, J. B. (1976), Development of photon correlation anemometry for application to supersonic flows. AGARD CP 193.
- Ausherman, D. W. and Yanta, W. J. (1984), The three-dimensional turbulent transport properties in the boundary layers of conical body configurations at Mach 3. AIAA P-84-1528.
- Becker, H. A., Hottel, H. C., and Williams, G. C. (1967), On the light-scatter technique for the study of turbulence and mixing. J. Fluid Mech. 30, pp. 259-284.
- Binder, G., Tardu, S., and Blackwelder, R. (1986), An experimental investigation of LDA biasing using a large amplitude oscillatory channel flow. Third Int. Symp. Applications of Laser Anemometry to Fluid Mech., Lisbon, Portugal.
- Boutier, A., Pagon, D., and Soulevant, D. (1985), Measurements accuracy with 3D laser velocimetry. Int. Conf. on Laser Anemometry - Advances and Application, Manchester, England.
- Chen, T. H. and Lightman, A. J. (1985), Effects of particle arrival statistics on laser anemometer measurements. Int. Symp. Laser Anemometry, ASME Winter Annual Meeting, Miami Beach, Florida.
- Cobb, S. M. (1965), The distribution of intervals between zero-crossings of sine-wave plus random noise and applied topics. IEEE Trans. Info. Theory IT-11, pp. 220-233.
- Dimotakis, P. E., Collins, D. J., and Lang, D. B. (1979), Laser Doppler velocity measurements in subsonic, transonic and supersonic turbulent boundary layers. Laser Velocimetry and Particle Sizing, Hemisphere, Washington, D.C.
- Dupneuve, D. and Durst, F. (1979), High speed velocity measurements using laser Doppler anemometry. Laser Velocimetry and Particle Sizing, Hemisphere, Washington, D.C.
- Driver, D. M. and Hebbbar, S. K. (1987), Experimental study of a three-dimensional, shear-driven, turbulent boundary layer. AIAA J. 25, pp. 35-42.
- Durao, D. F. G., Laker, J., and Whitelaw, J. H. (1980), Bias effects in laser Doppler anemometry. J. of Phys. E: Sci. Instrum. 13, pp. 442-445.
- Edwards, R. V. and Jensen, A. S. (1983), Particle-sampling statistics in laser anemometers: sample-and-hold systems and saturable systems. J. Fluid Mech. 133, pp. 397-411.
- Edwards, R. V. and Meyers, J. F. (1984), An overview of particle sampling bias. Second Int. Symp. Applic. Laser Anemometry to Fluid Mech., Lisbon, Portugal.
- Gumprecht, R. O., Sung, N., Chin, J. H., and Sliepcevich, C.M. (1952), Angular distribution of intensity of light scattered by large droplets of water. J. Optical Soc. of Amer. 42, pp. 226-231.
- Johnson, D. A. and Rose, W. C. (1975), Laser velocimeter and hot-wire anemometer comparison in a supersonic boundary layer. AIAA J. 13, pp. 512-515.
- Johnson, D. A., Modarress D., and Owen, F. K. (1984), An experimental verification of laser-velocimeter sampling bias and its correction. J. Fluids Eng. 106, pp. 5-12.
- Kuntz, J. W., Amatiucci, V. A., and Addy, A. L. (1987), Turbulent boundary-layer properties downstream of the shock-wave/boundary-layer interaction. AIAA J. 25, pp. 668-675.
- Lau, J. C., Whiffen, M. C., Fisher, M. J., and Smith, D. M. (1981), A note on turbulence measurements with a laser velocimeter. J. Fluid Mech. 102, pp. 353-366.
- Lennert, A. E., Brayton, D. B., Crosswy, F. L., Smith, F. H. Jr., and Kalb, H. T. (1970), Summary report of the development of a laser velocimeter to be used in AEDC wind tunnels. AEDC-TR-70-101.
- Mayo, W. T., Jr. (1979), Ocean laser velocimetry systems: signal processing accuracy by simulation. Laser Velocimetry and Particle Sizing, Hemisphere, Washington, D.C.

- Mazumder, M. K. and Wankum, D. L. (1970), SNR and spectral broadening in turbulence structure measurement using a CW laser. Appl. Optics 9, pp. 633-637.
- McLaughlin, D. K. and Tiederman, W. G. (1973), Biasing correction for individual realization of laser anemometer measurements in turbulent flow. Phys. Fluids 16, pp. 2082-2088.
- McDarress, D. and Johnson, D. A. (1979), Investigation of turbulent boundary-layer separation using laser velocimetry. AIAA J. 17, pp. 747-752.
- Nakayama, A. (1985), Measurements of separating boundary layers and wake of an airfoil using laser Doppler velocimeter. AIAA P-85-0181.
- Owen, F. K. and Calarese, W. (1987), Turbulence measurements in hypersonic flow. AGARD CP 428.
- Peterson, J. C. and Maurer, F. (1975), A method for the analysis of laser-Doppler signals using a computer in connection with a fast A/D-converter. Proceedings of the LDA Symposium Copenhagen 1975, Hemisphere, Washington, D.C.
- Petrie, H. L. Saminy, M. and Addy, A. L. (1985), An evaluation of LDV velocity and fringe bias effects in separated high speed turbulent flows. International Congress on Instrumentation in Aerospace Simulation Facilities, Stanford, CA, IEEE Publication 85CH2210-3.
- Robinson, S. K., Seegmiller, H. L., and Kussoy, M. I. (1983), Hot-wire and laser Doppler anemometer measurements in a supersonic boundary layer. AIAA P-83-1723.
- Rudd, M. J. (1969), A new theoretical model for the laser Dopplerimeter. J. Phys. E. Sci. Instrum. 2, pp. 55-58.
- Scharier, E. T. (1980), Turbulence measurements in the boundary layer of a low-speed wind tunnel using laser velocimetry. NASA TM 81165.
- Stevenson, W. H., Thompson, H. D., and Roesler, T. C. (1982), Direct measurement of laser velocimeter bias errors in a turbulent flow. AIAA J. 20, pp. 1720-1723.
- van de Hulst, H. C. (1957), Light Scattering by Small Particles. John Wiley and Sons, New York.
- Yanta, W. J. and Lee, R. E. (1974), Determination of turbulence transport properties with the laser Doppler velocimeter and conventional time-averaged mean flow measurements at Mach 3. AIAA P-74-575.

## CHAPTER 7

LASER DOPPLER ANEMOMETRY IN SUPERSONIC FLOWS:  
PROBLEMS OF SEEDING AND ANGULAR BIASBY  
M. ELENAInstitut de Mécanique Statistique de la Turbulence  
Unité Mixte Université C.N.R.S. No. 380033  
12, Avenue du Général Leclerc  
13003 MARSEILLE  
FRANCE1. INTRODUCTION

In Chapter 6, D. Johnson discussed the application of L.D.A. to supersonic flows, and described many of the problems that can be encountered. Here, we continue that discussion by considering two important additional difficulties: the problems of seeding and angular bias.

2. THE SEEDING PROBLEM

One would think that because the L.D.A. is an optical technique, it is non intrusive, that is, it does not alter the flow in any way. In reality, it is not so simple. For supersonic flows, it is necessary to have tracking particles which are small enough to follow the fluid motion, which can be difficult when the flow gradients are severe, as in the case of shock/boundary layer interaction. The response time of the particles was discussed in Chapter 6. It is often necessary to seed the flow with the appropriate size particles, and here we are particularly concerned with the problem of the seeding technique itself, that is, how the particles can be introduced without disturbing the flow.

Whatever naturally occurring particles exist in the flow, it is preferable to remove them by filtering, and then seed the flow in the plenum chamber with "good particles", where a good particle is one that faithfully follows the flow. In the supersonic flows, the frequency range of the velocity fluctuation is extremely wide, and it is difficult to ensure that the particles are "good". In low density flows, this problem is considerably aggravated because of low seeding densities and the augmentation of particle drag with increasing Knudsen number.

To study the response of particles to an abrupt change in the flow condition in the absence of turbulence, Boutier et al (1986) investigated the behavior of particles crossing a shock. In this type of study, it is necessary to use receiving optics with a wide light-collection angle, and a very sensitive photomultiplier to observe the smallest particles with a reasonable signal-to-noise ratio. Boutier et al found that latex balls of 0.3  $\mu\text{m}$  diameter displayed the shortest response distance downstream of the shock. Paradoxically, they observed almost the same response distance for latex balls of 2  $\mu\text{m}$  diameter. They did not offer an explanation for this surprising result. This could bring into question the equation of Tchen (1947) for the movement of spherical particles across a discontinuity, as suggested by Guin and Elena (1987). Furthermore, it is also necessary to emphasize the importance of the quality of flow seeding. The quality of the measurements obtained by L.D.A. depends greatly on the method of seeding the flow. It is essential that the flow upstream of the measuring point remains undisturbed by the introduction of the particles, and it is therefore necessary to inject the particles into the flow at a speed equal to the local mean flow velocity. This is a general result, first demonstrated by Favre (1938).

Elena and Gaviglio (1983) showed that when an injector is used, the wake of the injector can perturb the flow significantly, even if the speed of injection equalled the flow speed. They compared the L.D.A. output with the output of a hot-wire anemometer and other probes to determine the importance of streamlining the injector in reducing the perturbation of the downstream flow, including the case where the injector was placed upstream of the throat in the settling chamber.

To avoid the interference produced by the wake, it would seem preferable to inject the particles at the wall, especially for the study of boundary layers. However, Elena and Gaviglio showed that the resulting wall jet can also disturb the flow, even when it is placed upstream of the throat. Figure 1 shows the result for the turbulence intensities measured in the boundary layer on the wall of the tunnel a distance  $X$  downstream of the throat. In the figure,  $V$  is the mean velocity of the seeded air emitted from a simple

hole in the wall of the settling chamber,  $U_{ch}$  is the mean velocity of the flow in the settling chamber,  $\delta$  is the boundary layer thickness,  $y$  is the wall distance, and  $\sqrt{e'^2}$  and  $\sqrt{e''^2}$  are the rms voltage fluctuation levels measured by a hot-wire anemometer with and without injection, respectively. The results show that the ratio  $V/U_{ch}$  must be very small ( $< 0.05$ ) to avoid significant errors in the rms turbulence measurement. Higher injection velocities can produce large errors, even far downstream of the throat. The effects of the injection are felt at all points in the boundary layer, but they have the strongest relative effect in the outer region of the layer.

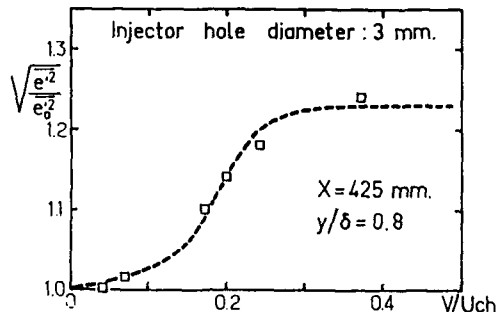


Figure 1. Effect of the seeding process

It is also possible to seed the entire upstream flow, to avoid all of the problems associated with injectors and wall injection. Unfortunately, when the whole flow is seeded, it may be necessary to stop the experiment frequently to clean the windows. In the case of a blowdown tunnel, this may not be such a problem because of the intermittent nature of operation. However, the cost of this type of seeding may be high, especially when using latex balls. Finally, the seeding of the boundary layer flow close to the wall may not be sufficiently dense when this kind of global seeding is used.

### 3. THE ANGULAR BIAS

Among the mechanisms that distort L.D.A. measurement results in supersonic flows, angular bias is particularly important. Angular bias is related to the number of fringes crossed by a particle in its flight through the measurement volume and it can produce significant errors when the number of fringes is small. Whiffen (1975) has shown how the angular bias can be reduced by using a Bragg cell, but in supersonic flow where the measured Doppler frequencies are already very high (about 40 MHz), this solution is not always possible. A Bragg cell typically shifts Doppler frequency to approximately 100 MHz, a value far higher than the cut-off frequency of the counter preamplifiers used to improve the signal-to-noise ratio. To retain a high precision of measurements with the presently available counters, a frequency of 45 MHz must not be exceeded. Furthermore, although angular bias is usually insignificant in single component measurements of a low turbulence flow, it becomes highly significant in two-component measurements of very turbulent, and especially, supersonic flows.

Consider the example of a typical commercial two channel L.D.A. with the optics arranged so that the initially parallel beams form the vertices of a right isosceles triangle on the focussing lens (Fig 2). The probe volume is formed by a combination of two measurement volumes whose normals to the fringe planes form the angles  $\phi_{fb}$  and  $\phi_{fg}$  with the horizontal plane (the subscripts b and g refer to the blue and green components of an argon ion laser beam).



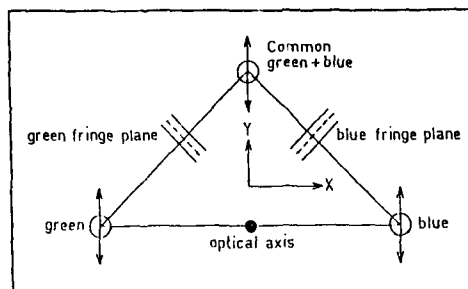


Figure 2. Emission beam configuration

For each measurement volume, the cross section of the flow which intersects the required minimum number of fringes  $N_n$  constitutes what may be called the "useful seeding cross section"  $S$  of the measurement volume. This area  $S$  was calculated for a one-component system by Buchhave (1975) and Dimotakis (1976), and by Whiffen (1975) when a Bragg cell is used. The calculation was extended to a two-component configuration by Lacharme (1984), and Lacharme and Elena (1987) who obtained:

$$S_g = S_{og} \left[ 1 - \left( \frac{N_n/N_{a_g}}{\cos(\psi - \varphi_{fg})} \right)^2 \right]$$

$$S_b = S_{ob} \left[ 1 - \left( \frac{N_n/N_{a_b}}{\cos(\psi - \varphi_{fb})} \right)^2 \right]$$

$S_o = \pi cd$  is the reference cross section of the measurement volume, (the measurement volume is assumed to be an ellipsoid with  $c$  the optical semi-axis and  $d$  the vertical semi-axis).  $N_n$  and  $N_a$  correspond respectively to the number of fringes required for validation and the actual number of fringes.  $\psi$  is the angle formed on a vertical plane by the longitudinal velocity  $U$  and the normal to the fringe plane.

For classical L.D.A. systems,  $\varphi_{fg} = +45^\circ$  and  $\varphi_{fb} = -45^\circ$ . Simultaneous validation of a particle with velocity  $\vec{u}$  on both channels implies that the cross sections  $S_g$  and  $S_b$  corresponding to the direction  $\vec{u}$  are different from zero. This allows a simultaneous "useful" cross section  $S_{20}$  to be defined (Lacharme 1984), that is,  $S_{20} = S_g \cap S_b = \inf(S_g, S_b)$ . Figure 3, which shows  $S_{20}(\psi)$  in polar form, illustrates the magnitude of this bias. When the measurement volume contains just enough fringes required for validation ( $N_g = N_{g0}$ ), validation occurs only for the particles which have a velocity direction close to the direction normal to the fringe plane. Validation cones for each component become very narrow, and the overlap angle that characterizes the useful cross section for simultaneous validation approaches zero. Simultaneous measurement is no longer possible in this case. To obtain accurate measurements using two-component L.D.A. systems, it is therefore necessary to increase the number of fringes  $N_{a_g}$  and  $N_{a_b}$  to reduce blind angles, and to reduce the angle  $|\varphi_{fb} - \varphi_{fg}|$  formed between the normals to the blue and green fringe planes, thereby increasing the area of angular overlap between the measurement volumes. It is straightforward to show that for supersonic flows the bias is negligible for single component configurations. A two-component configuration is more critical: angular bias is no longer negligible because various instrumental factors strongly aggravate it. These factors include the particle characteristics and the velocimeter parameters (laser power, diameter and focal length of optics, photomultiplier gain, counter gain and thresholds, etc.).

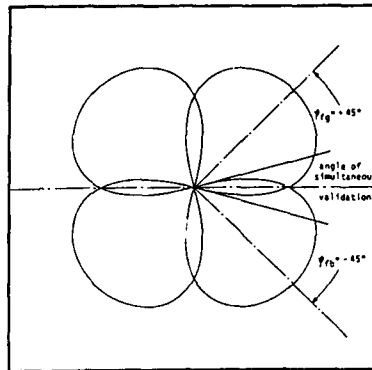


Figure 3. Simultaneous two-component validation angle

The analysis of angular bias given by Lacharme 1984 shows that for supersonic boundary layers, a decrease in  $\sqrt{v'^2}$  is expected when fluctuations are significant. This is also the case for longitudinal intensities when the correlation coefficient  $R_{uv}$  is close to 1. The experimental study of a supersonic turbulent boundary layer by Elena et al (1985) illustrates the existence of this angular bias. For example, Figure 4 shows measurements taken by single and two-component L.D.A. systems. It may be observed that the values of  $\sqrt{u'^2}/U_e$  obtained using a two-component L.D.A. are much lower than those obtained using a single component L.D.A. in the region close to the wall ( $y/\delta_{99} < 0.2$ ), where  $R_{uv}$  is near -1.  $\delta_{99}$  is the boundary layer thickness corresponding to  $U = 0.99 U_e$ , where  $U_e$  is the velocity at the edge of the boundary layer. On the other hand, the results obtained by both systems are similar for  $y/\delta_{99} > 0.7$ , where the fluctuations are small and the correlation coefficient  $R_{uv}$  approaches zero. Figure 4 also gives results obtained using a two-component L.D.A. for the distribution of  $\sqrt{v'^2}$  in the same boundary layer. A direct comparison of the two systems cannot, of course, be made on the transverse component. However, using results from the subsonic boundary layer studied by Klebanoff (1955), it was shown by Elena et al (1985) that the unbiased results obtained for  $\sqrt{u'^2}$  through single-component L.D.A. are very close to Klebanoff's, whereas the results obtained for  $\sqrt{u'^2}$  and  $\sqrt{v'^2}$  through two-component L.D.A. are lower than those obtained by Klebanoff. This reduction can be attributed, at least in part, to the effects of angular bias.

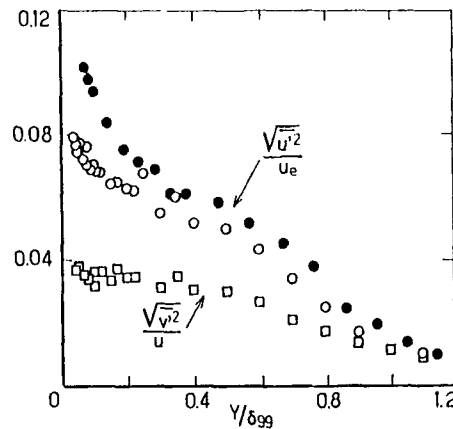


Figure 4. Distribution of turbulence intensity

- a) Fluctuation of  $u'$ 
  - single-component L.D.A.
  - two-component L.D.A.
- b) Fluctuation of  $v'$ 
  - two-component L.D.A.

Measurements of Reynolds shear stresses are best obtained using a two-component L.D.A. since the longitudinal and transverse velocity components are measured simultaneously, in contrast to the case of a one-component system where measurements must be taken at two different beam orientations. Besides the necessary to assume stationarity, errors can arise from distortions and displacements of the L.D.A. measurement volume during the rotation of the optics.

Given the uncertainty of the values of the boundary thickness  $\delta_{999}$  corresponding to  $U = 0.999 U_e$  and the wall friction  $\tau_w$ , the various measurements of Reynolds stresses by Johnson and Rose (1975), Robinson et al (1983), Elena et al (1985) agree to a satisfactory degree throughout a large portion of the boundary layer (see Figure 5). For the inner region of the boundary layer, the values given by L.D.A. in supersonic flow are generally lower than the subsonic boundary layer result of Klebanoff (1955), and the estimations of  $-\overline{uv}$  made by Sandborn (1976). This decrease is also related to the consequences of the angular bias.

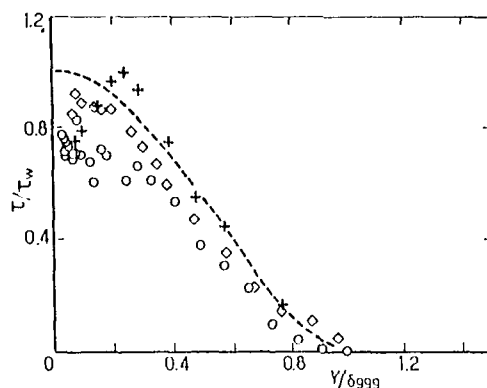


Figure 5. Turbulent shear stresses

- Elena et al (1985)
- + Johnson, D.A.; Rose, W.C. (1975)
- ◇ Robinson, S.K. et al (1983)
- Klebanoff, P.S. (1955)

These low values of  $-\overline{uv}$  near the wall were also observed by Johnson and Rose (1975) using a one-component L.D.A., as well as by Dimotakis et al (1978). Robinson et al (1983) suggested that "the roll-off in shear stress near the wall may be due to the use of L.D.A. systems with stationary fringes". The results obtained by these authors, using Bragg cells to provide moving fringes, seem to show that at least some of the effects of angular bias can be eliminated in this way, when it is possible. In other cases, it should be possible to reduce angular bias by decreasing the angle  $\phi$ . Angular bias also affects the measurement of the third velocity component in the case of a three-component configuration. The validation cross section then depends on the intersection of three-component probe volumes. Angular bias then becomes a problem of utmost importance.

## 4. REFERENCES

- Boutier, A., Lefèvre, J., Labbé, J., Eléna, M., Lacharme, J.P., "Etude expérimentale de la réponse d'une vélocimètre laser à divers types d'aérosols", Rapport Technique ONERA 27/1883 PN, 1985.
- Buchhave, P., 1975, "Biasing Errors in Individual Particle Measurements with L.D.A. Counter Signal Processor", Proceedings of the L.D.A. Symposium, Copenhagen.
- Dimotakis, P.E., 1976, "Single Scattering Particle Laser Doppler Measurements of Turbulence", AGARD Conference Proceedings on Application of Non-intrusive Instrumentation in Fluid Flow Research. Neuilly.
- Dimotakis, P.E., Collins, D.J., Lang, D.B., 1978, "Laser Doppler Velocimetry Measurements in Subsonic, Transonic and Supersonic Turbulent Boundary Layers", Laser Velocimetry and Particle Sizing, 208-219, Hemisphere Publishing Corporation, Washington.
- Eléna, M., Gaviglio, J., 1983 "Confrontation de mesures par anémomètres à laser et à fil chaud, en couches limites turbulentes, à vitesse supersonique", 20<sup>e</sup> coll. Acro. Appel., Toulouse.
- Eléna, M., Lacharme, J.P., Gaviglio, J., 1985; "Comparison of Hot-Wire and Laser Doppler Anemometry Methods in Supersonic Turbulent Boundary Layers", International Symposium on Laser Anemometry, Dybb, A. and Pfund, P.A. ed. A.S.M.E. New York.
- Favre, A., 1938, "Contribution à l'étude expérimentale des mouvements hydrodynamiques à deux dimensions", P.S.T. Ministère de l'air, no. 137.
- Gouin, H., Eléna, M., 1987, "Résolution de l'équation du mouvement de particules à travers un choc", 8<sup>e</sup> Congrès Français de Mécanique, Nantes.
- Johnson, D.A., Rose, W.C., 1975, "Laser Velocimeter and Hot-Wire Anemometer Comparison in a Supersonic Boundary Layer", A.I.A.A Journal, Vol. 13, No. 4, 512-515.
- Klebanoff, P.S., 1955, "Characteristics of Turbulence in a Boundary Layer with Zero Pressure Gradient", N.A.C.A. Rapport No. 1247.
- Lacharme, J.P., 1984, "Vélocimétrie laser Doppler bidimensionnelle pour écoulement turbulent supersonique : quelques aspects spécifiques des processus de mesure", Thèse de Docteur Ingénieur, Marseille II.
- Lacharme, J.P., Eléna, M., 1987, "Effect of an angular bias on LDA measurements in supersonic turbulent flow", Experiments in fluids, to be published.
- Robinson, S.K., Seegmiller, M.L., Kussoy, M.I., 1983, "Hot-Wire and Laser Doppler Anemometer Measurements in a Supersonic Boundary Layer", A.I.A.A Paper 83-1723.
- Sanborn, V.A., 1976, "Effect of Velocity Gradient on Measurements of Turbulent Shear Stress", A.I.A.A Journal, Vol. 14, No. 3.
- Tchen, C.M., 1947, "Mean value and correlation problems connected with the motion of small particles suspended in a turbulent fluid", Ph.D. Thesis, Technical University, Delft, Netherlands.
- Whiffen, M.C., 1975, "Polar Response of an LV Measurement Volume", Proceedings of Minnesota Symposium on Laser Velocimetry, Minneapolis.

## CHAPTER 8

### FLUCTUATING WALL-PRESSURE MEASUREMENTS

by

D. S. Dolling

Department of Aerospace Engineering and Engineering Mechanics,  
University of Texas at Austin  
Austin, Texas 78712, USA

and

J. P. Dussauge

Institut de Mécanique Statistique de la Turbulence  
12 Avenue Général Leclerc,  
13003 Marseille, France

#### Summary

This chapter is concerned with the wall pressure fluctuations under zero pressure gradient and perturbed compressible turbulent boundary layers. The method of measurement, common sources of error and calibration methods are discussed. Analysis of the published data in zero pressure gradient shows that due largely to poor spatial resolution there are few, if any, really reliable measurements. Within the accuracy of the measurements, it does appear that the structure of turbulence in equilibrium supersonic boundary layers is not significantly altered by compressibility. In perturbed flows most of the data are in shock/boundary layer interactions. Attention is focussed on the separation process which is characterized by large amplitude, low frequency shock-induced pressure fluctuations, on the separated flow, and on the outgoing boundary layer. Results are presented for two- and three-dimensional flows.

## 1 Introduction

Knowledge of the wall pressure fluctuations under supersonic turbulent boundary-layers is frequently required in aeronautical design. From the most general point of view, the wall pressure depends on the surrounding flow, and consequently reflects the salient features of that particular flow. Its prediction is, therefore, a complex problem. Since a wall pressure transducer is a non-intrusive device it is very tempting to use it extensively in such situations as separated flows or shockwave/boundary-layer interactions. The making of such measurements, however, shows that they can be very difficult, particularly in supersonic flows and even in zero-pressure gradient boundary layers, the validity of many of the measurements is questionable.

An attempt is made here to provide a brief introduction to the method of measurement, emphasizing those points which the experimentalist must pay careful attention to. Two types of transducers are popular for measurements in supersonic flows; piezoelectric and diaphragm sensors. The analysis will be restricted to these two types. Various sources of errors will be described briefly. The data for zero pressure gradient boundary-layers will then be analyzed, and an assessment of their accuracy will be given. Following that, the main features of pressure fluctuations in rapidly distorted flows will be discussed. The few data existing in this case are mainly in shock wave/boundary-layer interactions.

## 2 Method of Measurement

### 2.1 Types of Transducers and Sources of Errors

In recent studies in supersonic boundary-layers only two types of transducers were used: piezoelectric and diaphragm transducers. Only these types will be considered here. Those points which must be examined and the precautions which must be taken when measurements are made in supersonic boundary-layers will be described. For more basic considerations and for other types of sensors the reader is referred to Blake (1986).

Piezoelectric transducers make use of the fact that some crystals or ceramics output a voltage when a pressure difference is applied across them. In diaphragm transducers, the pressure difference deforms a membrane and this deformation is measured. The main disadvantage of piezoelectric transducers is their sensitivity to acceleration and cable vibrations. This type of instrument can be used only in facilities free from vibrations and must be mounted with great care, using, if necessary, special materials. In diaphragm sensors, there is generally a cavity, so that in addition to the natural frequency of the membrane resonance and anti-resonances may occur. For example, for a cavity of 0.1mm depth and 0.7mm diameter, transverse and longitudinal waves may be expected. For waves travelling transversely, the lowest resonance frequency corresponds to fluctuations for which one quarter of the wave length equals the depth of the cavity; in the example cited, this corresponds

to frequencies of about 700 kHz. For longitudinal waves, the lowest frequency is such that the width of the cavity is one half of the wave length. In the same example, this would correspond to frequencies around 200 kHz. In such cases it is important to check that the major contributions to the phenomena under investigation do not occur at frequencies near the resonance of the transducer. Moreover the use of "pinholes" and/or screens which protect the diaphragm from damage from dust particles can change the shape of the measured spectrum. Finally, the main advantage of diaphragm sensors is that they are practically insensitive to acceleration and for this reason are easily installed and used.

These transducers have to measure fluctuations at rather high frequencies. In a turbulent flow of thickness  $\delta$  with an external velocity  $U_e$ , a typical frequency for the energy-containing eddies is  $U_e/\delta$ . The upper frequency limit is of order  $U_e/\xi$ , where  $\xi$  is the Kolmogorov scale; it depends on the turbulent Reynolds number. However, for the flows commonly investigated it is assumed that the velocity fluctuations can be safely measured if the frequency cut-off of the instrumentation is greater than  $5U_e/\delta$  (Kistler 1959, Garigliis et al. 1981). For example, in a Mach 2.3 boundary-layer with  $U_e = 550$  m/s and  $\delta = 1$  cm, the typical frequency is 55 kHz; this means a minimum bandwidth of 275 kHz is needed. It will be assumed that the same rule applies to pressure fluctuations.

## 2.2 Common Sources of Errors

Generally, transducers are affected by moisture and dust. However, in wind tunnels where the quality of air can be controlled, these difficulties can be easily overcome. Two other areas of great practical importance are the spatial resolution and the flushness of the transducer mounting.

The question of spatial resolution has been examined in detail in low speed equilibrium boundary layers [see for example Willmarth (1975) or Blake (1986)]. An important contribution was made by Corcos (1963) who developed a theory for calculating the damping due to spatial integration. In this theory, it is assumed that the two-dimensional spectra of pressure (or two-point filtered correlations) are known; they were taken from experiments. In summary, the 3dB damping point is predicted to occur roughly at a non-dimensional frequency  $\omega r/U_e \approx 1$ , where  $\omega$  is the circular frequency,  $r$  the radius of the transducer and  $U_e$  the convection velocity of the perturbation considered. The results are generally in good agreement with measurements, at least in the medium frequency range.

A similar theory has not been developed for supersonic flows; in the next section, it will be shown that within the range of accuracy of the available measurements, it is reasonable to assume that the statistical properties are comparable in supersonic and in subsonic zero pressure gradient boundary-layers. Considering again a boundary-layer with  $U_e = 550$  m/s, for a transducer with  $2r = 0.7$  mm and  $U_e \approx 0.6U_\infty$ , the value  $f = 150$  kHz is obtained for the frequency limit given by  $2\pi fr/U_e = 1$ .

Moreover if the frequency  $f = U_e/2\pi r$  is constrained to be larger than  $5U_e/\delta$ , a rough but simple criterion for the required diameter  $d$  of the transducer is given by

$$d < \frac{1}{5\pi} \frac{U_e}{U_\infty} \delta \quad \text{i.e. } d < 0.04\delta \quad (1)$$

This "outer flow scaling" formula provides a means of determining quickly the size of a transducer, knowing only the thickness of the layer.

Another approach has been used by Emmerling (1973) and Schewe (1983) for subsonic flows. It uses the fact that the wall pressure fluctuations depend on some volume surrounding the point where the measurement is made, but are mainly influenced by the wall region. In particular, Schewe deduced from his measurements that an ideal transducer should have a diameter less than twenty times the viscous length scale  $\nu_w/u_\tau$ , where  $\nu_w$  is the wall kinematic viscosity and  $u_\tau$  the friction velocity. Schewe indicates that in his boundary-layer, for which the Reynolds number is rather low, there is still an appreciable amount of energy at the "viscous" frequency  $u_\tau^2/\nu_w$ . An example shows the correspondence between this viscous scale and frequencies which can be found in the flow. The Kolmogorov length scale  $\xi = (\nu^3/\epsilon)^{1/4}$  ( $\epsilon$  is the dissipation rate per unit mass) can be calculated at the point  $y^+ = 10$ ; at this point  $\rho_w \epsilon \approx \tau_w^2/4\mu_w$ , so that  $\xi \approx \sqrt{2}\nu_w/u_\tau$ . If Taylor's hypothesis is now used, as  $U \approx 10u_\tau$  for  $y^+ \approx 10$ , a frequency scale is deduced,  $f = 5\sqrt{2}u_\tau^2/\nu_w$ . The viscous frequency scale  $u_\tau^2/\nu_w$  is then a factor of magnitude below the upper frequency limit in the zone of maximum production. If these results hold also for supersonic boundary-layers, two criteria are obtained for the diameter of the transducer  $d$  and the bandwidth  $f_i$  of the system:

$$\begin{aligned} d &< 20\nu_w/u_\tau \\ f_i &> u_\tau^2/\nu_w \end{aligned} \quad (2)$$

It can be seen that condition (1) can be fulfilled, and not condition (2), if  $\delta^+ (\equiv \delta u_\tau/\nu_w)$  is larger than 500, i.e., in high Reynolds number boundary-layers.

Finally, a common source of error that should be carefully checked is the transducer flushness. It is obvious that, to keep the flow undisturbed, the departure from flushness has to be smaller than  $\nu_w/u_\tau$ . To the best of the authors knowledge, no systematic test of this scaling has been made; however the measurements of Coe (1969) and Hanly (1975) support this idea. Moreover, their results show that if the sensor is protruding, the measurements can be seriously in error: the r.m.s. pressure is changed and the coherence and phase functions are significantly modified in the energetic range, so that two point measurements can be drastically changed. On the other hand, if the transducer is slightly recessed, the changes in the measurements are less significant. In practice, it is difficult to install the transducer flush with the wall with an accuracy better than 0.01 mm. If  $\nu_w/u_\tau$  is less than 0.01 mm, as is often the case in high pressure blowdown tunnels, the best recommendation is to recess the transducer slightly.

## 2.3 Calibration

Calibration problems are of the same basic nature in subsonic and supersonic layers. Only those problems typical of supersonic flows are emphasized here. The fluctuations to be measured are typically in the range  $10^2 - 10^3$  N/m<sup>2</sup>; their frequency range is often larger than 100 kHz.

One possibility is to use a loudspeaker to calibrate the transducers; due to the very high level pressure fluctuations special equipment will probably have to be built. Another approach, and a more common one, [see Kistler and Chen (1962), Doebelin (1966), Raman (1974)] is to use a shock tube to produce a pressure step. The frequency response of the transducer can be obtained with the possible resonances. An interesting variant of this procedure is to use the pressure step across the shock wave produced by a bullet in supersonic flight (Raman 1974). In this way, a very rapid pressure change is produced, allowing calibration at high frequency. From the response to this step the transfer function of the transducer can be deduced. Frequently static calibrations only are made. The shock tube tests of Raman showed that, for the diaphragm type transducers which are widely used, static calibrations differ by only a few percent from dynamic calibrations. When dynamic calibrations are not possible and if multi-point measurements are to be performed, it is recommended that comparisons are made of the output of different transducers placed at the same location. From the comparisons at least consistent sets of data can be obtained (Dussauge 1983).

Finally, with many commercially available transducers, the lack of spatial resolution, the problems of cavity resonance, etc., may make it difficult to measure fluctuations at frequencies beyond 100 kHz. However, for lower frequencies accurate measurements can be performed.

## 3 Pressure Fluctuations in Zero Pressure Gradient Supersonic Boundary-Layers

### 3.1 Introductory Remarks

As discussed in the previous section, the main sources of errors are:

1. Spatial integration which acts like a low pass filter, and reduces the standard deviation. By reducing the contribution of the (weakly correlated) high frequencies, this increases the autocorrelation and two-point correlations.
2. Spurious signals due to tunnel noise and vibration; this increases the r.m.s. value.
3. Electronic noise which increases the standard deviation; as its spectral content is usually located at high frequencies, its characteristic time scale is very small, so that generally correlations are reduced by such noise.

The available data may be affected by all of these problems. As a first step, an attempt has been made to evaluate their influence on the published results. For obvious reasons, it is very difficult to determine the noise level in the experiments. However in most cases it is possible to determine approximately the frequency cut-off, and to check if the measurements are affected by bandwidth limitations. In this case, the analysis is also difficult, because the pressure fluctuations depend on both Mach number and Reynolds number. For this reason, the ratio  $\sigma_p/\tau_w$ , where  $\sigma_p$  is the standard deviation of the pressure fluctuations and  $\tau_w$  the wall friction, will be examined, because it is probably a weak function of the Mach number. There is no widely accepted correlation which gives this functional dependence for supersonic zero-pressure gradient boundary-layers. Moreover, inspection of the available data shows that the range of Reynolds number explored is rather limited: for example, the Karman number  $u_*\delta/\nu_w$  ranges from about 800 for Debieve's data (1983) to 10,000 for Dolling and Murphy's results (1983). We now assume that low speed formulations give a reasonable indication of the Reynolds number influence on  $\sigma_p/\tau_w$ , for a fixed Mach number. For example, Simpson et al. (1987), using the numerical results of Panton and Linebarger (1974) found that  $\sigma_p/\tau_w$  varies as  $[\ln(u_*\delta/\nu_w) + 9.24]^{1/2}$ . Such a law gives a variation of only 7% for  $\sigma_p/\tau_w$ , in the case of the present flows. Thus, it is believed that the observed trends are not the consequence of Reynolds number variations.

The effective bandwidth for each set of measurements was also evaluated. It was done as follows: the cut-off frequency  $f_1$  of the electronics circuits was first noted. The equivalent cut-off frequency  $f_2$  due to spatial integration was calculated from Corcos's work; it was defined by the relation  $2\pi f_2 r/U_c = 1$ . The frequency  $f_2$  was determined in each case with  $U_c = 0.6U_\infty$ . The smaller of  $f_1$  and  $f_2$  was then chosen as the upper frequency limit of the measurements.

This upper limit was then compared to characteristic frequencies: the first was the frequency scale of the energetic structures of the boundary-layer  $U_\infty/\delta$ ; the second was the viscous scale  $u_*^2/\nu_w$  defined in Section 2.2. Finally, the influence of the transducer diameter  $d^+$  ( $\equiv du_*/\nu_w$ ) was examined.

The various parameters defining the boundary-layer, namely  $U_\infty$ ,  $\delta$ ,  $u_*$ ,  $\nu_w$ , also had to be defined. When these quantities were given in the original papers, they were used unchanged. When all the quantities were not given, the flow was assumed adiabatic, with a recovery factor of 0.89; the stagnation temperature was taken as 293 K; finally the integral thickness and the friction coefficient were calculated using the formulas proposed by Michel (1960). In general, the accuracy of  $\delta$  is questionable, as pointed out by Fernholz and Finley (1980), but in the absence of any other information, the values reported by the authors were accepted. This may be the cause of additional scatter in the data, but as it will be demonstrated in the next section, does not change the conclusions of the analysis.

### 3.2 Analysis

Figure 1 shows the ratio  $\sigma_p/\tau_w$  plotted versus the nondimensional cut-off frequency  $f\delta/U_\infty$ . The values of  $\sigma_p$  are not corrected for spatial resolution errors, except in the case of Chyu and Hanly (1969) and of Speaker and Ailman (1969), who did not publish the raw data.

Symbols	Author	Mach No.	Reynolds Number $Re \times 10^{-4}$
$\Delta$	Speaker and	1.4	1.81
$\nabla$	Ailman	1.81	2.30
$\triangleleft$		2.52	3.08
$\circ$		3.45	5.33
$\ominus$	Muck et al.	2.84	8.54
$\triangle$	Tan et al.	2.99	5.42
$\times$	Dussauge	1.76	0.50
$\nabla$	Debieve	2.3	0.42
$\triangleleft$	Maestrello	1.42	2.99
$\gamma$		1.98	2.67
$\boxtimes$		2.99	1.83
$\circ$		3.03	3.53
$\triangle$		3.98	1.55
$+$	Kistler and	1.33	3.5
$\wedge$	Chen	2.01	1.57
$\times$		2.6	1.51
$\circ$		3.5	1.55
$\triangle$		3.99	1.65
$\triangle$		4.54	1.47
$\bullet$		5.00	2.22
$\circ$	Chyu and	1.6	1.80
$\circ$	Hanly	2	1.36
$\circ$		2.5	0.93

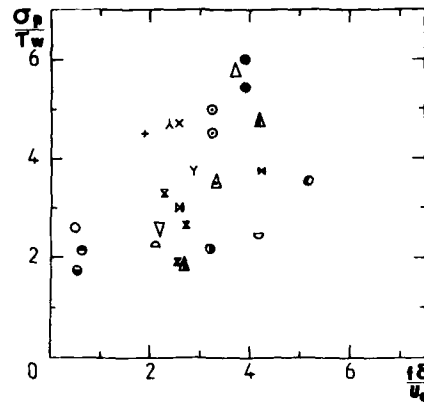


Figure 1: Influence of Cut-Off Frequency on Pressure Fluctuations

A first observation is that few data points have an effective cut-off frequency larger than  $4U_\tau/\delta$ ; this is generally due to poor spatial resolution rather than to the limitations of the electronics. Only Maestrello, Kistler and Chen, and Muck et al. took measurements with a cut-off frequency larger than  $4U_\tau/\delta$ . A second disturbing observation is that the results obtained by the same author, i.e., in the same wind tunnel and with the same electronics, have very close values, nearly independent of Mach number, Reynolds number and non-dimensional frequency limits. This suggests that the measurements reflect in some way the peculiarities of the particular experimental set-up and consequently the real evolution may be masked. For example, Kistler and Chen's data have systematically high values. The third observation is that no clear conclusion can be drawn about the dependence of  $\sigma_p/\tau_w$  on either cut-off frequency or Mach number.

The same data are replotted versus  $f\nu_w/u_\tau^2$  in Figure 2. There are only six points with an abscissa larger than 0.05, indicating that a large part of the high frequency contribution from the flow close to the wall is suppressed because of poor spatial resolution. It is not clear if in high Reynolds number flows it is necessary to reach the dissipative range to obtain accurate r.m.s. values. It is, however, clear that all measurements have been performed with a too narrow a bandwidth. As with Figure 1, no obvious underlying trends are apparent.

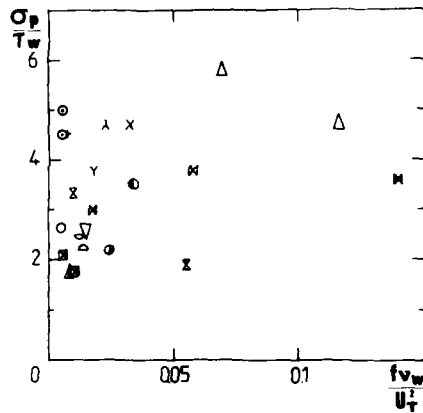


Figure 2: Influence of Cut-Off Frequency on Pressure Fluctuations (continued). Symbols as in Fig. 1

A final attempt was made by plotting  $\sigma_p/\tau_w$  versus  $d^+ = d\nu_w/\nu$  (Fig. 3), as proposed by Emmerling (1973) and Schewe (1983). Data with  $d^+ > 500$  were excluded. The number next to each data point is the Mach number. If the results of Schewe can be extended to the present experiments, the measurements underestimate  $\sigma_p$  if  $d^+$  is larger than 20; in particular for  $d^+$  larger than 100,  $\sigma_p$  should probably be multiplied by 2, if there is no other source of error. Again, no identifiable trends appear in this form, neither for the influence of  $d^+$  or for the Mach number dependence.

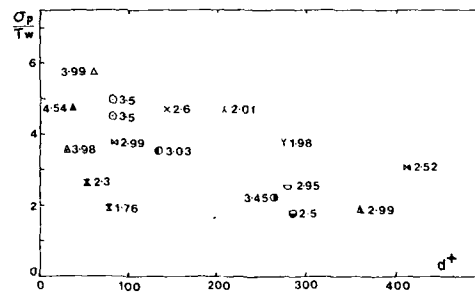


Figure 3: Effect of Transducer Size on the rms Values of Pressure Fluctuations (Symbols as in Fig. 1) (Numbers adjacent to symbols indicate Mach Number)



It should be noted finally, that for the higher Mach numbers, the measurements of Maestrello seem to have the better bandwidth. Some measurements of Kistler and Chen were performed with a reasonable bandwidth, although the results seem systematically too high; this suggests that their results could be affected by noise or spurious signals. As far as the value of  $d^+$  is concerned, the measurements of Debieve (1983) and Dussauge (1985) are satisfactory, whereas those obtained by Muck et al. (1983) have a good  $f\delta_e/U_e$  parameter.

In conclusion, it appears that the measured values of  $\sigma_p$  in zero pressure gradient supersonic boundary-layers are probably too low, if they are not affected by noise. As a consequence of the damping of the high frequencies, the shape of the spectra can be distorted; in particular if they are normalized to unity, the low frequency level will be in error  $\sim 10\%$ . Moreover, with the data presently available it is not possible to define the effect of the Mach number on  $\sigma_p/\tau_w$ .

### 3.3 Characteristic Scales - Space-Time Correlations

An examination was made to determine if some characteristic scales could be deduced from the measurements. The first one was the integral time scale deduced from the integral of the autocorrelation coefficient or from the extrapolated value of the spectrum at zero frequency. A length scale was deduced by using Taylor's hypothesis. This determination was either very difficult or impossible, for, very often, spectra had "bumps" at low frequency which prevented extrapolation. However, when this was possible, it appeared that the integral scale could be much larger than the boundary layer thickness, if the effective bandwidth was too small. For measurements with  $d^+ < 100$ , the integral scale was typically 0.1 $\delta$ , a value consistent with the results obtained in low speed flows.

Space-time correlations were examined, and in particular the locus of the maxima for various values of the separation distance  $x$ . They are shown in Figure 4. It is common to plot these results versus  $x/\delta^*$ ,  $\delta^*$  being the displacement thickness;  $\delta^*$  is widely used for scaling quantities in low speed studies, and is unambiguous, for it is proportional to  $\delta$  but can be determined much more accurately. In supersonic flows, the ratio  $\delta^*/\delta$  depends on the external Mach number, and may produce some scatter. Hence an alternative approach based on the following reasoning was preferred [see for example Corrsin (1963)]. It is well known that from the maximum of the space-time correlation a "convection time" for the eddies can be obtained. During this time, the structure loses a part of its coherence and there is a decrease in the correlation. This loss of correlation for large separations leads to the definition of a characteristic time ("eddy lifetime" or "turnover time") of the large eddies. This time should be proportional to the time scale of turbulence in the boundary-layer which is then the appropriate scaling quantity, and can be defined by  $\Lambda/\sqrt{u'^2}$ , where  $\Lambda$  is some length scale, for example an integral scale, and  $\sqrt{u'^2}$  a typical value of the velocity fluctuations. In the present case such measurements were not available so the friction velocity  $u_\tau$  was chosen as the velocity scale, and  $\delta$  as the length scale of the energetic eddies; the kinematic displacement thickness  $\delta_n^* \approx \int_0^\delta (1 - U/U_e) dy$  would probably have been easier to use, but was not in general given by the authors. It should be noted that the effective bandwidth of these measurements is generally lower than for the determination of the r.m.s. values: either an analog correlator introducing a lower cut-off was used, or the sampling rate was decreased to record two channels of data. A subsonic result is plotted for the sake of comparison.

Chyu & Hanly	M = 1.6	— — — — —
	M = 2.0	— x — — —
	M = 2.5	— • — — —
Muck et al.	M = 2.84	— — — — —
Speaker & Ailman	M = 3.45	— — — — —
Maestrello	M = 1.98	— ○ — — —
	M = 3.03	— • • • • •
Schewe	M = 0.02	— — — — —
Debieve	M = 2.3	— + + — —
Tan et al.	M = 2.99	— • • — —
Dussauge	M = 1.76	— ⊙ — — —
Bonnet et al.	M = 2.27	— — — — —
Kistler & Chen	1.3 < M < 5	shaded zone

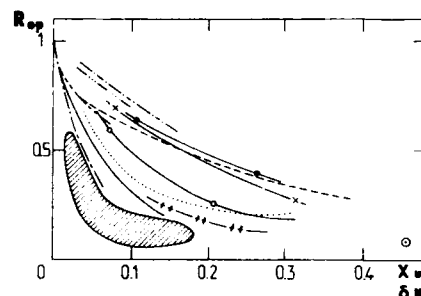


Figure 4: Optimum space-time correlations of wall pressure fluctuations in supersonic boundary layers

Some of the curves in Figure 4 have rather high values. They correspond essentially to cases with a very limited frequency range. When  $d^+$  is small, the curve lies in a range near the subsonic values, whatever the Mach number. A particular trend is observed for Kistler and Chen's results: they fall under the low speed data, whatever  $d^+$  and  $M_e$ . This result and the fact that the values of  $\sigma_p$  reported by these authors are the larger ones suggest that the signal-to-noise ratio of this measurement could be low.

Considering the accuracy of the measurements, a first conclusion is that the characteristic time scale of the energetic part of the pressure fluctuations seems to be of the same order of magnitude as in subsonic flows. This confirms that the structure of turbulence in equilibrium supersonic boundary-layers does not seem to be significantly changed by compressibility. Another conclusion is that there are no reliable measurements of the variance of the wall pressure in these flows. The reasons are the poor spatial resolution and probably the noise and vibration in many wind tunnels. These phenomena largely affect the high frequency part of the fluctuations so that all the phenomena involving the low frequency part of the spectrum can be measured reasonably accurately. For example, the pressure fluctuations produced by an oscillating shock wave in a compression ramp flow occur at low frequency, typically  $0.1U_e/\delta$ , and can be measured with confidence.

## 4 Measurements in Perturbed Flows

### 4.1 Introductory Remarks

There are many flows of interest in which compressible turbulent boundary layers are subjected to sudden perturbations. Buffeting in the transonic regime is one example and has much in common with other performance-limiting phenomena such as dynamic inlet distortion and buzz. The interaction of a shock wave with a turbulent boundary-layer is probably the most important class of flows in which extremely rapid perturbations in pressure and temperature are applied to the boundary-layer. There have been many experimental studies of such phenomena, but only in a small fraction of these studies have wall pressure fluctuations been measured.

The earliest study in which measurements were made is probably that of Kistler (1964) who investigated forward-facing step flows at Mach numbers of 3 and 4.5. In the late 1960's and early 70's, Robertson (1969,1971), Speaker and Ailman (1969), Chyu and Hanly (1960) and Coe et al. (1973), made measurements at speeds from transonic to supersonic. Much of this work was motivated by the need to predict the fluctuating pressure field about high-speed vehicles. From the late 70's to the present, wall pressure fluctuation measurements have contributed to the understanding of forced and self-excited oscillations in transonic diffuser flows (Chen et al. (1979), Sajben and Kroutil (1981), Bogar et al. (1983), Sajben et al. (1984) and Bogar (1986)). There is currently renewed interest in unsteady aspects of shock boundary-layer interaction in external flows, particularly the separation process. Wall pressure fluctuation measurements are the majority of the new data. In this section an attempt is made to summarise what has been learned from these measurements. Only naturally unsteady flows are included. Forced unsteadiness, induced by oscillating boundaries or time-varying upstream or downstream boundary conditions, is excluded.

The review is split into three parts. The first deals with the region bounded by  $X_0$  and  $S$ , where  $X_0$  is the interaction start (defined as where the mean pressure  $\bar{P}_w$  first increases above the undisturbed level  $\bar{P}_{w0}$ ) and  $S$  is the separation location (as indicated by surface tracer techniques). Because of the nature of the pressure signal, this region is called intermittent. The second part deals with the separated flow and the third concerns the outgoing boundary layer downstream of reattachment,  $R$ . For organizational purposes, results from nominally 2-D and 3-D studies are discussed later in separate sections. However, since they share many common features, they are discussed together where appropriate.

### 4.2 Two-Dimensional Flows

#### 4.2.1 Features of the Intermittent Region

Typical pressure signals measured upstream of  $S$  in a separated compression ramp flow at Mach 3 are shown in Figure 5. The moving separation shock generates an intermittent wall pressure signal,  $P_w$ , whose level fluctuates between the range characteristic of the undisturbed boundary layer and that of the disturbed flow downstream of the shock. There is some evidence to suggest that the instantaneous separation point and shock foot are essentially at the same location and that  $S$  is the downstream boundary of a region of intermittent separation [Chen et al. (1979), Gramann and Dolling (1986)]. The fraction of the time that the flow at a point is disturbed (given by the intermittency,  $\gamma$ ) increases downstream of  $X_0$  until just upstream of  $S$ ,  $\gamma = 1.0$ . Kistler (1964) was probably the first to observe this behavior. The same phenomenon has since been seen in flows generated by unswept and swept compression ramps, hemicylindrically blunted fins, sharp fins at angle-of-attack, circular cylinders, and in shock-induced separation in transonic diffusers and on transonic airfoils.

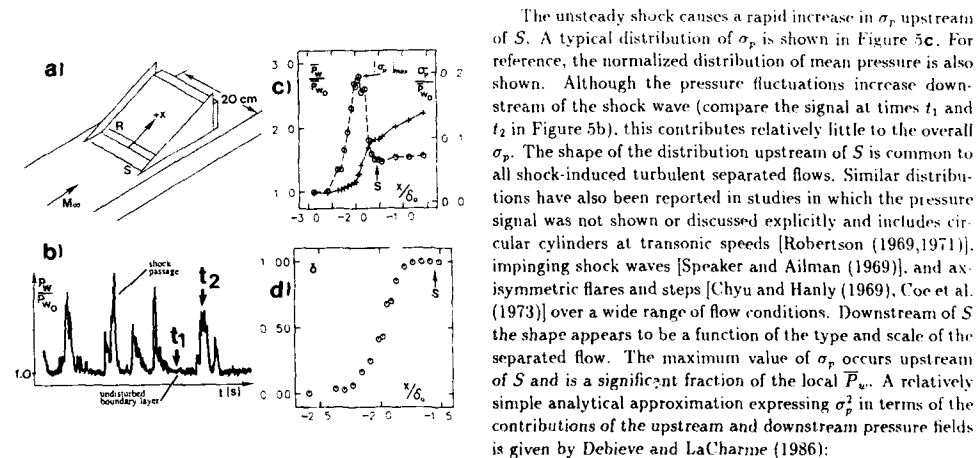


Figure 5: Mach 3 compression ramp flow (a) flow features (b) pressure signal upstream of "S" (c) distribution of mean pressure and rms of pressure fluctuations (d) intermittency

The unsteady shock causes a rapid increase in  $\sigma_p$  upstream of  $S$ . A typical distribution of  $\sigma_p$  is shown in Figure 5c. For reference, the normalized distribution of mean pressure is also shown. Although the pressure fluctuations increase downstream of the shock wave (compare the signal at times  $t_1$  and  $t_2$  in Figure 5b), this contributes relatively little to the overall  $\sigma_p$ . The shape of the distribution upstream of  $S$  is common to all shock-induced turbulent separated flows. Similar distributions have also been reported in studies in which the pressure signal was not shown or discussed explicitly and includes circular cylinders at transonic speeds [Robertson (1969,1971)], impinging shock waves [Speaker and Ailman (1969)], and axisymmetric flares and steps [Chyu and Hanly (1969), Coe et al. (1973)] over a wide range of flow conditions. Downstream of  $S$  the shape appears to be a function of the type and scale of the separated flow. The maximum value of  $\sigma_p$  occurs upstream of  $S$  and is a significant fraction of the local  $\bar{P}_w$ . A relatively simple analytical approximation expressing  $\sigma_p^2$  in terms of the contributions of the upstream and downstream pressure fields is given by Debieve and LaCharme (1986):

$$\frac{\sigma_p^2}{(\Delta p)_s^2} = (1 - \gamma) \frac{\sigma_p^2}{(\Delta p)_s^2} + \gamma \frac{\sigma_p^2}{(\Delta p)_s^2} + \gamma(1 - \gamma)$$

where  $(\Delta p)_s$  is the mean pressure rise across the shock and subscripts  $u$  and  $d$  refer to the pressure fields upstream and downstream of the shock respectively. The only inherent assumption is that the upstream and downstream fields are statistically homogeneous. If  $\sigma_{p_u}$  and  $\sigma_{p_d}$  are small compared to  $(\Delta p)_s$ , which, based on experimental evidence, is a reasonable approximation, then the expression can be simplified to:

$$\frac{\sigma^2 p}{(\Delta p)_s^2} \approx \gamma(1 - \gamma)$$

which has a maximum at  $\gamma = 0.5$ . As a check,  $(\Delta p)_s$  was calculated from  $(\sigma p)_{\max}$  for the 24°, Mach 3 compression ramp flow of Muck et al. (1985). The calculated shock pressure ratio was 1.6 compared to a value of about 1.7 "eyeballed" from the pressure signal. In practice,  $(\sigma p)_{\max}$  appears to occur a little further downstream at  $\gamma \approx 0.6 - 0.7$ , but as a first approximation the above works well.

For comparison of results from different flows and for determining the length scale of the shock motion, it is necessary to quantify  $\gamma$ . Different authors have used different techniques. In all methods, the objective is to calculate the fraction of the time that the flow is disturbed. Dolling and Murphy (1983) used the criterion  $P_w > \bar{P}_{w0} + 3\sigma_p$ ; Narlo (1986) used  $P_w > \bar{P}_{w0} + 4.5\sigma_p$ , and Andreopoulos and Muck (1986) used  $P_w > T$  where  $T$  is an "eyeballed" threshold. Methods using two thresholds have also been employed [Narlo (1986)], Dolling and Brusniak (1987). A brief description is given in section 4.2.3.

In practice,  $\gamma$  increases or decreases as the threshold is changed, but the curves do not change shape: they are simply shifted streamwise. The distribution shape is similar to the normal probability distribution function (Fig. 5d). For all cases for which  $\gamma$  has been reported, the intermittent region extends from  $X_u$  to just upstream of  $S$ . Up to this point, there is no evidence that it correlates with any incoming flow parameter.

Muck et al. (1985) and Dussauge et al. (1985) used a rotatable wall plug in which 4 Kulite transducers were installed in-line with spacing,  $\xi = 0.23\delta$ . Figure 6a shows simultaneously sampled signals upstream of  $S$  in a Mach 3 separated compression ramp flow, for the transducers aligned longitudinally. When the shock is upstream of a given transducer (i.e., channel 2 at time  $t_1$ ), the pressure indicated by it and the 2 downstream transducers is essentially the same and about equal to the pressure level at  $S$ . This suggests that the instantaneous shock structure in the intermittent zone can be described by a single shock wave. The traditional view, that  $\bar{P}_w$  increases through a nominally steady compression fan appears to be incorrect.

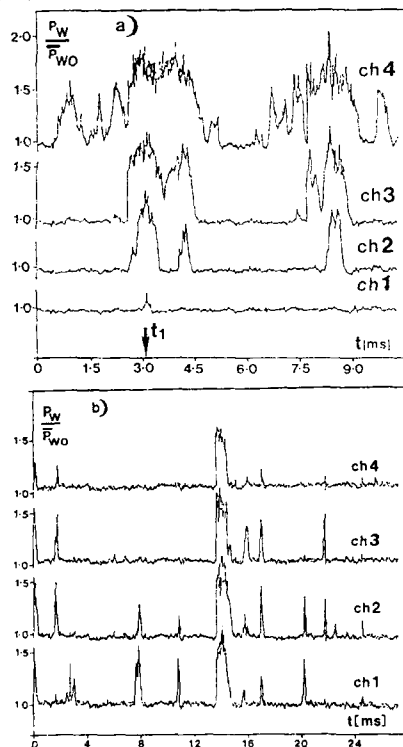


Figure 6. Simultaneous Sampled Pressure signals upstream of "S" in Mach 3 compression ramp flow (a) transducers aligned streamwise (b) transducers aligned spanwise

Pressure signals in the same flow with the plug rotated 90° (Fig. 6b) show that the shock front has spanwise ripples with wavelengths as small (if not smaller) than  $0.23\delta$ , and as large (if not larger) than  $0.69\delta$ . Dussauge et al. (1983) also noted spanwise non-uniformities in the auto-correlations of the signals at different spanwise locations. The intermittency also displayed strong spanwise non-uniformities. These observations agree qualitatively with the results of Settles (1979) which show that the separation line is wavy with a repetitive spanwise character. Reliable quantitative data on the spanwise structure, if any, are lacking and is a fruitful area for future work.

#### 4.2.2 Power Spectra in the Intermittent Region

Power spectra at the location of  $(\sigma_{pw})_{\max}$  are shown in Fig. 7. The model geometries and flow conditions are given in the legend as is the frequency resolution,  $\Delta f$ , and the number of data records,  $N_R$ , the spectrum is based on. All of these results were obtained in the Princeton University Mach 3 blowdown tunnel either at Station 1 ( $\delta \approx 1.6$  cm) or at Station 2 ( $\delta \approx 2.2$  cm) in the tunnel floor boundary layer. The data in Fig. 7 are presented in the commonly employed form  $fG(f)/\sigma_p^2$  vs  $f$ , plotted on linear-log axes, where  $G(f)$  is the one-sided, auto-spectral density function. The choice of plotting axes is an important consideration. Since  $\sigma_p^2 = \int_0^\infty G(f)df$  then for visualising the contribution of a given frequency range to  $\sigma_p^2$ , linear-linear axes, although awkward, are probably the least misleading. An alternative approach which has the advantage that the area under a given curve segment is linearly proportional to the contribution of that frequency range to  $\sigma_p^2$  is to plot  $f \cdot G(f)$  vs  $f$  on linear-log axes. The frequency range of shock oscillation which is characterised by high amplitude fluctuations is then more evident than when plotted as  $G(f)$  vs  $f$  on log-log scales as is done for curve 1 in the inset at the top of the figure.

Curve	Star./Geom.	$\sigma_p$	$\Delta f$ [Hz]	NR
1	2/24° ramp	0.85	39	-
2	2/24° ramp	0.80	488	750
3	1/24° ramp	0.72	488	600
4	2/20° ramp	0.64	195	200
5	2/16° ramp	0.47	195	200
6	1/D=1.27 cm	0.70	156	36
7	1/D=2.54 cm	0.84	156	36
8	1/16° sharp fin	0.21	97	≥72
9	1/20° sharp fin	0.33	97	≥72
10	1/12° sharp fin	-	97	≥72

- indicates unknown;  $\sigma_p$  in psi

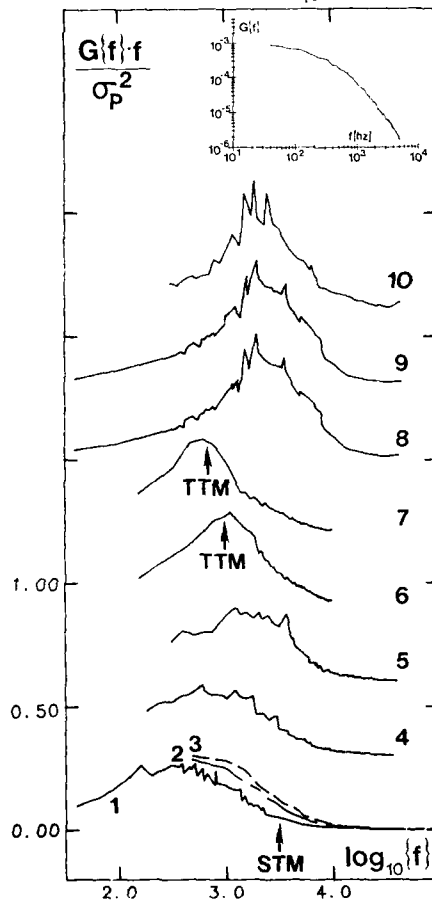


Figure 7 Power spectra at location of  $(\sigma_p)_{\max}$

(curves 1-3 on axes as shown; curves 4-10 are shifted 0.3 units of  $f \cdot G(f)/\sigma_p^2$  upwards)

However, plotting  $f \cdot G(f)$  vs.  $f$  does suffer from several drawbacks and care must be taken in the interpretation. Compared to the linear-linear form, the logarithmic representation may mask the low frequency component which is rejected to zero. Second, maxima in  $fG(f)$  occur at each point where  $G(f)$  vs  $f$  in linear-linear form has a slope of  $-1$ . This point has no particular physical meaning and is not always in the dominant frequency range. Third, peaks evident in the original linear-linear plot can be aliased to lower frequencies leading to misleading interpretations. Normalizing by  $\sigma_p^2$ , to force the area under the curve to unity, can also be misleading, unless the true spectrum and the true  $\sigma_p^2$  have been measured. If there exists a frequency cut-off, then as the area is forced to unity the low frequency range of the spectrum will be incorrect, even if the original dimensional spectrum was correct. In the incoming boundary layer and separated flow zones, frequency cut-off is a pervasive problem, and normalizing by  $\sigma_p^2$  is not recommended. On the other hand at  $(\sigma_p)_{\max}$ , where a large fraction of the energy is at low frequency, little error will be incurred.

Power spectra in the intermittent region of other 2-D flows, in transonic normal shock interaction in diffusers, and shock-induced separation on transonic airfoils all have similar characteristics. Even at very high freestream velocities and with thin boundary layers, which generates extremely small time-scales,  $\delta/U_\infty$ , power spectra indicate low shock oscillation frequencies; spectral center frequencies are typically 2 kHz or less. Although an idea of the range of shock frequencies can be deduced from power spectra, several authors have tried to isolate the shock motion component of the pressure signal, and determine the shock properties separately. A brief description of the techniques employed and some of the results follow in the next section.

#### 4.2.3 Separation Shock Wave Frequency Estimates

To isolate the shock component of the pressure signal, several authors have employed conditional sampling algorithms. Their common feature is the conversion of the pressure signal (Fig. 8a) into a "box-car" of amplitude unity and varying frequency (Fig. 8b). The time  $T_i$  between consecutive passages of the shock over the transducer is determined and statistics performed to obtain the probability distribution of  $T_i$  and the mean value  $T_m (\equiv \frac{1}{N} \sum_{i=1}^N T_i)$ , where  $N$  is the number of periods. It should be noted that  $1/T_m$  is the shock zero crossing frequency,  $f_c$ , not the mean shock frequency.  $f_c$  is the number of crossings per second of the transducer by the shock wave, whereas the mean shock frequency is  $\frac{1}{N} \sum_{i=1}^N f_i$  where  $f_i = 1/T_i$ . Since the pressure signal is of a turbulent flow, precautions must be taken to ensure that high-frequency turbulent fluctuations are not inadvertently counted as shock waves. This problem, and others, are discussed below.

In earlier work (Dolling & Murphy, (1983)) a single threshold  $T$  was used, as indicated in Fig. 8a.  $T$  was set equal to  $\bar{P}_w + 3\sigma_{P_w}$ , where subscript  $w$  refers to properties of the undisturbed boundary layer. Thus, when  $P_w$  increased above  $T$ , this indicated the start of the shock passage upstream over the transducer. When  $P_w$  fell below  $T$ , this indicated the end of the shock passage. However, because drift and zero shifts cause small dc offsets from test to test; the results can be inconsistent. Andreopoulos and Muck (1985) improved on this by "eyeballing" each signal and choosing  $T$  just above the largest fluctuations of the boundary layer fraction of this signal. This technique was used in the 24° compression ramp

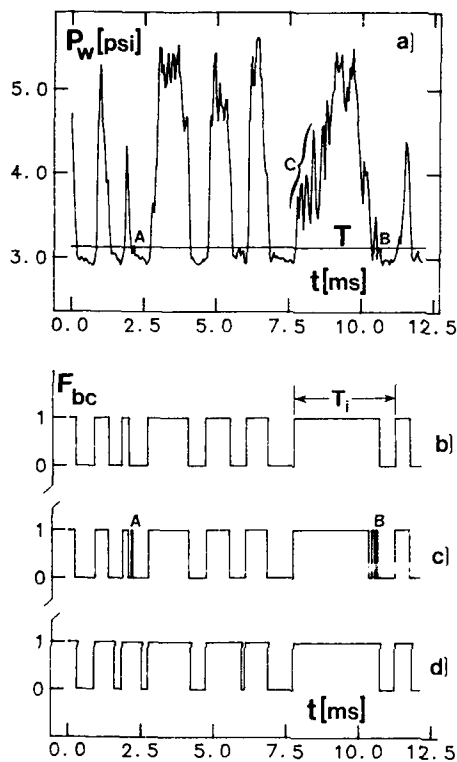


Figure 8: Conversion of pressure signal into box-car (a) original signal (b) box-car judged by eye (c) box car from two-threshold algorithm

no subjective input from the user.

Initially, if  $P_w < T_2$ , a flag is set "off". The algorithm then checks successive data points. If the first point is less than  $T_2$  and the second point is greater than  $T_2$  and the flag is "off", this marks the start of the passage of a shock. The counter that records the time between successive shock waves is then initialized and the flag is then set "on". Further crossings of  $T_2$  are not counted until  $P_w$  is less than  $T_1$ . Termination of the shock occurs when this happens, and the flag is reset. As shown in Fig. 8d this process largely eliminates the counting of turbulent fluctuations as shock waves.

Distributions of  $f_c$  using this approach are shown in Fig. 9a for cylinder flows at Mach 5.  $f_c$  is a maximum at  $\gamma \approx 0.5$  in both cases; about 1.6 kHz for  $D \approx 1.27$  cm and about 1.2 kHz for  $D = 1.91$  cm. These values are indicated by arrows labelled TTM on their corresponding power spectra in Fig. 9b and fall close to the center frequency of the spectrum. Narlo (1986) also calculated  $f_c$  using the single threshold method. These values are indicated by arrows labelled STM in Fig. 9b and, consistent with the ramp results mentioned earlier, are significantly higher than the center frequency. The two-threshold algorithm was also used by Dolling and Narlo in Mach 3 blunt fin flows. With only a few measurement stations in the intermittent zone neither the distribution of  $f_c$  or  $(f_c)_{\max}$  could be defined very accurately. For  $D = 1.27$  cm and 2.54 cm  $(f_c)_{\max}$  was estimated to be about 1 kHz and 0.7 kHz, respectively. Again, these values fell close to the power spectra center frequencies (curves 6 and 7, Fig. 7).

flow at Mach 3.  $T_m$  was found to be approximately  $7.7\delta_0/U_\infty$ . Further,  $T_m$  was independent of position in the intermittent region and ramp angle (i.e., independent of downstream flow conditions).  $f_c$  was equal to  $0.13U_\infty/\delta_0$ , which the authors claim is the same order as the estimated bursting frequency of the turbulent boundary layer. These two results led these authors to conclude that "the incoming boundary layer is the most likely cause triggering the shock wave oscillation."

Although this method avoids the problems noted above, it is subjective and difficult to apply consistently. However, a far more serious problem is that many "false shocks" are counted. Fig. 8 illustrates the problem. Fig. 8b shows the "ideal" box-car, as judged by eye, for the pressure signal in Fig. 8a. Fig. 8c shows the box-car from the algorithm, in which turbulent fluctuations such as A and B (Fig. 8a) are inadvertently counted as shock waves. Because these "shocks" are actually turbulent fluctuations they occur at high frequency and their inclusion in the box-car drives  $f_c$  higher. No matter what level  $T$  is set at, fluctuations such as A and B or the series around C (Fig. 8a) will always create false shocks. That this problem is significant can be seen by locating the value of  $f_c$  ( $0.13 U_\infty/\delta_0 \approx 3.1$  kHz) on the corresponding power spectrum in Fig. 7.  $f_c$ , indicated by the arrow labelled "STM", is around the upper boundary of the shock frequency range.

To avoid this problem an algorithm using two thresholds was developed by Dolling and Narlo (1987). In this case, the upper threshold  $T_2 = \bar{P}_o + 4.5\sigma_{P_o}$  and the lower one  $T_1 = \bar{P}_o$ . To calculate  $\bar{P}_o$ , a "window" of width  $\Delta P$  is stepped through the pressure signal in small increments, starting at the minimum in the signal. At each step, the number of data points in the window is counted. Since the transducers used in these experiments showed that the pressure fluctuations in the undisturbed boundary layer are distributed normally the position at which the greatest number of data points occurs brackets  $\bar{P}_o$ .

The standard deviation,  $\sigma_{P_o}$ , of the boundary layer portion of the signal is then calculated.  $\bar{P}_o + 4.5\sigma_{P_o}$  was chosen for  $T_2$ , since the probability of finding points greater than  $4.5\sigma_{P_o}$  above  $\bar{P}_o$  is very low (i.e., 0.0000068). Hence, pressures above  $T_2$  are characteristic of the flow downstream of the shock, and pressures below  $T_2$  are characteristic of the undisturbed boundary layer. This approach sets  $T_2$  consistently just above the largest fluctuations of the boundary layer, and automatically takes care of d.c. offsets or drift. The process requires

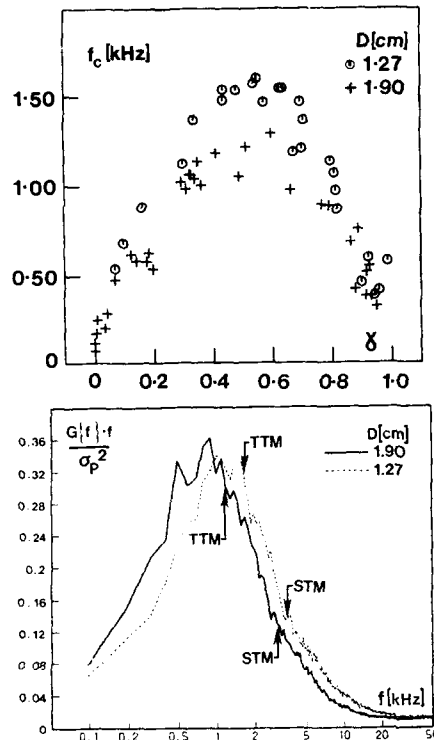


Figure 9: (a) Shock zero crossing frequency as a function of  $\gamma$ .  
(b) power spectra at  $\gamma \approx 0.5$  (cylinders at Mach 5)

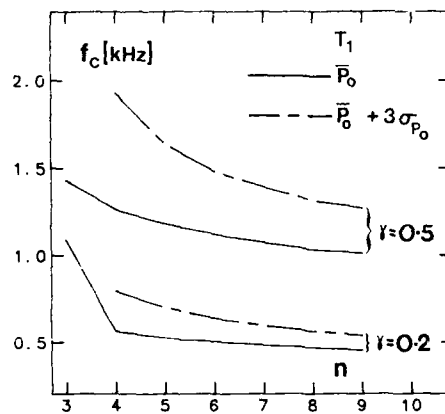


Figure 10: Sensitivity of shock zero crossing frequency to threshold settings

However, this algorithm introduces a new problem. If two shock passages are closely spaced  $P_c$  may not fall below  $\bar{P}_0$  before increasing again, and the flag is not reset. Two shock passages are then counted as only one. To examine this, and also assess the sensitivity of  $f_c$  to the threshold settings,  $T_1$  and  $T_2$  were systematically varied. First, with  $T_1 = \bar{P}_0$ ,  $T_2$  was varied through a series of values given by  $\bar{P}_0 + n\sigma_{P_0}$ ,  $3 \leq n \leq 9$ . Next,  $T_1$  was increased to  $\bar{P}_0 + 3\sigma_{P_0}$  and  $T_2$  varied as before. With this higher value of  $T_1$ ,  $P_c$  only has to fall back within the range of the turbulent boundary layer in order to reset the shock counter, whereas with  $T_1 = \bar{P}_0$  the pressure must decrease to below the mean value. Some typical results at  $\gamma \approx 0.2$  and  $0.5$  are shown in Fig. 10. At low  $\gamma$ , when relatively long periods of undisturbed boundary layer flow occur between successive shock passages, the choice of  $T_1$  is less critical than at higher  $\gamma$ . Also, at higher values of  $\gamma$ , when  $T_1 = \bar{P}_0 + 3\sigma_{P_0}$ ,  $T_2$  must be set significantly higher in order to avoid turbulent fluctuations being counted as shock waves (i.e., if  $T_1$  and  $T_2$  are too close the method becomes similar to a single threshold method and has similar problems). If  $T_2$  is set  $3\sigma_{P_0}$  above  $T_1$  or higher,  $f_c$  is then relatively insensitive to further increases in  $T_2$ .

It is evident that although  $f_c$  cannot be pinpointed precisely, it can be bracketed within a narrow range. The lower boundary of the range corresponds to  $T_1 = \bar{P}_0$ ,  $T_2 = \bar{P}_0 + 4.5\sigma_{P_0}$  since this requires that  $P_c$  fall below  $\bar{P}_0$  between shock waves. The upper boundary is set by  $T_1 = \bar{P}_0 + 3\sigma_{P_0}$ ,  $T_2 = \bar{P}_0 + 6\sigma_{P_0}$ . With these as bounds,  $f_c$  is in the range 0.55–0.65 kHz for  $\gamma \approx 0.2$ . At the higher  $\gamma$ , the variation is larger, 1.2–1.5 kHz.

In summary, results from single threshold methods give unrealistically high estimates of  $f_c$ . The two-threshold results are more representative and show that with physically sensible choices of  $T_1$  and  $T_2$ ,  $f_c$  can be bracketed within a fairly narrow range. Quantitatively, the values of  $(f_c)_{\max}$  from the two-threshold algorithm correlate reasonably well with the spectrum center frequency suggesting either technique could be used to estimate the maximum zero crossing frequency. However, statistical information concerning  $T_1$  and  $f_c$  can only be provided by the algorithm.

#### 4.2.4 Space-Time Correlations/Shock Velocities in Intermittent Region

Longitudinal space-time correlations  $R_{pp}(\xi, \tau)$  calculated by Muck et al. (1985) in a Mach 3, 24° compression ramp flow are shown in Fig. 11. The spacing,  $\xi$ , between transducers varied from 0.23–0.69  $\delta_0$ , although only curves for the smaller value are shown here. The case  $X/\delta_0 = 2.18$ ,  $\xi/\delta_0 = 0.23$  has the upstream transducer at  $(\sigma_{P_0})_{\max}$  and shows the features of such correlations and the difficulties of interpretation. One source of difficulty is that two different physical phenomena occur together. There is shock motion in the upstream and downstream directions superposed on convective transport of turbulent eddies largely in the downstream direction only. This leads to difficulties in interpreting the values of  $\tau$  at which maxima in  $R_{pp}$  occur.

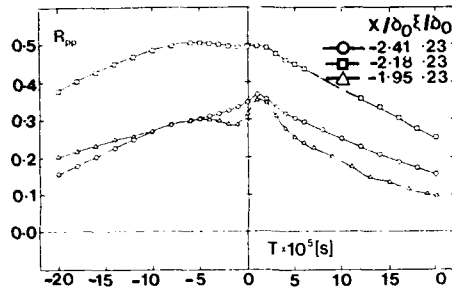


Figure 11: Longitudinal space-time correlations in intermittent region: compression ramp at Mach 3

minima in  $T_r$  and  $T_f$  (Fig. 12c) and not at an average (or broadband) value of  $T_d$  as occurs for the sequential signals (Fig. 12d). Thus, although correlations of the box-car signals from the TTM reveal a maximum in  $R_{pp}$  at positive  $\tau$  which corresponds to downstream motion of the shock wave, in addition to a maximum at negative  $\tau$  corresponding to upstream motion, the shock speeds calculated from these values of  $\tau$  and  $\xi$  are essentially maximum values, not broadband values.

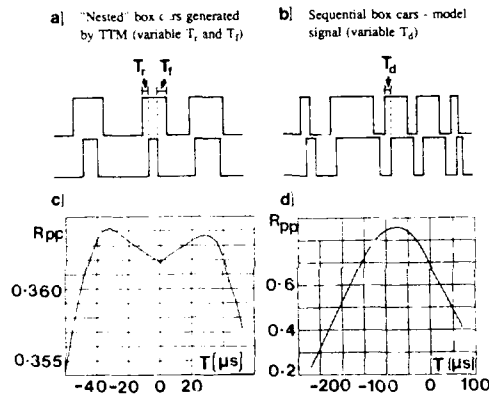


Figure 12: Cross-correlations of "nested" and "sequential" box-car signals in intermittent region: cylinders at Mach 5

the same approach in the Mach 5 cylinder flows. In this case the two-threshold algorithm was used to generate the box-car signal and at any given station, up to 700 pairs of nested  $T_r$  box-cars were examined. Upstream and downstream shock speeds were again found to be the same but the average values were substantially lower, about  $0.06 - 0.07 U_\infty$ . Probability distributions of the shock speeds in both directions are shown in Fig. 13.  $U_s$  is the shock speed,  $N$  is the number of occurrences of a given velocity and  $N_T$  is the total number of events. It is possible that this discrepancy is partly due to the smaller number of samples in the ramp study but it could also be due to the use of a single threshold algorithm to generate the box-cars which biases the results to shorter times and hence higher velocities. Further at this stage there is no reason to assume that  $U_\infty$  is an appropriate normalizer. Even so, it is clear that in two different flows the shock speeds are essentially the same in both direction and at a small fraction of  $U_\infty$ . No satisfactory explanation for this result is available.

The correlation at  $X/\xi_s = -2.18$  has two maxima: one at  $\tau \approx -60 \mu s$  and one at  $\tau \approx +10 \mu s$ . The latter corresponds to turbulent eddy convection downstream. This is evident from correlations in the incoming boundary layer (Fig. 3; Muck et al., 1986) since the maximum in  $R_{pp}$  is at the same positive  $\tau$ . It was suggested that the maximum at negative  $\tau$  is "probably due to the shock motion". This has been confirmed by Baade and Dolling (1987). In this case, correlations were performed on the original signals, the box-cars obtained from the two-threshold algorithm, and a set of model signals. The model signals were either "nested" square waves (as would be generated by the algorithm) with variable rise and fall times,  $T_r$  and  $T_f$  (Fig. 12a) or "sequential" square waves with the delay time,  $T_d$  fixed for a given pair of waves but varying through the signal (Fig. 12b). These two signals have different cross-correlations with different physical interpretations. For the nested waves, maxima in  $R_{pp}$  occur at values of  $\tau$  close to

In the Mach 5 cylinder interactions the maximum upstream and downstream shock speeds deduced from the box-cars were about the same ( $\approx 100$  m/s) and independent of position in the intermittent region. In the Mach 5 facility, 100 m/s is about  $0.14 U_\infty$ . At Mach 3, only cross-correlations of the original signals were made. Since the shock-induced fluctuations are also nested then the maximum in  $R_{pp}$  at negative  $\tau$  is also heavily weighted towards the minimum  $T_r$  (maximum upstream velocity) rather than the broadband value. Further, correlations on the entire signal result in a somewhat higher  $\tau$  (and smaller maximum velocity) than on the corresponding box-cars. Bearing this in mind, for a spacing of  $0.23\lambda$  ( $\approx 5.5$  mm) the maximum in  $R_{pp}$  at a  $\tau$  of  $60 \mu s$  corresponds to 92 m/s ( $\approx 0.16 U_\infty$ ).

Andreopoulos and Muck (1986) identified individual pairs of nested box-cars from the 24° compression ramp flow and performed statistics on  $T_r$  and  $T_f$ . The objective was to calculate the probability distribution for the shock speed but the small number of samples (only 65) precluded an accurate result. The calculated speeds ranged from  $0.05 - 0.8 U_\infty$  with a mean of about  $0.15 U_\infty$ . Upstream and downstream shock speeds were about the same order. Baade and Dolling used

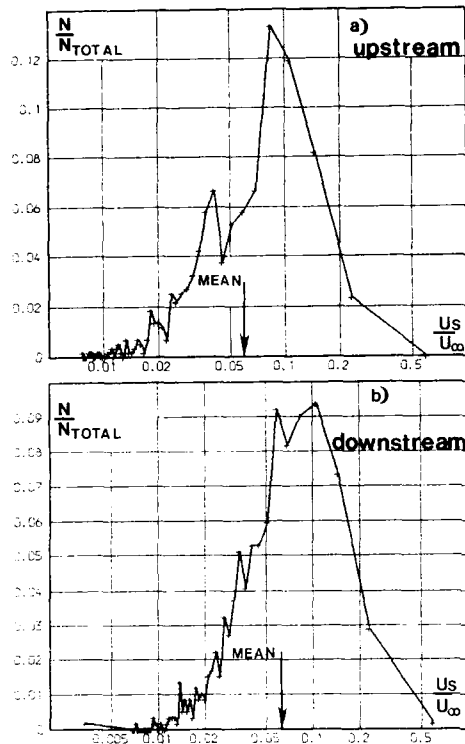


Figure 13. Probability density distributions for shock speeds in upstream and downstream directions: cylinders at Mach 5

levels [Chen and Hanly (1969), Coe et al. (1973)]. Compared to the undisturbed attached flow, both  $\sigma_p$  and  $\sigma_p/\bar{p}_s$  are significantly higher. Longitudinal space-time correlations for the Mach 3, 24° ramp are shown in Fig. 14. In this case, the extent of separation was relatively small, and the flow undergoes a continuous compression from separation through reattachment.  $R_{pp,max}$  is significantly less than in the upstream attached flow, and decreases much more rapidly with transducer separation distance suggesting a stronger contribution from high frequency (i.e., less correlated) fluctuations. An obvious feature is the double peak shape. However, the reasons for the second small peak at the larger positive  $\tau$  are not clear. Estimates of the broadband convection velocity from the first maxima at positive  $\tau$  gives a value of  $0.6U_\infty$  or  $0.8U_\infty$ , where  $U_\infty$  is the local freestream velocity (deduced assuming a 10° deflection through the separation shock). This agrees well with attached flow results. Although reverse flow occurs, the fluctuations are much more highly correlated in the streamwise direction, and eddies moving downstream are the major contributors. For the closest spacing, a peak is just discernible at  $\tau \approx -100\mu s$  but  $R_{pp}$  is low and of limited accuracy. Assuming that it reflects a physical feature present in the flow, it corresponds to an upstream convection velocity of about 55 m/s which is within a few percent of the maximum reversed flow velocities measured by Settles et al. (1976).

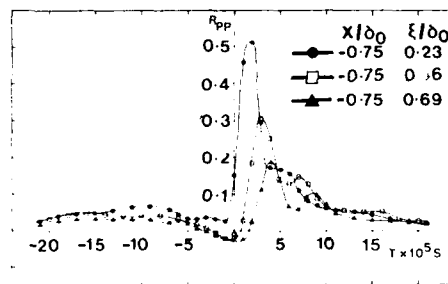


Figure 14. Space-time correlations in separated flow: compression ramp at Mach 3

Andreopoulos and Muck argued that the shock velocities are the same order as velocity fluctuations in the flow field and this result "represents further evidence that the turbulence of the incoming boundary layer is largely responsible for the shock wave motion." However, the shock is an interface and propagates with respect to the fluid at a velocity which depends on the upstream and downstream conditions and may be independent of velocity fluctuations. Hence, this is a questionable conclusion at this stage and is not supported by the results of Tran (1986) obtained using the VITA technique (Variable Interval Time Averaging). Tran's work was done in the same Mach 3 blowdown facility but with a 20° compression ramp. One transducer was placed on the upstream influence line and the other further upstream in the incoming boundary layer. The upstream channel was used as a trigger and sampling was carried out on the downstream one. The threshold setting (which determines if an 'event' has occurred) was fixed and integration times were varied from 16  $\mu s$  to 64  $\mu s$ . The latter had little effect on the magnitude of the downstream signals. Tran found little correlation between events detected on the upstream channel and the shock-induced pressure pulses on the downstream channel. Close observation showed that "in many instances, the details of the pressure fluctuations of the upstream signal were preserved at the downstream station at a time delay corresponding approximately to the time that it would take for the large-scale structure to travel between the two stations." Tran concluded that the pressure pulses in the intermittent region were independent of the large-scale structures in the upstream boundary layer which are convected into the interaction.

#### 4.2.5 Separated Region

At  $S$  or just downstream of it, the fluctuation amplitude distributions are again essentially Gaussian. If the separation length is large enough, both  $\bar{p}_s$  and  $\sigma_p$  reach constant plateau

Correlations further downstream (Muck et al., 1987) show that the maximum correlation at positive  $\tau$  increases, and the maximum at negative  $\tau$  disappears. It appears that convective phenomena dominate in the separated flow. Convection velocities at different separations were the same within the temporal resolution of the experiment. Spanwise correlations were symmetric about the  $\tau = 0$  axis with a peak correlation coefficient of about 0.4. Thus, the eddies are not strongly correlated spanwise and the time averaged flow can be regarded as uniform. These observations are in basic agreement with the work of Coe et al. (1973). Narrow band convection velocities determined in the separated flow upstream of a 15° axisymmetric flare at Mach 2 varied from  $0.2U_\infty$  (at  $f\delta/U_\infty = 0.06$ ) to a maximum of about  $0.8U_\infty$  (at  $f\delta/U_\infty = 0.8$ ). Upstream convection was not detected. Clearly, broad band velocities cannot be considered representative and the variation with frequency implies that the predominant turbulence



at different frequencies between  $0.03 \leq f\delta/U_\infty \leq 0.8$  is generated at different levels of the boundary layer, ranging from slightly above the zero velocity line to the free shear layer."

Roos (1980) obtained similar correlations in studies of transonic airfoil buffeting. For fully separated flow from the shock to the trailing edge, peak time delays were positive, indicative of disturbances moving downstream. By band-pass filtering before cross-correlation, the frequency dependence of the convection speeds was established. The results were similar to those of Coe et al. A more complex disturbance propagation pattern was found when shock-induced separation was followed by reattachment. The cross-correlations show upstream and downstream propagation of disturbances, indicative of acoustic and convective modes.

Coe et al. tried to determine the extent of the interaction between the shock oscillation and pressure fluctuations in the separated flow by simultaneously sampling the signals in both regions and calculating correlations and coherence functions. The results showed that the fluctuations were related only at low frequencies,  $f\delta/U_\infty < 0.04$  (in this case 200 Hz). The coherence at these low frequencies decreased rapidly downstream of the shock, but a coherence of about 0.2 persisted well into the separated region. Negative phase angles showed that the convection of the mean related turbulence was upstream, indicating that at low frequencies turbulence in the separated flow has a strong influence on the shock oscillation.

#### 4.2.6 Reattachment and Outgoing Boundary Layer

There exist few data near reattachment or in the outgoing boundary layer, largely because of tunnel constraints. Models such as compression ramps have to be long enough to avoid trailing-edge effects on reattachment, but short enough to avoid tunnel blockage. Generally outgoing boundary-layer lengths are short. In compression ramp flows  $\sigma p/\bar{P}_w$  increases towards reattachment. Chyu and Hanly (1969) report the same behavior in axisymmetric flare studies, although these data must be interpreted with caution since the cut-off frequency was low. Downstream of  $R$ ,  $\sigma p$  progressively decreases, and continues to do so after  $\bar{P}_w$  reaches a constant value. The slow readjustment is seen in the skewness and flatness coefficients. The skewness passes through zero about  $3\delta_0$  from the corner; close to where  $\bar{P}_w$  becomes constant. It then decreases and levels off at around -0.2. It is difficult to judge whether it remains constant or increases slowly back to zero. The results for the flatness are equally confusing. At the downstream boundary of the measurement region, the value is about 3 and apparently increasing. The power spectra (Murphy, 1983) are suggestive of some unusual features in the outgoing boundary layer. Downstream of  $R$ , a "bulge" developed in the spectrum; at the furthest downstream station, it spanned the range 5-12 kHz, corresponding to energetic structures of streamwise extent about  $2\delta_0$ .

Selig et al. (1986) made simultaneous wall pressure and mass flux measurements in the same compression ramp flow. Although correlations between the two signals were low and appeared to be dominated by tunnel noise, the mass flux measurements revealed some interesting results. From the wall to close to the middle of the boundary layer, probability density distributions centered around a single value equal to the incoming freestream mass flux. Further out than the middle of the boundary layer, the distribution centered around a single value equal to the mass flux downstream of the interaction. In the middle, the distributions were bimodal, indicative of an intermittent signal with peaks at both values. Similar findings have been reported by Hayakawa et al. (1984). Selig et al. suggest that this might be caused either by Taylor-Görtler vortices or low speed eruptions from the separation bubble and suggest that the latter is the more likely cause. In support, they cite the microsecond schlieren photographs of Ardonna (1984) which appear to show a "quasi-periodic" vortex sheet emerging from the separated flow and travelling downstream.

These observations agree qualitatively with the turbulence measurements of Lee (1979), Delery (1983) and Ardonna (1984). Lee made constant-temperature hot-wire measurements in  $8^\circ$ ,  $13^\circ$  and  $18^\circ$  compression ramp flows at  $M_\infty = 2.25$ . The maxima in the power spectra were located near 25 kHz before and after the interaction, inferring large-scale structures of  $O(2\delta_0)$  in extent in both cases. Some evidence of unsteadiness also was noted. The profiles close to the wall downstream of the interaction exhibited an intense peak around 1-10 kHz; assuming that transport phenomena are responsible, this corresponds to flow structures up to  $5\delta_0$  in extent. Lee concluded that this was not turbulence, but rather was due to a "a global displacement of the boundary layer linked with the separation instability."

Delery used a laser velocimeter in shock-induced separated flow in a 2-D transonic channel. The downstream relaxation to a new equilibrium state was very gradual due to the long lifetime of the large structures in the outgoing flow which formed near the shock root, a region of intense turbulence production. Ardonna made turbulence measurements in the same flows as Lee, using a laser velocimeter and a constant temperature hot wire. It was concluded that a large amount of turbulent energy was contained in large-scale structures. A typical scale is  $2\delta_0$  in the stream direction and  $1\delta_0$  spanwise. As Lee's more qualitative work had suggested, these structures do not lose their coherence during the interaction with the mean velocity field. Spanwise correlations showed a pattern of turbulent structures, with contiguous counter-rotating vortices. This agrees with the flow visualisation studies of Settles but contrasts with the work of Selig et al.

### 4.3 Three-Dimensional Flow

#### 4.3.1 Introductory Remarks

Fewer experiments have been made in 3-D flows, and the data are more difficult to interpret since the boundary layer can be highly skewed. The majority of the data are in shock-wave boundary-layer interactions. These include flows induced by sharp fins at angle of attack [Tran, (1986), Tan et al., (1985), Tran et al., (1985)] or by hemicylindrically blunted fins [Dolling and Bogdonoff, (1981), Dolling and Narlo, (1987)] or by circular cylinders and protuberances [Robertson, (1969), (1971), Narlo, (1986), Dolling and Narlo, (1987)]. Some additional unpublished work in swept compression ramp flows and flows induced by semi-cones adjacent to a flat surface is cited by Tran, (1986).

### 4.3.2 Blunt Fin and Cylinder Interactions

These two flows have much in common. The boundary layer separates, about two diameters upstream of the leading edge, and then rolls up into a vortical structure which develops spanwise and rearward as a horseshoe vortex system (as in incompressible flow). This structure gives rise to the characteristic double-peaked center-line mean pressure distribution. The streamwise scale of the flow field (and flow spanwise development) depends largely on  $D$ , and only weakly on  $\delta$  [Dolling and Bogdonoff, (1982)].

Between  $X_0$  and  $S$ , the pressure signal is intermittent as in 2-D flows and  $\sigma_p$  increases rapidly, with a maximum upstream of  $S$ . The magnitude of  $(\sigma_p)_{max}$  decreases spanwise, but not rapidly, [Dolling and Bogdonoff, (1981)]. Since the length of the streamwise region bounded by  $X_0$  and  $S$  scales with  $D$ , not  $\delta$ ,  $L_s$  may be a fraction of  $\delta_0$  to several  $\delta_0$ , dependent on  $D$ . Thus, the length scale of the shock motion can vary substantially in a given boundary layer.

Distributions of  $f_c$  as a function of  $\gamma$  for Mach 5 cylinder flows were shown earlier in Fig. 9. The distributions for both cylinders are similar in shape but have different maxima; as noted earlier for the 1.27 cm and 1.90 cm cases it is approximately 1.6 and 1.2 kHz, respectively. This suggests that the shock motion is in some way influenced by the downstream separated flow dynamics since the incoming flow conditions are constant, and only the cylinder diameter is changed. The maximum frequencies are low; more than two orders of magnitude less than a typical large eddy frequency,  $U_\infty/\delta_0$  ( $\approx 120$  kHz). Similar low frequencies are reported in blunt fin flows at Mach 3 (Dolling and Narlo, 1987).

Probability distributions for the shock wave period calculated using the two-threshold algorithm are highly skewed with the mean period about twice the most probable value. Some typical results at  $\gamma \approx 0.5$  are shown in Figure 15. The distribution for the smaller diameter cylinder has a higher probability for shorter periods and vice-versa. An interesting feature is that, although the mean period is a function of  $\gamma$  (for a fixed  $D$ ) and a function of  $D$  (for a fixed  $\gamma$ ), the most probable period is approximately constant ( $\approx 0.4 - 0.5$  ms) at all stations for both cylinders. No explanation is available to explain this result.

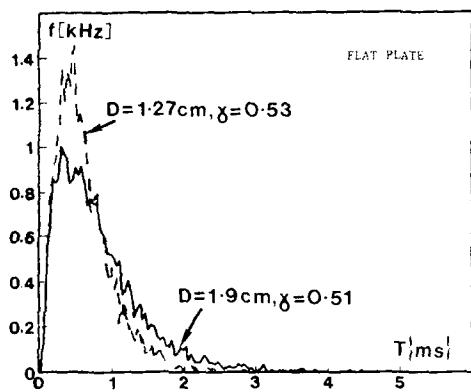


Figure 15: Probability density distributions for shock wave period, Mach 5 cylinder flows

In 3-D flows, a wide variety of separated flow structures can exist depending on the model geometry, shock strength, and parameters such as Reynolds number and Mach number. In blunt fin and cylinder-induced flows, the qualitative structure can best be understood in terms of vortex systems. How many vortices occur and their location appears to be a function of Reynolds number, certain dimensionless parameters, and flow type (Sedney, 1973). Since these vortices generate large streamwise and spanwise pressure gradients, it is obvious that they will play a dominant role in the wall pressure fluctuation behavior. This behavior is likely to be very complex and there are very few results available.

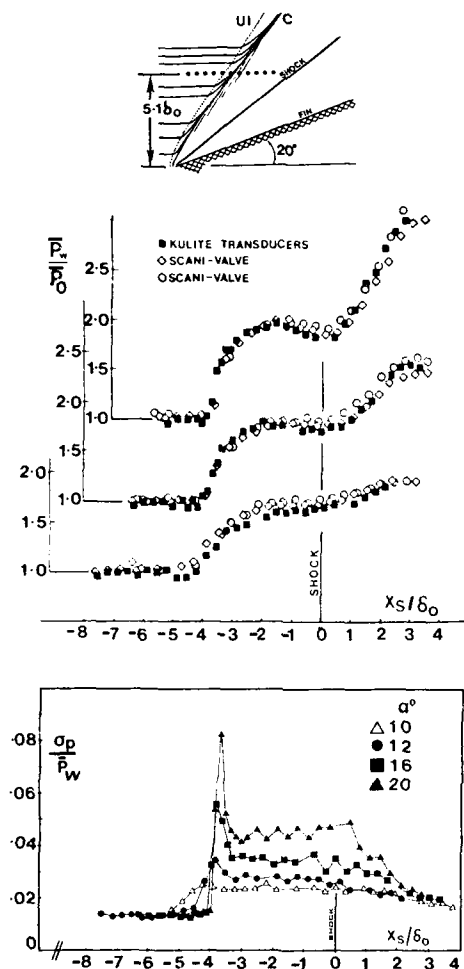
### 4.3.3 Sharp Fin Flows

The only known data are those of Tan et al. (1985), Tran et al. (1985) and Tran (1987). Tran made detailed measurements along a single survey line in the undisturbed freestream direction for fin angles of attack of  $10^\circ$ ,  $12^\circ$ ,  $16^\circ$  and  $20^\circ$  at Mach 3. Distributions of the normalized mean wall pressure and normalized  $\sigma_p$  are shown in Figure 16.  $X_s$  is measured from the inviscid shock location. The spanwise location of the

transducers is shown in the inset. On the figures, 'U' refers to the upstream influence line and 'C' refers to the line at coalescence of the surface streaks (generally considered as a line of separation).

At  $\alpha = 10^\circ$ , the pressure signals were not intermittent, were Gaussian throughout the entire region surveyed, and the distribution of  $\sigma_p$  had no discernible peak. On the basis of earlier work by Debieve and LaCharme (1985), among others, Tran states that this case "may be viewed as reflecting the amplification of turbulence through a region of relatively mild adverse pressure gradient". With increased shock strength, the rise in  $\sigma_p$  becomes more abrupt and a peak develops. It is just discernible at  $12^\circ$ . The pressure signals show that this development is associated with development of an unsteady shock structure and an intermittent pressure signal develops the same as in other 2-D and 3-D flows. The data suggests that the development of an intermittent pressure signal is associated with the onset of separation. As in 2-D flows,  $(\sigma_p)_{max}$  is upstream of  $S$ . Similar to large-scale 2-D separated flows, between  $C$  and the trace of the inviscid shock,  $\sigma_p$  is nearly constant (as is  $\bar{P}_w$ ). The value depends on the inviscid shock strength. From extrapolations of the data, Tran estimated that a new equilibrium value would be reached  $6 - 7\delta_0$  downstream of the inviscid shock.

Using a coordinate stretching technique, which makes use of the fact that the flow field footprint is quasi-conical, Tran correlated the data from sharp fin, semi cone and swept compression ramp flows. For a given inviscid shock strength, varying the geometry has little effect on the distribution of  $\bar{P}_w/\bar{P}_{\infty}$  and  $\sigma_p/\bar{P}_w$  (or  $\sigma_p/\sigma_{p0}$ ), at least from  $X_0$  to the inviscid shock location. It appears that the inviscid shock strength is the governing parameter in such interactions, and that the shock location is the reference point from which comparisons should be made.



Power spectra at 8 stations along the survey line for  $\alpha = 16^\circ$  and  $20^\circ$  have been reported by Tran. Both cases have common features. Between  $UI$  and  $C$ , the shock-induced fluctuations are the major contribution to  $\sigma p$  and are centered around 2 kHz (curves 8 and 9, Fig. 7). At  $C$ , the low frequency content decreases and the higher frequency range increases. In the plateau region of the  $\sigma_p$  distribution, spectra have the same shape with the higher frequency range centered around 10 kHz. Downstream of the inviscid shock, the spectra relax towards that of the incoming boundary layer. In the intermittent region, these results are qualitatively the same as in 2-D flows, and other 3-D flows.

The shock front undergoes much less rippling than in 2-D ramp flows. Space-time correlations were made by Tran along "UI" for both cases. Plots of the maxima of the space-time correlations as a function of transducer spacing showed that for close spacings, the signals are highly correlated for the swept flow; for the ramp, the correlation has already dropped significantly at  $\xi/\delta_w = 1$ . For larger spacings, the correlation is essentially zero for the ramp, but for the swept case is still relatively significant even at  $\xi/\delta_w = 3$ . The corresponding plots of the coherence function showed that for the swept case, the high-frequency components (due to turbulence) drop off rapidly while the low-frequency components (due to shock oscillation) remain highly correlated.

Tran also applied the VITA technique near the interaction, start in the sharp fin flows. The transducer configuration was similar to that in the  $20^\circ$  ramp case described earlier; one (the trigger) was in the undisturbed flow and the other on the upstream influence line. The same findings as reported for the 2-D flow were observed here.

Figure 16: Mean wall pressures and rms of the pressure fluctuations in sharp fin flows, Mach 3

## 5 Concluding Remarks

In this chapter the methods and difficulties of making fluctuating wall pressure measurements in supersonic flows have been outlined, and some of the results in zero pressure gradient and perturbed flows have been presented. No attempt is made in this section to summarize these findings and the questions they raise; rather, some brief general remarks are given.

As noted earlier, even for the case of zero pressure gradient there are few, if any, reliable data due largely to inadequate spatial resolution. Within the accuracy of the measurements it does appear that the structure of turbulence in equilibrium supersonic turbulent boundary layers is not significantly altered by compressibility. To confirm this, detailed measurements are needed over a range of flow conditions. Although the continuing miniaturization of sensors and improvements in the speed and resolution of signal processing hardware have made this task less difficult, it is still far from routine.

In perturbed flows, most of the measurements have been made in shock wave turbulent boundary layer interaction. Much of the attention has been on the unsteady separation process. In this case, the relatively low frequencies and large streamwise excursion of the separation shock have made spatial resolution and bandwidth limitations less of a problem and several data sets documenting shock properties are available. Some data in the separated flow are available, but there are very few near reattachment and in the outgoing boundary layer. The result of this paucity of experiments is that the basic information needed for improving engineering prediction methods and for devising physically accurate numerical models is, in most cases, lacking. The current poor understanding of the mechanism(s) driving the separation shock motion is just one example of how little is known. Bearing in mind the diversity of flows of interest, many with complex, separated flow structures dependent on such parameters as shock strength, Mach and Reynolds number, it is clear that much challenging research work remains to be done.

## Acknowledgements

A large fraction of the work of the first author and his graduate students which is reported in this chapter was sponsored by AFOSR Grant 86-0112 (monitored by Dr. James Wilson) and by the Center of Excellence of Hypersonics Training and Research (supported by NASA, AFOSR and ONR) at The University of Texas at Austin. These sources of support are gratefully acknowledged.

## References

- Alving, A.E., J.H. Watmuff, A.J. Smits, 1987, "The Relaxation of a Turbulent Boundary Layer far Downstream of a Short Region of Convex Curvature," *AIAA Paper* 87-0196.
- Andreopolulos, J. and K. C. Mack, 1986, "Some New Aspects of the Shock Wave Boundary Layer Interaction in Compression Ramp Flows," *AIAA Paper* 86-0342.
- Ardonceanu, P.L., 1984, "The Structure of Turbulence in a Supersonic Shock Wave Boundary Layer Interaction," *AIAA J.*, 22, 1254-1262.
- Blackwelder, R.F. and P. E. Kaplan, 1976, "On the Wall Structure of the Turbulent Boundary Layer," *J. Fluid Mech.*, 76.
- Blake, W.K., 1986, "Differential Pressure Measurements," in *Fluid Mechanics Measurement*, R.J. Goldstein Ed., Hemisphere Publishing Corp. and Springer-Verlag.
- Bogar, T.J., 1986, "Structure of Self-Excited Oscillations in Transonic Diffuser Flows," *AIAA J.*, 24, 54-61.
- Bogar, T. J., M. Sajben and J. C. Kroutil, 1983, "Characteristic Frequencies of Transonic Diffuser Flow Oscillations," *AIAA J.*, 21, 1232-1240.
- Bonnet, J. P., Chaput, E., Alziary de Roquefort, Mai 1986, "Détermination des fluctuations de pression pariétale dans une zone d'interaction onde de choc-couche limite turbulente en écoulement supersonique," *Rapport de Convention ONERA No. 20.391/SAT.2.CDC*
- Chen, C. P., M. Sajben and J. C. Kroutil, 1979, "Shock Wave Oscillations in a Transonic Diffuser Flow," *AIAA J.*, 17, 1076-1083.
- Chyu, W. J. and R. D. Hanly, 1969, "Power and Cross Spectra and Space-Time Correlations of Surface Fluctuating Pressures at Mach Numbers Between 1.6 and 2.5," *NASA TN-D-5440*.
- Coe, C. F., 1969, "Surface Pressure Fluctuations Associated with Aerodynamic Noise," *Basic Aerodynamic Noise Research*, I.R. Schwartz Ed., NASA SP-207.
- Coe, C. F., W. J. Chyu and J. B. Dods, 1973, "Pressure Fluctuations Underlying Attached and Separated Supersonic Turbulent Boundary Layers and Shock Waves," *AIAA Paper* 73-996.
- Corsico, G. M., 1963, "Resolution of Pressure in Turbulence," *J. Acoust. Soc. Am.*, Vol. 35, No. 2, pp. 192-199.
- Corsico, S., 1963, "Estimates of the Relations Between Eulerian and Lagrangian Scales in Large Reynolds Number Turbulence," *J. Atm. Sci.*, 20, p. 115.
- Debieve, J.F. and J. P. Lacharme, 1986, "A Shock Wave/Free Turbulence Interaction," *Proceedings, IUTAM Symposium, Turbulent Shear-Layer/Shock-Wave Interactions*, Springer-Verlag, 393-403.
- Debieve, J. F., Juin 1983 Etude d'une interaction turbulence - onde de choc. These de Doctorat d'Etat. Université Aix-Marseille II.
- Emmerling, R., 1973, "The Instantaneous Structure of the Wall Pressure Under a Turbulent Boundary-Layer Flow," *Max Planck-Institut für Strömungsforschung Rep. No. 9/1973*.
- Degrez, G., 1981, "Exploratory Experimental Investigation of the Unsteady Aspects of Blunt Fin-Induced Shock Wave Turbulent Boundary Layer Interactions," *MAE Dept., MS Thesis 1516-T, Princeton University*.
- Délery, J. M., 1983, "Experimental Investigation of Turbulence Properties in Transonic Shock/Boundary Layer Interactions," *AIAA J.*, 21, 180-185.
- Doebelin, E. O., 1966, *Measurement Systems, Application and Design*, International Student Edition, McGraw Hill, Kogakusha Ltd, Ed.
- Dolling, D. S., and Bugdonoff, S.M., 1982, "Blunt Fin-Induced Shock Wave/Turbulent Boundary Layer Interaction," *AIAA Journal*, Vol. 20, 1674-1680.
- Dolling, D. S., 1983, "On Upstream Influence in Shock Wave Turbulent Boundary Layer Interaction," *Royal Aero. Soc. J.*, 324-327.

- Dolling, D. S. and H. Baade, 1987, In preparation; available from first author.
- Dolling, D. S. and S. M. Bogdonoff, 1981, "An Experimental Investigation of the Unsteady Behavior of Blunt Fin-Induced Shock Wave Turbulent Boundary Layer Interactions," AIAA Paper 81-1287.
- Dolling, D. S. and M. T. Murphy, 1983, "Unsteadiness of the Separation Shock Wave Structure in a Supersonic Compression Ramp Flowfield," *AIAA J.*, 21, 1628-1634.
- Dolling, D. S. and J. C. Narlo, II, 1987, "Driving Mechanism of Unsteady Separation Shock Motion in Hypersonic Interactive Flow," AGARD Symposium on Aerodynamics of Hypersonic Lifting Vehicles (to be published as AGARD CP).
- Dolling, D. S. and C. T. Or, 1985, "Unsteadiness of the Shock Wave Structure in Attached and Separated Compression Ramp Flowfields," *Exp. in Fluids*, 3, 24-32.
- Dussauge, J. P., December 1983, "Retour à l'équilibre d'une couche limite turbulente, en aval d'une distorsion rapide, en écoulement supersonique," Rapport de Convention ONERA/IMIST No. 19891/SAT 2/JM.
- Dussauge, J. P., August 1985, "The Relaxation of a 'Relaminarized' Turbulent Boundary Layer in Supersonic Flow," 5th Turbulent Shear Flow Symposium, Cornell University, Ithaca, N. Y.
- Dussauge, J. P., K. C. Muck and J. Andreopoulos, 1985, "Properties of Wall Pressure Fluctuations in Separated Flow Over a Compression Ramp," *Proceedings, IUTAM Symposium, Turbulent Shear-Layer/Shock-Wave Interactions*, Springer Verlag.
- Fernholz, H. H., and P. J. Finley, May 1980, "A Critical Commentary on Mean Flow Data for Two-Dimensional Compressible Turbulent Boundary Layers," AGARDograph No. 253, AGARD, Neuilly.
- Gaviglio, J., Angillet, J. P., M. Elena, 1981, "On Application of Hot Wire Anemometry to the Solution of Problems Arising in Variable Temperature Turbulent Flows," *La Recherche Aérospatiale*, No. 1.
- Gramann, R. and D. S. Dolling, 1986, "Unsteady Separation in Shock Wave Turbulent Boundary Layer Interactions," AIAA Paper 86-1033.
- Hanly, R. D., March 1975, "Effects of Transducer Flushness on Fluctuating Surface Pressure Measurements," AIAA Paper 75-534.
- Hayakawa, K., A. J. Smits and S. M. Bogdonoff, 1984, "Turbulence Measurements in a Compressible Reattaching Shear Layer," *AIAA J.*, 22, 889-895.
- Hung, C. M. and P. E. Buning, 1984, "Simulation of Blunt Fin-Induced Shock Wave and Turbulent Boundary Layer Interaction," AIAA Paper 84-0457.
- Kistler, A. L., 1959, "Fluctuation Measurements in a Supersonic Turbulent Boundary Layer," *The Physics of Fluids*, Vol. 2, No. 3.
- Kistler, A. L., W. S. Chen, 1962, "The Fluctuating Pressure Field in a Supersonic Turbulent Boundary Layer," *Jet Propulsion Laboratory Tech. Report*, No. 32, p. 277.
- Kistler, A. L., 1961, "Fluctuating Wall Pressure Under a Separated Supersonic Flow," *J. Acoust. Soc. of America*, 30, 543-550.
- Lee, D. H., 1979, "Study of the Evolution of Turbulence in a Shock Wave Boundary Layer Interaction," Thesis (Docteur Ingénieur), University of Poitiers.
- Maestrello, L., September 1968, "Radiation From and Panel Response to a Supersonic Turbulent Boundary Layer," Boeing Scientific Research Laboratories document D1-82-0719.
- Michel, R., 1960, "Résultats sur la couche limite turbulente aux grandes vitesses," 10th Symposium of Applied Mechanics Stresa, TP ONERA No. 102.
- Muck, K. C., Andreopoulos, J. and Dussauge, J. P., 1987, "The Structure of a Separated Flow Over a Two-Dimensional Compression Ramp," submitted to AIAA Journal.
- Muck, K. C., J. P. Dussauge and S. M. Bogdonoff, 1985, "Structure of the Wall Pressure Fluctuations in a Shock Induced Separated Turbulent Flow," AIAA Paper 85-0179.
- Murphy, M., 1986, "An Experimental Investigation of the Separation Shock Wave Unsteadiness in a Compression Ramp Flowfield," M.S.E. Thesis 1605 T, MAF Dept., Princeton University.
- Narlo, J. C., II, 1986, "Experimental Investigation of the Driving Mechanisms of Separation Shock Wave Motion in Interactive Flows," MS Thesis, ASE/EM Dept., The University of Texas at Austin.

- Panton, R. L., H. G. Linebarger, 1974, "Wall Pressure Spectra Calculations for Equilibrium Boundary Layers," *J. Fluid Mech.*, 65, pp. 261-287.
- Raman, K. R., February 1974, "Surface Pressure Fluctuations in Hypersonic Turbulent Boundary Layers," NASA CR. 2386.
- Robertson, J. E., 1969, "Characteristics of the Static and Fluctuating-Pressure Environments Induced by Three-Dimensional Protuberances at Transonic Mach Numbers," Wyle Lab Rept. WR-69-3.
- Robertson, J.E., 1971, "Prediction of In-Flight Fluctuating Pressure Environments Including Protuberance Induced Flow," Wyle Lab Rept. WR-71-10.
- Roos, F. W., 1981, "Some Features of the Unsteady Pressure Field in Transonic Airfoil Buffeting," *J. Aircraft*, 17, 781-788.
- Roos, R. W., 1985, "The Buffeting Pressure Field of a High-Aspect-Ratio Swept Wing," AIAA Paper 85-1609.
- Sajben, M., T. J. Bogar and J. C. Kroutil, 1984, "Forced Oscillation Experiments in Supercritical Diffuser Flows," *AIAA J.*, 22, 465-474.
- Sajben, J. and J. C. Kroutil, 1981, "Effects of Initial Boundary Layer Thickness on Transonic Diffuser Flows," *AIAA J.*, 19, 1386-1393.
- Schewe, G., 1983, "On the Structure and Resolution of Wall Pressure Fluctuations Associated with Turbulent Boundary-Layer Flow," *J. Fluid Mech.*, Vol. 134, pp. 311-328.
- Sedney, R., June 1973, "A Survey of the Effects of Small Protuberances on Boundary Layer Flows," *AIAA Journal*, Vol. 11, 782-792.
- Selig, M. S., J. Andreopoulos, K. C. Muck, J. P. Dussauge and A. J. Smits, "Simultaneous Wall Pressure and Mass Flux Measurements Downstream of a Shock Wave/Turbulent Boundary Layer Interaction," AIAA Paper 87-0550.
- Settles, G. S., T. J. Fitzpatrick and S. M. Bogdonoff, 1979, "Detailed Study of Attached and Separated Compression Corner Flowfields in High Reynolds Number Supersonic Flow," *AIAA J.*, 17, 579-585.
- Simpson, R. L., M. Ghodbane, and B. E. McGrath, 1987, "Surface Pressure Fluctuations in a Separating Turbulent Boundary Layer," *J. Fluid Mech.*, Vol. 177, pp. 167-186.
- Speaker, W. V. and C. M. Ailman, 1969, "Spectra and Space-Time Correlations of the Fluctuating Pressures at a Wall Beneath a Supersonic Turbulent Boundary Layer Perturbed by Steps and Shock Waves," NASA CR-486.
- Tan, D. K. M., T. T. Tran and S. M. Bogdonoff, 1985, "Surface Pressure Fluctuations in a Three Dimensional Shock Wave/Turbulent Boundary Layer Interaction," AIAA Paper 85-0125.
- Tran, T. T., D. K. M. Tan and S. M. Bogdonoff, 1985, "Surface Pressure Fluctuations in a Three Dimensional Shock Wave/Turbulent Boundary Layer Interaction at Various Shock Strengths," AIAA Paper 85-1562.
- Willmarth, W. W., 1975, "Pressure Fluctuations Beneath Turbulent Boundary-Layers," *Ann. Rev. Fluid Mech.*, Vol. 7, pp. 13-38.

## 9. GENERAL COMMENTS ON THE INTERPRETATION OF DATA

### 9.1. Introduction

In the next chapter we discuss the mean flow for a number of the rapidly distorted turbulent boundary layers which form the subject matter of this AGARDograph. The approach will follow essentially that developed in AGARDograph 253, that is, the velocity profile material will be compared and contrasted with the wall and outer "laws" for an equilibrium zero pressure gradient boundary layer. The degree of disturbance undergone in the majority of the cases studied here is such that large departures are to be expected, but we have as yet found no other scaffold on which to hang, draw and quarter the estimable efforts of the experimental research workers in this field. Here we discuss some of the more general points which arise when attempting to interpret the data.

Chapters 10, 11 and 12 form an extension of the data compilation and survey of AGARDographs 223, 253 and 263. Individual ENTRIES will be referred to by their IDENTs - without succeeding letter if published in AG223, e.g. CAT7101, with a succeeding S if in AG263, e.g. CAT7802S and with a succeeding T for this volume. The next two numbers in the Idents indicate the series and the next two the profile numbers. For the most part, the current 12 entries represent flows subject to localised compression with wave systems of greater or lesser complexity. One case however describes an expansion, and another a ZPG flow. The entries are listed in arbitrary numerical order below (Table 9.1.1).

Table 9.1.1.  
List of ENTRIES in chapter 12.

ENTRY IDENT First author	Mach range	R THETA range	Type of flow Principal data
7904T Settles	2.9	80k	Compression corner flows, 8° - 24° PT2, P, T0 profiles. Preston tube CF.
8002T Délery	1.4	4k	Quasi-normal shock on bump LDV, mean flow, u', v' and u'v'.
8003T Copy	1.2- 1.45	2-3k	Quasi-normal shock on bumps LDV, mean flow, u', v', and u'v'.
8301T Debiève	2.3	4k	Compression corner flow, 6° PT2, P, T0 profiles. P' at wall.
8401T Taylor	2.9	80k	Curved compression surfaces PT2, P, T0 profiles. Preston tube CF.
8402T Ardonceanu	2.25	7k	Compression corner flows, 8° - 18° LDV, mean flow, u', v', u'v', PT2 profiles, normal HWP
8501T Liu	0.9- 1.8	16k	Quasi-normal shock on bumps, flat wall PT2 profiles, interferometer.
8601T Fernando	2.9	80k	Flat wall APG matching 8401T02 PT2, P, T0 profiles. Preston tube CF. Normal HWP.
8602T Dussauge	1.8	5k	Centred expansion, 12°. PT2, T0 profiles. Normal HWP.
8603T Spina	2.9	100k	Zero pressure gradient on tunnel wall PT2, P, T0 profiles. Preston CF. Normal and inclined HWP.
8701T Smits	2.9	80k	Compression corner flows, 8° - 24° Normal and inclined HWP.
8702T Jayaram	2.9	80k	Curved compression surfaces. Normal and inclined HWP.

## 9.2. Interpretation of data

### 9.2.1. A note on the nature of boundary-layer profiles

For historical reasons we are inclined to think that the immediate purpose of boundary layer studies is the prediction or measurement of the velocity profile, and through this the gross or integral properties of the layer - surface shear stress, displacement effect etc.. Within the context of low-speed fluid dynamics this is natural and easily understood - the variation of fluid properties is not a significant factor, and the velocity profile effectively provides a complete functional description. It is easy to forget, however, that there is no technological interest in the velocity profile as such, or, indeed, in the boundary layer itself, other than in its gross effects.

Given the "conventional" approach to mean profile measurements, when the velocities are such that the variation of fluid properties is significant, it becomes very difficult to measure the velocity profile - or any other profile - with confidence in any flow which might reasonably be called "complex". It is necessary to have values of two "static" or thermodynamic properties and one "dynamic" or relative property. These are most commonly derived from the values of the Pitot pressure, the static pressure and the total temperature, though the temperature information, often reasonably, and the static pressure, very much less so in any flow with interesting features, are not infrequently deduced from neighbouring values or a general hypothesis.

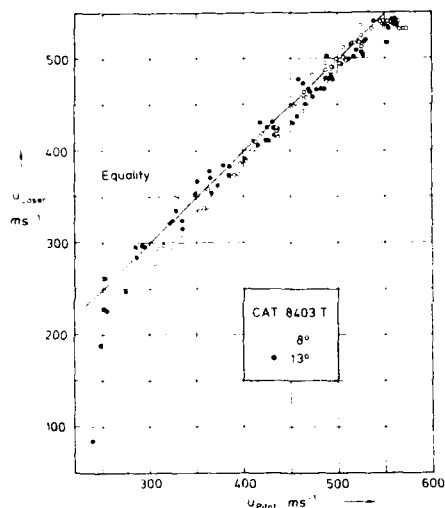


Fig. 9.2.1

Comparison between mean velocities as measured by LDV and Pitot tube.  $8^\circ$  and  $13^\circ$  CCF flows. Ardonceau (1984).

The flows to which our attention is principally directed at present are for the most part flows involving the "rapid distortion" of boundary layers and shear layers. As yet, we do not have cases with significant heat transfer so that temperature measurement is not vital. However, these flows are characterised by strong streamwise and normal pressure gradients, shock-wave structures and the possibility of separated flow regions. The traditional Pitot and static pressure measuring probes are likely to give notably untrustworthy results in flow fields of this nature, while to the great difficulties of using a hot-wire probe in any compressible flow are added those inherent to the use of such probes in regions of high turbulence and reversed mean or instantaneous flow.

The advent of the laser-doppler velocimeter (LDV or LDA) would seem to overcome these difficulties. There must remain problems arising from the principles of operation of the instrument - direct precise comparisons are rare, the usual evaluation being based on small scale figures in the literature. A direct comparison can be made using the original data of Ardonceau (1981), CAT8402T, (data - private communication), showing a likely systematic discrepancy between velocities derived from Pitot measurements and the LDV. Figure (9.2.1) shows the resultant velocity measured by the LDV plotted against the Pitot-derived velocity. The LDV values lie about 3% low. This is very good agreement, given the difficulties of using the instrument, but suggests a possible systematic bias. It is of interest that the remaining set of data for CAT8402T, with an  $18^\circ$  flow deflection, apparently show the laser as giving a systematically high value. We do not have data which allow us to make the comparison ourselves.



The virtues of the LDV - the non-intrusive nature, the ability to resolve the sense of the mean flow and the ability to provide statistical information on the fluctuating velocities - should not blind us to the uncertainties in its use. There remain questions as to the effects of the method and location of seeding and the problem of "parasitic" or false returns in addition to the need for very high frequency response in the associated electronic equipment.

A minor but at times significant problem arises from the need for a very rigid and therefore heavy mounting. The LDV is likely to be mounted on a traverse gear orientated in relation to the tunnel axis. Users to date seem to have made traverses at constant (tunnel) X, and thus not perpendicular to the local flow direction. It may therefore be difficult to interpret the results in normal terms. (See Brown et al., 1987, where the misalignment is up to 30°, so that the results can not be simply presented in boundary-layer axes.)

Above all, we should remember that, while the LDV gives us the velocity profile "directly" as a result of the "absolute" manner of its operation, it does not give us a functionally complete description of the flow field. A determination of the mean flow field will require, in addition, pressure or density values, and, though of less importance at present, temperature values. Those concerned with turbulence modelling may well heave a sigh of relief that at last they have relatively reliable values for the turbulence intensities, but they have not got the Reynolds stresses unless they also have the mean density.

### 9.2.2. The boundary-layer edge state and the influence of normal pressure gradients

In general a streamwise pressure gradient in a supersonic flow is likely to be accompanied by a normal pressure gradient. The properties of the free stream outside the boundary layer may well therefore be functions of the normal coordinate Y (AG 253 Ch.6). It then becomes impossible to use any directly measured quantity as the basis for a decision on the boundary-layer edge or "D-state". If the free stream adjacent to the edge is irrotational the edge state may be defined logically in terms of a total pressure deficit, and this (or implicitly, entropy) is the only mean flow property which can be so used (AG 253 § 7.1). Unfortunately, in supersonic flow, it is a derived property, so that no choice can be made until initial data processing is complete. If turbulence measurements become general, then there may be alternative rational definitions in terms of intermittency or approach to free-stream turbulence levels, and criteria of this nature would have the advantage that they could be used properly in rotational flows.

The boundary-layer edge can not be found with precision in any case if a deficit criterion is used, as unless the deficit is large the gradient of the chosen property is by definition small in the edge region. The boundary-layer thickness should not therefore be used as a scaling length. In the presence of normal pressure gradients, it is not even possible to define integral length scales with any precision, in part for the lack of a suitable reference flow, but more generally because, with the exception of the displacement thickness, the integral scales have no direct physical interpretation (AG 253 § 7.5).

Edge properties are commonly used in the formation of dimensionless quantities for data presentation. We are accustomed to think of most profile quantities in relation to the free stream value, and throughout the data compilation project we have provided data in this form. While wherever possible we base our choice on the P0 variation, the D-state properties should in general be regarded as arbitrary scaling quantities intended to represent an edge state, not necessarily with success. In particular, it can be difficult to transfer wall-friction data as CF changes with the choice of reference properties, and it is good practice to state the shear stress directly. We tend to think of wall shear as "high" or "low" in terms of the coefficient value. (In a 20° compression corner at M = 3, CF based on an edge state behind the shock would take more than double the value it would have if based on the free stream ahead of the shock.)

### 9.2.3. Effect of edge-state choice on the transformation.

The survey and comparisons made in AG 253, 263, and in chapter 10 below are all related to the incompressible form of the log-law. The profile in compressible flow is converted into an "equivalent incompressible profile" by the "transformation"

$$\bar{u}^* = \int_0^{\bar{u}} (\rho/\rho_w)^{1/2} d\bar{u} \quad (9.2.1)$$

This result embodies essentially the same assumptions as the derivation of the law of the wall in incompressible flow, with allowance made for the variation of density. It might therefore be expected to yield a log-law profile over broadly the same range of conditions as in the low speed case.

We have in general made use of the "Van Driest transformation"

$$\bar{u}_{V0}^+ = \left( \frac{u_\delta}{A} \right) \left[ \arcsin \left[ \frac{2A^2(\bar{u}/u_\delta) - B}{(4A^2 + B^2)^{1/2}} \right] + \arcsin \left[ \frac{B}{(4A^2 + B^2)^{1/2}} \right] \right] \quad (9.2.2)$$

$$\text{where} \quad A^2 = r \frac{\gamma - 1}{2} M_\delta^2 (T_\delta/T_w) ; \quad B = (1 + r \frac{\gamma - 1}{2} M_\delta^2) (T_\delta/T_w) - 1$$

which contains edge state properties which do not cancel out. This form of the transformation is further restricted by the incorporation of the Crocco temperature-velocity correlation, but our purpose here is not to demonstrate a correct result but rather to show the sensitivity of the transformation to the choice of edge state.

In a flow without normal pressure gradients, the free stream properties do not vary with  $Y$ , and the edge state, if taken far enough out, does not vary. Consequently, there is no problem. To demonstrate the effect when there is a normal gradient, we have performed a numerical experiment, using the data from the curved ramp experiments of Taylor, CAT8401T. Figure (9.2.2) shows the effect of choosing D-state points at various measurement stations outside the boundary layer edge (as determined from an inspection of the total pressure profile). The uppermost profile is that using the "best estimate" edge point, and for our present purpose, no particular significance should be placed on the fact that it does not agree very well with the wall law. The compression wave from the curved ramp here extends from the outer part of the layer into the free stream, so that as edge points are progressively chosen further out, the pressure, temperature, and density are falling while the velocity rises. The data are plotted in full for the curve obtained using the innermost and outermost edge points, the locus for selected points being shown for the intermediate curves. It is unlikely that an intelligent researcher would go out as far as we have here, but the possible effect is clearly demonstrated. It is apparent that a poor fit to the wall law can result from an ill-advised choice of D-state, independently of the accuracy of wall shear-stress measurement.

If the D-state is taken too far in, the change of state due to the boundary layer does not compensate, as is shown by figure (9.2.3), where the bottom curve represents data using a "sensible"  $P_0$  based edge state and the successive higher curves result from taking the edge point progressively further in.

It is clear that in an expansive wave generated at the wall, the effects of the normal pressure gradient and the boundary layer could oppose each other so as to make the transformation insensitive to the choice of edge state, but if this were to be the case, the edge point obviously lies within the layer and so is inappropriate.

An obvious measure to circumvent the secondary assumptions which give eqn. (9.2.2) is to use eqn. (9.2.1) directly, with experimental density values. The non-appearance of a log-law could then be confidently attributed to violation of the "low-speed" conditions required for the law to exist and for eqn. (9.2.1) to be valid. The choice of D-state would no longer have any influence. A number of such comparisons is made in § 5.2 of AGARDograph 263 (figs. 5.2.5-5.2.9), where it can be seen that the "pure" and "Van Driest" transformations give significantly different results. The flows in question are, however, so disturbed, that one would expect the log-law to break down in any case. At the time of writing that section, our interest was concentrated on the temperature/velocity relationship rather than the transformation itself, and further work remains to be done here. The effect of using no transformation in a well-behaved ZPG flow is shown in AGARDograph 253 fig. (3.3.0).

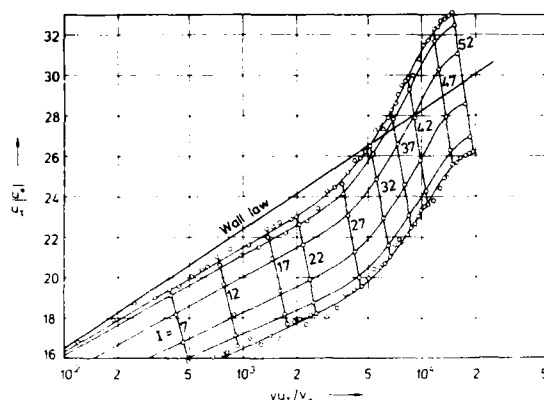


Fig. 9.2.2

Effect of choice of D-state on transformed velocity profiles in flow with normal pressure gradient outside the boundary layer. (data from 84010108, Taylor (1984)).

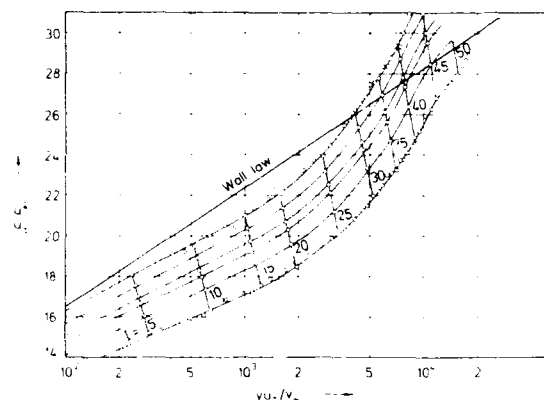


Fig. 9.2.3

Effect of choice of D-state on transformed velocity profiles in flow with normal pressure gradient inside the boundary layer. (Data from 84010107, Taylor (1984)).

#### 9.2.4. Preston tubes in compressible flow.

The Preston tube was originally developed for use in incompressible flow and depends on the assumption that the flow in the immediate neighbourhood of the wall is determined only by variables measurable at the wall. Thus the original accepted calibration in, and for use in, low-speed boundary layers in zero or small pressure gradients effectively implied that the velocity profile out to a scaled  $Y^+$  value comparable to  $d^+$  would follow the "universal" law of the wall, and that the calibration would break down when pressure gradients were such as to cause a significant departure from this "law", or the tube was overly large (Patel, 1965). A more convenient form of the basic calibration has been proposed by Head & Vasanta Ram (1971).

Pressure gradients can be scaled on wall variables and efforts have been made to extend the calibration to take account of this additional factor (Brown & Joubert, 1969; Frei & Thomann, 1980; Hirt & Thomann, 1986), resulting in corrections to the zero-pressure gradient calibration in terms of the scaled pressure gradient  $\alpha = [(v/\rho u^2)(dp/dx)]$ . All this is within the framework of wall similarity. The greater part of Frei & Thomann's calibrations were made in a range in which the universal law still holds (source, fig. 10), so that the correction allows for the use of a larger Preston tube than would be proper for the pressure gradient prevailing, should one attempt to use the ZPG calibration. However, the stronger (step flow) pressure gradients move into a range where the velocity profiles no longer appear to follow the universal "law" (source, fig. 11), though the authors ascribe the difference to the effect of normal pressure

gradients. It is worth emphasizing that with a two-parameter Preston-tube calibration there should go a two-parameter inner law, though the dependence on the second (pressure) parameter might be too weak to detect in the range covered. The later investigation by Hirt & Thomann perhaps leaves the question more open than before, but in principle a calibration of this nature should be possible so long as the rate of change of pressure gradient is not too great.

The simplicity of the Preston tube makes it very attractive for use in compressible flow, and a large part of the wall-shear data available to us is from this technique. In principle, all that is needed is to extend the wall similarity analysis to take account of compressibility. This approach, proposed by Rotta (1959) in an investigation of velocity and temperature profiles, was followed by Bradshaw & Unsworth (1973), the result being expressed as a compressibility correction to the low-speed calibration in terms of  $d^+$  and  $M_T (= u_T/a_w)$ . If used in pressure gradients, the gradients must be low enough for the (transformed) velocity profile to agree with the universal law, or a further pressure gradient correction calibration would be required. A first step would be boldly to apply the incompressible correction. In addition, there should be a heat-transfer parameter. Rotta and Bradshaw & Unsworth propose parameters based on the heat flux, which we would regard perhaps as more a variable dependent on a temperature parameter such as  $TW/TR$ . No serious attempt at assessing the sensitivity of the Preston tube to heat transfer is known to us, such evidence as is available (Yanta et al., 1969) suggesting that any influence is not large.

The case for the use of Preston tubes in compressible flow has been made strongly in zero pressure-gradient adiabatic flows by comparison with floating-element balance values and by the extensive agreement found between "transformed" velocity profiles and the universal profile, when using Preston-derived wall shear-stress values. Unfortunately the purist approach has not generally been applied, and the majority of compressible flow Preston correlations are based on formulations involving properties of the free-stream flow. The presumption is that the  $M_T$  dependence is subsumed in the correlation, which gives a true value for the shear stress, and that the transformation does likewise for the profile.

A characteristic of these correlations is that they call for property values at a "mean temperature" which is a function of wall temperature, free-stream temperature and free-stream Mach number, and not very close (77%  $TW$  for  $AW$  at Mach 3) to the wall temperature (Sommer & Short, 1955). Typical of these are Fenter & Stalmach (1958), Hopkins & Keener (1966) and Allen (1973, 1977). Because of the link between skin friction, Reynolds number and Mach number, these are functionally correct if restricted to ZPG adiabatic flows, though the success of the "mean temperature" approach is essentially empirical. Success is measured by the ability of the correlation to reduce compressible data to the incompressible Preston tube calibration. A good example is the much used "Hopkins & Keener T" correlation. The first step was to apply the incompressible correlation directly, evaluating fluid properties at the wall. This collapsed the data fairly well over the limited Mach number range used, but not onto the incompressible data, demonstrating a Mach number effect. The next step assumed that at low speeds the pressure difference recorded by the tube was the local dynamic pressure, so this should be used in the calibration rather than the Pitot pressure. Again, the fluid properties were taken at the wall, and for both of these the free-stream properties appearing in the calibrations cancel out. The implied "Mach correction" of the second attempt was however not great enough, and was supplemented by adoption of the "effective temperature" evaluation of fluid properties. The calibration then becomes edge-state dependent. Subsequent efforts (e.g. Allen, 1973, and, importantly, corrected, 1977) have been largely concerned with trying to improve the quality of the data, and the convenience and accuracy of the formulae used to describe it. (Allen's results prompted the development of the Bradshaw & Unsworth formulation, a corrected version of which is in Allen, 1977.)

By analogy with low-speed flows, the correlations are used in pressure gradients, when the Preston tube may be the only sensor which is remotely practical. With the usual restriction to gradients which are not "too great", the correlations may claim modest success (CAT 7102, 7007, 8601T along a straight wall, and 7101 on a curved surface - AG 253 figs. 5.3.2/13/15/16; fig 10.1.4 below). (A re-examination of the raw data for CAT7101, using the Bradshaw & Unsworth expression, shows poor agreement for the upstream profiles, with agreement improving to become almost complete at the downstream end.) However, in general, pressure gradients along a wall are accompanied by gradients normal to the surface, especially if the pressure gradient is changing, or the wall is curved (AG253 Ch. 6). The properties of the free stream therefore may vary rapidly along a profile normal, so that the choice of boundary-layer edge position critically affects the edge-state property values. Under these circumstances the wall shear-stress deduced from any of the correlations in terms of edge values will depend on the point chosen as the boundary-layer edge, which most evidently is not a quantity measurable at the wall, as wall similarity requires. We have already seen (§ 9.2.3, above) that the variation in edge state in a curved ramp flow (8401T) has a material effect on the Van Driest transformation, and so on the apparent success of measurements in realising the universal wall law, while retaining a fixed wall shear-stress value.

Discrepancies may therefore arise from sensitivity to selection of the edge state, from inherent errors of the correlation, from sensitivity of the calibration to longitudinal pressure gradients, or because the velocity profile in reality does not agree with the universal law of the wall. There is no reason to expect (rather than hope) that profiles in strong normal pressure gradients should agree with the universal law. Under these circumstances, we would not advise the acceptance of values derived from a fit to the wall law.

An alternative approach suggested by Settles (1975), CAT7904T, for flows experiencing a normal pressure gradient, is to use a fictitious edge state determined from the wall pressure and the free-stream total pressure. If there are shocks in the flow, it is not at present clear whether he and those following him (experiments performed at Princeton) would use upstream total pressure, or the pressure after the shock system for downstream flows - or how they would decide when to change from one to the other. In the downstream limit, the post-shock exterior flow obviously becomes the appropriate "exterior flow", but in the compression corner flows for which the procedure was proposed it is far from clear as to which, if any, would be appropriate. Preston tube wall shear-stress values derived in this way are used in Ch.10 below as being results based on measurements. The wall-law profiles which result do not fit the log-law well when the flow is disturbed. Some of the discrepancies may be accounted for by the effect of the edge state on the transformation (§ 9.2.3 above) but the authors also present values derived from a fit to the wall law (Taylor, 1984, CAT8401T; Smits & Muck, 1987, CAT8701T; Donovan & Smits, 1987). Jayaram et al. (1987, CAT8702T) show both values (source paper fig.5). If the profiles genuinely do have a wall-law region good enough for a profile fit, then logically a Preston tube should indicate the same shear-stress value. The longitudinal pressure gradients in CAT8702T were not so great as to suggest a large pressure gradient correction.

#### 9.2.5. Interpolation and profile alignment.

A functionally complete mean-flow profile requires measurement of three individual property profiles, and the Y-values for these will not in general match. Usually therefore two of the measured profiles must be interpolated to the Y-values of the third, generally that in which the greatest rate of change is observed, with conventional measurements, the Pitot profile. It is in this (authors') interpolated form that we present profile data when possible. A principal purpose of the additional entries in this volume is to present turbulence data, and in doing so there is inevitably a further stage of interpolation, generally from functionally complete mean flow profiles, to the Y-values of turbulence measurements. Interpolation within profiles measured on a common traverse line is inevitable and proper, though repeated interpolation will artificially smooth the original data. There are occasions however when a mean flow survey, already in being, does not include the traverse line to be used for turbulence measurements. The only possibility left, if turbulence data are to be matched to the mean flow, is to interpolate from neighbouring profiles. In an "interesting" flow this is inherently dangerous and to be avoided where possible. We have tried to indicate this possibility whenever we thought there was even a small chance that it had happened.

Many of the flows considered here are on walls which change direction more or less abruptly. In addition to arranging for profiles to be measured along the same traverse line, it may become necessary to ensure that probes have an appropriate alignment. The fluid at quite small distances from the local wall surface may be flowing in a very different direction from that of the wall. The extreme case is the compression corner flow, where for the most part the flow changes direction discontinuously at the shock. Probes which are parallel to the local wall direction may thus be seriously misaligned when they have passed outwards through the shock or compression front into a region where the flow is, as yet, undeflected. Readers will find a detailed discussion of some of the problems which arise in the editors' comments on CAT7904T (Settles et al., 1979). Static pressure probes and inclined hot wires are the sensors most affected, but all intrusive probe measurements will suffer to some degree. Optical techniques are not affected, but it is most important that there be a clear statement of the effective orientation of data, which may well not be obtained for the directions corresponding to natural or boundary layer axes. If the flow is at a large inclination to the measurement directions of a LDV for instance, the stress tensor obtained from the readings will need to be rotated to recover the kinematic Reynolds stresses normally encountered in boundary-layer theories or calculations. The rotation can not be accomplished for any one of the stresses unless all three components in the appropriate plane are available. In the cylinder/cone-flare experiment of Brown et al. (1987) for example, all measurements were made parallel and normal to the axis, while the deflection was 30°. A rotation would be needed before drawing any conclusions about the shear stress distribution behind the shock. Flow deflections in the quasi-normal shock flows of CAT8002T (Délery et al) and CAT8003T (Copy & Reisz) are small so that the effects of rotation can probably be ignored. This is perhaps not the case for the compression corner flows of CAT8402 (Ardonceanu), where the greatest deflection was 18°.

### 9.3. Interpretation of measurements

#### 9.3.1. Shock wave movements

In chapter 8 we presented a survey of the information to be obtained from wall pressure fluctuations. Much of these investigations were directed at the fluctuation mechanisms in separated compression-corner flows. It is concluded that at higher Mach numbers the principal mechanism of the "upstream influence" of a compression corner in such a flow is the oscillation of a single compression shock, the strength of which does not vary greatly as it moves (ch. 8.4.2.1) - and not the transmission of pressure signals through the low speed (time mean) part of the boundary layer. (Note that the oscillations still depend on upstream influence - in the recirculation zone - to close a feedback loop. The argument is that any upstream influence in the subsonic zone is negligible by comparison, perhaps, rather than non-existent.) The instantaneous separation point is near the foot of the shock, and the distributed rise in pressure ahead of the separation point is an expression of the intermittency of the wall pressure at a given point. The time-mean separation line indicated by surface-flow techniques is at or near the rearmost position of the shock because there is an intense rearward shear while the shock is downstream of any point, and only a weak forward shear when it is upstream, so that material accumulates at the downstream limit.

In a nominally two-dimensional flow, turbulence causes variations in the entry conditions and the shock front can develop ripples or wrinkles with a cross-flow wavelength of the order of one half of the entry boundary layer thickness (ch. 8.4.2.1). It follows that a short exposure schlieren photograph will tend to show a smudged double image corresponding to the forward and rearward "wavecrests" (there is no reason to expect uniform amplitude), while a long exposure picture will tend to record a gradient rather than a discontinuity. This gives rise to images apparently representing a coalescing compression fan or branched shock system, and has resulted in the traditional mean flow description of the interaction in those terms.

The turbulence-induced wrinkling of the shock front will however also occur in attached flows, and may result in intermittent separation in a compression corner flow which, in mean flow terms, is an incipient separation case. Both the relative magnitude and the range of movement of the shock fall off with shock strength (Dolling et al., 1983, figs. 8,10) so that with low enough deflection the movement of the shock will approach the turbulence induced wrinkling as a lower limit.

The shock unsteadiness appears to be the result of a complicated feedback process with at least four separately identifiable mechanisms: Firstly, the shock position and strength depends on the upstream and downstream flow conditions, and therefore it will be affected by the intensity and frequency content of the incoming and outgoing turbulence. Secondly, the shock is curved locally by the turbulent structures, and the entropy gradients can act as a source of fluctuating vorticity. Third, the pressure of significant regions of subsonic flow near the foot of the shock provides a feedback path for pressure disturbances to travel upstream. For low Mach numbers, the upstream subsonic layer can be quite thick, and the whole of the downstream layer can be subsonic. In this case, the pressure begins to rise well ahead of the shock position and this may be called a genuine upstream influence. At higher Mach numbers, the sonic line is very close to the wall (for CAT8603T, at Mach 2.9 the flow is subsonic for about  $y/\delta < 0.01$ ). The genuine upstream influence is very small, and the pressure rise ahead of the mean shock position is a direct indication of shock motion. Fourth, when separation occurs the size, shape, and position of the separated zone depends on the turbulence state as determined by the upstream boundary layer and the amplification/generation by the shock.

These four mechanisms modify the turbulence levels, alter the instantaneous shock position and distort its shape. However, the recent work by Selig (1988) and CAT870107T<sup>1</sup> indicates that the shock unsteadiness by itself has little effect on the downstream turbulence intensity, although it is obviously very important for the interaction zone itself.

#### 9.3.2. Three-dimensional effects

None of the experiments described in this volume were performed on axisymmetric configurations so that all will suffer in some degree from end-wall constraints.

With attached flows, the flow on the centreline in the vicinity of the experiment is probably properly representative of the equivalent two-dimensional flow. Many of the studies involve considerable disturbances, and these affect not only the test layer but also the boundary layers on the other tunnel walls. Generally, therefore, the downstream flows can not be considered truly representative of the recovery of a two-dimensional boundary layer from the disturbance which has been imposed, as the downstream pressure distribution will not be

appropriate. The quasi-normal shock flows, with downstream Mach numbers close to one, are likely to be particularly sensitive to the ratio of boundary-layer thickness to tunnel width because of the sensitivity of transonic flows to relatively small changes in their virtual boundaries. Even so, so long as the boundary layer is not exceptionally thick, the centreline development, for some way downstream, will correspond to a two-dimensional flow with the observed pressure distribution, and so may serve as a test case for calculation methods.

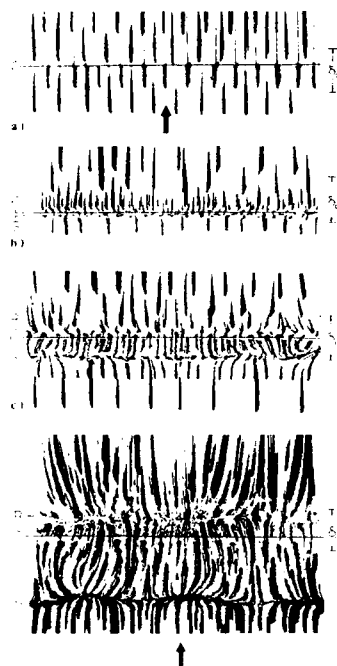


Fig. 9.3.1 Surface streak patterns from the 8, 16, 20 and 24 deg compression corner flowfields. (S, C, and R denote separation, corner, and reattachment locations, respectively. The streamwise direction is from bottom to top in each case. The incoming boundary-layer thickness is shown for comparison.)

It is not possible to have so much confidence in the accuracy with which the experiments represent two-dimensional flows when the flow separates. The configuration of a recirculation zone is critically dependent on the balance between entrainment by the free shear layer and the mass returned at reattachment. This may be materially disturbed by mass entering or leaving at the ends of the recirculation zone through the agency of the sidewall boundary layers. (See for example Heda & Murphy, 1973, figs. 3 & 4 and Schofield, 1985, fig. 2.) Three-dimensional effects therefore are not determined only by such factors as the ratio of the length of the separation to the entry boundary-layer thickness. In most tests with full width models on the floor of general purpose tunnels, the side wall boundary layers are related in a broadly similar way to that on the floor so that it may appear so. However the effects may be much reduced, though not entirely eliminated, by the use of side-plates, as in the Princeton compression corner flow experiments. Figure (9.3.1) shows the surface-streak patterns observed in those tests. The topmost set, for attached flow in an 8° compression corner, shows no detectable three dimensional effects. The remaining sets, for 16°, 20° and 24° corners, show increasingly extended separation regions. As the angle increases, a three-dimensional structure appears. This however is apparently a cellular structure and can not be regarded as an end effect except in so far as the end constraints may determine its cross-flow wavelength.

The appearance of cross-flow variations such as this implies that, for flows of this type, the nominally plane shock wave will always form an irregular surface, and seem to be of finite thickness in schlieren and interferometric photographs.

#### 9.4. Mean flow configurations

There follows a general description of the flows under discussion, with a brief outline of the main causes of measurement difficulties. The shock-wave interaction cases often include separated flow regions, and these present special instrumental problems. These will not be discussed individually or at length. The separation region is small, so that the problems of probe size are aggravated, and since the flows are usually unsteady, the size and position of the recirculating region will vary substantially with time. The direction of flow is also a function of both time and position. In such a region, the only truly trustworthy time mean readings would be values obtained from instrumentation with a linear response. There are few such available. In addition, there are usually relatively strong three-dimensional effects due to side-wall boundary layers, so that even when a flow appears substantially uniform over a central region, it does not follow that it represents the equivalent planar flow.

##### 9.4.1. Quasi-normal shock interactions (QNS)

At first sight it would seem that the simplest shock-boundary layer interaction should be that in which a normal shock enters the boundary layer, and in fact this was the first shock interaction to be studied (Ackeret et al., 1946). In practice, such flows are exceedingly difficult to study, principally because they always incorporate substantial mixed subsonic/

supersonic regions, and for that reason are often referred to as "transonic" interactions (e.g. Déler, 1985). The area/mass-flow relationship near Mach 1 is very sensitive, so that experiments are bedevilled by side-wall displacement effects and probe interference problems. There is therefore a very strong incentive for arranging experiments with non-intrusive instrumentation such as the LDV. Unfortunately, the velocity profile as such is not the sole aim of boundary layer research and LDV results need to be supported by data directly or implicitly containing pressure or density information. (See 9.2.1. above.) These flows are also very susceptible to three-dimensional effects, particularly when there is a separation bubble.

The rise in pressure caused by the shock wave exerts an upstream influence through the subsonic part of the boundary layer, which at the free stream Mach numbers characteristic of this type of interaction is a significant proportion of the whole. The boundary layer is retarded and thickens, so that, if the shock is not strong enough to cause a separation bubble to form, compression waves propagate away from the wall and coalesce into the free stream normal shock. There may or may not be a recognisable shock discontinuity within the boundary layer itself. (See Déler, 1985, figs. 4, 12.)

For stronger shocks, the flow may be sufficiently retarded to cause the boundary layer to separate and form a bubble under the "foot" of the shock. The displacement effect of the thickened boundary layer and bubble again causes compression waves to propagate out towards the free stream, and these coalesce to form a leading oblique shock wave which usually accounts for the major part of the overall pressure rise in the flow in the outer part of the layer and the adjacent free stream. The flow behind this shock is still just supersonic, and may be mildly accelerated as it passes over the convex separation bubble before entering a second, near-normal, shock at the end of the interaction. This second shock is, in general, technically "strong", with a subsonic outflow, although the pressure rise through it is less than that in the first, "weak", shock. The strength of the shock falls off as it penetrates the outer part of the boundary layer and in this region it is possible to have a "supersonic tongue" either immediately after the shock (e.g. Ackeret et al., 1946; Seddon, 1960; Abbis et al., 1976; Kooi, 1978; Schofield, 1985) or starting just downstream (East, 1976). The two shocks meet outside the boundary layer to form the characteristic branched "foot" of a normal shock interacting with a boundary layer. (See Déler, 1985, figs. 35, 36; and fig. 10.4.1 below.)

The changes of direction in flows of this type are not large, so that incidence effects on probes are not a serious problem. Transonic interference effects are however likely to be important, particularly near the wall. Gross effects caused by probes and their mountings can be ameliorated if there is provision for the active adjustment of shock-wave position (e.g. Schofield, 1985). The effects of strong pressure gradients on the probe readings themselves must remain problematical, and readings taken close to shock waves must be regarded with particular suspicion. In addition, flows with an extended separation bubble are likely to show significant oscillations in the shock-wave position, and this may cause "smudging" of probe readings near shocks. The Mach-number range is also such that it is difficult or impossible to calibrate hot-wire probes as a result of strong Mach-number effects.

Quasi-normal shock interactions considered here consist of a group of tests made at ONERA (Déler, 8002T, with an asymmetric configuration, and Copy et al., 8003T, three cases with the shock forming after a slight symmetric constriction in the tunnel) and a selection from a very large range of observations made at Cambridge (Liu & Squire, 8501T, with an asymmetric constriction). Shock entry Mach numbers are typically up to 1.5.

#### 9.4.2. Reflected shock wave flows (RSW)

No cases of this type are reported in this volume of the catalogue, and a very full account of an axisymmetric case is given in AG 263, § 5.3 (CAT7501S). The typical experiment uses an inclined surface in the free stream to generate an oblique shock which impinges on a straight surface supporting the test boundary layer. Close to the surface a complex interaction develops, the upstream influence of the pressure rise causing a relatively weak compression to form ahead of the point at which the incident shock approaches the wall. This coalesces to form the leading shock of the reflected wave system. The displacement surface moves towards the wall as a result of bulk compression, becoming convex, so that an expansion wave propagates outwards behind the leading shock, before becoming concave and returning to the direction of

the wall. This causes the main reflected shock wave to move out behind the expansion (AG 263 figs. 5.3.1/2). At large distances the waves run together to form a single shock of the strength appropriate to an ideal flow reflection. If the incident shock is strong enough, the boundary layer separates to form a bubble and all three components of the reflected wave become stronger. Locally, flow deflections may become large enough to cause alignment errors,



and in the region of interest shock-probe interactions are likely. Large-scale fluctuations are not in general a problem as the incident shock is "anchored" to its generator, and, the Mach-number level typically being higher, gross interference problems are unlikely. Really strong incoming shocks will cause the interaction to form at the foot of a Mach reflection, a case which has not yet been studied in detail.

#### 9.4.3. Compression-corner flows (CCF)

It will be seen that the most common configuration in table 9.1.1 is the compression-corner flow. The abrupt rise in pressure occasioned by the change in flow direction causes the boundary layer ahead of the corner to thicken, and if strong enough, to separate ahead of the corner itself. The question of when a corner flow is severe enough to cause separation has been comprehensively addressed by Settles (1975) and Settles et al. (1976) amongst others and will not be discussed here. A major problem is that, by virtue of the change in direction, there are large differences in static pressure along profile normals in the interaction region. Consequently it is difficult to determine an edge state, and many aspects of conventional data reduction which require edge values become ill-founded (§ 9.2 above).

For small deflections the flow remains attached, with the upstream influence of the corner flow causing a compression fan to form as though from the displacement surface and coalesce into a shock which, at moderate distances out into the free stream, is indistinguishable from the ideal flow plane shock apart from taking a slightly upstream position. The point at which the compression fan must be regarded as having formed a shock moves progressively inwards as the strength of the shock increases. For very small deflections and weak shocks, the point of coalescence may lie outside the boundary layer so that the edge flow undergoes an isentropic compression. For larger deflections the shock extends into the boundary layer (although its exact position is completely overshadowed by the background turbulence) steepening as the Mach number of the flow entering it falls. At representative Mach numbers, the fall in Mach number occurs, for the greater part, very close to the wall so that the shock appears to reach to the surface. (Settles, 1975, at  $M = 2.9$  - the sonic layer is at a  $Y$ -value given by  $Y/\delta = 2.63 Re_\delta^{-0.46}$ , or typically less than 0.005 of the layer thickness).

When the deflection is large enough to cause a separated return-flow region in the corner, the compression occurs predominately in two stages, possibly with a small degree of expansion interposed. A leading shock springs from the separation zone as the flow turns up and over the separation bubble. This shock tends to oscillate violently together with the leading edge of the separation (see chapter 8 and 9.3.1 above). The main turning and the greater pressure rise is accomplished by a compression springing from the reattachment zone. The compression runs into and reinforces the leading shock so that in the outer flow it has the same strength as in ideal flow.

The principal experimental difficulties in these flows, apart from the eternal problem of finding wall-shear stress, are those arising from probe alignment and, when separated, unsteadiness. The turning angles may become large - e.g. CAT7904T,  $20^\circ$ ,  $24^\circ$  - so that even the relatively insensitive Pitot tube gives misleading readings unless rotated to the stream direction, while a static probe will be seriously inaccurate. (See the editors' comments in the entry for CAT7904T and 9.2.5 above.) Quite systematic efforts have been made to quantify the extent of shock-wave movement for this configuration. The principal investigation is that of Dolling et al. (1983). The motion is such that for a  $20^\circ$  corner flow, the shock lies within an  $X$ -interval of 0.35 entry boundary layer thicknesses for 90% of the time. The observed range is about double this, and the range appears to scale on mean interaction length rather than  $\delta$ . The implication is that with this degree of movement a shock may well appear in time average measurements, as it affects probe measurements, to be a distributed compression. Compression-corner flows considered here consist of a group of tests made at Princeton (Settles, 7904T, Smits & Muck, 8701T) with models which did not span the whole tunnel but were fitted with end plates to minimise side-wall boundary-layer effects, and tests at Poitiers (Ardonneau, 8402T) and Marseille (Debiève, 8301T) in which the ramps were of tunnel width.

#### 9.4.4. Curved compression-surface flows (CCS)

Flow turned by a compression corner experiences an abrupt compression, even if the effects of shock motion and separation do in some degree distribute it. A flow turned by a ramp of relatively large curvature, or curved compression surface, will be compressed gradually, and the wave structure which propagates into the free stream exists as a distributed compression throughout the boundary layer. The normal pressure gradients, for any region in which the

Mach number is above  $\sqrt{2}$ , are greater than the streamwise pressure gradients, so that static pressure profiles are required if the data are to be functionally complete. (See Ch 6 in AG 253.) Cases of this type have been dealt with in previous volumes, the best documented being Sturek & Danberg, CAT7101.

If the radius of curvature is small, as for series 01 of Taylor, CAT8401T, there may be probe alignment problems of the same general nature as experienced for compression corners. The flow direction along a profile normal changes rapidly from that of the wall to that of the free stream in a relatively concentrated compression wave. For 8401T0105-7, the profiles in question, static probe measurements were replaced by a linear interpolation across the wave, while the free-stream pressure was probably obtained on a separate occasion. The presence of normal pressure gradients must also raise questions as to the validity of the transformation, demonstrated in § 9.2.3 above, and the use of Preston tubes (§ 9.2.4) unless with wall-law calibrations. Otherwise this configuration introduces no special difficulties apart from a slight unease as to the effects of strong streamwise pressure gradients on static probes.

Four curved ramp flows are represented, all from Princeton (Taylor, 8401T for the mean flow; Jayaram et al., 8702T for the turbulence data).

#### 9.4.5. Distributed compression by reflected wave.

We have one case of a boundary layer on a flat wall subjected to a distributed incident pressure wave. Flows of this type are discussed at length in AG 253, Ch. 6. Normal pressure gradients will be small except at the start and finish of the reflection (see AG 253, figs. 6.1.4, 6.2.2/3), and even there not too severe. Normal measurement methods should meet with little difficulty. It is instructive to compare figures 10.1.4 and 10.2.3 above, which give the inner-law plots for a reflected wave flow on a flat wall and a curved ramp flow with the same streamwise wall pressure gradient. The shear stress is deduced from Preston-tube measurements, and it is evident that the correlation is much more successful for the flat wall case. The discussion in § 9.2.4 above suggests that the lack of success on the curved wall may not be inherent to the Preston tube as the calibration used was edge-state dependent.

#### 9.4.6. Others

The other flows represented here are a flat plate flow, CAT8603T, and a centered expansion, CAT8602T. This last again presents the difficulties associated with a concentrated wave, and the authors overcame the profile-related problems by using the rotational method of characteristics to calculate the static pressure in the affected region. Preston tubes were not used, if they had been, there would have been an edge-state problem unless they used a wall based correlation.

#### CONCLUSIONS

- a) A majority of the problems arising in the interpretation of mean flow data for disturbed compressible boundary layers are related to the effects of normal pressure gradients.
- b) The most serious intractable problem is the determination of wall shear-stress. The flows in question include regions in which a Preston tube can never be expected to give a valid result, though it may be possible to extend the range of validity if calibrations are based on pure wall-law similarity.
- c) The Van Driest transformation should not be used for data affected by normal pressure gradients, and profile-derived wall shear-stress values deduced from such profiles can not be trusted.
- d) The direction of the mean flow may change significantly in a short distance so that it is necessary to take special measures to ensure that probes sensitive to misalignment, in particular static probes and oblique wires, are correctly oriented.

## 10. REVIEW OF MEAN FLOW DATA

Before we discuss the turbulence data we present the mean flow data for the 12 entries contained in this volume. We begin with the zero-pressure gradient flow (ZPG) of Spina & Smits (1987, CAT8603T), followed by the reflected wave case, Fernando & Smits (1986, CAT8601T), providing an adverse pressure gradient (APG) of the same order of magnitude as those in the concavely curved surface flows of Taylor (1984, CAT 8401T). The latter flows have appreciable normal pressure gradients as has the expansion flow of Dussauge (1987, CAT8602T). The remaining ten cases are shock/ boundary layer interactions which will be dealt with in two groups, quasi-normal shock interactions and compression corner flows (cf. chapter 9).

Comparisons between measurements and the logarithmic law of the wall (AG 253, eqn. (3.3.12)) on the one hand and the outer law (AG 253, eqn. (3.3.17)) on the other hand were made for all cases in this survey using the van Driest transformation (AG 253, eqns. (3.3.13 a and b)) with allowance for the recovery factor. The constants used for the log-law are  $K = 0.40$  and  $C = 5.10$ , and the Reynolds number is defined as  $Re_{\delta_2} = U_{\delta} \rho \delta_2 / \mu_w$ .

### 10.1. Zero, adverse, and favourable pressure gradient flows

Two of the three compressible boundary layers (ZPG and APG) discussed in this section were measured in the Princeton supersonic tunnel and provide comparative data for more complex flows discussed in sections 10.2 and 10.3. The flow was not quite adiabatic ( $T_w/T_r \approx 1.1$ ) but heat transfer to the wall has been assumed to have negligible effect. The skin friction was determined by Preston tubes using the calibration curve of Hopkins & Keener (1966). Total temperature was measured at selected stations and on the basis of those measurements, a linear variation giving  $T_0 = 1.04 T_{00}$  at the wall was assumed. The third flow accelerates round an expansion corner (Dussauge & Gaviglio (1987, CAT 8602T). The boundary layer has passed through the rapid expansion of the nozzle but ZPG development downstream is long enough for upstream history effects to be small.

Table 10.1.1 presents some characteristic data:

Table 10.1.1

CAT	Author	PG	$M_0$	$Re_{\delta_2} \times 10^{-3}$	Transition
8603T	Spina & Smits	ZPG	2.9	38	Natural
8601T	Fernando & Smits	APG	2.65 - 2.48	40 - 58	Natural
8602T	Dussauge & Gaviglio	FPG	1.76 - 2.25	3 - 2	Forced

The ZPG-flow is discussed first. Agreement between the log law and the measurements is good (fig. 10.1.1), the deviation at the smaller  $y$ -values probably being due to errors in measuring the distance from the wall. The outer law shows fair agreement (fig. 10.1.2) with the measurements although the older data in the same Reynolds - and Mach - number range from the same wind tunnel (Vas CAT7601) agree even better (fig. 4.2.16 AGARDograph 253). On the whole the data of Spina & Smits are characteristic of a fully developed ZPG boundary layer.

The longitudinal pressure gradient for the APG flow was provided by a wave generator mounted in the free stream and was identical to that measured on the curved ramp, model 2, of CAT8401T but without curvature (cf. fig. 10.2.1). All profiles show normal pressure gradients though, this being a reflected wave case, they are not very strong. The profiles describe the flow in the downstream region of the adverse pressure gradient, profile 01 being about halfway through the pressure rise. All outer-law profiles (fig. 10.1.3) show the typical APG behaviour for a modest streamwise pressure gradient and should be compared with the measurements of Thomas (fig. 5.3.12 AGARDograph 253). The profiles fit the logarithmic law reasonably (fig. 10.1.4), again with discrepancies in the range  $y^+ < 500$ . The data are in any case sparse near the wall as they have been interpolated from detailed mean flow surveys to the  $y$ -values used for the hot-wire experiment. In contrast, the data of Thomas go down to  $y^+ = 30$  without any deviation from the log law. The wake strength ( $\Delta(u^2/u_T) \sim 5-6$ ) shows values which are considerably higher than those for ZPG in the same Reynolds number range which is in agreement with results obtained in subsonic boundary layers.

For the FPG flow the tests were conducted on a continuation of the lower straight tunnel nozzle block. At a point 640 mm from the throat the surface turned down sharply at an angle of  $12^\circ$  forming the expansion corner, round which the flow accelerates. At about a further 120 mm along the tunnel axis the surface curved back to the free-stream direction. The reflection of

the expansion fan returned to the test surface downstream of this point. Profiles 01 to 09 were measured normal to the upstream wall, 10-23 normal to the sloping surface, with 09 and

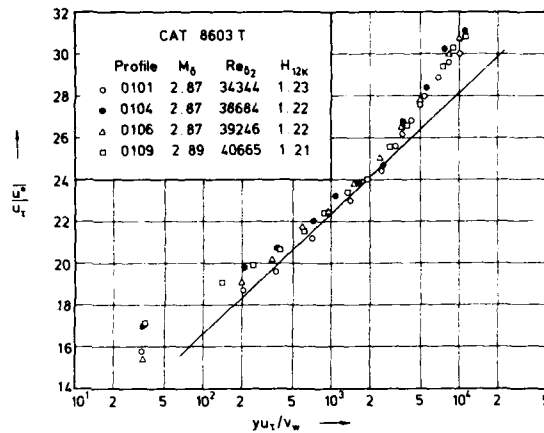


Fig. 10.1.1 Law of the wall for a compressible boundary layer with zero pressure gradient  $T_w/T_r \approx 1.10$ ,  $c_f$  from Preston tube). Spina & Smits (1986).

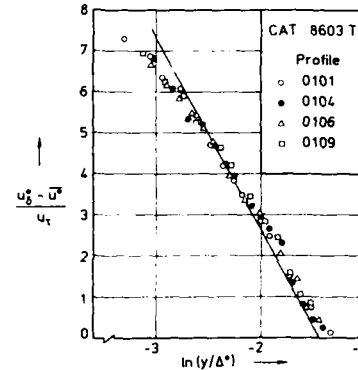


Fig. 10.1.2 Outer law for a compressible boundary layer with zero pressure gradient (origin not defined,  $T_w/T_r \approx 1.10$ ). Spina & Smits (1986).

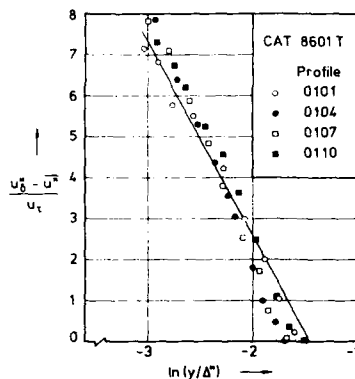


Fig. 10.1.3 Outer law for a compressible boundary layer with an adverse pressure gradient (origin not defined,  $T_w/T_r \approx 1.10$ ). Fernando & Smits (1986).

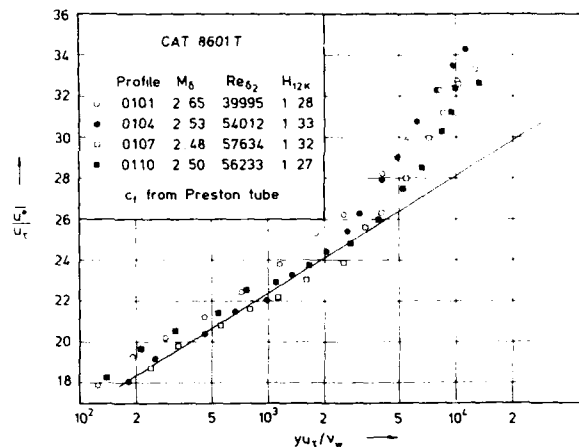


Fig. 10.1.4 Law of the wall for a compressible boundary layer with an adverse pressure gradient (origin not defined,  $T_w/T_r \approx 1.10$ ). Fernando & Smits (1986).

10 at the corner. Upstream skin friction data were obtained using a handfit to the transformed logarithmic law ( $K = 0.41$  and  $C = 5.7$ ). Downstream values were calculated according to Chew (1978). This flow was included in this volume because it appears to be the only reasonably fully documented study of a boundary layer passing through a concentrated expansion. Upstream influence by the subsonic layer next to the wall appears to be small, so that the boundary layer experiences a rapid distortion closely related to the corresponding ideal flow model. The comparison between measurements and the log law is shown in figure (10.1.5). The agreement for the three upstream profiles is very good due to the curve fit for  $u_r$  whereas the three downstream profiles appear to show a convergence towards the log-law. The wake strength  $\Delta(\bar{u}^2/u_r)$  is small and the acceleration effect on the boundary layer must be classified as being modest. Stronger effects of favourable pressure gradient may be observed in the boundary

layers investigated by Thomas (CAT7401) and Lewis et al. (CAT7201), both, however, reflected wave cases. Measurements agree with the outer law (fig. 10.1.6) - as they should - in the upstream region of the flow and show the behaviour of a FPG boundary layer in the expansion region (cf. fig. 5.2.4 in AGARDograph 253). Dussauge & Gaviglio (1987) claim that the turbulence intensities show a behaviour as to be found in a relaminarized boundary layer. This is not confirmed by the mean velocity profiles.

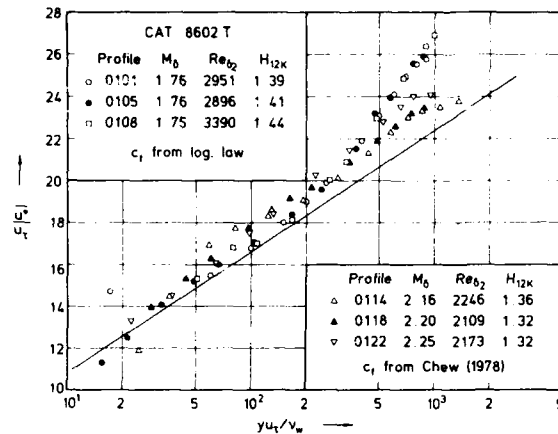


Fig. 10.1.5 Law of the wall for a compressible boundary layer with a rapid expansion (origin not defined, adiabatic wall). Dussauge & Gaviglio (1986).

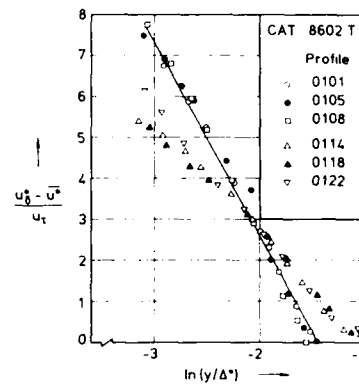


Fig. 10.1.6 Outer law for a compressible boundary layer with a rapid expansion (origin not defined, adiabatic wall). Dussauge & Gaviglio (1986).

## 10.2. Curved ramp flows

Before we discuss the compression corner flows, we present a milder version of this type of flow for which the abrupt compression corner was replaced by one of four curved ramps. These ramps had side fences since they were narrower than the tunnel so as to reduce side wall boundary-layer effects. The ramp curvature started at  $(X = 0)$  1.15 m from the nozzle exit plane and the four ramps had an initial circular arc section followed by a flat recovery section. The main geometric and flow parameters are presented in table 10.2.1. The initial mean flow studies were performed by Taylor (1984) and have been supplemented by a fourth case (Donovan & Smits (1987), presented as 840104T). There are no shock waves in the exterior flow near the boundary layers.

Table 10.2.1

CAT	R <sub>1</sub> mm	L <sub>1</sub> mm	L <sub>2</sub> mm	α°	M <sub>0</sub>	Re <sub>δ<sub>2</sub></sub> × 10 <sup>-3</sup>	Skin friction
840101T	254	35.5	145	8	2.9 - 2.5	37-59	Preston tube
840102T	1270	177.3	152	8	2.85-2.45	34-58	"
840103T	1270	354.7	77	16	2.88-2.18	35-98	"
840104T	350	97.7	156	16	2.88-2.14	31-68	"

Here R<sub>1</sub> denotes the radius of curvature, L<sub>1</sub> the length of the curved section, L<sub>2</sub> the length of the flat section, and α the turning angle. The respective turbulence data were measured by Jayaram et al. (1987) and by Donovan & Smits (1987). Comparable simple-wave APG studies are those of Sturek & Danberg (CAT7101) and Laderman (CAT7803S).

The wall static-pressure and the skin-friction distributions for the four test cases are presented in figure (10.2.1). For each turning angle there are two radii of curvature and the flow reaches about the same pressure level, however in half the downstream distance for

the smaller radius. This results in a steeper streamwise pressure gradient for cases 840101 and 840104 and corresponding effects on the mean flow and turbulence structure. As a curved-wall flow there are normal pressure gradients which, at these Mach numbers, are greater than the streamwise gradients. In the region affected therefore, integral values are not properly formed and no precise conclusions should be based on their values. The author has used an "effective" edge state as suggested by Settles (1975) and this must throw in doubt both the reduction of the Preston tube data - the Hopkins & Keener compressible adaptation requires edge-state values - and the value of the van Driest transformed velocity (see § 9.2.3 above).

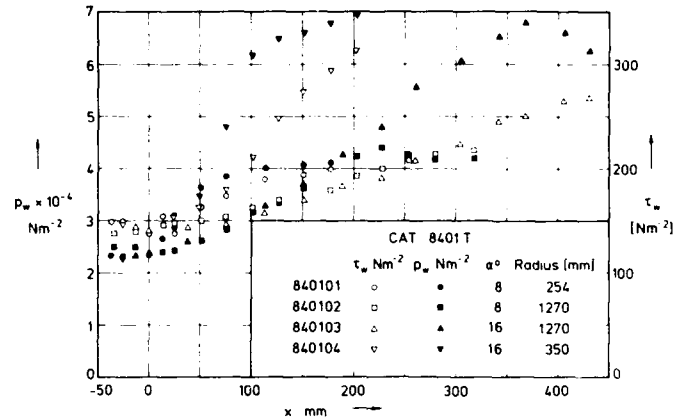


Fig. 10.2.1 Wall static-pressure and skin-friction distributions for compressible boundary layers along 4 concave compression surfaces with recovery sections (Taylor (1984)).

So the skin friction data in figure (10.2.1), in the affected region, should be regarded with some caution. For example, there is hardly any difference in the distributions of  $\tau_w$  for the two angles of curvature 8° and 16° for the same radius  $R_1$  of 1270 mm for values of  $x$  downstream of the affected region on the 8° model. The pressure distributions of course differ, but the recovery region is probably not long enough for significant differences to develop.

The wall-law velocity profiles, using the author's Preston-tube-derived wall shear stress,

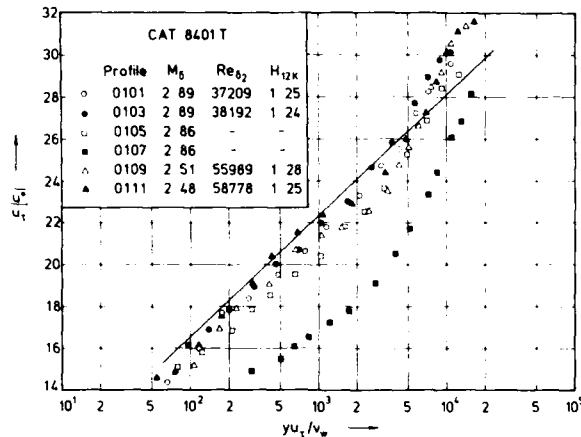


Fig. 10.2.2 Law of the wall for a compressible boundary layer along a concave compression surface (origin not defined,  $T_w/T_r \approx 1.10$ ,  $c_f$  from Preston tube). Taylor (1984).

show a considerable degree of scatter. They are presented in figures (10.2.2 to 10.2.4) for the first three cases. The initial profiles 0101, 0201 and 0301 (ZPG) agree well with the logarithmic law while the remainder in the less affected regions tend to lie low by up to 10% implying a wall shear stress value up to 20% too high. This may be a consequence of the use of the "effective" edge state when reducing the Preston-tube data (§ 9.2.3). If the Frei & Thomann (1980) pressure gradient correction may be taken as a guide to the validity of Preston-tube response to the streamwise pressure gradient, the maximum correction would be 3%, and related more to large probe size ( $d^+ = 1000$ ) than to pressure gradient ( $\alpha_{max} 5 \times 10^{-3}$  on model 1).

In the source paper and when shown in the open literature, these profiles have been presented with wall-shear values deduced by fitting the data to the wall law, and therefore initially appear to be in excellent agreement. We do not however, for the reasons outlined in § 9.2.3 above, feel that it is proper to rely on a curve fit in deducing wall shear in flows with normal pressure gradients, or in severely non-equilibrium conditions. In addition we must question the quality of the fit, as, at least for some of the downstream profiles, (0314/5) the profile as shown has points below the wall law in the range  $10^2 < y^+ < 10^3$  which if they were a decade further in would appear to indicate the sublayer very satisfactorily. It is not possible at present to come to any robust conclusion for flows of this type, with significant normal pressure gradients, as to the principal source of the discrepancies. Both the profile and the Preston-tube results are affected by the choice of edge state, and it may be that in reality the profiles do not show a standard log law.

It is evidently desirable to use a Preston tube calibration function which is not D-state dependent, such as that proposed by Bradshaw & Unsworth (1973), and the low value of the wall pressure gradient parameter suggests that the zero pressure gradient calibration might be appropriate. There is of course no ordered information as to the effect of curvature, if any, or of the normal pressure gradient. As for the log law we have plotted only a selection of data for the outer law. Again the measurements show a considerable degree of scatter (figures 10.2.5 a and b) without a definitive trend indicating the adverse pressure gradient. Only profiles 0309 and 0312 in figure (10.2.6) exhibit the APG behaviour in that they lie below the curve for the outer law in a ZPG. The measurements of series 4 in inner layer coordinates are presented in figure (10.2.7). They show the greatest scatter of the four test cases of CAT8401T and even the initial profile (401) which should be in a zero pressure gradient shows an anomalous behaviour.

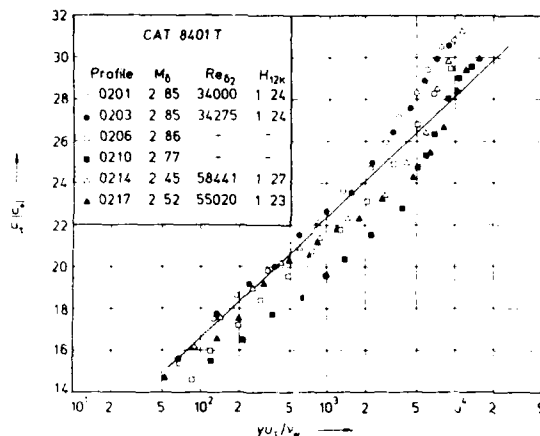


Fig. 10.2.3 Law of the wall for a compressible boundary layer along a concave compression surface (origin not defined,  $T_w/T_r \approx 1.10$ ,  $c_f$  from Preston tube). Taylor (1984).

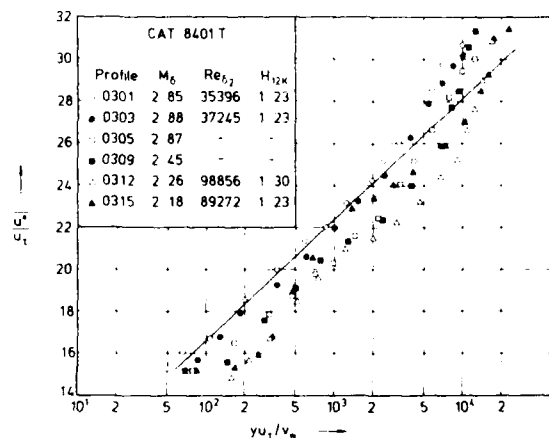


Fig. 10.2.4 Law of the wall for a compressible boundary layer along a concave compression surface (origin not defined,  $T_w/T_r \approx 1.10$ ,  $c_f$  from Preston tube). Taylor (1984).

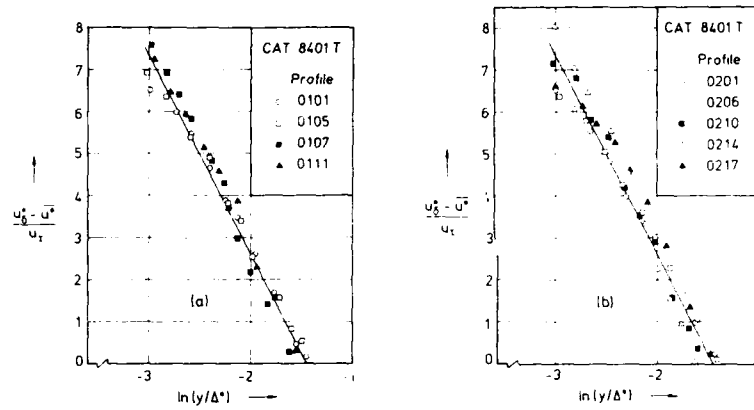


Fig. 10.2.5 Outer law for a compressible boundary layer along a concave compression surface (origin not defined,  $T_w/T_r \approx 1.10$ ). Taylor (1984).

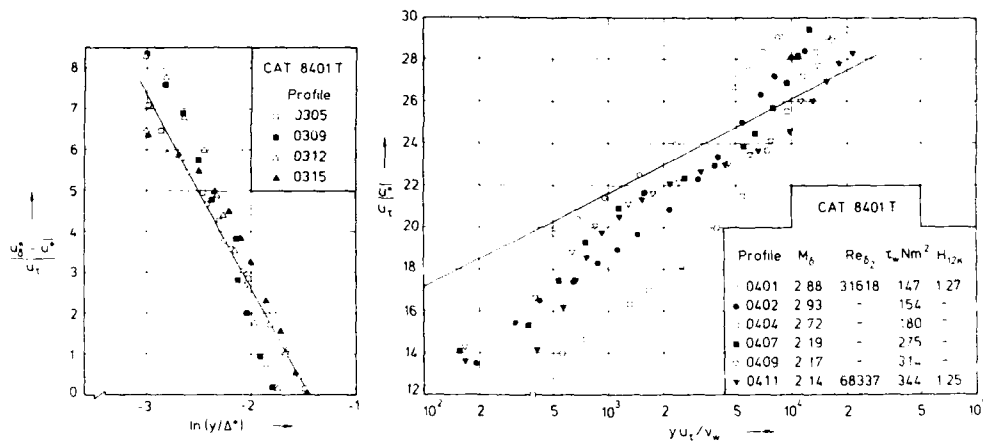


Fig. 10.2.6 Outer law for a compressible boundary layer along a concave compression surface (origin not defined,  $T_w/T_r \approx 1.10$ ). Taylor (1984).

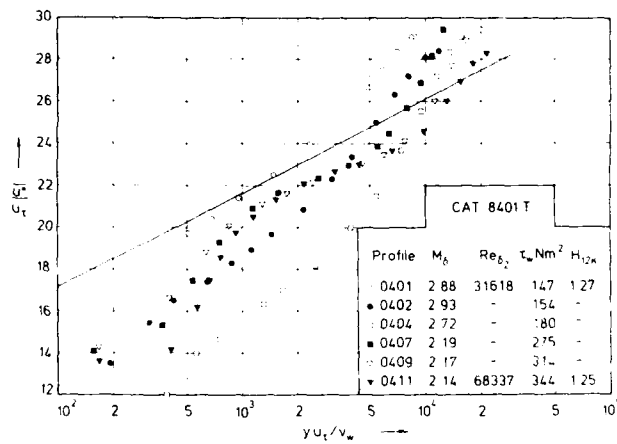


Fig. 10.2.7 Law of the wall for a compressible boundary layer along a concave compression surface (origin not defined,  $T_w/T_r \approx 1.10$ ,  $c_f$  from Preston tube). Donovan & Smits (1987).



### 10.3. Compression-corner flows

Compression-corner flows considered here consist of a group of tests made at Princeton (Settles et al. (1979) and Muck et al. (1983), the latter measured the turbulence field), and tests at Poitiers (Ardonceanu (1984) and Marseille (Debiève (1983)). In the former case (CAT 7904T) the models did not span the whole tunnel but were fitted with end plates to minimize side-wall boundary-layer effects, while in the latter two flows (CAT 8403T and 8303T) the ramps were of tunnel width.

Table 10.3.1

CAT	$\alpha^\circ$	$L_2$	$M_0$	$Re_{\delta_2} \times 10^{-3}$	Skin friction	Separation
8301 T	6	240	2.33-2.0	2.3-3.7	Calculated Chew (1978)	no
840201T	8	80	2.24-1.86	4-5.5	Calculated Fernholz(1971)	no
840202T	13	80	2.26-1.74	3.5-8		incipient
840203T	16	60	2.23-1.58	3.8-10		yes
790401T	8	not applicable	2.87	35-47	Preston tube	no
790402T	8	>107	2.76-2.43	24-56	" "	no
790403T	16	>140	2.83-2.2	32-63	" "	yes
790404T	20	>114	2.79-2.0	37-80	" "	yes
790405T	24	>142	2.8-2.7	33-40	" "	yes

$\alpha$  is the angle of inclination to the tunnel floor and  $L_2$  the length of the surface extending from the corner ( $L_1$  being zero). There are no other compression-corner flows in the three earlier AGARDographs by the authors which could be used for comparison.

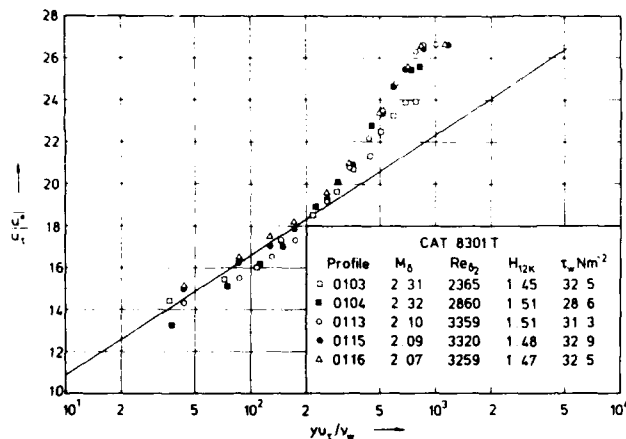


Fig. 10.3.1 Law of the wall for a compressible boundary layer along a compression surface (6°) (adiabatic wall, origin not defined,  $c_f$  from correlation of Chew (1978)). Debiève (1983).

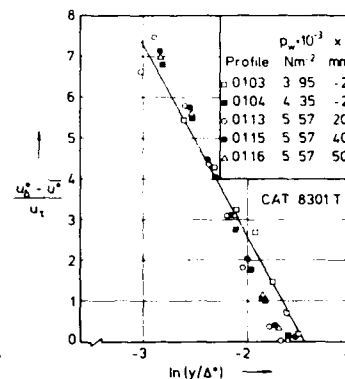


Fig. 10.3.2 Outer law for a compressible boundary layer along a compression surface (6°). Debiève (1983).

We begin our discussion of the mean flow profiles with CAT 8301T. The test boundary layer was formed on the floor of the wind tunnel, remaining under ZPG conditions for approximately 240 mm after leaving the nozzle which is about 350 mm axially from the throat to the exit plane. The turbulent boundary layer was shown to be fully developed with a normal energy spectrum. Transition was forced by a roughness strip upstream of the nozzle throat. The profiles (Pitot pressure, static pressure, and total temperature) form a single series running from the undisturbed upstream flow (01-06) through the compression-corner interaction and well downstream into the reattachment flow. Skin-friction values were not provided for all profiles,

downstream into the relaxing flow. Skin-friction values were not provided for all profiles, so the first and the last profiles which could be plotted were 03 and 16, respectively. We have plotted out all the mean-flow profiles for which the author gave us a value of the wall shear stress, none close to the interaction, and it is not surprising that they fit the logarithmic law (cf. figure 10.3.1) as the shear-stress values are profile derived. The outer region of the downstream profiles shows a typical APG character, inherited from the earlier retardation (figure 10.3.2). The last profile (0116) has not completed relaxation towards the ZPG profile.

As in the previous case the boundary layers of CAT 8402T developed under ZPG conditions on the tunnel floor before encountering the change in direction at the compression corner ( $X = 0$ ) a distance 546 mm from the throat and 219 mm from the exit of the nozzle. "The undisturbed boundary layer was found to be fully turbulent without any tripping" (Ardonceanu 1984). Pitot-pressure and static pressure profiles were measured normal to the axis in the range  $-0.02 < x < 0.06$  m and in reducing the Pitot data the author assumed constant total temperature. The wall pressure data were derived from the profile data adjacent to the wall. We present two of the three sets of profiles measured in turbulent boundary layers experiencing a shock-wave structure caused by a compression corner. Series 01 is wholly attached, series 02 is on the point of separation, while series 03 has a small separation region in the corner. The profiles cover the flow from upstream of the corner to about 8 undisturbed boundary-layer thicknesses downstream. Unfortunately there are no measured skin-friction values, preventing us from presenting the data in our usual way. We have therefore used the semi-empirical skin friction relationship derived for ZPG compressible boundary layers (Fernholz 1971) in order to plot the initial and the last profiles in inner and outer-law coordinates, at least for series 01 and 02 which have no separation.

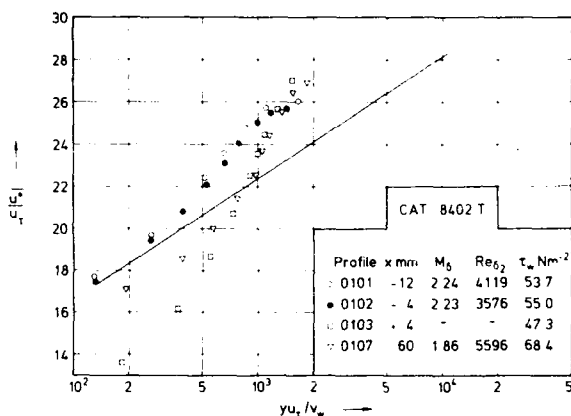


Fig. 10.3.3 Law of the wall for a compressible boundary layer along a compression surface (8°), (adiabatic wall, origin not defined, cf. from Fernholz (1971)). Ardonceanu (1984).

Figure (10.3.3) shows the first three and the last profile for the smallest ramp angle of 8°. The two upstream profiles (0101 and 0102) follow the logarithmic law whereas the downstream profiles, the first and the last of the deflected flow, show no agreement with the log law. Although the calculated skin friction for the latter profiles is probably incorrect, experience with this type of flow leads us to believe that the logarithmic law does not hold in the shock boundary-layer interaction and that the recovery length of the wall is too short to allow the profile to readjust to "normal" conditions. This is even more obvious in the case of the stronger flow deflection (13°) the profiles for which are shown in fig. (10.3.4). Overtly it would seem that the upstream effect on the pressure gradient is so strong that all the three upstream profiles (0201-0203) are affected. It would have been advantageous if velocity data

could have been measured closer to the wall, the lowest value of  $y^+$  being only about 130. This is, however, very difficult for any optical method as the effective position of measurement is much affected by refraction. The bad agreement at low values of  $y$  may be caused by this effect. Figure (10.3.5) presents the outer-law plot for some profiles of series 01 and 02 of CAT8402T.

In figure (10.3.6) we wish to draw attention to two observations which may be exemplified by the flows along the two small ramp angles 6° and 8° of CAT 830101T and 840201T, respectively: First, the large difference in the level of the calculated skin friction of the two boundary layers (full circles and squares) which is due to the different levels of total pressure and secondly, the close agreement, approximately  $\pm 3\%$ , between the calculation methods of Chew (1978) and Fernholz (1971). The former takes into account the APG, using the Ludwig & Tillmann relationship modified for compressible flow, whereas the latter is strictly valid only for ZPG. This is not fortuitous but can be explained by the rather weak influence of small and moderate pressure gradients on the change of the shape parameter  $H_{12,k}$  which is used in Chew's formula.  $H_{12,k}$  is defined as the ratio of displacement and momentum loss thickness for constant density.

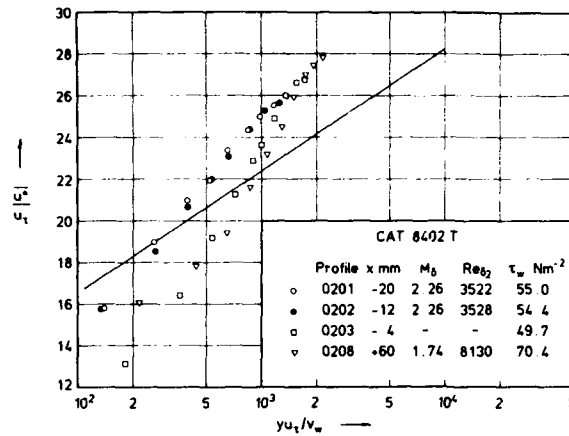


Fig. 10.3.4 Law of the wall for a compressible boundary layer along a compression corner (13°), (adiabatic wall, origin not defined,  $c_f$  from Fernholz (1971)). Ardouneau (1984).

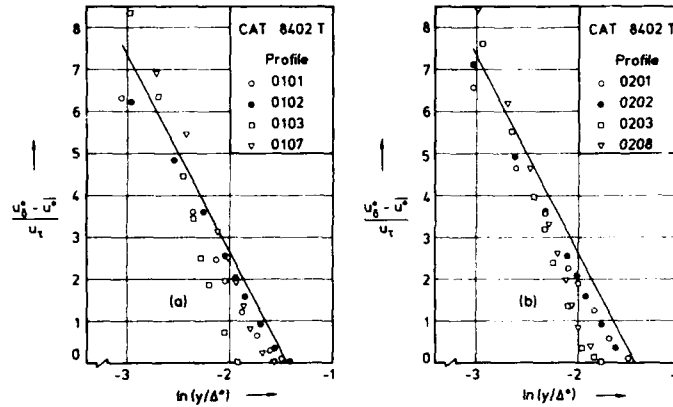
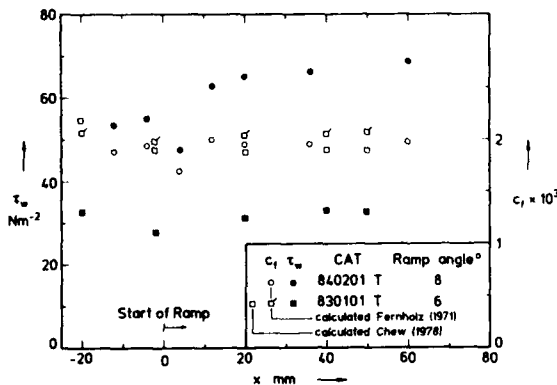


Fig. 10.3.5 Outer law for a compressible boundary layer along a compression corner (8° and 13°). Ardouneau (1984).



The next five cases form the mean flow base for the later turbulence measurements of Smits & Muck (1987). For this purpose they have been recovered from the archives and extensively reprocessed for this discussion. They were not available to us when we wrote AG 263. Since mean flow profiles were measured with a flattened Pitot probe and a static pressure probe there may be deviations due to probe misalignment and shock interference. For further general remarks the reader is referred to the editors' comments of the entry in CAT7904T.

Fig. 10.3.6 Skin friction and  $c_f$ -distributions in compressible boundary layers along two compression corners (Deblève 1983, Ardouneau 1984).  $2.3 > M_0 > 1.8$ ,  $5500 > Re_{\delta_2} > 2300$ .

Figure (10.3.7) presents the development of the wall shear stress as reported by the authors. The figure should be regarded as no more than an indication of the overall trends, as the reduction of the Preston tube data was made with the Hopkins & Keener (1966) correlation,

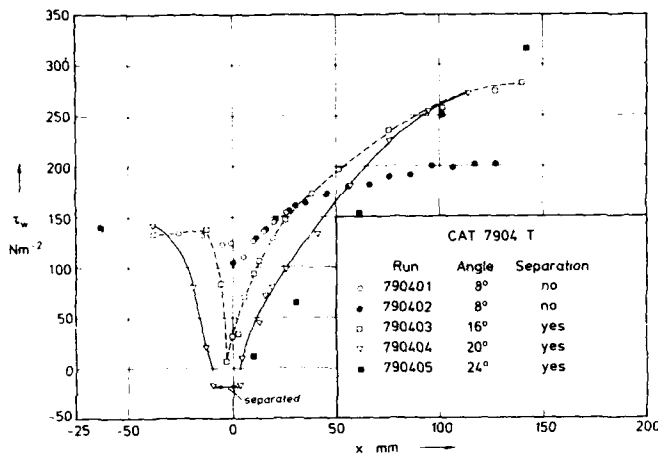


Fig. 10.3.7 Skin friction distributions for compressible boundary layers along 4 compression corners ( $c_f$  from Preston tube): Settles (1979). (Lines are for clarification only).

using a fictitious edge state (Settles et al., 1979) assuming free-stream total pressure and wall static pressure. The poor level of agreement with the log law in the figures below is at least in part due to this procedure, but it is questionable whether a Preston tube, unless so small to be considered a wall device, could provide shear stress values in the interesting part of these flow fields in any case (see § 9.2.3/ 9.2.4). Case 790403 shows a skin friction distribution with incipient separation where as cases 04 and 05 have extended separation regions followed by reattachment and a rise in skin friction with a parallel rise in wall pressure.

Figure (10.3.8) shows the mean velocity profiles upstream of the corner (0101-0104) and two

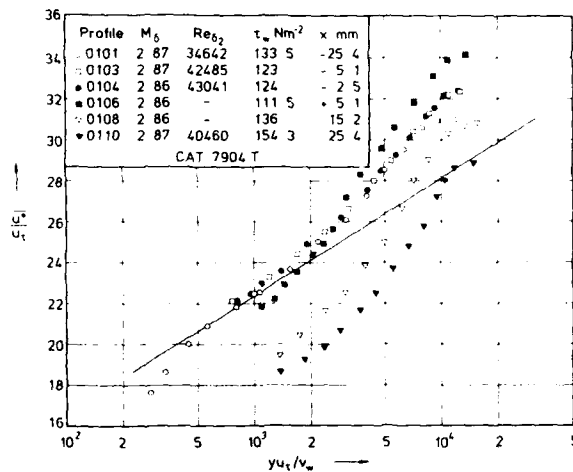


Fig. 10.3.8 Law of the wall for a compressible boundary layer along a compression corner (8°) (origin not defined,  $T_w/T_r \approx 1.10$ ,  $c_f$  from Preston tube). Settles (1979).

profiles along the ramp, with the probes aligned to the tunnel floor. In the upstream region agreement with the log law is good although discrepancies begin to show one decade too early for profile 0101. The discrepancies between the profiles and the log law are large down to about  $x = 30$  mm on the ramp and then suddenly decrease as is shown in figure (10.3.9) for profiles 0207 and 0208. This cannot be explained on physical reasons and we assume that the "jump" is due to an erroneous determination of the wall shear stress. Series 01 and 02 describe the same flow. For series 01 the probes are aligned with the axis, while for 02 they are parallel to the downstream ramp surface. Some profiles of series 01 and 02 are presented in outer-layer coordinates in figures (10.3.10 a and b). The profiles show ZPG (0101 and 0103) and moderate APG behaviour, respectively.

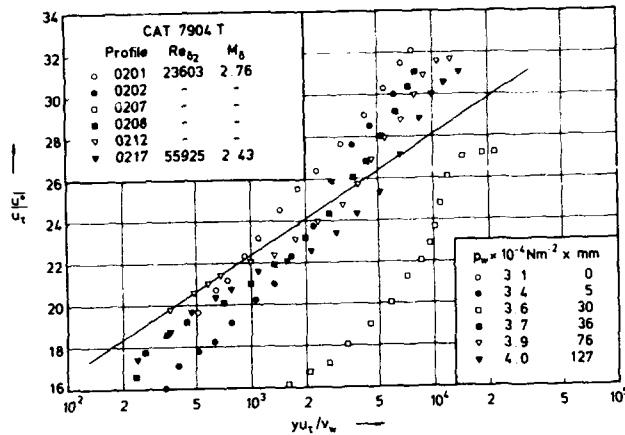


Fig. 10.3.9

Law of the wall for a compressible boundary layer along a compression corner (8°), (origin not defined,  $T_w/T_r = 1.10$ ,  $c_f$  from Preston tube). Settles (1979).

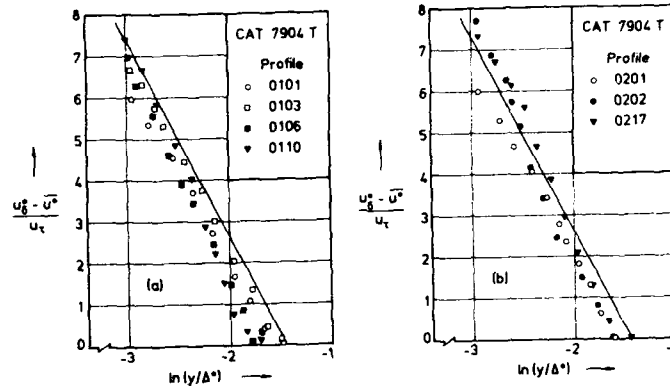


Fig. 10.3.10 Outer law for a compressible boundary layer along a compression corner (8°). Settles (1979).

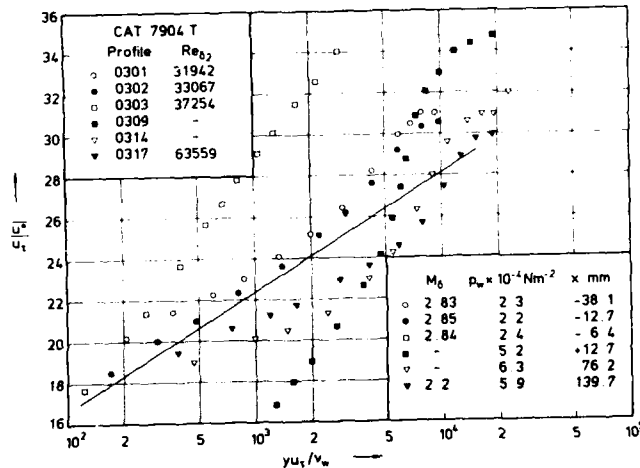


Fig. 10.3.11 Law of the wall for a compressible boundary layer along a compression corner (16°), (origin not defined,  $T_w/T_r = 1.10$ ,  $c_f$  from Preston tube). Settles (1979).

If the ramp angle is increased so that the boundary layer approaches incipient separation, the effects due to shock interference and separation become so severe that the logarithmic law breaks down completely (figures 10.3.11 and 10.3.12). The profiles shown are either upstream or downstream of separation and, although the latter profiles are in the reattached flow, the boundary layer did not recover to its "normal" behaviour, although a recovery to a logarithmic behaviour can be observed.

It is impossible at present to interpret the profiles presented in series 03 to 05 using our usual criteria. For this we need reliable skin-friction measurements and profile data obtained by a non-intrusive measuring technique.

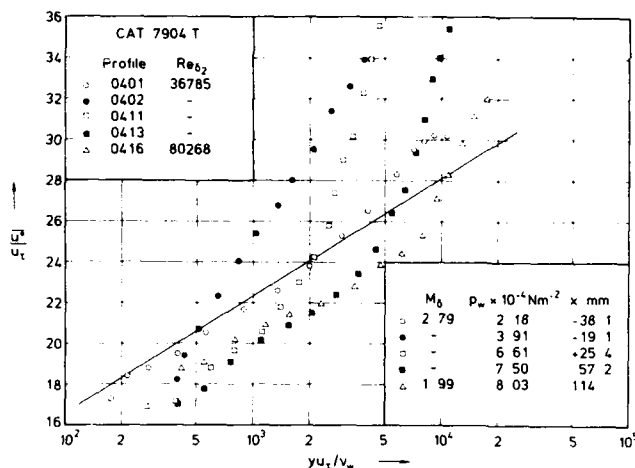


Fig. 10.3.12

Law of the wall for a compressible boundary layer along a compression corner ( $20^\circ$ ), (origin not defined,  $T_w/T_r = 1.10$ ,  $c_f$  from Preston tube). Settles (1979).

#### 10.4. Quasi-normal shock interactions

Quasi-normal shock interactions considered here consist of a group of tests made at ONERA (Délery et al., CAT 8002T, with an asymmetric configuration, and Copy et al., CAT 8003T, for three cases with the shock forming after a slight symmetric constriction in the tunnel), and three cases selected from a large number made at Cambridge (Liu & Squire CAT 8501T) on both the floor and the roof of a similar configuration to that used by Délery et al.. Table 10.4.1 gives the main parameters.

Table 10.4.1

CAT	$M_\delta$	$Re_{\delta_2} \times 10^{-3}$	Skin friction	Separation
800201	1.1 - 0.87	7 - 27	Not measured	yes
800301	1.3 - 0.80	1 - 10	Calculated from Fernholz (1971)	no
800302	1.3 - 0.81	2 - 11		incipient
800303	1.4 - 0.81	2 - 18	Not measured	yes
850101	1.1 - 0.80	5 - 27	Calculated from Winter (1970)*)	yes
850102	1.2 - 0.81	7 - 13		yes
850105	1.1 - 0.75	4 - 14		yes
850106	0.9 - 0.75	7 - 13		no

\*) Probably a profile fit

Délery et al. (1980) used a LDV to measure the velocity field in a boundary layer interacting with a quasi-normal shock and the succeeding recovery process. The shock was strong enough to cause the boundary layer to separate. They obtained a large number of profiles, at close intervals, which are plotted in full in the source paper. We show here (fig. 10.4.1) the Mach-number field in the exterior flow as deduced by them from an interferogram, with the assumption that the total pressure loss in the shock system can be neglected. With this assumption, the lines of constant Mach number are isobars. The figure illustrates well the complexity of this type of flow, but also indicates that, over most of the flow field, the normal pressure gradients are not large, so that some of the difficulties inherent in making mean flow measurements in compression-corner flows are avoided. All the measurements were non-intrusive, so that the data are not functionally complete, lacking pressure or density information in the boundary layer. More seriously, there are no wall shear-stress data so that we have not been able to make our standard velocity profile comparisons. The first traverse was at  $X = 270 \text{ mm}$ , behind the leading branch of the shock and with the recirculation region already established.

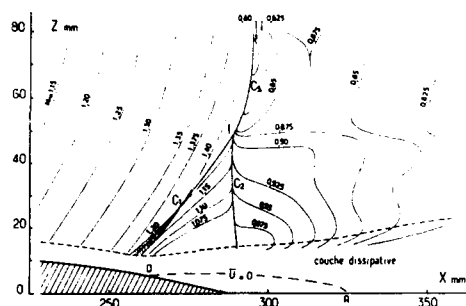


Fig. 10.4.1 Mach-number field of a quasi-normal shock/boundary-layer interaction as deduced from an interferogram. Délery et al. (CAT8002T), copied from author's Fig. 5.

The investigation of Copy & Reisz (CAT 8003T) supplements that of Délery et al. described above. Measurements started upstream of the wall pressure minimum in test boundary layers on the tunnel floor formed by convexly curved inserts let into the floor and roof. The throat was approximately 0.2 m from the start of the parallel part of the tunnel. Since no separation was observed for series 01 and 02 we have calculated skin-friction values using the calculation method of Fernholz (1971) in order to be able to plot the velocity profiles in inner and outer coordinates in the recovery region downstream of the shock. This is the region where the wall static pressure remains constant (fig. 10.4.2). The inner-layer plot (fig. 10.4.3) shows qualitatively that the velocity distribution recovers from the highly disturbed profile 0116 to profile 0120 which follows a straight line at least in a region  $350 < y^+ < 10^3$ , however, it would not be wise to claim that it is returning to the logarithmic law. The poor positioning of the curves in relation to the log law may well be a result of using a ZPG skin-friction correlation, but the shape of the curves suggests that this is not the sole problem. Some part of the variation at low  $y^+$  may be due to refraction. The same overall picture holds for the measurements of series 02 in figure (10.4.4). The outer law plot (fig. 10.4.5) is much clearer since the data do not suffer from wall effects. Here we observe clearly the recovery of an APG profile to a ZPG velocity distribution. Series 03 of CAT8003 includes a separation region. For this reason recovery to a ZPG boundary layer must take much longer so that it was considered inappropriate to calculate skin-friction values for this case.

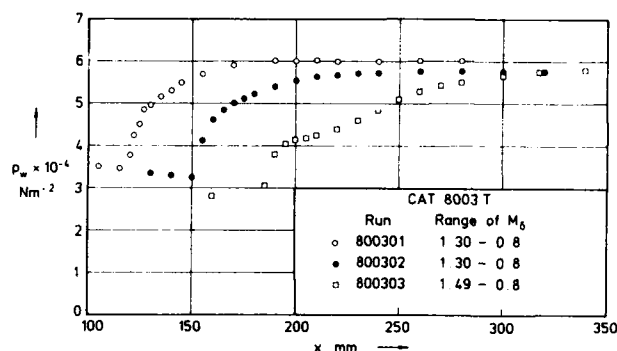


Fig. 10.4.2 Wall-pressure distributions for 3 shock boundary-layer interactions (adiabatic wall origin not defined). Copy & Reisz (1980).

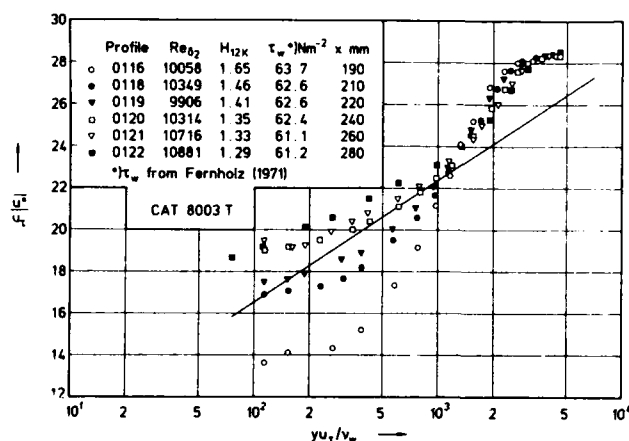


Fig. 10.4.3

Law of the wall for a compressible boundary layer downstream of a quasi-normal shock interaction (adiabatic wall,  $M_0 \approx 0.8$ ). Copy & Reisz (1980).

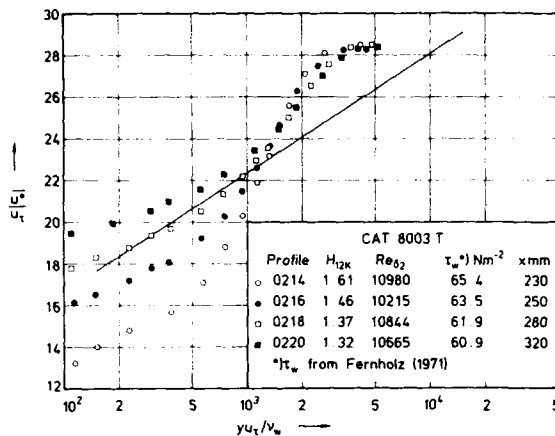


Fig. 10.4.4 Law of the wall for a compressible boundary layer downstream of a quasi-normal shock interaction (adiabatic wall,  $M_5 \approx 0.8$ ). Copy & Reisz (1980).

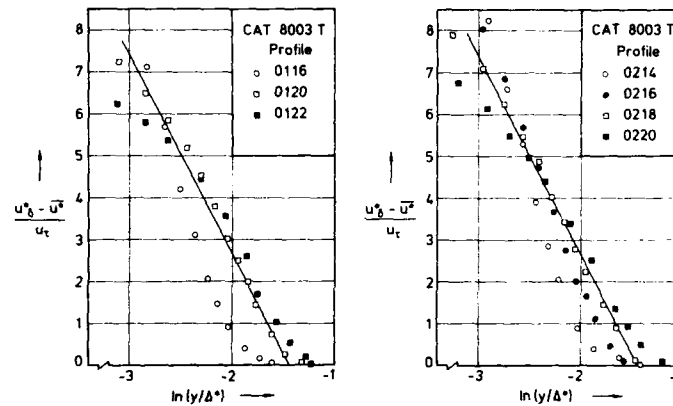


Fig. 10.4.5 Outer law for a compressible boundary layer downstream of a quasi-normal shock interaction (adiabatic wall,  $M_5 \approx 0.8$ ). Copy & Reisz (1980).

Liu & Squire (1985) performed their investigation of shock/boundary-layer interactions at transonic speeds. Five circular arc models could be mounted in the tunnel floor to form bumps. The origin  $x = 0$  is set at mid chord and the maximum height of the bump, 708 mm downstream of the start of the flat part of the floor. The flow approaching the test area is subsonic, so there are no incoming standing waves. It accelerates over the bump and at sufficiently low back pressure is retarded by a shock wave. The test region extended over the range  $-60 < x < 215$  mm. Pitot profiles were, in general, measured upstream of the interaction and in the recovery region downstream for both the boundary layers on the floor with bump (series 01, 03, and 05) and on the flat ceiling (series 02, 04, and 06). It is unfortunate again that no efforts were made to determine the wall shear stress other than by deducing it from the profiles. We show (fig. 10.4.6) the profiles of series 03, for a flow on the tunnel floor, on and downstream of the bump. They are plotted in wall coordinates, using skin-friction values corresponding to those shown in figure 18 of Liu & Squire (1988). The fit is not of a quality to justify us in presenting wall shear stress as data and only general qualitative conclusions can be drawn. The first two profiles 01, 02, show strongly accelerated characteristics, as might be expected. Profile 03 is at the  $X$ -value stated elsewhere as the separation point, so that its wayward character is not surprising. The remaining four profiles are downstream of the reattachment point and display a wake component which is progressively falling as the boundary layer relaxes after the interaction. Figure (10.4.7) shows a wall-law plot for series 02, on the flat tunnel ceiling. The disturbance is again large enough to cause separation, but it occurs further downstream than on the bump. Here there are four upstream profiles showing strongly accelerated characteristics followed by a single profile downstream of the reattachment. The outer-law plot, figure (10.4.8) again shows this clearly, while both presentations emphasise the enormous change in profile shape which occurs in the interaction.



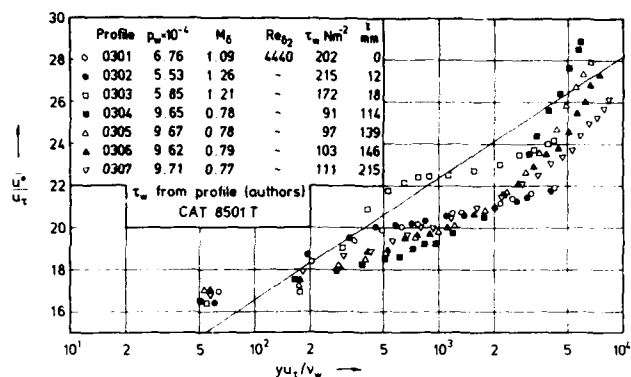


Fig. 10.4.6 Law of the wall for a compressible boundary layer with a quasi-normal shock interaction on the curved tunnel floor (adiabatic wall, origin not defined). Liu & Squire (1985).

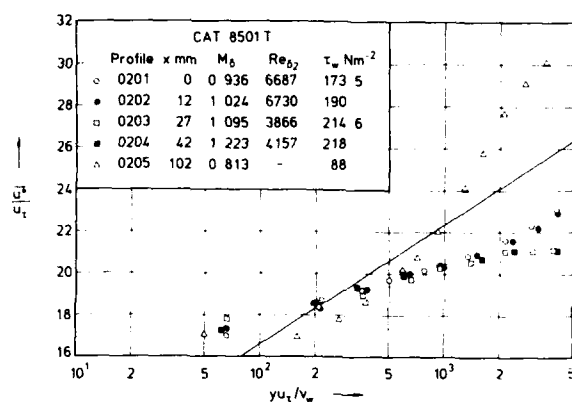


Fig. 10.4.7 Law of the wall for a compressible boundary layer with a quasi-normal shock interaction on the flat tunnel ceiling (origin not defined,  $\tau_w$  from profile (authors), adiabatic wall). Liu & Squire (1985).

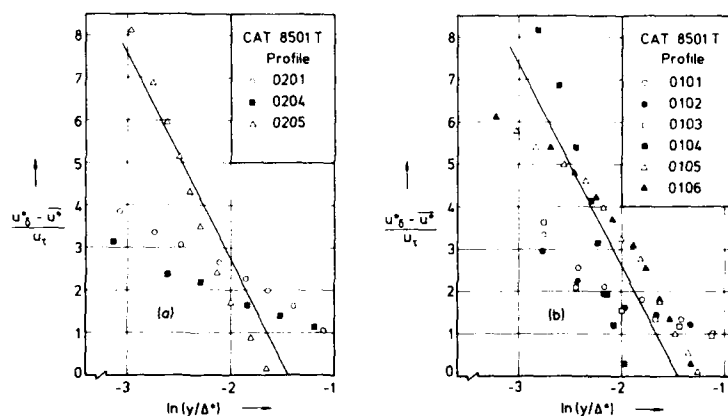


Fig. 10.4.8 Outer law for a compressible boundary layer with quasi-normal shock interaction on the flat tunnel ceiling. Liu & Squire (1985).

The data given in the entry for CAT8501T form only a small part of those measured. In all 68 configurations were tested, 53 with detailed wall pressure measurements and holograms giving the inviscid density distributions. Of these 16 included profile measurements (32 series in all).

Conclusions:

Compared with AG 223 and 263 the number of experiments with strong pressure gradients has risen considerably. Unfortunately most of the data sets are incomplete in that they are either functionally incomplete, requiring either pressure or density information, or lacking measurements of skin friction or both.

With the present experimental information it may be stated however, that the logarithmic law of the wall does not appear to hold in the region of the near-wall shock/ boundary layer interaction if no separation occurs and much further downstream of reattachment if the flow was separated.

## 11. REVIEW OF TURBULENCE DATA

### 11.1. General remarks

A discussion of turbulence data in compressible boundary layers may be found in Fernholz & Finley (1981) and in Détery & Marvin (1986), the latter authors dealing only with turbulence in shock/ boundary-layer interactions. Fernholz & Finley (1981) - henceforth denoted by AG 263 - have stated why investigations of the turbulence structure are necessary. We are interested in the

- changes of the turbulence structure due to compressibility
- changes due to pressure gradients
- changes due to shock/boundary-layer interaction (see ch. 9)
- relative order of magnitude of the Reynolds normal and shear-stress components.

AG 263 further provides surveys listing investigations in which measurements of single components of fluctuating quantities (table 3.1) and of Reynolds shear stresses (table 4.3.1) have been performed. These lists will be supplemented below.

Chapter 3 of AG 263 discusses in detail scaling velocities and scaling lengths so that a discussion will not be repeated here. Wherever possible we have used either inner-layer coordinates ( $y_+ / u_\tau$ ) as the characteristic length and the skin-friction velocity  $u_\tau$  as the characteristic velocity or outer-layer coordinates ( $(u_\tau^* y - \bar{u}^*) / u_\tau$  and  $\Delta^*$ , the Rotta-Clauser version for compressible boundary layers). In these cases - and they are the majority - where skin-friction data were not available or unreliable, velocities were made dimensionless by a constant reference velocity, either  $u_\tau$  or  $u_\delta$  in the upstream ZPG region, and plotted against  $y$ . As discussed in AG 263 we have rigidly excluded the boundary-layer thickness  $\delta$  as a scaling length, all the more since we deal mainly with shock/ boundary-layer interactions.

We begin our survey with table (11.1) listing investigations in which measurements of fluctuating components were performed. Their number is rather small but in comparison with AG 263 (table 3.1) there are several sequences of profiles showing the development of Reynolds normal and shear stresses upstream and downstream of a shock/boundary layer interaction along an adiabatic wall.

Table 11.1  
Number of profiles

Author	$M_{0\max}$	PG	$\langle u' \rangle$	$\langle v' \rangle$	$\langle u'v' \rangle$	$\alpha^\circ$	Anemometer wall geometry
Détery, Copy, Reisz (1980) CAT 8002T	1.4	QNS	28	28	28	—	LDA tunnel floor
Copy & Reisz (1980) CAT 8003T	$\approx 1.3$	QNS	22 20 17	22 20 17	22 20 17	— — —	LDA tunnel floor
Debiève (1983) CAT 8301T	$\approx 2.3$	CCF	2**)	—	—	6	CCHWA compression corner
Ardonceanu (1984) CAT 8402T	$\approx 2.3$	CCF	7 8 7	7 8 7	— — 7	8 13 18	LDV compression corner
Fernando & Smits (1986) CAT 8601T	2.9	APG	9 3*)	3*)	3*)	—	CTHWA tunnel floor
Dussauge & Gaviglio (1986) CAT 8602T	2.25	FPG	4	—	—	-12°	CCHWA expansion along tunnel floor
Spina & Smits (1986) CAT 8603T	2.9	ZPG	7 1*)	1*)	1*)	—	CTHWA tunnel floor
Jayaram et al. (1987) CAT 8702T	2.9	CCS	9 14	—	9 14	8 8	CTHW, curved compression surface
Donovan & Smits (1987) CAT 8702T	2.9	CCS	4*) 3	4*) —	4*) —	16 16	CTHWA, curved compression surface
Muck et al. (1983) CAT 8701T	2.8	CCF	23 13 11 3	— — — —	6 8 9 —	8 16 20 24	CTHWA compression corner

The profiles denoted by an asterisk were brought to our attention only after the figures for chapter 11 had been completed, those denoted by two asterisks are not available in tabulated form. They are therefore included on the tape and further details may be found in the following references:

For CAT8601T see Fernando (1988)

CAT8603T see Spina (1988)

CAT8702T see Donovan (1988).

There exist also two-point correlation data  $R_{uu}(r,0,0,r)$ ,  $R_{uu}(0,r,0,r)$ , and  $R_{uu}(0,0,r,r)$  available from Spina (ZPG) and Donovan (APG) as well as  $R_{uu}(0,r,0,r)$  and  $R_{uu}(0,0,r,r)$  for Fernando.

### 11.2. Reynolds normal stresses

The investigations of Spina & Smits (1986) in a ZPG and of Fernando & Smits (1986) in an APG boundary layer in the same test section with the same upstream conditions permit an interesting comparison between the distributions of the maxima of the Reynolds normal stresses as they develop in stream direction (fig. 11.2.1). For the ZPG case the  $u'^2$ -profiles display variations that lie within limits of less than  $\pm 10\%$  over the flow range under investigation. The adverse pressure gradient, however, leads to a rise of  $[(\bar{q} u'^2)_{\max}/\bar{q}_w u'^2]$  of about 300% at roughly the position of the maximum of the wall static pressure which itself increases by 50% compared with its level at the first measuring station. Since the ZPG upstream level for the APG flow is not given and since both flows have the same total pressure level it is reasonable to take the upstream ZPG flow as representative also for the APG case. The maximum static pressure rise is then 100%. Figure (11.2.2) shows distributions of the dimensionless Reynolds normal stress in inner-layer coordinates for the ZPG boundary layer. They display a "similar" behaviour which is not surprising since the Mach number remains constant and the Reynolds number hardly changes. Unfortunately the unavoidable sturdy design of the hot-wire probes does not permit an extension of the measurements closer to the wall so that the lowest value of  $y^+$  is only 1000. This is a very high value compared with measurements in subsonic boundary layers. This plot reveals an important deficiency of many fluctuation measurements presented in this chapter in that the maxima shown in the various diagrams are the maxima measured in the experiment but are often not the true maxima. These absolute maxima lie closer to the wall and are thus out of the range of present measuring techniques. This warning should be heeded when drawing conclusions from the fluctuation data. One example for this proposition are the data of Kussoy et al. (CAT7802S) which were measured at similar Mach and Reynolds numbers ( $M_0 \approx 2.3$  and  $Re_{\delta_2} \approx 16 \times 10^3$ ). They show qualitatively the same behaviour but extend closer to the wall, giving a value of  $(\bar{q} u'^2/\bar{q}_w u'^2) = 4$  at  $y^+$  of about 200 (AG 263, fig. 3.1.1). Figure (11.2.3) presents two of the profiles in outer-layer coordinates  $y/\Delta^*$  where  $\Delta^*$  is the transformed Rotta-Clausner length. In order to show the influence of the density distribution we have also plotted the specific Reynolds normal stress  $u'^2/u^2$  which is lower than the Reynolds normal stress. The trends of the ZPG data of Spina & Smits and of Kussoy et al. differ, however, as is shown more clearly when plotted in outer-layer coordinates (AG 263, fig. 3.1.3). The Kussoy-data display a plateau at about 2 in the range  $2 > y/\Delta^* > 0.5$  before they rise again towards the wall.

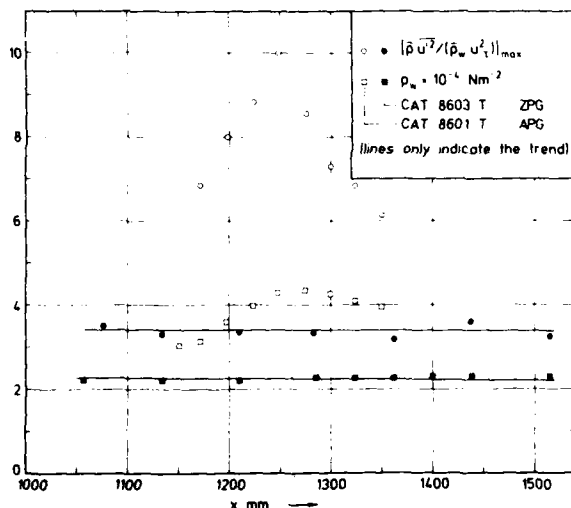


Fig. 11.2.1

Distributions of wall static pressure and of the maximum of the Reynolds normal stress in a ZPG and an APG compressible turbulent boundary layer ( $T_w/T_\infty = 1.10$ , (origin not defined). Spina & Smits (1986), Fernando & Smits (1986).

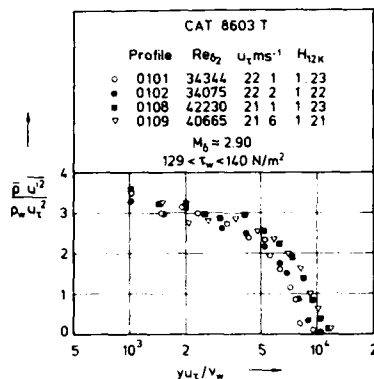


Fig. 11.2.2 Distributions of the Reynolds normal stress in a compressible boundary layer with zero pressure gradient ( $T_w/T_r = 1.10$ , origin not defined,  $c_f$  from Preston tube). Spina & Smits (1986). Inner scaling.

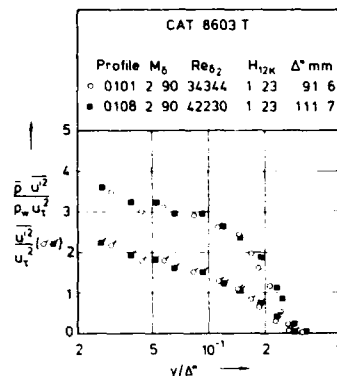


Fig. 11.2.3 Distributions of the Reynolds normal stress in a compressible boundary layer with zero pressure gradient ( $T_w/T_r = 1.10$ , origin not defined,  $c_f$  from Preston tube). Spina & Smits (1986). Outer scaling.

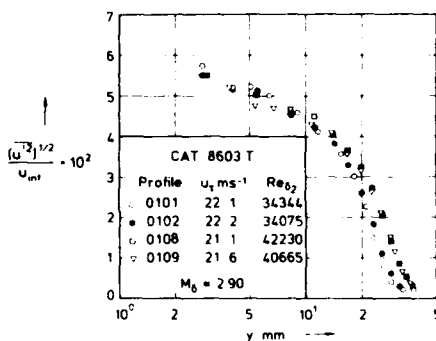


Fig. 11.2.4 Distributions of the mean square of the fluctuating velocity  $u'$  in a compressible boundary layer with zero pressure gradient ( $T_w/T_r = 1.10$ , origin not defined,  $u_{inf} = 569.4 \text{ ms}^{-1}$ ). Spina & Smits (1986).

There are several experiments where skin friction has not been determined and then it is impossible to present data in inner and outer layer coordinates. In order to set some sort of a standard for comparison, we present the ZPG data of Spina & Smits in a form (fig. 11.2.4) where  $(u'^2)^{1/2}$  is made dimensionless by an upstream undisturbed velocity  $u_{inf}$  plotted against the wall normal  $y$ . This procedure avoids an erroneous dimensionless presentation as a function of, for example,  $y/\delta$  since  $\delta$  cannot be defined properly in compressible boundary layers with pressure gradients. It also shows the streamwise development of the quantity in question in the boundary layer.

The discussion of the subsequent data of section 11 will be concerned with the behaviour of fluctuating quantities in APG compressible turbulent boundary layers. In AG 263 we remarked that such a discussion can only deal with case studies, and unfortunately, we have nothing to add to this comment today. It is appropriate therefore to quote the reasons given in § 3.2 of the earlier volume. "The two reasons for this are the scarcity of data and the lack of a suitable pressure-gradient parameter which could be used to compare data from different experiments. Such a pressure-gradient parameter would have to take account of boundary-layer flows with both streamwise and normal pressure gradients, and of flows where both pressure gradients are present." Such a pressure-gradient parameter does not yet exist, however, and none of the parameters which can be found in the literature has much meaning in the flows discussed below.

We continue the discussion of the behaviour of Reynolds normal stresses with the APG boundary layer of Fernando & Smits (1986), CAT 8601T, with the flat wall static-pressure distribution as given in figure (11.2.1). Since the first two profiles in figure (11.2.6) are already affected by the pressure rise, profile (0102) has values which are about twice as high as those in the ZPG case (fig. 11.2.2), and the largest values of  $\bar{\rho} u'^2 / \rho_w u_\tau^2$  occur close to the maximum of the pressure gradient, and upstream of the maximum wall pressure. This agrees with the comparable APG boundary layer of Kussoy et al. (1978), CAT 7802S, in figure (3.2.1) of AG 263, although there the maximum value of  $(\bar{\rho} u'^2 / \rho_w u_\tau^2)$  is about 11 compared with 9 in figure (11.2.5). For a comparison of the same profiles in outer-layer coordinates the reader is referred to figure (11.2.6) and (3.2.3) in AG 263).

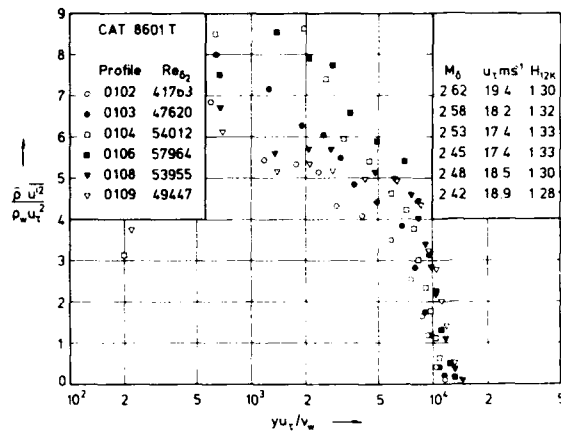


Fig. 11.2.5

Distributions of the Reynolds normal stress in a compressible boundary layer with an adverse pressure gradient ( $T_w/T_r \approx 1.10$ , origin not defined,  $c_f$  from Preston tube). Fernando & Smits (1986).

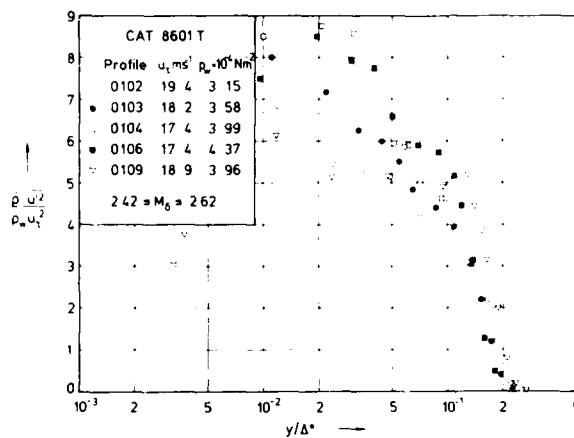


Fig. 11.2.6

Distributions of the Reynolds normal stress in a compressible boundary layer with an adverse pressure gradient ( $T_w/T_r \approx 1.10$ , origin not defined,  $c_f$  from Preston tube). Fernando & Smits (1986).

Figure (11.2.7) shows the absolute change in  $(u'^2)^{1/2}$  caused by the rise in pressure and should be compared with the ZPG data in fig. (11.2.4). The use of a common scaling quantity makes it evident that the rise is surprisingly small.

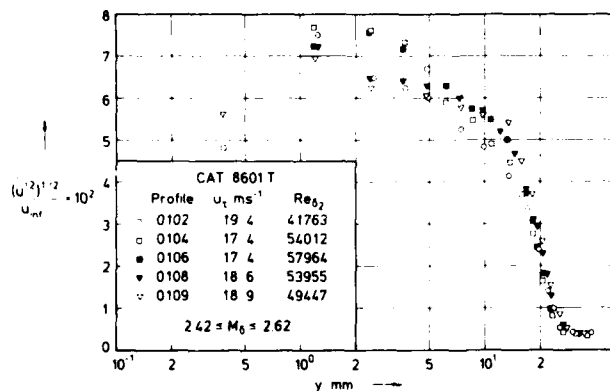


Fig. 11.2.7

Distributions of the root mean square of the fluctuating velocity  $u'$  in a compressible boundary layer with an adverse pressure gradient ( $T_w/T_r \approx 1.10$ , origin not defined,  $u_{inf} = 569.4 \text{ m}^s$ ). Fernando & Smits (1986).

The development of the few FPG profiles of  $\overline{u'^2}$  measured by Dussauge & Gaviglio (1986) is shown in figure (11.2.8). Compared with figure (11.2.3) the ZPG profile (0108) reaches the same peak value,  $(\overline{u'^2}/u_\tau^2)_{\max} = 2.2$ . The remaining three distributions display much scatter but show distinctly the damping influence of the FPG on the turbulence structure. There are no comparable measurements except three profiles measured by Kussoy et al. (CAT7802S) in a boundary layer with flow acceleration downstream of a severe pressure rise.

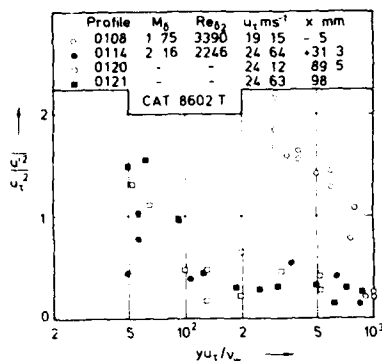


Fig. 11.2.8 Distributions of the specific Reynolds normal stress in a compressible boundary layer with a rapid expansion. (origin not defined, adiabatic wall,  $u_\tau$  from Chew (1978)). Dussauge & Gaviglio (1986).

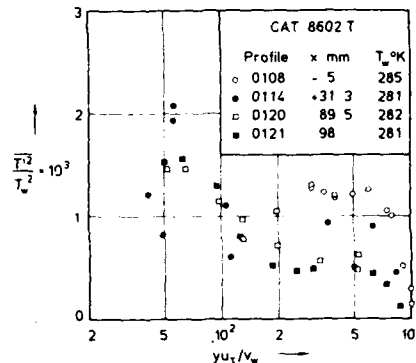


Fig. 11.2.9 Distributions of the intensity of the temperature fluctuation in a compressible boundary layer with a rapid expansion. (origin not defined, adiabatic wall). Dussauge & Gaviglio (1986).

#### Intensity of the temperature fluctuations

These are the only measurements known to us where distributions of the temperature fluctuation intensity in a favourable pressure gradient have been obtained (fig. 11.2.9). The ZPG profile (0108) may be compared with that measured by Kistler (58030101 fig. 3.4.2, AG 263) which shows a qualitatively similar behaviour. Compared with the ZPG profile we notice the same damping influence as in figure (11.2.8).

#### Curved ramp flows

As in chapter 10 we discuss first the influence of the curved ramp on the turbulence field before we discuss shock/boundary-layer interactions. The turbulence measurements were performed by Jayaram et al. (1987) using the respective mean flow profiles of Taylor (1984) (cf. section (10.2) and table (10.2.1)). The respective distributions of static pressure and wall shear stress in streamwise direction may be found in figure (10.2.1). A comparison with the APG flow of Fernando & Smits (fig. 11.2.1) reveals that this flow and the first two compression-surface flows (870201/03T) and (870202/04T) reach about the same overall pressure level only at different downstream positions. These three flows may therefore be interesting test cases for numerical computations. The maximum values of the specific Reynolds normal stress were made dimensionless by the ZPG upstream value of the skin-friction velocity  $u_{\tau ref}$  and plotted against  $x$  in figure (11.2.10). The distributions of  $(\overline{u'^2})_{\max}/u_{\tau ref}^2$  reflect the influence of the pressure distribution in the stream direction. There is little difference in the value of the "absolute" maximum nor in its  $x$ -position for cases 860101T and 870203T. Since the curvature of case 870204T is smaller than that of 870203T, the absolute maximum is reached further downstream. In none of these cases separation was observed.

Profiles 0303 to 0311 (fig. 11.2.11) show the development of  $(\overline{\rho} \overline{u'^2})/\rho_w u_\tau^2$  along one of the ramp flows. Station 03 is upstream of the start of the APG and at 05 the compression has yet to spread significantly up into the boundary layer, so the profiles are similar to those in figure (11.2.2). At 06 the compression has reached about  $\delta/2$ , and the profile is showing an APG reaction. The curvature ceases at  $x = 35.4$  mm but the compression continues to propagate in the outer part of the boundary layer, finally ceasing before 09. The turbulence levels continue to increase until a fall appears within the layer for the last station 0311. The maximum value of  $(\overline{\rho} \overline{u'^2})/\rho_w u_\tau^2$  is approximately 8 for profile 0309, about three times the "measured" ZPG maximum value and about the same as for the reflected wave case presented in figure (11.2.5). Again we note that the minimum value of  $y^+$  is about 1400 which is very high. Without taking into account the variation of the density across the boundary layer  $(\overline{u'^2}/u_\tau^2)$  increases by a factor of 4 (fig. 11.2.12). Such a plot is needed for comparison with measurements, e.g. obtained by LDA, where no density distributions were obtained.

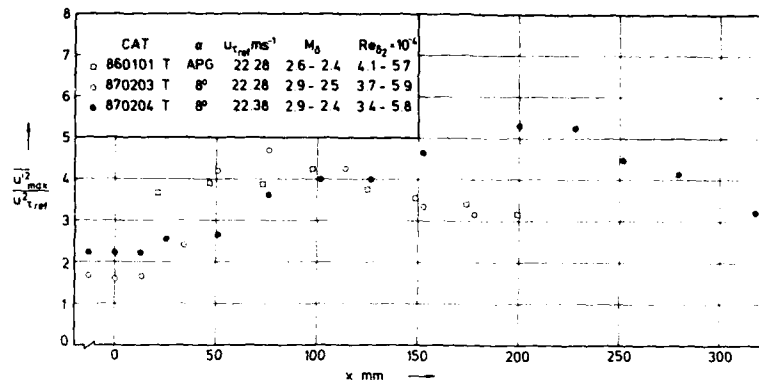


Fig. 11.2.10 Distributions of the maxima of the specific Reynolds normal stress in a compressible boundary layer in an APG and along two concave compression surfaces with a recovery section ( $T_w/T_r \approx 1.10$ , origin not defined). Fernando & Smits (1986), Jayaram et al. (1987).

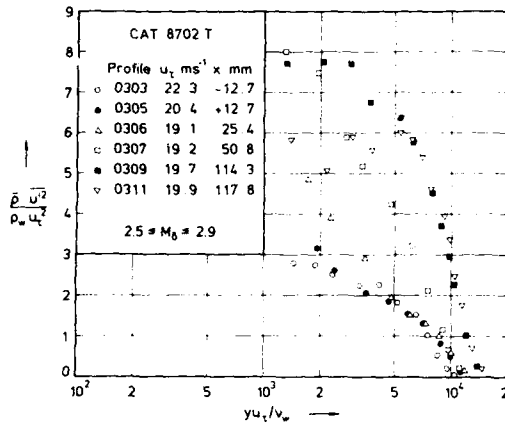


Fig. 11.2.11

Distributions of the Reynolds normal stress in a compressible boundary layer along a concave compression surface with a recovery section ( $T_w/T_r \approx 1.10$ , origin not defined,  $c_f$  from Preston tube). Jayaram et al. (1987).

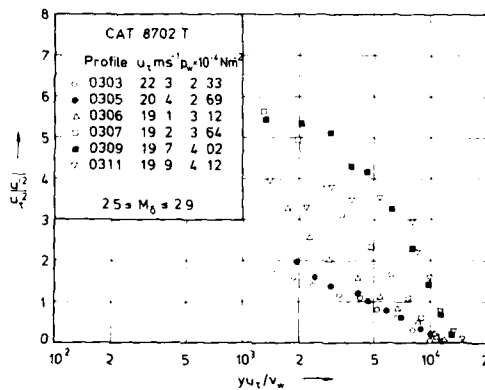


Fig. 11.2.12

Distributions of the specific Reynolds normal stress in a compressible boundary layer along a concave compression surface with a recovery section ( $T_w/T_r \approx 1.10$ , origin not defined,  $c_f$  from Preston tube). Jayaram et al. (1987).



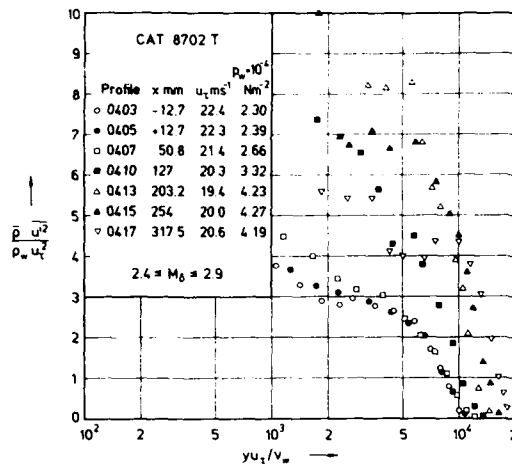


Fig. 11.2.13 Distributions of the Reynolds normal stress in a compressible boundary layer along a concave compression surface with a recovery section ( $T_w/T_r \approx 1.10$ , origin not defined). Jayaram et al. (1987).

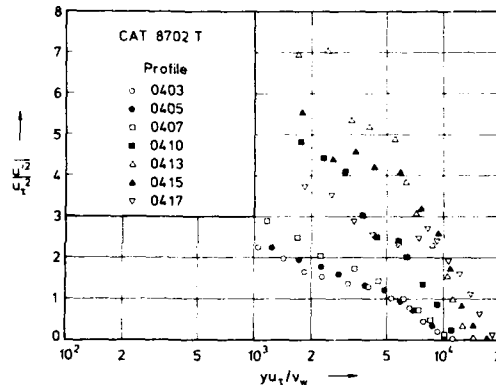


Fig. 11.2.14

Distributions of the specific Reynolds normal stress in a compressible boundary layer along a concave compression surface with a recovery section ( $T_w/T_r \approx 1.10$ , origin not defined). Jayaram et al. (1987).

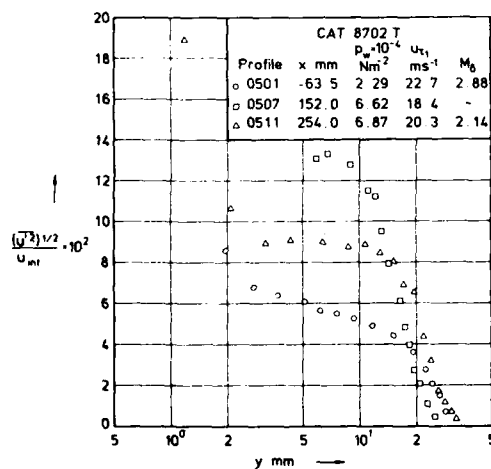


Fig. 11.2.15 Distributions of the root mean square of the fluctuating velocity  $u'$  in a compressible boundary layer along a concave compression surface with a recovery section ( $T_w/T_r \approx 1.10$ , origin not defined,  $u_{inf} = 519.6$  ms<sup>-1</sup>). Donovan & Smits (1987).

On the less acutely curved ramp (870202/04T, mean flow 840102T) the changes occur more gradually, the curvature ending between stations 10 and 13. The peak values are about the same (compare fig. 11.2.11 and fig. 11.2.13), and again the start of the relaxation can be seen in the last profiles. Figure (11.2.14) shows the distributions of  $(u'^2/u_\infty^2)$  for comparison. It would be important to know the distributions of the other two components  $\bar{v}^2$  and  $\bar{w}^2$  in order to prove the expected large anisotropy of the turbulence structure. The latter two components were not measured in this experiment but the data of Kussoy et al. (1978) (AG 263, figs. 3.2.4 and 3.2.5) allow an estimate. The ratio between the maximum values of the three components  $\bar{u}^2$ ,  $\bar{v}^2$ , and  $\bar{w}^2$  shown there is about 14:4:3 (see also ch. 5 for possible effects of bandwidth).

Larger pressure changes were generated in the 16° curved-ramp flows where some turbulence data were measured by Donovan & Smits (1987). For a comparison which avoids the measured skin-friction values,  $u'^2$  is plotted against  $y$  in figure (11.2.15). Comparing (11.2.15) with (11.2.7) shows that the level of  $(u'^2)^{1/2}$  increases by at least 50% if the angle of the compression corner is changed from 8° to 16°, the APG reflected wave case and the 8° curved compression surface being little different from each other. The differences between the three profiles are still more distinct if  $\bar{u}^2$  is plotted in inner-law coordinates (fig. 11.2.16) but here we cannot exclude problems with the measurement of  $u_t$ .

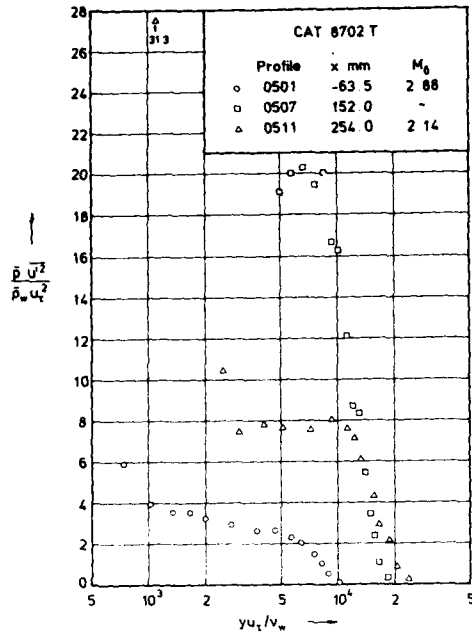


Fig. 11.2.16

Distributions of the Reynolds normal stress in a compressible boundary layer along a concave compression surface with a recovery section ( $T_w/T_r \approx 1.10$ , origin not defined,  $c_f$  from Preston tube). Jayaram et al. (1987).

#### Shock/boundary layer interactions

##### a) Compression corner flows

As was indicated in table (11.1) there are three experimental investigations of the turbulence structure in compressible boundary layers along compression corners: Debiève (1983), Ardonneau (1984), and Muck et al. (1984, 1987). The turbulence data of Debiève is restricted in quantity, and we present only copies of two figures from the source paper in the entry (CAT 8301 T).

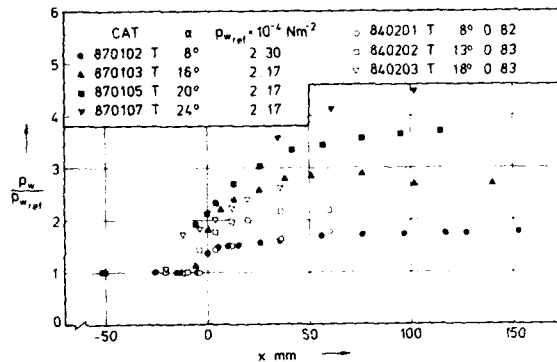


Fig. 11.2.17 Wall static pressure distributions in compression-corner flows (nearly adiabatic wall, origin not defined).

We begin the discussion of the cases investigated by Ardonneau and the Princeton group by presenting their distributions of the wall static pressure (fig. 11.2.17) with  $x = 0$  as the start of the ramp. Figures (11.2.18 and 11.2.19) show the development of the maxima of the specific Reynolds normal stresses. The values of  $u'^2_{max}$  were made dimensionless by  $u_{\tau,ref}^2$  which is the measured (Princeton) or calculated (Ardonneau) skin-friction velocity upstream of the shock interaction. For the two 8° ramps there appears to be a long plateau - despite some scatter in the data - after the almost immediate sharp increase at the corner. Lines were inserted only to indicate the trend. Since the Mach-number range of the two experiments is approximately the same and  $u_{\tau,ref}$  differs only by 10%, we have no explanation for the discrepancy

between the peak levels of  $(u'^2)_{max}/u_{\tau,ref}^2$  which is 60%. It is unlikely that this is due to a Reynolds-number effect - the Reynolds numbers differ by about one order of magnitude - but more probably due to the different measuring techniques LDA and hot-wire anemometry. These discrepancies continue to appear in the data of the 13° (840202T) and the 16° (870103T) compression-corner flows (fig. 11.2.19). At these higher deflection angles the trend of the distributions is different from that of the smaller deflections - (8°) - in that  $((u'^2)_{max}/u_{\tau,ref}^2)$  decreases more or less linearly downstream of the peak value at the corner. Again the lines in figure (11.2.19) serve for clarification only.

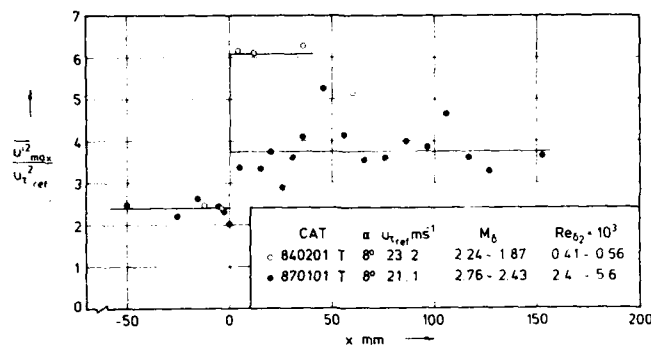


Fig. 11.2.18 Distributions of the maxima of the specific Reynolds normal stress in compressible boundary layers along two compression surfaces (adiabatic wall, origin not defined).

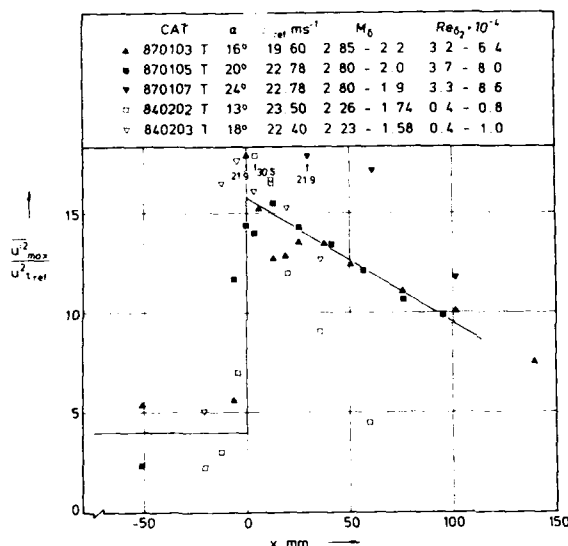


Fig. 11.2.19

Distributions of the maxima of the specific Reynolds normal stress in compressible boundary layers along 5 compression surfaces (adiabatic wall, origin not defined).

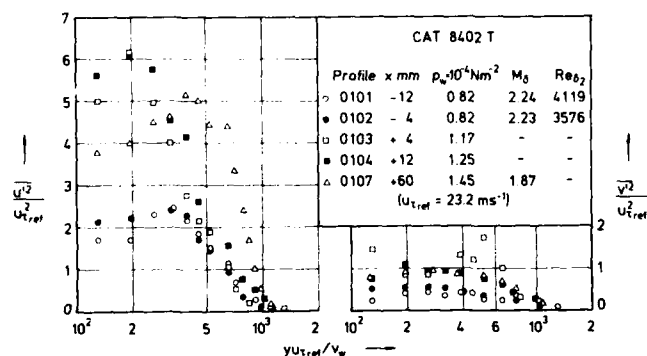


Fig. 11.2.20 Distributions of the specific Reynolds normal stress in a compressible boundary layer along a compression corner (8°), adiabatic wall, origin not defined). Ardonceau (1984).

Ardonceau has measured both  $\overline{u'^2}$  and  $\overline{v'^2}$  and they are plotted for the 8° and the 18° case in figures (11.2.20 and 11.2.21). For this experiment we have no wall shear-stress measurements and therefore we have made the data dimensionless by using a reference skin-friction velocity, calculated according to Fernholz (1971) at a presumably ZPG position upstream of the corner. This allows at least a qualitative description of the data distributions. The obvious observation is the anisotropy between the two specific Reynolds normal stresses which is about 4:1 in both ramp flows, a much greater ratio than could be accounted for by any error resulting from the fact that the axes for the traverse are aligned with the tunnel axis and not the local surface of the ramp.

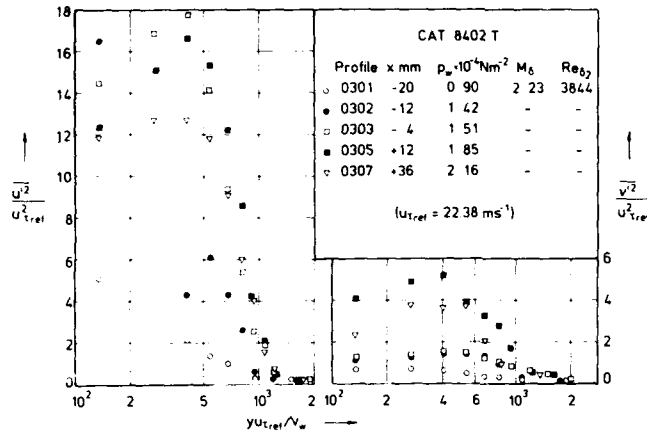


Fig. 11.2.21

Distributions of the specific Reynolds normal stress in a compressible boundary layer along a compression corner (18°), (adiabatic wall, origin not defined). Ardouneau (1984).

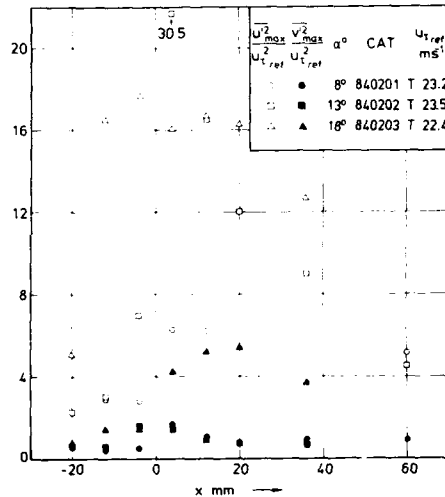


Figure (11.2.22) displays the development of the maxima of the two specific Reynolds normal stress components  $u'^2$  and  $v'^2$  for the 8°, 13° and 18° ramp flows. For the 8° case the absolute peaks for  $u'^2_{max}$  and  $v'^2_{max}$  occur at about  $x = +4 \text{ mm}$  with  $u'^2_{max}$  forming a long plateau up to about 40 mm and  $v'^2_{max}$  falling fast to its initial value upstream of the shock. The 13° ramp flow shows the peak value for  $v'^2_{max}$  upstream of the corner ( $x = -4 \text{ mm}$ ) and for  $u'^2_{max}$  at  $x = +36 \text{ mm}$ . Finally, for the 18° ramp the peak for  $v'^2_{max}$  is at  $x = +20 \text{ mm}$  and for  $u'^2_{max}$  upstream of the corner, indicating a strong upstream effect of the shock, possibly via the separation region. Some part of this may be a result of shock oscillation. As in the 8° case,  $u'^2_{max}$  forms a plateau, though shorter, for the 18° ramp flow. In summary (cf. figures 11.2.18, 11.2.19 and 11.2.22), both the shape of the  $u'^2_{max}$  and  $v'^2_{max}$  distributions and the magnitude and position of their absolute maximum are important for an interpretation of shock/boundary-layer interactions.

Fig. 11.2.22 Development of the maxima of specific Reynolds normal stresses in compressible boundary layers along 3 compression corners. Ardouneau (1984).

In order to complete the documentation of the Reynolds normal stress measurements, figures (11.2.23 to 11.2.25) display the Princeton data of  $\bar{q} u'^2$  for the 8°, 16° and 20° ramp flows. They are made dimensionless by the respective measured skin-friction velocities for which we have no error bounds (cf. chapter 9) and should thus only be regarded as qualitative. Note the change from linear to logarithmic scale for the ordinate in figures (11.2.23 and 24). The three cases have in common that the absolute maxima are upstream of the pressure maximum - as in all other flows with an APG - and that the position  $y'^2_{max}$  of the profile peak value moves away from the wall as long as the pressure is rising. The enormous increase of the absolute maximum rising from the 8° to the 20° case by a factor of about 30 is also due to the fall of  $u_\tau$ . Therefore plots of  $(u'^2/u_{trf}^2)$  as in figures (11.2.18, 19 and 22) give a more realistic picture of the influence of the shock structure on the turbulence. There are no  $v'^2$ -profiles provided by the Princeton group and  $\bar{q} u'v'$ -profiles will be discussed below.

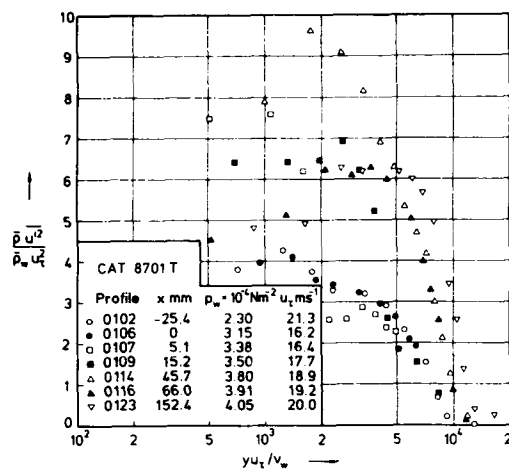


Fig. 11.2.23

Distributions of the Reynolds normal stress in a compressible boundary layer along a compression corner (8°). ( $T_w/T_r \approx 1.10$ , origin not defined),  $c_f$  from Preston tube). Muck et al. (1987).

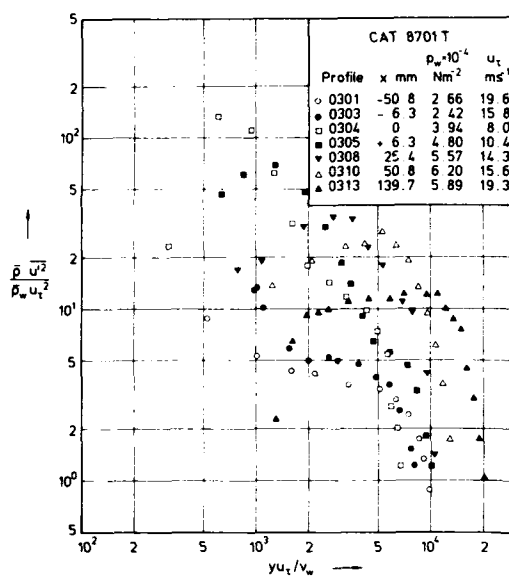


Fig. 11.2.24 Distributions of the Reynolds normal stress in a compressible boundary layer along a compression corner (16°). ( $T_w/T_r \approx 1.10$ , origin not defined,  $c_f$  from Preston tube). Muck et al. (1987).

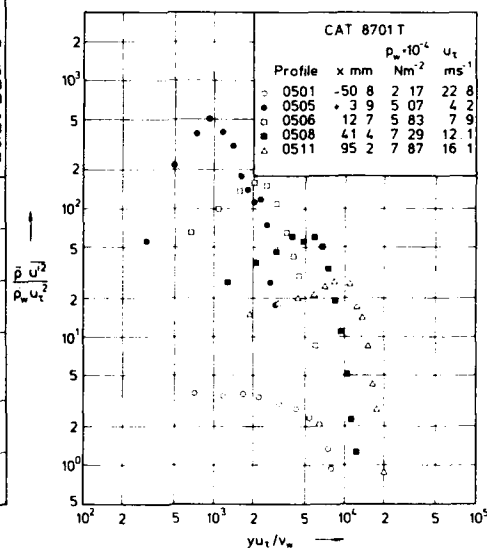


Fig. 11.2.25 Distributions of the Reynolds normal stress in a compressible boundary layer along a compression corner (20°). ( $T_w/T_r \approx 1.10$ , origin not defined,  $c_f$  from Preston tube). Muck et al. (1987).

## b) Quasi-normal shock interactions

When it comes to turbulence measurements only two of the three experimental investigations mentioned in chapter 10.4 remain. The ONERA group (cf. table 11.1) measured  $u'$ ,  $v'$  and  $u'v'$  using laser-Doppler anemometry. Neither mean density profiles nor skin-friction data were given. There are four cases altogether, Détery et al. (CAT 8002T) one and Copy & Reisz (CAT 8003T) three. Two cases of the latter investigation will be discussed in more detail.

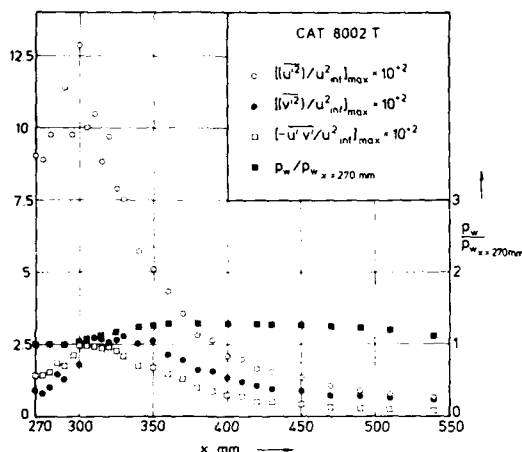


Fig. 11.2.26 Development of the wall static pressure and of the maxima of the specific Reynolds normal and shear stresses of a compressible boundary layer with a shock interaction (adiabatic wall, origin not defined,  $u_{inf} = 296.8 \text{ ms}^{-1}$ ). Détery et al. (1980).

Figure (11.2.26) presents the distributions of the wall static pressure,  $(u'^2)_{max}$ ,  $(v'^2)_{max}$ , and  $|-u'v'|_{max}$  in x-direction, the latter three quantities made dimensionless by a common value of  $u_{inf}$  as no upstream value of  $u_{inf}$  could be calculated due to incomplete information. Since three components of the specific Reynolds stress tensor were available, we have included  $u'v'$  in the following discussion. Apart from the rather mild static pressure rise in stream direction, which is deceptive as the greater part of the pressure change has taken place upstream (see entry CAT 8002T), one should notice the anisotropy of the turbulence field resulting in a maximum value of the ratio  $(u'^2/v'^2)_{max}$  of about 4. There is little difference in the value of the peaks of  $(v'^2)_{max}$  and  $|-u'v'|_{max}$  but  $|-u'v'|_{max}$  decays faster in streamwise direction, having a value of about 60% of that of  $(v'^2)_{max}$ . In the notation for x used here, the first leg of the shock is at about 260 mm from the start of the bump ( $x = 0$ ), the second leg at about 286 mm, and reattachment at about  $x = 325 \text{ mm}$ . At this latter position we notice the sudden fall of  $u'^2$  and the slower decrease of  $|-u'v'|$ .

The next two cases (Copy & Reisz, 1980) differ in that there was no separation for series 01

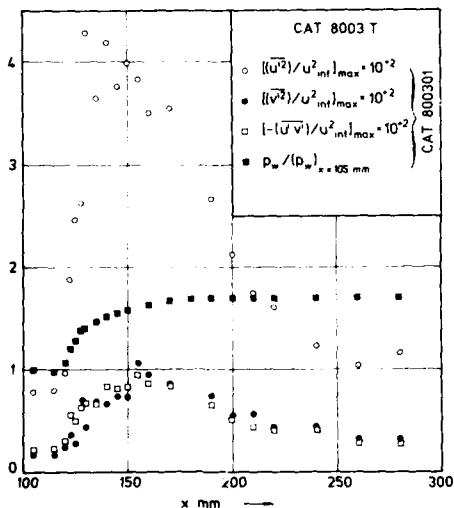


Fig. 11.2.27 Development of the wall static pressure and of the maxima of the specific Reynolds normal and shear stresses of a compressible boundary layer with a shock interaction (adiabatic wall, origin not defined,  $u_{inf} = 255.2 \text{ ms}$ ). Copy & Reisz (1980).

and 02 (the latter is not discussed here) but for series 03 over, approximately, the range  $195 < x < 240 \text{ mm}$  (authors). Figure (11.2.27) presents the equivalent quantities to those in fig. (11.2.26). Measurements started, however, upstream of the wall pressure minimum, thus displaying a more realistic wall-pressure distribution. The authors give the shock position at  $x = 128 \text{ mm}$  but the shock influence begins to show at about  $x = 120 \text{ mm}$  with the sharp increase of all turbulence quantities, especially of  $u'^2$ , which reaches its absolute peak at  $x = 130 \text{ mm}$  with an increase of more than a factor 5. The ratio of the two Reynolds normal stresses is again about 4 with the absolute peak of  $v'^2$  downstream ( $x = 155 \text{ mm}$ ) of that of  $u'^2$ . We have no explanation for the almost identical values of  $(v'^2)_{max}$  and  $|-u'v'|_{max}$  in series 01 and 03 (fig. 11.2.28) which differ from the distributions shown in fig. (11.2.26). For series 03 (fig. 11.2.28) the pressure increase is larger than in 01, resulting in a reverse-flow region and in about 20% higher values of  $(u'^2)_{max}$ . Other flow features are similar to those of series 01.

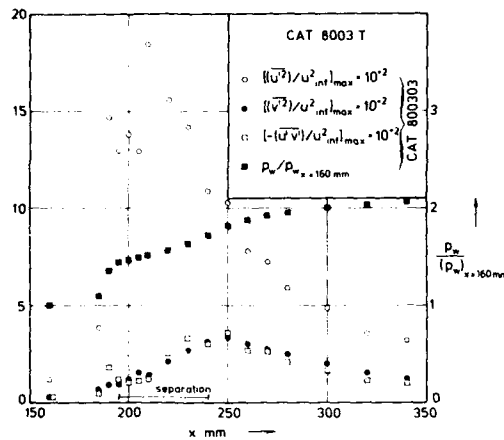


Fig. 11.2.28

Development of the wall static pressure and of the maxima of the specific Reynolds normal and shear stresses of a compressible boundary layer with shock interaction (adiabatic wall, origin not defined,  $u_{inf} = 257.9 \text{ ms}^{-1}$ ). Copy & Reisz (1980).

### 11.3. Reynolds shear stress

Table 11.1 contains a list of the available Reynolds shear-stress measurements. There are no data for the ZPG or the APG reflected wave case (they only available on the data tape) and so we begin our discussion with the data along the two  $8^\circ$  curved compression surfaces of Jayaram et al. (CAT 8702T).

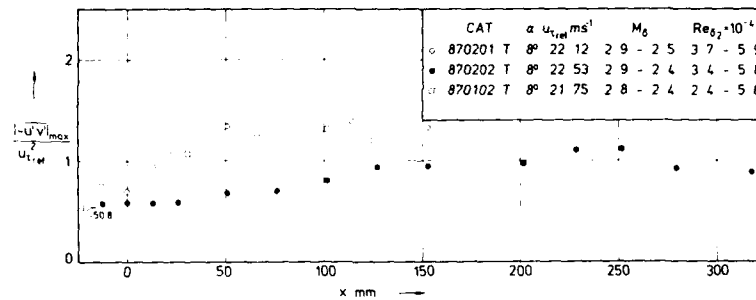


Fig. 11.3.1 Distributions of the maxima of the specific Reynolds shear stress in a compressible boundary layer along 3 compression surfaces with different concave curvature at the beginning ( $T_w/T_r \approx 1.10$ , origin not defined). Jayaram et al. (1987), Muck et al. (1987).

Figure (11.3.1) presents the distributions of the maximum specific Reynolds shear-stress value made dimensionless by the skin-friction velocity in the ZPG region upstream of the compression surface. The latter differ by the radius of curvature (for the geometry see CAT8401T), and the flow with the smaller radius of curvature followed by a flat section shows the sharper rise in  $|-(u'v')|_{max}$ . For a comparison we have plotted also the data for the  $8^\circ$  corner flow of Muck et al. (CAT 870104T). The increase of the specific maximum Reynolds shear stress follows closely that of the flow with the small radius of curvature indicating that the rate of curvature does not affect the flow much in this case. Figures (11.3.2 to 11.3.5) display the distributions of the Reynolds shear stress and  $|-(u'v')|$  without the influence of the density for the two  $8^\circ$  compression surfaces. Again  $u_r$  was measured by the Preston-tube method, the deficiencies of which are discussed in chapter 9.2.4. We find a behaviour very similar to incompressible APG boundary layers with an increase of  $|-(u'v')|$  and a shift of the profile maximum towards the edge of the boundary layer in the region with rising wall static pressure (e.g. figure 11.3.2). If the pressure falls, the magnitude of the maximum decreases and its position moves away from the boundary layer edge (fig. 11.3.4). As we have seen in figure (11.3.1) the absolute peak is higher for the faster pressure rise of case 1.

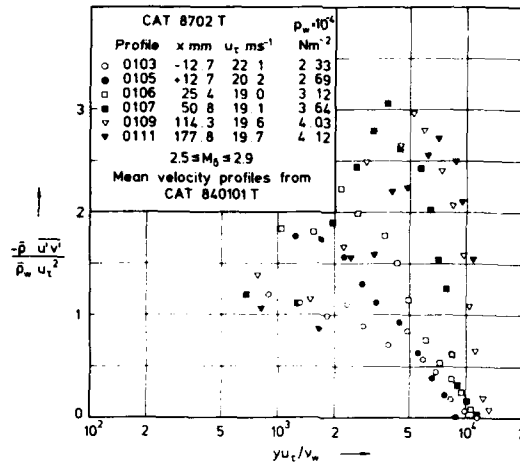


Fig. 11.3.2

Distributions of the Reynolds shear stress in a compressible boundary layer along a concave compression surface with a recovery section. (T<sub>w</sub>/T<sub>r</sub> ≈ 1.10, origin not defined, c<sub>f</sub> from Preston tube.) Jayaram et al. (1987).

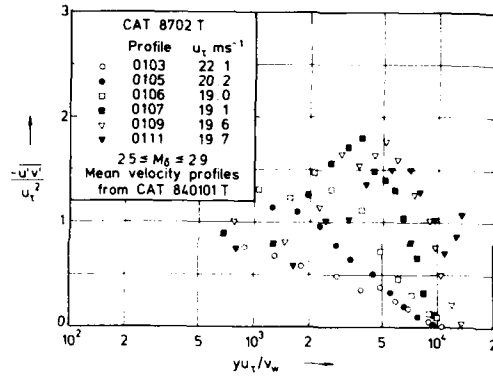


Fig. 11.3.3

Distributions of the specific Reynolds shear stress in a compressible boundary layer along a concave compression surface with a recovery section. (T<sub>w</sub>/T<sub>r</sub> ≈ 1.10, origin not defined, c<sub>f</sub> from Preston tube.) Jayaram et al. (1987).

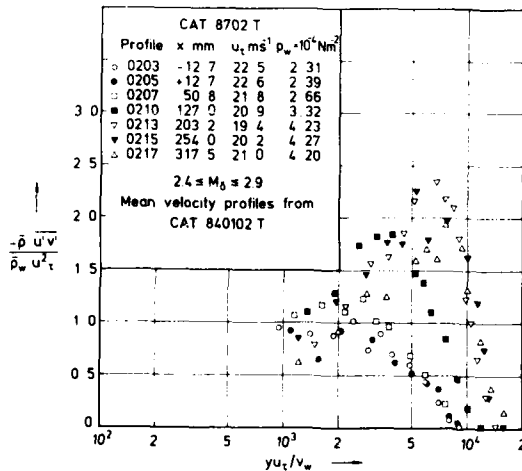


Fig. 11.3.4

Distributions of the Reynolds shear stress in a compressible boundary layer along a concave compression surface with a recovery section. (T<sub>w</sub>/T<sub>r</sub> ≈ 1.10, origin not defined, c<sub>f</sub> from Preston tube.) Jayaram et al. (1987).



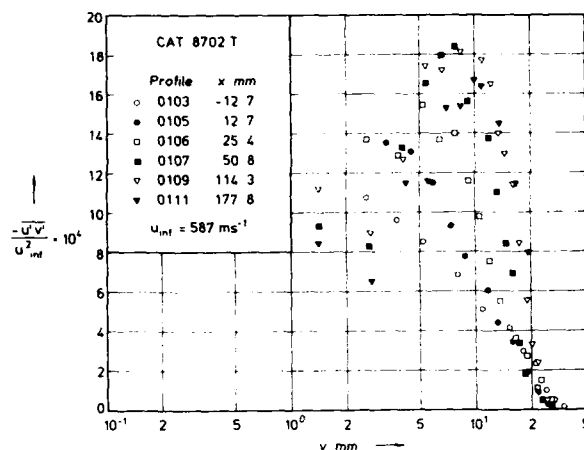


Fig. 11.3.5

Distributions of the specific Reynolds shear stress in a compressible boundary layer along a concave compression surface with a recovery section. ( $T_w/T_r \approx 1.10$ , origin not defined.) Jayaram et al. (1987).

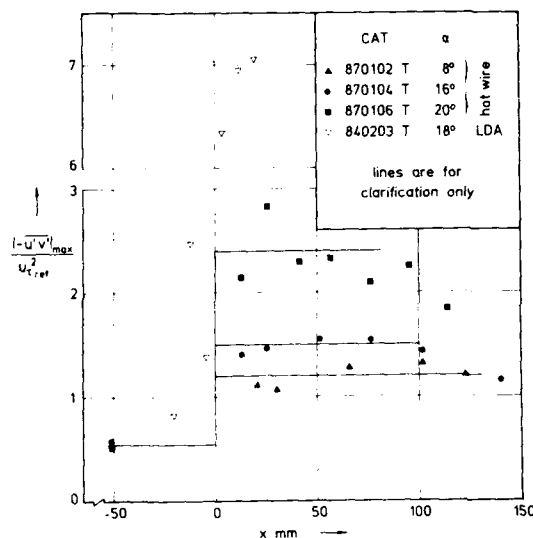


Fig. 11.3.6 Distributions of the maxima of the specific Reynolds shear stress in compressible boundary layers along 4 compression surfaces (adiabatic wall, origin not defined). Muck et al. (1987), Ardonneau (1984).

Figure (11.3.6) displays the maximum of the specific Reynolds shear stress against streamwise distance  $x$  (corner at  $x = 0$ ) for four compression corner flows and should be seen in connection with figure (11.2.19) for the specific Reynolds normal stress  $(u'^2)_{max}$ . With the exception of Ardonneau's data which only show the sharp increase due to the shock system, the other data (Princeton's) indicate a jump, a plateau, and a decrease, with peak values rising with the ramp angle. This type of distribution differs from that of the  $u'^2$ -data which decrease about linearly downstream of the absolute maximum (fig. 11.2.19). Such a behaviour could indicate that  $u'v'$ -containing structures change more slowly for flows at ramp angles larger than  $8^\circ$ . For the  $8^\circ$  degree case  $u'v'$  and  $u'^2$  (fig. 11.2.18) show a qualitatively similar behaviour. We have again no explanation why data for comparable ramp angles differ between Ardonneau and Muck et al. and guess that the discrepancies, especially near the corner, are due to the different experimental techniques. Figures (11.3.7 to 11.3.9) present the dimensionless Reynolds shear stress for the  $8^\circ$ ,  $16^\circ$  and  $20^\circ$  compression corner flows, respectively. Note that both  $(\bar{q}_w u_\tau^2)$  and  $|\bar{q}_w u'v'|$  change with  $x$ .

For the quasi-normal shock interaction there are four cases where  $|\bar{u'v'}|$  was measured and for which the distribution of  $|\bar{u'v'}|_{max}/u_\tau^2$  has been shown in figure (11.2.26). Figures (11.3.10) to (11.3.12) display the specific Reynolds shear stress for series 01 of Déjery et al. (CAT 8002T) and for series 01 and 03 of Copy & Reisz (CAT 8003T). These distributions are detailed and provide a sequence of so many profiles that they are especially suited for a comparison with numerical calculations.

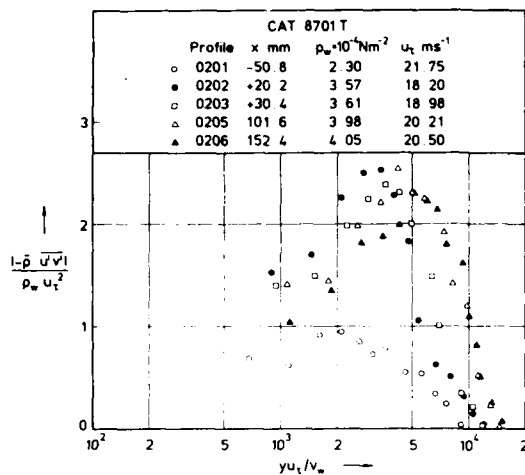


Fig. 11.3.7

Distributions of the Reynolds shear stress in a compressible boundary layer along a compression corner ( $8^\circ$ ). ( $T_w/T_r \approx 1.10$ , origin not defined,  $c_f$  from Preston tube.) Muck et al. (1987).

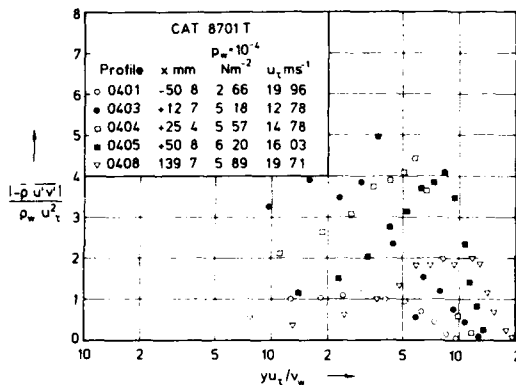


Fig. 11.3.8

Distributions of the Reynolds shear stress in a compressible boundary layer along a compression corner ( $16^\circ$ ). ( $T_w/T_r \approx 1.10$ , origin not defined,  $c_f$  from Preston tube.) Muck et al. (1987).

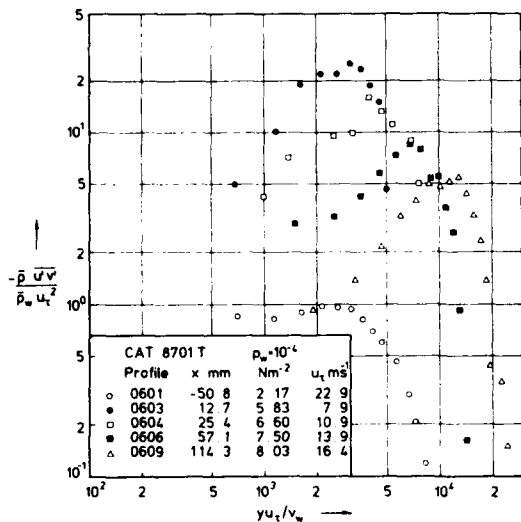


Fig. 11.3.9

Distributions of the Reynolds shear stress in a compressible boundary layer along a compression corner ( $20^\circ$ ). ( $T_w/T_r \approx 1.10$ , origin not defined,  $c_f$  from Preston tube.) Muck et al. (1987).

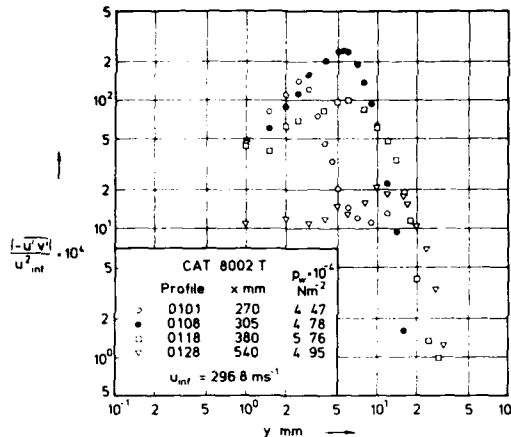


Fig. 11.3.10 Distributions of the specific Reynolds shear stress in a compressible boundary layer with a shock interaction (adiabatic wall, origin not defined). Détery et al. (1980).

Figure (11.3.10) presents four profiles, the first (0101) and the last (0128) measured, the profile with the absolute peak of  $|-u'v'|$  (0108), and one in the region where the absolute peak decreases but where its position still moves towards the edge of the boundary layer. The reader should remember that the first profiles in each of the subsequent figures is close to or just downstream of the shock structure, a fact which results in a very high absolute peak value (note the logarithmic scale of the ordinate). A more detailed sequence of profiles is shown in figure (11.3.11) for the case with the mildest shock interaction out of the 4 ONERA experiments. The trend of the data is very much the same as in (11.3.10) except that the absolute peak values are lower. Again it is interesting to note the plateau-like shape of the last measured profile (80030122) and to compare it with (80020128) in fig. (11.3.10). Furthermore it is certainly worth noting that the  $|-u'v'|$ -profiles extend down to 0.2 mm near to the wall which is extraordinarily low.

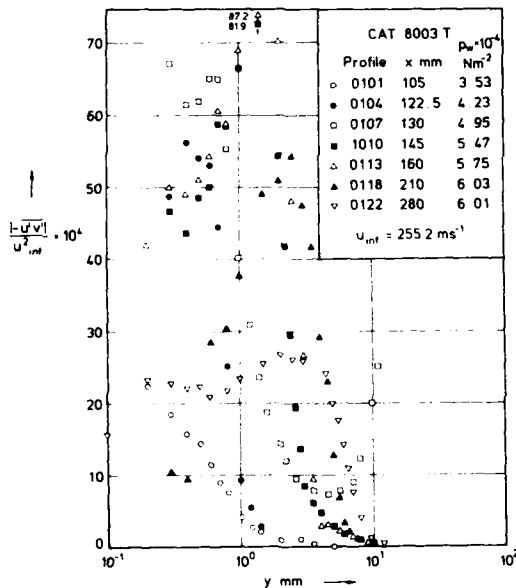


Fig. 11.3.11

Distributions of the specific Reynolds shear stress in a compressible boundary layer with a shock interaction (adiabatic wall, origin not defined). Copy & Reisz (1980).

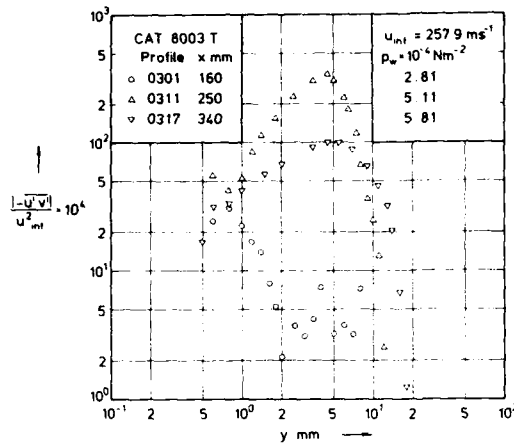


Fig. 11.3.12

Distributions of the specific Reynolds shear stress in a compressible boundary layer with a shock interaction (adiabatic wall, origin not defined). Copy & Reis (1980).

Figure (11.3.12) shows 3 characteristic profiles of series 03. Here the boundary layer separates and reattaches and it is therefore not surprising that the profile upstream of the shock (0301) and the peak profile (0311) differ by a factor 10. The variations of  $|u'v'|$  in the outer part of profile (0301) are probably due to the shock/ boundary-layer interaction.

#### The ratio "a" of Reynolds shear stress and turbulent kinetic energy

Klebanoff (1955) noted "that in the range of  $y/\delta = 0.1$  to  $y/\delta = 0.8$  the ratio of shear stress to turbulent energy is approximately constant". This statement concerned a two-dimensional ZPG incompressible turbulent boundary layer but has since been used for turbulence models in flows, both compressible and incompressible, with and without pressure gradients. Johnson & King (1985), for example, who present a "mathematically simple turbulence closure model for attached and separated turbulent boundary layers" assume the structure parameter  $|u'v'|_m/k_m$  to be constant and equal to 0.25. Here  $k_m$  denotes the maximum of the turbulent kinetic energy.

Unfortunately none of the experiments available to us provides all the Reynolds normal and shear stresses to check this assumption. At best we have  $-u'v'$ ,  $u'^2$ , and  $v'^2$  which we have used to form a modified structure parameter

$$a_{12} = \frac{|u'v'|}{u'^2 + v'^2}$$

Délery & Marvin (1986) have suggested that the missing term  $w'^2$  be substituted by  $0.5(u'^2 + v'^2)$ . We do not think this to be correct for shock/ boundary layer interactions which show a strong anisotropy between  $u'$  and  $v'$  and probably also for  $w'$ .

Figures (11.3.13 and 14) present distributions of  $a_{12}$  against the normal distance to the wall  $y$  for two compressible boundary layers with shock interaction (lines were inserted for clarity only). If  $w'^2$  were known, the value for  $a_{123}$  would be smaller than for  $a_{12}$  and, in the mean, below 0.20. In addition, the distributions show clearly that the structure parameter is not constant across a compressible boundary layer with a shock interaction, i.e. with an adverse pressure gradient. Smits & Muck (1987) made similar observations in discussing the ratio  $-u'v'/u'^2$  but show much smoother distributions (measured by hot-wire anemometry) than those obtained by LDA as presented in figures (11.3.13 and 14). Townsend (1976) compared the distributions of  $a_{123}$  for two APG incompressible boundary layers with the ZPG case and found an increase of  $a_{123}$  from 0.08 to about 0.16 at  $y/\delta \approx 0.8$  followed by a sharp decrease towards the edge of the boundary layer. This trend differs again from those shown above and from those presented by Smits & Muck (1987).

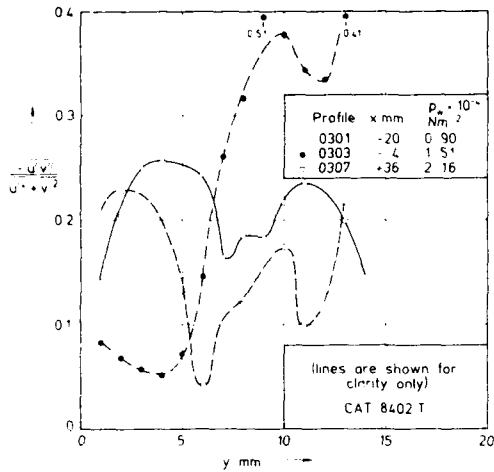


Fig. 11.3.13

Distributions of the modified structure parameter  $a_{12}$  in a compressible boundary layer along a compression corner ( $18^\circ$ ) Ardonceau (1984).

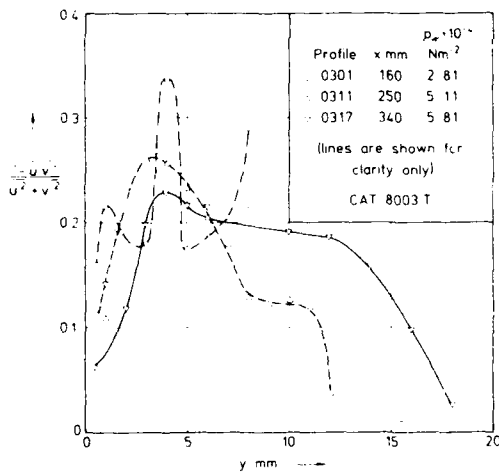


Fig. 11.3.14

Distributions of the modified structure parameter  $a_{12}$  in a compressible boundary layer with a shock interaction. Copy & Reisz (1980).

## 12. THE ENTRIES

### 12.1. Introduction

In preparing the first volume of this series, AG 223, we imposed certain restrictions on the flows considered as candidates for an entry. These were that the flow should be nominally two-dimensional, that the Mach number be high enough for the effects of compressibility to be significant, that the Reynolds number be high enough for at least some part of the flow to be recognisably turbulent, that there be no flow through the surface on which the boundary layer was formed, and that there be no discontinuities in the mean flow property profiles. We also required, as a general principle, that the information supplied must include profiles normal to the surface and that the principal part of the data be presented in tabular form.

This fourth volume contains 12 further entries and the data presentation follows the same pattern as for AG 263 (for an explanation of the numbering system see ch. 9). We have, however, included more cases in which shock waves impinge on and interact with a boundary layer, and inevitably many of the profiles in such flows incorporate what should be discontinuities in the flow properties concerned. The principal common feature of this volume in relation to AG 263 is that both mean flow and turbulence data are presented - this was not the case for AG 223. Again we have insisted on tabular data, some already published, but the majority was obtained on tapes as private communication. These tabular data have been prepared in a standard form, and samples appear as part of the entries. There is a full discussion of the planning and layout of an entry in AG 223, so that we only repeat the main points here. An entry is composed of four sections, A-D:

Section A This provides a description of the experiment in a standard format, and predominantly in a standard sequence. The description is keyed to a fixed set of topics indicated by numbers in the left hand margin. They may appear in any order, or be repeated if a topic recurs. The topics are

1. Description of test section
2. Flow quality
3. Observations of transition and tripping devices (trips)
4. Upstream history of the test boundary layer
5. Measures taken to test for, or ensure, two-dimensional flow
6. Measurements at the test-surface (wall measurements)
7. Probes used for boundary-layer traverses
8. Relative positions of measurement stations
9. Authors' interpolation procedure and assumptions
10. Corrections to the profile data
11. Viscosity law assumed by the authors
12. Editors' assumptions and interpolation procedures. Selection of data
13. Profiles presented
14. Wall data presented
- § Data summary
15. Editors' comments.

The topics marked 1-11 provides a description in which, so far as possible, we have restricted ourselves to statements which were verifiable either in the published reports or by correspondence with the authors. At various points, however, we have filled out the verifiable facts by an estimate or interpretation. Where this has happened we have inserted a marker (E). The end of the description, marked 12-14, describes the measures we found necessary in processing the data and is followed by (§ Data) a brief data summary which states what was in fact measured, in contrast to data which are deduced from the measurements. In § 15, Editors' comments, we have introduced our own interpretation and comment. These comments are supplemented by those in chapters 9, 10 and 11, either in general or particular. Chapters 10 and 11 deal with the mean flow and turbulence data, respectively, including graphical treatment.

Section B, the "Kopfdaten", contains tables of the principal boundary conditions and various derived quantities such as integral thicknesses. The table heading for a typical entry is shown here:

RUN	MD	TW/TR	REDZW	CF	H12	H12K	PW	PD
X	POD	PW/PD	RED2D	CQ	H32	H32K	TW	TD
RZ	TOD	TAUW	D2	PI2	H42	D2K	UD	TR

The list is reproduced in part at the start of this volume. Those quantities marked by a star (\*) represent the data used as input. In many cases these data would be entered directly, but the values shown often represent the results of preliminary calculations. In particular the D-state quantities (see AG 253 § 7.1 and chapter 9 of this volume) are often derived indirectly from the profile data. The stars indicate therefore the quantities which are, functionally, the independent variables rather than those which were directly available as numbers for processing. A good example is the wall shear stress  $\tau_{\text{AUW}}$ . Data are usually presented in the form of a skin-friction coefficient  $C_F$ . This quantity depends, in addition to the shear stress, on the reference values used in its formation, the D-state density and velocity. Many of the flows considered here have strong normal pressure gradients, so that the possible D-state properties are quite rapidly varying functions of the Y-value chosen to specify the boundary-layer edge. We have adopted the practice, therefore, of reducing authors'  $C_F$  input data to  $\tau_{\text{AUW}}$  values for use as program input, since we are then free to try various different D-states if we think it proper without having to consciously correct the normalization of  $C_F$ . For this reason a  $C_F$  value in our tables may well differ from that given by the original author. In this, and in many other features, our selection of a D-state, however carefully considered, may be ill advised. We hope however that it is self-consistent, so that the essential data may be recovered, and, at need, represented in a form better suited to the user's prejudices.

Section C, mean-profile tables, provides a selection from the available profile data. In an attempt to reduce the number of printed pages, the amount of space allotted to this section in this volume is significantly less than in AG 223. Readers will therefore need to have recourse to the computer tape data base (see the introduction to this volume).

I    Y    PT2/P    P/PD    TO/TOD    M/MD    U/UD    T/TD    R\*U/RD\*UD

The presentation is as in AG 223 save that for layout reasons the last column of data  $RHO*U/RHO*UD$  has been relabelled  $R*U/RD*UD$ . At the foot of each profile is a statement of the input used to construct the profile. As for the "Kopfdaten" tables of section B, quite often the data available to us did not directly fit our scheme of presentation. The boundary-layer edge state chosen or accepted by the editors is marked by the letter D. We have made clear in § 7 of AG 253 that this selection is essentially arbitrary. In using the information it is important to recognise that the scaled dimensionless information offered, while in principle more universal, is in fact critically dependent on the choice of the scaling quantity used. Thus it is the pressure, velocity, or shear stress rather than the pressure ratio, velocity ratio or shear-stress coefficient which represents the data entered to the catalogue. The dimensionless quantities are convenient, but coloured by the scaling process.

Section D supplies a miscellany of supplementary data. Of its very nature this does not fit the standard profile-based scheme. Typically, in AG 223, AG 263, and this volume, we present such information as wall-shear stress, temperature, or pressure distributions which have not been interpolated to the profile stations. Often far more detail is available, in terms of a streamwise distribution, for these quantities than for profile-derived data. We also present, at times, a selection of turbulence data. After due consideration we decided not to attempt a complete presentation of these data in the entries, since in certain cases this could run to many pages of tables. Nearly all the data available to us however appear in the magnetic tape data base.

Turbulence data present their own special problems and a presentation appropriate to the needs of research workers in turbulence modelling may well not fit that which allows an exact description of experimental results. It would, in general, be desirable to describe data in terms of "outer law" based quantities. The length scale in particular is usually so badly defined that it is in no way possible to arrange any comprehensive presentation in terms of "boundary-layer thickness" which has any generally agreed meaning. In contrast, the "wall values" are always well defined, if not always accurately measured. We have therefore, where possible, scaled all turbulence data on representative "wall values"  $RHO_w$ ,  $\tau_{\text{AUW}}$ ,  $\tau_{\text{TAUW}}$ ,  $T_w$  etc.. This may not be physically appropriate but does not compromise the accuracy of the original data. The choice of "outer-region scaling" is then open to the user.

The table heading for a typical entry may look like

Y    U'    V'    W'    RHO\*U' V'    RHO' U'    RHO' V'    RHO' W'    RHO\*U' T'    RHO' V' T'    RHO\*U' T' T'    RHO\*U' T' TW

We then give the profiles. For "single-component" terms these are the root mean square values of the quantity in question. For two-component or correlation terms they are the time means. Thus:

$$U' = \left[ \frac{u'^2}{T} \right]^{\frac{1}{2}} \quad T' = \left[ \frac{T'^2}{T} \right]^{\frac{1}{2}} \quad RHO' U' = \left[ \frac{(RHO' U')^2}{T} \right]^{\frac{1}{2}} \quad RHO*U' V' = \left[ \frac{(RHO*U' V')^2}{T} \right]^{\frac{1}{2}} \quad RHO' V' T' = \left[ \frac{(RHO' V' T')^2}{T} \right]^{\frac{1}{2}} \\ UT = \left[ \frac{u'^2}{T} \right]^{\frac{1}{2}} \quad TW = \left[ \frac{T'^2}{T} \right]^{\frac{1}{2}} \quad RHO*U' T' = \left[ \frac{(RHO*U' T')^2}{T} \right]^{\frac{1}{2}} \quad RHO*U' T' TW = \left[ \frac{(RHO*U' T' TW)^2}{T} \right]^{\frac{1}{2}}$$

Pagination. The description of an entry above implies a sequence of sections A-B-C-D. In the interest of saving pages, we have mixed sections freely according to convenience. An entry will always start as a right hand page - which will be numbered xxxx-A-1. The page numbers which follow may well be mixed - as for example in AG 223 72 04-A-2/B-1 which contains part of section A and part of section B.

While A, B and C will usually be in sequence, supplementary information from section D may well be attached to any page of any other section.

#### i) LIST OF ABBREVIATIONS

APG	-	adverse pressure gradient
AW	-	adiabatic wall
CC	-	constant current
CCF	-	compression-corner flow
CCP	-	cone-cylinder static pressure probe
CPP	-	circular Pitot probe
CSF	-	compression-surface flow
CT	-	constant temperature
D	-	D-state is the nominal boundary-layer edge state
E	-	estimated by editors
ECP	-	equilibrium cone probe
FEB	-	floating element balance
FPG	-	favourable pressure gradient
FPP	-	flattened Pitot probe
FWP	-	fine wire probe
H	-	height of the test section
HT	-	heat transfer
HWP	-	hot-wire probe
MHT	-	moderate heat transfer
NA	-	not available
NC	-	not computed
NM	-	not measured
NPG	-	normal pressure gradient
NX	-	number of X-stations
PC	-	private communication
QNS	-	quasi-normal shock
q.v.	-	quid vide
RUN	-	full 8-digit identification of the profile
RW	-	reflected wave
SH	-	severe heat transfer
SPP	-	static pressure probe
STP	-	static temperature probe
SW	-	simple wave
TPP	-	total pressure probe
TTP	-	total temperature probe
VPG	-	variable pressure gradient
W	-	width of the test wall
ZPG	-	zero pressure gradient



Probe dimensions

$d_1$	-	outside diameter
$d_2$	-	inside diameter
$h_1$	-	overall height of face
$h_2$	-	height of opening
$b_1$	-	overall width
$b_2$	-	width of opening
$l$	-	length of slender portion
$\alpha$	-	cone semi-angle

ii) GRAPHICAL PRESENTATION OF PROFILE DATA

Selected profile data from the sources below may be found in the figures listed.

Mean flow profiles and turbulence profiles

Source	"Inner" - Velocity	- "Outer"	Turbulence
7904	10.3.8-9, 11-12	10.3.10	See 8701
8002			11.2.26, 11.3.10
8003	10.4.3-4	10.4.5	11.2.27-28 11.3.11-12
8301	10.3.1	10.3.2	
8401	10.2.2-4, 7	10.2.5-6	See 8702
8402	10.3.3-4	10.3.5	11.2.20-22 11.3.6, 11.3.13-14
8501	10.4.6-7	10.4.8	
8601	10.1.4	10.1.3	11.2.5-7
8602	10.1.5	10.1.6	11.2.8-9
8603	10.1.1	10.1.2	11.2.2-4
8701	See 7904		11.2.19, 23-25 11.3.6-9
8702	See 8401		11.2.11-16 11.3.1-5

iii) PROPERTIES OF THE WORKING GAS, RECOVERY FACTORS

In data processing we have treated the working fluid as a perfect gas with constant specific heats.

The perfect gas properties assumed are:

Gas:	air
Gas constant $R$ in $\text{m}^2/\text{s}^2 \text{ K}$ :	287.1387
Specific heat ratio $\gamma$ :	1.40

The transport properties were calculated after Keyes (1952, see AGARDograph 223) for the diatomic gases (minor constituents of air being ignored).

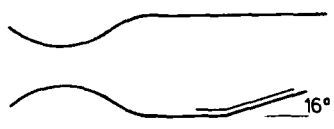
For the diatomic gases the expression

$$\mu = \frac{10^{-6} a_0 T^{1/2}}{1 + a T^{-1} 10^{-a_1 T^{1/2}}} \text{ NS/m}^2$$

was used, where the constants and the range of validity are given as

	$a_0$	$a$	$a_1$	range of validity
air:	1.488	122.1	5	$79 < T/K < 1845$

At present it is not possible to state a recovery factor with enough confidence to take account of upstream history effects, boundary conditions or other flow parameters. We have therefore chosen to use for all experiments a recovery factor  $r$  of 0.896, though this does not imply that we necessarily believe that there will be no heat transfer at a wall which is at the recovery temperature calculated using this. The numerical value represents the cube root of the Prandtl number for air, though a true recovery factor, if it could be defined, would of necessity be in some way a function of the shear stress distribution across the boundary layer, i.e. of the turbulence structure.

	M: 2.89 upstream	7904
	R Theta $\times 10^{-3}$ : 80	CCF
TW/TR: 1.11		
Blowdown tunnel with symmetrical contoured nozzle. Max. running time "several minutes", normally 60 seconds. $W = H = 0.203 \text{ m}$ L up to 2.7 m. PO: 0.69 MN/m <sup>2</sup> . T0: 265 K (+/- 6%). Air. $Re/m \times 10^{-6}$ : 63.		
SETTLES G.S., FITZPATRICK T.J., BOGDONOFF S.M., 1979. Detailed study of attached and separated compression corner flow fields in high Reynolds number supersonic flow. AIAA J <u>17</u> 579-586. <u>And:</u> Settles (1975), Settles et al. (1980). G.S. Settles and A.J. Smits, data tapes, private communications.		

- 1 The test boundary layer was formed on the floor of the wind tunnel, remaining under ZPG conditions for 1.14 m after leaving the nozzle. A recent investigation of this boundary layer is reported in CAT8603T, including a detailed study of the turbulent structure. The tests were performed on four compression surfaces 0.151 m long and 0.152 m wide, sharply inclined at 8 (Series 01 & 02 on the same model), 16 (03), 20 (04) and 24 (05) degrees to the floor. The inclined surface of the models was 50.8 mm narrower than the tunnel, leaving a gap on either side. The corner ( $X = 0$ ) region and the sloping surface were fitted with side fences so as to insulate the experiment from the effects of the tunnel side walls and improve the two-dimensionality of the test flow. The free stream Mach number was constant to +/- 0.02. The RMS free stream mass-flow fluctuation level was about 1%. The boundary layer was not tripped, but was fully turbulent. For details of the upstream flow see CAT8603T. Oil-flow patterns showing the surface flow are reproduced above as figure 9.3.1. The shock waves oscillated with increasing amplitude as the angle of the corner was increased. The discussions of flow unsteadiness in chapter 8 and 9.3.1 above are largely based on studies made in this flow.
- 6 Wall pressure was measured at 35 X-values (tapping dia. 0.81mm), with additional records at various stations across the model surface which showed variations of about 1%. Skin friction was determined at at least 19 stations using a Preston tube ( $d = 1.6 \text{ mm}$ ) and the Hopkins & Keener (1966) calibration. Mean flow profiles were measured with an FPP ( $h_1 = 0.178$ ,  $h_2 = 0.089$ ,  $b_1 = 0.762$ ,  $d = 0.61$ ,  $l = 15 \text{ mm}$ ), a CCP ( $d = 0.84 \text{ mm}$ ,  $15^\circ$  tip,  $0.25 \text{ mm}$  static holes in the horizontal plane 10d back from the shoulder,  $l = 15 \text{ mm}$  from the holes to the stem) and a FWP (dia. 0.1 mm) of the type described by Vas (1972), which was not however used for all profiles. The probes were mounted on supports passing through the roof of the tunnel, opposite the test surface. The profiles were measured along a line 12.7 mm off the centreline so as not to disturb the flow at adjacent static tapings.
- 8 The first few profiles were measured normal to the tunnel floor, with, in general, the remainder normal to the inclined compression surface. However, in the separated region for series 5, profiles were inclined at  $5.5^\circ$  to the vertical with the aim of having them normal to the zero-velocity line (Table 1). The Y-coordinate is set to zero at the model surface.

Table 1: Orientation of profile normals.

Series 01 and 02 were both measured on the  $8^\circ$  model. All the profiles of series 01 are normal to the tunnel floor, and all those for series 02 are inclined at  $8^\circ$ , normal to the ramp surface. For other series the profiles are presented as a single sequence.

Normal to floor:		Inclined at:	Inclined at:
Series 03	0301 - 04	0305 - 17	$16^\circ$
Series 04	0401 - 03	0404 - 08	$5.5^\circ$
Series 05		0501 - 05	$5.5^\circ$
			0409 - 16 $20^\circ$
			0506 - 09 $24^\circ$

(The orientation for series 05 is as given on a data tape prepared in 1987. The statement in Settles et al., 1980, should be disregarded. Elsewhere it is stated that 01 - 03 are normal to the floor.)

- 9 The measured T0 profiles were replaced by a linear approximation, accurate to within 2%. The authors have interpolated the original mean flow data to the measuring positions of the Pitot probes, and incorporated no profile corrections, though it is not certain whether the original Pitot profiles were corrected for shear. The editors have set the wall temperature at 1.04T0D, on the advice of A.J. Smits, as typical of normal operating conditions. The author has used an artificial edge state based on the tunnel total pressure and the local wall static pressure in reducing Preston-tube data. The selection of a D-state for flows of this nature is effectively arbitrary (9.2.2), the editors having attempted to indicate the edge of the wall-based dissipative layer after an inspection of the total pressure profiles.
- 13 The profiles are presented incorporating the assumptions and reduction procedures of the author. The wall data are also as given by the author with the profiles, which describe a boundary layer subjected to the shock-wave structure resulting from a range of compression corners. ("Author" here should be taken to include those working in the laboratory and preparing the data for us at a later date.)
- 5 DATA: 79040101 - 0509. Mean flow profiles from PT2, P and T0 probes. NX = 27 (01 & 02 combined), 17, 16 and 9. Wall shear from Preston tubes.

15 Editor's Comments:

The experimental work described here provides the mean flow data for the turbulence measurements in CAT8701T, (Smits & Muck, 1987). The data have been rescued from the archives and extensively reprocessed for us, but even so certain small discrepancies remain. Series 01 - 04 have been put together from the original experimental data tapes and give only slightly more than half of the profiles in that data collection. Series 5 is from the set of data prepared for the 1980 Stanford conference on complex turbulent flows (Kline et al., 1982), and represents only a small part of the data for the 24° corner reported in 1975.

Less fully documented compression-corner flows are described by Ardonneau, CAT8402T, with non-intrusive (LDV) instrumentation backed up by conventional probe measurements, and Debiève, CAT8301T, using conventional probes with some supporting hot-wire probe observations. Other recent investigations are described by Kuntz et al. (1987) and, using a cylinder/ cone-flare configuration, Brown et al. (1987).

The flow remains attached throughout in the 8° case. There is an exceedingly small separation region at the foot of the 16° ramp, while the separation region is estimated to extend from about  $X = -11.2$  to  $4.1$  mm and (very roughly)  $-35$  to  $10$  mm for the 20° and 24° cases respectively.

The profiles are given in fine detail and in most cases extend within the momentum deficit peak. They are compared to the inner and outer laws in Figs. 10.3.8-12 above. There we have used the shear-stress values declared by the author as derived from the Preston-tube results. Profiles for series 01-04 are shown in figure 5 of Smits & Muck (1987) using a profile fit to obtain a wall shear-stress value. The apparent fit is very good, and raises the question of why, if there is a log-law fit, the Preston tube does not give the same shear stress, and so not the same profile. All profiles in the interaction region, and to a lesser extent, those downstream, are subject to normal pressure gradients. Integral values therefore are improperly defined and should be treated with extreme reserve.

The wall pressure values given are those supplied by the author, and in many cases do not exactly match the inner part of the pressure profile. The pressure data and profile data were obtained in different runs, and as yet it has not proved possible to arrange a fully coherent normalisation.

Compression-corner flows inevitably cause problems with the alignment of probes. For the most part the flow is either broadly in line with the free stream, or with the downstream surface of the model. When the flow is separated there is also a small, but important region in which the flow is inclined roughly at 5-6° to the free stream. In that area of the flow which has the turning shock(s) embedded in the boundary layer, the desired alignment will change from the downstream to the upstream direction as the probe goes out through the shock. While a Pitot probe will tolerate a measure of misalignment, a static probe will be severely affected. (Settles, 1975, p.29. & Taylor, 1984, p.34 quote an error of 30% at 10° incidence.) When a probe is parallel to the downstream surface of a ramp and is traversed normal to the surface, it will eventually pass through the shock and become seriously misaligned, and error from this cause leads to anomalous results in the outer part of the profiles. The data as received are sometimes cut off at the shock when this happens, and sometimes extend beyond the shock, resulting in very high recorded Mach numbers (up to 3.9) and total pressures (more than double tunnel reservoir pressure). (79040411 - outermost point.) Our curiosity was aroused as to why this did not occur with

series 03, for the 16° ramp, and it is our opinion that, for this case and for series 05, the recorded static pressure outside the shock has been replaced by the upstream static pressure or by a separately measured value with the probe(s) locally aligned. (Settles p.29 could be stretched to imply this - but if so, why not for all?) If this is accepted as the explanation, it suggests that outside the shock, assuming Pitot alignment errors small, the mean flow data can be recovered in full, if not with complete accuracy, by assuming constant static pressure with a value of about  $22.5 \text{ kN m}^{-2}$ . It is not possible to apply a static correction to the recorded data, as this would be a function not only of inclination, but local Mach number and possibly Reynolds number.

Data in the immediate vicinity of the shock wave must be treated with some reserve. Even if the shock can be considered stationary, the response of probes, particularly static probes, is questionable. In general the shock oscillates (see above) and the probes do not respond simply by smoothing out the discontinuity, but display overshoots of both senses as they traverse the shock (figure 1). Settles (p.67) was of the opinion that "since much of the flow compression - occurs in the form of compression fans rather than overt shock waves, the problem of shock interference with the static probe does not appear to have been crucial" (see however section 9.3).

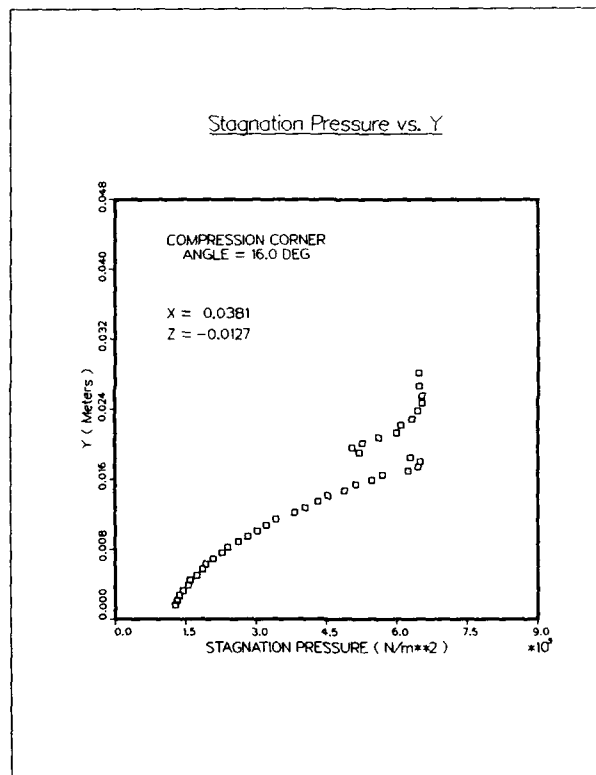


Fig. 1: 7904T

CAT 7904 SETTLES BOUNDARY CONDITIONS AND EVALUATED DATA, SI UNITS									
RUN X # RE	NO # MOD YDD	TU/TR PM/PO TAUW #	RED2H RED2D DZ	CF C2 PI2	M12 M32 M42	M12K M32K D2K	PW# TW# UD#	PJ# TD# TR	
79040101	2.8730	1.1120	3.4642+04	1.0355-03	5.7548	1.4395	2.3000+04	2.2315+04	
-2.5400-02	6.7675+05	1.0307	8.3397+04	NM	1.8104	1.7741	2.9299+02	1.0628+02	
INFINITE	2.8173+02	1.3350+02	1.4507-03	NM	-0.2257	2.3015-03	5.9393+02	2.6349+02	
79040102	2.8660	1.1119	4.3036+04	1.0152-03	5.5164	1.2830	2.3000+04	2.2648+04	
-1.5240-02	6.7959+05	1.0155	1.0634+05	NM	1.8500	1.8342	2.4810+02	9.0264+01	
INFINITE	2.3055+02	1.3220+02	1.4395-03	NM	-0.1895	2.1596-03	5.4595+02	2.2313+02	
79040103	2.8660	1.1119	4.2485+04	9.4615-04	5.7490	1.4318	2.3000+04	2.2591+04	
-5.1000-03	6.7788+05	1.0181	1.0514+05	NM	1.8611	1.8487	2.4584+02	8.9445+01	
INFINITE	2.3638+02	1.2290+02	1.4068-03	NM	-0.2134	2.0680-03	5.4346+02	2.2110+02	
79040104	2.8590	1.1117	4.3041+04	9.5096-04	5.6245	1.4449	2.3460+04	2.2592+04	
-2.5000-03	6.7075+05	1.0384	1.0624+05	NM	1.8515	1.8401	2.4536+02	8.9542+01	
INFINITE	2.3592+02	1.2370+02	1.4272-03	NM	-0.1878	2.1082-03	5.4242+02	2.2070+02	
79040105	2.8590	1.1117	4.2928+04	8.0518-04	5.4825	1.5392	3.1510+04	2.2552+04	
0.0000+00	6.6956+05	1.3972	1.0584+05	NM	1.8432	1.8407	2.4685+02	9.0098+01	
INFINITE	2.3739+02	1.0390+02	1.4375-03	NM	-0.2212	2.0454-03	5.4411+02	2.2207+02	
79040106	2.8590	1.1117	3.9527+04	8.5288-04	4.9029	1.5448	3.3810+04	2.2449+04	
5.1000-03	6.7838+05	1.4797	9.5235+04	NM	1.8173	1.8162	2.8229+02	1.0302+02	
INFINITE	2.7143+02	1.1150+02	1.5537-03	NM	-0.2228	2.0850-03	5.8181+02	2.5392+02	
79040107	2.8440	1.1114	3.6187+04	9.7354-04	4.0297	1.6578	3.4270+04	2.2824+04	
1.0160-02	6.6236+05	1.5015	8.6601+04	NM	1.7193	1.8074	2.8303+02	1.0397+02	
INFINITE	2.7214+02	1.2580+02	1.4410-03	NM	-0.1647	1.7582-03	5.8141+02	2.5467+02	
79040108	2.8590	1.1117	4.9205+04	1.0539-03	3.5417	1.6461	3.4960+04	2.2553+04	
1.5240-02	6.6959+05	1.5501	1.1933+05	NM	1.7442	1.7400	2.7451+02	1.0164+02	
INFINITE	2.6790+02	1.3600+02	1.9259-03	NM	-0.1207	2.4181-03	5.7790+02	2.5052+02	
79040109	2.8660	1.1119	4.6886+04	1.1260-03	2.7429	1.6459	3.5649+04	2.2427+04	
2.0320-02	6.7294+05	1.5896	1.1344+05	NM	1.7400	1.7439	2.8027+02	1.0197+02	
INFINITE	2.6949+02	1.4520+02	1.8531-03	NM	-0.1793	2.2017-03	5.8026+02	2.5206+02	
79040110	2.8660	1.1119	4.0460+04	1.1969-03	1.2976	1.6374	3.5550+04	2.2420+04	
2.5400-02	6.7275+05	1.5901	9.7818+04	NM	1.8370	1.8164	2.8148+02	1.0241+02	
INFINITE	2.7065+02	1.5430+02	1.6084-03	NM	-0.2018	1.6539-03	5.8152+02	2.5315+02	
79040201	2.7590	1.1096	2.3603+04	1.0020-03	3.3283	1.4731	3.1511+04	1.9641+04	
0.0000+00	4.9605+05	1.6192	5.4148+04	NM	1.8121	1.3080	2.9455+02	1.1240+02	
INFINITE	2.8352+02	1.0390+02	1.2197-03	NM	-0.1124	1.5596-03	5.8646+02	2.6572+02	
79040202	2.6040	1.1062	2.2025+04	1.2016-03	2.0010	1.4109	3.3910+04	1.9547+04	
5.0800-03	3.9250+05	1.7295	4.6994+04	NM	1.7760	1.7795	3.1094+02	1.2689+02	
INFINITE	2.9897+02	1.1150+02	1.3287-03	NM	-0.0862	1.3902-03	5.8912+02	2.8103+02	
79040203	2.8870	1.1123	3.8789+04	1.1225-03	2.1059	1.4228	3.4269+04	1.9207+04	
1.0160-02	5.2503+05	1.7841	3.3632+04	NM	1.7595	1.7572	2.9731+02	1.0719+02	
INFINITE	2.8587+02	1.2590+02	1.2074-03	NM	0.0084	2.0442-03	5.9929+02	2.6729+02	
79040204	2.9790	1.1141	4.6290+04	1.1442-03	1.9862	1.4138	3.4961+04	1.9134+04	
1.5240-02	6.8103+05	1.8272	1.1652+05	NM	1.7592	1.7546	2.9127+02	1.0093+02	
INFINITE	2.8007+02	1.3600+02	2.1145-03	NM	-0.0761	2.2494-03	6.0005+02	2.6144+02	
79040205	3.1700	1.1176	5.7557+04	1.1067-03	2.1027	1.3893	3.5550+04	1.9545+04	
2.0320-02	8.0226+05	1.9113	1.5749+05	NM	1.7681	1.7432	2.8416+02	9.0782+01	
INFINITE	2.7323+02	1.4520+02	2.3586-03	NM	-0.1615	2.5460-03	6.0558+02	2.5425+02	
79040206	3.1200	1.1147	5.2082+04	1.1846-03	1.6323	1.3967	3.5651+04	1.9114+04	
2.5400-02	4.3978+05	1.8650	1.6620+05	NM	1.7712	1.7617	2.8514+02	9.3371+01	
INFINITE	2.7515+02	1.5430+02	2.5718-03	NM	-0.1412	2.6745-03	6.0445+02	2.5625+02	
79040207	3.1490	1.1173	7.0338+04	1.2294-03	1.1991	1.4100	3.6109+04	1.8737+04	
3.0490-02	8.5923+05	1.9272	1.9037+05	NM	1.7637	1.7513	2.8610+02	9.2213+01	
INFINITE	2.7509+02	1.5990+02	2.9266-03	NM	-0.1454	2.8961-03	6.0629+02	2.5607+02	
79040208	2.3840	1.1009	3.7867+04	1.1989-03	3.4874	1.3818	3.6800+04	3.4342+04	
3.5560-02	4.8969+05	1.0716	7.4633+04	NM	1.7791	1.7328	2.8798+02	1.2960+02	
INFINITE	2.7692+02	1.6380+02	1.3530-03	NM	-0.0613	1.8121-03	5.4414+02	2.6159+02	
79040209	2.4620	1.1029	4.4178+04	1.1390-03	3.7923	1.3409	3.7950+04	3.5715+04	
4.5720-02	5.7517+05	1.0626	9.9918+04	NM	1.8095	1.7962	2.8935+02	1.2576+02	
INFINITE	2.7822+02	1.7260+02	1.4531-03	NM	-0.0591	1.9984-03	5.5357+02	2.6236+02	
79040210	2.5050	1.1039	4.6996+04	1.1143-03	4.1901	1.3539	3.8641+04	3.6693+04	
5.5880-02	6.3143+05	1.0531	9.4967+04	NM	1.8161	1.7997	2.9476+02	1.2654+02	
INFINITE	2.8535+02	1.7960+02	1.5124-03	NM	-0.0900	2.1408-03	5.6698+02	2.6883+02	
79040211	2.5400	1.1047	4.7041+04	1.0912-03	4.3694	1.3184	3.9100+04	3.7071+04	
6.6040-02	6.7402+05	1.0547	1.0276+05	NM	1.9203	1.8062	2.9514+02	1.2391+02	
INFINITE	2.8379+02	1.8100+02	1.5194-03	NM	-0.1557	2.1776-03	5.6688+02	2.6717+02	
79040212	2.4690	1.1031	4.5657+04	1.1271-03	4.8630	1.3384	3.9100+04	3.9296+04	
7.6200-02	6.3978+05	0.9950	9.3062+04	NM	1.8282	1.8159	2.9259+02	1.2677+02	
INFINITE	2.8133+02	1.8900+02	1.3786-03	NM	-0.2247	2.0231-03	5.5738+02	2.6525+02	
79040213	2.5190	1.1042	5.0792+04	1.1285-03	4.5980	1.3489	3.9327+04	3.8185+04	
8.6360-02	6.7199+05	1.0300	1.0590+05	NM	1.8180	1.8048	2.9004+02	1.2291+02	
INFINITE	2.7889+02	1.9140+02	1.5127-03	NM	-0.1841	2.1962-03	5.5992+02	2.6267+02	
79040214	2.5050	1.1039	5.0478+04	1.1815-03	4.4637	1.3230	3.9560+04	3.8460+04	
9.6520-02	6.6226+05	1.0286	1.0445+05	NM	1.8162	1.8018	2.9172+02	1.2439+02	
INFINITE	2.8050+02	1.9960+02	1.5166-03	NM	-0.1379	2.1954-03	5.6016+02	2.6426+02	

BOUNDARY CONDITIONS AND EVALUATED DATA, SI UNITS									
CAT 7904	SETTLES								
RUM X * RZ	M0 * P00 T00	FW/TR PW/PO TAUM *	RED2W RED2D DZ	C* CJ PEZ	H1Z H4Z	H12K H32K D2K	PW* T4* U0*	P0* T0* YR	
79040215	2.5050	1.1039	5.2245*+04	1.1617*-03	4.5200	1.3174	3.9790*+04	3.8303*+04	
1.0670*-01	6.6816*+05	1.0254	1.0828*+05	NM	1.9185	1.8057	2.8859*+02	1.2306*+02	
INFINITE	2.7750*+02	1.9800*+02	1.5346*-03	NM	-0.1445	2.2176*-03	5.5715*+02	2.6144*+02	
79040216	2.5050	1.1038	5.1017*+04	1.1931*-03	4.6676	1.3377	4.0020*+04	3.8583*+04	
1.1680*-01	6.6437*+05	1.0372	1.0595*+05	NM	1.8149	1.8008	2.8467*+02	1.2139*+02	
INFINITE	2.7374*+02	2.0220*+02	1.4810*-03	NM	-0.2050	2.1468*-03	5.5335*+02	2.5789*+02	
79040217	2.4270	1.1020	5.5925*+04	1.1967*-03	4.1611	1.3099	4.0020*+04	4.0390*+04	
1.2700*-01	6.2491*+05	0.9766	1.1229*+05	NM	1.8217	1.8095	2.8766*+02	1.2699*+02	
INFINITE	2.7659*+02	2.0220*+JZ	1.5268*-03	NM	-0.1562	2.2800*-03	5.4836*+02	2.6103*+02	
79040301	2.8300	1.1111	3.1942*+04	1.0436*-03	5.3753	1.2911	2.2510*+04	2.2870*+04	
-3.8100*-02	6.4970*+05	0.9843	7.5849*+04	NM	1.8600	1.8492	2.8630*+02	1.0581*+02	
INFINITE	2.7529*+02	1.3380*+02	1.2985*-03	NM	-0.2354	1.8783*-03	5.8366*+02	2.5767*+02	
79040302	2.8510	1.1116	3.3067*+04	1.0703*-03	5.5645	1.2850	2.1700*+04	2.2742*+04	
-1.2700*-02	6.6704*+05	0.9542	7.9265*+04	NM	1.8550	1.8419	2.8523*+02	1.0448*+02	
INFINITE	2.7425*+02	1.3850*+02	1.3293*-03	NM	-0.2531	1.9719*-03	5.8421*+02	2.5659*+02	
79040303	2.8440	1.1115	3.7254*+04	6.4661*-04	4.3227	1.3393	2.4260*+04	2.2807*+04	
-6.3500*-03	6.6196*+05	1.0637	9.9292*+04	NM	1.8214	1.8113	2.8085*+02	1.0316*+02	
INFINITE	2.7804*+02	9.3500*+01	1.4699*-03	NM	-0.2136	2.0787*-03	5.7917*+02	2.5244*+02	
79040304	2.8510	1.1115	4.1499*+04	2.7245*-05	4.2373	1.4975	3.4320*+04	2.2579*+04	
-3.1800*-03	6.6226*+05	1.5200	9.9639*+04	NM	1.7696	1.7561	2.8249*+02	1.0345*+02	
INFINITE	2.7162*+02	3.5000*+J0	1.6597*-03	NM	-0.2183	2.1604*-03	5.8139*+02	2.5413*+02	
79040305	2.8160	1.1109	5.0770*+04	2.5580*-04	3.5091	1.5983	3.9379*+04	3.3629*+04	
0.0000*+00	6.4041*+05	1.7100	1.1945*+05	NM	1.7487	1.7425	2.9205*+02	1.0559*+02	
INFINITE	2.8081*+02	3.2700*+J1	2.1192*-03	NM	-0.1542	2.6004*-03	5.8836*+02	2.6290*+02	
79040306	2.8230	1.1110	5.1550*+04	2.7165*-04	2.3738	1.4937	4.4980*+04	2.3030*+04	
1.8000*-03	6.4731*+05	1.9531	1.2142*+05	NM	1.7540	1.7523	2.9537*+02	1.0949*+02	
INFINITE	2.8400*+02	3.4900*+01	2.1746*-03	NM	-0.1692	2.5268*-03	5.9226*+02	2.6585*+02	
79040307	2.8160	1.1109	5.8413*+04	5.6242*-04	2.3995	1.5554	4.8019*+04	2.3030*+04	
4.3500*-03	6.4044*+05	2.0851	1.3746*+05	NM	1.7226	1.7252	2.9175*+02	1.0948*+02	
INFINITE	2.8053*+02	7.1900*+01	2.4350*-03	NM	-0.1544	2.5969*-03	5.8806*+02	2.6263*+02	
79040308	2.8230	1.1110	6.2033*+04	7.4028*-04	1.8757	1.5413	5.0050*+04	2.3029*+04	
9.5300*-03	6.4725*+05	2.1734	1.4693*+05	NM	1.7109	1.7131	2.8684*+02	1.0633*+02	
INFINITE	2.7581*+02	9.5100*+01	2.5206*-03	NM	-0.1767	2.4799*-03	5.8365*+02	2.5818*+02	
79040309	2.8230	1.1110	5.2126*+04	8.3207*-04	1.6275	1.5824	5.1799*+04	2.3030*+04	
1.2700*-02	6.4731*+05	2.2492	1.4723*+05	NM	1.7039	1.7043	2.8487*+02	1.0560*+02	
INFINITE	2.7391*+02	1.0690*+J2	2.5020*-03	NM	-0.1870	2.3501*-03	5.8164*+02	2.5641*+02	
79040310	2.8370	1.1113	7.7237*+04	1.0697*-03	0.9063	1.5392	5.4370*+04	2.3031*+04	
1.9100*-02	6.6128*+05	2.3607	1.8406*+05	NM	1.7075	1.7050	2.8519*+02	1.0508*+02	
INFINITE	2.7423*+02	1.3880*+J2	3.0901*-03	NM	-0.1423	2.6304*-03	5.8308*+02	2.5664*+02	
79040311	2.8160	1.1108	1.0057*+05	1.1522*-03	0.0897	1.5265	5.5700*+04	2.3032*+04	
2.5400*-02	6.4049*+05	2.4194	2.3773*+05	NM	1.7195	1.7100	2.8591*+02	1.0531*+02	
INFINITE	2.7491*+02	1.4730*+J2	4.0893*-03	NM	-0.1227	3.1238*-03	5.8214*+02	2.5738*+02	
79040312	2.8300	1.1111	1.0804*+05	1.3379*-03	-0.5176	1.4732	6.0850*+04	2.3050*+04	
3.8100*-02	6.5481*+05	2.6399	2.5611*+05	NM	1.7390	1.7266	2.8923*+02	1.0689*+02	
INFINITE	2.7810*+02	1.7290*+J2	4.4149*-03	NM	-0.1440	3.1384*-03	5.8664*+02	2.6030*+02	
79040313	2.8370	1.1113	1.2503*+05	1.5205*-03	-1.1174	1.4496	6.2000*+04	2.3033*+04	
5.0400*-02	6.6134*+05	2.4918	2.9613*+05	NM	1.7649	1.7504	2.9542*+02	1.0885*+02	
INFINITE	2.8407*+02	1.9730*+J2	5.2321*-03	NM	-0.1150	3.4996*-03	5.9344*+02	2.6584*+02	
79040314	2.3060	1.0989	8.7159*+04	1.1439*-03	2.1906	1.3466	6.2800*+04	5.4152*+04	
7.6200*-02	6.8352*+05	1.1597	1.6655*+05	NM	1.8175	1.8028	2.8751*+02	1.1397*+02	
INFINITE	2.7645*+02	2.3460*+02	2.0735*-03	NM	-0.0992	2.5096*-03	5.3514*+02	2.6163*+02	
79040315	2.1720	1.0953	6.4768*+04	1.2511*-03	4.0172	1.3787	5.8500*+04	6.2303*+04	
1.0160*-01	6.3763*+05	0.9390	1.1709*+05	NM	1.8042	1.7975	2.8912*+02	1.4304*+02	
INFINITE	2.7800*+02	2.5740*+J2	1.4754*-03	NM	-0.1205	2.0247*-03	5.2083*+02	2.6396*+02	
79040316	2.1930	1.0958	5.9906*+04	1.3329*-03	4.1445	1.3558	5.8000*+04	6.0958*+04	
1.2700*-01	6.4470*+05	0.9515	1.0938*+05	NM	1.8271	1.8213	2.8578*+02	1.4007*+02	
INFINITE	2.7480*+02	2.7350*+02	1.3547*-03	NM	-0.1289	1.8293*-03	5.2038*+02	2.6078*+02	
79040317	2.1930	1.0959	5.3559*+04	1.3945*-03	3.8063	1.3027	5.8900*+04	6.0608*+04	
1.3970*-01	6.4100*+05	0.9718	1.1598*+05	NM	1.8330	1.8274	2.8918*+02	1.4173*+02	
INFINITE	2.7805*+02	2.4250*+02	1.4676*-03	NM	-0.1334	1.9339*-03	5.2346*+02	2.6388*+02	
79040401	2.7880	1.1102	3.6785*+04	1.1191*-03	5.4218	1.3166	2.1810*+04	2.3271*+04	
-3.8100*-02	6.2007*+05	0.9372	5.7170*+04	NM	1.8353	1.8132	2.6157*+02	9.8456*+01	
INFINITE	2.5151*+02	1.4170*+J2	1.3402*-03	NM	-0.2584	2.0224*-03	5.5466*+02	2.3560*+02	
79040402	2.7240	1.1089	6.0567*+04	6.3443*-04	4.6894	1.6424	3.9080*+04	2.4571*+04	
-1.9050*-02	5.9599*+05	1.5840	9.3017*+04	NM	1.7762	1.7571	2.7131*+02	1.0502*+02	
INFINITE	2.6087*+02	8.1300*+J1	1.5170*-03	NM	-0.1825	2.0815*-03	5.5970*+02	2.4466*+02	
79040403	2.7450	1.1093	5.4356*+04	1.5863*-04	3.5530	1.6403	4.0890*+04	2.4612*+04	
-1.2700*-02	6.1403*+05	1.6614	1.2655*+05	NM	1.7357	1.7259	2.6090*+02	1.0007*+02	
INFINITE	2.5048*+02	2.0600*+01	1.7135*-03	NM	-0.1873	2.3714*-03	5.5055*+02	2.3519*+02	

CAT 7904		SETTLER		BOUNDARY CONDITIONS AND EVALUATED DATA, SI UNITS						
RUN X # RZ	MD # POD TOD	TW/TR PM/PO TAUM #	REQ2W REQ2D DZ	CF CJ PI2	M12 M12 M42	M12K M12K D2K	PW# TW# UD#	POW TOW TR		
79040404	2.7590	1.1096	5.0592E+04	1.4172E-04	3.5491	1.8052	4.1089E+04	2.4859E+04		
-1.1100E-02	6.3364E+05	1.6529	1.4222E+05	NM	1.7153	1.7032	2.5748E+02	9.8151E+01		
INFINITE	2.4758E+02	1.7700E+01	2.0591E-03	NM	-0.1573	2.4961E-03	5.4804E+02	2.3204E+02		
79040405	2.8440	1.1114	5.3672E+04	7.7629E-02	2.7734	1.9307	4.1609E+04	2.2752E+04		
-6.3500E-03	6.6027E+05	1.8288	1.5471E+05	NM	1.8134	1.8556	2.5931E+02	9.5250E+01		
INFINITE	2.4933E+02	1.0000E+04	2.2721E-03	NM	-0.1408	2.3945E-03	5.5651E+02	2.3331E+02		
79040406	1.3590	1.0700	1.6596E+04	1.7038E-01	5.6105	4.2552	4.6150E+04	4.5398E+04		
0.0000E+00	1.3662E+05	1.0166	2.2144E+04	NM	1.5856	1.5719	2.7522E+02	1.9325E+02		
INFINITE	2.6463E+02	1.0000E+04	9.2740E-04	NM	0.0118	1.1044E-03	3.7878E+02	2.5721E+02		
79040407	1.6990	1.0812	3.3256E+04	1.2338E-04	5.8245	2.4301	5.0729E+04	4.4926E+04		
3.9700E-03	2.2142E+05	1.1292	5.0178E+04	NM	1.6047	1.5864	2.7656E+02	1.6859E+02		
INFINITE	2.6592E+02	1.1200E+01	1.4088E-03	NM	-0.0252	1.7923E-03	4.4230E+02	2.5580E+02		
79040408	1.2000	1.0648	1.0452E+04	8.3656E-04	4.2363	2.4470	5.8300E+04	5.4312E+04		
1.2700E-02	1.3170E+05	1.0734	3.9657E+04	NM	1.1245	1.2021	2.6881E+02	2.0067E+02		
INFINITE	2.5846E+02	4.5800E+01	1.6113E-03	NM	-0.0173	2.1749E-03	3.4083E+02	2.5245E+02		
79040409	3.1060	1.1165	1.1667E+05	6.0970E-04	0.3256	2.0748	6.0448E+04	1.7929E+04		
1.5880E-02	7.7145E+05	3.3715	3.1452E+05	NM	1.6194	1.5764	2.6765E+02	8.7852E+01		
INFINITE	2.5736E+02	7.3700E+01	4.7648E-03	NM	-0.0608	3.4265E-03	5.8370E+02	2.3973E+02		
79040410	2.2350	1.0970	7.2212E+04	5.1030E-04	2.7775	1.9081	6.2590E+04	4.5115E+04		
1.9050E-02	5.0957E+05	1.3873	1.3511E+05	NM	1.6303	1.6065	2.7061E+02	1.3016E+02		
INFINITE	2.6020E+02	8.0500E+01	1.9996E-03	NM	-0.0459	2.4613E-03	5.1124E+02	2.4667E+02		
79040411	2.1530	1.0949	7.4647E+04	5.5267E-04	3.1561	1.7152	6.6110E+04	5.4508E+04		
2.5400E-02	5.4577E+05	1.2129	1.3483E+05	NM	1.6694	1.6491	2.7831E+02	1.3856E+02		
INFINITE	2.6761E+02	9.4200E+01	1.8690E-03	NM	-0.0393	2.4552E-03	5.0930E+02	2.5419E+02		
79040412	2.2850	1.0993	1.0729E+05	6.4610E-04	2.5110	1.6272	7.2090E+04	5.6281E+04		
4.1300E-02	5.4743E+05	1.2809	2.0437E+05	NM	1.6913	1.6713	2.7590E+02	1.2978E+02		
INFINITE	2.6530E+02	1.3290E+02	2.3617E-03	NM	-0.0834	2.9068E-03	5.2191E+02	2.5121E+02		
79040413	2.1150	1.0937	7.4758E+04	8.3742E-04	3.9045	1.5430	7.5198E+04	6.8904E+04		
5.7150E-02	6.4505E+05	1.0913	1.6931E+05	NM	1.7104	1.6967	2.6402E+02	1.3399E+02		
INFINITE	2.5386E+02	1.7960E+02	1.8046E-03	NM	-0.1004	2.5769E-03	4.9086E+02	2.4140E+02		
79040414	2.0510	1.0919	9.2776E+04	1.0503E-03	3.5435	1.4365	7.7150E+04	7.2529E+04		
7.6200E-02	6.1442E+05	1.0637	1.6133E+05	NM	1.7453	1.7374	2.6614E+02	1.3898E+02		
INFINITE	2.5591E+02	2.2430E+02	1.7759E-03	NM	-0.0586	2.4414E-03	4.8478E+02	2.4375E+02		
79040415	2.0160	1.0909	9.5187E+04	1.1734E-03	3.5668	1.4703	7.8740E+04	7.6386E+04		
9.5250E-02	5.1275E+05	1.0308	1.6289E+05	NM	1.7439	1.7346	2.7059E+02	1.4352E+02		
INFINITE	2.6018E+02	2.5500E+02	1.9121E-03	NM	-0.0568	2.4584E-03	4.8424E+02	2.4905E+02		
79040416	1.9880	1.0901	9.0268E+04	1.2885E-03	3.2371	1.3431	8.0320E+04	7.6473E+04		
1.1430E-01	5.8730E+05	1.0503	1.3515E+05	NM	1.7941	1.7876	2.8255E+02	1.5174E+02		
INFINITE	2.7168E+02	2.7260E+02	1.6445E-03	NM	-0.0500	2.1308E-03	4.9100E+02	2.5721E+02		
79040501	2.3230	1.1110	3.2777E+04	1.0714E-03	5.4269	1.2337	2.2890E+04	2.2890E+04		
-6.3500E-02	6.4337E+05	1.0000	7.9056E+04	NM	1.8543	1.8398	2.5704E+02	9.5286E+01		
INFINITE	2.4716E+02	1.3916E+02	1.1633E-03	NM	-0.2183	1.7264E-03	5.5250E+02	2.3136E+02		
79040502	2.8300	1.1111	5.0329E+04	NM	3.5354	1.7574	4.1160E+04	2.2889E+04		
-3.0480E-02	6.5024E+05	1.7982	1.2149E+05	NM	1.6929	1.6790	2.6032E+02	9.6207E+01		
INFINITE	2.5031E+02	NM	1.8046E-03	NM	-0.2189	2.2003E-03	5.5654E+02	2.3428E+02		
79040503	2.8510	1.1116	1.1018E+05	NM	1.7349	2.5220	5.0749E+04	2.2889E+04		
-1.0160E-02	6.7132E+05	2.2173	2.6637E+05	NM	1.6310	1.5945	2.7012E+02	9.8922E+01		
INFINITE	2.5973E+02	NM	4.1003E-03	NM	-0.0602	3.6842E-03	5.6953E+02	2.4301E+02		
79040504	2.7740	1.1100	1.4002E+05	NM	1.1260	2.5351	5.3370E+04	2.3120E+04		
0.0000E+00	6.0300E+05	2.3084	3.3041E+05	NM	1.4230	1.5753	2.5803E+02	9.7716E+01		
INFINITE	2.4810E+02	NM	5.0858E-03	NM	-0.0994	4.3066E-03	5.4979E+02	2.3246E+02		
79040505	2.7310	1.1090	1.5374E+05	1.0191E-04	0.2872	2.4079	6.1571E+04	2.2892E+04		
1.0160E-02	5.5839E+05	2.6896	3.5534E+05	NM	1.4204	1.5803	2.6320E+02	1.0157E+02		
INFINITE	2.5308E+02	1.2180E+01	5.7337E-03	NM	-0.1102	4.4135E-03	5.5184E+02	2.3732E+02		
79040506	2.7100	1.1036	1.5158E+05	5.5191E-04	-1.0071	2.1019	7.7570E+04	2.2891E+04		
3.0480E-02	5.4122E+05	3.3837	3.4919E+05	NM	1.5429	1.6113	2.6755E+02	1.0420E+02		
INFINITE	2.5725E+02	5.4950E+01	5.4497E-03	NM	-0.1200	4.0773E-03	5.5465E+02	2.4133E+02		
79040507	2.7170	1.1088	2.3393E+05	1.2925E-03	-2.3753	1.6319	8.9698E+04	2.2891E+04		
6.0960E-02	5.4708E+05	3.7185	5.3829E+05	NM	1.6970	1.6687	2.6090E+02	1.0130E+02		
INFINITE	2.5096E+02	1.5239E+02	9.0004E-03	NM	-0.1162	4.4781E-03	5.4828E+02	2.3531E+02		
79040508	2.6820	1.1080	4.0777E+05	2.1937E-03	-2.5643	1.3833	9.7152E+04	2.2899E+04		
1.0160E-01	5.1836E+05	4.2445	9.2952E+05	NM	1.7759	1.7570	2.5236E+02	9.9503E+01		
INFINITE	2.4265E+02	2.5167E+02	1.5340E-02	NM	-0.0716	6.3927E-03	5.3640E+02	2.2776E+02		
79040509	1.8890	1.0371	9.5996E+04	1.3496E-03	3.6415	1.4463	9.4460E+04	9.3922E+04		
1.4220E-01	6.1874E+05	1.0057	1.4036E+05	NM	1.8297	1.8249	2.6221E+02	1.4713E+02		
INFINITE	2.5213E+02	3.1661E+02	1.4036E-03	NM	-0.1130	1.7742E-03	4.5940E+02	2.4121E+02		



79040304		SETTLES	PROFILE TABULATION			54 POINTS, DELTA AT POINT 44		
I	Y	PT2/P	P/P3	T0/T30	M/MD	U/UD	T/T0	R/R0=U/UD
1	0.0000*-00	1.0000*-00	1.51999	1.03997	0.00000	0.00000	2.73059	0.00000
2	8.3540*-04	1.5015*-00	1.73837	1.04721	0.29765	0.46145	2.40344	0.33385
3	1.2700*-03	2.0645*-00	1.73695	1.04495	0.37636	0.55204	2.23014	0.43019
4	1.6350*-03	2.3671*-00	1.67199	1.04136	0.41599	0.60783	2.13495	0.47602
5	2.0900*-03	2.6890*-00	1.62943	1.03638	0.45317	0.64727	2.04007	0.51638
6	2.5330*-03	2.9936*-00	1.58535	1.03335	0.48544	0.68008	1.96264	0.54934
7	3.0780*-03	3.2060*-00	1.53823	1.03173	0.50649	0.70030	1.91172	0.56348
8	3.6120*-03	3.5395*-00	1.45512	1.02947	0.53771	0.72914	1.83877	0.59097
9	4.1350*-03	3.8212*-00	1.39976	1.02766	0.56261	0.75094	1.78155	0.59001
10	4.6480*-03	4.0693*-00	1.33410	1.02644	0.58365	0.76868	1.73453	0.59122
11	5.1510*-03	4.3108*-00	1.26930	1.02934	0.60330	0.78603	1.69750	0.58798
12	5.6460*-03	4.6192*-00	1.21159	1.02791	0.62750	0.80496	1.64558	0.59266
13	6.2380*-03	5.0164*-00	1.15352	1.02573	0.65731	0.82676	1.59202	0.60282
14	6.9290*-03	5.3629*-00	1.09348	1.02346	0.69222	0.84400	1.53054	0.60299
15	7.5820*-03	5.7049*-00	1.04180	1.02300	0.71940	0.86888	1.45876	0.62053
16	8.2140*-03	6.0583*-00	1.02691	1.02354	0.72957	0.87572	1.44077	0.62416
17	8.8950*-03	6.4818*-00	1.01292	1.02171	0.75693	0.89207	1.38896	0.65055
18	9.5580*-03	6.8771*-00	1.00046	1.02155	0.76920	0.89941	1.36719	0.65815
19	1.0190*-02	6.9615*-00	1.00000	1.02139	0.78674	0.90961	1.33675	0.68047
20	1.0780*-02	7.3423*-00	1.00000	1.02019	0.79165	0.91189	1.32684	0.68727
21	1.1570*-02	7.2878*-00	0.99696	1.02033	0.80638	0.92052	1.30310	0.70426
22	1.2260*-02	7.5439*-00	0.99301	1.02153	0.82147	0.92904	1.27905	0.72127
23	1.2940*-02	7.7559*-00	0.99119	1.02010	0.83374	0.93488	1.25734	0.73639
24	1.3550*-02	8.0207*-00	0.99042	1.01873	0.84832	0.94212	1.23130	0.75744
25	1.4220*-02	8.0642*-00	0.99073	1.02009	0.85129	0.94400	1.22971	0.76055
26	1.4730*-02	8.4173*-00	0.99352	1.01932	0.87092	0.95332	1.19817	0.79057
27	1.5630*-02	8.4173*-00	0.99853	1.01850	0.87092	0.95312	1.19767	0.79472
28	1.6310*-02	8.5486*-00	0.99863	1.01845	0.88335	0.95917	1.17349	0.81278
29	1.7130*-02	8.9757*-00	0.99574	1.01833	0.89583	0.96431	1.16019	0.82814
30	1.7860*-02	9.2550*-00	0.99331	1.01943	0.91542	0.97413	1.13140	0.85524
31	1.8460*-02	9.3492*-00	0.99260	1.01632	0.92073	0.97532	1.12210	0.86259
32	1.9290*-02	9.5331*-00	0.99210	1.01474	0.93055	0.97899	1.10681	0.87752
33	2.0010*-02	9.7862*-00	0.99179	1.01432	0.94318	0.98414	1.08875	0.89650
34	2.0680*-02	9.9803*-00	0.99210	1.01292	0.95300	0.98761	1.07396	0.91233
35	2.1330*-02	1.0276*-01	0.99377	1.01356	0.96773	0.99405	1.05514	0.93623
36	2.2010*-02	1.0177*-01	0.99544	1.01371	0.96282	0.99207	1.06168	0.93017
37	2.2820*-02	1.0326*-01	0.99742	1.00961	0.97019	0.99306	1.04771	0.94539
38	2.3620*-02	1.0393*-01	0.99939	1.00933	0.97239	0.99405	1.04376	0.95180
39	2.4520*-02	1.0685*-01	1.00000	1.00553	0.98772	0.99302	1.02095	0.97754
40	2.5240*-02	1.0685*-01	1.00000	1.00553	0.98772	0.99302	1.02095	0.97754
41	2.5960*-02	1.0685*-01	1.00000	1.00353	0.98772	0.99703	1.01892	0.97851
42	2.6820*-02	1.0838*-01	1.00000	1.00775	0.99509	1.00198	1.01330	0.98824
43	2.7610*-02	1.0883*-01	1.00000	1.00138	0.99754	1.00000	1.00493	0.99510
44	2.8520*-02	1.0940*-01	1.00000	1.00000	1.00000	1.00000	1.00000	1.00000
45	2.9540*-02	1.0940*-01	1.00000	1.00000	1.00000	1.00000	1.00000	1.00000
46	3.0530*-02	1.0940*-01	1.00000	1.00000	1.00000	1.00000	1.00000	1.00000
47	3.1900*-02	1.0999*-01	1.00000	0.99935	1.00281	1.00099	0.99638	1.00462
48	3.3450*-02	1.0999*-01	1.00000	0.99935	1.00281	1.00099	0.99638	1.00462
49	3.5230*-02	1.1050*-01	1.00000	0.99997	1.00526	1.00198	0.99349	1.00855
50	3.7330*-02	1.0999*-01	1.00000	0.99737	1.00281	1.00000	0.99441	1.00562
51	3.9420*-02	1.0940*-01	1.00000	1.00000	1.00000	1.00000	1.00000	1.00000
52	4.1760*-02	1.0999*-01	1.00000	0.99935	1.00281	1.00099	0.99638	1.00462
53	4.4910*-02	1.0889*-01	1.00000	0.99771	0.99754	0.99902	1.00095	0.99707
54	4.5720*-02	1.0999*-01	1.00000	0.99737	1.00281	1.00000	0.99441	1.00562

79040309		SETTLES	PROFILE TABULATION			43 POINTS, DELTA AT POINT 38			
I	Y	PTZ/P	P/PD	T0/T00	M/M0	U/U0	T/T0	R/R0=U/U0	
1	0.0000**00	1.0000**00	2.24921	1.04000	0.00000	0.00000	2.69763	0.00000	
2	7.6170**04	1.6114**00	2.28970	1.05167	0.30269	0.45700	2.38028	0.44323	
3	9.4110**04	1.6367**00	2.28295	1.04879	0.31792	0.48664	2.34297	0.47417	
4	1.3930**03	1.7998**00	2.26720	1.04769	0.33858	0.51336	2.29752	0.50659	
5	1.8530**03	1.9356**00	2.24719	1.04334	0.36096	0.54048	2.24197	0.54174	
6	2.2980**03	2.1251**00	2.23842	1.04246	0.38859	0.57368	2.17944	0.58920	
7	2.8450**03	2.3077**00	2.23617	1.03811	0.41263	0.60090	2.11947	0.63388	
8	3.2740**03	2.4901**00	2.22132	1.03852	0.43500	0.62582	2.06979	0.67164	
9	3.9370**03	2.7104**00	2.21155	1.03411	0.46015	0.65165	2.02552	0.71862	
10	4.3710**03	2.9845**00	2.20955	1.03432	0.47892	0.67129	1.95454	0.75507	
11	4.8410**03	3.0562**00	2.20760	1.03332	0.49653	0.68993	1.92489	0.79023	
12	5.4640**03	3.2570**00	2.18498	1.03271	0.51647	0.70808	1.87960	0.82308	
13	6.1420**03	3.4703**00	2.17813	1.03237	0.53656	0.72722	1.83622	0.86263	
14	6.7890**03	3.7045**00	2.16239	1.03251	0.55792	0.74646	1.79039	0.90171	
15	7.4930**03	3.9943**00	2.08952	1.03102	0.58337	0.76790	1.73447	0.92508	
16	7.9600**03	4.3900**00	2.03014	1.03021	0.61556	0.79462	1.66585	0.96333	
17	8.7400**03	5.0154**00	1.84773	1.03047	0.66393	0.83130	1.57009	0.97839	
18	9.3650**03	5.6866**00	1.61258	1.03066	0.71165	0.86530	1.47842	0.94389	
19	9.9870**03	6.3991**00	1.40936	1.02813	0.75912	0.89501	1.39007	0.90743	
20	1.0670**02	6.9155**00	1.24921	1.02661	0.79171	0.91376	1.33268	0.85692	
21	1.1310**02	7.3291**00	1.14030	1.02435	0.81696	0.92692	1.23762	0.82123	
22	1.2020**02	7.7559**00	1.06702	1.02512	0.84201	0.94079	1.24835	0.80413	
23	1.2810**02	8.1518**00	1.03014	1.02196	0.86469	0.95095	1.20948	0.80974	
24	1.3610**02	8.4173**00	1.01889	1.02114	0.87955	0.95793	1.18613	0.82236	
25	1.4410**02	8.5583**00	1.00877	1.01921	0.88735	0.96032	1.17122	0.82712	
26	1.5120**02	8.9227**00	1.00202	1.01859	0.90719	0.96989	1.14360	0.95026	
27	1.5810**02	9.0151**00	1.00000	1.01704	0.91215	0.97139	1.13410	0.85653	
28	1.6380**02	9.2081**00	1.00000	1.01502	0.92242	0.97507	1.11742	0.87261	
29	1.7160**02	9.5391**00	1.00000	1.01669	0.93978	0.98355	1.09531	0.89796	
30	1.7970**02	9.6828**00	1.00000	1.01552	0.94722	0.98524	1.08439	0.90974	
31	1.8750**02	9.7379**00	1.00000	1.01416	0.95005	0.98674	1.07872	0.91473	
32	1.9530**02	9.9319**00	1.00000	1.01049	0.95997	0.99392	1.05168	0.93167	
33	2.0640**02	1.0079**01	1.00000	1.00858	0.96741	0.99133	1.05005	0.94407	
34	2.1550**02	1.0326**01	1.00000	1.00756	0.97931	0.99531	1.03233	0.95406	
35	2.2580**02	1.0483**01	1.00000	1.00773	0.98750	0.99900	1.02322	0.97633	
36	2.3920**02	1.0634**01	1.00000	1.00536	0.99504	1.00100	1.01201	0.99312	
37	2.5500**02	1.0634**01	1.00000	1.00395	0.99504	1.00000	1.00939	0.99011	
38	2.7610**02	1.0736**01	1.00000	1.00000	1.00000	1.00000	1.00000	1.00000	
39	2.9950**02	1.0787**01	1.00000	1.00009	1.00248	1.00100	0.99704	1.00336	
40	3.2740**02	1.0838**01	1.00000	1.00217	1.00496	1.00299	0.99608	1.00693	
41	3.6120**02	1.0838**01	1.00000	1.00217	1.00496	1.00299	0.99608	1.00693	
42	4.0640**02	1.0787**01	1.00000	1.00009	1.00248	1.00100	0.99704	1.00336	
43	4.5720**02	1.0787**01	1.00000	1.00208	1.00248	1.00199	0.99903	1.00297	

79040311		SETTLES	PROFILE TABULATION		49 POINTS, DELTA AT POINT 42				
I	Y	PT2/P	P/PD	T0/T00	M/MD	U/U0	T/T0	R/RD*U/U0	
1	0.0000E+00	1.0000E+00	2.41837	1.04000	0.00000	0.00000	2.68940	0.00000	
2	7.6170E-04	1.7606E+00	2.57073	1.05134	0.33256	0.50578	2.31301	0.56214	
3	1.1520E-03	1.8320E+00	2.55622	1.04778	0.34506	0.52094	2.27914	0.58427	
4	1.6040E-03	1.9540E+00	2.53446	1.04521	0.35470	0.54487	2.23205	0.61869	
5	2.0640E-03	2.0719E+00	2.50785	1.04240	0.38210	0.56530	2.19880	0.64771	
6	2.5860E-03	2.1536E+00	2.49818	1.04212	0.39347	0.57876	2.15366	0.66825	
7	3.0780E-03	2.2382E+00	2.49334	1.03848	0.41122	0.59840	2.11757	0.70459	
8	3.5000E-03	2.3272E+00	2.48609	1.03657	0.42365	0.61197	2.03659	0.72913	
9	4.0360E-03	2.5445E+00	2.48125	1.03635	0.44247	0.63290	2.04598	0.76755	
10	4.6510E-03	2.7104E+00	2.47158	1.03147	0.46129	0.65145	1.99436	0.80733	
11	4.9250E-03	2.8510E+00	2.47158	1.03251	0.47656	0.66770	1.96300	0.84059	
12	5.5730E-03	2.9217E+00	2.46191	1.03234	0.48492	0.67527	1.94641	0.85412	
13	6.0660E-03	3.1807E+00	2.45949	1.03139	0.51030	0.70110	1.89759	0.91351	
14	6.5410E-03	3.3644E+00	2.46191	1.03095	0.52805	0.71795	1.84853	0.95617	
15	7.0560E-03	3.4971E+00	2.45707	1.03229	0.54048	0.73001	1.82429	0.99322	
16	7.4680E-03	3.5667E+00	2.46191	1.03056	0.54688	0.73529	1.80778	1.00135	
17	7.9680E-03	3.7045E+00	2.45465	1.02971	0.55930	0.74616	1.77979	1.02909	
18	8.5450E-03	3.8907E+00	2.45949	1.02917	0.57564	0.76032	1.74458	1.07189	
19	8.9510E-03	3.9943E+00	2.46191	1.03033	0.58452	0.76839	1.72812	1.09467	
20	9.4030E-03	4.1422E+00	2.45707	1.02956	0.59695	0.77856	1.70166	1.12459	
21	9.8860E-03	4.4078E+00	2.45223	1.02891	0.61851	0.79601	1.65580	1.17889	
22	1.0430E-02	4.5015E+00	2.45465	1.02879	0.62607	0.80190	1.64057	1.19981	
23	1.0990E-02	4.6558E+00	2.45465	1.02813	0.63814	0.81107	1.61541	1.23244	
24	1.1370E-02	4.9497E+00	2.45707	1.02819	0.66031	0.82902	1.57151	1.29461	
25	1.2080E-02	4.9830E+00	2.44931	1.02833	0.66300	0.82991	1.56699	1.29755	
26	1.2570E-02	5.1564E+00	2.44014	1.02573	0.67573	0.83819	1.53839	1.32950	
27	1.2930E-02	5.2935E+00	2.43530	1.02576	0.68572	0.84526	1.51945	1.35475	
28	1.3510E-02	5.2591E+00	2.42321	1.02519	0.68324	0.84327	1.52331	1.34143	
29	1.4190E-02	5.1224E+00	2.37338	1.02113	0.67330	0.83450	1.53617	1.28957	
30	1.4860E-02	5.1564E+00	2.16251	1.02017	0.67573	0.83599	1.52999	1.18146	
31	1.5530E-02	5.3282E+00	1.94657	1.01934	0.68821	0.84457	1.50600	1.09135	
32	1.6130E-02	6.2085E+00	1.61814	1.01333	0.74858	0.88195	1.39809	1.02812	
33	1.6910E-02	7.7132E+00	1.30810	1.01148	0.84162	0.93410	1.23184	0.99193	
34	1.7610E-02	8.5069E+00	1.19855	1.00565	0.83672	0.95394	1.15736	0.98798	
35	1.8330E-02	9.3492E+00	1.09770	1.00725	0.93217	0.97557	1.09528	0.97773	
36	1.9020E-02	9.9808E+00	1.04111	1.00484	0.96434	0.98834	1.04929	0.98063	
37	1.9700E-02	1.0276E+01	1.01499	1.00463	0.97976	0.99432	1.02994	0.97939	
38	2.0470E-02	1.0383E+01	1.01040	1.00274	0.98509	0.99551	1.02128	0.98490	
39	2.1250E-02	1.0433E+01	1.00677	1.00195	0.98757	0.99611	1.01737	0.98573	
40	2.2210E-02	1.0584E+01	1.00604	1.00337	0.99503	1.00000	1.01002	0.99607	
41	2.3170E-02	1.0634E+01	1.00121	1.00193	0.99751	1.00000	1.00499	0.99624	
42	2.4420E-02	1.0685E+01	1.00000	1.00000	1.00000	1.00000	1.00000	1.00000	
43	2.6160E-02	1.0685E+01	1.00000	1.00000	1.00000	1.00000	1.00000	1.00000	
44	2.8320E-02	1.0685E+01	1.00000	0.99602	1.00000	0.99801	0.99602	1.00200	
45	3.1090E-02	1.0635E+01	1.00000	0.99602	1.00000	0.99801	0.99602	1.00200	
46	3.4520E-02	1.0736E+01	1.00000	0.99809	1.00249	1.00000	0.99505	1.00498	
47	3.8460E-02	1.0838E+01	1.00000	0.99809	1.00746	1.00199	0.99918	1.01295	
48	4.1910E-02	1.0838E+01	1.00000	1.00025	1.00746	1.00299	0.99115	1.01194	
49	4.5720E-02	1.0838E+01	1.00000	0.99827	1.00746	1.00199	0.99918	1.01295	

77040313		SETTLES	PROFILE TABULATION			36 POINTS, DELTA AT POINT 31		
I	Y	PT2/P	P/PD	T0/T0D	M/MO	U/UD	T/TJ	R/RD=U/UD
1	0.0000*-00	1.0000**+00	2.63179	1.03945	0.00000	0.00000	2.71401	0.00000
2	9.3750*-04	2.1354**+00	2.71063	1.04050	0.33879	0.57376	2.19575	0.71154
3	1.5220*-03	2.2138**+00	2.68398	1.03572	0.33937	0.58569	2.15074	0.73090
4	2.0690*-03	2.2771**+00	2.66939	1.04147	0.43677	0.59592	2.14630	0.74133
5	2.6240*-03	2.4075**+00	2.64458	1.04035	0.42298	0.61412	2.10793	0.77049
6	3.2840*-03	2.5324**+00	2.64334	1.03416	0.43779	0.62873	2.05254	0.80578
7	3.9070*-03	2.6745**+00	2.62746	1.03273	0.45435	0.64622	2.02292	0.83934
8	4.5310*-03	2.7915**+00	2.62190	1.03300	0.46659	0.65934	1.99603	0.86605
9	5.4000*-03	3.0318**+00	2.62153	1.03063	0.49172	0.68420	1.93611	0.92641
10	6.3020*-03	3.1555**+00	2.60946	1.02837	0.50405	0.69593	1.90567	0.95299
11	7.2920*-03	3.5240**+00	2.60511	1.02924	0.53895	0.72913	1.83025	1.03792
12	8.3920*-03	3.4361**+00	2.60700	1.02733	0.57526	0.76102	1.75019	1.13360
13	9.6010*-03	4.4073**+00	2.59973	1.02479	0.61403	0.79215	1.66431	1.23737
14	1.0910*-02	4.6879**+00	2.60135	1.02631	0.63583	0.80994	1.62238	1.29867
15	1.1860*-02	5.1564**+00	2.60350	1.02527	0.67078	0.83559	1.55176	1.40192
16	1.3160*-02	5.4679**+00	2.60969	1.02502	0.69299	0.85119	1.53972	1.47234
17	1.4420*-02	5.9692**+00	2.61534	1.02231	0.72048	0.86869	1.45374	1.56291
18	1.5460*-02	6.1331**+00	2.60754	1.01995	0.73810	0.87993	1.41799	1.61626
19	1.6310*-02	6.2464**+00	2.60242	1.01656	0.74551	0.89221	1.40036	1.63949
20	1.7200*-02	6.4813**+00	2.60404	1.01030	0.76066	0.88897	1.36590	1.69491
21	1.8070*-02	6.5595**+00	2.59923	1.00857	0.76560	0.89095	1.35428	1.70340
22	1.9010*-02	6.5336**+00	2.56555	1.01013	0.76806	0.89314	1.35221	1.69455
23	1.9950*-02	6.9153**+00	2.48237	1.00636	0.78780	0.90298	1.31378	1.70617
24	2.1080*-02	7.6707**+00	2.13436	1.00632	0.83292	0.92803	1.24142	1.53593
25	2.2230*-02	8.6940**+00	1.51133	1.00479	0.89033	0.95567	1.15203	1.25426
26	2.3000*-02	9.3728**+00	1.31090	1.00415	0.87275	0.94692	1.17718	1.05448
27	2.3740*-02	9.3432**+00	1.15132	1.00266	0.92527	0.97028	1.09965	1.01631
28	2.4550*-02	1.0227**+01	1.05974	1.00096	0.97004	0.98867	1.03878	1.00863
29	2.5320*-02	1.0483**+01	1.03634	1.00113	0.98273	0.99384	1.02274	1.00706
30	2.6620*-02	1.0695**+01	1.01023	0.99975	0.99260	0.99702	1.00893	0.99830
31	2.8700*-02	1.0333**+01	1.00000	1.00000	1.00000	1.00000	1.00000	1.00000
32	3.1650*-02	1.0787**+01	1.00000	0.99991	0.99753	0.99901	1.00296	0.99666
33	3.3680*-02	1.0787**+01	1.00000	0.99732	0.99753	0.99801	1.00096	0.99705
34	3.8100*-02	1.0787**+01	1.00000	0.99991	0.99753	0.99901	1.00296	0.99666
35	4.1910*-02	1.0787**+01	1.00000	0.99533	0.99753	0.99702	0.99897	0.99805
36	4.5720*-02	1.0787**+01	1.00000	0.99533	0.99753	0.99702	0.99897	0.99805

79040317		SETTLES	PROFILE TABULATION			63 POINTS, DELTA AT POINT 28		
I	Y	PT2/P	P/PO	TO/TOD	M/MO	U/UD	T/TO	R/RD*U/UD
1	0.0000+00	1.0000+00	0.97192	1.04032	0.00000	0.00000	2.04036	0.00000
2	4.9990+04	2.4812+00	1.03984	1.01935	0.55860	0.69279	1.53817	0.46834
3	9.5450+04	2.7686+00	1.02527	1.01541	0.60055	0.73035	1.47901	0.50629
4	1.5480+03	2.9081+00	1.02138	1.01777	0.61970	0.74830	1.45811	0.52417
5	2.1410+03	3.0318+00	1.01652	1.02120	0.63611	0.76391	1.44215	0.53845
6	2.6950+03	3.1555+00	1.01059	1.02195	0.65207	0.77750	1.42171	0.55273
7	3.6530+03	3.3906+00	1.01059	1.01871	0.68126	0.80080	1.38174	0.58576
8	4.3840+03	3.4019+00	1.00777	1.02014	0.68263	0.80248	1.38196	0.58519
9	5.2350+03	3.4214+00	1.00194	1.01629	0.70862	0.82165	1.34446	0.61233
10	6.0270+03	3.5783+00	0.99417	1.01554	0.70360	0.81741	1.34967	0.60211
11	6.6500+03	3.7605+00	0.99320	1.01582	0.72458	0.83380	1.32419	0.62538
12	7.6070+03	3.9651+00	0.99028	1.01371	0.74738	0.85007	1.29369	0.65070
13	8.3310+03	4.0699+00	0.98737	1.01254	0.75878	0.85799	1.27859	0.66256
14	9.2890+03	4.2368+00	0.98445	1.01428	0.77656	0.87147	1.25938	0.68123
15	1.0150+02	4.4078+00	0.98348	1.01201	0.79435	0.88296	1.23554	0.70242
16	1.1140+02	4.6558+00	0.98251	1.01405	0.81943	0.90900	1.20875	0.73228
17	1.2230+02	5.0164+00	0.98348	1.01327	0.85454	0.92342	1.16771	0.77773
18	1.3340+02	5.1905+00	0.98445	1.01366	0.87095	0.93390	1.14976	0.79962
19	1.4430+02	5.5437+00	0.98834	1.01107	0.90333	0.95229	1.11134	0.84689
20	1.5430+02	5.7589+00	0.99125	1.01014	0.92249	0.96299	1.09976	0.87594
21	1.6540+02	6.0211+00	0.99223	1.00877	0.94528	0.97525	1.06442	0.90911
22	1.7720+02	6.3225+00	0.99125	1.00779	0.97082	0.98863	1.03703	0.94499
23	1.8880+02	6.5206+00	0.99320	1.00763	0.98723	0.99721	1.02032	0.97070
24	2.0070+02	6.5595+00	0.99514	1.00496	0.99042	0.99755	1.01444	0.97857
25	2.1150+02	6.6771+00	0.99708	1.00446	1.00000	1.00223	1.00446	0.99487
26	2.2250+02	6.6771+00	0.99806	1.00022	1.00000	1.00011	1.00022	0.99795
27	2.3340+02	6.6771+00	0.99903	1.00335	1.00000	1.00167	1.00335	0.99736
28	2.4430+02	6.6771+00	1.00000	1.00000	1.00000	1.00000	1.00000	1.00000
29	2.5430+02	6.6378+00	1.00097	0.99568	0.99631	0.99621	0.99880	0.99933
30	2.6420+02	6.6771+00	1.00194	0.99844	1.00000	0.99922	0.99844	1.00273
31	2.7410+02	6.6378+00	1.00389	0.99523	0.99681	0.99599	0.99835	1.00151
32	2.8330+02	6.5986+00	1.00583	0.99674	0.99362	0.99521	1.00320	0.99781
33	2.9670+02	6.6378+00	1.00777	0.99530	0.99681	0.99632	0.99902	1.00505
34	3.0380+02	6.5986+00	1.00777	0.99761	0.99362	0.99554	1.00388	0.99940
35	3.1450+02	6.6378+00	1.00875	0.99635	0.99681	0.99654	0.99947	1.00579
36	3.2160+02	6.6378+00	1.01069	0.99635	0.99681	0.99654	0.99947	1.00773
37	3.3050+02	6.6378+00	1.01059	0.99613	0.99681	0.99643	0.99925	1.00784
38	3.3930+02	6.6771+00	1.00875	0.99339	1.00000	0.99699	0.99399	1.01179
39	3.4800+02	6.5986+00	1.00777	0.99404	0.99362	0.99376	1.00028	1.00120
40	3.5890+02	6.6378+00	1.00777	0.99412	0.99681	0.99543	0.99724	1.00595
41	3.6800+02	6.6771+00	1.00583	0.99339	1.00000	0.99599	0.99399	1.00897
42	3.7590+02	6.5986+00	1.00389	0.99404	0.99362	0.99376	1.00028	0.99734
43	3.8280+02	6.6771+00	1.00292	0.99399	1.00000	0.99699	0.99399	1.00594
44	3.9370+02	6.6378+00	1.00194	0.99412	0.99631	0.99543	0.99724	1.00013
45	4.0340+02	6.6378+00	1.00000	0.99412	0.99681	0.99543	0.99724	0.99819
46	4.1250+02	6.6771+00	0.99806	0.99399	1.00000	0.99699	0.99399	1.00107
47	4.2110+02	6.5986+00	1.00097	0.99404	0.99362	0.99376	1.00028	0.99444
48	4.3050+02	6.5986+00	1.00292	0.99404	0.99362	0.99376	1.00028	0.99637
49	4.3990+02	6.5986+00	0.99806	0.99404	0.99362	0.99376	1.00028	0.99154
50	4.4960+02	6.5771+00	0.99611	0.99399	1.00000	0.99699	0.99399	0.99912
51	4.5900+02	6.6378+00	1.00000	0.99412	0.99681	0.99543	0.99724	0.99819
52	4.6890+02	6.5986+00	1.00292	0.99404	0.99362	0.99376	1.00028	0.99637
53	4.7980+02	6.6378+00	1.00097	0.99412	0.99681	0.99543	0.99724	0.99916
54	4.9050+02	7.0829+00	0.94140	0.99396	1.03238	1.01304	0.96290	0.99043
55	5.0010+02	7.7986+00	0.84636	0.99406	1.08710	1.03857	0.91271	0.96306
56	5.0770+02	6.4432+00	0.68659	0.99399	0.98085	0.98707	1.01272	0.66920
57	5.1130+02	6.8755+00	0.61098	0.99423	1.01536	1.09513	0.97879	0.62732
58	5.2070+02	9.3020+00	0.45493	0.99401	1.19380	1.09271	0.82255	0.59764
59	5.2860+02	1.0079+01	0.41701	0.99413	1.24533	1.10177	0.78274	0.58697
60	5.4310+02	1.0584+01	0.39815	0.99399	1.27770	1.11292	0.75870	0.58404
61	5.6290+02	1.0940+01	0.38210	0.99391	1.30005	1.12028	0.74256	0.57751
62	5.8060+02	1.1050+01	0.37998	0.99390	1.30699	1.12251	0.73774	0.57816
63	6.3500+02	1.1102+01	0.37998	0.99394	1.31008	1.12362	0.73561	0.58041

77040403		SETTLES	PROFILE TABULATION			99 POINTS, DELTA AT POINT 32			
I	Y	PT2/P	P/P3	T0/T00	M/M0	U/U0	T/T0	R/R0=U/U0	
1	0.0000+00	1.2030+00	1.07342	1.04003	0.00000	0.00000	1.33956	0.00000	
2	1.3330+03	1.2359+00	1.04931	1.01236	0.46633	0.51672	1.22779	0.44182	
3	1.4210+03	1.2645+00	1.04640	1.01245	0.49075	0.54193	1.21946	0.46520	
4	1.5550+03	1.2920+00	1.03735	1.01253	0.51350	0.55520	1.21149	0.43396	
5	1.6440+03	1.3023+00	1.03821	1.01167	0.52167	0.57344	1.20332	0.49271	
6	1.7330+03	1.3106+00	1.03811	1.01113	0.52817	0.57990	1.20549	0.49938	
7	1.7990+03	1.3364+00	1.03510	1.01106	0.54767	0.59961	1.19870	0.51778	
8	1.9320+03	1.3498+00	1.03210	1.01016	0.55742	0.60915	1.19422	0.52645	
9	2.0210+03	1.3730+00	1.02995	1.00952	0.57375	0.62530	1.18778	0.54221	
10	2.1320+03	1.3897+00	1.02759	1.00923	0.58508	0.63645	1.18331	0.55270	
11	2.2210+03	1.4046+00	1.02547	1.00872	0.59492	0.64599	1.17905	0.56206	
12	2.3540+03	1.3947+00	1.02372	1.00856	0.53842	0.63936	1.13065	0.55438	
13	2.4430+03	1.4351+00	1.02233	1.00855	0.61442	0.66489	1.17104	0.53045	
14	2.5760+03	1.4617+00	1.02050	1.00758	0.63067	0.69056	1.15649	0.59641	
15	2.6640+03	1.5094+00	1.01943	1.00691	0.65833	0.73630	1.15238	0.62502	
16	2.8420+03	1.5330+00	1.01717	1.00593	0.67142	0.71902	1.14683	0.63773	
17	2.9770+03	1.5511+00	1.01432	1.00552	0.68117	0.72807	1.14244	0.64630	
18	3.1320+03	1.6114+00	1.01224	1.00511	0.71208	0.75683	1.12962	0.67818	
19	3.2870+03	1.6535+00	1.00923	1.00437	0.73483	0.77751	1.11952	0.70091	
20	3.4210+03	1.6620+00	1.00644	1.00376	0.73650	0.77880	1.11817	0.70038	
21	3.5760+03	1.5974+00	1.00623	1.00313	0.75275	0.79334	1.11076	0.71868	
22	3.7540+03	1.5857+00	1.00849	1.00237	0.74732	0.78866	1.11192	0.71529	
23	3.8520+03	1.7569+00	1.01020	1.00196	0.77833	0.81629	1.09850	0.75067	
24	4.1300+03	1.8278+00	1.00902	1.00141	0.80933	0.84198	1.03555	0.78254	
25	4.2380+03	1.9130+00	1.00805	1.00023	0.84033	0.86993	1.07041	0.81925	
26	4.4550+03	1.9703+00	1.00633	0.99950	0.86167	0.83738	1.06057	0.84200	
27	4.6530+03	2.0545+00	1.00403	0.99974	0.89033	0.91210	1.04432	0.87361	
28	4.8410+03	2.1432+00	0.99667	1.00051	0.92000	0.94650	1.03619	0.90078	
29	5.0850+03	2.1641+00	0.99740	0.99994	0.92667	0.94135	1.03194	0.90633	
30	5.2430+03	2.2279+00	1.00140	1.00000	0.94667	0.95799	1.02437	0.93678	
31	5.4200+03	2.3077+00	1.00236	0.99951	0.97083	0.97689	1.01253	0.96709	
32	5.7070+03	2.4075+00	1.00000	1.00000	1.00000	1.00000	1.00000	1.00000	
33	5.9310+03	2.4603+00	0.99914	0.99945	1.01500	1.01131	0.99274	1.01783	
34	6.1290+03	2.5568+00	0.99837	0.99831	1.04167	1.03102	0.97957	1.05072	
35	6.3530+03	2.6311+00	0.99603	0.99839	1.06167	1.04605	0.97080	1.07324	
36	6.6190+03	2.7323+00	0.99292	0.99609	1.03833	1.06495	0.95750	1.10435	
37	6.8860+03	2.8145+00	0.99523	0.99560	1.10917	1.07934	0.94693	1.13444	
38	7.1960+03	2.9558+00	0.99420	0.99440	1.14417	1.10373	0.93057	1.17921	
39	7.4450+03	3.0318+00	0.99173	0.99317	1.16250	1.11553	0.92082	1.20144	
40	7.7950+03	3.2060+00	0.99054	0.99239	1.20333	1.14316	0.90249	1.25444	
41	8.0190+03	3.3382+00	0.98980	0.99176	1.23333	1.16239	0.88826	1.29526	
42	8.3740+03	3.4703+00	0.98738	0.99121	1.25250	1.13097	0.87501	1.33343	
43	8.6410+03	3.5395+00	0.98755	0.99058	1.27750	1.18985	0.86749	1.35452	
44	8.9280+03	3.6371+00	0.98433	0.98900	1.29833	1.20278	0.85922	1.37951	
45	9.3730+03	3.8620+00	0.97631	0.99007	1.34500	1.23154	0.83941	1.43485	
46	9.5960+03	3.9195+00	0.97357	0.99000	1.35667	1.23849	0.83337	1.44688	
47	9.8500+03	4.1234+00	0.97252	0.98954	1.39333	1.25272	0.81545	1.50595	
48	1.0220+02	4.1123+00	0.97005	0.98952	1.39500	1.26073	0.81683	1.49728	
49	1.0570+02	4.3591+00	0.96609	0.98909	1.44250	1.28745	0.79658	1.56140	
50	1.0900+02	4.4336+00	0.96071	0.98912	1.46593	1.30037	0.73698	1.58743	
51	1.1110+02	4.6558+00	0.95548	0.98833	1.49750	1.31685	0.77329	1.62706	
52	1.1700+02	4.7202+00	0.95148	0.98803	1.50917	1.32299	0.76849	1.63801	
53	1.2080+02	4.9437+00	0.94633	0.93811	1.55000	1.34432	0.75222	1.69123	
54	1.2530+02	5.1544+00	0.93903	0.93752	1.58583	1.35209	0.73773	1.73375	
55	1.2880+02	5.2935+00	0.93195	0.93756	1.60917	1.37357	0.72461	1.75698	
56	1.3330+02	5.5437+00	0.92100	0.93756	1.65033	1.39360	0.71264	1.80105	
57	1.3700+02	5.8316+00	0.90939	0.93821	1.69750	1.41574	0.69558	1.85132	
58	1.4020+02	5.9840+00	0.90135	0.93810	1.72157	1.42656	0.67657	1.87284	
59	1.4530+02	6.1703+00	0.89418	0.93734	1.75033	1.43933	0.67582	1.93308	
60	1.4900+02	6.5206+00	0.85423	0.93704	1.80417	1.46146	0.65618	1.90256	
61	1.5370+02	7.0018+00	0.81194	0.98573	1.97500	1.43926	0.63096	1.91670	
62	1.5790+02	7.2373+00	0.76664	0.98435	1.91533	1.53445	0.61665	1.87039	
63	1.6170+02	7.6707+00	0.72574	0.98416	1.96917	1.52333	0.59834	1.84675	
64	1.6560+02	7.5013+00	0.72091	0.98276	1.94533	1.51430	0.60564	1.80252	
65	1.7100+02	7.9416+00	0.66778	0.98243	1.99200	1.53094	0.59037	1.73169	
66	1.7550+02	9.3020+00	0.53281	0.94135	2.18167	1.59299	0.53315	1.59497	
67	1.7810+02	9.7852+00	0.49216	0.93014	2.24033	1.60979	0.51608	1.53518	
68	1.7990+02	1.0227+01	0.46392	0.97839	2.23333	1.62385	0.50137	1.50225	
69	1.8150+02	1.0227+01	0.45953	0.97833	2.23333	1.62385	0.50137	1.48834	
70	1.8460+02	1.0695+01	0.43323	0.97675	2.34667	1.63678	0.43649	1.45759	
71	1.8860+02	1.1414+01	0.40221	0.97611	2.42917	1.65778	0.46574	1.43167	
72	1.9230+02	1.2007+01	0.33095	0.97433	2.43417	1.67232	0.44956	1.41672	
73	1.9610+02	1.2450+01	0.36722	0.97450	2.54167	1.64353	0.43879	1.40991	
74	2.0140+02	1.2893+01	0.35466	0.97345	2.59833	1.69333	0.42800	1.40317	
75	2.0810+02	1.3467+01	0.34113	0.97151	2.64750	1.73444	0.41457	1.40269	
76	2.1410+02	1.3996+01	0.32975	0.96976	2.70033	1.71433	0.40230	1.40311	
77	2.2030+02	1.4283+01	0.32170	0.96877	2.73000	1.71918	0.39657	1.39464	
78	2.2740+02	1.4535+01	0.31734	0.96731	2.75417	1.72241	0.39110	1.39975	
79	2.3340+02	1.4654+01	0.31677	0.96627	2.75583	1.72433	0.38854	1.40555	
80	2.4030+02	1.4654+01	0.31655	0.96627	2.75583	1.72433	0.38854	1.40460	
81	2.4830+02	1.4714+01	0.31601	0.96631	2.77157	1.72564	0.38733	1.40682	
82	2.5730+02	1.4774+01	0.31516	0.96555	2.77750	1.72564	0.38601	1.40891	


79040411		SETTLES	PROFILE TABULATION		96 POINTS, DELTA AT POINT 70			
I	Y	PTZ/P	P/PD	T0/T0D	M/MD	U/UD	T/TD	R/RD=U/UD
1	0.0000+00	1.0000+00	1.21286	1.03997	0.00000	0.00000	2.00859	0.00000
2	4.8690+04	1.2960+00	1.24924	1.03315	0.28735	0.39115	1.85293	0.26371
3	6.8610+04	1.3064+00	1.23833	1.03213	0.29189	0.39668	1.84688	0.26597
4	9.2940+04	1.3320+00	1.22498	1.03054	0.30273	0.40996	1.83384	0.27385
5	1.0620+03	1.3801+00	1.21771	1.02972	0.32173	0.43332	1.81392	0.29089
6	1.1730+03	1.3947+00	1.21225	1.02840	0.32720	0.43973	1.80614	0.29514
7	1.3940+03	1.4248+00	1.20592	1.02830	0.33804	0.45291	1.79501	0.30425
8	1.6810+03	1.4351+00	1.20146	1.02757	0.34166	0.45711	1.79002	0.30681
9	1.9690+03	1.4754+00	1.19369	1.02653	0.35524	0.47316	1.77412	0.31836
10	2.1900+03	1.4894+00	1.18557	1.02520	0.35978	0.47825	1.76703	0.32088
11	2.4780+03	1.5450+00	1.18047	1.02346	0.37697	0.49806	1.74565	0.33681
12	2.6540+03	1.5792+00	1.17914	1.02277	0.38693	0.50946	1.73362	0.34652
13	2.8980+03	1.6246+00	1.16932	1.02179	0.39958	0.52374	1.71799	0.35647
14	3.0760+03	1.6347+00	1.16543	1.02036	0.40232	0.52662	1.71338	0.35820
15	3.2970+03	1.6551+00	1.16107	1.01935	0.40774	0.53237	1.70479	0.36258
16	3.4950+03	1.6902+00	1.15937	1.01815	0.41677	0.54223	1.69261	0.37140
17	3.6730+03	1.7230+00	1.15791	1.01725	0.42493	0.55108	1.68187	0.37940
18	3.8940+03	1.8197+00	1.15149	1.01600	0.44754	0.57554	1.65378	0.40073
19	4.0490+03	1.8278+00	1.14542	1.01535	0.44935	0.57731	1.65062	0.40062
20	4.2240+03	1.8464+00	1.14154	1.01467	0.45343	0.58152	1.64477	0.40360
21	4.4250+03	1.8631+00	1.14372	1.01397	0.45704	0.58517	1.63925	0.40828
22	4.6230+03	2.0107+00	1.14409	1.01379	0.45703	0.61682	1.60405	0.43995
23	4.7350+03	2.0203+00	1.14227	1.01314	0.48888	0.61848	1.60050	0.44141
24	4.9990+03	2.0447+00	1.13826	1.01378	0.49351	0.62346	1.59598	0.44466
25	5.1540+03	2.1251+00	1.13911	1.01350	0.50834	0.63852	1.57774	0.46100
26	5.3090+03	2.2091+00	1.13996	1.01264	0.52317	0.65313	1.55851	0.47773
27	5.5520+03	2.2279+00	1.13960	1.01125	0.52641	0.65589	1.55244	0.48147
28	5.7510+03	2.2279+00	1.13814	1.01023	0.52641	0.65556	1.55087	0.48110
29	5.9510+03	2.3671+00	1.13669	1.00877	0.54958	0.67770	1.52057	0.50661
30	6.0600+03	2.4812+00	1.13523	1.00895	0.56766	0.69496	1.49884	0.52637
31	6.2610+03	2.5233+00	1.13244	1.00928	0.57414	0.70116	1.49141	0.53240
32	6.4360+03	2.5568+00	1.13014	1.00899	0.57924	0.70581	1.48477	0.53723
33	6.7030+03	2.6531+00	1.13159	1.01041	0.59361	0.71953	1.46929	0.55416
34	6.9010+03	2.7556+00	1.13291	1.00976	0.60843	0.73271	1.45021	0.57234
35	7.1220+03	2.8510+00	1.13354	1.00802	0.62187	0.74400	1.43132	0.58921
36	7.3430+03	2.9081+00	1.13123	1.00823	0.62975	0.75097	1.42202	0.59740
37	7.4980+03	3.0318+00	1.12966	1.00711	0.64643	0.76491	1.40017	0.61713
38	7.7650+03	3.0562+00	1.12699	1.00655	0.64968	0.76746	1.39547	0.61981
39	8.0090+03	3.1951+00	1.12456	1.00632	0.66775	0.78251	1.37328	0.64079
40	8.2300+03	3.2314+00	1.12311	1.00672	0.67238	0.78650	1.36824	0.64559
41	8.4510+03	3.2716+00	1.12347	1.00594	0.67748	0.79037	1.36104	0.65241
42	8.7150+03	3.4284+00	1.12383	1.00625	0.69694	0.80620	1.33811	0.67710
43	9.0470+03	3.6371+00	1.12371	1.00516	0.72196	0.82535	1.30689	0.70966
44	9.2680+03	3.6648+00	1.12359	1.00475	0.72521	0.82767	1.30253	0.71396
45	9.5120+03	3.7485+00	1.12335	1.00504	0.73494	0.83520	1.29144	0.72649
46	9.8220+03	3.9195+00	1.12311	1.00552	0.75440	0.84992	1.26925	0.75206
47	9.9970+03	4.0236+00	1.12286	1.00514	0.76599	0.85822	1.25531	0.76766
48	1.0310+02	4.0826+00	1.12032	1.00533	0.77247	0.86298	1.24805	0.77466
49	1.0530+02	4.1764+00	1.11850	1.00464	0.78267	0.86995	1.23547	0.78758
50	1.0820+02	4.3108+00	1.11607	1.00491	0.79703	0.88013	1.21939	0.80556
51	1.1020+02	4.4389+00	1.11449	1.00430	0.81047	0.88910	1.20343	0.82339
52	1.1350+02	4.6192+00	1.11170	1.00442	0.82901	0.90160	1.18291	0.84740
53	1.1570+02	4.6558+00	1.10939	1.00399	0.83272	0.90382	1.17806	0.85151
54	1.1920+02	4.9835+00	1.10673	1.00410	0.85542	0.91865	1.15329	0.88156
55	1.2120+02	4.9497+00	1.10491	1.00428	0.86191	0.92286	1.14642	0.88944
56	1.2230+02	4.9165+00	1.10382	1.00418	0.85857	0.92075	1.14984	0.88390
57	1.2520+02	5.0885+00	1.10067	1.00282	0.87535	0.93060	1.13023	0.90626
58	1.2670+02	5.1564+00	1.09885	1.00254	0.88194	0.93448	1.12296	0.91442
59	1.2920+02	5.1905+00	1.09592	1.00133	0.88508	0.93614	1.11870	0.91699
60	1.3250+02	5.2935+00	1.08937	1.00127	0.89481	0.94178	1.10774	0.92659
61	1.3470+02	5.5437+00	1.08514	1.00077	0.91798	0.95528	1.08293	0.95724
62	1.3620+02	5.5437+00	1.08150	1.00077	0.91798	0.95517	1.08268	0.95414
63	1.3850+02	5.6866+00	1.07447	1.00061	0.93095	0.96270	1.06936	0.96730
64	1.4220+02	5.8316+00	1.05931	1.00051	0.94393	0.97001	1.05601	0.97303
65	1.4440+02	5.9417+00	1.05361	1.00050	0.95366	0.97543	1.04617	0.98236
66	1.4670+02	6.0211+00	1.04876	1.00014	0.96061	0.97908	1.03882	0.98844
67	1.4950+02	6.0957+00	1.04124	1.00014	0.96710	0.98262	1.03236	0.99107
68	1.5310+02	6.2844+00	1.02959	1.00044	0.98332	0.99148	1.01666	1.00409
69	1.5550+02	6.3608+00	1.02098	1.00045	0.98981	0.99491	1.01034	1.00539
70	1.5930+02	6.4818+00	1.00000	1.00000	1.00000	1.00000	1.00000	1.00000
71	1.6150+02	6.6378+00	0.98581	0.99975	1.01297	1.00653	0.97332	1.00499
72	1.6410+02	6.6378+00	0.96689	0.99777	1.01297	1.00553	0.98536	0.98668
73	1.6570+02	6.7165+00	0.95476	0.99677	1.01946	1.00830	0.97822	0.98412
74	1.6860+02	6.7560+00	0.93475	0.99465	1.02271	1.00886	0.97310	0.96910
75	1.6940+02	6.7560+00	0.92929	0.99421	1.02271	1.00863	0.97267	0.96365
76	1.7170+02	6.7165+00	0.91073	0.99348	1.01946	1.00664	0.97500	0.94029
77	1.7320+02	6.5206+00	0.89727	0.99313	1.00324	0.99823	0.99003	0.90470
78	1.7540+02	6.7957+00	0.87726	0.99321	1.02595	1.00974	0.98865	0.91447
79	1.7610+02	6.6378+00	0.86756	0.99295	1.01297	1.00310	0.98059	0.88747
80	1.7760+02	6.5986+00	0.84694	0.99270	1.00973	1.00133	0.98342	0.86236
81	1.7960+02	6.6378+00	0.81941	0.99251	1.01297	1.00288	0.98016	0.83839
82	1.8180+02	6.7165+00	0.79102	0.99217	1.01946	1.00598	0.97372	0.81723

79040412		SETTLES		PROFILE TABULATION		97 POINTS, DELTA AT POINT 72			
I	Y	PT2/P	P/PD	TO/TOD	M/MO	U/UD	T/TD	R/RO=U/UD	
1	0.0000+00	1.0000+00	1.28030	1.03935	0.00000	0.03000	2.12591	0.00000	
2	4.4270+04	1.3299+00	1.41412	1.04504	0.29563	0.40004	1.96920	0.23728	
3	5.7560+04	1.3613+00	1.40643	1.04014	0.23702	0.41445	1.94694	0.23939	
4	7.5230+04	1.3971+00	1.39746	1.03573	0.30985	0.42932	1.92437	0.31214	
5	9.7360+04	1.4644+00	1.37825	1.03560	0.33209	0.45755	1.89841	0.33218	
6	1.1730+03	1.4617+00	1.37056	1.03512	0.33120	0.45635	1.89853	0.32945	
7	1.3280+03	1.4951+00	1.36544	1.03518	0.34149	0.45903	1.89645	0.33949	
8	1.5040+03	1.5390+00	1.35331	1.03515	0.35431	0.48462	1.87084	0.35072	
9	1.7260+03	1.5634+00	1.35135	1.03516	0.36114	0.49285	1.86247	0.35760	
10	1.8310+03	1.5822+00	1.34623	1.03531	0.35626	0.49902	1.85639	0.36189	
11	2.1460+03	1.6015+00	1.33726	1.03515	0.37138	0.50509	1.84970	0.36516	
12	2.4340+03	1.6290+00	1.32573	1.03334	0.37825	0.51278	1.83782	0.36990	
13	2.7660+03	1.6724+00	1.30993	1.03162	0.38932	0.52534	1.82082	0.37770	
14	3.1620+03	1.7342+00	1.30396	1.02893	0.41733	0.54148	1.79731	0.39284	
15	3.3170+03	1.7693+00	1.29683	1.02830	0.41155	0.55003	1.78617	0.39996	
16	3.6070+03	1.8153+00	1.29243	1.02701	0.42134	0.56129	1.77048	0.40974	
17	3.8940+03	1.8402+00	1.28346	1.02666	0.42696	0.56693	1.76312	0.41263	
18	4.3360+03	1.9356+00	1.27757	1.02693	0.44535	0.58794	1.73313	0.43215	
19	4.5800+03	2.0035+00	1.27131	1.02535	0.45854	0.60126	1.71857	0.44495	
20	4.9100+03	2.0107+00	1.26502	1.02535	0.45996	0.60266	1.71679	0.44407	
21	5.3090+03	2.1072+00	1.25951	1.02377	0.47702	0.61032	1.69301	0.46203	
22	5.5940+03	2.2279+00	1.25695	1.02274	0.49716	0.64089	1.66192	0.43440	
23	5.8390+03	2.2469+00	1.25293	1.02203	0.50022	0.64382	1.65654	0.43697	
24	6.1060+03	2.3077+00	1.25003	1.01939	0.50935	0.65291	1.63395	0.43767	
25	6.4920+03	2.3671+00	1.24619	1.01930	0.51904	0.66179	1.62573	0.50729	
26	6.7460+03	2.4435+00	1.24414	1.01903	0.53129	0.67392	1.60899	0.52110	
27	7.0330+03	2.5558+00	1.24017	1.01810	0.54705	0.68837	1.59351	0.53876	
28	7.3660+03	2.7323+00	1.23477	1.01850	0.57155	0.71215	1.55250	0.56641	
29	7.5210+03	2.8014+00	1.23415	1.01840	0.58074	0.72060	1.53963	0.57762	
30	7.7420+03	2.9091+00	1.23312	1.01733	0.53475	0.73316	1.51960	0.53434	
31	8.0290+03	2.9744+00	1.23120	1.01613	0.59037	0.72883	1.52405	0.53874	
32	8.2300+03	3.0318+00	1.22890	1.01631	0.61050	0.74680	1.49637	0.51332	
33	8.4710+03	3.1305+00	1.22621	1.01634	0.62276	0.75753	1.47954	0.52778	
34	8.7810+03	3.1555+00	1.22493	1.01652	0.62532	0.76032	1.47484	0.53123	
35	9.1140+03	3.2974+00	1.22390	1.01619	0.64289	0.77442	1.45195	0.56319	
36	9.4230+03	3.3644+00	1.22416	1.01537	0.65077	0.78070	1.43920	0.66405	
37	9.7330+03	3.4856+00	1.22198	1.01475	0.65477	0.79207	1.41967	0.58178	
38	1.0110+02	3.7204+00	1.21929	1.01439	0.69133	0.81237	1.33408	0.71618	
39	1.0180+02	3.7767+00	1.21916	1.01452	0.69716	0.81774	1.37585	0.72451	
40	1.0310+02	3.9351+00	1.21890	1.01458	0.71422	0.83094	1.35322	0.74838	
41	1.0710+02	3.9313+00	1.21865	1.01353	0.71904	0.83409	1.34562	0.75538	
42	1.0970+02	4.0639+00	1.21855	1.01350	0.72823	0.84091	1.33343	0.76853	
43	1.1130+02	4.1393+00	1.21865	1.01357	0.74048	0.85001	1.31771	0.78611	
44	1.1370+02	4.2693+00	1.21865	1.01324	0.72823	0.84080	1.33305	0.76853	
45	1.1720+02	4.4523+00	1.21865	1.01377	0.76674	0.85885	1.29410	0.82457	
46	1.2010+02	4.4073+00	1.21634	1.01354	0.76236	0.86571	1.29951	0.81659	
47	1.2210+02	4.6192+00	1.21448	1.01434	0.73293	0.89033	1.24429	0.84579	
48	1.2500+02	4.7851+00	1.21455	1.01336	0.73869	0.89084	1.24407	0.86970	
49	1.2830+02	4.7851+00	1.21570	1.01420	0.79867	0.89035	1.24437	0.87042	
50	1.2980+02	4.9165+00	1.21583	1.01443	0.81094	0.89918	1.22945	0.88921	
51	1.3210+02	5.0164+00	1.21533	1.01458	0.82013	0.90524	1.21832	0.90339	
52	1.3380+02	5.0500+00	1.21593	1.01475	0.82319	0.90730	1.21478	0.90809	
53	1.3570+02	5.1305+00	1.21532	1.01423	0.83589	0.91521	1.19879	0.92783	
54	1.3850+02	5.2591+00	1.21468	1.01437	0.84201	0.91910	1.19149	0.93639	
55	1.4070+02	5.1905+00	1.21378	1.01423	0.83589	0.91521	1.19379	0.92655	
56	1.4330+02	5.2935+00	1.21212	1.01444	0.84508	0.92105	1.18789	0.93984	
57	1.4670+02	5.4679+00	1.20943	1.01413	0.86039	0.93036	1.15926	0.96232	
58	1.5000+02	5.5083+00	1.20597	1.01230	0.86339	0.93138	1.16359	0.96582	
59	1.5260+02	5.7227+00	1.20405	1.01259	0.83229	0.94282	1.14195	0.99409	
60	1.5570+02	5.7589+00	1.20213	1.01238	0.89534	0.94433	1.13771	0.99790	
61	1.5860+02	5.9417+00	1.19992	1.01135	0.90066	0.95311	1.11987	1.02116	
62	1.6150+02	6.0533+00	1.19726	1.01012	0.91028	0.95776	1.10704	1.03592	
63	1.6500+02	6.0957+00	1.19316	1.00877	0.91335	0.95895	1.10211	1.03806	
64	1.6680+02	6.0593+00	1.19085	1.00734	0.91029	0.95668	1.10344	1.03144	
65	1.7030+02	6.1708+00	1.18535	1.00663	0.91947	0.96123	1.09289	1.04255	
66	1.7410+02	6.1708+00	1.17817	1.00474	0.91947	0.96036	1.09091	1.03718	
67	1.7730+02	6.2844+00	1.16844	1.00374	0.92857	0.96502	1.07983	1.04421	
68	1.8140+02	6.3608+00	1.15947	1.00339	0.93479	0.96794	1.07219	1.04674	
69	1.8710+02	6.4818+00	1.12975	1.00135	0.94442	0.97228	1.05956	1.04556	
70	1.9330+02	6.6378+00	1.12708	1.00052	0.95657	0.97934	1.04591	1.03556	
71	1.9840+02	6.9155+00	1.09546	1.00033	0.97812	0.99328	1.02295	1.02072	
72	2.0130+02	7.2054+00	1.00000	1.00000	1.00000	1.00000	1.00000	1.00000	
73	2.0610+02	7.5860+00	0.92955	0.99950	1.02331	1.01321	0.97142	0.96954	
74	2.0730+02	7.7132+00	0.90239	0.99950	1.03720	1.01743	0.96225	0.95415	
75	2.0900+02	7.7996+00	0.86525	0.99929	1.04333	1.02014	0.95605	0.92325	
76	2.1060+02	7.9273+00	0.93556	0.99917	1.05252	1.02426	0.94702	0.90381	
77	2.1150+02	8.1073+00	0.81914	0.99857	1.06521	1.02967	0.93439	0.90256	
78	2.1230+02	8.1357+00	0.80423	0.99850	1.07133	1.03233	0.92960	0.89416	
79	2.1390+02	8.1073+00	0.76252	0.99825	1.06521	1.02946	0.93400	0.84045	
80	2.1520+02	8.5069+00	0.72734	0.99813	1.09279	1.04137	0.90812	0.83372	
81	2.1680+02	8.4173+00	0.68323	0.99801	1.08635	1.03956	0.91362	0.77674	
82	2.1790+02	8.5034+00	0.65057	0.99745	1.09934	1.04375	0.90142	0.75329	



79040415		SETTLES	PROFILE TABULATION				113 POINTS, DELTA AT POINT 68	
I	Y	PTZ/P	P/PJ	TQ/TJD	M/MD	U/UD	T/TO	R/RD=U/UD
1	0.0000+00	1.0000+00	1.93032	1.04001	0.09000	0.00000	1.89538	0.00000
2	5.9890+04	1.5950+00	1.09999	1.02037	0.41900	0.53315	1.61910	0.36218
3	6.8780+04	1.7083+00	1.09885	1.01725	0.45099	0.56734	1.58250	0.39395
4	8.4300+04	1.7645+00	1.09679	1.01457	0.45553	0.58200	1.56302	0.40840
5	9.5380+04	1.8402+00	1.09651	1.01413	0.48393	0.60141	1.54447	0.42468
6	1.0430+03	1.8300+00	1.08649	1.01453	0.49311	0.61111	1.53590	0.43230
7	1.1980+03	1.9137+00	1.08030	1.01574	0.50199	0.62058	1.52834	0.43866
8	1.3530+03	1.9968+00	1.07412	1.01595	0.51637	0.63502	1.51235	0.45101
9	1.4860+03	2.0203+00	1.06896	1.01553	0.52331	0.64218	1.50588	0.45596
10	1.6640+03	2.0276+00	1.06175	1.01707	0.52490	0.64414	1.50653	0.45397
11	1.9300+03	2.0719+00	1.05659	1.01773	0.53373	0.65327	1.49810	0.46074
12	2.1520+03	2.1174+00	1.05247	1.01323	0.54266	0.66228	1.49946	0.46797
13	2.4520+03	2.1719+00	1.04422	1.01955	0.55308	0.67290	1.48025	0.47463
14	2.6850+03	2.1825+00	1.03977	1.01831	0.55506	0.67452	1.47676	0.47460
15	3.0380+03	2.2198+00	1.03135	1.01819	0.55200	0.68110	1.46875	0.47850
16	3.3930+03	2.2382+00	1.02247	1.01757	0.57440	0.69277	1.45459	0.48697
17	3.6140+03	2.3151+00	1.01742	1.01909	0.57937	0.69762	1.44988	0.48954
18	3.8580+03	2.3471+00	1.01526	1.01647	0.58482	0.70224	1.44186	0.49447
19	4.1710+03	2.3872+00	1.01309	1.01572	0.59177	0.70848	1.43335	0.50075
20	4.5240+03	2.4192+00	1.00897	1.01412	0.59722	0.71298	1.42523	0.50474
21	4.9130+03	2.4435+00	1.00526	1.01423	0.60218	0.71760	1.42007	0.50798
22	5.1890+03	2.4812+00	1.00093	1.01282	0.60764	0.72211	1.41225	0.51179
23	5.5680+03	2.5324+00	0.99629	1.01269	0.61627	0.72973	1.40302	0.51819
24	5.8780+03	2.5875+00	0.99268	1.01155	0.62530	0.73735	1.39184	0.52589
25	6.1470+03	2.6437+00	0.98959	1.01055	0.63393	0.74498	1.39104	0.53392
26	6.5860+03	2.7232+00	0.98701	1.01021	0.64633	0.75572	1.36713	0.54560
27	6.9650+03	2.7556+00	0.98402	1.01071	0.65129	0.76022	1.36248	0.54905
28	7.2970+03	2.7734+00	0.98093	1.01037	0.65476	0.76311	1.35834	0.55103
29	7.7190+03	2.8980+00	0.97856	1.00942	0.67262	0.77801	1.33792	0.56904
30	8.1410+03	2.9333+00	0.97722	1.00830	0.68502	0.78817	1.32394	0.58180
31	8.6060+03	3.0562+00	0.97536	1.00832	0.69544	0.79660	1.31211	0.59216
32	8.9610+03	3.1807+00	0.97652	1.00852	0.71280	0.81081	1.29392	0.60816
33	9.2280+03	3.2460+00	0.96969	1.00769	0.72173	0.81762	1.29340	0.61777
34	9.6700+03	3.3906+00	0.96856	1.00722	0.74107	0.83264	1.26239	0.63884
35	1.0070+02	3.4598+00	0.97072	1.00619	0.75000	0.83911	1.25174	0.65073
36	1.0450+02	3.5240+00	0.97033	1.00625	0.75843	0.84558	1.24300	0.66042
37	1.0760+02	3.6371+00	0.97052	1.00523	0.77292	0.85597	1.22677	0.67717
38	1.1000+02	3.7838+00	0.96990	1.00571	0.79167	0.87006	1.20786	0.69865
39	1.1180+02	3.7898+00	0.96938	1.00544	0.79167	0.86995	1.20754	0.69837
40	1.1330+02	3.7888+00	0.96938	1.00544	0.79167	0.86995	1.20754	0.69837
41	1.1550+02	3.9651+00	0.96938	1.00523	0.81300	0.88519	1.19550	0.72383
42	1.1870+02	4.0404+00	0.96969	1.00516	0.82192	0.89143	1.17628	0.73497
43	1.2070+02	4.0693+00	0.97052	1.00516	0.82540	0.89385	1.17276	0.73979
44	1.2150+02	4.0996+00	0.97103	1.00545	0.82897	0.89640	1.16958	0.74423
45	1.2290+02	4.1593+00	0.97176	1.00557	0.83581	0.90125	1.16271	0.75324
46	1.2510+02	4.2368+00	0.97269	1.00534	0.84474	0.90725	1.15348	0.76505
47	1.2870+02	4.2358+00	0.97292	1.00560	0.84474	0.90737	1.15377	0.76585
48	1.3150+02	4.4078+00	0.97474	1.00630	0.86409	0.92054	1.13492	0.79062
49	1.3310+02	4.4836+00	0.97557	1.00672	0.87252	0.92643	1.12738	0.80167
50	1.3480+02	4.5015+00	0.97639	1.00665	0.87450	0.92770	1.12535	0.80490
51	1.3770+02	4.6192+00	0.97734	1.00729	0.88740	0.93636	1.11339	0.82236
52	1.4130+02	4.6558+00	0.97887	1.00728	0.89137	0.93890	1.10949	0.82836
53	1.4390+02	4.7851+00	0.97949	1.00795	0.90526	0.94302	1.09672	0.84669
54	1.4750+02	4.8335+00	0.98165	1.00861	0.91567	0.95484	1.08737	0.86200
55	1.5150+02	5.0164+00	0.98392	1.00839	0.92956	0.96350	1.07435	0.88231
56	1.5390+02	5.0385+00	0.98332	1.00791	0.93700	0.96755	1.06625	0.89274
57	1.5700+02	5.1564+00	0.98413	1.00742	0.94395	0.97167	1.05916	0.90255
58	1.6080+02	5.2247+00	0.98538	1.00677	0.95089	0.97528	1.05196	0.91402
59	1.6430+02	5.3282+00	0.98753	1.00607	0.96131	0.98106	1.04151	0.93021
60	1.6810+02	5.3973+00	0.98990	1.00539	0.96825	0.98475	1.03437	0.94241
61	1.7210+02	5.5083+00	0.99196	1.00417	0.97917	0.99041	1.02310	0.96016
62	1.7610+02	5.5792+00	0.99340	1.00325	0.99611	0.99388	1.01582	0.97195
63	1.8030+02	5.6149+00	0.99589	1.00235	0.98959	0.99538	1.01175	0.97976
64	1.8430+02	5.6149+00	0.99835	1.00142	0.99958	0.99492	1.01031	0.98265
65	1.8810+02	5.5507+00	0.99876	1.00054	0.99306	0.99642	1.00679	0.98848
66	1.9250+02	5.6865+00	0.99918	0.99931	0.99653	0.99804	1.00303	0.99420
67	1.9540+02	5.6866+00	0.99948	0.99911	0.99653	0.99804	1.00303	0.99451
68	1.9980+02	5.7227+00	1.00000	1.00000	1.00000	1.00000	1.00000	1.00000
69	2.0490+02	5.7227+00	1.00216	1.00000	1.00000	1.00000	1.00000	1.00216
70	2.1000+02	5.7227+00	1.00330	1.00000	1.00000	1.00000	1.00000	1.00330
71	2.1650+02	5.6956+00	1.00371	0.99875	0.99653	0.99746	1.00187	0.99929
72	2.2330+02	5.6356+00	1.00371	0.99757	0.99653	0.99677	1.00048	0.99999
73	2.3020+02	5.6866+00	1.00196	0.99575	0.99653	0.99536	0.99885	0.99895
74	2.3980+02	5.6866+00	1.00144	0.99357	0.99653	0.99492	0.99677	0.99958
75	2.5220+02	5.6537+00	1.00155	0.99123	0.99306	0.99180	0.99747	0.99585
76	2.5650+02	5.6507+00	0.99969	0.99174	0.99306	0.99203	0.99794	0.99377
77	2.5930+02	5.6507+00	0.99825	0.99174	0.99306	0.99215	0.99817	0.99222
78	2.6570+02	5.6537+00	0.99464	0.99257	0.99306	0.99249	0.99886	0.98829
79	2.7310+02	5.6507+00	0.99237	0.99313	0.99306	0.99272	0.99933	0.98581
80	2.8070+02	5.6537+00	0.98856	0.99313	0.99306	0.99272	0.99933	0.98202
81	2.9180+02	5.6507+00	0.98278	0.99313	0.99306	0.99272	0.99933	0.97629
82	3.0120+02	5.6149+00	0.97977	0.99317	0.99959	0.99076	1.00238	0.95772

79040416		SETTLES	PROFILE TABULATION			119 POINTS, DELTA AT POINT 71			
I	Y	PTZ/P	P/PD	T0/T0J	M/MD	U/UD	T/TD	R/RD=U/UD	
1	0.0000+00	1.0000+00	1.05031	1.04001	0.00000	0.00000	1.86207	0.00000	
2	4.4270-04	1.9197+00	1.06606	1.02051	0.50905	0.62689	1.51652	0.44068	
3	5.7560-04	1.9540+00	1.06922	1.01895	0.51660	0.63408	1.50656	0.45001	
4	7.3030-04	2.0545+00	1.05871	1.01914	0.53773	0.65533	1.49524	0.46713	
5	8.4100-04	2.1251+00	1.05661	1.01932	0.55181	0.66926	1.47099	0.48073	
6	9.7360-04	2.1825+00	1.05556	1.01771	0.56298	0.67948	1.45720	0.49219	
7	1.2390-03	2.2279+00	1.05136	1.02019	0.57143	0.68853	1.45185	0.49860	
8	1.4160-03	2.3077+00	1.04726	1.02005	0.58602	0.70235	1.43642	0.51206	
9	1.6150-03	2.3161+00	1.04453	1.02199	0.58753	0.70443	1.43757	0.51184	
10	1.8590-03	2.3471+00	1.04149	1.02140	0.59306	0.70943	1.43094	0.51635	
11	2.1680-03	2.3959+00	1.03193	1.02186	0.60161	0.71755	1.42258	0.52051	
12	2.4340-03	2.4192+00	1.02942	1.02019	0.60563	0.72069	1.41603	0.52402	
13	2.9410-03	2.5021+00	1.02332	1.01953	0.61972	0.73334	1.40031	0.53591	
14	3.2510-03	2.5568+00	1.01712	1.01843	0.62877	0.74112	1.38928	0.54259	
15	3.6270-03	2.5993+00	1.01450	1.01772	0.63581	0.74716	1.38090	0.54896	
16	3.8710-03	2.6092+00	1.01397	1.01754	0.63732	0.74843	1.37907	0.55029	
17	4.3130-03	2.6658+00	1.01103	1.01593	0.64638	0.75586	1.36745	0.55885	
18	4.6460-03	2.7329+00	1.00599	1.01521	0.65694	0.76480	1.35533	0.56767	
19	4.9330-03	2.8278+00	1.00494	1.01365	0.67153	0.77676	1.33796	0.58342	
20	5.2200-03	2.7915+00	1.00441	1.01323	0.66600	0.77188	1.34326	0.57717	
21	5.5090-03	2.8014+00	1.00273	1.01323	0.66751	0.77316	1.34162	0.57786	
22	5.8390-03	2.8990+00	1.00073	1.01192	0.68209	0.78500	1.32451	0.59311	
23	6.1930-03	2.9217+00	0.99517	1.01108	0.69561	0.79767	1.31987	0.59390	
24	6.5020-03	2.9695+00	0.99317	1.01061	0.69256	0.79336	1.31191	0.60061	
25	6.8350-03	3.0422+00	0.99443	1.01029	0.70322	0.80195	1.30051	0.61321	
26	7.2110-03	3.0562+00	0.99244	1.00907	0.70523	0.80311	1.29685	0.61460	
27	7.6100-03	3.1305+00	0.99013	1.00880	0.71579	0.81159	1.28556	0.62508	
28	7.8970-03	3.2060+00	0.98845	1.00853	0.72636	0.81994	1.27429	0.63602	
29	8.2730-03	3.2060+00	0.98887	1.00795	0.72636	0.81971	1.27356	0.63647	
30	8.6720-03	3.3234+00	0.98876	1.00617	0.74245	0.83167	1.25476	0.65536	
31	8.9150-03	3.4019+00	0.98845	1.00491	0.75302	0.83933	1.24238	0.66778	
32	9.0020-03	3.4538+00	0.98834	1.00353	0.76056	0.84456	1.23306	0.67694	
33	9.2020-03	3.5125+00	0.98729	1.00249	0.76761	0.84943	1.22456	0.68485	
34	9.4230-03	3.6490+00	0.98572	1.00151	0.78521	0.86220	1.20571	0.70488	
35	9.5780-03	3.6648+00	0.98457	1.00157	0.79722	0.86371	1.20376	0.70651	
36	9.6670-03	3.6925+00	0.98393	1.00213	0.79074	0.86650	1.20077	0.71002	
37	9.8880-03	3.7324+00	0.98435	1.00329	0.79577	0.87068	1.19711	0.71593	
38	1.0090-02	3.6371+00	0.98519	1.00312	0.78370	0.86174	1.20906	0.70218	
39	1.0400-02	3.7045+00	0.98635	1.00467	0.79225	0.86870	1.20230	0.71267	
40	1.0750-02	3.7045+00	0.98697	1.00440	0.79225	0.86859	1.20198	0.71314	
41	1.0990-02	4.0531+00	0.98719	1.00421	0.83501	0.89900	1.15914	0.76564	
42	1.1100-02	3.9485+00	0.98698	1.00442	0.82243	0.89029	1.17183	0.74985	
43	1.1210-02	4.0699+00	0.98656	1.00359	0.83702	0.90016	1.15656	0.76785	
44	1.1440-02	4.0996+00	0.98572	1.00371	0.84054	0.90260	1.15311	0.77157	
45	1.1790-02	4.2672+00	0.98456	1.00320	0.86016	0.91572	1.13335	0.79550	
46	1.2010-02	4.3294+00	0.98592	1.00331	0.86720	0.92048	1.12664	0.80543	
47	1.2120-02	4.2803+00	0.98635	1.00352	0.86167	0.91688	1.13225	0.79873	
48	1.2450-02	4.4078+00	0.98824	1.00265	0.87626	0.92617	1.11716	0.81929	
49	1.2610-02	4.3284+00	0.98908	1.00210	0.86720	0.92025	1.12607	0.80829	
50	1.2760-02	4.5150+00	0.98908	1.00318	0.88833	0.93429	1.10616	0.83540	
51	1.2980-02	4.5873+00	0.98908	1.00302	0.89638	0.93940	1.09830	0.84538	
52	1.3210-02	4.6879+00	0.98908	1.00212	0.90744	0.94602	1.08682	0.86094	
53	1.3360-02	4.5150+00	0.98908	1.00243	0.88833	0.93394	1.10533	0.83571	
54	1.3540-02	4.6558+00	0.98939	1.00142	0.90392	0.94346	1.08940	0.85685	
55	1.3800-02	4.6879+00	0.98971	1.00039	0.90744	0.94544	1.08549	0.86201	
56	1.4050-02	4.8178+00	0.99055	1.00069	0.92153	0.95414	1.07204	0.88162	
57	1.4240-02	4.9165+00	0.99170	1.00019	0.93209	0.96041	1.06169	0.89710	
58	1.4510-02	4.8835+00	0.99329	0.99961	0.92857	0.95798	1.06433	0.89402	
59	1.4820-02	4.9497+00	0.99506	1.00008	0.93561	0.96250	1.05831	0.90499	
60	1.5130-02	4.9830+00	0.99580	1.00022	0.93913	0.96471	1.05520	0.91040	
61	1.5440-02	5.1564+00	0.99632	1.00015	0.95724	0.97550	1.03852	0.93587	
62	1.5820-02	5.1905+00	0.99632	1.00042	0.95076	0.97771	1.03559	0.94064	
63	1.6100-02	5.3282+00	0.99643	1.00025	0.97485	0.98584	1.02267	0.96054	
64	1.6410-02	5.2247+00	0.99811	0.99975	0.96429	0.97945	1.03170	0.94756	
65	1.6590-02	5.7735+00	0.99916	0.99943	0.97133	0.98340	1.02501	0.95860	
66	1.6880-02	5.4328+00	1.00010	0.99927	0.98541	0.99141	1.01221	0.97955	
67	1.7190-02	5.5083+00	1.00073	0.99838	0.99236	0.99524	1.00460	0.99141	
68	1.7480-02	5.5792+00	1.00010	0.99834	1.00000	0.99942	0.99884	1.00059	
69	1.7790-02	5.5437+00	0.99947	0.99930	0.99648	0.99768	1.00241	0.99476	
70	1.8030-02	5.5792+00	0.99905	0.99954	1.00000	0.99977	0.99954	0.99929	
71	1.8360-02	5.5792+00	1.00000	1.00000	1.00000	1.00000	1.00000	1.00000	
72	1.8760-02	5.6507+00	1.00158	0.99933	1.00704	1.00383	0.99363	1.01186	
73	1.9150-02	5.6149+00	1.00289	0.99840	1.00352	1.00116	0.99530	1.00990	
74	1.9690-02	5.6149+00	1.00704	0.99655	1.00352	1.00023	0.99346	1.01391	
75	2.0260-02	5.5507+00	1.00861	0.99614	1.00704	1.00197	0.98996	1.02085	
76	2.0790-02	5.6866+00	1.00987	0.99712	1.01056	1.00441	0.98786	1.02679	
77	2.1390-02	5.5507+00	1.01250	0.99821	1.00704	1.00302	0.99202	1.02372	
78	2.1960-02	5.6507+00	1.01691	0.99650	1.00704	1.00221	0.99042	1.02901	
79	2.2560-02	5.6149+00	1.02143	0.99378	1.00352	0.99884	0.99069	1.02983	
80	2.3360-02	5.6507+00	1.02038	0.99129	1.00704	0.99954	0.99515	1.03528	
81	2.3980-02	5.5792+00	1.02343	0.99374	1.00000	0.99687	0.99374	1.02685	
82	2.4550-02	5.5792+00	1.02416	0.99629	1.00000	0.99814	0.99629	1.02606	

	M: Appr. 1.4 upstream of shock.  R Theta $\times 10^{-3}$ : 4  TW/TR: Appr. 1	8002
		QNS
Continuous tunnel with symmetric convergent nozzle. W = 0.12, H = 0.10, L = 0.53 m. PO: 95 kN/m <sup>2</sup> . T0: 290 K. Dried atmospheric air. Re/m $\times 10^{-6}$ : 14.		
DELERY J.M., COPY C., REISZ J., 1980. Analyse au vélocimètre laser bidirectionnel d'une interaction choc-couche limite turbulente avec décollement étendu. Rap. Tech. 37/7078 AY 014.  <u>And:</u> Délery (1983), J.M. Délery, private communications, data tapes.		

- 1 The test boundary layer was formed on a "half profile" or bump let into the surface of the tunnel floor. This was 0.286 m long and consisted of a 4° ramp followed by a circular arc profile with radius 0.423 m. The maximum height was 12 mm, while the ends were faired into the floor with circular arcs of radius 20 mm. The flow accelerated to supersonic velocity in the throat so formed. It then entered a shock boundary-layer interaction with the first leg at about 0.260 m from the start (X = 0) of the bump. The second leg of the interaction, and the shock in the free stream, occurred opposite the end of the bump. The two branches of the shock met at about Y = 50 mm. The pressure history is given in table 1. Measurements were made on the tunnel centreline and began at X = 0.27 m, after the start of the interaction, with the flow already separated. Reattachment occurred at about the 12<sup>th</sup> profile station (X = 0.325). A further 16 profiles were taken at increasing intervals back to X = 0.540 m. The position of the shock was controlled by an adjustable second throat mounted on the top surface with its area minimum at about X = (8) 0.524 m.
- 2 Boundary layer transition was natural and the mean flow and turbulence distributions at the onset of the interaction showed the layer to be fully developed.
- 3 Oil flow visualisations showed that the separation line was nearly straight and perpendicular to the flow, but that there was "a rather strong distortion of the reattachment line. However the presence of three-dimensional effects was not thought to alter radically the general features of the flow and the behaviour of turbulence. The shock system can be considered as steady in the sense that no large-scale oscillations of the shock were revealed by optical observations" (interferometry with short time exposure).
- 4 Wall pressure was measured at 40 tappings on the bump, 21 on the tunnel wall downstream, and also at 72 stations on the top wall. Profiles were measured normal to the tunnel axis with a LDA developed by ONERA. This was a two-component device using a modulation frequency of 7.5 MHz, allowing the simultaneous measurement of mean velocities and the Reynolds stress tensor components. The flow was seeded with incense smoke injected well upstream of the test section. The cross section of the measurement volume was about 300 micron in diameter. An experimental point is constructed from about 5000 samples. The data were processed with a DISA 55L analyser. The mean flow field was also surveyed with a holographic interferometer and the authors' sketch of the flow is reproduced above as figure 10.4.1.
- 5 The source paper presents profiles of the mean velocity components U and V, their fluctuation intensities and  $u'v'$  while the data tape (PC) gives the Mach number. This was derived from the velocity and the total temperature of the flow, measured in the settling chamber. In the boundary layer the modified Crocco temperature distribution was assumed. The wall temperature was assumed to equal the recovery temperature as runs lasted several hours. The Mach number in the free stream was also deduced from the density as measured from the holograms, assuming that entropy changes in the shocks were negligible. Profiles for stations 4, 6, 8 and 10 are interpolated by the authors from neighbouring data.
- 6 In order to complete the profile presentation in section C, the editors have set the static pressure equal to the wall value. (See the remarks in the editors' comments below.) We have chosen to set the zero for Y at the surface of the bump. We have interpolated wall pressure data for stations 18, 19, 20, 22, 23, 25, 27, and 28. The data describe the velocity field in a boundary layer interacting with a quasi-normal shock, and the succeeding recovery process.
- 7 DATA: 80020101-0128 Two-component LDV profiles for the mean and fluctuating velocities, and their cross correlation. NX = 28. Wall pressures. Holographic interferometry.

15 Editors' comments:

The entry describes the first of a series of investigations designed to provide basic data on the quasi-normal shock (QNS) boundary-layer interaction. Succeeding experiments are described in CAT8003T, and use a different, symmetrical, geometry. These experiments and many others are discussed in detail in Délery (1986)/ Délery & Marvin (1986). A wide range of similar flows has been studied by Liu & Squire (1988) and a selection are reported in CAT 8501T.

The large number of profiles, at close intervals, is most valuable. Given the desire to use only non-intrusive measurements, the data are, inevitably, functionally incomplete, requiring either pressure or density information. This might have been obtained from the interferometer, though possibly such data would not be sufficiently accurate in a region with large gradients. We repeat here our warning that without the density, the velocity fluctuation values do not give the Reynolds stresses. Skin-friction data would also have been most valuable. The separation and reattachment points were not recorded. The authors suggest that the reattachment point can be found by an interpolation to determine where the recirculation region has become vanishingly small, but are less hopeful about determining the separation point using such a procedure. The values suggested by the sketch in fig. (10.4.1) are  $X = 262$  and  $324$  mm.

The editors' assumption of constant static pressure along a normal appears reasonable for the majority of the profiles. However, inspection of the total pressure profiles suggests that the static pressure may fall by up to 8% in the outer part of the boundary layer just ahead of the shock (see the isobars in figure (10.4.1), while it is rising in the region just behind the shock. The profiles most affected are 01, 2, 5, 6, and integral values for these profiles will be inaccurate and improperly defined. The D-state has been set at the outermost point and is essentially arbitrary.

We must have some reservations as to the influence of three-dimensional effects and shock steadiness, as discussed in § 9.3 above. There is likely to be a very similar interaction on all the other three tunnel walls, with substantial secondary flows in the separated flow region. The high subsonic flow downstream will be sensitive to small changes in effective wall position and the thickened and disturbed boundary layers will give a strong displacement effect. (See for instance Schofield, 1985 and Reda & Murphy, 1973.)

The interpolated profiles 04, 06, 08, 10 have been retained at the suggestion of the authors, to assist in any reconstruction of the flow field as a whole. Since there are no wall shear-stress values, we are unable to comment on the profile quality in any detail. Turbulence profiles are presented as figures (11.2.26, 11.3.10). (Note that the representative  $R_{\theta}$  value in the heading to this entry is the authors' value for the boundary layer upstream of the data reported here.)

Table 1: Pressure distribution on the test surface.

X	$\frac{P}{P_1}$	X	$\frac{P}{P_1}$	X	$\frac{P}{P_1}$	X	$\frac{P}{P_1}$
-.0800	.7619	.1299	.6565	.2300	.3780	.3050	.5310
-.0400	.7758	.1400	.6415	.2350	.3662	.3099	.5414
-.0200	.7792	.1500	.6174	.2400	.3534	.3150	.5542
.0000	.7999	.1600	.5830	.2450	.3430	.3199	.5698
.0100	.7796	.1699	.5410	.2500	.3342	.3299	.5936
.0200	.7670	.1799	.5134	.2550	.4261	.3400	.6148
.0299	.7558	.1850	.4976	.2600	.4813	.3500	.6277
.0399	.7491	.1900	.4870	.2650	.4935	.3600	.6346
.0500	.7408	.1950	.4710	.2700	.4952	.3700	.6381
.0600	.7336	.1999	.4570	.2749	.4980	.4100	.6347
.0699	.7222	.2049	.4450	.2800	.4987	.4500	.6271
.0800	.7160	.2100	.4320	.2850	.5020	.4900	.6083
.0900	.7061	.2149	.4176	.2900	.5034	.5300	.5661
.0999	.6970	.2200	.4022	.2949	.5073	.5700	.4899
.1100	.6854	.2249	.3911	.3000	.5163	.6100	.3691
.1199	.6730						

$$P_1 = q \times 10^4 \text{ N/m}^2$$

CAT 8002	DELERY COPY, REISZ	BOUNDARY CONJUNCTIONS AND EVALUATED DATA, SI UNITS						
RUN X # RZ	MD # P00 T00	TW/TR# P4/PD TAUM	SE02W R020 02	C# CQ PIZ	H12 H32 H42	H12K H32K D2K	PW# TW UD#	PO TJ TR
80020101 2.7000E-01 INFINITE	1.1140 9.7514E+04 2.8758E+02	1.0000 1.0000 NM	7.0030E+03 9.2322E+03 5.3721E-04	NM NM NM	7.0889 1.3346 -0.0031	5.1717 1.8499 5.7671E-04	4.4558E+04 2.8160E+02 3.4000E+02	4.4659E+04 2.3007E+02 2.8160E+02
80020102 2.7500E-01 INFINITE	1.0910 9.3480E+04 2.4926E+02	1.0000 1.0000 NM	2.6556E+03 3.0921E+03 2.1220E-04	NM NM NM	23.3242 3.1506 -0.9373	11.0004 2.1892 4.1565E-04	4.4320E+04 2.8258E+02 3.3130E+02	4.4320E+04 2.3365E+02 2.8258E+02
80020103 2.8000E-01 INFINITE	1.0590 9.1135E+04 2.8791E+02	1.0000 1.0000 NM	4.3931E+03 5.0843E+03 3.5870E-04	NM NM NM	15.3073 2.1553 0.0701	16.2816 2.3175 3.4170E-04	4.4883E+04 2.8242E+02 3.2560E+02	4.4883E+04 2.3515E+02 2.8242E+02
80020104 2.8500E-01 INFINITE	1.0400 8.9663E+04 2.8771E+02	1.0000 1.0000 NM	5.9543E+03 5.7427E+03 4.3491E-04	NM NM NM	15.5627 2.1652 -0.1839	11.4400 1.9997 6.3033E-04	4.5180E+04 2.8239E+02 3.2070E+02	4.5180E+04 2.3554E+02 2.8239E+02
80020105 2.9000E-01 INFINITE	1.0570 9.1771E+04 2.8773E+02	1.0000 1.0000 NM	2.9106E+03 3.2511E+03 2.2758E-04	NM NM NM	37.9111 4.2144 0.0497	46.9219 5.5361 1.7969E-04	4.5305E+04 2.8226E+02 3.2500E+02	4.5305E+04 2.3513E+02 2.8227E+02
80020106 2.9500E-01 INFINITE	0.9761 8.4068E+04 2.8765E+02	1.0000 1.0000 NM	5.8921E+03 7.8127E+03 5.0911E-04	NM NM NM	12.1160 1.9130 0.0005	10.8626 1.9392 6.5993E-04	4.5557E+04 2.8285E+02 3.0420E+02	4.5557E+04 2.4161E+02 2.8285E+02
80020107 3.0000E-01 INFINITE	0.9937 9.7316E+04 2.8735E+02	1.0000 1.0000 NM	6.2940E+03 7.1654E+03 5.3559E-04	NM NM NM	15.4536 2.2635 -0.3044	14.2283 2.3199 5.6463E-04	4.6467E+04 2.8292E+02 3.0893E+02	4.6467E+04 2.4038E+02 2.8292E+02
80020108 3.0500E-01 INFINITE	0.9559 9.5933E+04 2.8806E+02	1.0000 1.0000 NM	1.1850E+04 1.3367E+04 1.0273E-03	NM NM NM	7.1725 1.5542 0.0294	6.3981 1.6517 1.1087E-03	4.7793E+04 2.8343E+02 2.9913E+02	4.7793E+04 2.4355E+02 2.8343E+02
80020109 3.1000E-01 INFINITE	0.9388 8.6007E+04 2.8795E+02	1.0000 1.0000 NM	1.2393E+04 1.3911E+04 1.0750E-03	NM NM NM	7.6796 1.7359 0.0124	6.8217 1.7378 1.1441E-03	4.8726E+04 2.8346E+02 2.9650E+02	4.8726E+04 2.4480E+02 2.8346E+02
80020110 3.1500E-01 INFINITE	0.9231 8.6998E+04 2.8786E+02	1.0000 1.0000 NM	1.7257E+04 1.9339E+04 1.4327E-03	NM NM NM	4.9437 1.5637 0.0374	4.3103 1.5462 1.5903E-03	4.9879E+04 2.8347E+02 2.9160E+02	4.9379E+04 2.4556E+02 2.8346E+02
80020111 3.2000E-01 INFINITE	0.9146 8.4126E+04 2.8793E+02	1.0000 1.0000 NM	2.3760E+04 2.6544E+04 2.0203E-03	NM NM NM	3.5293 1.4691 0.2143	4.0086 1.5667 1.7810E-03	5.1282E+04 2.8364E+02 2.8800E+02	5.1291E+04 2.4566E+02 2.8363E+02
80020112 3.2500E-01 INFINITE	0.8934 8.7960E+04 2.8782E+02	1.0000 1.0000 NM	2.2195E+04 2.4654E+04 1.8959E-03	NM NM NM	3.6124 1.5355 0.0314	3.1399 1.5282 2.0563E-03	5.2380E+04 2.8370E+02 2.8220E+02	5.2380E+04 2.4420E+02 2.8370E+02
80020113 3.3000E-01 INFINITE	0.8859 8.8993E+04 2.8771E+02	1.0000 1.0000 NM	2.3892E+04 2.6517E+04 2.0215E-03	NM NM NM	3.3371 1.5444 0.1436	2.9237 1.5374 2.1747E-03	5.3424E+04 2.8365E+02 2.8010E+02	5.3424E+04 2.4368E+02 2.8365E+02
80020114 3.4000E-01 INFINITE	0.8650 9.0242E+04 2.8784E+02	1.0000 1.0000 NM	2.7876E+04 3.0903E+04 2.3371E-03	NM NM NM	2.5090 1.5829 0.7397	2.2509 1.5751 2.5119E-03	5.5332E+04 2.8394E+02 2.7470E+02	5.5332E+04 2.5030E+02 2.8394E+02
80020115 3.5000E-01 INFINITE	0.8492 9.0435E+04 2.8791E+02	1.0000 1.0000 NM	3.0251E+04 3.3308E+04 2.5476E-03	NM NM NM	2.3047 1.5164 0.0338	1.9723 1.6098 2.7265E-03	5.6493E+04 2.8414E+02 2.6980E+02	5.6493E+04 2.5163E+02 2.8414E+02
80020116 3.6000E-01 INFINITE	0.8358 9.0246E+04 2.8803E+02	1.0000 1.0000 NM	3.0220E+04 3.3174E+04 2.5606E-03	NM NM NM	2.1227 1.5455 0.0259	1.7985 1.6402 2.7369E-03	5.7114E+04 2.8436E+02 2.6640E+02	5.7114E+04 2.5272E+02 2.8435E+02
80020117 3.7000E-01 INFINITE	0.8316 9.0374E+04 2.8798E+02	1.0000 1.0000 NM	3.0853E+04 3.3850E+04 2.6152E-03	NM NM NM	2.0003 1.5762 0.0195	1.6910 1.6719 2.7859E-03	5.7429E+04 2.8434E+02 2.6520E+02	5.7429E+04 2.5299E+02 2.8434E+02
80020118 3.8000E-01 INFINITE	0.8291 9.0412E+04 2.8798E+02	1.0000 1.0000 NM	3.0906E+04 3.3770E+04 2.6115E-03	NM NM NM	1.9096 1.7050 0.0109	1.5973 1.7024 2.7764E-03	5.7500E+04 2.8436E+02 2.6450E+02	5.7500E+04 2.5317E+02 2.8435E+02
80020119 3.9000E-01 INFINITE	0.8273 9.9954E+04 2.8800E+02	1.0000 1.0000 NM	3.0694E+04 3.3632E+04 2.6167E-03	NM NM NM	1.9526 1.7235 0.0048	1.5299 1.7263 2.7748E-03	5.7420E+04 2.8438E+02 2.6400E+02	5.7420E+04 2.5332E+02 2.8439E+02
80020120 4.0000E-01 INFINITE	0.8246 8.7759E+04 2.8798E+02	1.0000 1.0000 NM	3.1273E+04 3.4253E+04 2.6728E-03	NM NM NM	1.7905 1.7510 0.0052	1.4745 1.7483 2.8226E-03	5.7330E+04 2.8439E+02 2.6380E+02	5.7330E+04 2.5335E+02 2.8438E+02
80020121 4.1000E-01 INFINITE	0.8254 9.3417E+04 2.8810E+02	1.0000 1.0000 NM	2.9308E+04 3.2657E+04 2.5539E-03	NM NM NM	1.7525 1.7687 0.0056	1.4404 1.7664 2.6954E-03	5.7123E+04 2.8451E+02 2.6380E+02	5.7123E+04 2.5349E+02 2.8450E+02
80020122 4.2000E-01 INFINITE	0.8294 8.9592E+04 2.8801E+02	1.0000 1.0000 NM	3.0978E+04 3.3960E+04 2.5503E-03	NM NM NM	1.7254 1.7824 0.0018	1.4099 1.7903 2.7869E-03	5.7060E+04 2.8433E+02 2.6460E+02	5.7060E+04 2.5319E+02 2.8433E+02
80020123 4.3000E-01 INFINITE	0.8233 8.9159E+04 2.8807E+02	1.0000 1.0000 NM	3.0416E+04 3.3342E+04 2.6155E-03	NM NM NM	1.6954 1.7957 0.0029	1.3939 1.7949 2.7426E-03	5.6790E+04 2.8445E+02 2.6460E+02	5.6790E+04 2.5324E+02 2.8445E+02

## CAT 8002 DELERY,COPY,REISZ BOUNDARY CONDITIONS AND EVALUATED DATA, SI UNITS

RUN	NO *	TM/TR*	RE224	CF	M12	M12K	P#	PD
X *	P00	PM/PO	RE223	CJ	M32	M32K	Td	TJ
RZ	T00	TAUW	DZ	PIZ	M42	D2K	UD#	TR
80020124	0.8348	1.3000	3.7193**04	NM	1.5991	1.3589	5.6433**04	5.6433**04
4.5000*-01	8.9108**04	1.0000	3.3126**04	NM	1.8058	1.8041	2.8432**02	2.5276**02
INFINITE	2.8799**02	NM	2.5911**03	NM	-0.0017	2.7153**03	2.6610**02	2.8433**02
80020125	0.4360	1.0000	2.6095**04	NM	1.6423	1.3552	5.5900**04	5.5300**04
4.7000*-01	8.8208**04	1.0000	2.6636**04	NM	1.8352	1.8340	2.8445**02	2.5279**02
INFINITE	2.8812**02	NM	2.2626**03	NM	0.0039	2.3560**03	2.6550**02	2.8445**02
80020126	0.8597	1.0000	2.7149**04	NM	1.6524	1.3281	5.4747**04	5.4747**04
4.9000*-01	8.8605**04	1.0000	2.9951**04	NM	1.8466	1.8455	2.8424**02	2.5105**02
INFINITE	2.9808**02	NM	2.3274**03	NM	0.0020	2.4226**03	2.7280**02	2.8423**02
80020127	0.8827	1.0000	2.4277**04	NM	1.6595	1.3182	5.3100**04	5.3100**04
5.1000*-01	8.8151**04	1.0000	2.6925**04	NM	1.8640	1.8631	2.8403**02	2.4923**02
INFINITE	2.8807**02	NM	2.0796**03	NM	0.0004	2.1596**03	2.7940**02	2.8403**02
80020128	0.9471	1.0000	2.3591**04	NM	1.6900	1.3057	4.9500**04	4.9500**04
5.4000*-01	8.8190**04	1.0000	2.5534**04	NM	1.9776	1.8766	2.8356**02	2.4430**02
INFINITE	2.8913**02	NM	1.7968**03	NM	0.0044	2.0774**03	2.9680**02	2.8357**02

80020101 DELERY,COPY,REISZ PROFILE TABULATION 16 POINTS, DELTA AT POINT 16								
I	Y	PT2/P	P/PO	TO/TOD	M/MD	U/UD	T/TD	R/RD=U/UD
1	0.0000**00	1.0000**00	1.00000	0.97919	0.00000	0.00000	1.22358	0.00000
2	1.0000*-03	1.0085**00	1.00000	0.93942	0.09857	-0.10671	1.17192	-0.09105
3	1.5000*-03	1.0017**00	1.00000	0.79356	0.04454	-0.04435	0.99145	-0.04474
4	2.0000*-03	1.0045**00	1.00000	0.95566	0.07194	0.07847	1.19303	0.06577
5	2.5000*-03	1.0466**00	1.00000	1.00145	0.22898	0.25453	1.23560	0.20600
6	3.0000*-03	1.1632**00	1.00000	1.00227	0.42021	0.46029	1.19985	0.38363
7	3.5000*-03	1.3841**00	1.00000	1.00153	0.62397	0.65647	1.14086	0.58418
8	4.0000*-03	1.6109**00	1.00000	1.00138	0.75404	0.79853	1.09231	0.73105
9	4.5000*-03	1.7728**00	1.00000	1.00158	0.84320	0.86941	1.06313	0.81778
10	5.0000*-03	1.9339**00	1.00000	1.00130	0.89079	0.91059	1.04495	0.87142
11	6.0000*-03	2.0035**00	1.00000	1.00217	0.93739	0.95000	1.02709	0.92494
12	7.0000*-03	2.0325**00	1.00000	1.00142	0.94812	0.95853	1.02207	0.93783
13	8.0000*-03	2.0620**00	1.00000	1.00201	0.95996	0.96765	1.01842	0.95014
14	9.0000*-03	2.1149**00	1.00000	1.00134	0.97764	0.98265	1.01027	0.97266
15	1.0000*-02	2.1174**00	1.00000	1.00106	0.97853	0.98324	1.00963	0.97385
D 16	1.2000*-02	2.1798**00	1.00000	1.00000	1.00000	1.00000	1.00000	1.00000

## 80020101 Delery/Copy/Reisz Turbulence Data

X = 2.7000E-01 DELTA = 1.2000E-02 UINF = 2.9680E+02

I	Y	U	V	M	U'	V'	-U'V'
		UINF	UINF		UINF	UINF	UINF2
1	1.0000E-3	-1.2224E-1	3.1176E-2	1.1020E-1	1.4367E-1	6.3106E-2	4.6884E-3
2	1.5000E-3	-5.0809E-2	2.6021E-2	4.9800E-2	1.8932E-1	7.7257E-2	8.2461E-3
3	2.0000E-3	8.9892E-2	1.9768E-2	8.0320E-2	2.3608E-1	8.1772E-2	1.1067E-2
4	2.5000E-3	2.9158E-1	-4.3228E-3	2.5600E-1	2.8042E-1	9.5620E-2	1.4076E-2
5	3.0000E-3	5.2729E-1	-6.1590E-3	4.6980E-1	3.0037E-1	9.0195E-2	1.2022E-2
6	3.5000E-3	7.6348E-1	-3.8376E-3	6.9760E-1	2.3710E-1	6.6846E-2	7.5355E-3
7	4.0000E-3	9.1476E-1	-5.1617E-3	8.5420E-1	1.6792E-1	5.5526E-2	4.5862E-3
8	4.5000E-3	9.9596E-1	5.8962E-3	9.4270E-1	1.1338E-1	5.2190E-2	3.3500E-3
9	5.0000E-3	1.0431E+0	-9.2554E-3	9.9590E-1	7.2540E-2	4.6867E-2	2.0570E-3
10	6.0000E-3	1.0883E+0	-8.2042E-3	1.0480E+0	5.0135E-2	4.9191E-2	1.4633E-3
11	7.0000E-3	1.0980E+0	-1.1125E-2	1.0600E+0	4.1611E-2	4.7069E-2	1.2147E-3
12	8.0000E-3	1.1085E+0	-1.6516E-2	1.0720E+0	4.7945E-2	6.7251E-2	2.4021E-3
13	9.0000E-3	1.1257E+0	-2.3420E-2	1.0930E+0	3.6388E-2	4.6563E-2	1.0909E-3
14	1.0000E-2	1.1263E+0	-2.6048E-2	1.0940E+0	3.8443E-2	4.8012E-2	1.2464E-3
D 15	1.2000E-2	1.1456E+0	-3.9522E-2	1.1180E+0	3.5849E-2	4.8383E-2	1.3202E-3

80020108		DELERY,COPY,REISZ		PROFILE TABULATION		26 POINTS, DELTA AT POINT 26			
I	Y	PT2/P	P/PO	TQ/TQD	M/MQ	U/UD	T/TD	R/RD=U/UD	
1	0.0000E+00	1.0000E+00	1.00000	0.98393	0.00000	0.00000	1.16374	0.00000	
2	1.0000E-03	1.0084E+00	1.00000	0.99917	0.11476	-0.12461	1.17896	-0.10569	
3	1.5000E-03	1.0060E+00	1.00000	0.99969	0.07703	-0.10542	1.18035	-0.08931	
4	2.0000E-03	1.0025E+00	1.00000	0.99743	0.06260	-0.06797	1.17892	-0.05766	
5	2.5000E-03	1.0008E+00	1.00000	0.99608	0.03570	-0.03875	1.17784	-0.03290	
6	3.0000E-03	1.0002E+00	1.00000	0.61176	0.01694	0.01441	0.72352	0.01991	
7	3.5000E-03	1.0010E+00	1.00000	0.95881	0.04026	0.04286	1.13370	0.03781	
8	4.0000E-03	1.0061E+00	1.00000	0.98218	0.09727	0.10475	1.15967	0.09033	
9	4.5000E-03	1.0170E+00	1.00000	0.97798	0.16257	0.17442	1.15115	0.15152	
10	5.0000E-03	1.0330E+00	1.00000	0.98623	0.22576	0.24269	1.15569	0.21000	
11	5.5000E-03	1.0538E+00	1.00000	0.99038	0.28727	0.30859	1.15397	0.26742	
12	6.0000E-03	1.0843E+00	1.00000	0.99234	0.35778	0.38315	1.14686	0.33409	
13	6.5000E-03	1.1202E+00	1.00000	0.99261	0.42463	0.45269	1.13656	0.39830	
14	7.0000E-03	1.1591E+00	1.00000	0.99399	0.48562	0.51555	1.12707	0.45742	
15	7.5000E-03	1.2197E+00	1.00000	0.99535	0.56523	0.59612	1.11231	0.53593	
16	8.0000E-03	1.3134E+00	1.00000	0.99722	0.66576	0.69542	1.09108	0.63737	
17	8.5000E-03	1.3555E+00	1.00000	0.99784	0.70489	0.73320	1.08195	0.67766	
18	9.0000E-03	1.4335E+00	1.00000	0.99809	0.77006	0.79472	1.06507	0.74617	
19	9.5000E-03	1.4897E+00	1.00000	0.99966	0.81243	0.83450	1.05508	0.79094	
20	1.0000E-02	1.5532E+00	1.00000	0.99991	0.85647	0.87462	1.04284	0.83869	
21	1.1000E-02	1.6597E+00	1.00000	0.99972	0.92321	0.93380	1.02307	0.91275	
22	1.2000E-02	1.7308E+00	1.00000	0.99989	0.96359	0.96891	1.01106	0.95831	
23	1.4000E-02	1.7934E+00	1.00000	1.00000	1.00000	1.00000	1.00000	1.00000	
24	1.6000E-02	1.8243E+00	1.00000	1.00000	1.01266	1.01070	0.99613	1.01462	
25	1.8000E-02	1.8096E+00	1.00000	0.99936	1.00523	1.00435	0.99824	1.00612	
D 26	2.0000E-02	1.7994E+00	1.00000	1.00000	1.00000	1.00000	1.00000	1.00000	

80020108 Delery/Copy/Reisz Turbulence Data

X = 3.0500E-01 DELTA = 2.0000E-02 UINF = 2.9680E+02

I	Y	U UINF	V UINF	X	U' UINF	V' UINF	-U'V' UINF <sup>2</sup>
1	1.0000E-3	-1.2557E-1	-2.7955E-3	1.0970E-1	1.6840E-1	9.5687E-2	4.7497E-3
2	1.5000E-3	-1.0623E-1	8.4771E-4	9.2750E-2	1.8410E-1	1.0499E-1	6.1244E-3
3	2.0000E-3	-6.8497E-2	-3.5782E-3	5.9840E-2	2.0310E-1	1.1685E-1	8.8523E-3
4	2.5000E-3	-3.9050E-2	-2.2557E-3	3.4130E-2	2.1941E-1	1.3154E-1	1.1534E-2
5	3.0000E-3	1.4518E-2	-1.1557E-2	1.6190E-2	2.5539E-1	1.3794E-1	1.5836E-2
6	3.5000E-3	4.3194E-2	-8.8814E-3	3.8480E-2	2.5927E-1	1.4474E-1	1.7755E-2
7	4.0000E-3	1.0556E-1	-1.4107E-2	9.2980E-2	2.8568E-1	1.4960E-1	2.0570E-2
8	4.5000E-3	1.7577E-1	-2.6253E-2	1.5540E-1	2.9208E-1	1.5485E-1	2.2000E-2
9	5.0000E-3	2.4458E-1	-2.8474E-2	2.1580E-1	3.0593E-1	1.5788E-1	2.4282E-2
10	5.5000E-3	3.1098E-1	-3.0927E-2	2.7460E-1	3.1082E-1	1.6095E-1	2.4520E-2
11	6.0000E-3	3.8612E-1	-3.4872E-2	3.4200E-1	3.1614E-1	1.5320E-1	2.3975E-2
12	6.5000E-3	4.5620E-1	-3.8679E-2	4.0590E-1	3.1637E-1	1.5179E-1	2.1376E-2
13	7.0000E-3	5.1954E-1	-3.8410E-2	4.6420E-1	3.1580E-1	1.4606E-1	1.9389E-2
14	7.5000E-3	6.0074E-1	-3.9892E-2	5.4030E-1	3.0623E-1	1.3534E-1	1.6084E-2
15	8.0000E-3	7.0081E-1	-3.8949E-2	6.3640E-1	2.8635E-1	1.2385E-1	1.3895E-2
16	8.5000E-3	7.3888E-1	-3.6152E-2	6.7380E-1	2.7975E-1	1.1924E-1	1.2430E-2
17	9.0000E-3	8.0088E-1	-3.2834E-2	7.3610E-1	2.4869E-1	1.1122E-1	9.4233E-3
18	9.5000E-3	8.4097E-1	-2.2392E-2	7.7660E-1	2.2965E-1	1.0425E-1	8.3551E-3
19	1.0000E-2	8.8140E-1	-1.6995E-2	8.1870E-1	2.0020E-1	9.6092E-2	6.2901E-3
20	1.1000E-2	9.4104E-1	-4.5013E-3	8.8250E-1	1.5273E-1	8.5276E-2	4.7338E-3
21	1.2000E-2	9.7642E-1	8.9555E-4	9.2110E-1	1.0162E-1	6.9575E-2	2.2034E-3
22	1.4000E-2	1.0077E+0	1.1220E-2	9.5590E-1	5.4043E-2	5.2527E-2	9.4380E-4
23	1.6000E-2	1.0185E+0	1.1631E-2	9.6800E-1	3.4198E-2	3.6826E-2	1.6029E-4
24	1.8000E-2	1.0121E+0	1.1024E-2	9.6090E-1	2.8268E-2	3.1071E-2	3.2251E-6
D 25	2.0000E-2	1.0077E+0	7.2305E-3	9.5590E-1	2.3929E-2	2.5644E-2	4.3365E-5

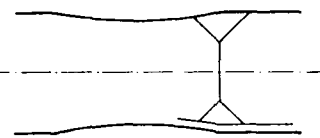
80020128		DELERY,COPYREISZ		PROFILE TABULATION		26 POINTS, DELTA AT POINT 26			
Z	Y	PT2/P	P/PD	TOT/TOU	M/MO	U/UD	T/TD	R/RD=U/UD	
1	0.0000E+00	1.0000E+00	1.00000	0.98415	0.00000	0.00000	1.16070	0.00000	
2	1.0000E-03	1.4035E+00	1.00000	0.99937	0.75293	0.77898	1.07038	0.72776	
3	2.0000E-03	1.4541E+00	1.00000	1.00022	0.79326	0.81671	1.05999	0.77049	
4	3.0000E-03	1.4804E+00	1.00000	0.99998	0.81311	0.83491	1.05432	0.79189	
5	4.0000E-03	1.4982E+00	1.00000	0.99975	0.82610	0.84670	1.05049	0.80600	
6	5.0000E-03	1.5018E+00	1.00000	0.99963	0.82874	0.84906	1.04963	0.80891	
7	6.0000E-03	1.5231E+00	1.00000	0.99932	0.84384	0.86287	1.04562	0.82523	
8	7.0000E-03	1.5280E+00	1.00000	0.99975	0.84722	0.86590	1.04460	0.82894	
9	8.0000E-03	1.5421E+00	1.00000	0.99971	0.85693	0.87466	1.04181	0.83956	
10	9.0000E-03	1.5571E+00	1.00000	0.99955	0.86707	0.88376	1.03887	0.85069	
11	1.0000E-02	1.5630E+00	1.00000	0.99935	0.87097	0.88713	1.03744	0.85511	
12	1.1000E-02	1.5784E+00	1.00000	0.99941	0.88111	0.89623	1.03460	0.86625	
13	1.2000E-02	1.5922E+00	1.00000	0.99960	0.89009	0.90431	1.03222	0.87608	
14	1.3000E-02	1.6033E+00	1.00000	0.99935	0.89716	0.91071	1.03044	0.88331	
15	1.4000E-02	1.6178E+00	1.00000	0.99997	0.90624	0.91890	1.02791	0.89385	
16	1.5000E-02	1.6321E+00	1.00000	0.99991	0.91511	0.92655	1.02516	0.90381	
17	1.6000E-02	1.6483E+00	1.00000	1.00010	0.92493	0.93531	1.02257	0.91466	
18	1.7000E-02	1.6622E+00	1.00000	0.99962	0.93327	0.94239	1.01963	0.92424	
19	1.8000E-02	1.6726E+00	1.00000	0.99973	0.93939	0.94778	1.01793	0.93109	
20	2.0000E-02	1.7003E+00	1.00000	0.99949	0.95544	0.96159	1.01291	0.94933	
21	2.2000E-02	1.7300E+00	1.00000	0.99972	0.97213	0.97608	1.00815	0.96819	
22	2.4000E-02	1.7454E+00	1.00000	0.99939	0.98057	0.98315	1.00527	0.97800	
23	2.6000E-02	1.7573E+00	1.00000	0.99985	0.98701	0.98888	1.00379	0.98515	
24	2.8000E-02	1.7709E+00	1.00000	0.99957	0.99430	0.99495	1.00130	0.99365	
25	3.0000E-02	1.7796E+00	1.00000	0.99977	0.99894	0.99899	1.00009	0.99890	
D 26	3.2000E-02	1.7816E+00	1.00000	1.00000	1.00000	1.00000	1.00000	1.00000	

80020128 Delery/Copy/Reisz Turbulence Data

X = 5.4000E-01 DELTA = 3.2000E-02 UINF = 2.9680E+02

Z	Y	U UINF	V UINF	M	U' UINF	V' UINF	-U'V' UINF2
1	1.0000E-3	7.7898E-1	-1.6567E-3	7.1310E-1	8.5344E-2	4.0364E-2	1.0809E-3
2	2.0000E-3	8.1671E-1	-6.2264E-3	7.5130E-1	8.1840E-2	4.8349E-2	1.1738E-3
3	3.0000E-3	8.3491E-1	-2.9434E-3	7.7010E-1	8.1031E-2	5.7345E-2	1.0904E-3
4	4.0000E-3	8.4670E-1	-3.3053E-3	7.8240E-1	7.8841E-2	6.2230E-2	1.1749E-3
5	5.0000E-3	8.4906E-1	-4.5115E-3	7.8490E-1	8.0964E-2	6.5600E-2	1.5110E-3
6	6.0000E-3	8.6287E-1	-1.4185E-3	7.9920E-1	7.8673E-2	7.0586E-2	1.3077E-3
7	7.0000E-3	8.6590E-1	-2.9067E-3	8.0240E-1	7.9582E-2	7.2170E-2	1.5666E-3
8	8.0000E-3	8.7466E-1	-3.1664E-3	8.1160E-1	7.7022E-2	7.2204E-2	1.5847E-3
9	9.0000E-3	8.8376E-1	-1.0876E-2	8.2120E-1	7.9009E-2	7.3349E-2	1.6994E-3
10	1.0000E-2	8.8713E-1	-2.5071E-3	8.2490E-1	7.7493E-2	7.3922E-2	2.1285E-3
11	1.1000E-2	8.9623E-1	-3.4063E-3	8.3450E-1	7.7055E-2	7.2776E-2	1.9276E-3
12	1.2000E-2	9.0431E-1	-5.3639E-3	8.4360E-1	7.5539E-2	7.0519E-2	1.8447E-3
13	1.3000E-2	9.1071E-1	-4.3834E-3	8.4970E-1	7.6550E-2	6.9811E-2	1.8504E-3
14	1.4000E-2	9.1880E-1	-6.1489E-3	8.5830E-1	7.4629E-2	6.6442E-2	1.9139E-3
15	1.5000E-2	9.2655E-1	-5.5121E-3	8.6670E-1	7.3585E-2	6.8632E-2	1.8753E-3
16	1.6000E-2	9.3531E-1	-9.4306E-3	8.7600E-1	7.0485E-2	6.6071E-2	1.8470E-3
17	1.7000E-2	9.4239E-1	-8.6186E-3	8.8390E-1	6.9306E-2	6.3646E-2	1.5359E-3
18	1.8000E-2	9.4778E-1	-7.3888E-3	8.8970E-1	6.7588E-2	6.1927E-2	1.6290E-3
19	2.0000E-2	9.6159E-1	-8.5849E-3	9.0490E-1	5.8962E-2	5.5627E-2	1.0645E-3
20	2.2000E-2	9.7608E-1	-1.2032E-2	9.2070E-1	5.1348E-2	4.7473E-2	8.1394E-4
21	2.4000E-2	9.8315E-1	-1.1681E-2	9.2870E-1	4.6125E-2	4.5047E-2	6.9270E-4
22	2.6000E-2	9.8888E-1	-1.1018E-2	9.3480E-1	3.8713E-2	3.8106E-2	3.5781E-4
23	2.8000E-2	9.9495E-1	-1.0758E-2	9.4170E-1	3.4704E-2	3.3962E-2	3.4499E-4
24	3.0000E-2	9.9899E-1	-1.3588E-2	9.4610E-1	2.9805E-2	2.9973E-2	2.1773E-4
D 25	3.2000E-2	1.0000E+0	-1.1557E-2	9.4710E-1	2.5836E-2	2.7217E-2	1.2510E-4



	M: 1.26, 1.30, 1.45 (nominal ahead of shock)	8003
	R Theta $\times 10^{-3}$ : 2-3 TW/TR: Appr. 1	QNS
Continuous tunnel with symmetric contoured nozzle. W = 0.12, H = 0.10, L = 0.53 m. P0: 90 kN/m <sup>2</sup> . T0: 300 K. Dried atmospheric air. Re/m $\times 10^{-6}$ : 14.		
COPY C., REISZ J., 1980-1983. Analyses expérimentales d'une interaction choc-couche limite turbulente à M = 1.26, 1.30 & 1.45. ONERA R.T. 42, 44 & 59/7078. And: Délerly (1983), CAT8002T, J.M. Délerly, private communication and data tapes.		

- 1 The test boundary layer was formed on the floor of the tunnel downstream of the nozzle throat, formed by inserts let into the floor and the roof. The forepart of these was a circular arc with radius 0.452 m (01/02) or 0.4 m (03), faired into the floor with a 20 mm radius. The coordinates of the afterparts ( $X = 0$  at the start of the bump) are given in tables 1 & 2 below. The maximum heights were 5.14 mm (01/02) and 10 mm (03). The throat was approximately (E) 0.2 m from the start of the parallel part of the tunnel. An adjustable second throat about (E) 0.63 m from the start was used to control the position of the shock wave, and isolate the flow from disturbances originating in the diffuser.
- 8 Measurements started upstream of the wall pressure minimum. Separation was not observed for series 01 or 02 - nominally "incipient", but for 03 it was separated over the approximate range  $0.195 < X < 0.24$  m. The range of measurements and the approximate shock positions on the tunnel centreline were:

Series:	Range of profile X-values:	NX:	Shock at:
01	$0.105 < X < 0.280$	22	0.128
02	$0.130 < X < 0.320$	20	0.163
03	$0.160 < X < 0.340$	17	0.203

Wall pressure was measured at 35 points on the tunnel roof and 56 points on the floor. The distribution for series 02 is given in table 3. Instrumentation and procedures were the same as for Délerly et al., CAT8002, save that there was no interferometric survey reported. The profiles were supplemented by traverses made at constant Y both in the "inviscid" flow, and at low values of Y near the shock foot.

- As for CAT8002T, the editors have presented the data obtained from the magnetic tape (PC) with the additional assumption that errors introduced by setting the pressure for a profile at the wall value will not be too serious, so as to present functionally complete data. The editors have interpolated these pressure values to the X-values of the profiles. There are three series at increasing nominal peak pre-shock Mach number. The profiles cover the boundary layer as it passes through the shock/boundary-layer interaction and recovers downstream, with no separation, incipient separation and a relatively small recirculation zone.

- § DATA: 80030101-0317. Two-component LDV profiles for the mean and fluctuating velocities, and their cross correlation. NX = 22, 20 & 17. Wall pressures.

#### Editors' Comments:

- 15 These studies continue the work done in the asymmetric arrangement of CAT8002T, and the same general criticisms apply. The interactions here are not so extended - two of them not involving separation - so that three-dimensional effects would not play so strong a role. Taken together, within those reservations, they provide impressively complete coverage of the velocity field of a side-wall bounded quasi-normal shock boundary-layer interaction. The experiment is again discussed in Délerly (1986), Délerly & Marvin (1986).

The editors' assumption of constant static pressure along a normal again leads to dubious values near the interaction. On the evidence of the total pressure profiles, profiles 0102-7, 0204/5, 0302-8 seem to be significantly affected. The assumed pressure is up to 50% too high in front of the final shock (0106). The low values behind the shock are not so marked, and could not be seen in series 02. Integral values in this region are wrongly evaluated and in any case have little meaning.

Again, the lack of wall shear-stress values makes it impossible for us to carry out our usual detailed profile criticism.

However, downstream mean-flow profiles are plotted above in figures (10.4.3-5) using wall shear stress values calculated from the ZPG correlation of Fernholz (1971). Turbulence data are shown in figures (11.2.27-28) and (11.3.11-12).

Table 1: Coordinates of test surface for series 01 & 02.

X, mm	Z, mm	X <sub>1</sub>	Z	X <sub>1</sub>	Z
0	5.141	46	3.064	92	0.636
2	137	48	2.928	94	570
4	123	50	794	96	608
6	100	52	661	98	450
8	068	54	532	100	396
10	028	56	405	102	345
12	4.979	58	281	104	298
14	922	60	159	106	255
16	856	62	041	108	217
18	782	64	1.924	110	181
20	699	66	812	112	150
22	608	68	701	114	121
24	508	70	594	116	097
26	400	72	490	118	075
28	284	74	389	120	057
30	162	76	292	122	041
32	033	78	198	124	028
34	3.901	80	107	126	017
36	764	82	020	128	010
38	625	84	0.936	130	004
40	484	86	856	132	0
42	344	88	779		
44	203	90	706		

Table 2: Coordinates of test surface for series 03.

X, mm	Z, mm	X <sub>1</sub>	Z	X <sub>1</sub>	Z
0	9.997	64	5.723	128	0.993
2	991	66	519	130	913
4	975	68	318	132	836
6	949	70	119	134	764
8	914	72	4.922	136	695
10	869	74	729	138	630
12	815	76	540	140	569
14	751	78	354	142	511
16	677	80	171	144	458
18	595	82	3.993	146	408
20	504	84	818	148	361
22	403	86	647	150	318
24	294	88	480	152	278
26	176	90	317	154	241
28	048	92	157	156	208
30	8.912	94	002	158	177
32	767	96	2.851	160	150
34	614	98	704	162	125
36	453	100	561	164	103
38	284	102	422	166	082
40	109	104	287	168	060
42	7.928	106	156	170	043
44	741	108	029	172	029
46	550	110	1.907	174	019
48	354	112	788	176	010
50	155	114	674	178	004
52	6.954	116	564	180	0
54	751	118	459		
56	545	120	357		
58	340	122	260		
60	134	124	167		
62	5.928	126	078		

Table 3: Pressure distribution on test surface for series 02.

X	$\frac{P}{P_1}$	X	$\frac{P}{P_1}$	X	$\frac{P}{P_1}$	X	$\frac{P}{P_1}$
-.1120	.7139	.0830	.4665	.1630	.5300	.2680	.6395
-.0720	.7364	.0880	.4371	.1680	.5480	.2780	.6408
-.0520	.7342	.0980	.4105	.1780	.5748	.2880	.6416
-.0320	.7344	.1030	.3960	.1830	.5870	.2980	.6407
-.0120	.7427	.1080	.3915	.1880	.5977	.3080	.6415
-.0020	.7653	.1130	.3845	.1980	.6144	.3180	.6405
.0080	.7295	.1180	.3817	.2030	.6198	.3280	.6406
.0180	.6832	.1230	.3774	.2080	.6279	.3380	.6403
.0280	.6468	.1280	.3746	.2180	.6308	.3780	.6378
.0380	.6105	.1380	.3684	.2230	.6325	.4180	.6296
.0480	.5784	.1430	.3626	.2280	.6341	.4580	.6090
.0580	.5450	.1480	.3596	.2380	.6357	.4980	.5724
.0680	.5085	.1530	.4179	.2480	.6382	.5380	.4996
.0780	.4758	.1580	.4994	.2580	.6384	.5780	.3863

$$P_1 = 9.6 \times 10^4 \text{ N/m}^2$$

CAT 9903		COPY, REISS		BOUNDARY CONDITIONS AND EVALUATED DATA, SI UNITS							
RUN	MD *	TW/TR*	RE02M	CE	H12	H12K	Pd4	PD			
X *	POD	PW/PD	RE02D	CJ	H32	H32K	T4	TD			
RZ	YOD	TAUM *	D2	PI2	H42	D2K	UD*	TR			
80030101	1.2440	1.0000	2.4620E+02	NM	2.3039	1.8001	3.5290E+04	3.5280E+04			
1.0500E-01	9.0658E+04	1.0000	1.2003E+03	NM	1.4923	1.8920	2.7987E+02	2.1911E+02			
INFINITE	2.8693E+02	NM	3.3547E-05	NM	0.1430	8.8463E-05	3.6923E+02	2.7987E+02			
80030102	1.2940	1.0000	1.7745E+03	NM	2.2391	1.6492	3.4560E+04	3.4560E+04			
1.1500E-01	9.4979E+04	1.0000	2.1931E+03	NM	1.9256	1.9240	2.7934E+02	2.1494E+02			
INFINITE	2.8691E+02	NM	1.4594E-04	NM	0.0946	1.5215E-04	3.8030E+02	2.7933E+02			
80030103	1.3060	1.0000	2.2460E+03	NM	2.1966	1.5911	3.7800E+04	3.7800E+04			
1.2000E-01	1.0559E+05	1.0000	2.7858E+03	NM	1.9119	1.9100	2.7933E+02	2.1394E+02			
INFINITE	2.8692E+02	NM	1.5697E-04	NM	0.0968	1.7570E-04	3.8300E+02	2.7933E+02			
80030104	1.3120	1.0000	3.9987E+03	NM	2.1792	1.4492	4.2300E+04	4.2300E+04			
1.2200E-01	1.1914E+05	1.0000	4.3444E+03	NM	1.9902	1.8964	2.7926E+02	2.1343E+02			
INFINITE	2.8691E+02	NM	2.5746E-04	NM	0.0162	2.7522E-04	3.8430E+02	2.7927E+02			
80030105	1.3200	1.0000	7.7521E+03	NM	2.3113	1.4777	4.5000E+04	4.5000E+04			
1.2500E-01	1.2814E+05	1.0000	9.5550E+03	NM	1.9485	1.8409	2.7914E+02	2.1272E+02			
INFINITE	2.8685E+02	NM	4.7734E-04	NM	-0.0336	5.2390E-04	3.8600E+02	2.7914E+02			
80030106	1.2890	1.0000	1.5996E+04	NM	2.2164	1.4174	4.8600E+04	4.8600E+04			
1.2700E-01	1.3266E+05	1.0000	1.9740E+04	NM	1.7874	1.7799	2.7953E+02	2.1540E+02			
INFINITE	2.8698E+02	NM	7.4084E-04	NM	-0.0214	1.0579E-03	3.7930E+02	2.7953E+02			
80030107	1.0600	1.0000	7.5525E+03	NM	2.1739	1.6526	4.9500E+04	4.9500E+04			
1.3000E-01	1.0063E+05	1.0000	9.8587E+03	NM	1.7693	1.7552	2.8267E+02	2.3529E+02			
INFINITE	2.8816E+02	NM	5.5657E-04	NM	0.0067	6.1179E-04	3.2600E+02	2.8267E+02			
80030108	0.9263	1.0000	3.7204E+03	NM	3.4221	2.7473	5.1750E+04	5.1750E+04			
1.3500E-01	9.0094E+04	1.0000	4.1737E+03	NM	1.4464	1.4489	2.8364E+02	2.4584E+02			
INFINITE	2.7503E+02	NM	3.0934E-04	NM	-0.0038	3.5232E-04	2.9120E+02	2.8364E+02			
80030109	0.9016	1.0000	5.0673E+03	NM	3.1327	2.6169	5.3100E+04	5.3100E+04			
1.4000E-01	8.9964E+04	1.0000	3.0441E+03	NM	1.5019	1.4970	2.8398E+02	2.4787E+02			
INFINITE	2.8817E+02	NM	4.2355E-04	NM	0.0154	4.7043E-04	2.8460E+02	2.8399E+02			
80030110	0.8909	1.0000	5.3190E+03	NM	2.9031	2.4282	5.4720E+04	5.4720E+04			
1.4500E-01	9.1643E+04	1.0000	7.0211E+03	NM	1.5499	1.5415	2.8384E+02	2.4454E+02			
INFINITE	2.8799E+02	NM	5.1926E-04	NM	0.0106	5.7083E-04	2.8160E+02	2.8383E+02			
80030111	0.9732	1.0000	5.5050E+03	NM	2.8228	2.3743	5.5710E+04	5.5710E+04			
1.5000E-01	9.1553E+04	1.0000	7.3112E+03	NM	1.5436	1.5361	2.8392E+02	2.4979E+02			
INFINITE	2.9788E+02	NM	5.4542E-04	NM	0.0137	5.9301E-04	2.7670E+02	2.8392E+02			
80030112	0.8575	1.0000	7.7696E+03	NM	2.4755	2.0992	5.6880E+04	5.6880E+04			
1.5500E-01	9.1942E+04	1.0000	4.5693E+03	NM	1.5994	1.5915	2.8411E+02	2.5103E+02			
INFINITE	2.8795E+02	NM	5.4172E-04	NM	0.0276	6.9455E-04	2.7240E+02	2.8411E+02			
80030113	0.9450	1.0000	3.2247E+03	NM	2.3150	1.7563	5.7510E+04	5.7510E+04			
1.6000E-01	9.1758E+04	1.0000	7.0510E+03	NM	1.5170	1.6099	2.8414E+02	2.5191E+02			
INFINITE	2.8788E+02	NM	5.8339E-04	NM	0.0210	7.3463E-04	2.6990E+02	2.8414E+02			
80030114	0.8261	1.0000	3.4116E+03	NM	2.1737	1.8366	5.8950E+04	5.8950E+04			
1.7000E-01	9.2249E+04	1.0000	1.0311E+04	NM	1.6353	1.6295	2.8426E+02	2.5124E+02			
INFINITE	2.8735E+02	NM	7.8235E-04	NM	0.0168	8.3997E-04	2.6360E+02	2.8425E+02			
80030115	0.4144	1.0000	3.1538E+03	NM	1.7015	1.6043	5.9580E+04	5.9580E+04			
1.9000E-01	9.2137E+04	1.0000	1.0000E+04	NM	1.7075	1.7033	2.8433E+02	2.5413E+02			
INFINITE	2.8734E+02	NM	7.4513E-04	NM	0.0194	9.0992E-04	2.6030E+02	2.8433E+02			
80030116	0.4082	1.0000	1.3058E+04	NM	1.7652	1.6504	6.0030E+04	6.0030E+04			
1.9000E-01	9.2257E+04	1.0000	1.0977E+04	NM	1.5483	1.6935	2.8449E+02	2.5469E+02			
INFINITE	2.8795E+02	NM	4.4206E-04	NM	0.0072	8.9541E-04	2.5980E+02	2.8449E+02			

CAT 8003		COPY, REISL		BOUNDARY CONDITIONS AND EVALUATED DATA, SI UNITS							
RUN X # RZ	NO # POD TOD	Td/TR# PM/PO TAUM #	RED2W RED2D D2	CF CQ PI2	H12 H32 H42	H12K H32K D2K	P4# T4 U3#	P3# TJ TR			
80030117	0.8017	1.0000	1.0026**04	NM	1.4007	1.5095	6.0120**04	6.0120**04			
2.0000*-01	9.1738**04	1.0000	1.0929**04	NM	1.7346	1.7312	2.8464**02	2.5524**02			
INFINITE	2.8805**02	NM	3.4524**04	NM	0.0125	8.9237**04	2.5480**02	2.8464**02			
80030118	0.8007	1.0000	1.0349**04	NM	1.7503	1.4515	6.0300**04	6.0307**04			
2.1000*-01	9.1982**04	1.0000	1.1278**04	NM	1.7514	1.7491	2.8461**02	2.5529**02			
INFINITE	2.3801**02	NM	3.7290**04	NM	0.0032	9.1682**04	2.5650**02	2.8461**02			
80030119	3.7979	1.0000	9.9060**03	NM	1.6764	1.4107	6.0210**04	6.0210**04			
2.2000*-01	9.1590**04	1.0000	1.0798**04	NM	1.7773	1.7752	2.8462**02	2.5547**02			
INFINITE	2.8830**02	NM	3.3914**04	NM	0.0055	8.7893**04	2.5570**02	2.8462**02			
80030120	0.8002	1.0000	1.0314**04	NM	1.4369	1.3564	6.0120**04	6.0120**04			
2.4000*-01	9.1652**04	1.0000	1.1249**04	NM	1.8030	1.8014	2.8470**02	2.5540**02			
INFINITE	2.8811**02	NM	3.7259**04	NM	0.0084	9.1053**04	2.5540**02	2.8471**02			
80030121	0.7943	1.0000	1.0715**04	NM	1.6089	1.3321	6.0120**04	6.0120**04			
2.6000*-01	9.1128**04	1.0000	1.1661**04	NM	1.8152	1.8137	2.8470**02	2.5578**02			
INFINITE	2.8805**02	NM	3.1396**04	NM	0.0058	9.5114**04	2.5470**02	2.8470**02			
80030122	0.7962	1.0000	1.0381**04	NM	1.5676	1.2979	6.0120**04	6.0120**04			
2.8000*-01	9.1299**04	1.0000	1.1846**04	NM	1.8254	1.8241	2.8459**02	2.5556**02			
INFINITE	2.8796**02	NM	3.2516**04	NM	0.0020	9.6151**04	2.5523**02	2.8459**02			
80030201	1.2950	1.0000	1.9652**03	NM	2.2351	1.6166	3.3480**04	3.3430**04			
1.3000*-01	9.1837**04	1.0000	2.3044**03	NM	1.9126	1.9102	2.7967**02	2.1520**02			
INFINITE	2.8716**02	NM	1.5874**04	NM	0.0343	1.6735**04	3.8030**02	2.7367**02			
80030202	1.3060	1.0000	2.3568**03	NM	4.1830	3.3506	3.2943**04	3.2943**04			
1.4000*-01	9.2017**04	1.0000	2.3230**03	NM	1.7176	1.7105	2.7962**02	2.1415**02			
INFINITE	2.8722**02	NM	2.0132**04	NM	0.1819	2.3073**04	3.8320**02	2.7362**02			
80030203	1.3220	1.0000	2.3116**03	NM	2.4859	1.7063	3.2670**04	3.2670**04			
1.5000*-01	9.3292**04	1.0000	2.8906**03	NM	1.9591	1.8543	2.7990**02	2.1307**02			
INFINITE	2.8755**02	NM	1.9623**04	NM	0.0126	2.1316**04	3.8630**02	2.7980**02			
80030204	1.3330	1.0000	6.4649**03	NM	2.4352	1.5463	4.1220**04	4.1220**04			
1.5500*-01	1.1949**05	1.0000	3.0834**03	NM	1.7953	1.7799	2.7973**02	2.1217**02			
INFINITE	2.8757**02	NM	4.3049**04	NM	-0.0154	4.8199**04	3.4930**02	2.7793**02			
80030205	1.2990	1.0000	1.4240**04	NM	2.4997	1.7033	4.6170**04	4.6170**04			
1.6000*-01	1.2775**05	1.0000	1.7623**04	NM	1.7490	1.7317	2.8047**02	2.1533**02			
INFINITE	2.8803**02	NM	3.7706**04	NM	0.0119	9.9139**04	3.4223**02	2.8047**02			
80030206	0.9854	1.0000	5.4644**03	NM	3.4623	2.7846	4.8603**04	4.8603**04			
1.6500*-01	2.0450**04	1.0000	5.2091**03	NM	1.5155	1.5050	2.8162**02	2.3984**02			
INFINITE	2.8647**02	NM	4.4626**04	NM	-0.0095	5.0605**04	3.0605**02	2.8162**02			
80030207	0.9329	1.0000	5.8224**03	NM	3.2335	2.6666	4.9950**04	4.9950**04			
1.7000*-01	8.7590**04	1.0000	7.6544**03	NM	1.5226	1.5139	2.8327**02	2.4505**02			
INFINITE	2.8770**02	NM	5.9140**04	NM	0.0020	6.4772**04	2.9280**02	2.8327**02			
80030208	0.9347	1.0000	7.3275**03	NM	3.2172	2.6394	5.1030**04	5.1030**04			
1.7500*-01	8.9863**04	1.0000	3.7893**03	NM	1.5078	1.4992	2.8340**02	2.4439**02			
INFINITE	2.8746**02	NM	6.5029**04	NM	0.0003	7.2754**04	2.9390**02	2.8339**02			
80030209	0.9109	1.0000	8.7292**03	NM	3.0163	2.5128	5.2200**04	5.2200**04			
1.8000*-01	8.9340**04	1.0000	9.7493**03	NM	1.5307	1.5222	2.8396**02	2.4712**02			
INFINITE	2.8813**02	NM	7.3328**04	NM	0.0100	8.0946**04	2.8710**02	2.8395**02			
80030210	0.8874	1.0000	9.8367**03	NM	2.5607	2.2181	5.4090**04	5.4090**04			
1.9000*-01	9.0247**04	1.0000	1.0921**04	NM	1.5624	1.5546	2.8382**02	2.4372**02			
INFINITE	2.8789**02	NM	3.2110**04	NM	0.0099	8.9409**04	2.8060**02	2.8382**02			
80030211	0.8643	1.0000	1.0595**04	NM	2.4100	2.0131	5.5440**04	5.5440**04			
2.0000*-01	9.0256**04	1.0000	1.1693**04	NM	1.5009	1.5037	2.8410**02	2.5055**02			
INFINITE	2.8798**02	NM	3.3229**04	NM	0.0110	9.5693**04	2.7430**02	2.8403**02			
80030212	0.8507	1.0000	1.1201**04	NM	2.1683	1.8015	5.6250**04	5.6250**04			
2.1000*-01	9.0281**04	1.0000	1.2336**04	NM	1.6394	1.6334	2.8413**02	2.5151**02			
INFINITE	2.8791**02	NM	3.4376**04	NM	0.0083	1.0168**03	2.7050**02	2.8413**02			
80030213	0.8460	1.0000	1.0755**04	NM	2.0373	1.6784	5.6790**04	5.6790**04			
2.2000*-01	9.0704**04	1.0000	1.2053**04	NM	1.6749	1.6595	2.8413**02	2.5188**02			
INFINITE	2.8733**02	NM	3.2112**04	NM	0.0021	9.8782**04	2.6920**02	2.8419**02			
80030214	0.8504	1.0000	1.0930**04	NM	1.9525	1.6090	5.7060**04	5.7060**04			
2.3000*-01	9.1552**04	1.0000	1.2091**04	NM	1.6950	1.6906	2.8431**02	2.5163**02			
INFINITE	2.8809**02	NM	3.1327**04	NM	0.0042	9.7745**04	2.7050**02	2.8431**02			
80030215	0.8338	1.0000	1.0423**04	NM	1.8223	1.4971	5.7240**04	5.7240**04			
2.4000*-01	9.0230**04	1.0000	1.1437**04	NM	1.7368	1.7335	2.8450**02	2.5299**02			
INFINITE	2.8916**02	NM	3.8412**04	NM	0.0060	9.3756**04	2.6590**02	2.8450**02			
80030216	0.8293	1.0000	1.0215**04	NM	1.7770	1.4565	5.7240**04	5.7240**04			
2.5000*-01	8.9866**04	1.0000	1.1178**04	NM	1.7534	1.7508	2.8445**02	2.5324**02			
INFINITE	2.8807**02	NM	3.7151**04	NM	0.0029	9.2094**04	2.6460**02	2.8445**02			
80030217	0.8183	1.0000	2.1279**03	NM	1.7641	1.4485	5.7510**04	5.7510**04			
2.6000*-01	9.9297**04	1.0000	3.9851**03	NM	1.7563	1.7547	2.8452**02	2.5404**02			
INFINITE	2.8806**02	NM	7.9710**04	NM	0.0011	8.3125**04	2.6150**02	2.8452**02			
80030218	0.8232	1.0000	1.0844**04	NM	1.4838	1.3736	5.7600**04	5.7600**04			
2.8000*-01	8.7538**04	1.0000	1.1365**04	NM	1.7926	1.7905	2.8443**02	2.5383**02			
INFINITE	2.8733**02	NM	3.3055**04	NM	-0.0015	9.7519**04	2.6209**02	2.8443**02			

## CAT 8003 COPY, REISZ BOUNDARY CONDITIONS AND EVALUATED DATA, SI UNITS

RUN X RZ	MD # P00 T00	TW/TR# PW/PO TAUM #	RE02J RE02N J2	CF CJ PI2	M12 M32 M42	M12K M12K M2K	P4# T4 UJ#	P0 TJ T2
80030219	0.8129	1.0000	1.1052**04	NM	1.6342	1.3415	5.7690**04	5.7690**04
3.0000*-01	3.9080**04	1.0000	1.2073**04	NM	1.8096	1.8068	2.8461**02	2.8461**02
INFINITE	2.8611**02	NM	1.5717**04	NM	0.0048	9.9939**04	2.6000**02	2.8461**02
80030220	0.8108	1.0000	1.0665**04	NM	1.6037	1.3157	5.7690**04	5.7690**04
3.2000*-01	8.8892**04	1.0000	1.1646**04	NM	1.8254	1.8239	2.8462**02	2.8462**02
INFINITE	2.8810**02	NM	9.2613**04	NM	0.0046	9.6382**04	2.5940**02	2.8462**02
80030301	1.4350	1.0000	1.4542**03	NM	3.0427	2.1261	2.8080**04	2.8080**04
1.6000*-01	9.3897**04	1.0000	2.3916**03	NM	1.3556	1.8528	2.7773**02	2.8087**02
INFINITE	2.8642**02	NM	1.6371**04	NM	0.0523	1.8113**04	4.0380**02	2.7773**02
80030302	1.4840	1.0000	3.3516**03	NM	2.9972	1.9062	3.0600**04	3.0600**04
1.3500*-01	1.1056**05	1.0000	4.4019**03	NM	1.9148	1.4037	2.7787**02	1.9845**02
INFINITE	2.8704**02	NM	2.5920**04	NM	-0.0064	2.9039**04	4.2100**02	2.7787**02
80030303	1.4470	1.0000	4.0151**03	NM	3.2345	2.1067	3.9160**04	3.9160**04
1.9000*-01	1.3358**05	1.0000	1.1755**04	NM	1.7408	1.7171	2.7851**02	2.0100**02
INFINITE	2.8751**02	NM	5.7154**04	NM	-0.0134	6.6906**04	4.1700**02	2.7851**02
80030304	1.2750	1.0000	7.3058**03	NM	4.4323	3.4384	4.0500**04	4.0500**04
1.9500*-01	1.0848**05	1.0000	9.9777**03	NM	1.5623	1.6379	2.8011**02	2.1592**02
INFINITE	2.8745**02	NM	5.2399**04	NM	0.0404	6.0127**04	3.7650**02	2.3011**02
80030305	1.2300	1.0000	4.6162**03	NM	4.5384	3.5347	4.1407**04	4.1407**04
2.0000*-01	1.0443**05	1.0000	1.1663**04	NM	1.7108	1.6868	2.7975**02	2.1730**02
INFINITE	2.8566**02	NM	7.0039**04	NM	0.0314	7.9358**04	3.6520**02	2.7975**02
80030306	1.0950	1.0000	4.2633**03	NM	9.5655	7.8289	4.1940**04	4.1940**04
2.0500*-01	8.8995**04	1.0000	4.9896**03	NM	1.5468	1.5622	2.7731**02	2.2427**02
INFINITE	2.8301**02	NM	3.5034**04	NM	0.0254	4.1735**04	3.3170**02	2.7731**02
80030307	1.0250	1.0000	3.2648**03	NM	14.1774	11.4317	4.2570**04	4.2570**04
2.1000*-01	8.3085**04	1.0000	3.7478**03	NM	1.4382	1.4549	2.8949**02	2.3597**02
INFINITE	2.8565**02	NM	2.8994**04	NM	-0.0356	3.4972**04	3.1600**02	2.8949**02
80030308	1.0330	1.0000	6.4233**03	NM	8.9180	7.4350	4.4010**04	4.4010**04
2.2000*-01	8.6614**04	1.0000	7.3904**03	NM	1.5079	1.5216	2.6277**02	2.3737**02
INFINITE	2.8803**02	NM	5.5136**04	NM	0.0209	6.2745**04	3.1910**02	2.8745**02
80030309	1.0280	1.0000	1.1145**04	NM	5.3632	4.7452	4.6170**04	4.6170**04
2.3000*-01	9.0326**04	1.0000	1.2796**04	NM	1.4777	1.4950	2.8276**02	2.3774**02
INFINITE	2.8799**02	NM	3.1714**04	NM	0.0677	9.9208**04	3.1780**02	2.8775**02
80030310	0.9943	1.0000	1.5857**04	NM	3.7300	3.1201	4.8690**04	4.8690**04
2.4000*-01	9.1770**04	1.0000	1.8074**04	NM	1.5225	1.5127	2.8294**02	2.4022**02
INFINITE	2.8791**02	NM	1.2848**03	NM	0.0332	1.4273**03	3.0960**02	2.8295**02
80030311	0.9605	1.0000	1.3704**04	NM	2.9909	2.4566	5.1120**04	5.1120**04
2.5000*-01	3.2465**04	1.0000	2.1123**04	NM	1.5520	1.5408	2.8299**02	2.4284**02
INFINITE	2.8765**02	NM	1.5047**03	NM	0.0255	1.6683**03	3.0010**02	2.8299**02
80030312	0.9323	1.0000	2.1202**04	NM	2.4948	2.0463	5.2920**04	5.2920**04
2.6000*-01	9.2736**04	1.0000	2.3783**04	NM	1.5909	1.5826	2.9339**02	2.4522**02
INFINITE	2.8782**02	NM	1.7076**03	NM	0.0225	1.8732**03	2.9270**02	2.8333**02
80030313	0.9015	1.0000	1.9913**04	NM	2.4911	2.0421	5.4270**04	5.4270**04
2.7000*-01	9.1937**04	1.0000	2.2179**04	NM	1.5006	1.5329	2.8363**02	2.4749**02
INFINITE	2.8792**02	NM	1.6262**03	NM	0.0173	1.7752**03	2.8440**02	2.8364**02
80030314	0.8834	1.0000	2.1323**04	NM	2.1205	1.7343	5.5170**04	5.5170**04
2.8000*-01	9.1656**04	1.0000	2.3653**04	NM	1.6448	1.6432	2.8384**02	2.4702**02
INFINITE	2.8789**02	NM	1.7542**03	NM	0.0127	1.8994**03	2.7950**02	2.8384**02
80030315	0.8471	1.0000	2.0155**04	NM	1.9411	1.5915	5.6430**04	5.6430**04
3.0000*-01	9.0231**04	1.0000	2.2180**04	NM	1.6903	1.6866	2.8414**02	2.5179**02
INFINITE	2.8791**02	NM	1.7013**03	NM	0.0056	1.8226**03	2.6950**02	2.8415**02
80030316	0.8178	1.0000	1.9462**04	NM	1.7864	1.4582	5.7420**04	5.7420**04
3.2000*-01	8.9102**04	1.0000	2.1294**04	NM	1.7290	1.7268	2.8440**02	2.5394**02
INFINITE	2.8771**02	NM	1.6807**03	NM	0.0034	1.7423**03	2.6130**02	2.8440**02
80030317	0.8056	1.0000	1.8415**04	NM	1.7373	1.4441	5.8050**04	5.8050**04
3.4000*-01	9.8983**04	1.0000	2.0087**04	NM	1.7550	1.7525	2.8459**02	2.5434**02
INFINITE	2.8803**02	NM	1.6007**03	NM	0.0094	1.6851**03	2.5799**02	2.8459**02

80030301		COPY, REISZ		PRFLE TABULATION		17 POINTS, DELTA AT POINT 17			
I	Y	PTZ/P	P/PD	TO/TDD	M/MD	U/UD	T/TD	R/RD+U/UD	
1	0.0000E+00	1.0000E+00	1.00000	0.96956	0.00000	0.00000	1.36900	0.00000	
2	6.0000E-04	2.0819E+00	1.00000	0.99640	0.75261	0.80381	1.14067	0.70468	
3	8.0000E-04	2.2011E+00	1.00000	0.99676	0.78467	0.83138	1.12261	0.74058	
4	1.0000E-03	2.4133E+00	1.00000	0.99805	0.83763	0.87579	1.09320	0.80113	
5	1.2000E-03	2.6248E+00	1.00000	0.99752	0.88641	0.91435	1.06403	0.85933	
6	1.4000E-03	2.7849E+00	1.00000	0.99820	0.92125	0.94143	1.04429	0.90151	
7	1.6000E-03	2.9115E+00	1.00000	0.99807	0.94774	0.96120	1.02862	0.93446	
8	1.8000E-03	2.9971E+00	1.00000	0.99734	0.96516	0.97389	1.01818	0.95650	
9	2.0000E-03	3.0527E+00	1.00000	0.99826	0.97631	0.98219	1.01208	0.97046	
10	2.5000E-03	3.1198E+00	1.00000	0.99827	0.98955	0.99170	1.00436	0.98740	
11	3.0000E-03	3.1448E+00	1.00000	0.99864	0.99443	0.99536	1.00189	0.99349	
12	3.5000E-03	3.1591E+00	1.00000	0.99858	0.99721	0.99732	1.00021	0.99711	
13	4.0000E-03	3.1627E+00	1.00000	0.99906	0.99791	0.99805	1.00028	0.99777	
14	5.0000E-03	3.1807E+00	1.00000	0.99900	1.00139	1.00049	0.99819	1.00230	
15	6.0000E-03	3.1843E+00	1.00000	0.99851	1.00209	1.00073	0.99729	1.00345	
16	7.0000E-03	3.2023E+00	1.00000	0.99944	1.00557	1.00366	0.99620	1.00749	
17	8.0000E-03	3.1735E+00	1.00000	1.00000	1.00000	1.00000	1.00000	1.00000	

80030301

Copy/Reisz

Turbulence Data

X = 1.6000E-01 DELTA = 8.0000E-03 UINF = 2.5790E+02

I	Y	U UINF	V UINF	M	U' UINF	V' UINF	-U'V' UINF2
1	6.0000E-4	1.2772E+0	-1.2586E-1	1.0800E+0	1.0896E-1	5.9829E-2	2.4687E-3
2	8.0000E-4	1.3211E+0	-1.2346E-1	1.1260E+0	1.0845E-1	5.1183E-2	3.0761E-3
3	1.0000E-3	1.3916E+0	-1.2264E-1	1.2020E+0	9.0655E-2	4.7111E-2	2.2597E-3
4	1.2000E-3	1.4529E+0	-1.3009E-1	1.2720E+0	7.6464E-2	4.2613E-2	1.6854E-3
5	1.4000E-3	1.4959E+0	-1.2935E-1	1.3220E+0	6.6150E-2	4.0171E-2	1.4148E-3
6	1.6000E-3	1.5273E+0	-1.3172E-1	1.3600E+0	5.2889E-2	3.3928E-2	7.9233E-4
7	1.8000E-3	1.5475E+0	-1.3606E-1	1.3850E+0	4.3350E-2	2.9093E-2	5.2396E-4
8	2.0000E-3	1.5607E+0	-1.3827E-1	1.4010E+0	3.6840E-2	2.7472E-2	2.1304E-4
9	2.5000E-3	1.5758E+0	-1.3625E-1	1.4200E+0	3.1694E-2	2.8193E-2	3.7797E-4
10	3.0000E-3	1.5816E+0	-1.3594E-1	1.4270E+0	3.0485E-2	2.8488E-2	3.1272E-4
11	3.5000E-3	1.5847E+0	-1.3528E-1	1.4310E+0	2.8821E-2	2.6642E-2	4.1346E-4
12	4.0000E-3	1.5859E+0	-1.3044E-1	1.4320E+0	3.2745E-2	3.3470E-2	7.3866E-4
13	5.0000E-3	1.5898E+0	-1.3261E-1	1.4370E+0	2.9465E-2	3.1291E-2	3.2144E-4
14	6.0000E-3	1.5902E+0	-1.3265E-1	1.4380E+0	3.1183E-2	3.1958E-2	3.7782E-4
15	7.0000E-3	1.5948E+0	-1.2908E-1	1.4430E+0	2.7390E-2	2.8996E-2	3.2415E-4
16	8.0000E-3	1.5890E+0	-1.2338E-1	1.4350E+0	3.5355E-2	3.5518E-2	7.2783E-4

80030306

Copy/Reisz

Turbulence Data

X = 2.0500E-01 DELTA = 1.2000E-02 UINF = 2.5790E+02

I	Y	U UINF	V UINF	M	U' UINF	V' UINF	-U'V' UINF2
1	4.0000E-4	-1.4157E-1	5.5952E-3	1.0750E+1	1.7301E-1	7.1733E-2	1.9981E-3
2	5.0000E-4	-1.5432E-1	2.7817E-3	1.1710E+1	1.7887E-1	7.3711E-2	3.2761E-3
3	6.0000E-4	-1.4765E-1	1.6231E-3	1.1210E+1	1.9550E-1	7.6503E-2	3.2400E-3
4	8.0000E-4	-1.0810E-1	8.7902E-4	8.1980E+0	2.2544E-1	9.1004E-2	6.5837E-3
5	1.0000E-3	-9.4339E-2	2.3916E-3	7.1570E+0	2.4335E-1	9.0074E-2	4.8487E-3
6	1.2000E-3	-4.2613E-2	3.2420E-3	3.2390E+0	2.6867E-1	9.8371E-2	6.5762E-3
7	1.4000E-3	8.3792E-3	6.0954E-3	7.8530E+0	2.8554E-1	1.0962E-1	8.0962E-3
8	1.6000E-3	7.5339E-2	7.5611E-3	5.7420E+0	3.0446E-1	1.1466E-1	9.2374E-3
9	1.8000E-3	1.5227E-1	3.3800E-3	1.1560E+1	3.1202E-1	1.1559E-1	9.0359E-3
10	2.0000E-3	1.8922E-1	1.0097E-2	1.4390E+1	3.2094E-1	1.1931E-1	1.1063E-2
11	2.5000E-3	3.5995E-1	2.7235E-2	2.7570E+1	3.4067E-1	1.2129E-1	1.0866E-2
12	3.0000E-3	5.4750E-1	4.4126E-2	4.2370E+1	3.4812E-1	1.2489E-1	1.0980E-2
13	3.5000E-3	7.4680E-1	7.4254E-2	5.8800E+1	3.5824E-1	1.1722E-1	9.3261E-3
14	4.0000E-3	9.2788E-1	1.0314E-1	7.4580E+1	3.5983E-1	1.0744E-1	5.8831E-3
15	4.5000E-3	1.0869E+0	1.3203E-1	8.9350E+1	2.9899E-1	9.0229E-2	2.7559E-3
16	5.0000E-3	1.2078E+0	1.5785E-1	1.0130E+0	1.9550E-1	7.2703E-2	1.4283E-3
17	5.5000E-3	1.2741E+0	1.7200E-1	1.0830E+0	1.1039E-1	6.0605E-2	1.5877E-3
18	6.0000E-3	1.2959E+0	1.8527E-1	1.1070E+0	7.6774E-2	5.6417E-2	1.0562E-3
19	7.0000E-3	1.3083E+0	1.9035E-1	1.1210E+0	4.6646E-2	4.7034E-2	1.2250E-4
20	8.0000E-3	1.3172E+0	1.8817E-1	1.1300E+0	4.9670E-2	4.4320E-2	-5.5749E-4
21	9.0000E-3	1.3137E+0	1.8732E-1	1.1260E+0	5.4401E-2	4.4979E-2	-6.5251E-4
22	1.0000E-2	1.3090E+0	1.8581E-1	1.1210E+0	6.6460E-2	4.6607E-2	-1.2017E-3
23	1.2000E-2	1.2862E+0	1.7088E-1	1.0950E+0	8.9453E-2	4.6956E-2	-1.5245E-3

80030311		COPY, REISZ		PROFILE TABULATION		29 POINTS, DELTA AT POINT 29		
I	Y	PT2/P	P/PD	TQ/TOD	M/MD	U/UD	T/TD	R/RD=U/UD
1	0.0000E+00	1.0000E+00	1.00000	0.98381	0.00000	0.00000	1.16534	0.00000
2	6.0000E-04	1.0216E+00	1.00000	0.99732	0.18199	0.19720	1.17417	0.16795
3	7.0000E-04	1.0225E+00	1.00000	0.99660	0.19605	0.20150	1.17299	0.17178
4	8.0000E-04	1.0220E+00	1.00000	0.99859	0.18376	0.19923	1.17552	0.16949
5	1.0000E-03	1.0253E+00	1.00000	0.99965	0.19708	0.21370	1.17567	0.18177
6	1.2000E-03	1.0290E+00	1.00000	0.99789	0.21093	0.22839	1.17239	0.19481
7	1.4000E-03	1.0299E+00	1.00000	0.99541	0.21406	0.23146	1.16919	0.19796
8	1.5000E-03	1.0323E+00	1.00000	0.99545	0.22238	0.24039	1.16846	0.20573
9	1.8000E-03	1.0390E+00	1.00000	0.99540	0.24404	0.26355	1.16625	0.22598
10	2.0000E-03	1.0431E+00	1.00000	0.99544	0.25643	0.27677	1.16498	0.23758
11	2.5000E-03	1.0595E+00	1.00000	0.99042	0.30036	0.32266	1.15396	0.27961
12	3.0000E-03	1.0866E+00	1.00000	0.98569	0.36075	0.38520	1.14018	0.33785
13	3.5000E-03	1.1078E+00	1.00000	0.98734	0.40115	0.42752	1.13584	0.37639
14	4.0000E-03	1.1446E+00	1.00000	0.98832	0.46174	0.49017	1.12694	0.43496
15	4.5000E-03	1.1825E+00	1.00000	0.98619	0.51567	0.54415	1.11352	0.48868
16	5.0000E-03	1.2502E+00	1.00000	0.98707	0.59750	0.62579	1.09694	0.57749
17	5.5000E-03	1.2955E+00	1.00000	0.98976	0.64508	0.67311	1.08879	0.61822
18	6.0000E-03	1.3027E+00	1.00000	0.99009	0.70796	0.73342	1.07353	0.68319
19	6.5000E-03	1.4340E+00	1.00000	0.99267	0.76679	0.78974	1.06075	0.74451
20	7.0000E-03	1.4886E+00	1.00000	0.99332	0.80770	0.82772	1.05019	0.78817
21	7.5000E-03	1.5361E+00	1.00000	0.99443	0.84092	0.85838	1.04197	0.82381
22	8.0000E-03	1.5992E+00	1.00000	0.99555	0.88204	0.89570	1.03122	0.86859
23	9.0000E-03	1.5873E+00	1.00000	0.99781	0.93472	0.94302	1.01783	0.92650
24	1.0000E-02	1.7404E+00	1.00000	0.99828	0.96419	0.96868	1.00934	0.95971
25	1.1000E-02	1.7794E+00	1.00000	0.99891	0.98490	0.98667	1.00359	0.98314
26	1.2000E-02	1.7955E+00	1.00000	0.99945	0.99323	0.99400	1.00155	0.99246
27	1.3000E-02	1.8108E+00	1.00000	0.99958	1.00104	1.00067	0.99925	1.00142
28	1.4000E-02	1.8049E+00	1.00000	1.00001	0.99902	0.99833	1.00063	0.99771
D 29	1.6000E-02	1.8088E+00	1.00000	1.00000	1.00000	1.00000	1.00000	1.00000

80030311 Copy/Reisz Turbulence Data

X = 2.5000E-01 DELTA = 1.6000E-02 UINF = 2.5790E+02

I	Y	U	V	M	U'	V'	-U'V'
		UINF	UINF		UINF	UINF	UINF2
1	6.0000E-4	2.2947E-1	-1.4765E-2	1.7480E-1	2.0132E-1	8.9880E-2	5.5072E-3
2	7.0000E-4	2.3447E-1	-1.6359E-2	1.7870E-1	1.9213E-1	9.8333E-2	6.5161E-3
3	8.0000E-4	2.3183E-1	-1.2245E-2	1.7650E-1	1.8724E-1	9.9961E-2	4.2263E-3
4	1.0000E-3	2.4866E-1	-1.2005E-2	1.8930E-1	1.8961E-1	1.1621E-1	5.2937E-3
5	1.2000E-3	2.6576E-1	-1.4661E-2	2.0260E-1	2.0415E-1	1.2474E-1	8.3383E-3
6	1.4000E-3	2.6933E-1	-2.1415E-2	2.0560E-1	2.1338E-1	1.3645E-1	1.1550E-2
7	1.5000E-3	2.7972E-1	-2.1369E-2	2.1360E-1	2.1660E-1	1.4409E-1	1.2942E-2
8	1.8000E-3	3.0667E-1	-2.4277E-2	2.3440E-1	2.2606E-1	1.5045E-1	1.5606E-2
9	2.0000E-3	3.2206E-1	-2.5591E-2	2.4630E-1	2.3912E-1	1.6142E-1	1.8162E-2
10	2.5000E-3	3.7546E-1	-3.9977E-2	2.8850E-1	2.5878E-1	1.6894E-1	2.2823E-2
11	3.0000E-3	4.4824E-1	-5.7658E-2	3.4650E-1	2.7546E-1	1.7433E-1	2.7604E-2
12	3.5000E-3	4.9748E-1	-6.0527E-2	3.8530E-1	2.9003E-1	1.8352E-1	3.0536E-2
13	4.0000E-3	5.7038E-1	-6.3513E-2	4.4350E-1	2.9705E-1	1.7879E-1	3.0972E-2
14	4.5000E-3	6.3319E-1	-7.9682E-2	4.9530E-1	3.2094E-1	1.8391E-1	3.5798E-2
15	5.0000E-3	7.2819E-1	-8.6661E-2	5.7390E-1	3.1993E-1	1.7208E-1	3.0671E-2
16	5.5000E-3	7.8325E-1	-8.6933E-2	6.1960E-1	3.1415E-1	1.6359E-1	2.8055E-2
17	6.0000E-3	8.5343E-1	-9.2361E-2	6.7990E-1	2.9380E-1	1.5211E-1	2.2507E-2
18	6.5000E-3	9.1896E-1	-8.7902E-2	7.3650E-1	2.7801E-1	1.4378E-1	1.8237E-2
19	7.0000E-3	9.6316E-1	-8.5925E-2	7.7580E-1	2.5855E-1	1.3408E-1	1.5050E-2
20	7.5000E-3	9.9844E-1	-8.6351E-2	8.0770E-1	2.3575E-1	1.2582E-1	1.1784E-2
21	8.0000E-3	1.0423E+0	-7.9256E-2	8.4720E-1	2.0151E-1	1.0950E-1	6.7551E-3
22	9.0000E-3	1.0973E+0	-6.6266E-2	8.9780E-1	1.4703E-1	9.1508E-2	3.6730E-3
23	1.0000E-2	1.1272E+0	-6.1458E-2	9.2610E-1	1.1539E-1	8.1970E-2	2.5138E-3
24	1.1000E-2	1.1481E+0	-5.8511E-2	9.4600E-1	7.8325E-2	7.0725E-2	1.3354E-3
25	1.2000E-2	1.1566E+0	-5.1105E-2	9.5400E-1	5.6999E-2	5.9015E-2	2.5018E-4
26	1.3000E-2	1.1644E+0	-4.9864E-2	9.6150E-1	4.7732E-2	5.0291E-2	-1.9199E-4
27	1.4000E-2	1.1617E+0	-4.1877E-2	9.5860E-1	4.5715E-2	4.8352E-2	-2.7709E-5
D 28	1.6000E-2	1.1636E+0	-4.0946E-2	9.6050E-1	3.8344E-2	4.2885E-2	-2.0658E-4

80030317 COPY, REISZ PROFILE TABULATION 26 POINTS, DELTA AT POINT 26								
I	Y	PTZ/P	P/PD	T0/T00	M/M0	U/UD	T/TD	R/RD=U/UD
1	0.0000E+00	1.0000E+00	1.00000	0.98805	0.00000	0.00000	1.11630	0.00000
2	5.0000E-04	1.1357E+00	1.00000	1.00024	0.53414	0.55758	1.08971	0.51168
3	6.0000E-04	1.1423E+00	1.00000	1.00036	0.54630	0.56999	1.08860	0.52360
4	8.0000E-04	1.1515E+00	1.00000	0.99952	0.56233	0.58627	1.08464	0.54052
5	1.0000E-03	1.1642E+00	1.00000	1.00009	0.58491	0.60838	1.08186	0.56234
6	1.5000E-03	1.1875E+00	1.00000	1.00057	0.62264	0.64599	1.07639	0.60014
7	2.0000E-03	1.2070E+00	1.00000	0.99916	0.65231	0.67468	1.06977	0.63068
8	2.5000E-03	1.2221E+00	1.00000	0.99942	0.67403	0.69601	1.06627	0.65275
9	3.0000E-03	1.2383E+00	1.00000	0.99905	0.69650	0.71772	1.06186	0.67591
10	3.5000E-03	1.2528E+00	1.00000	0.99874	0.71586	0.73633	1.05800	0.69596
11	4.0000E-03	1.2698E+00	1.00000	0.99958	0.73771	0.75766	1.05481	0.71829
12	4.5000E-03	1.2857E+00	1.00000	0.99918	0.75732	0.77627	1.05066	0.73884
13	5.0000E-03	1.2982E+00	1.00000	0.99832	0.77234	0.79023	1.04685	0.75486
14	5.5000E-03	1.3169E+00	1.00000	0.99857	0.79394	0.81078	1.04286	0.77746
15	6.0000E-03	1.3292E+00	1.00000	0.99878	0.80785	0.82396	1.04030	0.79204
16	7.0000E-03	1.3594E+00	1.00000	0.99807	0.84049	0.85421	1.03290	0.82700
17	8.0000E-03	1.3958E+00	1.00000	0.99840	0.87751	0.88872	1.02548	0.86664
18	9.0000E-03	1.4195E+00	1.00000	0.99812	0.90057	0.90965	1.02028	0.89158
19	1.0000E-02	1.4523E+00	1.00000	0.99864	0.93099	0.93757	1.01421	0.92444
20	1.1000E-02	1.4710E+00	1.00000	0.99867	0.94774	0.95269	1.01048	0.94281
21	1.2000E-02	1.4881E+00	1.00000	0.99907	0.96264	0.96627	1.00755	0.95902
22	1.3000E-02	1.5094E+00	1.00000	0.99947	0.98064	0.98255	1.00391	0.97872
23	1.4000E-02	1.5213E+00	1.00000	0.99956	0.99057	0.99147	1.00183	0.98966
24	1.6000E-02	1.5416E+00	1.00000	0.99930	1.00708	1.00620	0.99827	1.00795
25	1.8000E-02	1.5464E+00	1.00000	0.99932	1.01092	1.00931	0.99680	1.01254
D 26	2.0000E-02	1.5329E+00	1.00000	1.00000	1.00000	1.00000	1.00000	1.00000

80030317

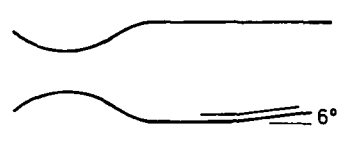
Copy/Reisz

Turbulence Data

X = 3.4000E-01 DELTA = 2.0000E-02 UINF = 2.5790E+02

I	Y	U UINF	V UINF	M	U' UINF	V' UINF	-U'V' UINF2
1	5.0000E-4	5.5758E-1	-9.0190E-3	4.3030E-1	1.4672E-1	7.1384E-2	1.6749E-3
2	6.0000E-4	5.6999E-1	-2.9201E-3	4.4010E-1	1.4102E-1	5.8589E-2	3.1137E-3
3	8.0000E-4	5.8627E-1	1.0993E-3	4.5350E-1	1.5165E-1	6.1535E-2	3.3092E-3
4	1.0000E-3	6.0838E-1	-1.7972E-3	4.7120E-1	1.5746E-1	6.8941E-2	4.2158E-3
5	1.5000E-3	6.4599E-1	-6.6848E-3	5.0160E-1	1.6227E-1	8.6080E-2	5.5869E-3
6	2.0000E-3	6.7468E-1	-1.4831E-2	5.2550E-1	1.7115E-1	9.2051E-2	6.8198E-3
7	2.5000E-3	6.9601E-1	-1.5200E-2	5.4300E-1	1.7251E-1	1.0058E-1	7.8091E-3
8	3.0000E-3	7.1772E-1	-1.8903E-2	5.6110E-1	1.7580E-1	1.0271E-1	8.2150E-3
9	3.5000E-3	7.3633E-1	-2.1834E-2	5.7670E-1	1.7507E-1	1.0644E-1	9.2795E-3
10	4.0000E-3	7.5766E-1	-2.3300E-2	5.9430E-1	1.7693E-1	1.0954E-1	9.8809E-3
11	4.5000E-3	7.7627E-1	-2.7026E-2	6.1010E-1	1.7906E-1	1.1202E-1	1.0028E-2
12	5.0000E-3	7.9023E-1	-3.4827E-2	6.2220E-1	1.7569E-1	1.0981E-1	9.3080E-3
13	5.5000E-3	8.1078E-1	-3.0151E-2	6.3960E-1	1.7573E-1	1.0942E-1	9.8448E-3
14	6.0000E-3	8.2396E-1	-3.3967E-2	6.5080E-1	1.7200E-1	1.0950E-1	8.9547E-3
15	7.0000E-3	8.5421E-1	-3.6475E-2	6.7710E-1	1.6677E-1	1.0671E-1	8.8420E-3
16	8.0000E-3	8.8872E-1	-3.5998E-2	7.0700E-1	1.5560E-1	1.0198E-1	7.5039E-3
17	9.0000E-3	9.0965E-1	-3.8294E-2	7.2550E-1	1.5114E-1	9.7402E-2	6.4680E-3
18	1.0000E-2	9.3757E-1	-3.6956E-2	7.5000E-1	1.3463E-1	8.6739E-2	4.9059E-3
19	1.1000E-2	9.5269E-1	-3.2532E-2	7.6350E-1	1.2621E-1	8.6584E-2	4.6412E-3
20	1.2000E-2	9.6627E-1	-2.9290E-2	7.7550E-1	1.1609E-1	7.9992E-2	3.7271E-3
21	1.3000E-2	9.8255E-1	-2.6444E-2	7.9000E-1	9.9767E-2	7.4719E-2	3.1723E-3
22	1.4000E-2	9.9147E-1	-2.6297E-2	7.9800E-1	8.7980E-2	7.2005E-2	2.0583E-3
23	1.6000E-2	1.0062E+0	-2.1687E-2	8.1130E-1	6.1458E-2	5.5215E-2	6.7266E-4
24	1.8000E-2	1.0093E+0	-1.8872E-2	8.1440E-1	4.9748E-2	4.7034E-2	1.2362E-4
D 25	2.0000E-2	1.0000E+0	-1.5173E-2	8.0560E-1	4.6840E-2	4.3195E-2	-1.2831E-4



	M: Appr. 2.32 upstream	8301
	R Theta $\times 10^{-3}$ : 4	CCF
TW/TR: Appr. 1		
Continuous tunnel with symmetric contoured nozzle. W = 170, H = 116 mm P0: 50.6 kN/m <sup>2</sup> . T0: 293 K. Air. Re/m $\times 10^{-6}$ : 0.44.		
DEBIEVE J.F., 1983. Etude d'une Interaction Turbulence-Onde Choc. Thèse, Docteur ès-Sciences, Université d'Aix Marseille II. And: Debiève et al. (1981). Data tables, J.-P. Dussauge (PC)		

- 1 The test boundary layer was formed on the floor of the wind tunnel, remaining under ZPG
- 4 conditions for approximately 240 mm after leaving the nozzle, which is about 350 mm axially from throat to the exit plane. The tests were performed on a compression surface spanning the tunnel and sharply inclined at 6° to the tunnel floor. The surface extended
- 3 for 240 mm from the corner (X = 0). Transition was forced by a roughness strip upstream of the throat, and in a series of tests over a range of tunnel stagnation pressure the
- 2 boundary layer was shown to be fully developed with a normal turbulent energy spectrum. No significant free-stream disturbances could be detected in schlieren photographs. Pitot
- 5 profiles at X = 70 mm on the centreline and at Z =  $\pm 35.5$  mm were within 1.5% except near the shock front, here well outside the boundary layer, where the variation reached 4%. Surface flow visualisation "showed no sign of any anomaly in the two-dimensionality
- 2 of the flow". Free-stream turbulence at frequencies above 100 Hz was less than 0.1% for velocity fluctuations.
- 6 Wall pressure was measured at 8 stations upstream of the corner and 13 downstream with
- tappings 0.5 mm in diameter. At three upstream and three downstream stations measurements
- were made of the wall-pressure fluctuations using a piezo-electric transducer ("LEM 20H
- 48A") 0.8 mm in diameter with a frequency response of the electronics up to 400 kHz (see
- ch. 8).
- 7 Pitot profiles were measured with a FPP ( $h_1 = 0.28$ ,  $h_2 = 0.08$ ,  $b_1 = 2.12$ ,  $b_2 = 1.92$ , length to holder 35 mm). The static pressure probe used was "ONERA 20 K 10 biseautée",
- with holes ( $d = 0.4$  mm) on the vertical faces of a slender wedge of 6.3° included angle,
- 6 mm from the tip, length to holder 35 mm. Mean total temperatures were found using a
- FWP, the active element having  $d = 3.8$   $\mu$ m,  $l = 1$  mm. Fluctuation measurements were made
- with a normal HWP ( $d = 2.5$   $\mu$ m, active length 0.7 mm) operating in the constant-current
- mode, with 12 overheat ratios. Data reduction was by modal analysis after Morkovin (1966)
- as developed by Gaviglio (1978) and others. The estimated bandwidth is 200 kHz. All
- traverses were made normal to the tunnel axis.
- 8 The entry has 5 profiles upstream, one at, and 14 downstream of the corner. They do not
- match those presented in the thesis exactly, and do not correspond in general to wall
- 9 pressure tappings. The author has derived TAUW values from 8 profiles using the correlation
- of Chew (1978). The editors have accepted the authors data reduction procedures. The wall
- 12 pressure values are taken from the static pressure profiles. In most cases this is
- straightforward, but at the foot of the shock (profiles 04-09) the values are not very
- trustworthy as the extrapolation was not well conditioned, and in any case the readings
- of a static probe near a shock are dubious. The values are consistent with the author's
- graphical presentation of PW as measured at the wall tappings. The TAUW values, profile
- 13 derived, were received privately from the author. The profiles form a single series
- running from the undisturbed upstream flow through the compression corner interaction and
- well downstream into the relaxing flow. We have presented all profiles available to us in
- tabular form, with some supporting information scaled from figures. The turbulence data
- is restricted in quantity, and we present only copies of two figures from the source
- paper (figs. 1 & 2.).
- 8 DATA: 83060101-0120. PT2, T0, P profiles, NX = 20. Some normal hot-wire data, and wall
- pressure fluctuations.
- 15 Editors' comments:  
 This experiment is part of a programme of experimental and theoretical studies of rapidly distorted flows undertaken at IMST - see CAT8602T, chapter 2 above, and the associated

bibliography. Unfortunately the available copies of the data tables are in very bad condition so that we were unable to read profiles at stations 4, 5, 8 and 14, while, for the same reason, some of the scatter in the data may not be of experimental origin. The profiles are functionally complete, with reservations (expressed by the author also) as to the validity of static pressure data near the shock. They do not reach in past the momentum deficit peak, but the H12K value is appropriate to a fully developed boundary layer at this relatively low Reynolds number. We have plotted out all the mean flow profiles for which the author gave us a wall shear stress as figures (10.3.1-2).

The turbulence data are very fully analysed in the source paper - unfortunately the main effort went into taking data along the " $y/\delta = 0.4$ " streamline, and this does not fit well into our handling scheme. There is much other graphical information on correlations, length scales, spectra etc. in the source paper.

Comparisons may be drawn with the investigation of Ardonneau, CAT8402T, using an LDV, and the Princeton experiments reported in CAT7904T and CAT8701T using hot wires. Both cover a wider and more severe range of corner flows in closer detail.

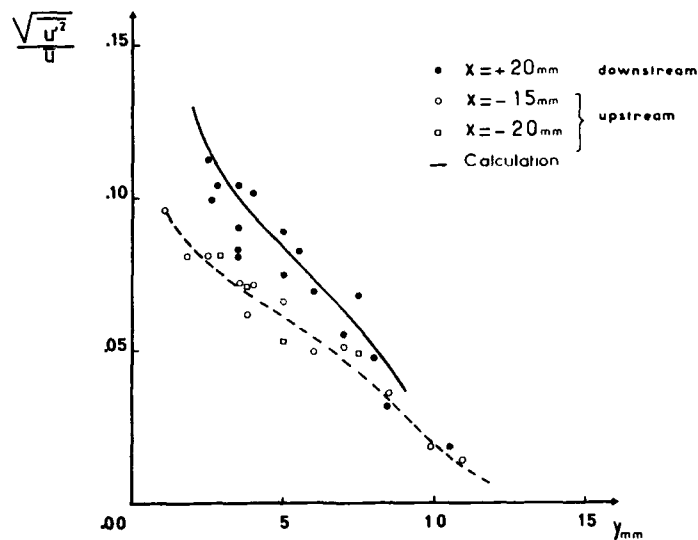


Fig. 1: Streamwise component of turbulent fluctuations (Normal HWP, CC mode).

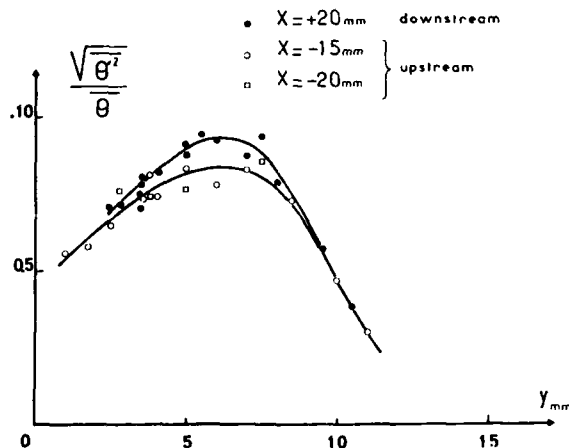


Fig. 2: Turbulent temperature fluctuations.


BOUNDARY CONDITIONS AND EVALUATED DATA, SI UNITS									
CAT #301	DEBIEVE								
RUN	MD #	TM/TR*	RED2W	C#	M12	M12K	P#	PO-	
X *	P00	PM/PO	RFOZD	C2	M32	-37K	TM	TO*	
RZ	T00	TAUM *	D2	P12	M42	D2K	UD#	TR	
83010101	2.3063	1.0000	2.3054**03	NM	3.9086	1.4551	3.9468**03	3.9923**03	
-4.0000**02	5.0415**04	0.9896	4.9602**03	NM	1.7998	1.7881	2.7793**02	1.4230**02	
INFINITE	2.9368**02	NM	7.4568**04	NM	0.0424	1.0073**03	5.5160**02	2.7794**02	
83010102	2.3053	1.0000	2.3649**03	2.1964**03	3.7492	1.4509	3.9463**03	3.9923**03	
-2.0000**02	5.0415**04	0.9896	4.1651**03	NM	1.7995	1.7985	2.7793**02	1.4230**02	
INFINITE	2.9368**02	3.2500**01	7.5576**04	NM	0.0629	1.0277**03	5.5160**02	2.7794**02	
83010103	2.3216	1.0000	2.9603**03	1.8981**03	3.1475	1.5090	4.3516**03	3.9923**03	
-2.0000**03	5.1637**04	1.0900	5.0671**03	NM	1.7637	1.7541	2.7797**02	1.4140**02	
INFINITE	2.9382**02	2.8600**01	7.1724**04	NM	0.0343	1.1483**03	5.5350**02	2.7797**02	
83010104	2.3294	1.0000	3.6267**03	NM	2.3642	1.6787	4.8070**03	3.9923**03	
0.0000**00	5.2270**04	1.2041	5.4457**03	NM	1.5993	1.6454	2.7752**02	1.4070**02	
INFINITE	2.9339**02	NM	1.1548**03	NM	0.2953	1.2217**03	5.5400**02	2.7751**02	
83010107	2.3175	1.0000	3.1557**03	NM	2.6450	1.5788	5.2320**03	3.9923**03	
-2.0000**03	5.1306**04	1.3105	5.5804**03	NM	1.7317	1.7235	2.7847**02	1.4190**02	
INFINITE	2.9432**02	NM	1.0170**03	NM	0.0455	1.1939**03	5.5350**02	2.7947**02	
83010109	2.3166	1.0000	3.5532**03	NM	2.1754	1.6098	5.4091**03	3.9923**03	
5.0000**03	5.1234**04	1.3549	6.2918**03	NM	1.7175	1.7060	2.7777**02	1.4160**02	
INFINITE	2.9358**02	NM	1.1437**03	NM	0.0167	1.2773**03	5.5270**02	2.7778**02	
83010110	2.3336	1.0000	3.6578**03	NM	1.9901	1.5635	5.4496**03	3.9923**03	
6.5000**03	5.2359**04	1.3550	6.5252**03	NM	1.7366	1.7233	2.7827**02	1.4000**02	
INFINITE	2.9209**02	NM	1.1692**03	NM	-0.0254	1.2748**03	5.5290**02	2.7527**02	
83010111	2.3178	1.0000	4.0130**03	NM	1.6195	1.5429	5.4749**03	3.9923**03	
8.0000**03	5.1331**04	1.3714	7.1014**03	NM	1.7438	1.7304	2.7713**02	1.4120**02	
INFINITE	2.9291**02	NM	1.2850**03	NM	0.0178	1.3548**03	5.5220**02	2.7713**02	
83010112	2.2955	1.0000	4.1027**03	NM	1.4269	1.5264	5.5002**03	4.0480**03	
1.0000**02	5.0262**04	1.3597	7.1974**03	NM	1.7522	1.7366	2.7745**02	1.4170**02	
INFINITE	2.9309**02	NM	1.3154**03	NM	-0.0098	1.3902**03	5.4980**02	2.7745**02	
83010113	2.1030	1.0000	3.3539**03	1.8795**03	3.2719	1.5103	5.5660**03	3.9923**03	
-2.0000**02	4.9418**04	1.0348	5.4799**03	NM	1.7629	1.7490	2.7641**02	1.5420**02	
INFINITE	2.9059**02	3.1300**01	7.1758**04	NM	-0.0541	1.1391**03	5.5236**02	2.7541**02	
83010115	2.0875	1.0000	3.3195**03	1.7065**03	3.5559	1.4941	5.5560**03	5.6571**03	
4.0000**02	5.0732**04	0.9439	5.3795**03	NM	1.7717	1.7605	2.7871**02	1.5550**02	
INFINITE	2.9289**02	3.2300**01	7.4077**04	NM	0.0163	1.1734**03	5.5236**02	2.7771**02	
83010116	2.0741	1.0000	3.2590**03	1.3942**03	3.6151	1.4750	5.5660**03	5.6976**03	
5.0000**02	5.0038**04	0.9767	5.2548**03	NM	1.7769	1.7661	2.7892**02	1.5750**02	
INFINITE	2.9301**02	3.2500**01	9.5739**04	NM	0.0005	1.1575**03	5.5219**02	2.7592**02	
83010117	2.0994	1.0000	3.3943**03	NM	4.0323	1.4554	5.5660**03	5.7380**03	
7.0000**02	5.2423**04	0.9700	5.5389**03	NM	1.7844	1.7742	2.7420**02	1.5320**02	
INFINITE	2.8825**02	NM	3.6395**04	NM	-0.1635	1.1925**03	5.5210**02	2.7420**02	
83010118	2.0675	1.0000	3.6403**03	NM	3.5296	1.3941	5.5660**03	5.8342**03	
1.3000**01	5.0712**04	0.9540	5.3522**03	NM	1.3115	1.8031	2.8026**02	1.5870**02	
INFINITE	2.9437**02	NM	7.5644**04	NM	0.0432	1.2485**03	5.5220**02	2.8026**02	
83010119	2.0491	1.0000	3.7058**03	NM	3.5443	1.3998	5.5660**03	5.8443**03	
1.5000**01	4.9363**04	0.9524	5.9206**03	NM	1.8069	1.7980	2.7934**02	1.5940**02	
INFINITE	2.9326**02	NM	9.8058**04	NM	0.0142	1.2352**03	5.1870**02	2.7934**02	
83010120	2.0449	1.0000	3.7354**03	NM	3.5315	1.3952	5.5660**03	5.8595**03	
1.6400**01	4.9160**04	0.9499	5.9547**03	NM	1.8096	1.8006	2.7935**02	1.5970**02	
INFINITE	2.9325**02	NM	9.8853**04	NM	0.0142	1.2917**03	5.1310**02	2.7935**02	

83010103 DEBIEVE PROFILE TABULATION 21 POINTS, DELTA AT POINT 14									
I	Y	PT2/P	P/PO	TO/TOD	M/MD	U/UD	T/TD	R/RD=U/UD	
1	0.0000**00	1.0000**00	1.08999	0.94604	0.00000	0.00000	1.96584	0.00000	
2	5.0000**04	1.9159**00	1.12674	0.94391	0.43517	0.55537	1.62872	0.38421	
3	1.0000**03	2.2863**00	1.16096	0.97391	0.49851	0.62981	1.59617	0.45809	
4	1.5000**03	2.6156**00	1.17364	0.95976	0.54662	0.67136	1.50848	0.52234	
5	2.0000**03	2.8201**00	1.17364	0.98011	0.57403	0.70370	1.50282	0.54956	
6	3.0000**03	3.4289**00	1.15463	0.99757	0.64788	0.77398	1.42716	0.62618	
7	4.0000**03	3.9527**00	1.10773	0.99176	0.70469	0.81644	1.34230	0.67377	
8	5.0000**03	4.6273**00	1.06094	0.99833	0.77135	0.86739	1.26451	0.72768	
9	6.0000**03	5.3562**00	1.02155	1.00019	0.83721	0.91093	1.18388	0.78603	
10	7.0000**03	5.9836**00	1.00740	1.00307	0.88987	0.94363	1.12447	0.84556	
11	8.0000**03	6.5315**00	1.00000	1.00443	0.93339	0.96838	1.07639	0.89966	
12	9.0000**03	6.9810**00	1.00000	1.00386	0.96760	0.98591	1.03819	0.94964	
13	1.0000**02	7.2424**00	1.00000	1.00260	0.98694	0.99494	1.01627	0.97901	
14	1.1000**02	7.4218**00	1.00000	1.00000	1.00000	1.00000	1.00000	1.00000	
15	1.2000**02	7.4460**00	1.00000	0.99615	1.00175	0.99892	0.99434	1.00460	
16	1.3000**02	7.4461**00	1.00000	0.99637	1.00176	0.99928	0.99505	1.00424	
17	1.4000**02	7.4287**00	1.00000	0.99697	1.00050	0.99874	0.99647	1.00228	
18	1.5000**02	7.4607**00	1.00000	0.99370	1.00281	0.99819	0.99081	1.00745	
19	1.6000**02	7.4015**00	1.00000	0.99708	0.99854	0.99783	0.99859	0.99924	
20	1.7000**02	7.3990**00	1.00000	0.99639	0.99835	0.99765	0.99859	0.99906	
21	2.0000**02	7.3990**00	1.00000	0.99639	0.99835	0.99765	0.99859	0.99906	

83010112		DEBIEVE	PROFILE TABULATION			22 POINTS, DELTA AT POINT 20		
I	Y	PT2/P	P/PO	T0/TUD	M/MD	U/UD	T/TO	R/RDEU/UD
1	0.0000+00	1.0000+00	1.35875	0.94655	0.00000	0.00000	1.94429	0.00000
2	5.0000-04	1.7145+00	1.36125	0.97673	0.39751	0.52128	1.71969	0.41263
3	1.0000-03	1.9413+00	1.36500	0.97936	0.44500	0.57421	1.66502	0.47074
4	1.5000-03	2.1770+00	1.36500	0.98267	0.48658	0.61841	1.61528	0.52259
5	2.0000-03	2.4269+00	1.36875	0.98905	0.52566	0.65933	1.57324	0.57363
6	3.0000-03	2.9502+00	1.36875	0.99119	0.59742	0.72663	1.47932	0.67232
7	4.0000-03	3.4263+00	1.37125	1.00673	0.65496	0.78156	1.42396	0.75263
8	5.0000-03	4.0224+00	1.36875	1.00084	0.71998	0.83012	1.32936	0.85471
9	6.0000-03	4.5869+00	1.36125	1.00523	0.77627	0.87232	1.26278	0.94034
10	7.0000-03	5.1807+00	1.34875	1.00883	0.83119	0.91015	1.19902	1.02381
11	7.5000-03	5.4367+00	1.33500	1.00891	0.85809	0.92688	1.16678	1.06052
12	8.0000-03	5.7784+00	1.31250	1.00871	0.88293	0.94162	1.13735	1.08662
13	8.5000-03	6.0560+00	1.27625	1.00727	0.90593	0.95417	1.10932	1.09775
14	9.0000-03	6.2050+00	1.22750	1.00566	0.91803	0.96017	1.09390	1.07743
15	9.5000-03	6.2978+00	1.18125	1.00429	0.92549	0.96362	1.08409	1.04998
16	1.0000-02	6.4446+00	1.13875	1.00324	0.93716	0.96944	1.07008	1.03165
17	1.0500-02	6.6515+00	1.09500	1.00202	0.95337	0.97745	1.05115	1.01822
18	1.1000-02	6.9374+00	1.04875	1.00161	0.97530	0.98854	1.02733	1.00915
19	1.1500-02	7.1245+00	1.02000	1.00076	0.98940	0.99527	1.01191	1.00323
20	1.2000-02	7.2671+00	1.00000	1.00000	1.00000	1.00000	1.00000	1.00000
21	1.3000-02	7.3374+00	0.99000	0.99970	1.00518	1.00236	0.99460	0.99793
22	1.4000-02	7.3618+00	0.98625	0.99943	1.00698	1.00309	0.99230	0.99698

83010115		DEBIEVE	PROFILE TABULATION			29 POINTS, DELTA AT POINT 17			
I	Y	PT2/P	P/PD	T0/T0D	M/M0	U/UD	T/T0	R/R0=U/UD	
1	0.0000+00	1.0000+00	0.98390	0.95157	0.00000	0.00000	1.78089	0.00000	
2	5.0000-04	1.9373+00	0.98390	0.97239	0.48851	0.59950	1.50607	0.39165	
3	1.0000-03	2.1736+00	0.98390	0.97477	0.53443	0.64591	1.45071	0.43507	
4	1.5000-03	2.3597+00	0.98658	0.97723	0.56690	0.67762	1.42875	0.46791	
5	2.0000-03	2.5405+00	0.98658	0.97934	0.59625	0.70550	1.40001	0.49716	
6	3.0000-03	2.9563+00	0.98837	0.98501	0.65780	0.76108	1.33865	0.56193	
7	4.0000-03	3.3952+00	0.99106	0.99112	0.71626	0.81092	1.28179	0.62699	
8	5.0000-03	3.8844+00	0.99374	0.99573	0.77579	0.85772	1.22237	0.69729	
9	6.0000-03	4.4010+00	0.99374	1.00005	0.83376	0.90011	1.16550	0.76744	
10	7.0000-03	4.9036+00	0.99553	1.00428	0.88636	0.93621	1.11565	0.83541	
11	8.0000-03	5.3944+00	0.99821	1.00678	0.93477	0.96677	1.06965	0.90220	
12	9.0000-03	5.7698+00	0.99821	1.00676	0.97011	0.98701	1.03514	0.95180	
13	1.0000-02	5.9708+00	1.00000	1.00516	0.98351	0.99637	1.01597	0.98071	
14	1.1000-02	6.0671+00	1.00000	1.00377	0.99720	1.00038	1.00639	0.99403	
15	1.2000-02	6.0805+00	1.00000	1.00171	0.99840	1.00000	1.00320	0.99681	
16	1.3000-02	6.0891+00	1.00000	1.00050	0.99917	0.99981	1.00128	0.99853	
17	1.4000-02	6.0963+00	1.00000	1.00000	1.00000	1.00000	1.00000	1.00000	
18	1.5000-02	6.1019+00	1.00000	0.99956	1.00032	1.00000	0.99936	1.00064	
19	1.6000-02	6.1240+00	0.99821	1.00022	1.00230	1.00134	0.99808	1.00147	
20	1.7000-02	6.1298+00	0.99821	1.00076	1.00281	1.00153	0.99744	1.00230	
21	2.2500-02	6.4001+00	0.99528	1.00023	1.02667	1.01413	0.97572	0.99288	
22	2.3000-02	6.4395+00	0.93649	1.00020	1.03010	1.01585	0.97252	0.97822	
23	2.3500-02	6.4874+00	0.89445	0.99970	1.02557	1.01337	0.97636	0.92836	
24	2.4000-02	6.4730+00	0.83810	1.00024	1.03301	1.01738	0.96997	0.87907	
25	2.4500-02	6.4302+00	0.78175	1.00000	1.06350	1.03247	0.94249	0.85638	
26	2.5000-02	7.0736+00	0.73882	0.99079	1.08378	1.03743	0.91630	0.83649	
27	2.6000-02	7.4630+00	0.71288	0.99846	1.11546	1.05615	0.89649	0.83984	
28	2.7000-02	7.4732+00	0.70841	0.99992	1.11627	1.05730	0.89713	0.83488	
29	3.0000-02	7.4958+00	0.70572	1.00018	1.11808	1.05825	0.89585	0.83366	

83010116		DEBIEVE	PROFILE TABULATION			24 POINTS, DELTA AT POINT 14		
I	Y	PT2/P	P/PD	T0/T0D	M/M/D	U/U/D	T/T/D	R/RD/U/D
1	0.0000+00	1.0000+00	0.97691	0.95191	0.00000	0.00000	1.77092	0.00000
2	5.0000-04	1.9391+00	0.97691	0.97607	0.49203	0.60318	1.50286	0.39209
3	1.0000-03	2.2018+00	0.97957	0.97854	0.54301	0.65434	1.45208	0.44142
4	1.5000-03	2.4144+00	0.97957	0.98111	0.57970	0.68979	1.41587	0.47723
5	2.0000-03	2.5945+00	0.98135	0.98334	0.60858	0.71680	1.38731	0.50705
6	3.0000-03	2.9800+00	0.97957	0.98732	0.66537	0.76758	1.33081	0.56500
7	4.0000-03	3.4110+00	0.98648	0.99295	0.72291	0.81606	1.27430	0.63187
8	5.0000-03	4.3494+00	0.99112	1.00169	0.83351	0.90017	1.16635	0.76493
9	6.0000-03	5.2781+00	0.99290	1.00670	0.92949	0.96340	1.07429	0.89041
10	7.0000-03	5.6949+00	0.99556	1.00731	0.96939	0.98678	1.03620	0.94808
11	8.0000-03	5.9180+00	0.99556	1.00659	0.99006	0.99789	1.01588	0.97793
12	1.1000-02	5.9936+00	0.99822	1.00481	0.99697	1.00077	1.00763	0.99143
13	1.2000-02	6.0354+00	0.99822	1.00262	1.00077	1.00172	1.00191	0.99804
D 14	1.4000-02	6.0269+00	1.00000	1.00000	1.00000	1.00000	1.00000	1.00000
15	1.6000-02	6.0248+00	1.00000	0.99932	0.99981	0.99981	1.00000	0.99981
16	1.8000-02	6.0304+00	1.00000	0.99956	1.00031	1.00000	0.99937	1.00063
17	2.0000-02	6.0614+00	0.99822	0.99971	1.00312	1.00153	0.99683	1.00293
18	2.7500-02	6.3446+00	0.95392	0.99974	1.02842	1.01495	0.97397	0.99394
19	2.8000-02	6.3320+00	0.93961	0.99956	1.02731	1.01418	0.97460	0.97776
20	2.8500-02	6.1218+00	0.91395	0.99965	1.00858	1.00441	0.99175	0.92552
21	2.9000-02	6.1989+00	0.85968	0.99963	1.01549	1.00805	0.98540	0.87944
22	2.9500-02	6.5129+00	0.80639	0.99971	1.04316	1.02242	0.96064	0.85826
23	3.0000-02	6.9522+00	0.75222	0.99951	1.08066	1.04081	0.92762	0.84401
24	4.0000-02	7.4657+00	0.70071	0.99943	1.12288	1.06055	0.89207	0.83305

	M(inf): 2.89 upstream R Theta $\times 10^{-3}$ : 86 TW/TR: 1.11	8401
		CSF
Blowdown tunnel with symmetrical contoured nozzle. Max. running time "several minutes", normally 60 seconds. W = H = 203 mm. L up to 2.7 m. PO: 0.69 MN/m <sup>2</sup> . T0: 240 - 280 K. Air. Re/m $\times 10^{-6}$ : 63.		
TAYLOR M.W., 1984. A supersonic turbulent boundary layer on concavely curved surfaces. Princeton, Gas Dyn. Lab. Rep. MAE-1684 And: Jayaram et al, (1987), Donovan & Smits (1987), A.J.Smits, data tapes and private communications.		

- 1 The general arrangements for the experiment were as for Settles, CAT7904T, q.v.. The abrupt compression corner of that experiment was replaced by one of four curved ramps, again narrower than the tunnel and with side fences. The ramp curvature started ( $X = 0$ ) 1.15 m from the nozzle exit plane. The four ramps had an initial circular arc section followed by a flat recovery section. Model 1 turned the flow through  $8^\circ$  with a radius of curvature of 254 mm ( $0 < x < 35.5$  mm) followed by a flat section 145 mm long. Model 2 also turned the flow  $8^\circ$  but with radius 1270 mm ( $0 < x < 177.3$  mm), again followed by a 152 mm recovery section. Model 3 turned the flow  $16^\circ$  with radius 1270 mm ( $0 < x < 354.7$  mm), followed by a flat plate 77 mm long and model 4 (Donovan & Smits) turned the flow  $16^\circ$  with radius 350 mm ( $0 < x < 97.7$  mm) followed by a flat section ( $E$ ) > 156 mm long.
  - 6 Wall pressure was measured at tappings 0.8 mm in diameter. The number of X-stations and the number of tappings were, for model 1, 17 along the centreline and 20 in four spanwise rows. The corresponding figures for models 2-4 are 27, 30 in 6 rows, 38, 40 in 8 rows and not known. Wall shear stress was measured for all profiles and at some additional stations using a Preston tube ( $d_1 = 1.6$ ,  $d_2 = 0.96$  mm) with the Hopkins & Keener (1966) calibration. Measurements of wall pressure across the ramps showed variations of less than 7%, while skin friction varied by about 10%. Surface flow visualisation showed no sign of any steady vortex structure on the models.
  - 7 Pitot profiles were measured with a FPP ( $h_1 = 0.18$ ,  $h_2 = 0.08$  mm) (model 4,  $h_1 = 0.33$  mm) and static profiles with a CCP ( $d = 0.84$  mm) with static holes about 10 diameters downstream of the tip. These were "very sensitive to incidence" and calibrated individually against wall-pressure readings. Total temperature was measured with a thermo-couple FWP of the type described by Vas (1972).
  - 8 The main mean flow profile measurements were made on a line 12.7 mm (model 4 - 0 mm) from the centreline. The X-values for these profiles, which start upstream of the ramps and continue onto the flat recovery sections, are in the tables of Section B. In addition, on models 1 & 2, profiles were measured for nine stations across the model at three X-stations, upstream of, on, and downstream of the curved portion. All profiles were measured normal to the local test surface.
  - 9 Owing to the difficulty of specifying a proper unambiguous boundary-layer state, the author has used an "effective" edge state based on free stream (reservoir) total pressure and the wall static pressure. Properties of this state are used for forming dimensionless quantities and integral thicknesses and in the reduction of Preston-tube data, following Settles, CAT7904T. The tunnel total pressure and temperature states are average values for a run, the total temperature falling by "several degrees" during a 30 second run as a result of expansion in the reservoir.
- The author found that the overall variation in the total temperature profiles was only 4%. They were therefore not measured at every station. The measured profiles were replaced by a linear approximation, introducing errors estimated to be less than 2% in T0. Static pressure values were interpolated from the measured profiles for each Pitot-pressure reading. For the profiles at 12.7, 25.4 and 50.8 mm on model 2, the measured static pressure profile was replaced by a linear variation through the compression wave, from the wall pressure to the free-stream pressure. No corrections were applied to the profile data.
- 10

- 12 The editors have set the wall temperature at 1.04 TOD on the advice of A.J. Smits as being typical of operating conditions. We have accepted the author's calibration and data reduction procedures. The tabulation used is based on the original experimental record, and contains more data points than the source paper, which gives interpolated values (AJS). The D-state has been selected on the basis of the total pressure profiles (there are no shock waves in the exterior flow near the boundary layer).

This entry contains the mean flow for the three models used by Taylor and reported in the source paper. To these have been added the results of a similar recent investigation. In each case there is a sequence of functionally complete profiles describing the development of a shock free boundary layer on a concave compression surface.

§ DATA: 84010101-0411. PT2, P, T0 profiles, NX = 11, 17, 15 and 11. Wall shear stress from Preston tubes.

16 Editors' comments:

These experiments constitute part of a long series of related tests performed in the same tunnel and with predominantly the same instrumentation. Turbulence measurements on models 1, 2 and 4 are discussed in CAT8702T (Jayaram et al., 1987 and Donovan & Smits (1987). Models 1 & 2 both deflect the flow by 8° and can be, and are, compared with the 8° compression corner flow of Settles, CAT7904T, giving three different rates of turning. Likewise models 3 & 4 can be compared to the 16° corner flow. Comparable simple wave APG studies are those of Sturek & Danberg, CAT7101, and Laderman, CAT 7803S.

The profiles are given in close detail near the wall, extending within the momentum deficit peak. The flow outside the boundary layer is shock-free, though model 4 was designed with the expectation that the shock would coalesce only just outside the layer (the data appear to show the shock in the outer part of the traverses at X = 127 and 152.4 mm). It is therefore possible to examine the total pressure profile as an aid to choosing an appropriate D-point. For profiles 0105-7 there is a substantial pressure difference across the boundary layer, and the flow in the outer region has yet to start turning. There is therefore the possibility of significant probe misalignment. The outer region static pressures which are reported are precisely constant, and not showing the small variations found in the other profiles. It seems probable therefore that the free stream static pressure was deduced from other measurements, with the measured value discarded because of misalignment. The mean flow profiles (figs. 10.2.2-7) are discussed at length in Ch. 10.2.

The pressure gradients are not very severe, the wall law pressure-gradient parameter reaching a maximum of about  $5 \times 10^{-3}$  for profile 5 on model 1. As a curved wall case however, there are normal pressure gradients which, at these Mach numbers, are greater than the streamwise gradients. In the region affected therefore, integral values are not properly formed and no precise conclusions should be based on their values. The author has used an "effective" edge state as suggested by Settles (1975) and this must throw in doubt both the reduction of the Preston tube data (the Hopkins and Keener compressible adaptation requires edge state values) and the value of the Van Driest transformed velocity. (See § 9.2.3 above.) It is probable that the outer parts of profiles 0402-0406 are affected by misalignment of probes with the local flow direction.

BOUNDARY CONDITIONS AND EVALUATED DATA, SI UNITS											
CAT 8401	TAYLOR										
RUN X # RZ	MO # POD TOD	TM/TR P4/P3 TAYL #	Q1/Q2 Q1/Q2 Q2	CF CJ Q12	+12 +12 +42	+124 +124 +124	PWR TWR UWR	PWR TWR UWR			
84010101	2.8900	1.1124	3.7297E+04	1.1295E-03	5.1326	1.2463	2.3170E+04	2.2390E+04			
-3.8100E-02	6.9676E+05	1.0348	3.1456E+04	N4	1.3418	1.9258	2.7105E+02	9.7500E+01			
INFINITE	2.6063E+02	1.4826E+02	1.3933E-03	N4	-0.2196	2.0943E-03	5.7320E+02	2.4369E+02			
84010102	2.8830	1.1122	3.7092E+04	1.1150E-03	5.2976	1.2456	2.3250E+04	2.2680E+04			
-2.5400E-02	6.9517E+05	1.0251	3.0653E+04	N4	1.8434	1.8268	2.7192E+02	9.8300E+01			
INFINITE	2.6137E+02	1.4948E+02	1.3313E-03	N4	-0.2271	2.0750E-03	5.7250E+02	2.4441E+02			
84010103	2.8900	1.1124	3.8172E+04	1.0386E-03	5.1462	1.2397	2.3330E+04	2.2502E+04			
-1.2700E-02	7.0018E+05	1.0369	3.3656E+04	N4	1.8460	1.8300	2.7467E+02	9.8300E+01			
INFINITE	2.6410E+02	1.4373E+02	1.4437E-03	N4	-0.2017	2.1465E-03	5.7730E+02	2.4492E+02			
84010104	2.8400	1.1113	3.5593E+04	1.0635E-03	5.4849	1.2444	2.3710E+04	2.3050E+04			
0.0000E+00	6.9515E+05	1.0232	3.5648E+04	N4	1.8423	1.8275	2.7749E+02	9.9900E+01			
INFINITE	2.6105E+02	1.3830E+02	1.3341E-03	N4	-0.2335	2.0052E-03	5.6850E+02	2.4423E+02			
84010105	2.8600	1.1113	3.9136E+04	1.1435E-03	4.3096	1.2457	2.6720E+04	2.2340E+04			
1.2700E-02	6.8033E+05	1.1756	3.2858E+04	N4	1.9370	1.8451	2.6638E+02	9.7700E+01			
INFINITE	2.5306E+02	1.5440E+02	1.4045E-03	N4	-0.2403	2.0002E-03	5.6710E+02	2.4140E+02			
84010106	2.8600	1.1118	4.2743E+04	1.0471E-03	3.7137	1.3338	3.1200E+04	2.2150E+04			
-2.5400E-02	6.5862E+05	1.4095	1.0439E+05	N4	1.8041	1.7955	2.6617E+02	9.7100E+01			
INFINITE	2.5595E+02	1.3780E+02	1.5055E-03	N4	-0.2004	2.1017E-03	5.6430E+02	2.3741E+02			
84010107	2.8600	1.1119	4.5492E+04	1.2604E-03	1.1877	1.3170	3.6420E+04	2.2570E+04			
-0.0800E-02	6.7111E+05	1.5137	1.5374E+05	N4	1.7945	1.7921	2.6372E+02	9.6200E+01			
INFINITE	2.5358E+02	1.4270E+02	2.3376E-03	N4	-0.1344	2.5112E-03	5.6210E+02	2.3721E+02			
84010108	2.6000	1.1061	5.4776E+04	1.0647E-03	3.7670	1.2466	3.4510E+04	3.5100E+04			
7.6200E-02	7.0039E+05	1.1000	1.2332E+05	N4	1.8074	1.7934	2.6587E+02	9.7000E+01			
INFINITE	2.5660E+02	1.7330E+02	1.5747E-03	N4	-0.1615	2.1747E-03	5.4390E+02	2.4125E+02			
84010109	2.9100	1.1040	5.6949E+04	1.1331E-03	4.2056	1.2445	4.0250E+04	3.2300E+04			
1.1430E-01	6.5130E+05	1.0257	1.1713E+05	N4	1.8139	1.8109	2.7523E+02	1.1710E+02			
INFINITE	2.6465E+02	1.3070E+02	1.5732E-03	N4	-0.1635	2.2134E-03	5.4510E+02	2.4423E+02			
84010110	2.9100	1.1040	5.9101E+04	1.1233E-03	4.2817	1.2553	4.0750E+04	3.9510E+04			
1.5240E-01	6.8565E+05	1.0314	1.2419E+05	N4	1.8219	1.8105	2.6912E+02	1.1550E+02			
INFINITE	2.5877E+02	1.3510E+02	1.5583E-03	N4	-0.1735	2.2097E-03	5.3750E+02	2.4377E+02			
84010111	2.4870	1.1033	5.3773E+04	1.1792E-03	4.5643	1.2499	4.1230E+04	4.1050E+04			
1.7780E-01	6.8035E+05	1.0041	1.2199E+05	N4	1.8319	1.8205	2.8535E+02	1.1710E+02			
INFINITE	2.5668E+02	1.3939E+02	1.5017E-03	N4	-0.2259	2.1517E-03	5.3260E+02	2.4165E+02			
84010201	2.9500	1.1116	3.4000E+04	1.0537E-03	5.3243	1.2390	2.2940E+04	2.2150E+04			
-3.6580E-02	6.7212E+05	1.1013	1.1574E+04	N4	1.8472	1.8312	2.8105E+02	1.0370E+02			
INFINITE	2.7216E+02	1.3776E+02	1.3493E-03	N4	-0.2253	2.0275E-03	5.2240E+02	2.5464E+02			
84010202	2.8770	1.1120	3.4471E+04	1.0317E-03	5.4234	1.2353	2.7340E+04	2.1600E+04			
-2.5400E-02	7.0100E+05	1.0322	4.3354E+04	N4	1.8430	1.8427	2.9056E+02	1.0110E+02			
INFINITE	2.6777E+02	1.3457E+02	1.5137E-03	N4	-0.2602	1.9453E-03	5.8010E+02	2.5231E+02			
84010203	2.8400	1.1113	4.3744E+04	1.0731E-03	5.3159	1.2353	2.3050E+04	2.3130E+04			
-1.2700E-02	6.9717E+05	1.0765	3.0736E+04	N4	1.4435	1.4430	2.4073E+02	1.0430E+02			
INFINITE	2.6944E+02	1.4245E+02	1.3135E-03	N4	-0.2091	1.9571E-03	5.7340E+02	2.5241E+02			
84010204	2.9500	1.1116	3.4272E+04	1.1135E-03	4.9913	1.2446	2.3640E+04	2.2670E+04			
0.0000E+00	6.6392E+05	1.0428	3.2133E+04	N4	1.8455	1.8312	2.8387E+02	1.0400E+02			
INFINITE	2.7205E+02	1.4440E+02	1.3735E-03	N4	-0.1314	2.0775E-03	5.6320E+02	2.5534E+02			
84010205	2.8400	1.1117	3.4501E+04	1.1177E-03	4.9473	1.2402	2.3100E+04	2.2420E+04			
1.2700E-02	6.6655E+05	1.0600	4.3246E+04	N4	1.8439	1.8307	2.8729E+02	1.0400E+02			
INFINITE	2.7624E+02	1.4510E+02	1.4145E-03	N4	-0.2108	2.0562E-03	5.6590E+02	2.5341E+02			
84010206	2.4600	1.1110	3.5111E+04	1.1492E-03	4.7518	1.2457	2.4360E+04	2.2570E+04			
-2.5400E-02	6.7052E+05	1.0323	1.4427E+04	N4	1.8429	1.8279	2.8757E+02	1.0400E+02			
INFINITE	2.7651E+02	1.4920E+02	1.4327E-03	N4	-0.2194	2.0562E-03	5.8720E+02	2.5341E+02			
84010207	2.6700	1.1110	3.4216E+04	1.1413E-03	4.2645	1.2544	2.6650E+04	2.2740E+04			
-0.6800E-02	6.8651E+05	1.1676	3.2270E+04	N4	1.8353	1.8212	2.9662E+02	1.0410E+02			
INFINITE	2.7559E+02	1.5000E+02	1.5236E-03	N4	-0.2049	2.1189E-03	5.8740E+02	2.5775E+02			
84010208	2.4900	1.1122	4.3417E+04	1.1462E-03	4.4247	1.2546	2.4360E+04	2.2570E+04			
7.6200E-02	7.0314E+05	1.2330	1.0410E+05	N4	1.8376	1.8127	2.8746E+02	1.0410E+02			
INFINITE	2.7679E+02	1.5530E+02	1.7371E-03	N4	-0.1789	2.2313E-03	5.3910E+02	2.5785E+02			
84010209	2.4200	1.1104	4.6043E+04	1.1443E-03	4.4844	1.2462	3.1060E+04	2.5350E+04			
1.0160E-01	7.0797E+05	1.2277	1.0842E+05	N4	1.8221	1.8081	2.9327E+02	1.0700E+02			
INFINITE	2.7713E+02	1.5240E+02	1.7135E-03	N4	-0.2116	2.2401E-03	5.3420E+02	2.5944E+02			
84010210	2.7700	1.1039	5.0043E+04	1.1711E-03	4.2673	1.2444	3.2210E+04	2.7100E+04			
1.2700E-01	7.0379E+05	1.2232	1.1574E+05	N4	1.8201	1.8054	2.8890E+02	1.0700E+02			
INFINITE	2.7779E+02	1.7040E+02	1.7935E-03	N4	-0.2071	2.3467E-03	5.8040E+02	2.6031E+02			
84010211	2.7000	1.1034	5.5067E+04	1.1577E-03	4.3721	1.2472	3.2730E+04	3.0710E+04			
1.5240E-01	7.1013E+05	1.1357	1.2379E+05	N4	1.8157	1.8014	2.9335E+02	1.1290E+02			
INFINITE	2.7726E+02	1.5040E+02	1.8226E-03	N4	-0.1409	2.4773E-03	5.7550E+02	2.6115E+02			
84010212	2.5270	1.1055	6.1037E+04	1.1222E-03	4.3767	1.2474	4.0490E+04	3.4310E+04			
1.7780E-01	7.0340E+05	1.1110	1.2379E+05	N4	1.8041	1.7917	2.8729E+02	1.1770E+02			
INFINITE	2.7834E+02	1.4020E+02	1.7147E-03	N4	-0.1749	2.4794E-03	5.6470E+02	2.6141E+02			
84010213	2.5170	1.1034	6.4417E+04	1.1744E-03	4.4412	1.2465	4.2320E+04	3.2530E+04			
2.0120E-01	7.2126E+05	1.1341	1.1466E+05	N4	1.8113	1.7987	2.8445E+02	1.1750E+02			
INFINITE	2.7759E+02	1.4740E+02	1.7137E-03	N4	-0.1664	2.5714E-03	5.6750E+02	2.6141E+02			

BOUNDARY CONDITIONS AND EVALUATED DATA, SI UNITS										
CAT 8401	YAYL3R									
RUN	MD *	Tw/TR	SEDW	CF	M12	M12K	P**	P**		
X *	POB	PM/PO	SEDW	CJ	M12	M12K	Tw	Tw		
RZ	TOD	TAJH *	02	PI2	M12	M12K	UW	UW		
84010214	2.4500	1.1026	1.9441E+04	1.1333E-03	4.6927	1.2718	4.3960E+04	4.3340E+04		
2.2860E-01	5.8504E+05	1.0143	1.1932E+05	NM	1.9178	1.9060	2.8736E+02	1.2570E+02		
INFINITE	2.7340E+02	2.0060E+02	1.6016E-03	NM	-0.1755	2.3170E-03	5.5250E+02	2.6294E+02		
84010215	2.5100	1.1040	5.5320E+04	1.1751E-03	4.2376	1.2551	4.2590E+04	4.0390E+04		
2.5400E-01	7.0092E+05	1.0559	1.1684E+05	NM	1.9271	1.8146	2.9075E+02	1.2370E+02		
INFINITE	2.7956E+02	2.0840E+02	1.6030E-03	NM	-0.1874	2.2462E-03	5.5853E+02	2.6335E+02		
84010216	2.4400	1.1023	5.7155E+04	1.2070E-03	4.2382	1.2449	4.1300E+04	4.2470E+04		
2.7940E-01	6.6890E+05	1.0342	1.1524E+05	NM	1.9314	1.8213	2.9026E+02	1.2745E+02		
INFINITE	2.7910E+02	2.1340E+02	1.5031E-03	NM	-0.1545	2.2577E-03	5.5240E+02	2.6332E+02		
84010217	2.5200	1.1042	5.5070E+04	1.2380E-03	4.3764	1.2314	4.1990E+04	3.9623E+04		
2.1750E-01	6.9833E+05	1.0573	1.1462E+05	NM	1.9404	1.8311	2.9062E+02	1.2310E+02		
INFINITE	2.7945E+02	2.1740E+02	1.5819E-03	NM	-0.2124	2.2186E-03	5.6040E+02	2.6313E+02		
84010301	2.9500	1.1000	3.4509E+04	1.0567E-03	5.2768	1.2325	2.3400E+04	2.2100E+04		
-3.9100E-01	6.7065E+05	1.0218	3.5465E+04	NM	1.9507	1.8346	2.4556E+02	1.0300E+02		
INFINITE	2.6245E+02	1.3712E+02	1.3352E-03	NM	-0.2133	1.9903E-03	5.7197E+02	2.4555E+02		
84010302	2.4400	1.0000	3.9366E+04	1.1037E-03	5.4933	1.2451	2.3440E+04	2.3210E+04		
-1.2700E-01	6.6947E+05	1.0079	3.7017E+04	NM	1.9448	1.8275	2.4551E+02	1.0645E+02		
INFINITE	2.6236E+02	1.4445E+02	1.3559E-03	NM	-0.2387	2.0466E-03	5.7020E+02	2.4551E+02		
84010303	2.4800	1.1000	4.0546E+04	1.0321E-03	5.7979	1.2345	2.3620E+04	2.2560E+04		
0.0000E+00	6.9147E+05	1.0470	4.1143E+04	NM	1.9499	1.8335	2.4341E+02	9.7900E+01		
INFINITE	2.6030E+02	1.4134E+02	1.3981E-03	NM	-0.2313	2.0342E-03	5.7153E+02	2.4341E+02		
84010304	2.9100	1.1000	4.1274E+04	1.1173E-03	4.4356	1.2422	2.5950E+04	2.1630E+04		
3.9100E-02	6.9572E+05	1.1344	3.7800E+04	NM	1.9379	1.8257	2.4535E+02	9.7700E+01		
INFINITE	2.6317E+02	1.4352E+02	1.4568E-03	NM	-0.2202	2.0466E-03	5.7533E+02	2.4535E+02		
84010305	2.8700	1.1000	4.5930E+04	1.1337E-03	3.5561	1.2577	2.8740E+04	2.2730E+04		
7.6200E-02	6.9406E+05	1.2591	1.0258E+05	NM	1.9312	1.8175	2.4562E+02	9.8200E+01		
INFINITE	2.6252E+02	1.4660E+02	1.5715E-03	NM	-0.2405	2.0497E-03	5.7240E+02	2.4562E+02		
84010306	2.7400	1.1000	5.2652E+04	1.1154E-03	3.6236	1.2743	3.2970E+04	2.7200E+04		
1.1430E-01	6.7342E+05	1.1121	1.1177E+05	NM	1.9203	1.8075	2.4597E+02	1.0630E+02		
INFINITE	2.5341E+02	1.5735E+02	1.4646E-03	NM	-0.2078	2.2188E-03	5.6361E+02	2.4647E+02		
84010307	2.7500	1.1000	5.4753E+04	1.0744E-03	3.1710	1.2946	3.7163E+04	2.9700E+04		
1.5240E-01	7.5320E+05	1.2423	1.4677E+05	NM	1.9133	1.7934	2.4376E+02	1.0253E+02		
INFINITE	2.6004E+02	1.7083E+02	1.3073E-03	NM	-0.1707	2.4163E-03	5.6160E+02	2.4376E+02		
84010308	2.6200	1.1000	7.3436E+04	1.1133E-03	2.7933	1.3334	4.2900E+04	3.4250E+04		
1.9050E-01	7.0490E+05	1.2526	1.4483E+05	NM	1.7949	1.7462	2.4487E+02	1.0490E+02		
INFINITE	2.6054E+02	1.3315E+02	1.9379E-03	NM	-0.1828	2.4495E-03	5.5020E+02	2.4487E+02		
84010309	2.4500	1.0000	3.2573E+04	1.0475E-03	3.2311	1.3116	4.7310E+04	4.2270E+04		
2.2840E-01	6.9373E+05	1.1972	1.3770E+05	NM	1.7965	1.7446	2.3542E+02	1.1395E+02		
INFINITE	2.5064E+02	1.7117E+02	1.3244E-03	NM	-0.1396	2.5423E-03	5.2537E+02	2.3542E+02		
84010310	2.3800	1.1000	4.7163E+04	1.0423E-03	3.4516	1.3205	5.5730E+04	4.8830E+04		
2.6070E-01	6.9892E+05	1.1451	1.7975E+05	NM	1.7892	1.7793	2.3555E+02	1.1395E+02		
INFINITE	2.4933E+02	2.0350E+02	1.3330E-03	NM	-0.1540	2.6701E-03	5.1530E+02	2.3555E+02		
84010311	2.3400	1.0000	1.1210E+05	1.1133E-03	3.3317	1.3177	6.0753E+04	5.3330E+04		
3.0480E-01	7.0991E+05	1.1331	2.0451E+05	NM	1.7892	1.7793	2.3130E+02	1.1703E+02		
INFINITE	2.4513E+02	2.2426E+02	1.3344E-03	NM	-0.1563	2.7930E-03	5.0640E+02	2.3130E+02		
84010312	2.2600	1.0000	1.0650E+05	1.1775E-03	3.2957	1.3017	6.6370E+04	5.7330E+04		
3.4290E-01	6.9131E+05	1.1275	1.3703E+05	NM	1.7745	1.7877	2.4439E+02	1.2763E+02		
INFINITE	2.5775E+02	2.4510E+02	2.3670E-03	NM	-0.1145	2.7163E-03	5.1230E+02	2.4439E+02		
84010313	2.2100	1.1000	1.0976E+05	1.1133E-03	3.3785	1.2935	6.6110E+04	6.1570E+04		
3.6830E-01	6.7199E+05	1.1009	1.4256E+05	NM	1.8053	1.7774	2.4503E+02	1.3370E+02		
INFINITE	2.5937E+02	2.4984E+02	2.0076E-03	NM	-0.1479	2.6366E-03	5.0400E+02	2.4503E+02		
84010314	2.1900	1.1000	1.1105E+05	1.2362E-03	3.5197	1.2452	6.4280E+04	6.3720E+04		
4.0360E-01	6.7076E+05	1.0402	1.9349E+05	NM	1.8120	1.8015	2.4542E+02	1.3360E+02		
INFINITE	2.6175E+02	2.4537E+02	2.0712E-03	NM	-0.1364	2.7420E-03	5.0443E+02	2.4542E+02		
84010315	2.1300	1.1000	1.6003E+04	1.2501E-03	4.2605	1.2314	6.2640E+04	6.4470E+04		
4.3180E-01	6.7019E+05	1.0532	1.6321E+05	NM	1.8421	1.8324	2.4793E+02	1.2330E+02		
INFINITE	2.6117E+02	2.4584E+02	1.7315E-03	NM	-0.1344	2.4403E-03	5.0553E+02	2.4793E+02		
84010401	2.8300	1.1122	3.1618E+04	1.1417E-03	5.1980	1.2688	2.2493E+04	2.1780E+04		
-2.5400E-02	6.6758E+05	1.0510	7.9641E+04	NM	1.8447	1.8280	2.4656E+02	1.0340E+02		
INFINITE	2.7554E+02	1.4640E+02	1.3134E-03	NM	-0.1920	1.9442E-03	5.5782E+02	2.5766E+02		
84010402	2.9200	1.1131	3.4628E+04	1.2173E-03	3.5639	1.3223	2.4540E+04	2.1170E+04		
2.5400E-02	6.9952E+05	1.3468	9.8054E+04	NM	1.9097	1.7351	2.9403E+02	1.3015E+02		
INFINITE	2.7508E+02	1.5370E+02	1.5426E-03	NM	-0.1674	2.1416E-03	5.4101E+02	2.5711E+02		
84010403	2.8900	1.1124	5.3280E+04	1.2551E-03	1.5349	1.3431	3.6461E+04	2.1751E+04		
5.0000E-02	6.7942E+05	1.7036	1.2393E+05	NM	1.7553	1.7793	2.9403E+02	1.3015E+02		
INFINITE	2.7540E+02	1.6350E+02	2.2045E-03	NM	-0.1000	2.3561E-03	5.3915E+02	2.5711E+02		
84010404	2.7170	1.1037	7.0033E+04	1.2233E-03	1.2114	1.4144	4.2170E+04	2.8432E+04		
7.6200E-02	6.7945E+05	1.6343	1.5859E+05	NM	1.7553	1.7793	2.9403E+02	1.3015E+02		
INFINITE	2.7528E+02	1.7340E+02	2.4451E-03	NM	-0.0945	2.4545E-03	5.3915E+02	2.5711E+02		



CAT 8401		TAYLOR		BOUNDARY CONDITIONS AND EVALUATED DATA, SI UNITS							
RUN	MD *	TH/TR	RED24	CF	H12	H12K	P44	P38			
X *	P00	P4/P0	RED20	CJ	H32	H32K	TW4	TJ			
RZ	T00	TAUW *	32	R12	H42	D1K	UU4	TR			
84010405	2.4750	1.1032	9.2151E+04	1.1711E-03	1.6047	1.4033	6.1809E+04	4.2222E+04			
1.0160E-01	6.9495E+05	1.4639	1.6839E+05	NM	1.7595	1.7457	2.8688E+02	1.2391E+02			
INFINITE	2.7584E+02	2.1220E+02	2.2410E-03	NM	-0.0851	2.4644E-03	5.5261E+02	2.6004E+02			
84010406	2.2070	1.0962	5.7855E+04	1.1735E-03	3.7258	1.3550	6.4731E+04	6.2329E+04			
1.2700E-01	6.7381E+05	1.0395	1.2449E+05	NM	1.7853	1.7737	2.8780E+02	1.4018E+02			
INFINITE	2.7674E+02	2.4940E+02	1.5090E-03	NM	-0.0853	2.0529E-03	5.2390E+02	2.6254E+02			
84010407	2.1930	1.0959	5.9270E+04	1.3032E-03	3.6699	1.3200	6.4200E+04	6.2592E+04			
1.5240E-01	6.5199E+05	1.0576	1.2471E+05	NM	1.9008	1.7911	2.8495E+02	1.3365E+02			
INFINITE	2.7399E+02	2.7460E+02	1.4979E-03	NM	-0.0888	2.0287E-03	5.1962E+02	2.6002E+02			
84010408	2.2030	1.0961	6.9334E+04	1.3733E-03	3.5591	1.2788	6.7880E+04	6.3441E+04			
1.7780E-01	6.7836E+05	1.0700	1.2673E+05	NM	1.8207	1.8151	2.9041E+02	1.4190E+02			
INFINITE	2.7944E+02	2.9530E+02	1.5329E-03	NM	-0.1128	2.0176E-03	5.2561E+02	2.6514E+02			
84010409	2.1650	1.0951	7.2834E+04	1.4394E-03	3.6655	1.2673	6.9300E+04	6.6507E+04			
2.0320E-01	6.7324E+05	1.0420	1.3139E+05	NM	1.8294	1.8204	2.9229E+02	1.4357E+02			
INFINITE	2.7816E+02	3.1410E+02	1.5642E-03	NM	-0.1306	2.0675E-03	5.2011E+02	2.6415E+02			
84010410	2.1430	1.0745	5.8497E+04	1.4654E-03	4.0232	1.2471	7.1040E+04	6.8387E+04			
2.2860E-01	6.7472E+05	1.0298	1.2229E+05	NM	1.9438	1.8357	2.9091E+02	1.4580E+02			
INFINITE	2.7972E+02	3.2500E+02	1.4499E-03	NM	-0.1649	1.9279E-03	5.1932E+02	2.6373E+02			
84010411	2.1430	1.0745	5.8337E+04	1.5763E-03	3.9795	1.2516	6.8700E+04	6.7952E+04			
2.5400E-01	6.5446E+05	1.0169	1.2130E+05	NM	1.8477	1.8374	2.9273E+02	1.4475E+02			
INFINITE	2.9154E+02	3.4450E+02	1.4735E-03	NM	-0.1551	1.9421E-03	5.2050E+02	2.6752E+02			

34010401		TAYLOR		PROFILE TABULATION		45 POINTS, DELTA AT POINT 40			
I	Y	PTZ/P	P/PD	T0/TD0	M/MD	U/UD	T/TD	R/RJ/U/UD	
1	0.0000E+00	1.0090E+00	1.05097	1.04000	0.00000	0.00000	2.76522	0.00000	
2	1.8000E-04	1.6213E+00	1.03857	1.03211	0.29875	0.46189	2.39036	0.20068	
3	4.1780E-04	2.1432E+00	1.03857	1.03229	0.38333	0.56945	2.20679	0.26800	
4	6.5940E-04	2.7556E+00	1.03857	1.03235	0.45590	0.65124	2.04052	0.33147	
5	9.0200E-04	3.1448E+00	1.03395	1.03069	0.49549	0.69144	1.94737	0.36712	
6	1.1390E-03	3.3644E+00	1.03626	1.03044	0.51632	0.71164	1.89970	0.38819	
7	1.3870E-03	3.5940E+00	1.03353	1.03060	0.53715	0.73124	1.85322	0.40781	
8	1.6290E-03	3.7605E+00	1.03216	1.03056	0.55174	0.74448	1.82070	0.42205	
9	1.8630E-03	3.9072E+00	1.03027	1.02965	0.56424	0.75522	1.79155	0.43431	
10	2.1110E-03	4.0699E+00	1.02849	1.02919	0.57778	0.76677	1.76118	0.44777	
11	2.3520E-03	4.2066E+00	1.02830	1.02903	0.58889	0.77612	1.73696	0.45974	
12	2.5820E-03	4.3284E+00	1.03027	1.02903	0.59851	0.78418	1.71609	0.47079	
13	3.0850E-03	4.5015E+00	1.03626	1.02820	0.61215	0.79482	1.68587	0.48856	
14	3.5720E-03	4.7202E+00	1.03679	1.02743	0.62832	0.80766	1.64970	0.50759	
15	4.0580E-03	4.9165E+00	1.02943	1.02715	0.64340	0.81871	1.61916	0.52052	
16	4.5430E-03	5.1224E+00	1.02207	1.02622	0.65833	0.82935	1.58703	0.53411	
17	5.0220E-03	5.3282E+00	1.01703	1.02579	0.67292	0.83980	1.55751	0.54838	
18	5.4970E-03	5.5083E+00	1.01282	1.02496	0.68542	0.84826	1.53160	0.56094	
19	5.9770E-03	5.6507E+00	1.01062	1.02440	0.69514	0.85473	1.51185	0.57135	
20	6.4500E-03	5.7952E+00	1.00915	1.02358	0.70486	0.86099	1.49208	0.58232	
21	6.9410E-03	5.9840E+00	1.00778	1.02318	0.71736	0.86905	1.46764	0.59675	
22	7.4290E-03	6.0957E+00	1.00694	1.02235	0.72465	0.87343	1.45277	0.60539	
23	8.3310E-03	6.4432E+00	1.00463	1.02101	0.74688	0.88686	1.41000	0.63199	
24	9.3830E-03	6.7957E+00	1.00463	1.02017	0.76875	0.89970	1.35970	0.65990	
25	1.0340E-02	7.0829E+00	1.00453	1.01852	0.78611	0.90905	1.33725	0.69294	
26	1.1290E-02	7.3706E+00	1.00539	1.01752	0.80313	0.91821	1.30712	0.70667	
27	1.2260E-02	7.6707E+00	1.00672	1.01532	0.82049	0.92696	1.27612	0.73265	
28	1.3240E-02	8.0207E+00	1.01138	1.01450	0.84023	0.93662	1.24244	0.75288	
29	1.4210E-02	8.3233E+00	1.01514	1.01357	0.85729	0.94478	1.21451	0.78969	
30	1.5180E-02	8.5583E+00	1.01787	1.01205	0.86979	0.95015	1.19331	0.81046	
31	1.6130E-02	8.8767E+00	1.01832	1.01110	0.88681	0.95791	1.16655	0.83651	
32	1.7100E-02	9.2550E+00	1.01934	1.00955	0.90650	0.96617	1.13573	0.86715	
33	1.8080E-02	9.5391E+00	1.01787	1.00848	0.92118	0.97214	1.11370	0.88849	
34	1.9040E-02	9.9832E+00	1.01514	1.00720	0.93854	0.97891	1.08786	0.91346	
35	2.0010E-02	1.0177E+01	1.01240	1.00613	0.95313	0.98458	1.06709	0.93412	
36	2.0980E-02	1.0433E+01	1.00872	1.00429	0.95563	0.98876	1.04848	0.95126	
37	2.1960E-02	1.0635E+01	1.00547	1.00317	0.97778	0.99303	1.03145	0.96802	
38	2.2930E-02	1.0889E+01	1.00326	1.00156	0.99750	0.99602	1.01733	0.98225	
39	2.3880E-02	1.1050E+01	1.00095	0.99969	0.99514	0.99801	1.00578	0.99321	
40	2.4840E-02	1.1154E+01	1.00000	1.00000	1.00000	1.00000	1.00000	1.00000	
41	2.5780E-02	1.1206E+01	0.99905	0.99818	1.00243	1.00020	0.99516	1.00392	
42	2.6750E-02	1.1258E+01	0.99821	0.99637	1.00486	1.00000	0.99035	1.00794	
43	2.8690E-02	1.1362E+01	0.99454	0.99477	1.00972	1.00099	0.98279	1.01296	
44	3.0640E-02	1.1362E+01	0.99170	0.99279	1.00972	1.00000	0.98094	1.01108	
45	3.2570E-02	1.1414E+01	0.99222	0.99299	1.01215	1.00099	0.97807	1.01548	

94010101	TAYLOR	PROFILE TABULATION	71 POINTS, DELTA AT POINT 57					
I	Y	PT2/P	P/PD	T0/T10	M/MD	U/UD	T/TD	R/RD=U/UD
1	0.0000E+00	1.0000E+00	1.03484	1.0401	0.09000	0.00000	2.77725	0.00000
2	8.8900E-05	1.6913E+00	1.03494	1.03810	0.31142	0.48098	2.33545	0.20866
3	1.7190E-04	1.9844E+00	1.03434	1.04015	0.35986	0.54379	2.29344	0.24644
4	2.9320E-04	2.3500E+00	1.03494	1.03672	0.40830	0.60084	2.16544	0.28713
5	3.6570E-04	2.5568E+00	1.03434	1.03813	0.43253	0.62858	2.11199	0.30799
6	4.4610E-04	2.6186E+00	1.05593	1.03431	0.43945	0.63521	2.09398	0.32039
7	5.2680E-04	2.7734E+00	1.06119	1.03435	0.45675	0.65370	2.04835	0.33866
8	5.4910E-04	2.8444E+00	1.06174	1.03930	0.46367	0.66277	2.04320	0.34499
9	7.2030E-04	3.0144E+00	1.05895	1.03513	0.48097	0.67917	1.99399	0.36069
10	8.5740E-04	3.1915E+00	1.05752	1.03433	0.49827	0.69644	1.95362	0.37703
11	9.4040E-04	3.3011E+00	1.05895	1.03331	0.50865	0.70604	1.92670	0.38805
12	1.0090E-03	3.3392E+00	1.06074	1.03735	0.51211	0.71075	1.92620	0.39140
13	1.2180E-03	3.4133E+00	1.05032	1.03819	0.51903	0.71772	1.91218	0.39446
14	1.4090E-03	3.4894E+00	1.05360	1.03833	0.52595	0.72457	1.89766	0.40226
15	1.5830E-03	3.5650E+00	1.05593	1.03465	0.53979	0.73537	1.85844	0.41807
16	1.7990E-03	3.8050E+00	1.05226	1.03612	0.55363	0.74895	1.83006	0.43064
17	2.0080E-03	3.8456E+00	1.04824	1.03315	0.55709	0.75105	1.81752	0.43316
18	2.1350E-03	3.9273E+00	1.05002	1.03411	0.56401	0.75750	1.80380	0.44095
19	2.3690E-03	3.9633E+00	1.05226	1.03757	0.56747	0.76169	1.80162	0.44487
20	2.5390E-03	3.9273E+00	1.05270	1.03679	0.56401	0.75837	1.80795	0.44157
21	2.7700E-03	4.2238E+00	1.05649	1.03391	0.58824	0.77809	1.74957	0.46894
22	2.9540E-03	4.3547E+00	1.05538	1.03756	0.59862	0.78921	1.73374	0.47991
23	3.4080E-03	4.3939E+00	1.05717	1.03214	0.60209	0.78890	1.71690	0.48576
24	3.9170E-03	4.5695E+00	1.05002	1.03571	0.62284	0.80687	1.67827	0.50482
25	4.3390E-03	4.5635E+00	1.04536	1.03431	0.62284	0.80653	1.67582	0.50290
26	4.5550E-03	5.0452E+00	1.04243	1.03214	0.65052	0.82676	1.61525	0.53356
27	5.3540E-03	5.1905E+00	1.03707	1.03077	0.65030	0.83374	1.59144	0.54331
28	5.8000E-03	5.2334E+00	1.03171	1.03274	0.66436	0.83706	1.57745	0.54631
29	6.2910E-03	5.3381E+00	1.03171	1.03214	0.67128	0.84194	1.57309	0.55013
30	6.7890E-03	5.6913E+00	1.03439	1.02715	0.69550	0.85694	1.51412	0.59333
31	7.2000E-03	5.6913E+00	1.03523	1.02714	0.69550	0.85677	1.51751	0.59451
32	7.7130E-03	6.1117E+00	1.03454	1.02557	0.72318	0.87439	1.46198	0.61840
33	8.2000E-03	6.0051E+00	1.04377	1.02335	0.71626	0.86916	1.47243	0.61610
34	8.6900E-03	6.2193E+00	1.04824	1.02836	0.73310	0.87997	1.45257	0.63472
35	9.2210E-03	6.2193E+00	1.04630	1.02338	0.73010	0.87805	1.44635	0.63556
36	9.6750E-03	6.5434E+00	1.04511	1.02513	0.75037	0.89149	1.40963	0.65045
37	1.0120E-02	6.7730E+00	1.04422	1.02514	0.75471	0.90004	1.39526	0.67240
38	1.0660E-02	6.7155E+00	1.03930	1.02251	0.76125	0.89672	1.38760	0.67154
39	1.1090E-02	6.9442E+00	1.03205	1.01931	0.77509	0.90370	1.35940	0.68475
40	1.1560E-02	7.1761E+00	1.02932	1.02047	0.78893	0.91130	1.33604	0.70296
41	1.2090E-02	7.4122E+00	1.02858	1.02072	0.80277	0.91975	1.31258	0.72069
42	1.2570E-02	7.2937E+00	1.02456	1.01918	0.79585	0.91521	1.32245	0.70905
43	1.3500E-02	7.3537E+00	1.01921	1.01632	0.83391	0.93440	1.25554	0.75952
44	1.4470E-02	8.2083E+00	1.01608	1.01874	0.84775	0.94250	1.23629	0.77470
45	1.5420E-02	8.3992E+00	1.01251	1.01653	0.85813	0.94679	1.21731	0.78750
46	1.6400E-02	8.9161E+00	1.00993	1.01427	0.89591	0.95900	1.17207	0.82625
47	1.7350E-02	9.3154E+00	1.01027	1.01177	0.90657	0.96738	1.13863	0.85832
48	1.8310E-02	9.3829E+00	1.00893	1.01144	0.91004	0.96877	1.13325	0.85249
49	1.9290E-02	9.3624E+00	1.00670	1.00739	0.93426	0.97757	1.09510	0.89975
50	2.0250E-02	1.0426E+01	1.00402	1.00816	0.96134	0.98913	1.05745	0.93920
51	2.1280E-02	1.0563E+01	1.00223	1.00732	0.96986	0.99145	1.04718	0.94839
52	2.2210E-02	1.0859E+01	1.00045	1.00413	0.99270	0.99546	1.02615	0.97053
53	2.3200E-02	1.0359E+01	1.00134	1.00443	0.93270	0.99564	1.02651	0.97123
54	2.4170E-02	1.1030E+01	1.00253	1.00243	0.93308	0.99308	1.01116	0.99023
55	2.5220E-02	1.1030E+01	0.99921	1.00103	0.99303	0.99731	1.00974	0.98651
56	2.6160E-02	1.1223E+01	0.99643	1.00000	1.00000	1.00000	1.00000	0.99643
57	2.7180E-02	1.1223E+01	1.00000	1.00000	1.00000	1.00000	1.00000	1.00000
58	2.8080E-02	1.1377E+01	0.99821	0.99950	1.00692	1.00132	0.99009	1.01014
59	2.9120E-02	1.1377E+01	0.99330	1.00043	1.00692	1.00279	0.99181	1.00429
60	3.0080E-02	1.1302E+01	1.00134	0.99916	1.00346	1.00037	0.99484	1.00740
61	3.1090E-02	1.1377E+01	1.00259	1.00043	1.00692	1.00279	0.99131	1.01379
62	3.2050E-02	1.1377E+01	1.00000	1.00043	1.00692	1.00279	0.99131	1.01107
63	3.3000E-02	1.1377E+01	1.00670	1.00043	1.00692	1.00279	0.99181	1.01794
64	3.4010E-02	1.1377E+01	1.00357	0.99869	1.00692	1.00192	0.99009	1.01556
65	3.4960E-02	1.1377E+01	1.00432	1.00043	1.00692	1.00279	0.99131	1.01513
66	3.5980E-02	1.1302E+01	1.00447	0.99916	1.00346	1.00087	0.99131	1.01055
67	3.6940E-02	1.1377E+01	1.00179	1.00043	1.00692	1.00279	0.99131	1.01248
68	3.7930E-02	1.1452E+01	0.99052	0.99952	1.01038	1.00366	0.99131	1.00761
69	3.8910E-02	1.1452E+01	0.99419	0.99952	1.01038	1.00366	0.99131	1.01124
70	3.9910E-02	1.1452E+01	0.99419	0.99952	1.01038	1.00366	0.99131	1.01124
71	4.0960E-02	1.1452E+01	0.99973	0.99952	1.01038	1.00366	0.99131	1.00670

84010105		TAYLOR		PROFILE TABULATION		TI POINTS, DELTA AT POINT 56		
I	Y	PT2/P	P/PD	TO/TOD	M/MD	U/UD	T/TD	R/RD=U/UD
1	0.0000*-00	1.0000*-00	1.17657	1.04000	0.00000	0.00000	2.74137	0.00000
2	8.8900*-05	1.9379*-00	1.17657	1.04493	0.35664	0.53853	2.28008	0.27789
3	1.5740*-04	2.1351*-00	1.17657	1.03763	0.39151	0.57909	2.13668	0.31159
4	2.5850*-04	2.3500*-00	1.17657	1.04232	0.41259	0.60501	2.15026	0.33195
5	3.2340*-04	2.5568*-00	1.17657	1.03473	0.43706	0.63005	2.07807	0.35672
6	4.4610*-04	2.6186*-00	1.17614	1.04035	0.44406	0.63957	2.07444	0.36262
7	5.5790*-04	2.7453*-00	1.17439	1.04345	0.45904	0.65544	2.04765	0.37592
8	6.3370*-04	2.9115*-00	1.17351	1.03850	0.47552	0.67219	1.99821	0.37476
9	7.4920*-04	2.9115*-00	1.17177	1.03850	0.47552	0.67219	1.99821	0.37418
10	8.2850*-04	2.9798*-00	1.17045	1.03975	0.49252	0.67977	1.98474	0.40088
11	9.0430*-04	3.1555*-00	1.16914	1.03833	0.50000	0.69706	1.94354	0.41931
12	1.0090*-03	3.1915*-00	1.16783	1.04330	0.50350	0.70199	1.94339	0.42174
13	1.1680*-03	3.2278*-00	1.16521	1.03628	0.50699	0.70305	1.92296	0.42631
14	1.3770*-03	3.5279*-00	1.16171	1.03433	0.53497	0.72897	1.85682	0.45608
15	1.6260*-03	3.5667*-00	1.15822	1.04154	0.53846	0.73461	1.86127	0.45713
16	1.7920*-03	3.5667*-00	1.15559	1.03755	0.53846	0.73338	1.85502	0.45686
17	1.9940*-03	3.8456*-00	1.15210	1.03492	0.56294	0.75454	1.79558	0.48387
18	2.1820*-03	3.8866*-00	1.14948	1.03803	0.56643	0.75877	1.79442	0.48606
19	2.3440*-03	3.8456*-00	1.14685	1.04024	0.56234	0.75648	1.80582	0.48643
20	2.5710*-03	4.0110*-00	1.14336	1.03867	0.57632	0.76812	1.77264	0.49544
21	2.7550*-03	4.0531*-00	1.14073	1.03912	0.58042	0.77129	1.76535	0.49825
22	2.9790*-03	4.2238*-00	1.13724	1.03753	0.59441	0.78258	1.73336	0.51344
23	3.4260*-03	4.4880*-00	1.13068	1.03735	0.61539	0.79951	1.68791	0.53556
24	3.8850*-03	4.5783*-00	1.12325	1.03033	0.62239	0.80268	1.66332	0.54205
25	4.4110*-03	4.6635*-00	1.11495	1.03530	0.62937	0.81009	1.65672	0.54518
26	4.8770*-03	4.9023*-00	1.10795	1.02995	0.64685	0.82120	1.61169	0.55453
27	5.3280*-03	4.9973*-00	1.10140	1.01054	0.65395	0.82666	1.59847	0.56960
28	5.8510*-03	5.1418*-00	1.09353	1.02844	0.66434	0.83354	1.57426	0.57900
29	6.3270*-03	5.3878*-00	1.08610	1.03195	0.68192	0.84747	1.54494	0.59578
30	6.7890*-03	5.5894*-00	1.07867	1.02833	0.69590	0.85576	1.51261	0.61026
31	7.2580*-03	5.5894*-00	1.07168	1.02792	0.69530	0.85558	1.51199	0.60643
32	7.7780*-03	5.8473*-00	1.06391	1.02670	0.71329	0.86687	1.47599	0.62437
33	8.1890*-03	5.8936*-00	1.05726	1.02833	0.71678	0.86996	1.47274	0.62446
34	8.6800*-03	6.3280*-00	1.04993	1.02676	0.74475	0.88715	1.41833	0.65637
35	9.1880*-03	6.2735*-00	1.04136	1.02734	0.74126	0.88521	1.42609	0.66677
36	9.6610*-03	6.5602*-00	1.03453	1.02633	0.76573	0.90002	1.38149	0.67398
37	1.0190*-02	6.7730*-00	1.02656	1.02337	0.77273	0.90266	1.36458	0.67913
38	1.0560*-02	6.8869*-00	1.01923	1.02326	0.77972	0.90672	1.35228	0.68340
39	1.1110*-02	7.0597*-00	1.01224	1.02155	0.79021	0.91201	1.33202	0.69306
40	1.1620*-02	7.4719*-00	1.00491	1.02137	0.81469	0.92559	1.29079	0.72052
41	1.2130*-02	7.6525*-00	1.00000	1.02290	0.82517	0.93193	1.27549	0.73065
42	1.2580*-02	7.7742*-00	1.00000	1.02250	0.83217	0.93546	1.26366	0.74028
43	1.3570*-02	8.0207*-00	1.00000	1.01935	0.84615	0.94128	1.23748	0.76064
44	1.4510*-02	8.2093*-00	1.00000	1.01701	0.85664	0.94551	1.21824	0.77613
45	1.5440*-02	8.6551*-00	1.00000	1.01587	0.88112	0.95697	1.17959	0.81128
46	1.6370*-02	8.8505*-00	1.00000	1.01395	0.89161	0.96103	1.16179	0.82720
47	1.7400*-02	9.1146*-00	1.00000	1.01134	0.90559	0.96720	1.14069	0.84791
48	1.8390*-02	9.6553*-00	1.00000	1.01352	0.93357	0.97972	1.10132	0.88959
49	1.9360*-02	9.9319*-00	1.00000	1.01031	0.94755	0.98413	1.07870	0.91233
50	2.0280*-02	1.0072*-01	1.00000	1.00933	0.95455	0.98660	1.06829	0.92353
51	2.1280*-02	1.0283*-01	1.00000	1.00743	0.96504	0.98995	1.05230	0.94075
52	2.2270*-02	1.0569*-01	1.00000	1.00642	0.97902	0.99506	1.03304	0.95324
53	2.3230*-02	1.0797*-01	1.00000	1.00453	0.98951	0.99824	1.01772	0.98086
54	2.4230*-02	1.0787*-01	1.00000	1.00311	0.98951	0.99753	1.01628	0.98155
55	2.5180*-02	1.0859*-01	1.00000	1.00239	0.99301	0.99877	1.01153	0.98728
56	2.6180*-02	1.1006*-01	1.00000	1.00000	1.00000	1.00000	1.00000	1.00000
57	2.7150*-02	1.1030*-01	1.00000	0.99911	1.00350	1.00088	0.99479	1.00613
58	2.8110*-02	1.1030*-01	1.00000	1.00037	1.00350	1.00176	0.99654	1.00524
59	2.9100*-02	1.1223*-01	1.00000	0.99952	1.01049	1.00370	0.99661	1.01733
60	3.0040*-02	1.1154*-01	1.00000	1.00037	1.00679	1.00242	0.99174	1.01118
61	3.1010*-02	1.1228*-01	1.00000	0.99952	1.01049	1.00370	0.99661	1.01733
62	3.2020*-02	1.1154*-01	1.00000	1.00037	1.00679	1.00242	0.99174	1.01118
63	3.3030*-02	1.1080*-01	1.00000	1.00037	1.00350	1.00176	0.99654	1.00524
64	3.3980*-02	1.1154*-01	1.00000	1.00037	1.00679	1.00242	0.99174	1.01118
65	3.4960*-02	1.1030*-01	1.00000	0.99911	1.00350	1.00088	0.99479	1.00613
66	3.5920*-02	1.1080*-01	1.00000	1.00037	1.00350	1.00176	0.99654	1.00524
67	3.6910*-02	1.1080*-01	1.00000	0.99911	1.00350	1.00088	0.99479	1.00613
68	3.7930*-02	1.1080*-01	1.00000	1.00037	1.00350	1.00176	0.99654	1.00524
69	3.8900*-02	1.1080*-01	1.00000	1.00037	1.00350	1.00176	0.99654	1.00524
70	3.9890*-02	1.1080*-01	1.00000	0.99911	1.00350	1.00088	0.99479	1.00613
71	4.0940*-02	1.1080*-01	1.00000	1.00037	1.00350	1.00176	0.99654	1.00524

34910107		TAYLOR		PROFILE TABULATION		61 POINTS, DELTA AT POINT 53		
I	Y	PTZ/P	P/PD	T0/T50	M/MD	U/UD	T/TD	R/RD=U/UD
1	0.0000**00	1.0000**00	1.61265	1.04031	0.00000	0.00000	2.74137	0.00000
2	8.9900**05	1.6378**00	1.61355	1.03959	0.30420	0.46931	2.39022	0.31817
3	1.5700**04	1.9235**00	1.61355	1.03155	0.33916	0.51398	2.29850	0.36178
4	2.9250**04	2.0325**00	1.61355	1.03876	0.37052	0.55417	2.23568	0.39999
5	3.8640**04	2.1851**00	1.61355	1.02912	0.39151	0.57641	2.16651	0.42932
6	4.4730**04	2.2661**00	1.63447	1.03072	0.40210	0.58940	2.14856	0.44837
7	5.4770**04	2.2737**00	1.63314	1.03646	0.40559	0.59509	2.15269	0.45146
8	6.3730**04	2.3786**00	1.47667	1.03427	0.41603	0.60649	2.12454	0.46721
9	7.6280**04	2.4075**00	1.63934	1.02970	0.41953	0.60914	2.10771	0.47373
10	8.4980**04	2.4663**00	1.62423	1.03155	0.42657	0.61751	2.09554	0.48151
11	9.6350**04	2.5875**00	1.63048	1.03003	0.44056	0.63245	2.05084	0.50033
12	1.0350**03	2.5875**00	1.63226	1.03003	0.44056	0.63245	2.06084	0.50092
13	1.2500**03	2.7136**00	1.62634	1.02856	0.45434	0.64704	2.02631	0.51351
14	1.4510**03	2.6816**00	1.62551	1.03125	0.45125	0.64437	2.04030	0.51325
15	1.6270**03	2.8112**00	1.62635	1.03453	0.45534	0.66007	2.01442	0.53273
16	1.8240**03	2.9115**00	1.62295	1.03204	0.47552	0.67017	1.93618	0.54761
17	2.0170**03	2.9778**00	1.61852	1.03127	0.47203	0.65625	1.99224	0.54127
18	2.1890**03	3.0492**00	1.61808	1.03064	0.49951	0.63336	1.95171	0.55696
19	2.4080**03	3.1555**00	1.61935	1.03615	0.50030	0.63614	1.93844	0.53173
20	2.5870**03	3.1198**00	1.61896	1.02731	0.49650	0.58731	1.93083	0.57343
21	2.7590**03	3.1915**00	1.61852	1.03536	0.50350	0.69952	1.93022	0.58656
22	2.9740**03	3.3756**00	1.61852	1.02814	0.52078	0.71375	1.87696	0.61548
23	3.4440**03	3.4894**00	1.61836	1.02671	0.53147	0.72233	1.84974	0.62264
24	3.9530**03	3.6450**00	1.61320	1.02738	0.54545	0.73635	1.82241	0.65181
25	4.4150**03	3.7245**00	1.61232	1.02513	0.55245	0.74158	1.80241	0.66345
26	4.9030**03	3.9273**00	1.60922	1.02333	0.56933	0.75663	1.76247	0.69034
27	5.3620**03	4.0531**00	1.60301	1.03073	0.59042	0.76919	1.75168	0.70243
28	5.9530**03	4.2672**00	1.62134	1.02951	0.59770	0.78242	1.71247	0.73150
29	6.3330**03	4.3939**00	1.59991	1.02433	0.62839	0.73918	1.68253	0.75039
30	6.9100**03	4.5237**00	1.59534	1.02433	0.62537	0.93324	1.64635	0.77903
31	7.2790**03	4.7619**00	1.59149	1.02313	0.63636	0.81053	1.62229	0.77514
32	7.7420**03	4.9023**00	1.59398	1.02577	0.64635	0.81961	1.60545	0.81135
33	8.2220**03	5.2394**00	1.59149	1.02112	0.67133	0.93552	1.54933	0.85836
34	8.6910**03	5.2394**00	1.59618	1.02505	0.67133	0.83722	1.55527	0.85336
35	9.1900**03	5.3381**00	1.58618	1.02503	0.67332	0.84220	1.54155	0.85655
36	9.6630**03	5.6918**00	1.58751	1.02013	0.70230	0.85714	1.43747	0.91479
37	1.0160**02	5.6918**00	1.53307	1.01935	0.70230	0.85697	1.48685	0.91242
38	1.0630**02	5.9523**00	1.57554	1.01814	0.72023	0.86817	1.45281	0.94151
39	1.1130**02	6.1654**00	1.57023	1.01912	0.73427	0.87725	1.42737	0.96505
40	1.1610**02	6.4377**00	1.56092	1.01816	0.75175	0.88774	1.39453	0.99366
41	1.2000**02	6.3280**00	1.54187	1.01704	0.74475	0.88294	1.40551	0.98850
42	1.2480**02	6.7730**00	1.51833	1.01537	0.77273	0.89913	1.35391	1.00836
43	1.3450**02	7.4122**00	1.47142	1.01570	0.81119	0.92101	1.28909	1.05128
44	1.4440**02	7.7742**00	1.42313	1.01271	0.83217	0.93037	1.25156	1.05859
45	1.5400**02	8.2033**00	1.37661	1.01132	0.85654	0.94289	1.21150	1.07139
46	1.6380**02	8.3982**00	1.32920	1.01005	0.86713	0.94841	1.19624	1.05392
47	1.7350**02	8.4505**00	1.28223	1.00834	0.89151	0.95837	1.15536	1.05351
48	1.8330**02	9.1146**00	1.23438	1.00721	0.90559	0.96442	1.13413	1.04966
49	1.9260**02	9.2482**00	1.18919	1.00649	0.91253	0.96709	1.12301	1.02408
50	2.0250**02	9.5853**00	1.14039	1.00433	0.93007	0.97403	1.09676	1.01322
51	2.1220**02	1.0002**01	1.09393	1.00229	0.95125	0.98163	1.06544	1.00792
52	2.2200**02	1.0569**01	1.04652	1.00233	0.97932	0.99306	1.02889	1.01008
53	2.3160**02	1.1006**01	1.00070	1.00070	1.00000	1.00000	1.00000	1.00000
54	2.4140**02	1.1302**01	0.98449	0.99913	1.01339	1.02430	0.98196	1.00740
55	2.5120**02	1.1228**01	0.98449	0.99640	1.01049	1.00213	0.99352	1.00312
56	2.6100**02	1.1228**01	0.98449	0.99711	1.01049	1.00249	0.99423	1.00276
57	2.7070**02	1.1302**01	0.99449	0.99610	1.01339	1.00338	0.97918	1.00882
58	2.8030**02	1.1302**01	0.99449	0.99610	1.01339	1.00338	0.97918	1.00882
59	2.9030**02	1.1377**01	0.98449	0.99552	1.01748	1.00427	0.97420	1.01438
60	3.0010**02	1.1302**01	0.98449	0.99610	1.01339	1.00338	0.97918	1.00882
61	3.1000**02	1.1302**01	0.98449	0.99610	1.01339	1.00338	0.97918	1.00882

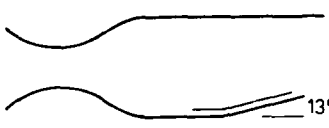
34010109		TAYLOR	PROFILE TABULATION			66 POINTS, DELTA AT POINT 57		
I	Y	PT2/P	P/PJ	T0/TJD	M/MJ	U/UD	T/TD	R/R0=U/UD
1	0.0000E+00	1.0000E+00	1.05671	1.03938	0.00000	0.00000	2.35038	0.00000
2	8.8900E-05	1.5336E+00	1.05671	1.04359	0.32271	0.46597	2.09494	0.23617
3	1.7940E-04	1.7874E+00	1.05671	1.03551	0.37849	0.53293	1.98263	0.28404
4	2.8800E-04	2.0570E+00	1.05671	1.03954	0.42629	0.59943	1.91183	0.32579
5	3.8580E-04	2.2383E+00	1.05671	1.04031	0.45419	0.62044	1.85609	0.35133
6	4.9440E-04	2.3500E+00	1.05592	1.03354	0.47012	0.63548	1.82720	0.36724
7	5.8490E-04	2.4361E+00	1.05750	1.03756	0.49004	0.65749	1.80020	0.38624
8	7.0070E-04	2.4961E+00	1.05556	1.03633	0.49004	0.65731	1.79920	0.38557
9	7.8400E-04	2.5558E+00	1.05277	1.03845	0.49801	0.66593	1.78809	0.39208
10	8.9260E-04	2.7458E+00	1.05497	1.03433	0.52191	0.68850	1.74025	0.41734
11	9.7220E-04	2.7138E+00	1.05146	1.02837	0.51793	0.68281	1.73804	0.41308
12	1.0190E-03	2.7458E+00	1.04935	1.02937	0.52191	0.68703	1.73283	0.41605
13	1.1390E-03	2.9455E+00	1.05203	1.03017	0.54592	0.71015	1.69278	0.44176
14	1.2620E-03	2.3773E+00	1.05172	1.03231	0.53795	0.70336	1.71014	0.43256
15	1.3920E-03	2.9738E+00	1.05014	1.03416	0.54930	0.71528	1.69256	0.44379
16	1.5040E-03	2.9455E+00	1.04804	1.02954	0.54582	0.70996	1.69190	0.43978
17	1.5590E-03	3.0144E+00	1.04639	1.03073	0.55378	0.71785	1.69029	0.44729
18	1.6670E-03	3.0144E+00	1.04831	1.03073	0.55378	0.71785	1.69029	0.44786
19	1.8080E-03	3.1198E+00	1.04778	1.03257	0.56574	0.72959	1.66314	0.45964
20	1.9240E-03	3.0844E+00	1.04752	1.03529	0.56175	0.72694	1.67412	0.45479
21	2.0370E-03	3.1198E+00	1.04621	1.02852	0.56574	0.72812	1.65646	0.45988
22	2.1780E-03	3.1198E+00	1.04773	1.03579	0.56574	0.73069	1.66817	0.45835
23	2.5760E-03	3.2643E+00	1.04952	1.03019	0.59157	0.74317	1.63235	0.47786
24	3.0510E-03	3.3332E+00	1.05172	1.02734	0.59964	0.74922	1.61452	0.49805
25	3.4630E-03	3.5279E+00	1.04936	1.02651	0.60556	0.76628	1.53030	0.50893
26	3.3100E-03	3.4133E+00	1.05146	1.03425	0.59761	0.75976	1.61203	0.49491
27	4.2230E-03	3.4934E+00	1.04752	1.03134	0.60559	0.76463	1.59427	0.50240
28	4.4500E-03	3.9050E+00	1.04439	1.02834	0.63745	0.79050	1.53733	0.53711
29	4.9980E-03	3.7646E+00	1.04279	1.03070	0.63347	0.78793	1.54713	0.53108
30	5.4000E-03	3.3456E+00	1.02339	1.03035	0.64143	0.79453	1.53433	0.53923
31	5.8490E-03	3.3456E+00	1.03896	1.02421	0.64143	0.79197	1.52443	0.53970
32	6.2870E-03	4.0110E+00	1.03676	1.02573	0.65737	0.80536	1.50031	0.55630
33	6.6920E-03	4.2233E+00	1.03337	1.02217	0.67729	0.81948	1.45396	0.57873
34	7.1410E-03	4.3547E+00	1.03208	1.02236	0.68924	0.82884	1.44609	0.59212
35	7.4960E-03	4.3108E+00	1.03177	1.02714	0.68526	0.82756	1.45843	0.58546
36	7.9450E-03	4.3547E+00	1.03072	1.02422	0.68924	0.82939	1.44801	0.59037
37	8.3650E-03	4.3084E+00	1.03124	1.02411	0.72908	0.85838	1.38611	0.63861
38	8.7080E-03	4.7156E+00	1.02898	1.02271	0.72112	0.85214	1.39640	0.62786
39	9.1390E-03	4.6695E+00	1.03045	1.02428	0.71713	0.84994	1.40467	0.62350
40	9.5340E-03	5.0452E+00	1.02852	1.02225	0.74900	0.87140	1.35353	0.66223
41	9.9720E-03	4.9973E+00	1.03255	1.01873	0.74502	0.86718	1.35482	0.66090
42	1.0360E-02	5.2394E+00	1.02835	1.01732	0.75494	0.88021	1.32408	0.69362
43	1.1130E-02	5.3878E+00	1.02940	1.02004	0.77689	0.88901	1.30946	0.69887
44	1.2000E-02	5.3473E+00	1.02308	1.01531	0.81275	0.90974	1.25292	0.75012
45	1.2880E-02	6.2193E+00	1.03619	1.01874	0.84064	0.92772	1.21791	0.78472
46	1.3790E-02	6.3827E+00	1.02914	1.01238	0.85259	0.93194	1.19480	0.80273
47	1.4730E-02	6.7165E+00	1.02914	1.01332	0.87649	0.94552	1.16369	0.83619
48	1.5580E-02	6.7730E+00	1.02809	1.01054	0.89049	0.94643	1.15543	0.84213
49	1.6540E-02	7.3528E+00	1.02573	1.01171	0.92032	0.96790	1.10606	0.89760
50	1.7490E-02	7.5319E+00	1.02520	1.00937	0.93227	0.97303	1.09936	0.91573
51	1.8400E-02	7.7742E+00	1.02310	1.00923	0.94321	0.98055	1.06939	0.93811
52	1.9310E-02	8.0829E+00	1.01995	1.00745	0.96813	0.98918	1.04396	0.96643
53	2.0280E-02	8.2083E+00	1.01419	1.00432	0.97610	0.99119	1.03117	0.97486
54	2.1160E-02	8.4620E+00	1.01155	1.00344	0.99203	0.99817	1.01240	0.99732
55	2.2060E-02	8.5261E+00	1.00751	1.00037	0.99602	0.99872	1.00543	1.00088
56	2.2960E-02	8.5261E+00	1.00499	0.99937	0.99602	0.99817	1.00432	0.99893
57	2.3830E-02	8.5905E+00	1.00000	1.00000	1.00000	1.00000	1.00000	1.00000
58	2.4790E-02	8.7200E+00	0.99790	0.99631	1.00737	1.00165	0.99750	1.01220
59	2.5740E-02	8.7200E+00	0.99217	0.99486	1.00737	1.00092	0.99606	1.00814
60	2.6620E-02	8.6550E+00	0.99031	0.99540	1.00398	0.99945	0.99100	0.99926
61	2.7570E-02	8.7200E+00	0.99697	0.99448	1.00737	1.00073	0.99559	1.00194
62	2.8470E-02	8.7851E+00	0.99110	0.99530	1.01135	1.00312	0.99262	1.00156
63	2.9340E-02	8.7200E+00	0.97611	0.99705	1.00737	1.00202	0.99823	0.99873
64	3.0370E-02	8.7200E+00	0.97243	0.99705	1.00737	1.00202	0.99823	0.98600
65	3.1330E-02	8.8505E+00	0.96771	0.99492	1.01534	1.00440	0.97741	0.99443
66	3.2240E-02	8.9505E+00	0.96640	0.99492	1.01534	1.00440	0.97741	0.99308

34010404		TAYLOR		PROFILE TABULATION		46 POINTS, DELTA AT POINT 39			
I	Y	PT2/P	P/PD	T0/T0D	M/MD	U/UD	T/TD	R/RD=U/UD	
1	0.0000**+00	1.0000**+00	1.69434	1.03996	0.00000	0.00000	2.57539	0.00000	
2	1.8000**+04	1.5330**+00	1.70112	1.02828	0.29654	0.44519	2.25384	0.33601	
3	4.1310**+04	1.4754**+00	1.70112	1.02817	0.28215	0.42589	2.27839	0.31798	
4	5.1160**+04	1.5792**+00	1.70112	1.02775	0.30732	0.45931	2.23367	0.34980	
5	7.4360**+04	1.8800**+00	1.70112	1.02775	0.36588	0.53337	2.12512	0.42696	
6	9.9650**+04	2.0035**+00	1.77398	1.02720	0.39572	0.55705	2.08563	0.47381	
7	1.2340**+03	2.1536**+00	1.75873	1.02670	0.40730	0.58265	2.04132	0.50199	
8	1.4740**+03	2.2661**+00	1.74687	1.02754	0.42326	0.60043	2.01236	0.52121	
9	1.7200**+03	2.3671**+00	1.73840	1.02539	0.43651	0.61465	1.99275	0.53890	
10	1.9720**+03	2.4485**+00	1.72823	1.02601	0.44682	0.62593	1.96240	0.55123	
11	2.2030**+03	2.5324**+00	1.71976	1.02638	0.45712	0.63710	1.94247	0.56406	
12	2.3700**+03	2.5660**+00	1.71457	1.02563	0.46117	0.64117	1.93294	0.56877	
13	2.8460**+03	2.7329**+00	1.69943	1.02477	0.48058	0.66128	1.89263	0.59378	
14	3.3240**+03	2.8845**+00	1.68553	1.02447	0.49761	0.67825	1.85782	0.61535	
15	3.8090**+03	3.0318**+00	1.67249	1.02311	0.51343	0.69339	1.82382	0.63585	
16	4.2930**+03	3.1807**+00	1.66367	1.02231	0.52889	0.70812	1.79258	0.65720	
17	4.7690**+03	3.2974**+00	1.65537	1.02229	0.54067	0.71899	1.76840	0.67304	
18	5.2530**+03	3.4971**+00	1.64470	1.02150	0.56018	0.73656	1.72891	0.70069	
19	5.7410**+03	3.6925**+00	1.63030	1.02070	0.57859	0.75251	1.69162	0.72523	
20	6.2240**+03	3.8334**+00	1.62217	1.02039	0.59146	0.76347	1.66629	0.74327	
21	6.6510**+03	3.9485**+00	1.61132	1.01997	0.60177	0.77202	1.64590	0.75580	
22	7.1390**+03	4.1294**+00	1.59990	1.01932	0.61759	0.78492	1.61437	0.77750	
23	8.0230**+03	4.5150**+00	1.57937	1.01832	0.64938	0.81002	1.55306	0.82406	
24	8.9150**+03	4.8173**+00	1.55541	1.01667	0.67427	0.82759	1.50648	0.85447	
25	9.8790**+03	5.2247**+00	1.52854	1.01523	0.70556	0.84933	1.44908	0.89596	
26	1.0840**+02	5.6149**+00	1.50017	1.01402	0.73427	0.86823	1.33818	0.93156	
27	1.1730**+02	5.9840**+00	1.47205	1.01310	0.75040	0.88459	1.35332	0.90219	
28	1.2640**+02	6.4432**+00	1.43934	1.01144	0.73169	0.90299	1.30092	0.99905	
29	1.3530**+02	6.8755**+00	1.40241	1.01076	0.82002	0.91903	1.25605	1.02612	
30	1.4510**+02	7.2878**+00	1.36039	1.00938	0.84615	0.93274	1.21514	1.00453	
31	1.5400**+02	7.7559**+00	1.32006	1.00840	0.87486	0.94727	1.17238	1.00659	
32	1.6280**+02	8.1957**+00	1.27550	1.00677	0.90099	0.95957	1.13424	1.07907	
33	1.7160**+02	8.6034**+00	1.22857	1.00551	0.92455	0.97003	1.10080	1.00262	
34	1.7970**+02	8.9227**+00	1.18706	1.00457	0.94258	0.97785	1.07623	1.07854	
35	1.8850**+02	9.2031**+00	1.13995	1.00365	0.95841	0.98435	1.05487	1.05375	
36	1.9750**+02	9.4914**+00	1.09032	1.00254	0.97387	0.99045	1.03434	1.00453	
37	2.0660**+02	9.7379**+00	1.04439	1.00113	0.99712	0.99533	1.01670	1.02244	
38	2.1550**+02	9.9803**+00	1.00070	1.00000	1.00000	1.00000	1.00000	1.00000	
39	2.2460**+02	1.0177**+01	0.95849	0.99907	1.01031	1.00366	0.99688	0.97478	
40	2.3350**+02	1.0276**+01	0.92054	0.99736	1.01546	1.00508	0.97967	0.94442	
41	2.4250**+02	1.0433**+01	0.88272	0.99644	1.02356	1.00752	0.96891	0.91811	
42	2.5140**+02	1.0685**+01	0.84758	0.99516	1.03644	1.01179	0.95300	0.89997	
43	2.7030**+02	1.1154**+01	0.79888	0.99224	1.05939	1.01900	0.92415	0.88098	
44	2.8890**+02	1.1414**+01	0.77804	0.99119	1.07287	1.02306	0.90930	0.87539	
45	3.0730**+02	1.1520**+01	0.76754	0.98965	1.07803	1.02408	0.90242	0.87102	
46	3.2500**+02	1.1572**+01	0.75839	0.98938	1.09050	1.02509	0.89990	0.86399	

84010407		TAYLOR		PROFILE TABULATION		41 POINTS, DELTA AT POINT 30			
I	Y	PT2/P	P/P0	T0/T00	M/M0	U/U0	T/T0	R/R0*U/U0	
1	0.0000+00	1.0000+00	1.05764	1.03939	0.00000	0.00000	2.04031	0.00000	
2	1.8000+04	1.5573+00	1.04643	1.02338	0.37451	0.49827	1.77010	0.29456	
3	4.2270+04	1.6939+00	1.04643	1.02345	0.41104	0.54013	1.72717	0.32728	
4	6.1810+04	1.9868+00	1.04643	1.02249	0.47469	0.60950	1.64855	0.38686	
5	8.7580+04	2.3161+00	1.04643	1.02290	0.53260	0.66875	1.57660	0.44387	
6	1.1130+03	2.5233+00	1.03533	1.02253	0.56498	0.69994	1.53493	0.47215	
7	1.3450+03	2.6658+00	1.03035	1.02205	0.58596	0.71940	1.50733	0.49175	
8	1.5790+03	2.7556+00	1.02443	1.02219	0.59872	0.73114	1.49123	0.50227	
9	1.8180+03	2.8510+00	1.02126	1.02112	0.61195	0.74265	1.47279	0.51497	
10	2.0500+03	2.8980+00	1.01819	1.02059	0.61833	0.74824	1.46433	0.52027	
11	2.2930+02	2.9217+00	1.01692	1.02112	0.62152	0.75115	1.46061	0.52297	
12	2.5370+03	2.9695+00	1.01512	1.02049	0.62731	0.75651	1.45158	0.52905	
13	3.0140+03	3.0318+00	1.01037	1.01995	0.63611	0.76344	1.44040	0.53552	
14	3.4930+03	3.0914+00	1.00814	1.01979	0.64397	0.77004	1.43032	0.54275	
15	3.9760+03	3.1448+00	1.00730	1.01858	0.65071	0.77540	1.41999	0.55005	
16	4.4520+03	3.2060+00	1.00878	1.01846	0.65846	0.78189	1.41004	0.55938	
17	4.9430+03	3.2460+00	1.00825	1.01775	0.66347	0.78580	1.40274	0.56481	
18	5.4260+03	3.3122+00	1.00476	1.01657	0.67163	0.79217	1.39096	0.57223	
19	5.9120+03	3.4019+00	1.00328	1.01678	0.68263	0.80123	1.37768	0.58349	
20	6.3850+03	3.4856+00	1.00127	1.01551	0.69266	0.80872	1.36320	0.59401	
21	6.8550+03	3.5783+00	0.99798	1.01533	0.70350	0.81733	1.34939	0.60442	
22	7.3380+03	3.6925+00	0.99609	1.01457	0.71693	0.82717	1.33155	0.61877	
23	8.3030+03	3.8497+00	0.99408	1.01330	0.73461	0.84025	1.30827	0.63845	
24	9.2680+03	4.1294+00	0.99196	1.01157	0.76516	0.86216	1.26960	0.67362	
25	1.0030+02	4.3284+00	0.99291	1.01079	0.73614	0.87690	1.24396	0.69985	
26	1.0930+02	4.5873+00	0.99376	1.01013	0.81259	0.89458	1.21199	0.73350	
27	1.2510+02	5.1905+00	0.99503	1.00753	0.97095	0.93114	1.14237	0.81061	
28	1.4440+02	5.8316+00	0.99810	1.00533	0.92886	0.96434	1.07784	0.89299	
29	1.6380+02	6.3608+00	1.00042	1.00290	0.97401	0.98793	1.02878	0.96069	
30	1.8330+02	6.6771+00	1.00000	1.00000	1.00000	1.00000	1.00000	1.00000	
31	2.0250+02	6.8355+00	1.00032	0.99741	1.01277	1.00514	0.98500	1.02078	
32	2.2150+02	6.8755+00	0.99547	0.99515	1.01596	1.00559	0.97969	1.02589	
33	2.4110+02	6.9155+00	0.99662	0.99254	1.01915	1.00593	0.97421	1.02906	
34	2.6050+02	6.9155+00	0.99154	0.99004	1.01915	1.00458	0.97162	1.02518	
35	2.7980+02	6.9615+00	0.98403	0.98733	1.02230	1.00503	0.96556	1.02426	
36	2.9940+02	6.9615+00	0.98001	0.98475	1.02280	1.00369	0.96298	1.02144	
37	3.1860+02	6.8755+00	0.98033	0.98477	1.01596	1.00033	0.96948	1.01153	
38	3.3700+02	6.8355+00	0.96848	0.98502	1.01277	0.99888	0.97277	0.99448	
39	3.5640+02	5.9840+00	0.85045	0.98451	0.94209	0.96165	1.04197	0.78490	
40	3.7570+02	8.6486+00	0.45785	0.98460	1.14865	1.05991	0.85129	0.57000	
41	3.9490+02	1.0999+01	0.35822	0.98461	1.30369	1.11627	0.73314	0.54543	

84010411		TAYLOR		PROFILE TABULATION		51 POINTS, DELTA AT POINT 41			
I	Y	PT2/P	P/PD	T0/T0D	M/MD	U/U0	T/TD	R/RD*U/U0	
1	0.0000*-00	1.0000*-00	1.01092	1.03996	0.07000	0.00000	1.99516	0.00000	
2	1.8000*-04	1.6080*-00	0.99535	1.03072	0.33791	0.52252	1.72531	0.30145	
3	4.4460*-04	1.6690*-00	0.99535	1.02929	0.41423	0.54102	1.70583	0.31568	
4	6.1930*-04	1.9773*-00	0.99535	1.02944	0.48390	0.61693	1.62539	0.37779	
5	7.1900*-04	2.2198*-00	0.99535	1.02977	0.52870	0.66266	1.57095	0.41986	
6	8.1640*-04	2.4397*-00	0.99292	1.02835	0.56510	0.69795	1.52546	0.45430	
7	9.8700*-04	2.7104*-00	0.99595	1.02895	0.60615	0.73641	1.47593	0.49647	
8	1.2330*-03	2.9081*-00	0.99555	1.02899	0.63416	0.76138	1.44146	0.52590	
9	1.4750*-03	3.0914*-00	0.99393	1.02835	0.65839	0.78271	1.41115	0.55124	
10	1.6390*-03	3.1555*-00	0.99252	1.02841	0.67529	0.79963	1.40029	0.55969	
11	1.8100*-03	3.2205*-00	0.99030	1.02757	0.67569	0.79632	1.39895	0.56776	
12	1.9810*-03	3.2716*-00	0.98797	1.02769	0.69222	0.80177	1.39118	0.57351	
13	2.3160*-03	3.3906*-00	0.98504	1.02703	0.69715	0.81368	1.36224	0.58838	
14	2.6490*-03	3.4436*-00	0.98342	1.02668	0.70369	0.81879	1.35390	0.59474	
15	3.0620*-03	3.5240*-00	0.98514	1.02650	0.71349	0.82651	1.34190	0.60677	
16	3.4660*-03	3.5940*-00	0.98858	1.02535	0.72199	0.83263	1.33036	0.61872	
17	3.8780*-03	3.6057*-00	0.98939	1.02546	0.72329	0.83377	1.32884	0.62110	
18	4.2870*-03	3.6648*-00	0.98757	1.02413	0.73028	0.83865	1.31878	0.62802	
19	4.7680*-03	3.7204*-00	0.98494	1.02353	0.73682	0.84341	1.31027	0.63393	
20	5.1870*-03	3.7767*-00	0.98049	1.02314	0.74335	0.84818	1.30193	0.63877	
21	5.6590*-03	3.8334*-00	0.97756	1.02294	0.74988	0.85306	1.29410	0.64439	
22	6.0750*-03	3.8334*-00	0.97503	1.02239	0.74938	0.85283	1.29342	0.64290	
23	7.0570*-03	3.9651*-00	0.97130	1.02060	0.76482	0.86316	1.27369	0.65857	
24	7.8600*-03	4.0996*-00	0.97048	1.01964	0.77975	0.87360	1.25520	0.67544	
25	8.7610*-03	4.1422*-00	0.97109	1.01879	0.78441	0.87666	1.24993	0.68158	
26	9.6580*-03	4.2803*-00	0.97129	1.01768	0.79935	0.88664	1.23035	0.69996	
27	1.0550*-02	4.3768*-00	0.97321	1.01573	0.80961	0.89300	1.21660	0.71435	
28	1.1520*-02	4.5556*-00	0.97412	1.01496	0.82823	0.90525	1.19451	0.73824	
29	1.2500*-02	4.7202*-00	0.97564	1.01343	0.84508	0.91569	1.17410	0.76691	
30	1.3380*-02	4.9178*-00	0.97665	1.01240	0.85488	0.92159	1.16217	0.77447	
31	1.4280*-02	5.0500*-00	0.97736	1.01159	0.87774	0.93578	1.13661	0.80516	
32	1.5030*-02	5.1905*-00	0.97918	1.01029	0.89127	0.94349	1.12061	0.82441	
33	1.6000*-02	5.4328*-00	0.98079	1.00925	0.91414	0.95677	1.09544	0.85663	
34	1.6900*-02	5.5437*-00	0.98251	1.00754	0.92441	0.96199	1.08297	0.87276	
35	1.7780*-02	5.7589*-00	0.98453	1.00676	0.94400	0.97289	1.06211	0.90182	
36	1.8760*-02	5.9417*-00	0.98706	1.00569	0.95034	0.98150	1.04457	0.92747	
37	1.9660*-02	6.0211*-00	0.99020	1.00431	0.96734	0.98468	1.03619	0.94098	
38	2.0550*-02	6.2085*-00	0.99323	1.00296	0.98367	0.99285	1.01876	0.96797	
39	2.1360*-02	6.2464*-00	0.99596	1.00219	0.98693	0.99421	1.01481	0.97575	
40	2.2180*-02	6.3608*-00	0.99808	1.00114	0.99673	0.99886	1.00428	0.99270	
41	2.3040*-02	6.3991*-00	1.00000	1.00000	1.00000	1.00000	1.00000	1.00000	
42	2.3930*-02	6.4818*-00	0.99990	0.99842	1.00700	1.00284	0.99175	1.01108	
43	2.5810*-02	6.5206*-00	1.00091	0.99593	1.01027	1.00329	0.98624	1.01811	
44	2.7610*-02	6.5206*-00	1.00051	0.99373	1.01027	1.00216	0.98401	1.01896	
45	2.9470*-02	6.5206*-00	1.00121	0.99103	1.01027	1.00079	0.98134	1.02107	
46	3.1280*-02	6.4818*-00	1.00091	0.99053	1.00700	0.99886	0.98391	1.01613	
47	3.3220*-02	6.4432*-00	1.00293	0.99043	1.00373	0.99716	0.98695	1.01331	
48	3.5070*-02	6.3225*-00	1.00960	0.99072	0.99347	0.99194	0.99694	1.00455	
49	3.7000*-02	6.2085*-00	1.01799	0.99052	0.98357	0.98672	1.00622	0.99827	
50	3.8850*-02	6.1331*-00	1.02305	0.99032	0.97713	0.98309	1.01223	0.99360	
51	4.0710*-02	6.1331*-00	1.03013	0.99032	0.97713	0.98309	1.01223	1.00047	



	$M(\infty): 2.25$ upstream $R \text{ Theta} \times 10^{-3}: 7$ $TW/TR: \text{Appr. } 1$	8402
		CCF
<p>Ejector-driven blow down tunnel with symmetrical contoured nozzle. Running time: 90 secs. <math>W = H = 0.15 \text{ m}</math>. <math>L = 0.495 \text{ m}</math>.  <math>P_0: 90 \text{ kN/m}^2</math>. <math>T_0: 300 \text{ K}</math>. Air. <math>Re/m \times 10^{-6}: 11</math>.</p>		
<p>ARDONCEAU P.L., 1984. The structure of turbulence in a supersonic shock-wave/boundary-layer interaction. AIAA J 22 1254-1262.          And: Ardonceau (1981), Data tables, P.L.Ardonceau, private communication.</p>		

- 1 The test boundary layer developed under ZPG conditions on the tunnel floor before encountering an abrupt change in direction at the compression corner ( $X = 0$ ) a distance 219 mm from the exit of the nozzle, and 546 mm from the throat. The compression ramps ran the full width of the tunnel at angles of 8, 13 & 18 degrees to the tunnel floor. The ramps extended for 80 mm downstream. The 18° ramp had to be cut off parallel to the tunnel floor from 60 mm on to prevent blockage. "The undisturbed boundary layer was found to be fully turbulent - - without any tripping". Wall pressure was found on lines 2 mm either side of the centreline at 2.33 mm axial spacing with tappings 0.5 mm in dia.. - - spanwise pressure measurements and surface flow visualisations revealed good transverse uniformity over a 90 mm centre part of the flow free from perturbations". Schlieren observations on high speed film suggested that there were periodic structures present of large lateral extent, which imply an associated unsteadiness in the position of mean flow features.
- 2
- 7 Pressure profiles were measured with a FPP (shank dia. 1.0 mm, flattened) and a static probe (CCP,  $d = 1.0 \text{ mm}$ , 4 static holes 12 d from nose). A HWP (DISA 55P11), operated in the constant temperature mode, was used to find the mass-flow fluctuation intensity. The length of all probes between the sensing wire or orifice and the mounting to the traverse gear was 45 mm. A single beam LDV, measurement volume diameter 600  $\mu$ , was used in the forward scatter mode with six orientations to pick up, with a statistical fit, the velocity fluctuations in the streamwise and the vertical directions. Mean velocities were also recorded. The flow was seeded with a range of 1-3  $\mu$  particles by a DOP (Diocetylphthalate) generator, to give about 3000 records/second. Data points were based on 1000 instantaneous frequency readings clipped at the 3  $\sigma$  point.
- 8 The X-coordinate is measured in the direction of the tunnel axis. Profiles were measured normal to the axis in the range  $-0.02 < X < 0.06 \text{ m}$ , with  $NX = 7, 8 \text{ \& } 8$  for the pressure and hot-wire profiles. For series 01 & 02, these are matched by LDV profiles. For series 03, 9 sets of LDV data were supplied, of which 7 match the pressure profiles. The pressure probes were aligned with the local wall direction.
- 9 In reducing the Pitot data the author assumed constant total temperature. To obtain functionally complete profiles from the data supplied, we have used the Mach number, the velocity and the specific mass-flow values from the Pitot-static surveys, as forming a self-consistent set, in principle representing the resultant velocity parallel to the wall. We do not have the original wall pressure data, and have used values derived from the profile data adjacent to the wall. The author notes that " - - the inclination of the isobars is small near the wall - - ". In processing the LDV data for series 03, we have set the author's scaling velocity  $U_i$  equal to the upstream velocity reported in the Pitot measurements for profile 0301.
- 12
- 13 We present three sets of profiles measured in turbulent boundary layers experiencing a shock-wave structure caused by a compression corner. Series 01 is wholly attached, series 02 is on the point of separation, while series 03 has a small separation region in the corner. The profiles cover the flow from upstream of the corner to about 8 undisturbed boundary layer thicknesses downstream.
- 8 DATA: 84020101-0308. Pitot and static, normal hot-wire profiles,  $NX$  7 or 8. Single element LDV profiles reduced to give both components of velocity and fluctuation intensity. Not all at same values of  $X$ .

Editors' comments:

This is a much quoted experiment, surprisingly sketchily reported in detail. The published paper is written round the 18° case, with separation largely ignored. It is for this case that we have the LDV data separately and normalised to an unknown velocity. The combination of conventional profiles, RWP, LDV is attractive, and it is a pity that we have not been able to make more of it. In this experiment there would be significant normal pressure gradients, and the functionally incomplete LDV data is backed up by static pressure information so that in principle there is no problem.

The author remarks that "the laser gives higher velocities than the Pitot tube", which may be the case for the profiles cited in the source paper, for the 18° CCF. We do not have data for this series in a form allowing direct comparison. For the other two series, we find that in general the laser velocities, as shown above in figure 9.2.1, are about 3% lower than those derived from the Pitot profiles.

The LDV profiles, and therefore the associated probe traverses, were made normal to the tunnel axis and so are inclined to the test surface downstream of the corner. The fluctuation measurements do not therefore relate directly to Reynolds stresses in the usual boundary layer axes. Unfortunately, the correlation for  $u'v'$  is only given for series 03, as it is required when rotating the stress tensor. It is probably reasonable to ignore the rotation for series 01, the 8° case, but less so for series 02 at 13°. For the 18° case at least there may be inaccuracies in the mean flow data resulting from static probe misalignment in the same way as for CAT7904.

The shocks do not appear "sharp" in the pressure record, suggesting either an influence of shock oscillation or of the response of probes adjacent to shock waves. The author remarks on the images of "macrostructures" which can be seen in ultra high speed film, principally as evidence of their ability to traverse the discontinuity, and these would cause some degree of fluctuation. The mechanism of relatively large scale shock movement and intermittent separation discussed in chapter 8 and 9.3.1 will also come into play. There are relatively few points in each profile and in most cases the measurements do not extend within the momentum deficit peak. It is for this reason rather than because of low Reynolds-number effects that the upstream H12K value is on the high side.

The mean profiles are shown in figures 10.3.3-5, and the turbulence data in figures 11.2.20-22, 11.3.6. For this purpose a CF value was derived from the Fernholz (1971) skin friction correlation for zero pressure gradient (fig. 10.3.6).

8402-B-1

12F-7

CAT 8402		AROUNDCAU		SOLARARY CONJUNCTIONS AND EVALUATED DATA, SI UNITS							
RUN	NO.	TD	TR	PD	PD	PD	PD	PD	PD	PD	PD
RZ	POD	POD	POD	POD	POD	POD	POD	POD	POD	POD	POD
	POD	POD	POD	POD	POD	POD	POD	POD	POD	POD	POD
34020101	2.2440	1.3000	4.1119E+03	NH	3.3752	1.6453	8.2007E+03	4.0705E+03			
-1.2000E-02	9.2554E+04	1.0149	7.0546E+03	NH	1.7713	1.7452	2.8535E+02	1.5051E+02			
INFINITE	3.0213E+02	NH	7.1246E-04	NH	3.2928	8.8057E-04	5.5200E+02	2.8535E+02			
34020102	2.2330	1.3000	4.5711E+03	NH	3.3031	1.6472	8.1761E+03	4.0705E+03			
-4.0000E-03	9.1170E+04	1.0110	5.0491E+03	NH	1.4271	1.8173	2.8784E+02	1.5201E+02			
INFINITE	3.0350E+02	NH	4.2254E-04	NH	-0.1073	8.1030E-04	5.5200E+02	2.8784E+02			
34020103	2.2430	1.3000	5.0155E+03	NH	1.5547	1.7903	1.1697E+04	7.2571E+03			
-4.0000E-03	9.2614E+04	1.5116	1.0644E+04	NH	1.7099	1.7021	2.8535E+02	1.4554E+02			
INFINITE	3.0432E+02	NH	1.0911E-03	NH	0.2072	1.0374E-03	5.5600E+02	2.8435E+02			
34020104	1.7340	1.3000	4.9074E+03	NH	3.2614	1.7561	1.2553E+04	1.1759E+04			
-1.2000E-02	8.5117E+04	1.0434	7.4370E+03	NH	1.7417	1.7377	2.9144E+02	1.7412E+02			
INFINITE	3.0505E+02	NH	7.2424E-04	NH	0.0117	9.1462E-04	5.1300E+02	2.9143E+02			
34020105	1.9400	1.3000	5.3629E+03	NH	3.4075	1.7164	1.2845E+04	1.2503E+04			
-2.0000E-02	8.3940E+04	1.0172	7.0441E+03	NH	1.7652	1.7531	2.9013E+02	1.7327E+02			
INFINITE	3.0359E+02	NH	7.1223E-04	NH	1.1305	9.3561E-04	5.1200E+02	2.9113E+02			
34020106	1.8350	1.3000	5.7246E+03	NH	3.3773	1.6344	1.3652E+04	1.3565E+04			
-3.6000E-02	8.8951E+04	1.0064	7.3830E+03	NH	1.7675	1.7577	2.9373E+02	1.7494E+02			
INFINITE	3.0281E+02	NH	7.6342E-04	NH	-0.2015	9.8147E-04	5.0300E+02	2.9372E+02			
34020107	1.3670	1.3000	5.5951E+03	NH	3.3550	1.6423	1.4433E+04	1.4159E+04			
-6.0000E-02	9.0119E+04	1.0233	8.3348E+03	NH	1.7757	1.7494	2.8985E+02	1.7342E+02			
INFINITE	3.0230E+02	NH	7.3074E-04	NH	-0.3447	9.2673E-04	5.0000E+02	2.8977E+02			
34020201	2.2570	1.3000	5.5319E+03	NH	3.3459	1.7339	8.2843E+03	7.4951E+03			
-2.0000E-02	9.3116E+04	1.0402	6.0714E+03	NH	1.7935	1.7769	2.9385E+02	1.5706E+02			
INFINITE	3.0696E+02	NH	5.2730E-04	NH	-0.2014	5.3123E-04	5.5800E+02	2.9745E+02			
34020202	2.2600	1.0000	5.5244E+03	NH	4.2137	1.6714	8.2434E+03	7.6535E+03			
-1.2000E-02	9.2315E+04	1.0495	6.3751E+03	NH	1.7751	1.7452	2.8741E+02	1.5117E+02			
INFINITE	3.0545E+02	NH	5.2733E-04	NH	-0.2007	8.5202E-04	5.5700E+02	2.8741E+02			
34020203	2.2550	1.3000	5.5736E+03	NH	3.3047	1.7796	1.1842E+04	7.8775E+03			
-4.0000E-03	9.2005E+04	1.5064	6.5259E+03	NH	1.7166	1.7111	2.8399E+02	1.5164E+02			
INFINITE	3.0600E+02	NH	1.0010E-03	NH	0.3145	1.0740E-03	5.5700E+02	2.9399E+02			
34020204	1.1380	1.3000	4.3753E+03	NH	2.7240	1.7391	1.4444E+04	1.2745E+04			
-4.0000E-03	9.2985E+04	1.1118	1.7619E+04	NH	1.5502	1.6472	2.9294E+02	1.7457E+02			
INFINITE	3.0443E+02	NH	1.0293E-03	NH	0.0077	1.0292E-03	5.1100E+02	2.9297E+02			
34020205	1.7350	1.3000	5.4657E+03	NH	2.3203	1.8741	1.6143E+04	1.3572E+04			
-1.2000E-02	9.0853E+04	1.1812	1.6671E+04	NH	1.7050	1.5501	2.9425E+02	1.7559E+02			
INFINITE	3.0735E+02	NH	1.1744E-03	NH	0.1249	1.3520E-03	5.1300E+02	2.9425E+02			
34020206	1.8010	1.0000	7.1753E+03	NH	3.2534	2.3393	1.5563E+04	1.5551E+04			
-2.0000E-02	9.0241E+04	1.0653	1.5755E+04	NH	1.5826	1.5701	2.9257E+02	1.5107E+02			
INFINITE	3.0504E+02	NH	4.2110E-04	NH	-0.3148	1.1717E-03	4.9100E+02	2.9257E+02			
34020207	1.7010	1.3000	7.3176E+03	NH	2.9454	1.7836	1.7317E+04	1.6774E+04			
-3.6000E-02	8.7953E+04	1.0310	1.0106E+04	NH	1.7014	1.6376	2.9643E+02	1.6975E+02			
INFINITE	3.0620E+02	NH	4.4278E-04	NH	0.0253	1.1353E-03	4.7500E+02	2.9433E+02			
34020209	1.7430	1.3000	4.1246E+03	NH	1.3503	1.6455	1.8050E+04	1.7763E+04			
-6.0000E-02	9.1017E+04	1.0436	1.1530E+04	NH	1.7476	1.7393	2.9380E+02	1.6921E+02			
INFINITE	3.0542E+02	NH	4.7042E-04	NH	0.2176	1.1445E-03	4.8200E+02	2.9377E+02			
34020301	2.2320	1.3000	5.4440E+03	NH	3.5547	1.6799	9.0023E+03	8.1270E+03			
-2.0000E-02	9.1363E+04	1.1077	6.5576E+03	NH	1.7933	1.7447	2.9402E+02	1.5070E+02			
INFINITE	3.0434E+02	NH	6.7476E-04	NH	-0.2422	8.5251E-04	5.5300E+02	2.8702E+02			
34020302	1.9830	1.3000	6.4319E+03	NH	4.4444	2.6701	1.4201E+04	1.0751E+04			
-1.2000E-02	9.1926E+04	1.1209	7.4944E+03	NH	1.5710	1.5529	2.9272E+02	1.5177E+02			
INFINITE	3.0677E+02	NH	7.1455E-04	NH	-0.3739	1.1329E-03	5.2100E+02	2.9277E+02			
34020303	2.0100	1.3000	6.0055E+03	NH	4.0742	3.1171	1.5123E+04	1.2317E+04			
-4.0000E-03	9.7335E+04	1.0278	1.4237E+04	NH	1.6370	1.6067	2.9253E+02	1.6171E+02			
INFINITE	3.0634E+02	NH	1.2411E-03	NH	0.0077	1.4571E-03	5.2500E+02	2.9257E+02			
34020304	1.9230	1.3000	3.1237E+03	NH	4.7159	2.9473	1.6673E+04	1.5161E+04			
-4.0000E-03	9.0234E+04	1.3197	1.3574E+04	NH	1.5706	1.5414	2.9243E+02	1.5341E+02			
INFINITE	3.0532E+02	NH	1.1755E-03	NH	-0.3042	1.5543E-03	4.9500E+02	2.9244E+02			
34020305	1.7270	1.3000	1.0219E+04	NH	3.3429	2.4367	1.8543E+04	1.7745E+04			
-1.2000E-02	9.3141E+04	1.0691	1.4533E+04	NH	1.5811	1.5544	2.9365E+02	1.9137E+02			
INFINITE	3.0552E+02	NH	1.2334E-03	NH	-0.0224	1.6143E-03	4.7900E+02	2.9355E+02			
34020306	1.6330	1.3000	1.3733E+04	NH	3.5711	2.1037	1.9413E+04	1.9443E+04			
-2.0000E-02	9.7801E+04	1.1154	1.4719E+04	NH	1.6119	1.5941	2.9534E+02	1.9137E+02			
INFINITE	3.0648E+02	NH	1.2345E-03	NH	0.3034	1.6131E-03	4.6600E+02	2.9534E+02			
34020307	1.5870	1.3000	1.1714E+04	NH	3.7947	1.9458	2.1563E+04	2.0757E+04			
-3.6000E-02	9.5516E+04	1.0392	1.5375E+04	NH	1.5451	1.6436	2.9677E+02	2.0446E+02			
INFINITE	3.0748E+02	NH	1.1015E-03	NH	0.0094	1.6253E-03	4.5500E+02	2.9677E+02			
34020308	1.5730	1.3000	4.3710E+03	NH	3.6747	1.5754	2.0742E+04	2.1277E+04			
-6.0000E-02	9.7522E+04	1.1751	1.3476E+04	NH	1.7635	1.7549	2.9643E+02	2.0500E+02			
INFINITE	3.0739E+02	NH	1.1117E-03	NH	-0.7323	1.3344E-03	4.5700E+02	2.9643E+02			

84020102 ARDONCEAU PROFILE TABULATION 21 POINTS, DELTA AT POINT 17

I	Y	PT/2	P/R	T/T	M/M	U/U	T/T	R/RD=U/U
1	0.0000E+00	1.0000E+00	1.01113	0.7481	0.00000	0.00000	1.69356	0.00000
2	1.0000E-03	2.7040E+00	1.01113	0.74774	0.53373	0.71739	1.47951	0.49023
3	2.0000E-03	3.4750E+00	1.01440	0.73814	0.47447	0.73946	1.57158	0.59398
4	3.0000E-03	4.1776E+00	1.01440	0.73814	0.47447	0.83977	1.30111	0.65430
5	4.0000E-03	4.8313E+00	1.00540	0.74977	0.73634	0.84225	1.22033	0.72656
6	5.0000E-03	5.4511E+00	1.00540	0.74977	0.85311	0.91848	1.15911	0.79687
7	5.5000E-03	5.4529E+00	1.00440	0.74977	0.87957	0.93478	1.11073	0.83008
8	6.0000E-03	5.7433E+00	1.00143	0.74129	0.74451	0.94928	1.10118	0.85328
9	6.5000E-03	5.9575E+00	1.00071	0.74218	0.72237	0.95014	1.03217	0.88955
10	7.0000E-03	6.1751E+00	1.00071	0.74218	0.74173	0.97101	1.06405	0.91534
11	7.5000E-03	6.3937E+00	1.00167	0.75027	0.75925	0.99007	1.04339	0.94043
12	8.0000E-03	6.6043E+00	0.99838	0.75027	0.77671	0.99113	1.01359	0.95259
13	8.5000E-03	6.8171E+00	1.00115	0.75027	0.79320	0.99275	1.02134	0.97256
14	9.0000E-03	7.0300E+00	1.00115	0.75027	0.81071	0.99457	1.01352	0.98422
15	9.5000E-03	7.2421E+00	1.00000	0.75027	0.82822	0.99619	1.00839	0.99023
16	1.0000E-02	7.4542E+00	0.99942	0.75027	0.84573	1.00000	1.00000	0.99492
17	1.1000E-02	7.6663E+00	1.00000	0.75027	0.86324	1.00000	1.00000	1.00000
18	1.2000E-02	7.8784E+00	1.00116	0.74977	0.88075	1.00000	0.99910	1.00115
19	1.3000E-02	8.0905E+00	1.00116	0.74977	0.89826	1.00000	0.99910	1.00233
20	1.4000E-02	8.3026E+00	1.00116	0.74977	0.91577	1.00000	0.99910	1.00351
21	1.5000E-02	8.5147E+00	1.00116	0.74977	0.93328	1.00000	1.00000	1.00469

84020102 Ardonceau Turbulence Data

X = -4.0000E-03 RHO\_R = 1.8695E-01 U\_R = 5.5200E+02

I	Y	M	U	(RU) <sup>2</sup>	U <sup>2</sup>	V <sup>2</sup>
			UR	RR UR	UR2	UR2
1	1.0000E-3	1.3170E+0	7.1739E-1	5.5163E+0	3.7493E-3	8.9349E-4
2	1.5000E-3				3.8836E-3	9.2628E-4
3	2.0000E-3	1.5060E+0	7.8986E-1	4.6706E+0	4.0203E-3	9.2628E-4
4	2.5000E-3				4.2533E-3	9.1528E-4
5	3.0000E-3	1.6420E+0	8.3877E-1	5.4861E+0	4.0664E-3	7.2861E-4
6	3.5000E-3				2.9932E-3	7.1886E-4
7	4.0000E-3	1.7830E+0	8.8225E-1	5.5225E+0	2.5546E-3	6.1597E-4
8	5.0000E-3	1.9050E+0	9.1848E-1	5.5034E+0	1.6467E-3	5.6320E-4
9	5.5000E-3	1.9630E+0	9.3478E-1	6.1281E+0	1.0871E-3	
10	6.0000E-3	2.0200E+0	9.4928E-1	6.0477E+0	6.4325E-4	3.2819E-4
11	6.5000E-3	2.0610E+0	9.6014E-1	5.8528E+0	4.6475E-4	
12	7.0000E-3	2.1020E+0	9.7101E-1	5.0120E+0	3.1519E-4	
13	7.5000E-3	2.1420E+0	9.8007E-1	4.7592E+0	1.9458E-4	
14	8.0000E-3	2.1810E+0	9.8913E-1	3.1052E+0	1.0292E-4	1.5625E-4
15	8.5000E-3	2.1930E+0	9.9275E-1	2.3357E+0	1.1040E-4	
16	9.0000E-3	2.2060E+0	9.9457E-1	2.9538E+0	1.1815E-4	
17	9.5000E-3	2.2190E+0	9.9819E-1	3.1934E+0	1.2616E-4	
18	1.0000E-2	2.2320E+0	1.0000E+0	2.0024E+0	1.3443E-4	9.2188E-5
19	1.1000E-2	2.2330E+0	1.0000E+0	6.7475E-1	1.4296E-4	
20	1.2000E-2	2.2340E+0	1.0000E+0	9.6439E-1	1.5175E-4	1.0292E-4
21	1.3000E-2	2.2340E+0	1.0000E+0	6.8668E-1	1.1424E-4	
22	1.4000E-2	2.2340E+0	1.0000E+0	4.4783E-1	8.2047E-5	
23	1.5000E-2	2.2330E+0	1.0000E+0	4.4740E-1	8.2047E-5	

84020103 ARDONCEAU PROFILE TABULATION 21 POINTS, DELTA AT POINT 18

I	Y	PT/2	P/R	T/T	M/M	U/U	T/T	R/RD=U/U
1	0.0000E+00	1.0000E+00	1.51157	0.74500	0.00000	0.00000	1.41124	0.00000
2	1.0000E-03	1.7915E+00	1.41157	0.74500	0.40000	0.56000	1.75591	0.49339
3	2.0000E-03	2.3100E+00	1.51157	0.74500	0.40000	0.63958	1.54748	0.62665
4	3.0000E-03	2.8173E+00	1.77701	0.74500	0.73444	0.73958	1.50676	0.76399
5	4.0000E-03	3.2355E+00	1.50701	0.74500	0.67450	0.73958	1.23352	0.85961
6	5.0000E-03	3.6537E+00	1.74657	0.74500	0.75735	0.85213	1.27607	0.91658
7	5.5000E-03	3.8175E+00	1.74657	0.74500	0.75735	0.85213	1.21846	0.94507
8	6.0000E-03	4.0313E+00	1.23127	0.74500	0.75735	0.85213	1.15951	0.96666
9	6.5000E-03	4.2451E+00	1.11510	0.74500	0.84374	0.84374	1.11440	0.97762
10	7.0000E-03	4.4589E+00	1.11046	0.74500	0.84374	0.84374	1.04515	0.99372
11	7.5000E-03	4.6727E+00	1.00843	0.74500	0.85753	0.87330	1.04456	0.99993
12	8.0000E-03	4.8865E+00	1.00000	0.74500	0.87530	0.87530	1.00590	0.99991
13	8.5000E-03	5.0993E+00	1.00000	0.74500	0.87530	0.87530	1.00000	1.00000
14	9.0000E-03	5.3121E+00	0.99823	0.74500	0.87530	0.87530	0.99332	1.00000
15	9.5000E-03	5.5249E+00	0.99823	0.74500	0.87530	0.87530	0.98757	1.01017
16	1.0000E-02	5.7377E+00	0.99823	0.74500	0.87530	0.87530	0.98182	1.01526
17	1.1000E-02	5.9505E+00	0.99823	0.74500	0.87530	0.87530	0.97607	1.01941
18	1.2000E-02	6.1633E+00	0.99823	0.74500	0.87530	0.87530	0.97032	1.02356
19	1.3000E-02	6.3761E+00	0.99823	0.74500	0.87530	0.87530	0.96457	1.02771
20	1.4000E-02	6.5889E+00	0.99823	0.74500	0.87530	0.87530	0.95882	1.03186
21	1.5000E-02	6.8017E+00	0.99823	0.74500	0.87530	0.87530	0.95307	1.03601

84020103 Ardonceau Turbulence Data

X = 4.0000E-03 RHO\_R = 1.8695E-01 U\_R = 5.5200E+02

I	Y	M	U UR	(RU) <sup>2</sup> RR UR	U <sup>2</sup> UR2	V <sup>2</sup> UR2
1	1.0000E-3	9.5200E-1	5.5435E-1	4.4319E+0	8.8401E-3	2.5546E-3
2	1.5000E-3				1.0888E-2	1.4611E-3
3	2.0000E-3	1.1660E+0	6.5580E-1	8.3031E+0	8.7721E-3	1.4890E-3
4	2.5000E-3				7.0657E-3	1.7361E-3
5	3.0000E-3	1.3910E+0	7.4819E-1	8.5509E+0	4.8141E-3	2.2873E-3
6	3.5000E-3				3.7938E-3	2.1340E-3
7	4.0000E-3	1.5830E+0	8.1884E-1	8.0163E+0	3.3397E-3	3.0131E-3
8	5.0000E-3	1.7860E+0	8.8406E-1	6.3997E+0	1.8746E-3	1.7664E-3
9	5.5000E-3	1.8950E+0	9.1667E-1	5.4643E+0	9.9362E-4	
10	6.0000E-3	2.0080E+0	9.4746E-1	4.9170E+0	1.8992E-4	5.5464E-4
11	6.5000E-3	2.0820E+0	9.6739E-1	4.4233E+0	1.1519E-4	
12	7.0000E-3	2.1590E+0	9.8551E-1	4.3104E+0	2.4841E-4	
13	7.5000E-3	2.2410E+0	1.0036E+0	3.2529E+0	1.8956E-4	
14	8.0000E-3	2.3290E+0	1.0236E+0	2.9284E+0	1.3866E-4	8.8742E-5
15	8.5000E-3	2.3400E+0	1.0254E+0	2.9624E+0	1.2212E-4	
16	9.0000E-3	2.3520E+0	1.0272E+0	1.9570E+0	1.0663E-4	
17	9.5000E-3	2.3630E+0	1.0290E+0	1.9630E+0	9.5699E-5	
18	1.0000E-2	2.3740E+0	1.0326E+0	1.4216E+0	8.2047E-5	8.2047E-5
19	1.1000E-2	2.3780E+0	1.0326E+0	5.7229E-1	1.0663E-4	
20	1.2000E-2	2.3810E+0	1.0344E+0	6.8103E-1	1.3866E-4	8.2047E-5
21	1.3000E-2	2.3810E+0	1.0344E+0	1.2259E+0	1.3866E-4	
22	1.4000E-2	2.3810E+0	1.0344E+0	1.2246E+0	1.3866E-4	9.9277E-5
23	1.5000E-2	2.3800E+0	1.0344E+0	1.2393E+0	1.3866E-4	

84020107 ARDONCEAU PROFILE TABULATION 21 POINTS, DELTA AT POINT 15

I	Y	PT./P	P/P0	TOT/T0	M/M0	U/U0	T/T0	R/R0(U/U0)
1	0.0000E+00	1.0000E+00	1.000000	0.957000	0.000000	0.000000	1.02459	0.000000
2	1.0000E-03	2.0015E+00	1.000000	1.000000	0.500000	0.500000	1.300000	0.400000
3	2.0000E-03	2.0079E+00	1.000000	1.000000	0.618000	0.618000	1.340000	0.500000
4	3.0000E-03	2.0131E+00	1.000000	1.000000	0.673000	0.673000	1.299000	0.600000
5	4.0000E-03	2.0182E+00	1.000000	1.000000	0.735000	0.735000	1.241000	0.675000
6	5.0000E-03	3.0433E+00	1.100000	1.176000	0.800000	0.800000	1.370000	0.750000
7	5.5000E-03	3.0433E+00	1.100000	1.176000	0.800000	0.800000	1.370000	0.750000
8	6.0000E-03	3.0433E+00	1.100000	1.176000	0.800000	0.800000	1.370000	0.750000
9	6.5000E-03	4.0133E+00	1.010000	1.000000	0.800000	0.800000	1.000000	0.800000
10	7.0000E-03	4.0133E+00	1.010000	1.000000	0.800000	0.800000	1.000000	0.800000
11	7.5000E-03	4.0133E+00	1.010000	1.000000	0.800000	0.800000	1.000000	0.800000
12	8.0000E-03	4.0133E+00	1.010000	1.000000	0.800000	0.800000	1.000000	0.800000
13	8.5000E-03	4.0133E+00	1.010000	1.000000	0.800000	0.800000	1.000000	0.800000
14	9.0000E-03	4.0133E+00	1.010000	1.000000	0.800000	0.800000	1.000000	0.800000
15	9.5000E-03	4.0133E+00	1.010000	1.000000	0.800000	0.800000	1.000000	0.800000
16	1.0000E-02	5.0000E+00	0.900000	0.900000	1.000000	1.000000	0.900000	1.000000
17	1.1000E-02	5.0000E+00	0.900000	0.900000	1.000000	1.000000	0.900000	1.000000
18	1.2000E-02	5.0000E+00	0.900000	0.900000	1.000000	1.000000	0.900000	1.000000
19	1.3000E-02	5.0000E+00	0.900000	0.900000	1.000000	1.000000	0.900000	1.000000
20	1.4000E-02	5.0000E+00	0.900000	0.900000	1.000000	1.000000	0.900000	1.000000
21	1.5000E-02	5.0000E+00	0.900000	0.900000	1.000000	1.000000	0.900000	1.000000

84020107 Ardonceau Turbulence Data

X = 6.0000E-02 RHO\_R = 1.8695E-01 U\_R = 5.5200E+02

I	Y	M	U UR	(RU) <sup>2</sup> RR UR	U <sup>2</sup> UR2	V <sup>2</sup> UR2
1	1.0000E-3	1.0530E+0	6.0326E-1	6.1223E+0	6.5869E-3	1.3927E-3
2	1.5000E-3				7.0962E-3	1.5312E-3
3	2.0000E-3	1.1550E+0	6.5036E-1	8.5810E+0	7.9442E-3	1.6467E-3
4	2.5000E-3				8.1719E-3	1.5170E-3
5	3.0000E-3	1.2580E+0	6.9565E-1	1.0612E+1	9.1147E-3	1.5170E-3
6	3.5000E-3				8.8061E-3	1.5312E-3
7	4.0000E-3	1.3740E+0	7.4275E-1	1.2553E+1	7.8476E-3	1.5030E-3
8	5.0000E-3	1.5070E+0	8.5688E-1	1.3158E+1	7.7836E-3	1.2098E-3
9	5.5000E-3	1.5690E+0	8.1341E-1	1.3485E+1	5.9000E-3	
10	6.0000E-3	1.6280E+0	8.3333E-1	1.4282E+1	4.2533E-3	8.9349E-4
11	6.5000E-3	1.6790E+0	8.4964E-1	1.1792E+1	2.8949E-3	
12	7.0000E-3	1.7280E+0	8.6594E-1	1.1648E+1	1.7970E-3	
13	7.5000E-3	1.7760E+0	8.8043E-1	9.7424E+0	9.4846E-4	
14	8.0000E-3	1.8230E+0	8.9312E-1	1.1302E+1	1.7574E-4	2.6583E-4
15	8.5000E-3	1.8370E+0	8.9855E-1	5.5036E+0	3.2166E-4	
16	9.0000E-3	1.8520E+0	9.0036E-1	6.4974E+0	2.6583E-4	
17	9.5000E-3	1.8670E+0	9.0580E-1	5.3529E+0	2.2067E-4	
18	1.0000E-2	1.8820E+0	9.0942E-1	4.7076E+0	1.7489E-4	1.1424E-4
19	1.1000E-2	1.8880E+0	9.1123E-1	1.6690E+0	1.7489E-4	
20	1.2000E-2	1.8940E+0	9.1304E-1	1.0476E+0	1.7489E-4	1.0663E-4
21	1.3000E-2	1.8940E+0	9.1123E-1	1.3450E+0	1.2212E-4	
22	1.4000E-2	1.8940E+0	9.1123E-1	1.0895E+0	8.2047E-5	6.6458E-5
23	1.5000E-2	1.8950E+0	9.1123E-1	1.1424E+0	8.2047E-5	

## 84020303 Ardonceau Turbulence Data

X = -4.0000E-03 RHO\_R = 1.8535E-01 U\_R = 5.5300E+02

I	Y	M	U UR	(RU)' RR UR	U'2 UR2	V'2 UR2	-U'V' UR2
1	1.0000E-3	2.6200E-1	1.6456E-1	-3.1483E+0	2.5373E-2	1.9430E-3	2.2679E-3
2	2.0000E-3	2.3000E-1	1.4467E-1	3.5102E+0	2.7656E-2	2.2170E-3	2.0437E-3
3	3.0000E-3	5.3100E-1	3.2731E-1	6.3939E+0	2.9005E-2	2.4097E-3	1.8058E-3
4	4.0000E-3	8.3500E-1	4.9548E-1	9.0972E+0	2.3188E-2	2.2170E-3	1.2977E-3
5	5.0000E-3	1.0700E+0	6.1302E-1	1.1354E+1	1.5432E-2	1.9430E-3	1.2430E-3
6	6.0000E-3	1.2450E+0	6.9078E-1	1.7123E+1	8.8680E-3	1.6871E-3	1.5394E-3
7	7.0000E-3	1.4500E+0	7.7215E-1	1.4894E+1	4.2403E-3	1.3007E-3	1.4467E-3
8	8.0000E-3	1.6340E+0	8.3725E-1	1.3207E+1	3.1474E-3	1.1602E-3	1.3682E-3
9	9.0000E-3	1.7370E+0	8.6980E-1	1.2612E+1	9.6448E-4	1.0277E-3	1.0115E-3
10	1.0000E-2	1.8360E+0	9.0054E-1	7.4683E+0	1.3007E-3	7.8684E-4	8.0021E-4
11	1.1000E-2	1.9190E+0	9.2405E-1	7.2295E+0	9.6448E-4	7.3164E-4	5.8214E-4
12	1.2000E-2	2.0100E+0	9.4937E-1	1.1794E+1	6.2726E-4	7.3164E-4	4.5592E-4
13	1.3000E-2	2.0350E+0	7.7777E+7	7.7777E+7	2.2581E-4	7.3164E-4	3.9427E-4
14	1.4000E-2	2.0650E+0	7.7777E+7	7.7777E+7	4.4260E-4	3.6231E-4	1.6138E-4

## 84020305 Ardonceau Turbulence Data

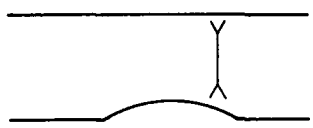
X = 1.2000E-02 RHO\_R = 1.8535E-01 U\_R = 5.5300E+02

I	Y	M	U UR	(RU)' RR UR	U'2 UR2	V'2 UR2	-U'V' UR2
1	1.0000E-3	3.1900E-1	2.0072E-1	5.6423E+0	2.0237E-2	6.5848E-3	7.6419E-3
2	2.0000E-3	4.0600E-1	2.5316E-1	6.4615E+0	2.4738E-2	7.9497E-3	9.9988E-3
3	3.0000E-3	5.5900E-1	3.4358E-1	8.0585E+0	2.7324E-2	8.4946E-3	1.1381E-2
4	4.0000E-3	7.7100E-1	4.6293E-1	9.9580E+0	2.5054E-2	6.4232E-3	8.4995E-3
5	5.0000E-3	1.0050E+0	5.8228E-1	1.3496E+1	1.9953E-2	5.3483E-3	7.0246E-3
6	6.0000E-3	1.1690E+0	6.5823E-1	1.8428E+1	1.4212E-2	4.5052E-3	6.1614E-3
7	7.0000E-3	1.3170E+0	7.2152E-1	2.1737E+1	6.5848E-3	2.8192E-3	2.9169E-3
8	8.0000E-3	1.4480E+0	7.7215E-1	2.0098E+1	3.4936E-3	2.1237E-3	2.1300E-3
9	9.0000E-3	1.5690E+0	8.1555E-1	1.5326E+1	9.0326E-4	9.6448E-4	5.4695E-4
10	1.0000E-2	1.6830E+0	8.5353E-1	1.1809E+1	3.6231E-4	7.3164E-4	3.0634E-4
11	1.1000E-2	1.7050E+0	8.6076E-1	5.6266E+0	4.4260E-4	7.3164E-4	3.4143E-4
12	1.2000E-2	1.7270E+0	8.6618E-1	3.5108E+0	3.6231E-4	6.2726E-4	3.6803E-4
13	1.3000E-2	1.7380E+0	8.6980E-1	2.7622E+0	1.9671E-4	5.3091E-4	2.0424E-4
14	1.4000E-2	1.7490E+0	8.7342E-1	2.8453E+0	1.9671E-4	5.3091E-4	2.3042E-4

## 84020307 Ardonceau Turbulence Data

X = 3.6000E-02 RHO\_R = 1.8535E-01 U\_R = 5.5300E+02

I	Y	M	U UR	(RU)' RR UR	U'2 UR2	V'2 UR2	-U'V' UR2
1	1.0000E-3	5.7600E-1	3.5443E-1	6.1320E+0	1.9391E-2	3.8579E-3	4.8003E-3
2	2.0000E-3	6.6100E-1	4.0325E-1	7.3373E+0	2.0811E-2	6.1060E-3	6.1549E-3
3	3.0000E-3	7.7800E-1	4.6655E-1	9.6961E+0	2.0811E-2	5.9505E-3	5.6086E-3
4	4.0000E-3	9.0800E-1	5.3526E-1	1.0408E+1	1.9391E-2	6.1060E-3	5.7562E-3
5	5.0000E-3	1.0450E+0	5.9675E-1	1.6109E+1	1.4938E-2	3.3762E-3	2.6986E-3
6	6.0000E-3	1.1400E+0	6.4557E-1	2.0746E+1	9.8165E-3	1.6058E-3	4.8884E-4
7	7.0000E-3	1.2780E+0	7.0524E-1	2.2476E+1	6.5848E-3	1.3007E-3	9.0723E-4
8	8.0000E-3	1.4000E+0	7.5407E-1	2.5984E+1	2.6104E-3	1.0929E-3	4.4592E-4
9	9.0000E-3	1.4860E+0	7.8662E-1	2.1543E+1	1.2294E-3	1.0277E-3	4.4625E-4
10	1.0000E-2	1.5690E+0	8.1555E-1	1.6381E+1	5.3091E-4	6.7845E-4	2.1126E-4
11	1.1000E-2	1.5870E+0	8.2278E-1	1.4637E+1	2.5693E-4	4.8575E-4	7.3481E-5
12	1.2000E-2	1.6050E+0	8.2821E-1	6.5518E+0	1.6961E-4	3.6231E-4	6.2221E-5
13	1.3000E-2	1.5950E+0	8.2459E-1	7.2844E+0	3.2517E-4	4.8575E-4	1.7686E-4
14	1.4000E-2	1.5850E+0	8.2098E-1	2.0246E+0	3.6231E-4	4.4260E-4	2.3426E-4

	M: (peak value) 0.9 to 1.82	8501
	R Theta $\times 10^{-3}$ : 16 upstream	QNS
Blowdown tunnel with symmetrical convergent nozzle. Running time: 30 secs. W = 0.114, H = 0.063, L = 1.4 m. PO: 150 kN/m <sup>2</sup> . TO: 290 K. Air. Re/m $\times 10^{-6}$ : 20.		
LIU X., SQUIRE L.C., 1988. An investigation of shock/ boundary layer interactions on curved surfaces at transonic speeds. <i>J. Fluid Mech.</i> <u>187</u> 467-486. And: Liu (1985), Liu & Squire (1985). L.C. Squire, private communications and data tables.		

- 1 The test boundary layers were formed on the floor and ceiling of the wind tunnel. Five circular arc models of chord 80 mm could be mounted in the tunnel floor to form "bumps" with radii of 401, 268, 163, 104 or 73 mm. The origin  $X = 0$  is set at mid chord, the maximum height of the bump, 708 mm downstream of the start of the flat part of the floor. The back pressure of the mean flow was controlled by a second throat formed by an adjustable incidence aerofoil, and the authors specify a configuration by the bump radius and the aerofoil incidence. Transition was natural, and the tunnel floor was set to diverge at  $0.3^\circ$  to counter boundary layer growth. The flow approaching the test area is subsonic,
- 2 so there are no incoming standing waves. The flow accelerates over the bump and at sufficiently low back pressure it is retarded by a shock wave, the  $X$ -positions of the peak Mach number, as indicated by the wall-pressure minimum, separation and reattachment being as below:

Series	M(Peak)	Separation	Reattachment
01 $X(\text{mm})$	21	23	62
02	39	45	90
03	15	18	56
04	27	--	--
05	9	30	46
06	3	--	--

- 2 These being for a bump radius of 163 mm and incidences of  $8.75^\circ$ ,  $9^\circ$  and  $9.5^\circ$  degrees, odd numbers on the floor, even numbers on the flat roof. No oscillation of the shock could be detected in schlieren studies, though there were small movements of the interaction foot on the flat upper surface for incoming Mach numbers close to one. The test zone extended over the range  $-60 < X < 215$  mm. Three-dimensional effects were assessed in the light of the results of surface oil-flow patterns, interferograms, pressure distributions on and off the centreline and a momentum balance based on profile measurements on the centreline. (See 15 below.)
- 6 The wall pressure was measured in great detail from a point well upstream of the bump to  $X = 132$  mm, at 45 stations along the centreline in the range  $-60 < X < 132$  mm, for both the floor-with-bump and the flat ceiling, for the greater part at 3 mm intervals. "Only a few measurements of pressure distributions off the centreline were obtained --."
- 7 Pitot profiles were measured with a single FPP ( $h_1 = 0.18$  mm). A survey of the entire density field was also obtained from laser holographic interferometry, supported by schlieren photographs. Profiles were, in general, measured upstream of the interaction and in the recovery region downstream. In several cases, some were downstream of the region covered by wall-pressure measurements ( $X > 132$  mm). There are no profiles in the separated zone, but 0204, 0303, 0403, 0502 and possibly 0602 appear to be in the zone of upstream influence, being close behind M(peak).
- 9 The authors have set the static pressure equal to the wall pressure and assumed isoenergetic/Grocco total temperature profiles. The editors have chosen to present six series of profiles drawn from three configurations using the same "bump", with radius 163 mm. These configurations provided the longest sequences of profiles. The wall pressures for these profiles are given in Section D. The editors have set the wall-pressure values

in the profile tables at the profile value closest to the wall. These differ slightly from the pressure values in the wall tables. There is a slight scatter in the profile pressure values as a result of rounding errors in the data as received. The wall temperature has been set at 290 K as representative of the values recorded in the wall-pressure runs. No value is given in association with the profiles.

The original data include profiles for a further ten configurations (20 series, 103 profiles) and information of some sort for 68 configurations, 53 of which have wall pressure surveys and holograms. The editors have accepted the authors' assumptions and data reduction procedures.

§ DATA: CAT8404 0101-0606. Pitot profiles, NX up to 9. Wall pressures, NX = 45. Support from holographic interferometry.

15 Editors' comments:

The experiments as a whole cover a wide range of quasi-normal shock/boundary-layer interactions on surfaces with systematically varied radius of curvature, and over a substantial range of Mach number. This is exploited in an account of the influence of wall curvature on the type of separation which occurs (source paper fig.14). The series presented here are those for the bump of 163 mm radius with second throat settings of 8.75, 9.0 and 9.5 degrees. Series 01, 02 and 03 are on the floor, with the bump, while series 02, 04 and 06 are on the flat ceiling. Each has at least one profile upstream of the interaction and several downstream. A calculation of the boundary layer development using the given wall pressure distribution will probably require a model of the shock structure, which would be much assisted by access to the holograms in the data report. Comparisons may be made with the studies by Déjery et al., reported as CAT8002/3T above.

The profiles are given in relatively fine detail, but, upstream, where they have strongly accelerated characteristics, do not approach the wall within the momentum deficit peak. For the greater part, they should not be severely affected by normal pressure gradients, but, by analogy with the QNS flows in CAT8002/3T, we would expect significant effects where the profile is close to the interaction. We do not find fictitious  $P_0$  variations here of the type observed for the ONERA data (80030102 - 7, 0204 - 5, 0302 - 5) because in this case the velocity has been deduced assuming  $P$  constant, as opposed to calculating  $P_0$  from measured velocities. We cannot therefore attempt any quantitative estimate. The profiles most likely to be affected are 0204, 0303, 0403, and 0502. Integral values for these profiles should be viewed with suspicion. Additionally, profiles taken just ahead of a shock are likely to suffer from probe-shock interactions. These may affect 0103, 0204, 0302, 0403 and 0502 over at least a part of their traverse.

A QNS flow of this nature is very susceptible to three-dimensional effects, particularly in separated cases, and we consider that it should only be considered as two-dimensional in the restricted sense implied by § 9.3.2 above. The authors' comment on their assessment is: "Taken together, these results suggest that for attached flows and for flows with small regions of separation, measurements along the tunnel centreline are representative of two-dimensional flow over the bump surfaces. However, in flows with larger regions of separation, the flow in the separation region is clearly affected by the presence of the walls and in particular by the shock interaction with the boundary layers on the side walls. Even in these cases the measured boundary layer development well down of reattachment satisfies the two-dimensional momentum integral equation". Reference is made to measured skin friction in this connection, and values are presented in figure 18 of the source paper. The values shown by open circles are for series 03 as presented here, and are the values also shown in the 1985 paper (fig. 10). These are based "on a fair fit to the law of the wall". Figure (10.4.6) shows these profiles in wall law coordinates, using the CF values of the source paper. We do not feel that the fit is good enough to justify presenting CF values as data, and in consequence the second author has stated "My own view about the boundary-layer profiles is that they provide valuable data on boundary layers through complicated interactions, but that we do not have reliable skin-friction coefficients to go with them".



CAT 8501 LIU/SQUIRE BOUNDARY CONDITIONS AND EVALUATED DATA, SI UNITS									
RUN X # RZ	MD # POD TOD	TW/TR PW/PO# TAUM	RED2W RED2D OZ	CF # CJ PIZ	M12 M32 M42	M12K M32K M42K	PW T4# UDW	P3# T0 TR	
85010101	1.0970	1.0216	4.8294**03	3.4800**-03	1.7129	1.2331	6.7720**04	6.7720**04	
0.0000**00	1.4406**05	1.0000	5.7386**03	NM	1.9109	1.9096	2.9000**02	2.3351**02	
INFINITE	2.8971**02	1.9852**02	2.5665**04	NM	0.0211	2.6633**04	3.3610**02	2.8337**02	
85010102	1.2620	1.0239	4.4595**03	3.3103**-03	1.8636	1.2451	5.5172**04	5.5172**04	
1.2000**02	1.4522**05	1.0000	5.5576**03	NM	1.9080	1.9055	2.9000**02	2.2035**02	
INFINITE	2.9054**02	2.0361**02	2.4563**04	NM	0.0396	2.5300**04	3.7560**02	2.8324**02	
85010103	1.3230	1.0318	4.2199**03	3.1113**-03	1.9733	1.2677	5.0930**04	5.0930**04	
1.8000**02	1.4562**05	1.0000	5.3890**03	NM	1.8977	1.8937	2.9000**02	2.1394**02	
INFINITE	2.8886**02	1.9414**02	2.3648**04	NM	0.0313	2.5131**04	3.8800**02	2.8107**02	
85010104	0.8110	1.0100	2.7946**04	1.8733**-03	1.7238	1.4439	9.3519**04	9.3519**04	
1.1400**01	1.4413**05	1.0000	3.0749**04	NM	1.7209	1.7189	2.9000**02	2.5685**02	
INFINITE	2.9064**02	8.0659**01	1.5256**03	NM	0.0227	1.6091**03	2.6060**02	2.8712**02	
85010105	0.8040	1.0068	2.6695**04	2.4337**-03	1.5621	1.2978	9.4434**04	9.4434**04	
1.6420**01	1.4452**05	1.0000	2.9255**04	NM	1.7946	1.7933	2.9000**02	2.5315**02	
INFINITE	2.9152**02	1.0399**02	1.4595**03	NM	0.0146	1.5209**03	2.5900**02	2.8805**02	
85010106	0.8040	1.0091	2.6813**04	2.5761**-03	1.5042	1.2491	9.4437**04	9.4437**04	
2.1460**01	1.4453**05	1.0000	2.9439**04	NM	1.8244	1.8232	2.9000**02	2.5755**02	
INFINITE	2.9085**02	1.1008**02	1.4642**03	NM	0.0147	1.5171**03	2.5970**02	2.8734**02	
85010201	0.9360	1.0137	6.6869**03	3.3800**-03	1.5739	1.2298	8.3709**04	8.3709**04	
0.0000**00	1.4730**05	1.0000	7.5855**03	NM	1.8881	1.8871	2.9000**02	2.4727**02	
INFINITE	2.9060**02	1.7351**02	3.4672**04	NM	0.0174	3.5836**04	2.9510**02	2.8609**02	
85010202	1.0240	1.0176	6.7297**03	3.3612**-03	1.6372	1.2215	7.7083**04	7.7083**04	
1.2000**02	1.5009**05	1.0000	7.8230**03	NM	1.8941	1.8930	2.9000**02	2.3390**02	
INFINITE	2.9021**02	1.9018**02	3.4117**04	NM	0.0086	3.5431**04	3.1300**02	2.8495**02	
85010203	1.0950	1.0125	3.8659**03	3.7179**-03	1.7133	1.2503	6.8773**04	6.8773**04	
2.7000**02	1.4535**05	1.0000	6.5590**03	NM	1.9213	1.9224	2.9000**02	2.3576**02	
INFINITE	2.9230**02	2.1462**02	2.0363**04	NM	0.0359	2.1015**04	3.3710**02	2.8542**02	
85010204	1.2230	1.0159	4.1568**03	3.5700**-03	1.8211	1.2333	5.8302**04	5.8302**04	
4.2000**02	1.4571**05	1.0000	5.0899**03	NM	1.9239	1.9227	2.9000**02	2.2511**02	
INFINITE	2.9245**02	2.1792**02	2.2598**04	NM	0.0450	2.3505**04	3.6790**02	2.8545**02	
85010205	0.8130	1.0044	1.2896**04	2.0336**-03	1.7012	1.4231	9.3916**04	9.3916**04	
1.0200**01	1.4503**05	1.0000	1.4132**04	NM	1.7497	1.7470	2.9000**02	2.5815**02	
INFINITE	2.9228**02	8.8365**01	7.0109**04	NM	0.0170	7.3620**04	2.6190**02	2.8373**02	
85010301	1.0920	1.0286	4.4445**03	3.5789**-03	1.7016	1.2376	6.7636**04	6.7636**04	
0.0000**00	1.4299**05	1.0000	5.3037**03	NM	1.9165	1.9152	2.9000**02	2.3230**02	
INFINITE	2.8770**02	2.0205**02	2.3695**04	NM	0.0416	2.4518**04	3.3370**02	2.8194**02	
85010302	1.2590	1.0278	4.0957**03	3.5122**-03	1.8563	1.2370	5.5275**04	5.5275**04	
1.2000**02	1.4491**05	1.0000	5.1157**03	NM	1.9229	1.9212	2.9000**02	2.1075**02	
INFINITE	2.8961**02	2.1541**02	2.2540**04	NM	0.0470	2.3504**04	3.7420**02	2.8217**02	
85010303	1.2070	1.0260	6.0050**03	2.8390**-03	1.8450	1.2563	5.8500**04	5.8500**04	
1.8000**02	1.4316**05	1.0000	7.3794**03	NM	1.8813	1.8770	2.9000**02	2.2413**02	
INFINITE	2.8943**02	1.7235**02	3.2894**04	NM	0.0392	3.4304**04	3.6230**02	2.8254**02	
85010304	0.7810	1.0078	2.5281**04	2.2152**-03	1.6317	1.3940	9.6456**04	9.6456**04	
1.1400**01	1.4431**05	1.0000	2.7599**04	NM	1.7487	1.7472	2.9000**02	2.5940**02	
INFINITE	2.9104**02	9.1231**01	1.3964**03	NM	0.0188	1.4598**03	2.5220**02	2.8775**02	
85010305	0.7760	1.0098	2.4655**04	2.3314**-03	1.5721	1.3235	9.6688**04	9.6688**04	
1.3900**01	1.4395**05	1.0000	2.6930**04	NM	1.7807	1.7794	2.9000**02	2.5922**02	
INFINITE	2.9044**02	9.7058**01	1.3668**03	NM	0.0233	1.4237**03	2.5050**02	2.8719**02	
85010306	0.7860	1.0090	2.5909**04	2.4805**-03	1.5405	1.2301	9.6217**04	9.6217**04	
1.4620**01	1.4466**05	1.0000	2.8231**04	NM	1.7993	1.7982	2.9000**02	2.5876**02	
INFINITE	2.9073**02	1.0321**02	1.4193**03	NM	0.0130	1.4738**03	2.5350**02	2.8741**02	
85010307	0.7730	1.0124	2.2870**04	2.7242**-03	1.4709	1.2339	9.7103**04	9.7103**04	
2.1460**01	1.4415**05	1.0000	2.5018**04	NM	1.8360	1.8351	2.9000**02	2.5976**02	
INFINITE	2.8966**02	1.1064**02	1.2662**03	NM	0.0160	1.3963**03	2.4930**02	2.8645**02	

CAT 8501 LIU/SQUIRE BOUNDARY CONDITIONS AND EVALUATED DATA, SI UNITS									
RUN X RZ	MO * POD TOD	TW/TR PW/PD* TAUW	POD2W RED2D OZ	CF * C1 PI2	M12 M32 M42	M12K M32K M42K	Pd TWS UD*	Pd* TJ TR	
85010601 0.0000*-00 INFINITE	0.9040 1.4773*+05 2.8907*+02	1.0181 1.0000 1.6771*+02	7.1242*+03 8.0503*+03 3.6902*-04	3.3709*-03 NM NM	1.5631 1.8811 0.0095	1.2319 1.8402 3.8148*-04	8.6968*+04 2.9000*+02 2.8570*+02	8.6361*+04 2.4446*+02 2.8455*+02	
85010602 1.2000*-02 INFINITE	0.9180 1.4767*+05 2.8889*+02	1.0191 1.0000 1.6449*+02	7.1213*+03 8.0795*+03 3.6808*-04	3.2570*-03 NM NM	1.5785 1.8782 0.0259	1.2374 1.8770 3.8112*-04	8.5611*+04 2.9000*+02 2.8940*+02	8.5511*+04 2.4722*+02 2.8455*+02	
85010603 2.7000*-02 INFINITE	0.8450 1.4701*+05 2.8874*+02	1.0176 1.0000 1.2781*+02	8.6657*+03 9.5613*+03 4.5708*-04	2.7753*-03 NM NM	1.5730 1.8432 0.0119	1.2777 1.8413 4.7424*-04	9.2137*+04 2.9000*+02 2.6930*+02	9.2137*+04 2.5266*+02 2.8499*+02	
85010604 5.7000*-02 INFINITE	0.7890 1.4696*+05 2.8763*+02	1.0200 1.0000 9.8459*+01	1.0979*+04 1.2142*+04 5.9099*-04	2.3183*-03 NM NM	1.5964 1.8039 0.0037	1.3313 1.8016 6.1469*-04	9.7461*+04 2.9000*+02 2.5300*+02	9.7461*+04 2.5373*+02 2.8431*+02	
85010605 7.2000*-02 INFINITE	0.7690 1.4696*+05 2.8839*+02	1.0158 1.0000 9.2609*+01	1.2001*+04 1.3152*+04 5.5155*-04	2.2513*-03 NM NM	1.4015 1.7917 0.0120	1.3469 1.7794 6.7779*-04	9.9374*+04 2.9000*+02 2.4760*+02	9.9374*+04 2.5787*+02 2.8521*+02	
85010606 1.0200*-01 INFINITE	0.7560 1.4700*+05 2.8827*+02	1.0163 1.0000 1.0063*+02	1.2636*+04 1.3824*+04 5.3005*-04	2.4983*-03 NM NM	1.5648 1.8007 0.0165	1.3192 1.7791 7.1627*-04	1.0065*+05 2.9000*+02 2.4387*+02	1.0065*+05 2.5477*+02 2.8523*+02	
85010401 0.0000*-00 INFINITE	0.9350 1.4719*+05 2.8915*+02	1.0187 1.0000 1.7177*+02	5.7642*+03 7.7020*+03 3.5014*-04	3.3518*-03 NM NM	1.5798 1.4846 0.0231	1.2327 1.8835 3.6229*-04	9.3745*+04 2.9000*+02 2.4410*+02	9.3745*+04 2.4412*+02 2.8463*+02	
85010402 1.2000*-02 INFINITE	1.0200 1.4976*+05 2.8953*+02	1.0199 1.0000 1.7463*+03	7.2176*+03 9.3970*+03 3.6621*-04	3.1027*-02 NM NM	1.6552 1.8799 0.0155	1.2381 1.8781 3.8193*-04	7.7281*+04 2.9000*+02 3.1560*+02	7.7281*+04 2.3464*+02 2.8433*+02	
85010403 2.7000*-02 INFINITE	1.0830 1.4593*+05 2.9088*+02	1.0171 1.0000 2.0575*+02	4.3030*+03 5.0759*+03 2.2590*-04	3.5928*-03 NM NM	1.7016 1.3115 0.0137	1.2491 1.9104 2.3396*-04	6.9750*+04 2.9000*+02 3.3330*+02	6.9750*+04 2.3561*+02 2.8513*+02	
85010404 4.2000*-02 INFINITE	0.9020 1.4696*+05 2.9160*+02	1.0092 1.0000 1.02.6*+02	9.0508*+03 1.0151*+04 4.7350*-04	2.0790*-03 NM NM	1.7094 1.9070 0.0248	1.3714 1.8024 4.9563*-04	4.6702*+04 2.9000*+02 2.8649*+02	4.6702*+04 2.4412*+02 2.8735*+02	
85010405 5.7000*-02 INFINITE	0.8600 1.4697*+05 2.9283*+02	1.0038 1.0000 9.0442*+01	1.0596*+04 1.1712*+04 5.6011*-04	1.1264*-03 NM NM	1.5994 1.7835 0.0306	1.3744 1.7795 5.8722*-04	9.0583*+04 2.9000*+02 7.7540*+02	9.0583*+04 2.5517*+02 2.8991*+02	
85010406 1.0200*-01 INFINITE	0.8020 1.4701*+05 2.9214*+02	1.0046 1.0000 9.5044*+01	1.3752*+04 1.5038*+04 7.4050*-04	2.1933*-03 NM NM	1.5320 1.7748 0.0103	1.3595 1.7724 7.7319*-04	9.6247*+04 2.9000*+02 2.5879*+02	9.6247*+04 2.5596*+02 2.8367*+02	
85010501 0.0000*-00 INFINITE	1.0910 1.4340*+05 2.9020*+02	1.0197 1.0000 2.1826*+02	3.9124*+03 4.5151*+03 2.0352*-04	3.8573*-03 NM NM	1.5848 1.9333 0.0158	1.2382 1.9327 2.0713*-04	6.7712*+04 2.9000*+02 3.3490*+02	6.7712*+04 2.3443*+02 2.8440*+02	
85010502 1.2000*-02 INFINITE	1.0560 1.4255*+05 2.9137*+02	1.0145 1.0000 1.7636*+02	5.0820*+03 5.9410*+03 2.7236*-04	3.2065*-03 NM NM	1.7219 1.7797 0.0196	1.2729 1.8772 2.8470*-04	7.0460*+04 2.9000*+02 3.2680*+02	7.0460*+04 2.3324*+02 2.8585*+02	
85010503 6.0000*-02 INFINITE	0.7230 1.4444*+05 2.8807*+02	1.0267 1.0000 4.8664*+01	1.7071*+04 1.8556*+04 9.6589*-04	1.3040*-03 NM NM	1.8259 1.5894 0.0090	1.5876 1.6858 1.0121*-03	1.0199*+05 2.9000*+02 2.3410*+02	1.0199*+05 2.6077*+02 2.8523*+02	
85010504 8.4000*-02 INFINITE	0.7450 1.4451*+05 2.8825*+02	1.0166 1.0000 8.4423*+01	1.6196*+04 1.7678*+04 9.0499*-04	2.1734*-03 NM NM	1.6344 1.7673 0.0037	1.3887 1.7554 9.4422*-04	9.9978*+04 2.9000*+02 2.4060*+02	9.9978*+04 2.5445*+02 2.8526*+02	
85010505 9.6000*-02 INFINITE	0.7410 1.4455*+05 2.8899*+02	1.0143 1.0000 9.7856*+01	1.6358*+04 1.7809*+04 9.1658*-04	2.2771*-03 NM NM	1.6037 1.7677 0.0012	1.3641 1.7561 9.5460*-04	1.0036*+05 2.9000*+02 2.3970*+02	1.0036*+05 2.6030*+02 2.8591*+02	
85010506 1.1400*-01 INFINITE	0.7410 1.4523*+05 2.8744*+02	1.0194 1.0000 1.0728*+02	1.3205*+04 1.4433*+04 7.3470*-04	2.7676*-03 NM NM	1.5181 1.9125 0.0016	1.2994 1.8115 7.5764*-04	1.0085*+05 2.9000*+02 2.3910*+02	1.0085*+05 2.5903*+02 2.8444*+02	
85010507 1.3900*-01 INFINITE	0.7570 1.4565*+05 2.8925*+02	1.0134 1.0000 1.1152*+02	1.3349*+04 1.4559*+04 7.3670*-04	2.7907*-03 NM NM	1.5009 1.8233 0.0179	1.2731 1.8223 7.6044*-04	9.9625*+04 2.9000*+02 2.4450*+02	9.9625*+04 2.5751*+02 2.8515*+02	
85010508 1.6427*-01 INFINITE	0.7590 1.4593*+05 2.8833*+02	1.0167 1.0000 1.1337*+02	1.4133*+04 1.5456*+04 7.7675*-04	2.4264*-03 NM NM	1.4842 1.8297 0.0151	1.2610 1.8286 9.0122*-04	9.9727*+04 2.9000*+02 2.4449*+02	9.9727*+04 2.5761*+02 2.8524*+02	
85010509 2.1460*-01 INFINITE	0.7550 1.4606*+05 2.8896*+02	1.0144 1.0000 1.1354*+02	1.4167*+04 1.5444*+04 7.7893*-04	2.8425*-03 NM NM	1.4494 1.9409 0.0309	1.2449 1.8398 9.0177*-04	1.0010*+05 2.9000*+02 2.4380*+02	1.0010*+05 2.5733*+02 2.8547*+02	

85010301		LIU/SQUIRE		PROFILE TABULATION		52 POINTS, DELTA AT POINT 20		
I	Y	PT2/P	P/PO	T0/TJD	M/MD	U/UD	T/TO	R/RD=U/UD
1	0.0000+00	1.0000+00	1.00000	1.00799	0.00000	0.00000	1.24839	0.00000
2	9.0000-05	1.5552+00	0.92899	0.99454	0.75032	0.78244	1.03572	0.71994
3	2.9000-04	1.6804+00	0.99933	0.99643	0.81868	0.84447	1.06400	0.77367
4	4.9000-04	1.7874+00	0.93885	0.99629	0.86936	0.88942	1.04523	0.84995
5	6.8000-04	1.8453+00	1.00056	0.99786	0.83550	0.91220	1.03740	0.87991
6	8.8000-04	1.8624+00	0.93941	0.99730	0.90233	0.91819	1.03409	0.88740
7	1.0700-03	1.8776+00	0.99957	0.99733	0.90934	0.92338	1.03224	0.89473
8	1.2700-03	1.8819+00	0.93925	0.99707	0.91117	0.92508	1.03077	0.89680
9	1.4700-03	1.9220+00	0.99996	0.99872	0.92766	0.93977	1.02628	0.91567
10	1.6600-03	1.9356+00	0.99845	0.99721	0.93315	0.94366	1.02266	0.92133
11	1.8600-03	1.9448+00	1.00024	0.99833	0.93681	0.94726	1.02242	0.92671
12	2.0500-03	1.9494+00	0.99949	0.99826	0.93864	0.94876	1.02166	0.92817
13	2.2400-03	1.9797+00	0.99843	0.99759	0.95055	0.95835	1.01647	0.94133
14	3.0300-03	2.0131+00	0.99945	0.99850	0.96337	0.96943	1.01263	0.95700
15	3.5200-03	2.0349+00	1.00038	0.99946	0.97161	0.97663	1.01035	0.96699
16	4.0100-03	2.0570+00	1.00054	0.99976	0.97985	0.98352	1.00749	0.97673
17	4.4900-03	2.0645+00	0.99898	0.99825	0.98260	0.98502	1.00492	0.97919
18	4.9800-03	2.0744+00	0.99860	0.99828	0.98626	0.98801	1.00355	0.98314
19	5.4700-03	2.0996+00	0.99819	0.99841	0.99542	0.99550	1.00017	0.99354
20	5.9600-03	2.1123+00	1.00000	1.00000	1.00000	1.00000	1.00000	1.00000
21	6.4500-03	2.1303+00	0.99816	0.99866	1.00641	1.00450	0.99620	1.00648
22	6.9400-03	2.1380+00	1.00063	1.00023	1.00916	1.00749	0.99670	1.01147
23	7.4200-03	2.1484+00	0.99912	0.99916	1.01282	1.00989	0.99422	1.01487

85010302		LIU/SQUIRE		PROFILE TABULATION		52 POINTS, DELTA AT POINT 20			
I	Y	PT2/P	P/PD	T0/TJD	M/MD	U/UD	T/TD	R/RD=U/UD	
1	0.0000+00	1.0000+00	1.00000	1.00232	0.00000	0.00000	1.31968	0.00000	
2	9.0000-05	1.7117+00	0.99828	0.99258	0.72359	0.76617	1.12115	0.68220	
3	2.9000-04	2.0252+00	0.99934	0.99538	0.83956	0.86905	1.07151	0.81052	
4	4.9000-04	2.1614+00	0.99992	0.99652	0.88245	0.90540	1.05270	0.85992	
5	6.8000-04	2.2388+00	0.99991	0.99756	0.90548	0.92464	1.04276	0.89664	
6	8.8000-04	2.2688+00	0.99924	0.99732	0.91422	0.93159	1.03836	0.89649	
7	1.0700-03	2.2854+00	0.99923	0.99712	0.91898	0.93533	1.03589	0.90223	
8	1.2700-03	2.2965+00	0.99922	0.99739	0.92216	0.93800	1.03465	0.90588	
9	1.4700-03	2.3133+00	0.99923	0.99724	0.92693	0.94174	1.03222	0.91164	
10	1.6600-03	2.3273+00	0.99856	0.99732	0.93090	0.94495	1.03042	0.91583	
11	1.8600-03	2.3358+00	0.99924	0.99793	0.93328	0.94709	1.02981	0.91898	
12	2.0500-03	2.3500+00	0.99812	0.99738	0.93725	0.95003	1.02745	0.92291	
13	2.2400-03	2.3815+00	0.99883	0.99747	0.94599	0.95697	1.02336	0.93403	
14	3.0300-03	2.4192+00	1.00013	0.99894	0.95631	0.96579	1.01992	0.94705	
15	3.5200-03	2.4515+00	0.99867	0.99811	0.96505	0.97221	1.01488	0.95657	
16	4.0100-03	2.4812+00	0.99835	0.99808	0.97299	0.97835	1.01105	0.96607	
17	4.4900-03	2.5172+00	0.99979	0.99944	0.98253	0.98637	1.00784	0.97849	
18	4.9800-03	2.5445+00	0.99955	0.99916	0.98967	0.99172	1.00413	0.98719	
19	5.4700-03	2.5629+00	0.99976	0.99937	0.99444	0.99546	1.00205	0.99319	
20	5.9600-03	2.5844+00	1.00000	1.00000	1.00000	1.00000	1.00000	1.00000	
21	6.4500-03	2.6030+00	0.99971	0.99972	1.00477	1.00347	0.99743	1.00577	
22	6.9400-03	2.6092+00	0.99868	0.99946	1.00635	1.00454	0.99640	1.00684	
23	7.4200-03	2.6217+00	0.99943	0.99943	1.00953	1.00695	0.99489	1.01155	
24	7.9100-03	2.6217+00	0.99936	1.00001	1.00953	1.00722	0.99542	1.01182	

85010303		LIU/SQUIRE		PROFILE TABULATION		52 POINTS, DELTA AT POINT 22		
I	Y	PT2/P	P/PO	T0/TJD	M/MD	U/UD	T/TD	R/RD=U/UD
1	0.0000+00	1.0000+00	1.00000	1.00135	0.00000	0.00000	1.29389	0.00000
2	9.0000-05	1.4976+00	1.00049	0.99235	0.64789	0.67252	1.14252	0.60643
3	2.9000-04	1.5396+00	0.99888	0.99174	0.67109	0.71405	1.13214	0.63000
4	4.9000-04	1.7325+00	0.99949	0.99415	0.75398	0.80017	1.09727	0.72886
5	6.8000-04	1.9494+00	0.99977	0.99604	0.84921	0.87552	1.06291	0.82351
6	8.8000-04	2.0595+00	0.99774	0.99538	0.89732	0.90754	1.04607	0.86560
7	1.0700-03	2.0996+00	0.99922	0.99721	0.90058	0.91913	1.04162	0.88172
8	1.2700-03	2.1380+00	0.99789	0.99650	0.91301	0.92906	1.03548	0.89534
9	1.4700-03	2.1484+00	0.99831	0.99720	0.91632	0.93210	1.03474	0.89929
10	1.6600-03	2.1588+00	0.99987	0.99800	0.91964	0.93514	1.03400	0.90427
11	1.8600-03	2.1667+00	0.99974	0.99730	0.92212	0.93707	1.03268	0.90717
12	2.0500-03	2.1693+00	0.99912	0.99754	0.92295	0.93762	1.03204	0.90771
13	2.2400-03	2.1904+00	0.99823	0.99725	0.92959	0.94287	1.02879	0.91486
14	3.0300-03	2.2225+00	0.99897	0.99778	0.93952	0.95115	1.02490	0.92708
15	3.5200-03	2.2497+00	0.99925	0.99823	0.94780	0.95805	1.02173	0.93697
16	4.0100-03	2.2826+00	1.00008	0.99900	0.95775	0.96633	1.01800	0.94932
17	4.4900-03	2.3105+00	0.99930	0.99852	0.96603	0.97267	1.01380	0.95876
18	4.9800-03	2.3415+00	0.99913	0.99905	0.97514	0.98013	1.01024	0.96934
19	5.4700-03	2.3642+00	0.99732	0.99857	0.98177	0.98510	1.00678	0.97642
20	5.9600-03	2.3815+00	1.00009	0.99964	0.98674	0.98951	1.00562	0.98407
21	6.4500-03	2.4075+00	0.99892	0.99961	0.99420	0.99531	1.00223	0.99202
22	6.9400-03	2.4279+00	1.00000	1.00000	1.00000	1.00000	1.00000	1.00000
23	7.4200-03	2.4426+00	0.99835	0.99912	1.00414	1.00276	0.99725	1.00386
24	7.9100-03	2.4456+00	0.99835	0.99943	1.00497	1.00359	0.99725	1.00469
25	8.4000-03	2.4515+00	0.99835	0.99915	1.00663	1.00469	0.99616	1.00690

85010304		LIU/SQUIRE		PROFILE TABULATION		52 POINTS, DELTA AT POINT 29		
I	Y	PT2/P	P/PD	T0/T00	M/M0	U/UD	T/T0	R/RD=U/UD
1	0.0000*-00	1.0000*-00	1.00030	0.99641	0.00000	0.00000	1.11796	0.00000
2	9.0000*-05	1.1382*-00	1.00295	0.99274	0.55570	0.57573	1.07341	0.53794
3	2.9000*-04	1.1568*-00	1.00406	0.99435	0.59027	0.61063	1.07017	0.57230
4	4.9000*-04	1.1656*-00	1.00051	0.99134	0.60563	0.62490	1.06454	0.58726
5	6.8000*-04	1.1723*-00	1.00342	0.99422	0.61716	0.63719	1.06598	0.59980
6	8.8000*-04	1.1784*-00	1.00342	0.99439	0.62740	0.64750	1.06510	0.61000
7	1.0700*-03	1.1799*-00	1.00016	0.99202	0.62996	0.64909	1.06164	0.61150
8	1.2700*-03	1.1878*-00	1.00257	0.99477	0.64277	0.65257	1.06257	0.62522
9	1.4700*-03	1.1934*-00	1.00159	0.99341	0.65173	0.67090	1.05969	0.63411
10	1.6600*-03	1.1934*-00	1.00396	0.99575	0.65173	0.67169	1.06219	0.63436
11	1.8600*-03	1.1967*-00	1.00206	0.99333	0.65685	0.67605	1.05932	0.63951
12	2.0500*-03	1.2041*-00	1.00148	0.99340	0.66837	0.68715	1.05698	0.65107
13	2.5400*-03	1.2031*-00	1.00010	0.99241	0.67606	0.69429	1.05467	0.65837
14	3.0300*-03	1.2221*-00	1.00061	0.99350	0.69526	0.71332	1.05263	0.67807
15	3.5200*-03	1.2391*-00	0.99950	0.99321	0.71959	0.73672	1.04817	0.70258
16	4.0100*-03	1.2493*-00	1.00059	0.99411	0.73367	0.75059	1.04666	0.71756
17	4.4900*-03	1.2725*-00	1.00107	0.99531	0.74440	0.78033	1.04211	0.74960
18	4.9800*-03	1.2877*-00	1.00105	0.99536	0.73361	0.79897	1.03959	0.76935
19	5.4700*-03	1.3033*-00	1.00194	0.99709	0.80282	0.81761	1.03718	0.78993
20	5.9600*-03	1.3306*-00	1.00171	0.99720	0.83483	0.84774	1.03117	0.82352
21	6.4500*-03	1.3453*-00	1.00076	0.99702	0.85147	0.86320	1.02775	0.84054
22	6.9400*-03	1.3688*-00	0.99943	0.99709	0.87708	0.88699	1.02273	0.86713
23	7.4200*-03	1.3785*-00	1.00032	0.99721	0.89732	0.93651	1.02081	0.87851
24	7.9100*-03	1.3971*-00	1.00092	0.99849	0.90653	0.91475	1.01822	0.89212
25	8.4000*-03	1.4241*-00	1.00137	1.00023	0.93342	0.94013	1.01443	0.92851
26	8.8900*-03	1.4401*-00	1.00250	1.00090	0.94878	0.95440	1.01188	0.94556
27	9.3800*-03	1.4592*-00	1.00278	1.00133	0.95671	0.97105	1.00901	0.96506
28	9.8700*-03	1.4788*-00	0.99993	0.99970	0.97844	0.98612	1.00302	0.99358
29	1.0360*-02	1.4961*-00	1.00000	1.00000	1.00000	1.00000	1.00000	1.00000
30	1.0640*-02	1.5034*-00	1.00222	1.00207	1.00640	1.00674	1.00067	1.00830
31	1.1330*-02	1.5183*-00	1.00118	1.00133	1.01921	1.01784	0.99733	1.02177
32	1.1820*-02	1.5213*-00	1.00160	1.00175	1.02177	1.02022	0.99698	1.02495
33	1.2310*-02	1.5304*-00	1.00210	1.00242	1.02945	1.02736	0.99594	1.03371
34	1.2800*-02	1.5289*-00	1.00073	1.00153	1.02817	1.02577	0.99535	1.03132
35	1.3290*-02	1.5259*-00	1.00107	1.00130	1.02561	1.02339	0.99569	1.02893
36	1.3770*-02	1.5239*-00	1.00150	1.00230	1.02817	1.02617	0.99611	1.03172
37	1.4260*-02	1.5274*-00	1.00167	1.00219	1.02639	1.02498	0.99629	1.03052
38	1.4750*-02	1.5304*-00	1.00132	1.00164	1.02945	1.02696	0.99517	1.03331

85010305		LIU/SQUIRE		PROFILE TABULATION		52 POINTS, DELTA AT POINT 31			
I	Y	PT2/P	P/P0	T0/T00	M/M0	U/UD	T/T0	R/RD=U/U0	
1	0.0000*-00	1.0000*-00	1.00000	0.99849	0.00000	0.00000	1.11874	0.00000	
2	9.0000*-05	1.1583*-00	0.99982	0.99331	0.59665	0.61637	1.06719	0.57746	
3	2.9000*-04	1.1626*-00	0.99837	0.99132	0.60438	0.62355	1.06445	0.58467	
4	4.9000*-04	1.1838*-00	1.00026	0.99425	0.64046	0.65988	1.06155	0.62178	
5	6.8000*-04	1.1910*-00	1.00078	0.99430	0.65206	0.67146	1.06037	0.63372	
6	8.8000*-04	1.1975*-00	1.00172	0.99571	0.66237	0.68194	1.05964	0.64457	
7	1.0700*-03	1.2074*-00	0.99776	0.99251	0.67784	0.69581	1.05373	0.65885	
8	1.2700*-03	1.2117*-00	1.00020	0.99512	0.68428	0.70299	1.05545	0.66619	
9	1.4700*-03	1.2177*-00	1.00046	0.99517	0.69330	0.71178	1.05401	0.67561	
10	1.6600*-03	1.2212*-00	1.00099	0.99570	0.69945	0.71697	1.05371	0.68109	
11	1.8600*-03	1.2256*-00	0.99736	0.99231	0.70490	0.72216	1.04957	0.68658	
12	2.0500*-03	1.2283*-00	1.00095	0.99570	0.70876	0.72695	1.05197	0.69169	
13	2.5400*-03	1.2382*-00	0.99790	0.99325	0.72294	0.73972	1.04697	0.70498	
14	3.0300*-03	1.2493*-00	0.99955	0.99512	0.73840	0.75529	1.04626	0.72157	
15	3.5200*-03	1.2637*-00	1.00016	0.99577	0.75773	0.77405	1.04354	0.74197	
16	4.0100*-03	1.2715*-00	1.00036	0.99614	0.76804	0.78403	1.04207	0.75245	
17	4.4900*-03	1.2836*-00	0.99922	0.99529	0.79351	0.79840	1.03839	0.76829	
18	4.9800*-03	1.2970*-00	0.99989	0.99653	0.80026	0.81477	1.03660	0.78592	
19	5.4700*-03	1.3151*-00	0.99922	0.99575	0.82216	0.83513	1.03179	0.80877	
20	5.9600*-03	1.3272*-00	1.00000	0.99745	0.83634	0.84910	1.03075	0.82426	
21	6.4500*-03	1.3419*-00	0.99730	0.99542	0.85309	0.86387	1.02543	0.84060	
22	6.9400*-03	1.3581*-00	0.99846	0.99636	0.87113	0.88104	1.02297	0.86001	
23	7.4200*-03	1.3664*-00	0.99837	0.99643	0.88015	0.88942	1.02117	0.86956	
24	7.9100*-03	1.3785*-00	0.99929	0.99731	0.89304	0.90180	1.01970	0.88375	
25	8.4000*-03	1.4034*-00	0.99752	0.99815	0.91831	0.92575	1.01515	0.91150	
26	8.8900*-03	1.4163*-00	0.99972	0.99861	0.93170	0.93772	1.01297	0.92545	
27	9.3800*-03	1.4387*-00	0.99842	0.99791	0.95361	0.95729	1.00773	0.94844	
28	9.8700*-03	1.4537*-00	0.99934	0.99859	0.96778	0.97046	1.00554	0.96448	
29	1.0360*-02	1.4647*-00	0.99953	0.99849	0.97809	0.97964	1.00317	0.97512	
30	1.0840*-02	1.4860*-00	0.99950	0.99931	0.99742	0.99760	1.00037	0.99694	
31	1.1330*-02	1.4889*-00	1.00000	1.00000	1.00000	1.00000	1.00000	1.00000	
32	1.1820*-02	1.5034*-00	0.99893	0.99941	1.01249	1.01118	0.99663	1.01351	
33	1.2310*-02	1.5094*-00	0.99900	0.99933	1.01804	1.01597	0.99593	1.01910	
34	1.2800*-02	1.5138*-00	1.00079	1.00094	1.02191	1.01996	0.99619	1.02467	
35	1.3290*-02	1.5183*-00	1.00026	1.00048	1.02577	1.02315	0.99490	1.02867	
36	1.3770*-02	1.5198*-00	0.99953	0.99903	1.02706	1.02355	0.99318	1.02907	
37	1.4260*-02	1.5183*-00	0.99794	0.99892	1.02577	1.02236	0.99335	1.02708	
38	1.4750*-02	1.5198*-00	0.99931	0.99991	1.02706	1.02395	0.99395	1.02947	

85010306		LIU/SQUIRE	PROFILE TABULATION			52 POINTS, DELTA AT POINT 33		
I	Y	PTZ/P	P/PO	TQ/TQD	M/MO	U/UO	T/TQ	R/RQ=U/UO
1	0.0000*-00	1.0000*+00	1.00000	0.99743	0.00000	0.00000	1.12073	0.00000
2	9.0000*-05	1.1708*+00	1.00094	0.99328	0.61069	0.63077	1.06695	0.53180
3	2.9000*-04	1.1807*+00	1.00100	0.99410	0.62723	0.64734	1.05515	0.60835
4	4.9000*-04	1.1950*+00	1.00321	0.99645	0.65013	0.67061	1.06401	0.63229
5	6.8000*-04	1.2125*+00	1.00292	0.99624	0.67684	0.69665	1.05937	0.65953
6	8.8000*-04	1.2134*+00	1.00143	0.99435	0.67812	0.69744	1.05779	0.66027
7	1.0700*-03	1.2283*+00	1.00096	0.99471	0.69975	0.71834	1.05386	0.63229
8	1.2700*-03	1.2309*+00	0.99994	0.99432	0.70356	0.72189	1.05279	0.68566
9	1.4700*-03	1.2355*+00	0.99908	0.99437	0.70992	0.72781	1.05163	0.69134
10	1.6600*-03	1.2391*+00	1.00073	0.99536	0.71501	0.73333	1.05190	0.69766
11	1.8600*-03	1.2428*+00	1.00022	0.99470	0.72010	0.73807	1.05052	0.70273
12	2.0500*-03	1.2484*+00	1.00202	0.99635	0.72774	0.74596	1.05070	0.71139
13	2.5400*-03	1.2579*+00	1.00046	0.99534	0.74046	0.75777	1.04736	0.72355
14	3.0300*-03	1.2656*+00	1.00166	0.99667	0.75064	0.76805	1.04693	0.73453
15	3.5200*-03	1.2775*+00	1.00044	0.99572	0.76590	0.78225	1.04714	0.75023
16	4.0100*-03	1.2918*+00	1.00176	0.99778	0.78372	0.80000	1.04199	0.76911
17	4.4900*-03	1.3033*+00	1.00222	0.99817	0.79771	0.81341	1.03976	0.78389
18	4.9800*-03	1.3086*+00	0.99950	0.99603	0.80407	0.81854	1.03631	0.78946
19	5.4700*-03	1.3283*+00	1.00059	0.99739	0.82697	0.84063	1.03331	0.81402
20	5.9600*-03	1.3430*+00	1.00137	0.99811	0.84351	0.85641	1.03082	0.83194
21	6.4500*-03	1.3499*+00	1.00055	0.99803	0.85115	0.86351	1.02927	0.83951
22	6.9400*-03	1.3676*+00	1.00196	0.99904	0.87023	0.88166	1.02644	0.86055
23	7.4200*-03	1.3617*+00	1.00058	0.99810	0.86397	0.87535	1.02675	0.85304
24	7.9100*-03	1.3761*+00	1.00267	1.00033	0.87913	0.89034	1.02544	0.87040
25	8.4000*-03	1.3896*+00	1.00151	0.99937	0.89313	0.90296	1.02213	0.88493
26	8.8900*-03	1.4072*+00	1.00249	1.00073	0.91094	0.91992	1.01941	0.90429
27	9.3800*-03	1.4241*+00	1.00027	0.99879	0.92748	0.93412	1.01437	0.92114
28	9.8700*-03	1.4334*+00	1.00236	1.00095	0.93639	0.94320	1.01459	0.93154
29	1.0360*-02	1.4468*+00	1.00235	1.00147	0.94911	0.95503	1.01251	0.94544
30	1.0840*-02	1.4619*+00	1.00094	0.99979	0.96310	0.96686	1.00782	0.95940
31	1.1330*-02	1.4802*+00	0.99930	1.00067	0.97964	0.98185	1.00452	0.97770
32	1.1820*-02	1.4831*+00	1.00107	1.00105	0.99219	0.98462	1.00495	0.98091
33	1.2310*-02	1.5034*+00	1.00000	1.00000	1.00000	1.00000	1.00000	1.00000
34	1.2800*-02	1.5034*+00	1.00158	1.00159	1.00000	1.00079	1.00158	1.00079
35	1.3290*-02	1.5123*+00	1.00127	1.00141	1.00763	1.00750	0.99973	1.00905
36	1.3770*-02	1.5228*+00	1.00237	1.00295	1.01654	1.01617	0.99928	1.01931
37	1.4260*-02	1.5259*+00	1.00046	1.00084	1.01908	1.01736	0.99661	1.02128
38	1.4750*-02	1.5259*+00	1.00124	1.00161	1.01908	1.01775	0.99739	1.02168

85010307		LIU/SQUIRE	PROFILE TABULATION			52 POINTS, DELTA AT POINT 35		
I	Y	PTZ/P	P/PO	TQ/TQC	M/MO	U/UO	T/TQ	R/RQ=U/UO
1	0.0000*-00	1.0000*+00	1.00000	1.00117	0.00000	0.00000	1.12072	0.00000
2	9.0000*-05	1.1776*+00	0.99874	0.99250	0.63250	0.65142	1.06040	0.61354
3	2.9000*-04	1.2033*+00	0.99946	0.99370	0.67400	0.69234	1.05517	0.65579
4	4.9000*-04	1.2229*+00	0.99994	0.99478	0.70375	0.72162	1.05143	0.68628
5	6.8000*-04	1.2309*+00	0.99853	0.99362	0.71539	0.73245	1.04825	0.69771
6	8.8000*-04	1.2428*+00	1.00239	0.99749	0.73221	0.75010	1.04946	0.71661
7	1.0700*-03	1.2512*+00	1.00150	0.99574	0.74386	0.76093	1.04644	0.72833
8	1.2700*-03	1.2608*+00	1.00113	0.99665	0.75677	0.77337	1.04428	0.74141
9	1.4700*-03	1.2627*+00	1.00029	0.99545	0.75938	0.77537	1.04256	0.74393
10	1.6600*-03	1.2637*+00	0.99938	0.99536	0.75067	0.77657	1.04225	0.74509
11	1.8600*-03	1.2755*+00	1.00084	0.99649	0.77620	0.79132	1.04065	0.76153
12	2.0500*-03	1.2785*+00	0.99975	0.99527	0.78008	0.79503	1.03969	0.76522
13	2.5400*-03	1.2887*+00	1.00049	0.99668	0.79301	0.80786	1.03780	0.77881
14	3.0300*-03	1.2991*+00	1.00006	0.99619	0.80535	0.81990	1.03490	0.79229
15	3.5200*-03	1.3086*+00	1.00017	0.99641	0.81759	0.83113	1.03318	0.80442
16	4.0100*-03	1.3162*+00	1.00190	0.99850	0.82645	0.84035	1.03343	0.81463
17	4.4900*-03	1.3272*+00	0.99956	0.99639	0.83959	0.85158	1.02879	0.82748
18	4.9800*-03	1.3362*+00	1.00015	0.99721	0.84994	0.86161	1.02767	0.83454
19	5.4700*-03	1.3419*+00	0.99969	0.99713	0.85640	0.86763	1.02639	0.84506
20	5.9600*-03	1.3534*+00	1.00143	0.99901	0.86934	0.88047	1.02576	0.85958
21	6.4500*-03	1.3628*+00	0.99927	0.99728	0.87969	0.88929	1.02195	0.86996
22	6.9400*-03	1.3785*+00	0.99940	0.99754	0.89651	0.90493	1.01889	0.88762
23	7.4200*-03	1.3724*+00	1.00244	1.00007	0.89004	0.90012	1.02278	0.88221
24	7.9100*-03	1.3724*+00	1.00244	1.00007	0.89004	0.90012	1.02278	0.88221
25	8.4000*-03	1.3834*+00	1.00104	0.99941	0.90169	0.91055	1.01977	0.89383
26	8.8900*-03	1.3983*+00	1.00051	0.99895	0.91721	0.92459	1.01616	0.91044
27	9.3800*-03	1.4124*+00	1.00058	0.99944	0.93144	0.93783	1.01377	0.92563
28	9.8700*-03	1.4124*+00	1.00058	0.99944	0.93144	0.93783	1.01377	0.92563
29	1.0360*-02	1.4347*+00	1.00094	1.00040	0.95343	0.95829	1.01021	0.94948
30	1.0840*-02	1.4455*+00	1.00155	1.00094	0.96373	0.96791	1.00959	0.96124
31	1.1330*-02	1.4482*+00	0.99877	0.99860	0.96636	0.96911	1.00950	0.96244
32	1.1820*-02	1.4647*+00	0.99956	0.99955	0.98189	0.98355	1.00339	0.97979
33	1.2310*-02	1.4647*+00	0.99956	0.99955	0.98189	0.98355	1.00339	0.97979
34	1.2800*-02	1.4746*+00	1.00060	1.00037	0.99094	0.99238	1.00290	0.99010
35	1.3290*-02	1.4845*+00	1.00000	1.00000	1.00000	1.00000	1.00000	1.00000
36	1.3770*-02	1.4889*+00	1.00023	1.00029	1.00398	1.00361	0.99946	1.00438
37	1.4260*-02	1.4932*+00	1.00045	1.00059	1.00776	1.00722	0.99893	1.00876
38	1.4750*-02	1.4976*+00	1.00059	1.00089	1.01164	1.01083	0.99819	1.01315

## SECTION D. WALL PRESSURE AND PEAK MACH NUMBER BEFORE SHOCK

(Facsimile from authors' tables)

850105-06

R = 163 mm, Second Throat = 8.75 deg.  
 $M_{pb} = 1.37$ ,  $M_{pt} = 1.23$   
 $T_{0w} = 289.6$  K,  $T_{tw} = 291.2$  K

X(mm)	Pb(mmHg)	Mb	Pt(mmHg)	Mt
-60	782	0.729	752	0.770
-54	789	0.720	749	0.775
-48	802	0.701	742	0.784
-42	823	0.671	735	0.794
-36	794	0.713	721	0.813
-30	736	0.792	711	0.827
-24	683	0.866	691	0.855
-18	629	0.941	674	0.878
-12	586	1.005	650	0.912
-6	541	1.070	630	0.940
0	496	1.141	606	0.976
3	472	1.179	593	0.993
6	456	1.204	579	1.014
9	437	1.237	567	1.032
12	417	1.273	559	1.044
15	399	1.305	540	1.072
18	381	1.338	527	1.092
21	366	1.366	515	1.110
24	350	1.214	500	1.134
27	540	1.071	487	1.155
30	552	1.053	471	1.180
33	563	1.037	459	1.199
36	566	1.032	451	1.213
39	572	1.024	444	1.226
42	580	1.012	436	1.188
45	579	1.013	553	1.052
48	592	0.994	598	0.986
51	605	0.976	622	0.962
54	622	0.951	643	0.922
57	637	0.929	652	0.909
60	648	0.915	658	0.900
63	659	0.899	661	0.897
66	667	0.888	662	0.894
69	676	0.875	668	0.887
72	682	0.867	669	0.886
75	687	0.859	676	0.875
78	693	0.852	678	0.873
81	696	0.849	682	0.866
84	696	0.848	683	0.865
87	696	0.848	688	0.859
90	696	0.848	688	0.859
93	696	0.848	688	0.859
96	696	0.848	688	0.859
99	696	0.848	688	0.859
102	696	0.848	688	0.859
105	696	0.848	688	0.859
108	696	0.848	688	0.859
111	696	0.848	688	0.859
114	696	0.848	688	0.859
117	696	0.848	688	0.859
120	696	0.848	688	0.859
123	696	0.848	688	0.859
126	696	0.848	688	0.859
129	696	0.848	688	0.859
132	696	0.848	688	0.859

850103-04

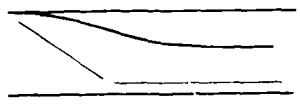
R = 163 mm, Second Throat = 9 deg.  
 $M_{pb} = 1.27$ ,  $M_{pt} = 1.14$   
 $T_{0w} = 289.6$  K,  $T_{tw} = 291.2$  K

X(mm)	Pb(mmHg)	Mb	Pt(mmHg)	Mt
-60	783	0.728	755	0.768
-54	791	0.718	750	0.774
-48	803	0.702	744	0.783
-42	825	0.670	737	0.792
-36	796	0.712	724	0.810
-30	737	0.793	711	0.828
-24	682	0.868	695	0.850
-18	631	0.939	676	0.877
-12	586	1.005	653	0.909
-6	541	1.071	632	0.938
0	497	1.140	608	0.972
3	472	1.179	594	0.993
6	456	1.206	581	1.011
9	437	1.238	567	1.031
12	420	1.268	559	1.044
15	405	1.294	543	1.068
18	389	1.317	529	1.096
21	374	1.345	515	1.112
24	359	1.366	503	1.130
27	344	1.389	498	1.138
30	330	1.412	508	1.121
33	317	1.435	516	1.102
36	304	1.456	520	1.085
39	292	1.476	524	1.068
42	280	1.495	529	1.052
45	269	1.514	533	1.036
48	258	1.532	537	1.020
51	247	1.550	541	1.004
54	236	1.567	545	0.988
57	225	1.584	549	0.972
60	214	1.600	553	0.956
63	203	1.616	557	0.940
66	192	1.632	561	0.924
69	181	1.647	565	0.908
72	170	1.662	569	0.892
75	159	1.677	573	0.876
78	148	1.691	577	0.860
81	137	1.706	581	0.844
84	126	1.720	585	0.828
87	115	1.734	589	0.812
90	104	1.748	593	0.796
93	93	1.762	597	0.780
96	82	1.776	601	0.764
99	71	1.790	605	0.748
102	60	1.804	609	0.732
105	49	1.818	613	0.716
108	38	1.832	617	0.700
111	27	1.846	621	0.684
114	16	1.860	625	0.668
117	5	1.874	629	0.652
120	-6	1.888	633	0.636
123	-17	1.902	637	0.620
126	-28	1.916	641	0.604
129	-39	1.930	645	0.588
132	-50	1.944	649	0.572

850101-02

R = 163 mm, Second Throat = 9.5 deg.  
 $M_{pb} = 1.20$ ,  $M_{pt} = 0.96$   
 $T_{0w} = 291.2$  K,  $T_{tw} = 292$  K

X(mm)	Pb(mmHg)	Mb	Pt(mmHg)	Mt
-60	789	0.724	757	0.769
-54	794	0.717	754	0.773
-48	809	0.697	747	0.782
-42	832	0.665	740	0.792
-36	800	0.709	730	0.806
-30	742	0.790	716	0.825
-24	690	0.861	700	0.847
-18	638	0.933	684	0.869
-12	583	0.998	664	0.896
-6	548	1.063	647	0.920
0	504	1.131	631	0.943
3	482	1.166	627	0.948
6	467	1.190	630	0.945
9	459	1.204	631	0.943
12	450	1.217	635	0.935
15	440	1.230	644	0.924
18	430	1.243	653	0.912
21	420	1.256	662	0.900
24	410	1.269	671	0.888
27	400	1.282	680	0.876
30	390	1.295	689	0.863
33	380	1.308	698	0.851
36	370	1.321	707	0.839
39	360	1.334	716	0.827
42	350	1.347	725	0.815
45	340	1.360	734	0.803
48	330	1.373	743	0.791
51	320	1.386	752	0.779
54	310	1.399	761	0.767
57	300	1.412	770	0.755
60	290	1.425	779	0.743
63	280	1.438	788	0.731
66	270	1.451	797	0.719
69	260	1.464	806	0.707
72	250	1.477	815	0.695
75	240	1.490	824	0.683
78	230	1.503	833	0.671
81	220	1.516	842	0.659
84	210	1.529	851	0.647
87	200	1.542	860	0.635
90	190	1.555	869	0.623
93	180	1.568	878	0.611
96	170	1.581	887	0.599
99	160	1.594	896	0.587
102	150	1.607	905	0.575
105	140	1.620	914	0.563
108	130	1.633	923	0.551
111	120	1.646	932	0.539
114	110	1.659	941	0.527
117	100	1.672	950	0.515
120	90	1.685	959	0.503
123	80	1.698	968	0.491
126	70	1.711	977	0.479
129	60	1.724	986	0.467
132	50	1.737	995	0.455

	$M(\infty)$ : 2.89, falling to 2.4 $R \text{ Theta} \times 10^{-3}$ : 80 upstream $TW/TR$ : 1.11	8601
		APG
Blowdown tunnel with symmetrical contoured nozzle. Max. running time "several minutes", normally 60 seconds. $W = H = 203 \text{ mm}$ , $L$ up to $2.7 \text{ m}$ . $PO$ : $0.67 \text{ MN/m}^2$ . $TO$ : $270 \text{ K}$ . Air. $Re/m \times 10^{-6}$ : 63.		
FERNANDO E.M., SMITS A.J., 1986. A data compilation for a supersonic turbulent boundary layer under conditions of an adverse pressure gradient. Princeton, Gas Dynamics Lab. Rep. MAE 1746. And: Fernando & Smits (1987), A.J.Smits, private communications, data tape.		

- 1 The general arrangements for the experiment were as for the CCF tests described in CAT7904T, q.v.. The test surface however was flush with the tunnel floor, starting  $0.902 \text{ m}$  from the nozzle exit ( $X = 0$ ). A wave generator was mounted in the free stream to provide a longitudinal pressure gradient identical to that measured on the curved ramp, model 2, of CAT8401T. The co-ordinates for this are given in the source paper. The pressure gradient started at about  $X = 1.0 \text{ m}$ , a little upstream of the start of the curvature in the ramp experiment. The two-dimensionality of the flow was checked by spanwise surveys of the mean flow quantities at the  $X$ -value of profile 08.
- 5 the ramp experiment. The two-dimensionality of the flow was checked by spanwise surveys of the mean flow quantities at the  $X$ -value of profile 08.
- 6 Wall pressure was measured at 47  $X$ -stations along the centreline, and at numerous points  $25.4$  and  $50.8 \text{ mm}$  to the side. Wall shear stress was measured with a Preston tube ( $d = 1.6 \text{ mm}$ ) at 10 values of  $X$ , and at a further 8 stations across the surface at  $X = 0.4191 \text{ m}$ , corresponding to profile 0108. The transverse variation was  $\pm 6\%$ . Velocity profiles
- 8 were measured at the same 18 positions. The  $X$ -values are given in section B. Normal wire turbulence profiles were obtained at the 10 profile stations along the centre of the floor.
- 7 The mean flow probes, instrumentation and data reduction procedures were largely as for CAT7904, except that the traverse gear was mounted on doubly eccentric plugs inserted in the test wall rather than on long supports passing through the tunnel roof, and the probes were in consequence of "goose-neck" form. Turbulence measurements were made with normal hot wires only, operating in the constant-temperature mode and using a DISA 55 M 10 anemometer. The copper-plated soft-soldered sensor wires ( $d = 5 \mu\text{m}$ , active length about  $0.8 \text{ mm}$ ) were slightly slackened, to avoid strain-gauging. The support prongs were about  $2-3 \text{ mm}$  long and mounted in a cylindrical holder ( $d = 2.5-4 \text{ mm}$ ) the front of which formed a wedge with  $30^\circ$  included angle. (Smits et al., 1983).
- 12 The editors have presented the profile data, 0101-0110, measured on the centreline of the tunnel, as interpolated to the hot-wire measuring positions by the authors. The authors' D-state has been replaced by a state selected on the basis of the total pressure profile, there being no shock waves in the exterior flow adjacent to the test layer, with additional consideration given to the reported turbulence levels.
- 9 Data: 86010101-10. Pitot, static pressure and  $TO$  profiles,  $NX = 10$ . CF from Preston tubes. Normal hot-wire profiles,  $NX = 8$ .
- 15 Editors' comments:  
 This is one of a series of experiments designed to subject boundary layers to a number of perturbations with features both in common and in contrast. The streamwise pressure gradient here is the same as for the curved ramp of series 2, CAT8401T, but without curvature. The "disturbance" of the layer - the change in mean pressure level - is the same as for that case, and also the more abrupt changes of series 1, CAT8401T/7904T. The choice of  $X$ -values for the profiles suggests a concentration on the "recovery" process rather than the APG flow itself - 01 is about halfway through the pressure rise, 05-10 cover a region in which the pressure actually falls slightly. All profiles show normal pressure-gradients though, this being a reflected wave case, they are not very strong. Zero pressure gradient observations using the same instruments, but supported from the tunnel roof as for CAT7904T, and covering a range of  $X$  from  $1.07$  to  $1.53 \text{ m}$  on the same tunnel floor are given by Spina & Smits, CAT8603T.

The authors' D-state is based on a 5% deficit in specific mass flow relative to an ideal flow computed from the local static pressure and the free-stream total pressure (for a discussion of the implications of this type of procedure, see § 9.2.2 above and AG253 Ch7). We again urge the desirability of basing the choice of edge point on the computed value of the total pressure.

The profiles are covered in fairly fine detail. The momentum deficit integrand has not reached its peak as the wall is approached, but the H12K values are low even for a modest pressure gradient. Normal pressure gradients are present, but are probably small enough for integral quantities to retain their conventional meanings with acceptable accuracy. The profiles fit the wall law reasonably well, with a tendency to lie a little high, (fig. 10.1.4) in contrast in this, and in the extent of the disagreement, with the profiles for series 2 of CAT8401T with the same streamwise pressure gradient on a curved wall (fig. 10.2.3). The outer law plot for the two cases is very similar and typical of those seen in modest adverse pressure gradients. (figs. 10.1.3, 10.2.5.)

Earlier investigations in similar flows are reported by Kussoy et al., CAT7802S, with hot wire measurements. Related mean flows are reported by Peake et al., CAT7102, Lewis et al., CAT7201, Thomas CAT7401 and Zwarts, CAT7007.

Fernando & Smits (1987) report additional measurements in this boundary layer including crossed wire traverses and multiple normal wire observations aimed at elucidating the large-scale structure of the flow.

CAT 8601		FERNANDO/SMITS		BOUNDARY CONDITIONS AND EVALUATED DATA, SI UNITS					
RUN	ND #	TW/TP	REDZ	CF	H12	H12K	P4*	PJ*	
X #	P00	PM/PO	RENZ	CJ	H32	H32K	T4*	TJ	
Z	T00	TAUW #	DZ	PI2	H42	D2K	UJ*	TR	
86010101	2.6530	1.1073	3.9995*+04	9.9203*-04	5.3056	1.2775	3.0490*+04	3.1311*+04	
1.1510*+00	6.7221*+05	0.9823	1.9483*+04	NM	1.9346	1.8234	2.8155*+02	1.1245*+02	
INFINITE	2.7074*+02	1.5170*+02	1.3004*-03	NM	-0.1726	1.9617*-03	5.6405*+02	2.5429*+02	
86010102	2.6140	1.1065	4.1753*+04	9.9537*-04	5.0535	1.2783	3.1500*+04	3.2697*+04	
1.1720*+00	6.7086*+05	0.9634	1.0345*+04	NM	1.8320	1.8179	2.8575*+02	1.1590*+02	
INFINITE	2.7477*+02	1.5630*+02	1.3415*-03	NM	-0.1463	1.9972*-03	5.6502*+02	2.5525*+02	
86010103	2.5750	1.1055	4.7620*+04	9.6721*-04	4.4348	1.3191	3.5833*+04	3.4750*+04	
1.1970*+00	6.6707*+05	1.0314	1.0197*+05	NM	1.3172	1.8049	2.8197*+02	1.1665*+02	
INFINITE	2.7113*+02	1.5600*+02	1.4523*-03	NM	-0.1340	2.0863*-03	5.5733*+02	2.5505*+02	
86010104	2.5330	1.1046	5.4012*+04	9.4299*-04	3.3003	1.3301	3.9890*+04	3.7281*+04	
1.2220*+00	6.7051*+05	1.0700	1.1378*+05	NM	1.3090	1.7940	2.7993*+02	1.1791*+02	
INFINITE	2.6921*+02	1.5790*+02	1.5612*-03	NM	-0.1201	2.1552*-03	5.5148*+02	2.5348*+02	
86010105	2.4900	1.1035	5.7938*+04	9.4420*-04	3.9700	1.3474	4.2870*+04	3.9812*+04	
1.2480*+00	6.7141*+05	1.0741	1.2002*+05	NM	1.3022	1.7985	2.7594*+02	1.1399*+02	
INFINITE	2.6629*+02	1.6390*+02	1.5834*-03	NM	-0.1277	2.1904*-03	5.4433*+02	2.5496*+02	
86010106	2.4480	1.1025	5.7954*+04	9.4116*-04	4.2739	1.3331	4.3650*+04	4.2492*+04	
1.2730*+00	6.7726*+05	1.0155	1.1791*+05	NM	1.9086	1.7942	2.7932*+02	1.2215*+02	
INFINITE	2.6857*+02	1.6970*+02	1.5277*-03	NM	-0.1314	2.1754*-03	5.4249*+02	2.5335*+02	
86010107	2.4760	1.1032	5.7634*+04	1.0111*-03	4.1206	1.3222	4.2510*+04	4.0923*+04	
1.2990*+00	6.7367*+05	1.0386	1.1854*+05	NM	1.9139	1.8011	2.8053*+02	1.2117*+02	
INFINITE	2.6974*+02	1.7760*+02	1.5761*-03	NM	-0.1267	2.2186*-03	5.4645*+02	2.5429*+02	
86010108	2.4760	1.1032	5.3955*+04	1.0664*-03	4.1961	1.3037	4.1003*+04	3.9770*+04	
1.3240*+00	6.5459*+05	1.0309	1.1091*+05	NM	1.8216	1.8100	2.8149*+02	1.2153*+02	
INFINITE	2.7067*+02	1.9200*+02	1.5252*-03	NM	-0.1326	2.1424*-03	5.4740*+02	2.5517*+02	
86010109	2.4200	1.1018	4.9447*+04	1.0845*-03	4.7100	1.2759	3.9630*+04	4.1493*+04	
1.3490*+00	6.2586*+05	0.9551	9.9159*+04	NM	1.8314	1.8190	2.8443*+02	1.2598*+02	
INFINITE	2.7354*+02	1.8450*+02	1.4068*-03	NM	-0.1379	2.0544*-03	5.4460*+02	2.5319*+02	
86010110	2.5050	1.1039	5.5233*+04	1.0429*-03	4.7111	1.2662	4.0170*+04	4.0170*+04	
1.3610*+00	6.9170*+05	1.0000	1.1758*+05	NM	1.8313	1.8202	2.7092*+02	1.1552*+02	
INFINITE	2.6050*+02	1.8400*+02	1.4713*-03	NM	-0.1546	2.1362*-03	5.3982*+02	2.4542*+02	



86010102		FERNANDO/SMITS		PROFILE TABULATION		53 POINTS, DELTA AT POINT 42		
I	Y	PTZ/P	P/PD	T0/TQD	N/MD	U/UD	T/TD	R/RD=U/UD
1	0.0000+00	1.0000+00	0.96339	1.03998	0.00000	0.00000	2.46557	0.00000
2	3.9700-04	2.3757+00	0.96339	1.02937	0.45416	0.62658	1.90342	0.31714
3	5.8160-04	2.5783+00	0.96339	1.02825	0.48014	0.65348	1.85239	0.33986
4	7.7420-04	2.7104+00	0.96339	1.02893	0.49618	0.67009	1.82386	0.35395
5	9.9080-04	2.9217+00	0.96339	1.02792	0.52053	0.69398	1.77680	0.37628
6	1.2070-03	3.0808+00	0.96339	1.02786	0.53820	0.71080	1.74427	0.39259
7	1.4160-03	3.0318+00	0.98748	1.02783	0.53285	0.70571	1.75406	0.39729
8	1.5770-03	3.2060+00	0.98555	1.02803	0.55157	0.72337	1.71997	0.41449
9	1.8010-03	3.3234+00	0.98459	1.02748	0.56379	0.73437	1.69668	0.42616
10	2.0020-03	3.3644+00	0.98266	1.02674	0.56799	0.73790	1.68778	0.42962
11	2.2190-03	3.4436+00	0.98266	1.02699	0.57601	0.74517	1.67359	0.43753
12	2.4270-03	3.4971+00	0.97977	1.02653	0.58136	0.74974	1.66316	0.44167
13	2.8850-03	3.6767+00	0.97881	1.02538	0.59893	0.75480	1.63057	0.45910
14	3.3020-03	3.8497+00	0.98266	1.02473	0.61536	0.77819	1.59928	0.47815
15	3.6870-03	3.9195+00	0.98362	1.02506	0.62185	0.78370	1.59828	0.48534
16	4.0000-03	4.0110+00	0.98555	1.02420	0.63025	0.79024	1.57213	0.49539
17	4.4180-03	4.0699+00	0.99037	1.02350	0.63560	0.79429	1.56167	0.50371
18	4.8910-03	4.2368+00	0.98748	1.02325	0.65050	0.80602	1.53534	0.51840
19	5.3400-03	4.4211+00	0.98555	1.02285	0.66654	0.81828	1.50712	0.53509
20	5.7020-03	4.4701+00	0.98362	1.02138	0.67074	0.82108	1.49852	0.53895
21	6.0230-03	4.6558+00	0.98266	1.02145	0.68640	0.83261	1.47137	0.55606
22	6.4160-03	4.7526+00	0.98362	1.02132	0.69442	0.83842	1.45773	0.55574
23	7.2180-03	5.0885+00	0.98362	1.01937	0.72154	0.85711	1.41108	0.53747
24	8.1090-03	5.2591+00	0.98844	1.01894	0.73491	0.86584	1.38904	0.61657
25	8.9280-03	5.4679+00	0.98940	1.01818	0.75095	0.87622	1.36144	0.63678
26	9.6500-03	5.7227+00	0.98844	1.01722	0.77005	0.88816	1.33028	0.65993
27	1.0440-02	5.9417+00	0.98844	1.01629	0.78610	0.89782	1.30445	0.68032
28	1.1220-02	6.2095+00	0.98748	1.01494	0.80519	0.90883	1.27397	0.70445
29	1.2120-02	6.5996+00	0.98555	1.01370	0.83231	0.92409	1.23269	0.73882
30	1.2960-02	6.7560+00	0.97977	1.01277	0.84301	0.92970	1.21624	0.74894
31	1.3660-02	7.0829+00	0.97592	1.01145	0.86478	0.94102	1.18408	0.77558
32	1.4460-02	7.3291+00	0.97110	1.01032	0.88083	0.94922	1.16133	0.79373
33	1.5260-02	7.5860+00	0.96532	1.00941	0.89725	0.95701	1.13764	0.81205
34	1.6110-02	8.0207+00	0.96435	1.00826	0.92437	0.96989	1.10091	0.84959
35	1.7020-02	8.1957+00	0.96339	1.00712	0.93506	0.97446	1.08603	0.86442
36	1.7690-02	8.3728+00	0.97013	1.00641	0.94576	0.97913	1.07181	0.88625
37	1.8470-02	8.6034+00	0.98073	1.00538	0.95951	0.98494	1.05371	0.91672
38	1.9260-02	8.8308+00	0.99037	1.00438	0.97288	0.99045	1.03644	0.94642
39	2.0150-02	8.9227+00	0.99807	1.00317	0.97823	0.99221	1.02880	0.96258
40	2.0990-02	9.0151+00	1.00193	1.00203	0.98358	0.99398	1.02126	0.97516
41	2.1730-02	9.2081+00	1.00193	1.00101	0.99465	0.99824	1.00722	0.99299
42	2.2490-02	9.3020+00	1.00000	1.00000	1.00000	1.00000	1.00000	1.00000
43	2.4050-02	9.3020+00	0.99229	0.99772	1.00000	0.99886	0.99772	0.99343
44	2.5720-02	9.4914+00	0.98362	0.99586	1.01070	1.00239	0.98363	1.00238
45	2.7310-02	9.4914+00	0.97977	0.99380	1.01070	1.00135	0.98159	0.99949
46	2.8850-02	9.5391+00	0.98170	0.99162	1.01337	1.00135	0.97642	1.00676
47	3.0550-02	9.5391+00	0.97881	0.99018	1.01337	1.00062	0.97500	1.00453
48	3.2020-02	9.6348+00	0.96917	0.99017	1.01872	1.00280	0.96901	1.00298
49	3.3590-02	9.6348+00	0.95915	0.99017	1.01872	1.00280	0.96901	0.99261
50	3.5180-02	9.6828+00	0.95395	0.99009	1.02139	1.00384	0.96594	0.99139
51	3.6780-02	9.7379+00	0.95915	0.99011	1.02445	1.00509	0.96257	1.00152
52	3.8400-02	9.6828+00	0.96724	0.99009	1.02139	1.00384	0.96594	1.00520
53	3.9980-02	9.5869+00	0.97698	0.99027	1.01604	1.00177	0.97209	1.00670

86010104

FERNANDO/SMTS

PROFILE TABULATION

53 POINTS, DELTA AT POINT 41

I	Y	PT2/P	P/P0	T0/T00	M/MD	U/UD	T/T0	R/RD#U/UD
1	0.0000**00	1.0000**00	1.06998	1.04033	0.00000	0.00030	2.37451	0.00000
2	3.4700**04	2.0276**00	1.06998	1.02871	0.41759	0.57853	1.91913	0.32261
3	4.8340**04	2.2198**00	1.06998	1.02793	0.44730	0.61126	1.86752	0.35022
4	7.0800**04	2.3757**00	1.06998	1.02796	0.46940	0.63495	1.82971	0.37130
5	8.7650**04	2.4693**00	1.06999	1.02743	0.43234	0.64800	1.80713	0.38357
6	1.1090**03	2.6092**00	1.06998	1.02737	0.50020	0.66653	1.77563	0.40164
7	1.2940**03	2.7104**00	1.06998	1.02707	0.51283	0.67905	1.75332	0.41440
8	1.4940**03	2.7329**00	1.09245	1.02709	0.51559	0.68179	1.74958	0.42596
9	1.6950**03	2.7784**00	1.09031	1.02659	0.52112	0.68705	1.73821	0.43096
10	1.8710**03	2.8377**00	1.08924	1.02577	0.52823	0.69369	1.72458	0.43913
11	2.1040**03	2.9553**00	1.08493	1.02659	0.54205	0.70716	1.70201	0.45123
12	2.3130**03	2.9558**00	1.08496	1.02583	0.54205	0.70695	1.70100	0.45092
13	2.6170**03	3.1807**00	1.07961	1.02519	0.56731	0.73021	1.65674	0.47564
14	2.9940**03	3.2854**00	1.07640	1.02437	0.57876	0.74011	1.63527	0.48716
15	3.4520**03	3.3906**00	1.07747	1.02374	0.58931	0.74979	1.61632	0.49931
16	3.9250**03	3.4971**00	1.07533	1.02300	0.60037	0.75937	1.59715	0.51127
17	4.2380**03	3.6490**00	1.07533	1.02232	0.61627	0.77221	1.57013	0.52886
18	4.6070**03	3.7324**00	1.07533	1.02234	0.62456	0.77916	1.55635	0.53934
19	5.0320**03	3.8050**00	1.07426	1.02208	0.63156	0.78474	1.54340	0.54620
20	5.5300**03	3.9651**00	1.06805	1.02138	0.64736	0.79634	1.51655	0.56119
21	5.9070**03	4.1294**00	1.06698	1.02062	0.66246	0.80834	1.49078	0.57890
22	6.2840**03	4.1764**00	1.06377	1.01930	0.66630	0.81190	1.48256	0.58255
23	7.1260**03	4.4836**00	1.05521	1.01923	0.69443	0.83263	1.43752	0.61115
24	7.7920**03	4.7526**00	1.05307	1.01833	0.71773	0.84916	1.39978	0.63893
25	8.7070**03	4.9830**00	1.04933	1.01714	0.73707	0.85221	1.36839	0.66117
26	9.4610**03	5.2591**00	1.04740	1.01577	0.75957	0.87694	1.33261	0.68918
27	1.0260**02	5.5437**00	1.04772	1.01453	0.78208	0.89095	1.29779	0.71927
28	1.1120**02	5.7227**00	1.05254	1.01335	0.79589	0.89937	1.27692	0.74133
29	1.1840**02	6.1703**00	1.05981	1.01290	0.82945	0.91926	1.22828	0.79318
30	1.2770**02	6.2844**00	1.06938	1.01173	0.83774	0.92558	1.25543	0.81396
31	1.3480**02	6.4818**00	1.07405	1.01073	0.85195	0.93126	1.19485	0.83477
32	1.4350**02	6.6771**00	1.06484	1.00973	0.85577	0.93553	1.17513	0.85044
33	1.5150**02	7.1645**00	1.06002	1.00835	0.89933	0.95589	1.12975	0.89690
34	1.5870**02	7.2878**00	1.05468	1.00773	0.90752	0.95989	1.11851	0.95511
35	1.6790**02	7.6707**00	1.04558	1.00625	0.93239	0.97190	1.08538	0.93626
36	1.7540**02	7.8846**00	1.03702	1.00541	0.94670	0.97821	1.06757	0.95013
37	1.8330**02	8.0642**00	1.02899	1.00417	0.95815	0.98305	1.05255	0.95036
38	1.9170**02	8.3283**00	1.02172	1.00323	0.97473	0.99032	1.03223	0.98024
39	1.9860**02	8.5063**00	1.01584	1.00230	0.98579	0.99494	1.01846	0.99228
40	2.0800**02	8.5583**00	1.00449	1.00034	0.98935	0.99558	1.01346	0.98677
41	2.1560**02	8.7395**00	1.00000	1.00000	1.00000	1.00000	1.00000	1.00000
42	2.2360**02	8.7395**00	0.99326	0.99874	1.00000	0.99937	0.99874	0.99399
43	2.3950**02	8.9757**00	0.98202	0.99701	1.00829	1.00211	0.99777	0.99628
44	2.5580**02	8.9227**00	0.97421	0.99465	1.01135	1.00211	0.99238	0.99373
45	2.7170**02	9.0151**00	0.96908	0.99230	1.01658	1.00358	0.97458	0.99791
46	2.8760**02	9.0151**00	0.96458	0.99032	1.01658	1.00253	0.97254	0.99432
47	3.0320**02	9.0615**00	0.96131	0.98913	1.01934	1.00294	0.96788	0.99665
48	3.1880**02	9.0615**00	0.95442	0.98913	1.01934	1.00294	0.96788	0.98889
49	3.3420**02	9.1613**00	0.94254	0.98901	1.02527	1.00526	0.96136	0.98559
50	3.5020**02	9.1613**00	0.92938	0.98901	1.02527	1.00526	0.96136	0.97192
51	3.6610**02	9.2550**00	0.92831	0.98863	1.03079	1.00737	0.95507	0.97915
52	3.8170**02	9.2081**00	0.93644	0.98831	1.02803	1.00632	0.95820	0.98346
53	3.9750**02	9.1613**00	0.94233	0.98901	1.02527	1.00526	0.96136	0.98536

86010106		FERNANDO/SMIIS		PROFILE TABULATION		53 POINTS, DELTA AT POINT 42			
I	Y	PT2/P	P/PD	T0/T0D	N/MD	U/UD	T/TD	R/RD=U/UD	
1	0.0000E+00	1.0000E+00	1.01554	1.04001	0.00000	0.00000	2.28651	0.00000	
2	3.9700E-04	2.0373E+00	1.01554	1.02937	0.43382	0.58952	1.84658	0.32421	
3	5.2540E-04	2.2279E+00	1.01554	1.02960	0.46405	0.62246	1.79923	0.35133	
4	7.0990E-04	2.3557E+00	1.01554	1.02961	0.48284	0.64225	1.76925	0.36864	
5	9.4250E-04	2.4192E+00	1.01554	1.02798	0.49183	0.65102	1.75208	0.37734	
6	1.1510E-03	2.5233E+00	1.01554	1.02836	0.50613	0.66567	1.72980	0.39080	
7	1.3680E-03	2.5875E+00	1.01554	1.02861	0.51471	0.67433	1.71644	0.39897	
8	1.5440E-03	2.6880E+00	1.01960	1.02783	0.52778	0.68695	1.69414	0.41343	
9	1.7690E-03	2.7556E+00	1.01462	1.02790	0.53636	0.69529	1.68047	0.41980	
10	1.9130E-03	2.8145E+00	1.01320	1.02730	0.54371	0.70214	1.66768	0.42659	
11	2.1220E-03	2.8980E+00	1.01279	1.02687	0.55392	0.71166	1.65061	0.43666	
12	2.3670E-03	2.9081E+00	1.01086	1.02695	0.55515	0.71283	1.64877	0.43704	
13	2.7560E-03	3.0422E+00	1.00579	1.02633	0.57108	0.72738	1.62230	0.45096	
14	3.1650E-03	3.1305E+00	1.00416	1.02550	0.58129	0.73636	1.60472	0.46078	
15	3.4300E-03	3.2716E+00	1.00091	1.02479	0.59722	0.75037	1.57864	0.47576	
16	3.8550E-03	3.3494E+00	1.00254	1.02525	0.60580	0.75797	1.56546	0.48541	
17	4.3520E-03	3.4284E+00	1.00457	1.02460	0.61438	0.76513	1.55096	0.49558	
18	4.7930E-03	3.5667E+00	1.00528	1.02331	0.62908	0.77711	1.52598	0.51134	
19	5.1300E-03	3.6925E+00	1.00508	1.02292	0.64216	0.78781	1.50507	0.52609	
20	5.4350E-03	3.7888E+00	1.00619	1.02328	0.65196	0.79594	1.49044	0.53734	
21	5.8200E-03	3.8497E+00	1.00812	1.02199	0.65809	0.80032	1.47897	0.54553	
22	6.3740E-03	3.9361E+00	1.00599	1.02140	0.66667	0.80695	1.46514	0.55407	
23	7.0560E-03	4.1764E+00	1.00386	1.02012	0.68995	0.82449	1.42803	0.57959	
24	7.9780E-03	4.3531E+00	1.00112	1.01923	0.70711	0.83701	1.40115	0.59804	
25	8.6840E-03	4.7202E+00	1.00020	1.01813	0.73979	0.86011	1.35173	0.63643	
26	9.5350E-03	4.9830E+00	1.00020	1.01752	0.76266	0.87562	1.31814	0.66442	
27	1.0370E-02	5.2247E+00	1.00162	1.01628	0.78309	0.88866	1.28781	0.69118	
28	1.1060E-02	5.3978E+00	1.00162	1.01545	0.79739	0.89754	1.26698	0.70956	
29	1.2030E-02	5.6149E+00	1.00112	1.01367	0.81495	0.90781	1.24087	0.74241	
30	1.2750E-02	5.9417E+00	1.00203	1.01360	0.84069	0.92332	1.20624	0.76701	
31	1.3550E-02	6.2464E+00	1.00457	1.01201	0.86397	0.93626	1.17433	0.80091	
32	1.4470E-02	6.3608E+00	1.00782	1.01096	0.87255	0.94064	1.16217	0.81571	
33	1.5130E-02	6.6771E+00	1.00853	1.00974	0.89583	0.95294	1.13156	0.84933	
34	1.6060E-02	6.9155E+00	1.00995	1.00867	0.91299	0.96160	1.10933	0.87546	
35	1.6760E-02	7.1236E+00	1.01391	1.00737	0.92770	0.96888	1.09075	0.90062	
36	1.7570E-02	7.4122E+00	1.01757	1.00663	0.94771	0.97840	1.06580	0.93412	
37	1.8460E-02	7.5860E+00	1.01858	1.00542	0.95956	0.98364	1.05081	0.95347	
38	1.9140E-02	7.7132E+00	1.01655	1.00491	0.96814	0.98749	1.04037	0.96488	
39	2.0070E-02	7.8846E+00	1.01229	1.00353	0.97958	0.99230	1.02615	0.97889	
40	2.0770E-02	7.9710E+00	1.01066	1.00244	0.98529	0.99444	1.01865	0.98664	
41	2.1600E-02	8.1079E+00	1.00741	1.00117	0.99428	0.99797	1.00743	0.99795	
42	2.2480E-02	8.1957E+00	1.00000	1.00000	1.00000	1.00000	1.00000	1.00000	
43	2.3990E-02	8.2840E+00	0.99812	0.99804	1.00572	1.00160	0.99183	0.99785	
44	2.5610E-02	8.3728E+00	0.97461	0.99592	1.01144	1.00310	0.98359	0.99395	
45	2.7300E-02	8.4173E+00	0.96649	0.99383	1.01430	1.00332	0.97846	0.99103	
46	2.8740E-02	8.4173E+00	0.95532	0.99192	1.01430	1.00235	0.97658	0.98052	
47	3.0450E-02	8.5069E+00	0.93622	0.99033	1.02002	1.00406	0.96897	0.97013	
48	3.2000E-02	8.6034E+00	0.91733	0.99012	1.02614	1.00663	0.96233	0.95956	
49	3.3500E-02	8.6486E+00	0.90667	0.99021	1.02900	1.00791	0.95943	0.95249	
50	3.5180E-02	8.6940E+00	0.89895	0.99031	1.03186	1.00920	0.95655	0.94843	
51	3.6630E-02	8.6940E+00	0.89387	0.99031	1.03186	1.00920	0.95655	0.94307	
52	3.8300E-02	8.6940E+00	0.89433	0.99031	1.03186	1.00920	0.95655	0.93300	
53	3.9870E-02	8.7851E+00	0.87032	0.99013	1.03758	1.01155	0.95045	0.92626	

86010108		FERNANDO/SHIYS		PROFILE TABULATION		53 POINTS, DELTA AT POINT 42		
I	Y	PT2/P	P/PD	T0/TD	M/MD	U/UD	T/TD	R/RD=U/UD
1	0.0000+00	1.0000+00	1.03093	1.03996	0.00000	0.00000	2.31508	0.00000
2	3.9700-04	2.2579+00	1.03093	1.02919	0.46325	0.62390	1.81383	0.35460
3	5.1730-04	2.4901+00	1.03093	1.02931	0.49596	0.65805	1.76043	0.38536
4	7.8210-04	2.6531+00	1.03093	1.02931	0.51737	0.67954	1.72518	0.40608
5	9.3450-04	2.7915+00	1.03093	1.02855	0.53473	0.69624	1.69531	0.42339
6	1.1910-03	2.9611+00	1.03093	1.02813	0.54321	0.70422	1.68066	0.43198
7	1.3200-03	2.9845+00	1.03093	1.02836	0.54604	0.70699	1.67639	0.43478
8	1.5600-03	3.0318+00	1.03072	1.02721	0.56341	0.72284	1.64604	0.45263
9	1.7610-03	3.0562+00	1.02515	1.02706	0.56624	0.72540	1.64117	0.45312
10	1.9530-03	3.1555+00	1.02742	1.02738	0.57754	0.73582	1.62321	0.46574
11	2.1220-03	3.1807+00	1.02742	1.02709	0.58037	0.73827	1.61814	0.46876
12	2.3380-03	3.1951+00	1.02216	1.02661	0.58199	0.73955	1.61474	0.46815
13	2.6510-03	3.2974+00	1.02155	1.02643	0.59330	0.74955	1.59609	0.47978
14	3.1730-03	3.3382+00	1.02010	1.02535	0.59774	0.75306	1.58722	0.48399
15	3.4620-03	3.4971+00	1.02412	1.02510	0.61470	0.76764	1.55949	0.50411
16	3.8950-03	3.5940+00	1.02639	1.02472	0.62480	0.77604	1.54273	0.51631
17	4.3680-03	3.5783+00	1.02918	1.02437	0.62318	0.77455	1.54479	0.51602
18	4.7610-03	3.7485+00	1.03093	1.02338	0.64055	0.78859	1.51566	0.53639
19	5.1300-03	3.8497+00	1.02918	1.02253	0.65065	0.79647	1.49847	0.54703
20	5.4590-03	3.9361+00	1.02515	1.02258	0.65913	0.80328	1.44522	0.55445
21	5.8760-03	4.0110+00	1.02361	1.02150	0.66640	0.80860	1.47230	0.56217
22	6.3580-03	4.2368+00	1.02041	1.02113	0.68780	0.82498	1.43867	0.58514
23	7.0880-03	4.4078+00	1.01887	1.02010	0.70355	0.83637	1.41318	0.60300
24	7.9700-03	4.5873+00	1.01258	1.01936	0.71971	0.84786	1.37871	0.61851
25	8.6920-03	4.8178+00	1.01237	1.01822	0.73990	0.86169	1.35628	0.64319
26	9.5910-03	4.9830+00	1.01082	1.01734	0.75404	0.87105	1.33444	0.65981
27	1.0380-02	5.2591+00	1.01031	1.01599	0.77706	0.88584	1.29957	0.68867
28	1.1090-02	5.5083+00	1.01103	1.01472	0.79725	0.89829	1.24951	0.71539
29	1.2040-02	5.6866+00	1.00979	1.01373	0.81139	0.90669	1.24871	0.73322
30	1.2750-02	5.9049+00	1.01381	1.01278	0.82835	0.91669	1.22467	0.75886
31	1.3590-02	6.2085+00	1.01258	1.01168	0.85137	0.92967	1.19240	0.78947
32	1.4450-02	6.4818+00	1.01351	1.01056	0.87157	0.94063	1.16476	0.81856
33	1.5210-02	6.7165+00	1.00907	1.00959	0.88853	0.94957	1.14211	0.83836
34	1.6030-02	6.9615+00	1.00907	1.00826	0.90590	0.95819	1.11877	0.86423
35	1.6760-02	7.2054+00	1.00629	1.00734	0.92286	0.96680	1.09750	0.88645
36	1.7630-02	7.4122+00	1.00474	1.00646	0.93700	0.97330	1.07898	0.90633
37	1.8440-02	7.6707+00	1.00423	1.00548	0.95436	0.98138	1.05742	0.93201
38	1.9190-02	7.8846+00	1.00278	1.00465	0.96850	0.98776	1.04018	0.95225
39	2.0080-02	8.1518+00	1.00000	1.00308	0.98586	0.99511	1.01884	0.97671
40	2.0740-02	8.2398+00	1.00155	1.00215	0.99152	0.99723	1.01156	0.98736
41	2.1630-02	8.3283+00	1.00175	1.00106	0.99717	0.99925	1.00418	0.99684
42	2.2480-02	8.3728+00	1.00000	1.00000	1.00000	1.00000	1.00000	1.00000
43	2.4080-02	8.4173+00	1.01206	0.99739	1.00283	1.00021	0.99479	1.01758
44	2.5610-02	8.4620+00	1.03711	0.99602	1.00565	1.00053	0.99394	1.04832
45	2.7350-02	8.2840+00	1.06186	0.99382	0.99435	0.99436	1.00003	1.05584
46	2.8820-02	8.3283+00	1.06392	0.99170	0.99717	0.99457	0.99480	1.06368
47	3.0470-02	8.3283+00	1.05876	0.99022	0.99717	0.99383	0.99330	1.05932
48	3.2070-02	8.3728+00	1.05258	0.99024	1.00000	0.99511	0.99024	1.05775
49	3.3520-02	8.3728+00	1.04845	0.99024	1.00000	0.99511	0.99024	1.05361
50	3.5260-02	8.3728+00	1.05155	0.99024	1.00000	0.99511	0.99024	1.05672
51	3.6760-02	8.2840+00	1.05567	0.99021	0.99435	0.99255	0.99640	1.05160
52	3.8380-02	8.2398+00	1.06082	0.99021	0.99152	0.99128	0.99951	1.05209
53	3.9980-02	8.1957+00	1.06082	0.99023	0.98869	0.99000	1.00265	1.04744

86010109		FERNANDO/SNII'S		PROFILE TABULATION		53 POINTS, DELTA AT POINT 42			
I	Y	PT2/P	P/PO	TO/T00	M/MD	U/UD	T/TD	R/RD#U/UD	
1	0.0000+00	1.0000+00	0.95511	1.04000	0.00000	0.00000	2.25814	0.00000	
2	2.7700+04	2.0895+00	0.95511	1.02911	0.44752	0.60206	1.80992	0.31771	
3	4.2940+04	2.4397+00	0.95511	1.02839	0.50041	0.65753	1.72652	0.36374	
4	6.2200+04	2.6311+00	0.95511	1.02913	0.52645	0.68376	1.68693	0.38713	
5	8.5470+04	2.8278+00	0.95511	1.02791	0.55165	0.70762	1.64539	0.41076	
6	1.1360+03	2.9081+00	0.95511	1.02873	0.56157	0.71697	1.63004	0.42011	
7	1.3280+03	2.9833+00	0.96084	1.02701	0.57066	0.72503	1.61421	0.43157	
8	1.4960+03	3.0808+00	0.95606	1.02756	0.58223	0.73578	1.59701	0.44048	
9	1.7050+03	3.1305+00	0.95463	1.02712	0.58802	0.74084	1.58732	0.44555	
10	1.8820+03	3.2460+00	0.95482	1.02676	0.60124	0.75244	1.56623	0.45872	
11	2.1220+03	3.2570+00	0.95224	1.02730	0.60248	0.75373	1.56514	0.45858	
12	2.3390+03	3.3382+00	0.94861	1.02622	0.61157	0.76126	1.54943	0.46607	
13	2.7560+03	3.4588+00	0.95005	1.02524	0.62479	0.77222	1.52761	0.48026	
14	3.1250+03	3.5240+00	0.94671	1.02577	0.63182	0.77835	1.51763	0.48554	
15	3.5020+03	3.5395+00	0.94976	1.02438	0.63347	0.77921	1.51306	0.48912	
16	3.9030+03	3.6490+00	0.95606	1.02431	0.64504	0.78878	1.49532	0.50432	
17	4.3370+03	3.6925+00	0.95702	1.02329	0.64959	0.79211	1.48695	0.50981	
18	4.7140+03	3.8212+00	0.95606	1.02264	0.66281	0.80254	1.46606	0.52336	
19	5.0670+03	3.8907+00	0.95606	1.02292	0.66983	0.80823	1.45592	0.53075	
20	5.4680+03	3.9818+00	0.95463	1.02173	0.67893	0.81490	1.44066	0.53998	
21	5.8930+03	4.1294+00	0.95129	1.02181	0.69339	0.82608	1.41935	0.55366	
22	6.2860+03	4.2368+00	0.94976	1.02111	0.70372	0.83360	1.40320	0.56423	
23	7.0970+03	4.4389+00	0.94546	1.01991	0.72273	0.84715	1.37394	0.58295	
24	7.9550+03	4.5873+00	0.94546	1.01933	0.73636	0.85671	1.35359	0.59840	
25	8.6770+03	4.7526+00	0.94422	1.01773	0.75124	0.86649	1.33038	0.61499	
26	9.6000+03	4.9165+00	0.94231	1.01689	0.76570	0.87606	1.30903	0.63064	
27	1.0330+02	5.2247+00	0.94422	1.01557	0.79215	0.89304	1.27096	0.66346	
28	1.1150+02	5.4328+00	0.94690	1.01498	0.80950	0.90390	1.24682	0.68647	
29	1.1890+02	5.6149+00	0.95482	1.01345	0.82438	0.91250	1.22521	0.71112	
30	1.2800+02	5.7227+00	0.97039	1.01240	0.83306	0.91734	1.21257	0.73412	
31	1.3540+02	6.0583+00	0.98281	1.01140	0.85950	0.93260	1.17733	0.77852	
32	1.4470+02	6.2464+00	0.99140	1.01040	0.87397	0.94045	1.15792	0.80520	
33	1.5240+02	6.3991+00	0.99331	1.00935	0.88554	0.94647	1.14235	0.82299	
34	1.6030+02	6.7165+00	0.99618	1.00827	0.90909	0.95883	1.11242	0.85864	
35	1.6800+02	6.9615+00	0.99809	1.00709	0.92686	0.96764	1.08994	0.88610	
36	1.7570+02	7.2054+00	0.99809	1.00601	0.94421	0.97603	1.06952	0.91169	
37	1.8420+02	7.4600+00	0.99713	1.00482	0.96198	0.98431	1.04695	0.93747	
38	1.9160+02	7.7132+00	0.99713	1.00413	0.97934	0.99237	1.02678	0.96371	
39	2.0100+02	7.7132+00	1.00095	1.00283	0.97934	0.99172	1.02545	0.96803	
40	2.0810+02	7.9710+00	0.99905	1.00219	0.99669	0.99957	1.00578	0.99288	
41	2.1640+02	7.9710+00	0.99905	1.00112	0.99669	0.99903	1.00470	0.99341	
42	2.2350+02	8.0207+00	1.00000	1.00000	1.00000	1.00000	1.00000	1.00000	
43	2.4010+02	8.0207+00	1.00478	0.99764	1.00000	0.99882	0.99764	1.00597	
44	2.5730+02	7.9278+00	1.01719	0.99562	0.99380	0.99495	1.00231	1.00973	
45	2.7350+02	7.8846+00	1.02388	0.99315	0.99091	0.99237	1.00294	1.01308	
46	2.9000+02	7.8846+00	1.02483	0.99143	0.99091	0.99151	1.00121	1.01490	
47	3.0560+02	7.9278+00	1.01815	0.98983	0.99380	0.99205	0.99647	1.01363	
48	3.2130+02	8.0207+00	1.00860	0.98971	1.00000	0.99484	0.98971	1.01383	
49	3.3540+02	8.1079+00	1.00287	0.98980	1.00579	0.99753	0.98365	1.01702	
50	3.5100+02	8.1518+00	0.99809	0.98976	1.00868	0.99882	0.98054	1.01669	
51	3.6690+02	8.1957+00	0.99427	0.98974	1.01157	1.00011	0.97746	1.01730	
52	3.8290+02	8.1957+00	0.99523	0.98974	1.01157	1.00011	0.97746	1.01828	
53	3.9870+02	8.2398+00	0.99140	0.98972	1.01446	1.00140	0.97441	1.01856	

96010110		FERNANDO/SMITS		PROFILE TABULATION		53 POINTS, DELTA AT POINT 43		
I	Y	PTZ/P	P/PD	T0/T00	M/MD	U/U0	T/T0	R/RD*U/U0
1	0.0000*-00	1.0000*-00	1.00000	1.04001	0.00000	0.00000	2.34522	0.00000
2	2.2700*-04	2.1825*-00	1.00000	1.03050	0.44671	0.60896	1.85839	0.32768
3	3.7100*-04	2.4693*-00	1.00000	1.03166	0.48743	0.65251	1.79206	0.36411
4	5.6310*-04	2.6658*-00	1.00000	1.03063	0.51297	0.67904	1.74710	0.38809
5	7.4710*-04	2.8145*-00	1.00000	1.03065	0.53134	0.69605	1.71608	0.40550
6	9.4710*-04	2.8744*-00	1.00000	1.02994	0.53852	0.70272	1.70278	0.41269
7	1.1630*-03	2.9833*-00	1.00000	1.02955	0.55130	0.71470	1.68062	0.42526
8	1.3470*-03	3.1807*-00	0.97650	1.02994	0.57365	0.73546	1.64359	0.43697
9	1.5470*-03	3.2205*-00	0.97390	1.02921	0.57804	0.73917	1.63518	0.44024
10	1.7470*-03	3.2716*-00	0.97190	1.02912	0.58353	0.74415	1.62570	0.44488
11	1.9390*-03	3.2864*-00	0.97040	1.02898	0.58523	0.74552	1.62282	0.44580
12	2.1790*-03	3.3756*-00	0.96810	1.02899	0.59481	0.75430	1.60689	0.45426
13	2.5150*-03	3.5395*-00	0.96640	1.02832	0.61198	0.75952	1.57744	0.47088
14	2.8680*-03	3.5511*-00	0.96690	1.02814	0.61317	0.76957	1.57519	0.47239
15	3.2840*-03	3.6767*-00	0.96710	1.02764	0.62595	0.78017	1.55346	0.48569
16	3.7320*-03	3.7324*-00	0.97340	1.02712	0.63154	0.78462	1.54354	0.49490
17	4.1640*-03	3.7767*-00	0.97830	1.02623	0.63593	0.78790	1.53507	0.50213
18	4.5480*-03	3.8907*-00	0.98110	1.02570	0.64711	0.79630	1.51617	0.51560
19	4.8760*-03	3.9361*-00	0.98250	1.02507	0.65150	0.80009	1.50316	0.52127
20	5.2600*-03	3.9818*-00	0.98560	1.02423	0.65599	0.80326	1.49988	0.52734
21	5.7480*-03	4.1593*-00	0.98810	1.02418	0.67265	0.81640	1.47307	0.54762
22	6.1480*-03	4.2438*-00	0.98630	1.02396	0.68104	0.82276	1.45949	0.55601
23	6.8600*-03	4.3900*-00	0.93410	1.02237	0.69391	0.83176	1.43719	0.56954
24	7.7090*-03	4.6132*-00	0.98430	1.02179	0.71417	0.84649	1.40487	0.59339
25	8.5330*-03	4.9165*-00	0.99380	1.02052	0.73972	0.86408	1.36443	0.62300
26	9.2370*-03	5.0500*-00	0.98810	1.02003	0.75090	0.87149	1.34697	0.63929
27	1.0170*-02	5.1905*-00	0.99230	1.01817	0.76248	0.87848	1.32744	0.65669
28	1.0950*-02	5.3978*-00	0.99030	1.01720	0.77924	0.88908	1.30177	0.67659
29	1.1690*-02	5.5732*-00	0.99390	1.01606	0.79351	0.89777	1.27970	0.69434
30	1.2580*-02	5.9049*-00	0.98830	1.01514	0.81976	0.91231	1.24321	0.72573
31	1.3260*-02	6.2454*-00	0.98630	1.01423	0.84431	0.92764	1.20713	0.75794
32	1.4190*-02	6.3608*-00	0.99160	1.01294	0.85269	0.93198	1.19435	0.76588
33	1.4940*-02	6.5986*-00	0.98060	1.01137	0.86936	0.94110	1.17049	0.78842
34	1.5770*-02	6.9615*-00	0.97910	1.01040	0.89541	0.95423	1.13570	0.82245
35	1.6580*-02	7.2878*-00	0.97610	1.00974	0.91776	0.96557	1.10699	0.85148
36	1.7250*-02	7.4600*-00	0.97540	1.00878	0.92934	0.97097	1.09160	0.86761
37	1.8170*-02	7.5860*-00	0.97680	1.00738	0.93772	0.97447	1.07991	0.88143
38	1.8900*-02	8.0207*-00	0.97810	1.00672	0.95607	0.98792	1.04554	0.92411
39	1.9760*-02	8.1518*-00	0.98010	1.00542	0.97445	0.99110	1.03446	0.93901
40	2.0580*-02	8.1957*-00	0.98530	1.00431	0.97725	0.99184	1.03010	0.94871
41	2.1290*-02	8.2398*-00	0.99130	1.00363	0.98004	0.99280	1.02620	0.95993
42	2.2200*-02	8.3728*-00	0.99530	1.00233	0.98842	0.99597	1.01534	0.97681
43	2.3670*-02	8.5583*-00	1.00000	1.00000	1.00000	1.00000	1.00000	1.00000
44	2.5420*-02	8.5583*-00	1.00100	0.99759	1.00000	0.99894	0.99789	1.00206
45	2.6970*-02	8.6486*-00	1.00100	0.99593	1.00559	1.00042	0.99975	1.01179
46	2.8530*-02	8.6034*-00	1.00200	0.99374	1.00279	0.99820	0.99086	1.00942
47	3.0160*-02	8.6486*-00	1.00100	0.99193	1.00559	0.99841	0.99578	1.01383
48	3.1630*-02	8.6486*-00	1.00100	0.99193	1.00559	0.99841	0.99578	1.01383
49	3.3290*-02	8.6486*-00	1.00600	0.99133	1.00559	0.99841	0.98578	1.01889
50	3.4790*-02	8.6034*-00	1.00300	0.99162	1.00279	0.99703	0.98354	1.01161
51	3.6370*-02	8.6940*-00	0.99500	0.99203	1.00838	0.99968	0.98282	1.01207
52	3.8040*-02	8.6940*-00	0.99530	0.99223	1.00838	0.99968	0.98282	1.00221
53	3.9560*-02	8.7395*-00	0.98460	0.99172	1.01118	1.00074	0.97947	1.00599

86010102

Fernando/Smits

Turbulence Data

X = 1.1710E+00 UTAU = 1.9410E+01 RHOW = 4.1488E-01 UREF = 5.6940E+02 MUEW = 1.6779E-05

I	Y	M	U UREF	(RU)' RW UT	R U'2 RW UT2	U'2 UT2
1	1.2410E-3	1.4070E+0	6.7806E-1	5.2974E+0	6.8492E+0	4.8351E+0
2	2.4900E-3	1.5280E+0	7.1802E-1	5.2616E+0	5.4430E+0	3.6041E+0
3	3.7190E-3	1.6300E+0	7.4916E-1	5.6912E+0	5.3310E+0	3.3617E+0
4	4.9480E-3	1.7080E+0	7.7128E-1	6.0044E+0	5.1702E+0	3.1367E+0
5	6.1600E-3	1.8040E+0	7.9717E-1	5.9512E+0	4.3242E+0	2.5233E+0
6	7.3920E-3	1.8960E+0	8.2017E-1	6.4100E+0	4.2755E+0	2.3880E+0
7	8.6160E-3	1.9500E+0	8.3307E-1	6.6093E+0	4.1196E+0	2.2331E+0
8	9.8350E-3	2.0260E+0	8.5042E-1	6.8180E+0	3.8533E+0	2.0191E+0
9	1.1050E-2	2.0970E+0	8.6569E-1	7.1105E+0	3.7120E+0	1.8826E+0
10	1.2500E-2	2.1830E+0	8.8335E-1	7.4384E+0	3.5155E+0	1.7171E+0
11	1.3450E-2	2.2470E+0	8.9545E-1	7.3642E+0	3.1177E+0	1.4891E+0
12	1.4670E-2	2.3170E+0	9.0854E-1	7.1115E+0	2.6030E+0	1.2126E+0
13	1.5880E-2	2.4010E+0	9.2292E-1	7.5041E+0	2.5348E+0	1.1413E+0
14	1.7070E-2	2.4500E+0	9.3095E-1	7.2979E+0	2.2100E+0	9.7260E-1
15	1.8270E-2	2.5030E+0	9.3928E-1	6.5986E+0	1.6319E+0	6.9032E-1
16	1.9480E-2	2.5500E+0	9.4632E-1	5.9323E+0	1.2023E+0	4.9016E-1
17	2.0670E-2	2.5700E+0	9.4870E-1	4.5582E+0	6.8151E-1	2.7280E-1
18	2.1840E-2	2.6060E+0	9.5356E-1	3.7490E+0	4.3372E-1	1.7036E-1
D 19	2.3050E-2	2.6180E+0	9.5465E-1	2.6520E+0	2.1369E-1	8.3765E-2
20	2.4250E-2	2.6210E+0	9.5436E-1	1.9344E+0	1.1352E-1	4.4608E-2
21	2.5440E-2	2.6410E+0	9.5674E-1	1.4657E+0	6.3458E-2	2.4838E-2
22	2.6640E-2	2.6460E+0	9.5674E-1	1.2109E+0	4.3080E-2	1.6866E-2
23	2.7830E-2	2.6480E+0	9.5634E-1	1.1998E+0	4.2138E-2	1.6474E-2
24	2.9050E-2	2.6530E+0	9.5624E-1	1.1302E+0	3.7023E-2	1.4409E-2
25	3.0220E-2	2.6530E+0	9.5575E-1	1.1948E+0	4.1375E-2	1.6107E-2
26	3.1410E-2	2.6610E+0	9.5684E-1	1.1202E+0	3.6146E-2	1.4111E-2
27	3.2580E-2	2.6670E+0	9.5773E-1	1.1533E+0	3.8257E-2	1.5014E-2
28	3.3780E-2	2.6680E+0	9.5783E-1	1.1336E+0	3.7169E-2	1.4686E-2
29	3.4970E-2	2.6730E+0	9.5862E-1	1.0797E+0	3.3580E-2	1.3294E-2
30	3.6190E-2	2.6790E+0	9.5951E-1	1.1687E+0	3.8874E-2	1.5308E-2
31	3.7410E-2	2.6790E+0	9.5941E-1	1.2122E+0	4.1602E-2	1.6295E-2

86010103

Fernando/Smits

Turbulence Data

X = 1.1970E+00 UTAU = 1.8217E+01 RHOW = 4.7005E-01 UREF = 5.6940E+02 MUEW = 1.6835E-05

I	Y	M	U UREF	(RU)' RW UT	R U'2 RW UT2	U'2 UT2
1	1.2530E-3	1.3360E+0	6.5470E-1	5.3869E+0	7.9951E+0	5.8372E+0
2	2.4660E-3	1.4470E+0	6.9308E-1	5.6001E+0	7.1722E+0	4.9884E+0
3	3.6980E-3	1.5490E+0	7.2600E-1	5.7132E+0	6.2744E+0	4.1692E+0
4	4.9310E-3	1.6650E+0	7.6080E-1	6.2005E+0	6.0581E+0	3.8242E+0
5	6.1340E-3	1.7380E+0	7.8109E-1	6.2615E+0	5.4954E+0	3.3853E+0
6	7.3510E-3	1.8290E+0	8.0535E-1	6.3363E+0	4.8497E+0	2.8899E+0
7	8.5940E-3	1.9110E+0	8.2553E-1	6.6704E+0	4.6822E+0	2.6951E+0
8	9.7840E-3	2.0020E+0	8.4691E-1	7.0116E+0	4.4383E+0	2.4581E+0
9	1.1010E-2	2.0590E+0	8.5944E-1	7.2211E+0	4.2822E+0	2.3178E+0
10	1.2200E-2	2.1270E+0	8.7366E-1	7.3167E+0	3.9422E+0	2.0804E+0
11	1.3420E-2	2.2200E+0	8.9265E-1	7.7987E+0	3.8430E+0	1.9523E+0
12	1.4610E-2	2.2700E+0	9.0170E-1	7.3123E+0	3.1128E+0	1.5489E+0
13	1.5830E-2	2.3310E+0	9.1274E-1	7.3863E+0	2.8396E+0	1.3600E+0
14	1.7030E-2	2.3920E+0	9.2328E-1	6.8791E+0	2.2053E+0	1.0176E+0
15	1.8210E-2	2.4580E+0	9.3422E-1	6.4784E+0	1.7483E+0	7.7989E-1
16	1.9400E-2	2.5070E+0	9.4178E-1	5.5684E+0	1.1934E+0	5.2110E-1
17	2.0590E-2	2.5400E+0	9.4645E-1	4.8859E+0	8.7237E-1	3.7585E-1
18	2.1780E-2	2.5580E+0	9.4864E-1	3.4023E+0	4.1325E-1	1.7759E-1
19	2.2970E-2	2.5790E+0	9.5142E-1	2.4296E+0	2.0411E-1	8.7087E-2
D 20	2.4160E-2	2.5900E+0	9.5232E-1	1.7330E+0	1.0225E-1	4.3484E-2
21	2.5370E-2	2.6010E+0	9.5311E-1	1.5314E+0	7.8373E-2	3.3129E-2
22	2.6570E-2	2.6120E+0	9.5401E-1	1.2636E+0	5.2596E-2	2.2193E-2
23	2.7770E-2	2.6160E+0	9.5391E-1	1.1583E+0	4.3976E-2	1.8552E-2
24	2.8960E-2	2.6110E+0	9.5222E-1	1.0098E+0	3.3568E-2	1.4137E-2
25	3.0140E-2	2.6050E+0	9.5103E-1	9.7077E-1	3.1226E-2	1.3156E-2

86010104

Fernando/Smits

Turbulence Data

X = 1.2230E+00 UTAU = 1.7438E+01 RHO = 5.1927E-01 UREF = 5.6940E+02 MUEW = 1.6935E-05

I	Y	M	U UREF	(RU)' RW UT	R U'2 RW UT2	U'2 UT2
1	3.8100E-4	1.0770E+0	5.5554E-1	2.7689E+0	3.1441E+0	2.5232E+0
2	1.1840E-3	1.2800E+0	6.3587E-1	5.3195E+0	8.4952E+0	6.3200E+0
3	2.3940E-3	1.3900E+0	6.7524E-1	5.9675E+0	8.8248E+0	6.1983E+0
4	3.6470E-3	1.5060E+0	7.1361E-1	6.4672E+0	8.5997E+0	5.7880E+0
5	4.8760E-3	1.5930E+0	7.4112E-1	6.4475E+0	7.3829E+0	4.7940E+0
6	6.0850E-3	1.6830E+0	7.6723E-1	6.2203E+0	5.9410E+0	3.7375E+0
7	7.3050E-3	1.7750E+0	7.9255E-1	6.6956E+0	5.9394E+0	3.6225E+0
8	8.5350E-3	1.8580E+0	8.1407E-1	6.8641E+0	5.4331E+0	3.2044E+0
9	9.7450E-3	1.9440E+0	8.3500E-1	7.3495E+0	5.3768E+0	3.0539E+0
10	1.0970E-2	2.0100E+0	8.5015E-1	7.2527E+0	4.6599E+0	2.5577E+0
11	1.2160E-2	2.1080E+0	8.7178E-1	7.6445E+0	4.3272E+0	2.2446E+0
12	1.3370E-2	2.1520E+0	8.8055E-1	7.8927E+0	4.2452E+0	2.1404E+0
13	1.4560E-2	2.2150E+0	8.9291E-1	7.8641E+0	3.8128E+0	1.8787E+0
14	1.5790E-2	2.2970E+0	9.0846E-1	7.4833E+0	3.0364E+0	1.4528E+0
15	1.6980E-2	2.3720E+0	9.2171E-1	6.9629E+0	2.3420E+0	1.0933E+0
16	1.8170E-2	2.4210E+0	9.2989E-1	6.3026E+0	1.7891E+0	8.2579E-1
17	1.9360E-2	2.4770E+0	9.3886E-1	5.2230E+0	1.1328E+0	5.1474E-1
18	2.0540E-2	2.5030E+0	9.4244E-1	3.9385E+0	6.2384E-1	2.8316E-1
D 19	2.1730E-2	2.5330E+0	9.4673E-1	2.5822E+0	2.5719E-1	1.1602E-1
20	2.2920E-2	2.5400E+0	9.4713E-1	2.0527E+0	1.6187E-1	7.3332E-2
21	2.4140E-2	2.5550E+0	9.4882E-1	1.4383E+0	7.8201E-2	3.5458E-2
22	2.5320E-2	2.5600E+0	9.4882E-1	1.3060E+0	6.4233E-2	2.9180E-2
23	2.6530E-2	2.5690E+0	9.4962E-1	1.0841E+0	4.3706E-2	1.9826E-2
24	2.7730E-2	2.5750E+0	9.4982E-1	9.7821E-1	3.5363E-2	1.6044E-2
25	2.8900E-2	2.5760E+0	9.4922E-1	1.0326E+0	3.9446E-2	1.7926E-2
26	3.0090E-2	2.5810E+0	9.4952E-1	9.6461E-1	3.4126E-2	1.5477E-2
27	3.1270E-2	2.5820E+0	9.4952E-1	1.0303E+0	3.9077E-2	1.7803E-2
28	3.2460E-2	2.5880E+0	9.5042E-1	1.0640E+0	4.1600E-2	1.9050E-2
29	3.3660E-2	2.5970E+0	9.5181E-1	1.1224E+0	4.6101E-2	2.1241E-2
30	3.4850E-2	2.5970E+0	9.5181E-1	1.1085E+0	4.5410E-2	2.1135E-2
31	3.6060E-2	2.6060E+0	9.5311E-1	9.4893E-1	3.2888E-2	1.5284E-2

86010106

Fernando/Smits

Turbulence Data

X = 1.2750E+00 UTAU = 1.7351E+01 RHO = 5.6365E-01 UREF = 5.6940E+02 MUEW = 1.7043E-05

I	Y	M	U UREF	(RU)' RW UT	R U'2 RW UT2	U'2 UT2
1	1.1700E-3	1.2410E+0	6.2408E-1	4.8462E+0	7.5130E+0	5.6832E+0
2	2.3890E-3	1.3630E+0	6.6896E-1	5.6822E+0	8.5267E+0	6.1732E+0
3	3.6380E-3	1.4720E+0	7.0621E-1	5.9764E+0	7.9376E+0	5.5373E+0
4	4.8640E-3	1.5470E+0	7.2985E-1	6.3020E+0	7.7507E+0	5.2137E+0
5	6.0970E-3	1.6220E+0	7.5259E-1	6.1977E+0	6.5845E+0	4.2768E+0
6	7.3140E-3	1.7010E+0	7.7542E-1	6.7647E+0	6.8731E+0	4.3253E+0
7	8.5180E-3	1.7920E+0	8.0036E-1	6.7680E+0	5.8923E+0	3.5671E+0
8	9.7280E-3	1.8790E+0	8.2280E-1	7.2146E+0	5.7726E+0	3.3616E+0
9	1.0980E-2	1.9480E+0	8.3963E-1	7.6454E+0	5.7427E+0	3.2348E+0
10	1.2150E-2	2.0060E+0	8.5265E-1	7.8061E+0	5.4168E+0	2.9687E+0
11	1.3340E-2	2.1000E+0	8.7368E-1	8.2771E+0	5.1686E+0	2.7052E+0
12	1.4550E-2	2.1430E+0	8.8239E-1	7.9763E+0	4.4420E+0	2.2689E+0
13	1.5770E-2	2.2220E+0	8.9802E-1	8.2308E+0	4.1280E+0	2.0278E+0
14	1.6950E-2	2.2830E+0	9.0944E-1	7.5775E+0	3.1427E+0	1.4927E+0
15	1.8140E-2	2.3390E+0	9.1945E-1	6.7464E+0	2.2606E+0	1.0424E+0
16	1.9350E-2	2.3760E+0	9.2576E-1	5.2925E+0	1.3081E+0	5.9362E-1
17	2.0540E-2	2.4070E+0	9.3067E-1	4.2550E+0	8.0572E-1	3.6162E-1
18	2.1720E-2	2.4360E+0	9.3488E-1	3.4098E+0	4.9518E-1	2.2005E-1
D 19	2.2910E-2	2.4520E+0	9.3688E-1	2.0641E+0	1.7822E-1	7.9266E-2



86010108

Fernando/Smits

Turbulence Data

X = 1.3240E+00 UTAU = 1.8581E+01 RHOW = 5.2717E-01 UREF = 5.6940E+02 MUEW = 1.7101E-05

I	Y	M	U UREF	(RU)' RW UT	R U'2 RW UT2	U'2 UT2
1	1.1940E-3	1.3450E+0	6.6444E-1	4.9860E+0	6.7340E+0	4.8923E+0
2	2.3950E-3	1.4460E+0	6.9937E-1	4.9234E+0	5.6061E+0	3.9388E+0
3	3.6330E-3	1.5320E+0	7.2727E-1	5.3624E+0	5.7371E+0	3.8724E+0
4	4.8670E-3	1.5930E+0	7.4604E-1	5.6484E+0	5.7023E+0	3.7252E+0
5	6.0710E-3	1.6710E+0	7.6903E-1	5.9033E+0	5.4862E+0	3.4867E+0
6	7.2840E-3	1.7510E+0	7.9141E-1	6.3068E+0	5.4904E+0	3.3844E+0
7	8.5190E-3	1.8200E+0	8.0978E-1	6.4663E+0	5.1474E+0	3.0895E+0
8	9.7230E-3	1.8770E+0	8.2403E-1	6.8691E+0	5.2757E+0	3.0895E+0
9	1.0940E-2	1.9630E+0	8.4490E-1	7.2002E+0	4.9885E+0	2.8056E+0
10	1.2140E-2	2.0150E+0	8.5665E-1	7.2320E+0	4.6064E+0	2.5299E+0
11	1.3350E-2	2.0920E+0	8.7351E-1	7.7278E+0	4.5995E+0	2.4313E+0
12	1.4550E-2	2.1640E+0	8.8846E-1	7.6971E+0	4.0376E+0	2.0638E+0
13	1.5770E-2	2.2290E+0	9.0131E-1	7.4409E+0	3.3865E+0	1.6845E+0
14	1.6950E-2	2.2930E+0	9.1336E-1	7.1924E+0	2.8539E+0	1.3827E+0
15	1.8150E-2	2.3480E+0	9.2309E-1	6.5189E+0	2.1387E+0	1.0107E+0
16	1.9330E-2	2.4050E+0	9.3293E-1	6.1790E+0	1.7511E+0	8.0730E-1
17	2.0520E-2	2.4500E+0	9.4005E-1	5.0891E+0	1.1018E+0	4.9735E-1
18	2.1690E-2	2.4690E+0	9.4266E-1	4.1600E+0	7.1188E-1	3.1786E-1
19	2.2880E-2	2.4780E+0	9.4337E-1	3.0174E+0	3.6863E-1	1.6356E-1
20	2.4090E-2	2.4830E+0	9.4357E-1	2.7183E+0	2.9320E-1	1.2834E-1
21	2.5280E-2	2.4880E+0	9.4377E-1	1.7625E+0	1.1978E-1	5.1258E-2
22	2.6480E-2	2.4760E+0	9.4096E-1	1.4709E+0	8.3569E-2	3.5305E-2
23	2.7680E-2	2.4640E+0	9.3805E-1	1.0587E+0	4.3569E-2	1.8254E-2
24	2.8860E-2	2.4690E+0	9.3825E-1	1.0707E+0	4.4057E-2	1.8361E-2
25	3.0040E-2	2.4690E+0	9.3775E-1	9.4035E-1	3.4060E-2	1.4229E-2
26	3.1210E-2	2.4720E+0	9.3815E-1	9.0584E-1	3.1551E-2	1.3208E-2
27	3.2410E-2	2.4760E+0	9.3875E-1	9.4541E-1	3.4297E-2	1.4392E-2
28	3.3610E-2	2.4760E+0	9.3875E-1	9.6180E-1	3.5594E-2	1.4979E-2
29	3.4810E-2	2.4760E+0	9.3875E-1	1.0375E+0	4.1352E-2	1.7371E-2
30	3.6010E-2	2.4690E+0	9.3755E-1	1.0081E+0	3.9358E-2	1.6534E-2

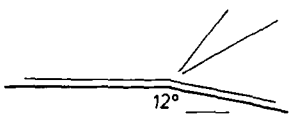
86010109

Fernando/Smits

Turbulence Data

X = 1.3490E+00 UTAU = 1.8877E+01 RHOW = 5.1778E-01 UREF = 5.6940E+02 MUEW = 1.6886E-05

I	Y	M	U UREF	(RU)' RW UT	R U'2 RW UT2	U'2 UT2
1	3.8100E-4	1.1700E+0	5.9269E-1	3.2399E+0	3.7410E+0	2.9025E+0
2	1.2060E-3	1.3670E+0	6.6676E-1	4.8497E+0	6.1328E+0	4.4051E+0
3	2.4280E-3	1.4870E+0	7.0728E-1	4.8914E+0	5.1577E+0	3.5544E+0
4	3.6720E-3	1.5450E+0	7.2550E-1	5.2489E+0	5.3612E+0	3.5876E+0
5	4.8870E-3	1.6120E+0	7.4591E-1	5.4781E+0	5.1838E+0	3.3534E+0
6	6.1110E-3	1.6920E+0	7.6901E-1	6.2296E+0	5.8839E+0	3.6961E+0
7	7.3430E-3	1.7580E+0	7.8713E-1	6.0567E+0	4.9816E+0	3.0504E+0
8	8.5740E-3	1.8130E+0	8.0127E-1	6.5491E+0	5.3076E+0	3.1732E+0
9	9.7820E-3	1.8690E+0	8.1530E-1	6.5898E+0	4.8826E+0	2.8481E+0
10	1.1010E-2	1.9520E+0	8.3552E-1	7.1846E+0	5.0133E+0	2.8049E+0
11	1.2210E-2	2.0020E+0	8.4677E-1	7.4856E+0	4.9115E+0	2.6429E+0
12	1.3410E-2	2.0670E+0	8.6100E-1	8.2232E+0	5.1934E+0	2.6556E+0
13	1.4590E-2	2.1190E+0	8.7195E-1	7.9973E+0	4.4425E+0	2.1916E+0
14	1.5820E-2	2.1850E+0	8.8500E-1	7.8835E+0	3.8456E+0	1.8322E+0
15	1.7000E-2	2.2540E+0	8.9824E-1	7.6196E+0	3.1854E+0	1.4646E+0
16	1.8200E-2	2.3170E+0	9.0969E-1	7.5206E+0	2.7920E+0	1.2469E+0
17	1.9390E-2	2.3700E+0	9.1905E-1	6.6655E+0	2.0067E+0	8.7382E-1
18	2.0560E-2	2.3970E+0	9.2323E-1	5.7485E+0	1.4221E+0	6.0965E-1
19	2.1770E-2	2.4130E+0	9.2552E-1	4.3749E+0	8.0130E-1	3.4075E-1
20	2.2960E-2	2.4200E+0	9.2582E-1	3.5399E+0	5.1673E-1	2.1814E-1
21	2.4160E-2	2.4190E+0	9.2482E-1	2.3241E+0	2.2199E-1	9.3231E-2
22	2.5350E-2	2.4080E+0	9.2233E-1	2.0346E+0	1.7137E-1	7.1614E-2
23	2.6560E-2	2.4010E+0	9.2034E-1	1.3810E+0	7.9236E-2	3.2955E-2
24	2.7770E-2	2.3980E+0	9.1895E-1	1.2102E+0	6.0861E-2	2.5218E-2
25	2.8940E-2	2.3980E+0	9.1835E-1	1.0253E+0	4.3613E-2	1.8041E-2
26	3.0130E-2	2.4030E+0	9.1875E-1	1.0579E+0	4.6213E-2	1.9139E-2
27	3.1310E-2	2.4120E+0	9.2004E-1	9.5350E-1	3.7177E-2	1.5419E-2
28	3.2500E-2	2.4240E+0	9.2213E-1	9.4320E-1	3.5925E-2	1.4917E-2

	$M(\text{inf}): 1.76 \text{ rising to } 2.1$ $R \text{ Theta} \times 10^{-3}: 5$ $TW/TR: 1.0$	8602
		FPG
Continuous tunnel with asymmetrical nozzle. $W = 150 \text{ mm}$ , $H = 100 \text{ mm}$ $PO: 40 \text{ KN/m}^2$ . $TO: 296 \text{ K}$ . Air. $Re/m \times 10^{-6}: 0.4$ .		
DUSSAUGE J.-P., GAVIGLIO J., 1987. The rapid expansion of a supersonic turbulent flow: Role of bulk dilation. J. Fluid. Mech. <u>174</u> , 81-112. And: Dussauge (1981), Dussauge J.-P., private communications.		

- 1 The tests were conducted on a continuation of the lower, straight, tunnel nozzle block. The models started 512 mm from the nozzle throat, continuing in the plane of the tunnel floor. At a point 640 mm from the throat the surface turned down sharply at an angle of  $12^\circ$  forming the expansion corner ( $X = 0$ ), round which the flow accelerates from  $M = 1.76$  to  $M = 2.1$ . At about a further 120 mm along the tunnel axis the surface curved back to the free stream direction. The reflection of the expansion fan returned to the test surface downstream of this point. The models ran across the full width of the tunnel, 150 mm. Two geometrically identical models were used, one with pressure tapings, the other with thermocouples.
- 2 Transition was forced by a sand-paper strip upstream of the throat. After the nozzle expansion, the boundary layer grew under essentially ZPG conditions, reaching the corner with a thickness of about 10 mm. Small disturbances in the flow which showed up in schlieren studies corresponded to Mach number perturbations of less than 1%. The free-stream turbulence level for velocity fluctuations was less than 0.1% above 100 Hz. The temperatures were allowed 15 minutes to settle so that the flow was effectively adiabatic. The wall temperature was constant to within 0.5 K over a distance of 100 mm. "Surface flow visualisations showed no particular spanwise streamline divergence".
- 3 Wall pressure was measured at 11 stations along the model with tapings ( $d = 0.3 \text{ mm}$ ) on the centreline and 20 or 40 mm to either side. Wall temperature was measured at 6 stations upstream and 6 downstream of the corner.
- 4 Pitot profiles were measured with a FPP ( $h_1 = 0.28$ ,  $h_2 = 0.08$ ,  $b_1 = 2.12$ ,  $b_2 = 1.92 \text{ mm}$ ,  $l$ , appr. 20 mm). (A wedge static probe is shown but the results were discarded because of yaw sensitivity in the expansion.) The mean total-temperature profile was measured with a fine wire probe,  $l = 1.5 \text{ mm}$   $d = 5 \text{ }\mu\text{m}$ . For fluctuation measurements a normal HWP was used (Platinum plated tungsten,  $d = 2.5 \text{ }\mu\text{m}$ ,  $l/d = 320$ ), operated in the constant-current mode and with the signal processed as described by Gaviglio (1971, 1978), following Laufer (1961). The band-width claimed is 100 Hz - 200 kHz.
- 5 Mean flow profiles were obtained at the stations listed in section B. Profiles 01-09 are measured normal to the upstream wall, 10-23 normal to the sloping surface, with 09 & 10 at the corner. Turbulent intensities were measured at a station well upstream of the corner, near profile 03, just upstream, at  $X = -10$ , -5 mm (profiles 07, 08) and downstream at  $X = 6$ , 15, 31.3, 61.5, 89.5 and 98 mm (Profiles 11, between 12 & 13, 14, 17, 20 and 21).

The authors obtained static pressure values in the free stream from Pitot readings, and these are used everywhere outside the expansion. Where wall pressure was measured, the

- 6 values were consistent. Within the expansion, pressures were calculated from the method of characteristics for rotational flow. The corresponding calculated Pitot pressures agreed with measured values to within 3%. No corrections were applied to the profile data.
- 7 The editors have accepted the data as supplied, incorporating the authors' assumptions and reduction procedures. We have chosen to give their skin-friction values as deduced from the profiles, hand fitted to the log-law upstream of the expansion and using the correlation of Chew (1978) downstream. We present all the profiles measured normal to the wall and the associated turbulence profiles, when available. They form a single series covering the approach to a centred expansion, the expansion itself and the recovery region downstream. Turbulence measurements were also made along the last characteristic of the expansion and along two streamlines, one close to the wall and one at about  $Y/D = 0.5$ , but have not been presented here.
- 8
- 9
- 10
- 11
- 12
- 13
- 14

S DATA: 86020101-0123. Pitot and T0 profiles, NX = 23. Normal hot-wire profiles, NX = 4.

# 15 Editors' comments:

While there have been many studies of boundary layers subjected to rapid compression by shock waves, this, with the exception of the weaker case in Chew & Squire (1979), CAT7902S, Series 01/02, appears to be the only reasonably fully documented study of a boundary layer passing through a concentrated, centred, expansion. Reflected wave cases are reported by Thomas, CAT7401, and Lewis et al., CAT7201.

Upstream influence by the subsonic layer next to the wall appears to be small, so that the boundary layer experiences a rapid distortion closely related to the corresponding ideal flow model. The authors refer to the effect as "relaminarisation", but the boundary layer does not undergo "reverse transition" in the sense observed in some subsonic flows. Turbulence levels are markedly reduced, and it is in the observation and prediction of the changes in the turbulence structure that the interest of the authors lies.

There are relatively few points in each profile, but for most stations the profile extends within the momentum deficit peak. The Reynolds number is low, but the H12K values are characteristic of fully developed mean flow. Integral values in the range where the profile goes through the expansion should be ignored (0109-0112) because of normal pressure gradient effects. The upstream profiles agree well with the inner and outer laws (figs. 10.1.5-6), as they should with a profile derived CF value. The downstream profiles, where CF values are given, for the same reason, fit the wall law well. The outer profiles retain the characteristics of an accelerated flow, relaxing slowly towards the ZPG profile. Some small differences are accounted for as the authors used a "non-standard" log-law additive constant ( $C = 5.7$ ). The turbulence data, profiles of  $u'^2$  and  $T'^2$ , are given in figures (11.2.8-9).

86020108 Dussauge/Gaviglio

Turbulence Data

86020114

Dussauge/Gaviglio

X = -5.000E-03 TW = 2.8485E+02 UINF = 4.7855E+02

X = 3.1300E-02 TW = 2.8114E+02 UINF = 4.7855E+02

I	Y	U' <sup>2</sup> UINF <sup>2</sup>	T' <sup>2</sup> TW <sup>2</sup>	R.TU
1	3.0000E-3	3.4628E-3	1.3055E-3	-8.0300E-1
2	3.0000E-3	2.9681E-3	1.3179E-3	-7.6400E-1
3	3.0000E-3	2.7010E-3	1.2808E-3	-7.5700E-1
4	3.5000E-3	2.5427E-3	1.2358E-3	-7.4100E-1
5	4.0000E-3	2.6317E-3	1.2108E-3	-8.0300E-1
6	4.0000E-3	2.5130E-3	1.1902E-3	-7.3700E-1
7	5.0000E-3	2.2657E-3	1.2108E-3	-7.7200E-1
8	6.0000E-3	2.0480E-3	1.2684E-3	-8.0800E-1
9	6.0000E-3	2.3052E-3	1.2520E-3	-8.4400E-1
10	7.5000E-3	1.2565E-3	1.0502E-3	-8.4400E-1
11	8.0000E-3	1.7314E-3	1.0049E-3	-8.6700E-1
12	9.0000E-3	3.3243E-4	5.2303E-4	-8.7800E-1
13	1.0000E-2	3.2748E-4	1.4867E-4	-8.5500E-1
14	1.0000E-2	4.1158E-4	2.9034E-4	-9.5600E-1

I	Y	U' <sup>2</sup> UINF <sup>2</sup>	T' <sup>2</sup> TW <sup>2</sup>	R.TU
1	6.0000E-4	2.6713E-3	1.2176E-3	-8.8000E-1
2	7.0000E-4	1.1872E-3	8.2018E-4	-8.0000E-1
3	8.0000E-4	2.0777E-3	1.9405E-3	-1.0000E+0
4	8.0000E-4	2.7702E-3	2.0800E-3	-9.6000E-1
5	1.5000E-3	1.0191E-3	1.1034E-3	-8.9000E-1
6	1.6000E-3	8.1128E-4	6.0034E-4	-6.8000E-1
7	5.1500E-3	1.4445E-3	9.3856E-4	-7.9000E-1
8	9.0000E-3	1.0883E-3	9.0473E-4	-8.5000E-1
9	1.2000E-2	3.5617E-4	4.5659E-4	-8.9000E-1

86020120 Dussauge/Gaviglio

Turbulence Data

86020121

Dussauge/Gaviglio

X = 8.9500E-02 TW = 2.8151E+02 UINF = 4.7855E+02

X = 9.8000E-02 TW = 2.8063E+02 UINF = 4.7855E+02

I	Y	U' <sup>2</sup> UINF <sup>2</sup>	T' <sup>2</sup> TW <sup>2</sup>	R.TU
1	8.0000E-4	3.3243E-3	1.4632E-3	-8.5000E-1
2	1.0000E-3	2.8494E-3	1.4674E-3	-8.5600E-1
3	1.5000E-3	1.2070E-3	1.1554E-3	-8.5000E-1
4	2.0000E-3	4.6500E-4	7.8851E-4	-7.9000E-1
5	2.0000E-3	1.2367E-3	9.7404E-4	-7.9000E-1
6	3.0000E-3	5.6394E-4	7.2104E-4	-7.7000E-1
7	3.0000E-3	1.6621E-3	1.0499E-3	-8.3000E-1
8	5.0000E-3	1.1675E-3	5.7346E-4	-7.7000E-1
9	8.0000E-3	7.1215E-4	4.8491E-4	-7.8000E-1
10	8.0000E-3	1.0685E-3	6.3671E-4	-8.3000E-1

I	Y	U' <sup>2</sup> UINF <sup>2</sup>	T' <sup>2</sup> TW <sup>2</sup>	R.TU
1	8.0000E-4	3.9674E-3	1.5275E-3	-8.8100E-1
2	1.0000E-3	4.1358E-3	1.5572E-3	-8.8400E-1
3	1.5000E-3	2.5526E-3	1.2984E-3	-8.5400E-1
4	2.0000E-3	1.1576E-3	8.0195E-4	-7.6900E-1
5	3.0000E-3	7.9249E-4	5.1766E-4	-7.5000E-1
6	3.0000E-3	7.6775E-4	5.5160E-4	-8.2700E-1
7	4.0000E-3	7.4796E-4	4.6674E-4	-7.6900E-1
8	5.0000E-3	4.3701E-4	4.8371E-4	-8.2600E-1
9	8.0000E-3	8.7361E-4	5.0493E-4	-8.2800E-1
10	1.0000E-2	3.7695E-4	4.4128E-4	-8.8000E-1
11	1.2000E-2	8.2217E-4	3.3096E-4	-8.6000E-1
12	1.4000E-2	6.9256E-5	1.1881E-4	-8.7000E-1

CAT 8602		DOSSAUGE/GAVIGLIO BOUNDARY CONDITIONS AND EVALUATED DATA, SI UNITS							
RUN X * RZ	MD * POD TOD#	TW/TR* PW/PO TAUM *	RED24 KED20 O2	CF CJ PI2	M12 M32 M42	M124 M324 M24	P44 T44 U4	PO4 T44 TR	
86020101	1.7588	1.0000	2.9513**03	2.2206*-03	2.5717	1.3457	7.3927**03	7.3311**03	
-7.2500*-02	3.9881**04	1.0002	4.2357**03	NM	1.7842	1.7761	2.8625**02	1.8415**02	
INFINITE	2.9810**02	3.5540**01	7.8797*-04	NM	0.0627	9.4731*-04	4.7855**02	2.8625**02	
86020102	1.7682	1.0000	2.9249**03	2.1206*-03	2.6883	1.3577	7.3521**03	7.3517**03	
-6.2500*-02	4.0240**04	1.0001	4.2151**03	NM	1.7916	1.7926	2.8483**02	1.8255**02	
INFINITE	2.9670**02	3.4120**01	7.7501*-04	NM	0.0426	9.3456*-04	4.7900**02	2.8437**02	
86020103	1.7691	1.0000	2.9876**03	2.3190*-03	2.7167	1.3733	7.3521**03	7.3317**03	
-5.2500*-02	4.0295**04	1.0001	4.3042**03	NM	1.7846	1.7752	2.8543**02	1.8285**02	
INFINITE	2.9730**02	3.7350**01	7.9258*-04	NM	0.0391	9.5894*-04	4.7963**02	2.8440**02	
86020104	1.7688	1.0000	2.9693**03	2.2298*-03	2.6952	1.3803	7.3521**03	7.3517**03	
-4.2500*-02	4.0277**04	1.0001	4.2758**03	NM	1.7819	1.7726	2.8538**02	1.8324**02	
INFINITE	2.9790**02	3.5900**01	7.8996*-04	NM	0.0596	9.5404*-04	4.8006**02	2.8597**02	
86020105	1.7558	1.0000	2.3976**03	2.2023*-03	2.7079	1.4081	7.4697**03	7.4697**03	
-3.2500*-02	4.0122**04	1.3030	4.1539**03	NM	1.7690	1.7594	2.8642**02	1.8450**02	
INFINITE	2.9825**02	3.5500**01	7.6785*-04	NM	0.0590	9.3300*-04	4.7817**02	2.8543**02	
86020106	1.7575	1.0000	2.9673**03	2.2613*-03	2.6644	1.3991	7.6319**03	7.4304**03	
-2.2500*-02	4.0014**04	1.0271	4.2563**03	NM	1.7777	1.7690	2.8645**02	1.8439**02	
INFINITE	2.9830**02	3.6330**01	7.3954*-04	NM	0.0684	9.5312*-04	4.7943**02	2.8645**02	
86020107	1.7273	1.0000	3.1232**03	2.2924*-03	2.6580	1.3370	7.5372**03	7.5372**03	
-1.0000*-02	3.9030**04	0.9999	4.4332**03	NM	1.7759	1.7653	2.8551**02	1.8470**02	
INFINITE	2.9810**02	3.6330**01	4.3337*-04	NM	0.0596	1.0041*-03	4.7320**02	2.8652**02	
86020108	1.7541	1.0000	3.3845**03	2.0907*-03	2.8266	1.4420	7.6277**03	7.6269**03	
-5.0000*-03	4.0860**04	1.0001	4.3596**03	NM	1.7845	1.7769	2.8485**02	1.8361**02	
INFINITE	2.9660**02	3.4180**01	9.7467*-04	NM	0.0127	1.0403*-03	4.7655**02	2.8495**02	
86020109	1.7279	1.0000	2.7935**03	NM	3.3307	1.2436	5.2491**03	7.6267**03	
0.0000**00	3.9262**04	0.6935	3.9659**03	NM	1.9349	1.8244	2.8651**02	1.8665**02	
INFINITE	2.9810**02	NM	7.4125*-04	NM	0.0618	9.6692*-04	4.7329**02	2.8452**02	
86020110	1.7355	1.0000	2.5798**03	NM	3.7474	1.3055	5.0703**03	7.6267**03	
0.0000**00	3.9723**04	0.6648	3.6729**03	NM	1.8494	1.4123	2.8577**02	1.8450**02	
INFINITE	2.9740**02	NM	4.7819*-04	NM	0.0525	9.0480*-04	4.7405**02	2.8578**02	
86020111	1.7400	1.0000	2.5843**03	NM	557.9746	2.6123	4.0328**03	7.5394**03	
6.1000*-03	3.9851**04	0.5307	3.6917**03	NM	-1.6501	1.4728	2.8516**02	1.8495**02	
INFINITE	2.9690**02	NM	5.7855*-06	NM	12.1700	1.0722*-04	4.7433**02	2.8415**02	
86020112	1.9048	1.0000	7.7693**02	NM	16.2753	1.5167	3.9673**03	5.9352**03	
1.0400*-02	4.0110**04	0.6719	1.1757**03	NM	1.7938	1.7935	2.8383**02	1.7175**02	
INFINITE	2.9630**02	NM	2.2350*-04	NM	0.0600	4.2013*-04	5.0155**02	2.8339**02	
86020113	2.1665	1.0000	2.0091**03	NM	3.1500	1.3553	3.9193**03	3.9201**03	
1.9500*-02	3.9776**04	0.9998	3.3472**03	NM	1.8401	1.8242	2.8252**02	1.5345**02	
INFINITE	2.9750**02	NM	7.4144*-04	NM	0.1275	9.0685*-04	5.3809**02	2.8525**02	
86020114	2.1604	1.0000	2.2455**03	2.3025*-03	3.3904	1.3576	4.0368**03	4.0364**03	
3.1300*-02	4.0571**04	1.0000	3.7346**03	NM	1.4329	1.4172	2.8114**02	1.5309**02	
INFINITE	2.9600**02	3.0370**01	9.0339*-04	NM	0.0075	1.0025*-03	5.3595**02	2.8113**02	
86020115	2.1496	1.0000	2.2499**03	2.3097*-03	3.1754	1.3112	4.0368**03	4.0352**03	
4.0600*-02	3.9813**04	1.0004	3.7256**03	NM	1.8348	1.8233	2.8229**02	1.5443**02	
INFINITE	2.9712**02	3.0120**01	9.1536*-04	NM	0.0625	1.0079*-03	5.3544**02	2.8229**02	
86020116	2.1596	1.0000	2.2151**03	2.3992*-03	3.2348	1.3225	3.9719**03	3.9719**03	
5.0900*-02	3.9859**04	1.0000	3.6832**03	NM	1.8355	1.8205	2.8213**02	1.5372**02	
INFINITE	2.9710**02	3.0980**01	9.0379*-04	NM	0.0601	1.0035*-03	5.3684**02	2.8219**02	
86020117	2.1721	1.0000	2.1959**03	2.3303*-03	3.2647	1.3255	3.9111**03	3.9111**03	
4.1500*-02	4.0034**04	1.0000	3.5696**03	NM	1.9330	1.8174	2.8210**02	1.5295**02	
INFINITE	2.9710**02	3.0100**01	8.0806*-04	NM	0.0595	1.0065*-03	5.3944**02	2.8210**02	
86020118	2.1994	1.0000	2.1094**03	2.3474*-03	3.3077	1.3211	3.7693**03	3.7693**03	
7.0500*-02	4.0266**04	1.0000	3.5609**03	NM	1.9360	1.8211	2.8191**02	1.5101**02	
INFINITE	2.9710**02	2.9960**01	7.4023*-04	NM	0.0599	9.8452*-04	5.4189**02	2.8191**02	
86020119	2.1781	1.0000	2.2493**03	2.2979*-03	3.2801	1.3186	3.8828**03	3.8823**03	
7.9100*-02	4.0119**04	1.0000	3.7665**03	NM	1.4290	1.4138	2.8206**02	1.5245**02	
INFINITE	2.9710**02	2.9500**01	3.3027*-04	NM	0.0559	1.0413*-03	5.3920**02	2.8205**02	
86020120	2.1999	1.0000	2.2653**03	2.1463*-03	3.4460	1.4211	3.8341**03	3.8341**03	
8.9500*-02	4.0291**04	1.0000	3.9107**03	NM	1.8510	1.8443	2.8151**02	1.5144**02	
INFINITE	2.9660**02	2.7600**01	9.3890*-04	NM	0.0324	1.0363*-03	5.4012**02	2.8150**02	
86020121	2.2332	1.0000	2.2453**03	2.1561*-03	4.5037	1.3222	3.7045**03	3.5604**03	
9.3000*-02	4.0183**04	1.0404	3.9412**03	NM	1.9268	1.8108	2.8063**02	1.4314**02	
INFINITE	2.9600**02	2.5850**01	9.6551*-04	NM	0.0052	1.1077*-03	5.4506**02	2.8063**02	
86020122	2.2513	1.0000	2.1734**03	2.2009*-03	3.5478	1.3218	3.4451**03	3.4451**03	
1.0840*-01	3.9917**04	1.0000	3.7440**03	NM	1.9250	1.8099	2.8050**02	1.4700**02	
INFINITE	2.9600**02	2.6900**01	9.5530*-04	NM	0.0025	1.1019*-03	5.4726**02	2.8051**02	
86020123	2.2039	1.0000	2.4329**03	2.1375*-03	3.3992	1.3355	3.7328**03	3.7324**03	
1.1910*-01	4.0158**04	1.0000	4.1141**03	NM	1.8142	1.8005	2.8168**02	1.5063**02	
INFINITE	2.9690**02	2.7130**01	9.1654*-04	NM	0.0402	1.1764*-03	5.4227**02	2.8164**02	

86020101		DUSSAUGE/GAVIGLIO		PROFILE TABULATION		20 POINTS, DELTA AT POINT 14			
I	Y	PTZ/P	P/PO	TO/TOD	M/MD	U/UD	T/TD	R/RD=U/UD	
1	0.0000+00	1.0000+00	1.00022	0.96026	0.00000	0.00000	1.55435	0.00000	
2	1.7193+04	1.7143+00	1.00000	0.96310	0.51875	0.59970	1.33645	0.44873	
3	6.0258+04	1.8045+00	1.00000	0.96947	0.54492	0.62742	1.32572	0.47327	
4	1.0060+03	2.0083+00	1.00000	0.97484	0.59700	0.67881	1.29287	0.52504	
5	1.5020+03	2.2250+00	1.00000	0.97920	0.64527	0.72441	1.26035	0.57477	
6	2.0198+03	2.4279+00	1.00000	0.98323	0.68626	0.75186	1.23243	0.61817	
7	2.5775+03	2.6252+00	1.00000	0.98524	0.72328	0.79391	1.20494	0.65893	
8	3.0085+03	2.7774+00	1.00000	0.98632	0.75034	0.81674	1.18481	0.68934	
9	3.9346+03	3.1326+00	1.00000	0.99123	0.83942	0.86489	1.14177	0.75750	
10	5.0244+03	3.4967+00	1.00000	0.99530	0.86531	0.90797	1.10104	0.82465	
11	6.0273+03	3.8220+00	1.00000	0.99849	0.91210	0.94218	1.06704	0.88239	
12	7.0291+03	4.1332+00	1.00000	1.00131	0.95457	0.97168	1.03617	0.93776	
13	8.0432+03	4.3684+00	1.00000	1.00134	0.98539	0.99156	1.01257	0.97925	
14	8.9697+03	4.4827+00	1.00000	1.00000	1.00000	1.00000	1.00000	1.00000	
15	1.0048+02	4.5249+00	1.00000	0.99698	1.00534	1.03178	0.99291	1.00893	
16	1.2027+02	4.5226+00	1.00000	0.99303	1.00506	0.99992	0.98979	1.01023	
17	1.4044+02	4.5226+00	1.00000	0.99236	1.00506	0.99958	0.98912	1.01057	
18	1.6039+02	4.5249+00	1.00000	0.99235	1.00534	0.99975	0.98990	1.01037	
19	1.8057+02	4.5294+00	1.00000	0.99236	1.00591	1.00010	0.98848	1.01176	
20	1.9045+02	4.5317+00	1.00000	0.99236	1.00620	1.00027	0.98826	1.01216	

86020105		DUSSAUGE/GAVIGLIO		PROFILE TABULATION		23 POINTS, DELTA AT POINT 19		
I	Y	PTZ/P	P/PO	TO/TOD	M/MD	U/UD	T/TD	R/RD=U/UD
1	0.0000+00	1.0000+00	1.00000	0.96031	0.00000	0.00000	1.55241	0.00000
2	1.5497+04	1.3615+00	1.00000	0.96245	0.38654	0.46148	1.42455	0.32395
3	2.1133+04	1.4578+00	1.00000	0.96261	0.42943	0.50761	1.37725	0.36329
4	3.2407+04	1.6255+00	1.00000	0.96295	0.49143	0.57203	1.35492	0.42219
5	5.0253+04	1.7711+00	1.00000	0.96597	0.53640	0.61774	1.32627	0.46577
6	6.7022+04	1.8641+00	1.00000	0.97267	0.56202	0.64475	1.31608	0.48990
7	1.0453+03	2.0317+00	1.00000	0.97435	0.60354	0.68467	1.29689	0.53203
8	1.3444+03	2.1575+00	1.00000	0.97754	0.63191	0.71158	1.26806	0.56115
9	1.6825+03	2.2760+00	1.00000	0.98075	0.65702	0.73495	1.25127	0.58736
10	2.0583+03	2.3950+00	1.00000	0.98206	0.68100	0.75666	1.23456	0.61290
11	2.4214+03	2.5321+00	1.00000	0.98331	0.70731	0.77994	1.21559	0.64153
12	2.7030+03	2.6173+00	1.00000	0.98503	0.72309	0.79350	1.20423	0.65893
13	3.6784+03	2.9919+00	1.00000	0.98950	0.79796	0.84752	1.15689	0.73259
14	4.6927+03	3.3640+00	1.00000	0.99340	0.84695	0.89381	1.11397	0.80236
15	5.6978+03	3.7329+00	1.00000	0.99370	0.90107	0.93233	1.07059	0.87096
16	6.6580+03	4.0140+00	1.00000	0.99715	0.94014	0.95031	1.04336	0.92040
17	6.6634+03	4.0644+00	1.00000	0.99933	0.94598	0.95611	1.04081	0.92822
18	7.6768+03	4.3151+00	1.00000	1.00034	0.98029	0.98879	1.01536	0.97256
19	8.6988+03	4.4692+00	1.00000	1.00000	1.00000	1.00000	1.00000	1.00000
20	9.5427+03	4.5107+00	1.00000	0.99732	1.00530	1.03217	0.99379	1.00843
21	1.0462+02	4.5154+00	1.00000	0.99547	1.00537	1.03134	0.99103	1.01041
22	1.5689+02	4.5033+00	1.00000	0.99245	1.00433	0.99888	0.99918	1.00991
23	1.8672+02	4.4956+00	1.00000	0.99245	1.00347	0.99836	0.99983	1.00962

86020108		DUSSAUGE/GAVIGLIO		PROFILE TABULATION		20 POINTS, DELTA AT POINT 18		
I	Y	PTZ/P	P/PO	TO/TOD	M/MD	U/UD	T/TD	R/RD=U/UD
1	0.0000+00	1.0000+00	1.00011	0.96039	0.00000	0.00000	1.55139	0.00000
2	5.0800+04	1.7108+00	1.00000	0.97134	0.51907	0.63219	1.34592	0.44742
3	5.9100+04	1.7600+00	1.00000	0.97438	0.53372	0.61765	1.33922	0.46120
4	8.0300+04	1.9267+00	1.00000	0.97775	0.57870	0.66224	1.30955	0.50570
5	1.0800+03	1.9390+00	1.00000	0.98112	0.53178	0.66630	1.31167	0.50798
6	1.6600+03	2.1264+00	1.00000	0.98433	0.62548	0.70843	1.28202	0.55259
7	2.1700+03	2.3007+00	1.00000	0.98820	0.66273	0.74293	1.25666	0.59119
8	2.6900+03	2.4395+00	1.00000	0.99056	0.69996	0.77612	1.22945	0.63127
9	2.9100+03	2.5580+00	1.00000	0.99158	0.71284	0.78743	1.22021	0.64532
10	3.3000+03	2.6813+00	1.00000	0.99326	0.73536	0.80695	1.20387	0.67021
11	3.8200+03	2.8654+00	1.00000	0.99562	0.76752	0.83398	1.18040	0.70644
12	4.8200+03	3.1828+00	1.00000	0.99956	0.81957	0.87604	1.14256	0.76673
13	5.8700+03	3.5067+00	1.00000	1.00037	0.86911	0.91422	1.10650	0.82622
14	6.9200+03	3.8334+00	1.00000	1.00573	0.91414	0.94824	1.07131	0.88512
15	7.9000+03	4.0877+00	1.00000	1.00641	0.95103	0.97192	1.04442	0.93058
16	8.9400+03	4.3148+00	1.00000	1.00506	0.99107	0.99055	1.01962	0.97159
17	9.8460+03	4.4175+00	1.00000	1.00236	0.99436	0.99767	1.00668	0.99105
18	1.0949+02	4.4616+00	1.00000	1.00000	1.00000	1.00000	1.00000	1.00000
19	1.2966+02	4.4638+00	1.00000	0.99793	1.00091	0.99955	0.99729	1.00227
20	1.4019+02	4.4670+00	1.00000	0.99738	1.00059	0.99941	0.99746	1.00196

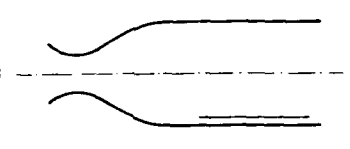
96920111 DUSSAUGE/GAVIGLIO PROFILE TABULATION 20 POINTS, DELTA AT POINT 16								
I	Y	PTZ/P	P/PD	T0/T00	M/MD	U/UD	T/TD	R/RD=U/UD
1	0.0000+00	1.0000+00	0.53057	0.96079	0.00000	0.00000	1.54257	0.00000
2	1.7370+04	1.3019+00	0.53057	0.96423	0.35960	0.43088	1.43576	0.15926
3	6.0688+04	3.1688+00	0.53057	0.96553	0.82397	0.86366	1.09868	0.41715
4	1.0614+03	3.5159+00	0.53057	0.96755	0.87753	0.90327	1.05954	0.45240
5	1.6123+03	3.7477+00	0.53057	0.97067	0.31138	0.92805	1.03693	0.47495
6	2.1141+03	3.9278+00	0.53057	0.97271	0.93679	0.94501	1.01980	0.49227
7	2.6509+03	4.1132+00	0.53057	0.97507	0.96218	0.96359	1.00314	0.50980
8	3.1408+03	4.2746+00	0.53057	0.97707	0.98374	0.97837	0.98912	0.52490
9	4.1256+03	4.6466+00	0.53057	0.98113	1.03161	1.00968	0.95793	0.55933
10	5.1336+03	4.7549+00	0.57120	0.98517	1.04511	1.01975	0.95204	0.61142
11	6.1119+03	4.7340+00	0.63573	0.98883	1.04253	1.02014	0.95751	0.67732
12	7.1434+03	4.7197+00	0.70560	0.99225	1.04075	1.02082	0.96208	0.74858
13	8.0384+03	4.7248+00	0.76597	0.99528	1.04138	1.02276	0.96455	0.81203
14	9.1548+03	4.7086+00	0.84000	0.99837	1.03937	1.02346	0.96963	0.83654
15	1.0062+02	4.6681+00	0.89867	1.00034	1.03431	1.02113	0.97468	0.94150
16	1.2163+02	4.3989+00	1.00000	1.00000	1.00000	1.00000	1.00000	1.00000
17	1.3202+02	4.4024+00	1.00353	0.99839	1.00046	0.99978	0.99884	1.00477
18	1.5201+02	4.4286+00	1.00353	0.99750	1.00385	1.00104	0.99441	1.01032
19	1.7209+02	4.4295+00	1.00353	0.99731	1.00377	1.00111	0.99433	1.01048
20	1.9233+02	4.4260+00	1.00353	0.99730	1.00351	1.00083	0.99467	1.00984

96020114 DUSSAUGE/GAVIGLIO PROFILE TABULATION 25 POINTS, DELTA AT POINT 23								
I	Y	PTZ/P	P/PD	T0/T00	M/MD	U/UD	T/TD	R/RD=U/UD
1	0.0000+00	1.0000+00	1.00000	0.94932	0.00000	0.00000	1.83644	0.00000
2	1.6090+04	1.1735+00	1.00000	0.96723	0.22387	0.29923	1.71652	0.16749
3	3.4874+04	1.7414+00	1.00000	0.96790	0.42392	0.54206	1.59713	0.33940
4	5.0630+04	2.3127+00	1.00000	0.96943	0.54009	0.55553	1.47322	0.44497
5	8.2662+04	3.0601+00	1.00000	0.97263	0.64946	0.75441	1.34929	0.55912
6	1.1547+03	3.3498+00	1.00000	0.97737	0.68647	0.78644	1.31217	0.59925
7	1.7497+03	3.5803+00	1.00000	0.98142	0.71445	0.80994	1.24518	0.63022
8	2.1557+03	3.7200+00	1.00000	0.98412	0.73084	0.82352	1.26971	0.64859
9	2.7084+03	3.8919+00	1.00000	0.98632	0.75046	0.83923	1.25055	0.67109
10	3.1707+03	4.0543+00	1.00000	0.98953	0.76852	0.85746	1.23328	0.69202
11	4.2027+03	4.3737+00	1.00000	0.99270	0.80277	0.87870	1.19857	0.71323
12	5.1785+03	4.6810+00	1.00000	0.99652	0.83434	0.90169	1.16798	0.77201
13	6.2004+03	4.9744+00	1.00000	1.00000	0.86336	0.92198	1.14015	0.80856
14	7.2064+03	5.2644+00	1.00000	1.00270	0.89146	0.94049	1.11303	0.84498
15	8.2217+03	5.5508+00	1.00000	1.00473	0.91761	0.95700	1.09770	0.87984
16	9.2105+03	5.8222+00	1.00000	1.00540	0.94205	0.97135	1.06317	0.91363
17	1.0161+02	6.0413+00	1.00000	1.00574	0.96130	0.98222	1.04339	0.94093
18	1.1241+02	6.2637+00	1.00000	1.00608	0.98047	0.99275	1.02523	0.95833
19	1.2164+02	6.3619+00	1.00000	1.00574	0.98880	0.99701	1.01658	0.98066
20	1.3236+02	6.4222+00	1.00000	1.00541	0.99389	0.99952	1.01135	0.98829
21	1.4274+02	6.4802+00	1.00000	1.00405	0.99875	1.00138	1.00527	0.99613
22	1.5263+02	6.4912+00	1.00000	1.00203	0.99958	1.00085	1.00234	0.99851
23	1.6250+02	6.4951+00	1.00000	1.00000	1.00000	1.00000	1.00000	1.00000
24	1.7272+02	6.5401+00	1.00000	1.00000	1.00375	1.00193	0.99638	1.00557
25	1.9279+02	6.6956+00	1.00000	1.00000	1.01662	1.00849	0.98408	1.02481

96020118 DUSSAUGE/GAVIGLIO PROFILE TABULATION 31 POINTS, DELTA AT POINT 24								
I	Y	PTZ/P	P/PD	T0/T00	M/MD	U/UD	T/TD	R/RD=U/UD
1	0.0000+00	1.0000+00	1.00000	0.94835	0.00000	0.00000	1.86633	0.00000
2	1.5639+04	1.4069+00	1.00000	0.96305	0.32543	0.42675	1.71975	0.24315
3	4.2758+04	2.2169+00	1.00000	0.96567	0.51464	0.63290	1.51239	0.41848
4	6.5467+04	2.6030+00	1.00000	0.96735	0.57516	0.69062	1.44179	0.47900
5	9.0430+04	2.9125+00	1.00000	0.97071	0.61949	0.73023	1.39397	0.52335
6	1.1794+03	3.1886+00	1.00000	0.97341	0.65436	0.76147	1.35418	0.55231
7	1.4341+03	3.4695+00	1.00000	0.97576	0.68873	0.79006	1.31589	0.60040
8	1.6825+03	3.6411+00	1.00000	0.97745	0.70883	0.80634	1.29406	0.62311
9	1.9445+03	3.8318+00	1.00000	0.97947	0.73047	0.82351	1.27096	0.64794
10	2.1788+03	3.9535+00	1.00000	0.98081	0.74393	0.83400	1.25680	0.66359
11	2.4345+03	4.0682+00	1.00000	0.98216	0.75639	0.84359	1.24387	0.67820
12	2.6908+03	4.1614+00	1.00000	0.98351	0.76635	0.85127	1.23393	0.68989
13	2.9304+03	4.2334+00	1.00000	0.98435	0.77394	0.85721	1.22676	0.69876
14	3.1933+03	4.3209+00	1.00000	0.98620	0.79308	0.86417	1.21783	0.70960
15	4.2196+03	4.6407+00	1.00000	0.99057	0.81554	0.88810	1.18586	0.74891
16	5.1660+03	4.9331+00	1.00000	0.99452	0.84429	0.90848	1.15838	0.78427
17	6.2208+03	5.2335+00	1.00000	0.99764	0.87242	0.92757	1.13043	0.82055
18	7.2439+03	5.5265+00	1.00000	1.00034	0.89915	0.94490	1.10434	0.85562
19	8.2376+03	5.7931+00	1.00000	1.00202	0.92280	0.95941	1.04092	0.89758
20	9.2380+03	6.0264+00	1.00000	1.00269	0.94298	0.97107	1.06046	0.91571
21	1.0251+02	6.2735+00	1.00000	1.00303	0.96390	0.98264	1.03926	0.94552
22	1.1264+02	6.4813+00	1.00000	1.00236	0.98113	0.97144	1.02113	0.97093
23	1.2268+02	6.6327+00	1.00000	1.00159	0.99350	0.97752	1.00811	0.98949
24	1.3294+02	6.7131+00	1.00000	1.00000	1.00000	1.00000	1.00000	1.00000
25	1.4302+02	6.7210+00	1.00000	0.99798	1.00064	0.99931	0.99736	1.00196
26	1.5310+02	6.7295+00	1.00000	0.99653	1.00132	0.99898	0.99534	1.00366
27	1.6315+02	6.7261+00	1.00000	0.99630	1.00105	0.99868	0.99527	1.00342
28	1.7320+02	6.7345+00	1.00000	0.99630	1.00173	0.99902	0.99461	1.00444
29	1.8330+02	6.7304+00	1.00000	0.99630	1.00141	0.99886	0.99492	1.00396
30	1.9331+02	6.7628+00	1.00000	0.99630	1.00400	1.00017	0.99239	1.00785
31	2.0342+02	6.7895+00	1.00000	0.99630	1.00614	1.00125	0.99030	1.01105

96-20120		DUSSAUGE/GAVIGLIO		PROFILE TABULATION		27 POINTS, DELTA AT POINT 23		
I	Y	PT2/P	P/PD	T0/T00	M/MD	U/UD	T/TD	R/RD*U/UD
1	0.0000**00	1.0000**00	1.00000	0.94913	0.00000	0.00000	1.85864	0.00000
2	9.0892*-04	2.8464**00	1.00000	0.97202	0.61245	0.72471	1.40018	0.51759
3	9.6158*-04	2.8724**00	1.00000	0.97269	0.61602	0.72806	1.39684	0.52122
4	1.1595*-03	3.0119**00	1.00000	0.97472	0.63470	0.74483	1.37713	0.54096
5	1.4148*-03	3.2071**00	1.00000	0.97741	0.65933	0.76681	1.35057	0.56777
6	1.6558*-03	3.3689**00	1.00000	0.97910	0.67988	0.78371	1.32876	0.58981
7	1.8541*-03	3.4971**00	1.00000	0.98045	0.69533	0.79647	1.31208	0.60703
8	2.0641*-03	3.6230**00	1.00000	0.98146	0.71013	0.80836	1.29579	0.62334
9	2.3162*-03	3.7577**00	1.00000	0.98348	0.72562	0.82096	1.28006	0.64134
10	2.6146*-03	3.8829**00	1.00000	0.98433	0.73969	0.83201	1.26521	0.65761
11	3.1314*-03	4.0831**00	1.00000	0.98753	0.76162	0.84911	1.24295	0.68314
12	3.6810*-03	4.2394**00	1.00000	0.99360	0.77829	0.86356	1.23111	0.70144
13	4.1982*-03	4.3900**00	1.00000	0.99225	0.79401	0.87388	1.21130	0.72144
14	5.1997*-03	4.6948**00	1.00000	0.99612	0.82484	0.89632	1.18081	0.75907
15	6.2111*-03	4.9682**00	1.00000	0.99933	0.85152	0.91500	1.15465	0.79245
16	7.2310*-03	5.2546**00	1.00000	1.00135	0.87857	0.93300	1.12774	0.82732
17	8.2238*-03	5.5280**00	1.00000	1.00371	0.90350	0.94888	1.10273	0.86049
18	9.2310*-03	5.8014**00	1.00000	1.00438	0.92735	0.96330	1.07763	0.89391
19	1.0242*-02	6.0562**00	1.00000	1.00472	0.95007	0.97594	1.05439	0.92497
20	1.1262*-02	6.2909**00	1.00000	1.00405	0.96998	0.98632	1.03396	0.95392
21	1.2286*-02	6.4852**00	1.00000	1.00303	0.98616	0.99436	1.01671	0.97802
22	1.3246*-02	6.6019**00	1.00000	1.00169	0.99575	0.99867	1.00586	0.99285
23	1.4100*-02	6.6540**00	1.00000	1.00000	1.00000	1.00000	1.00000	1.00000
24	1.5042*-02	6.7001**00	1.00000	0.99865	1.00375	1.00123	0.99500	1.00627
25	1.6167*-02	6.7396**00	1.00000	0.99798	1.00694	1.00251	0.99122	1.01140
26	1.7136*-02	6.7256**00	1.00000	0.99733	1.00589	1.00198	0.99224	1.00982
27	1.9332*-02	6.5996**00	1.00000	0.99733	1.00370	1.00087	0.99437	1.00654

86020121		DUSSAUGE/GAVIGLIO		PROFILE TABULATION		27 POINTS, DELTA AT POINT 23		
I	Y	PT2/P	P/PD	T0/T00	M/MD	U/UD	T/TD	R/RD*U/UD
1	0.0000**00	1.0000**00	1.04041	0.94807	0.00000	0.00000	1.89372	0.00000
2	1.5000*-04	1.4172**00	1.00000	0.96723	0.32407	0.42855	1.74879	0.24506
3	2.0000*-04	1.7951**00	1.00000	0.96723	0.42710	0.54605	1.63458	0.33406
4	3.0000*-04	2.1024**00	1.00000	0.96791	0.43724	0.60918	1.56318	0.38971
5	4.0000*-04	2.2298**00	1.00000	0.96926	0.50900	0.63134	1.53846	0.41037
6	5.0000*-04	2.3426**00	1.00000	0.97061	0.52723	0.64956	1.51789	0.42793
7	8.0000*-04	2.6012**00	1.00000	0.97399	0.56618	0.68743	1.47413	0.46632
8	1.0000*-03	2.7455**00	1.00000	0.97635	0.58656	0.70678	1.45194	0.48678
9	1.5000*-03	3.1645**00	1.00000	0.97973	0.64146	0.75559	1.38750	0.54457
10	2.0000*-03	3.5947**00	1.00000	0.98277	0.69232	0.79824	1.32747	0.60132
11	2.5000*-03	3.9088**00	1.00000	0.98531	0.72733	0.82613	1.29835	0.64123
12	3.0000*-03	4.1140**00	1.00000	0.98851	0.74978	0.84333	1.26512	0.66660
13	3.5000*-03	4.3117**00	1.00000	0.99038	0.77028	0.85892	1.24337	0.69030
14	4.0000*-03	4.4813**00	1.00000	0.99325	0.78744	0.87182	1.22582	0.71122
15	4.5000*-03	4.6160**00	1.00000	0.99527	0.80078	0.88176	1.21248	0.72724
16	5.0000*-03	4.7879**00	1.00000	0.99676	0.81748	0.89360	1.19490	0.74785
17	6.0000*-03	5.0721**00	1.00000	1.00068	0.84435	0.91257	1.16813	0.78122
18	8.0000*-03	5.6553**00	1.00000	1.00540	0.89637	0.94672	1.11425	0.84965
19	1.0000*-02	6.1778**00	1.00000	1.00642	0.94138	0.97243	1.06705	0.91133
20	1.2000*-02	6.6215**00	1.00000	1.00473	0.97757	0.99091	1.02749	0.96440
21	1.4000*-02	6.8503**00	1.00000	1.00237	0.99570	0.99902	1.00668	0.99239
22	1.5000*-02	6.8800**00	1.00000	1.00112	0.99803	0.99952	1.00299	0.99654
23	1.7000*-02	6.9052**00	1.00000	1.00000	1.00000	1.00000	1.00000	1.00000
24	1.8000*-02	6.9173**00	1.00000	1.00000	1.00094	1.00047	0.99906	1.00141
25	1.9000*-02	6.8652**00	1.00000	1.00000	0.99687	0.99931	0.99314	0.99531
26	2.0000*-02	6.9563**00	1.00000	1.00000	1.00399	1.00000	0.99603	1.00599
27	2.1000*-02	6.9598**00	1.00000	1.00000	1.00425	1.00000	0.99576	1.00639

	$M(\infty): 2.87$ $R \text{ Theta} \times 10^{-3}: 84-100$ $TW/TR: 1.11$	8603
		ZPG
Blowdown tunnel with symmetrical contoured nozzle. Max. running time "several minutes", normally 60 seconds. $W = R = 203 \text{ mm}$ . $L$ up to $2.7 \text{ m}$ . $PO: 0.69 \text{ MN/m}^2$ . $TO: 250-255 \text{ K}$ . Air. $Re/\mu \times 10^{-6}: 65$ .		
SPINA E.F., SMITS A.J., 1987. Organised structures in a supersonic turbulent boundary layer. <i>J. Fluid. Mech.</i> <b>182</b> , 85-109. And: Spina & Smits (1986). Data tapes, and private communications.		

- 1 The general arrangements for the experiment were as for the CCF tests described in CAT7904T, q.v.. The test surface however was flush with the tunnel floor starting  $0.892 \text{ m}$  (probably, in fact,  $0.902 \text{ m}$ ) from the nozzle exit ( $X=0$ ). The principal profile measurements were made over the range  $1.057 < X < 1.515 \text{ m}$  under ZPG conditions, along the centreline of the floor. Flow uniformity was carefully checked by very detailed static and Pitot pressure surveys, at fixed  $Y$ , both along the centre line and across the flow at  $X = 1.362 \text{ m}$ , backed up by five Pitot profiles at stations across the flow, again at  $X = 1.362 \text{ m}$ . The free-stream Mach number is quoted as  $2.87 \pm 0.05$ , with a mass-flux turbulence level of  $1 - 1.5\%$ . A spanwise "peak to peak variation of less than  $5\%$  in static pressure - with streamwise  $6\% - 1.4\%$  in Mach number" and a "slight adverse pressure gradient - considered small enough to be neglected" is, slightly confusingly, reported, with "a  $10\%$  variation in Pitot pressure - most probably due to the constriction of the side wall boundary layers through the - nozzle" (pp. 41-42, Spina & Smits 1986).
- 6 A  $50.8 \text{ mm}$  wall instrumentation plug could be inserted at  $X = 1.362 \text{ m}$ , which carried a static pressure tap ( $d = 0.81 \text{ mm}$ ) and four "Kulite" miniature pressure transducers mounted symmetrically in a straight line at  $5.08 \text{ mm}$  intervals. The transducer sensing element was  $0.71 \text{ mm}$  in diameter and the useful frequency range was estimated as  $0 - 40 \text{ kHz}$ . The plug could be rotated so as to yaw the line of transducers. Preston-tube measurements were made at 43 streamwise locations, and reduced using the Hopkins & Keener  $T'(1966)$  calibration.
- 7 The probes used for mean flow measurements were similar to those used for CAT7904T, q.v., and as in that experiment, mounted on supports fixed to the roof of the tunnel (in contrast to CAT8601T). Normal HWP surveys were made using both single wire probes and multiple wires mounted in an array operating in the CT mode. This consisted of two probes, each usually carrying two wires with a vertical separation of about  $2 \text{ mm}$ . The separation between the pairs of wires could be varied as desired. Double wire probes were used, with vertical separations of  $2.38, 2.58 \text{ mm}$ , and a triple wire probe with separations of  $2.58, 3.17$  and  $5.75 \text{ mm}$ . The active length was about  $0.8 \text{ mm}$  with a wire diameter of  $5 \mu\text{m}$ . The probes were operated in the constant-temperature mode. Total temperature was not measured, a linear variation giving  $TO = 1.04TOD$  at the wall being assumed, after Taylor, CAT8401T.
- 12 The editors have presented all the mean flow data, for nine stations along the centre-line. We have replaced the author's D-state by a state selected on the basis of the  $PO$  profile, with additional consideration given to the reported turbulence levels. The turbulence data are given in association with mean flow values as interpolated by the authors to the  $Y$ -values of hot-wire probe measurements. There are no HWP data for stations 05 & 07, while the original report includes two profiles for a station downstream of the last mean flow profile. These have not been presented here.
- 13 Data: 83030101-09. Pitot, static pressure and  $TO$  profiles,  $NX = 9$ . CF from Preston tubes. Normal hot-wire profiles,  $NX = 7$ .
- 15 Editors' comments:  
 The authors' D-state, based on a  $1\%$  specific mass flow deficit, is a consistent definition and at these Mach numbers should correspond to, approximately, a  $PO$  deficit of about  $5\%$ . Unless they can pick it out directly from the hot-wire data - which we doubt - it is a little clumsy, as it is defined as a deficit from a quantity which itself must be calculated for the "pressure-based reference flow". We again urge the use of  $PO$ . The tendency is then to a quantity which is in principle constant, even if there are substantial normal pressure gradients (Ch.7, AG 253).



Rather than use the earlier data for this boundary layer (Vas et al. CAT7601), fresh mean flow data was obtained specifically for use in conjunction with the turbulence data. These have been studied in unusual detail. Measurements taken extended far beyond the single component turbulence results and mean flow data presented here. There are large quantities of data, presented graphically, covering the space and time correlations between multiple wires, the four pressure transducers, and wire and pressure signals. The emphasis is on the information which spatial and temporal correlations, with and without conditional sampling, can give about the "large scale structures" of boundary layer turbulence.

These data, with CAT7601, provide the ZPG background for the various Princeton experiments described in this volume. The substantial amount of ZPG data, covering the whole area used in the other experiments, shows that the boundary layer turbulence structure is fully established at the start of those tests. Other workers will be able to compare their own undisturbed flow data with these and so allow for any systematic differences resulting from probe or data-reduction techniques, which are fully discussed in Spina & Smits, 1987.

The mean flow data are covered in fine detail, but do not quite extend within the momentum deficit peak. The values of H12K correspond to a fully developed layer. Agreement with the inner and outer laws is good (figs. 10.1.1-2) save close to the wall. Here it is arguable that the way in which the probes and their supporting fairings reach across the tunnel must inevitably introduce a proportionally large uncertainty in low values of  $Y$ . However, the lowest value of  $Y$  is identical for all profiles, suggesting that the probe is in contact with the wall, so that the lack of agreement at low  $Y$  values may well be ascribed to a lack of shear and wall probe corrections, probably the normal practice of the laboratory (e.g. Taylor, CAT8401T for a specific statement). The turbulence data are discussed in ch. 11.2 (figs. 11.2.2-4). Spina (1988) reports single  $v'^2$  and  $u'v'$  profiles which were not available to us at the time of writing but will be available on the data tape.

CAT 8603		SPINA/SMITS		BOUNDARY CONDITIONS AND EVALUATED DATA, SI UNITS					
RUN	MD *	TM/TP	RED2W	CF	H12	H12K	Pd	PJ*	
X *	POD	PM/PO	RED2D	CJ	H32	H32K	Tu*	TJ*	
RZ	Y0D	TAUW *	Q2	PI2	442	Q2K	U0*	T2	
86030101	2.8660	1.1119	3.4344*+04	1.1007*-03	5.5574	1.2294	2.1900*+04	2.1300*+04	
1.0570*+00	6.5715*+05	1.0000	8.3899*+04	NM	1.6535	1.8377	2.6520*+02	9.6489*+01	
INFINITE	2.5500*+02	1.3860*+02	1.2946*-03	NM	-0.2497	1.9509*-03	5.6445*+02	2.3352*+02	
86030102	2.9080	1.1127	3.4075*+04	1.0745*-03	5.7058	1.2224	2.2040*+04	2.2090*+04	
1.1340*+00	7.0641*+05	1.0000	9.4959*+04	NM	1.8558	1.8419	2.6076*+02	9.3163*+01	
INFINITE	2.5073*+02	1.4050*+02	1.2157*-03	NM	-0.2645	1.8465*-03	5.6275*+02	2.3434*+02	
86030103	2.9150	1.1128	3.5811*+04	1.0574*-03	5.6555	1.2168	2.1910*+04	2.1913*+04	
1.2100*+00	7.0811*+05	1.0000	8.3595*+04	NM	1.3591	1.8452	2.6016*+02	9.2670*+01	
INFINITE	2.5016*+02	1.3780*+02	1.2804*-03	NM	-0.2451	1.9303*-03	5.6262*+02	2.3373*+02	
86030104	2.8660	1.1119	3.9694*+04	1.0313*-03	5.4710	1.2173	2.2670*+04	2.2670*+04	
1.2860*+00	6.8025*+05	1.0000	9.4744*+04	NM	1.8573	1.9435	2.6124*+02	9.5350*+01	
INFINITE	2.5120*+02	1.3450*+02	1.3815*-03	NM	-0.2267	2.0564*-03	5.6022*+02	2.3495*+02	
86030105	2.8730	1.1120	3.9352*+04	1.0410*-03	5.4736	1.2147	2.2760*+04	2.2760*+04	
1.3240*+00	6.9025*+05	1.0000	9.6590*+04	NM	1.8576	1.8456	2.6239*+02	9.5174*+01	
INFINITE	2.5230*+02	1.3690*+02	1.4022*-03	NM	-0.2260	2.0900*-03	5.6197*+02	2.3596*+02	
86030106	2.8730	1.1120	3.9246*+04	1.0406*-03	5.4593	1.2160	2.2520*+04	2.2520*+04	
1.3620*+00	6.8297*+05	1.0000	9.5294*+04	NM	1.3619	1.8462	2.6300*+02	9.5393*+01	
INFINITE	2.5289*+02	1.3540*+02	1.4176*-03	NM	-0.2202	2.0994*-03	5.6262*+02	2.3651*+02	
86030107	2.8660	1.1119	4.2230*+04	9.7226*-04	5.4272	1.2259	2.3040*+04	2.3040*+04	
1.4000*+00	6.9136*+05	1.0000	1.0333*+05	NM	1.8529	1.8382	2.6193*+02	9.5320*+01	
INFINITE	2.5191*+02	1.2890*+02	1.4894*-03	NM	-0.2040	2.2407*-03	5.6102*+02	2.3563*+02	
86030108	2.8730	1.1120	4.1239*+04	9.9424*-04	5.4542	1.2128	2.3100*+04	2.3100*+04	
1.4380*+00	7.0056*+05	1.0000	1.0121*+05	NM	1.8602	1.8457	2.6146*+02	9.4940*+01	
INFINITE	2.5140*+02	1.3270*+02	1.4401*-03	NM	-0.2186	2.1421*-03	5.6097*+02	2.3512*+02	
86030109	2.8870	1.1123	4.0665*+04	1.0390*-03	5.5065	1.2100	2.2980*+04	2.2980*+04	
1.5150*+00	7.1188*+05	1.0000	1.0054*+05	NM	1.9607	1.8469	2.6034*+02	9.3961*+01	
INFINITE	2.5032*+02	1.3930*+02	1.4074*-03	NM	-0.2246	2.1035*-03	5.6079*+02	2.3405*+02	

86030101 SPINA/SMITS PROFILE TABULATION 41 POINTS, DELTA AT POINT 29								
I	Y	PT2/P	P/P3	T0/T0D	M/M0	U/UD	T/TD	R/RD*U/UD
1	0.0000E+00	1.0000E+00	1.00000	1.04020	0.00000	0.00000	2.74850	0.00000
2	8.8900E-05	2.2091E+00	1.00000	1.04014	0.39323	0.58302	2.19047	0.26616
3	5.5030E-04	2.9936E+00	1.00000	1.03976	0.49290	0.68066	1.98675	0.34260
4	9.8900E-04	3.2864E+00	1.00000	1.03823	0.51151	0.70859	1.91839	0.36925
5	1.4160E-03	3.6490E+00	1.00000	1.03839	0.54466	0.73983	1.84506	0.40098
6	1.8820E-03	3.9195E+00	1.00000	1.03711	0.56804	0.75052	1.79253	0.42427
7	2.4220E-03	4.1764E+00	1.00000	1.03625	0.59932	0.77820	1.74372	0.44629
8	2.8720E-03	4.2977E+00	1.00000	1.03537	0.59909	0.73624	1.72234	0.45649
9	3.3830E-03	4.6192E+00	1.00000	1.03527	0.62421	0.80623	1.65819	0.48329
10	3.8330E-03	4.7202E+00	1.00000	1.03426	0.63189	0.81175	1.65030	0.49138
11	4.3170E-03	4.8505E+00	1.00000	1.03336	0.64166	0.81898	1.62907	0.50273
12	4.8430E-03	5.1224E+00	1.00000	1.03233	0.66155	0.83345	1.58721	0.52510
13	5.7510E-03	5.2935E+00	1.00000	1.03113	0.67376	0.94179	1.56096	0.53927
14	6.7040E-03	5.6866E+00	1.00000	1.02994	0.70033	0.86027	1.50613	0.57118
15	7.6680E-03	6.1708E+00	1.00000	1.02842	0.73308	0.83076	1.44351	0.61016
16	8.6660E-03	6.3608E+00	1.00000	1.02710	0.74529	0.88749	1.41929	0.62559
17	9.6160E-03	6.7957E+00	1.00000	1.02540	0.77251	0.93367	1.36840	0.66038
18	1.0560E-02	7.0423E+00	1.00000	1.02361	0.78751	0.91160	1.33999	0.68031
19	1.1500E-02	7.2878E+00	1.00000	1.02260	0.80216	0.91944	1.31377	0.69985
20	1.2460E-02	7.6283E+00	1.00000	1.02078	0.82205	0.92948	1.27845	0.72704
21	1.3450E-02	7.9710E+00	1.00000	1.01963	0.84159	0.93923	1.24548	0.75411
22	1.4420E-02	8.3728E+00	1.00000	1.01755	0.86392	0.94957	1.20837	0.78591
23	1.6390E-02	8.9688E+00	1.00000	1.01539	0.89602	0.96374	1.15685	0.83307
24	1.8230E-02	9.3964E+00	1.00000	1.01196	0.91835	0.97237	1.12111	0.86733
25	2.0180E-02	9.8832E+00	1.00000	1.00928	0.94313	0.93192	1.08373	0.90596
26	2.2120E-02	1.0383E+01	1.00000	1.00603	0.96790	0.99046	1.04715	0.94586
27	2.4110E-02	1.0787E+01	1.00000	1.00321	0.99744	0.93678	1.01902	0.97818
28	2.5990E-02	1.0999E+01	1.00000	1.00034	0.99756	0.99909	1.00308	0.99602
29	2.7910E-02	1.1050E+01	1.00000	1.00000	1.00000	1.00000	1.00000	1.00000
30	2.9820E-02	1.1154E+01	1.00000	1.00034	1.00498	1.00201	0.99428	1.00777
31	3.1770E-02	1.1154E+01	1.00000	1.00034	1.00498	1.00201	0.99428	1.00777
32	3.3700E-02	1.1258E+01	1.00000	1.00010	1.00977	1.00372	0.98804	1.01586
33	3.5710E-02	1.1154E+01	1.00000	1.00034	1.00498	1.00201	0.99428	1.00777
34	3.7640E-02	1.1310E+01	1.00000	0.99990	1.01221	1.00452	0.98486	1.01996
35	3.9520E-02	1.1258E+01	1.00000	1.00010	1.00977	1.00372	0.98804	1.01586
36	4.1530E-02	1.1258E+01	1.00000	1.00010	1.00977	1.00372	0.98804	1.01586
37	4.3420E-02	1.1258E+01	1.00000	1.00010	1.00977	1.00372	0.98804	1.01586
38	4.5340E-02	1.1154E+01	1.00000	1.00034	1.00498	1.00201	0.99428	1.00777
39	4.7340E-02	1.1310E+01	1.00000	0.99990	1.01221	1.00452	0.98486	1.01996
40	4.9300E-02	1.1154E+01	1.00000	1.00034	1.00498	1.00201	0.99428	1.00777
41	5.1190E-02	1.1258E+01	1.00000	1.00010	1.00977	1.00372	0.98804	1.01586

86030101 Spina/Smits Turbulence Data

X = 1.0570E+00 UTAU = 2.2130E+01 RHOW = 2.8300E-01 UINF = 5.6939E+02 MUEW = 1.7033E-05

I	Y	M	U UINF	(RU) RW UT	R U' <sup>2</sup> RW UT <sup>2</sup>	U' <sup>2</sup> UT <sup>2</sup>
1	2.7800E-3	1.7110E+0	7.8400E-1	4.8633E+0	3.4976E+0	2.1964E+0
2	4.0490E-3	1.8230E+0	8.1431E-1	4.9656E+0	3.0041E+0	1.7923E+0
3	5.2740E-3	1.9130E+0	8.3670E-1	5.4976E+0	3.1562E+0	1.8069E+0
4	6.3420E-3	1.9790E+0	8.5255E-1	5.6569E+0	2.9800E+0	1.6547E+0
5	7.6220E-3	2.0970E+0	8.7905E-1	6.1511E+0	2.8835E+0	1.5172E+0
6	8.9720E-3	2.1610E+0	8.9230E-1	6.3195E+0	2.7239E+0	1.3893E+0
7	1.0280E-2	2.2440E+0	9.0856E-1	6.6513E+0	2.6181E+0	1.2836E+0
8	1.1730E-2	2.3130E+0	9.2111E-1	6.7275E+0	2.3862E+0	1.1323E+0
9	1.3190E-2	2.3970E+0	9.3586E-1	7.3098E+0	2.4456E+0	1.1149E+0
10	1.4330E-2	2.4700E+0	9.4791E-1	7.6248E+0	2.3602E+0	1.0403E+0
11	1.5410E-2	2.5220E+0	9.5594E-1	7.2699E+0	1.9668E+0	8.4507E-1
12	1.6210E-2	2.5590E+0	9.6166E-1	7.2860E+0	1.8592E+0	7.8543E-1
13	1.7090E-2	2.5920E+0	9.6628E-1	6.9486E+0	1.6026E+0	6.6628E-1
14	1.8170E-2	2.6300E+0	9.7129E-1	6.8332E+0	1.4571E+0	5.9472E-1
15	1.9600E-2	2.6820E+0	9.7822E-1	6.3727E+0	1.1649E+0	4.6375E-1
16	2.0900E-2	2.7290E+0	9.8424E-1	5.7094E+0	8.6597E-1	3.3692E-1
17	2.2050E-2	2.7710E+0	9.8936E-1	4.5875E+0	5.2288E-1	1.9944E-1
18	2.2860E-2	2.7950E+0	9.9197E-1	4.0724E+0	3.9652E-1	1.4943E-1
19	2.4300E-2	2.8130E+0	9.9619E-1	3.1920E+0	2.2934E-1	8.4875E-2
20	2.5750E-2	2.8550E+0	9.9799E-1	2.1263E+0	9.8064E-2	3.5847E-2
21	2.7200E-2	2.8630E+0	9.9890E-1	1.4486E+0	4.4922E-2	1.6354E-2
22	2.8670E-2	2.8710E+0	1.0000E+0	1.1572E+0	2.8352E-2	1.0294E-2
23	3.0040E-2	2.8800E+0	1.0012E+0	1.0165E+0	2.1580E-2	7.8035E-3
24	3.1550E-2	2.8800E+0	1.0012E+0	8.0356E-1	1.3484E-2	4.8759E-3
25	3.2990E-2	2.8890E+0	1.0023E+0	8.7349E-1	1.5718E-2	5.6614E-3
26	3.4450E-2	2.8890E+0	1.0023E+0	8.4199E-1	1.4605E-2	5.2604E-3
27	3.5910E-2	2.8820E+0	1.0015E+0	8.1593E-1	1.3857E-2	5.0063E-3
28	3.7360E-2	2.8980E+0	1.0033E+0	8.6516E-1	1.5202E-2	5.4522E-3

86030109 SPINA/SMITS PROFILE TABULATION 55 POINTS, DELTA AT POINT 43									
I	Y	PT2/P	P/PO	T0/T00	M/MD	U/UD	T/T0	R/RD=U/UD	
1	0.0000+00	1.0000+00	1.00000	1.04072	0.00000	0.00000	2.77368	0.00000	
2	8.8900+05	2.4603+00	1.00000	1.03375	0.42199	0.61701	2.13887	0.24867	
3	3.5360+04	2.9936+00	1.00000	1.04015	0.47939	0.67892	2.00568	0.33850	
4	6.1840+04	3.2460+00	1.00000	1.03925	0.50398	0.70327	1.94718	0.35117	
5	8.4150+04	3.4703+00	1.00000	1.03935	0.52477	0.72330	1.89980	0.38073	
6	1.0080+03	3.5395+00	1.00000	1.03836	0.53100	0.72881	1.88383	0.38698	
7	1.3265+03	3.7485+00	1.00000	1.03820	0.54936	0.74554	1.84176	0.40440	
8	1.5490+03	3.8784+00	1.00000	1.03775	0.55044	0.75536	1.81653	0.41593	
9	1.7870+03	3.8784+00	1.00000	1.03721	0.56044	0.75516	1.81557	0.41593	
10	2.0370+03	3.9943+00	1.00000	1.03677	0.57014	0.76357	1.79364	0.42571	
11	2.2670+03	4.2368+00	1.00000	1.03642	0.58889	0.77020	1.74937	0.44599	
12	2.5250+03	4.2195+00	1.00000	1.03657	0.59850	0.77910	1.75265	0.44453	
13	2.9750+03	4.6192+00	1.00000	1.03538	0.61967	0.80425	1.68443	0.47766	
14	3.4210+03	4.6879+00	1.00000	1.03438	0.62487	0.80775	1.67100	0.48339	
15	3.9770+03	5.0164+00	1.00000	1.03457	0.64912	0.82639	1.62077	0.50987	
16	4.4080+03	4.9497+00	1.00000	1.03366	0.64427	0.82238	1.62935	0.50473	
17	4.9410+03	5.0164+00	1.00000	1.03257	0.64912	0.82559	1.61763	0.51037	
18	5.3910+03	5.3292+00	1.00000	1.03136	0.67129	0.84151	1.57148	0.53549	
19	5.8410+03	5.3282+00	1.00000	1.03137	0.67129	0.84131	1.57074	0.53552	
20	6.3750+03	5.5437+00	1.00000	1.03018	0.68618	0.85133	1.53930	0.55306	
21	6.7910+03	5.7227+00	1.00000	1.02971	0.69830	0.85955	1.51513	0.56373	
22	7.3200+03	5.9417+00	1.00000	1.02914	0.71295	0.86896	1.49595	0.58478	
23	8.2500+03	6.2454+00	1.00000	1.02759	0.73259	0.88109	1.44647	0.60913	
24	9.2260+03	6.3603+00	1.00000	1.02602	0.73997	0.89499	1.43077	0.61854	
25	1.0180+02	6.6771+00	1.00000	1.02443	0.75951	0.91641	1.39262	0.64393	
26	1.1120+02	7.0829+00	1.00000	1.02231	0.78421	0.91014	1.34496	0.67570	
27	1.2130+02	7.2878+00	1.00000	1.02179	0.79633	0.91655	1.32473	0.69188	
28	1.3110+02	7.4600+00	1.00000	1.01939	0.80637	0.92126	1.30524	0.70582	
29	1.4040+02	7.7986+00	1.00000	1.01876	0.82577	0.93118	1.27158	0.73230	
30	1.4980+02	8.1518+00	1.00000	1.01723	0.84551	0.94069	1.23731	0.75997	
31	1.5940+02	8.1957+00	1.00000	1.01566	0.84794	0.94119	1.23205	0.76392	
32	1.6940+02	8.7395+00	1.00000	1.01412	0.87713	0.95492	1.14456	0.80164	
33	1.7910+02	9.0615+00	1.00000	1.01275	0.89435	0.96223	1.15755	0.83126	
34	1.8830+02	9.2550+00	1.00000	1.01133	0.90440	0.96614	1.14119	0.86660	
35	1.9800+02	9.6828+00	1.00000	1.00979	0.92622	0.97505	1.10923	0.87983	
36	2.0750+02	9.7379+00	1.00000	1.00814	0.92399	0.97546	1.10253	0.89474	
37	2.1740+02	9.9808+00	1.00000	1.00659	0.94112	0.97986	1.04604	0.90330	
38	2.2740+02	1.0326+01	1.00000	1.00535	0.95839	0.98627	1.05971	0.93071	
39	2.3680+02	1.0483+01	1.00000	1.00377	0.96571	0.98858	1.04793	0.94337	
40	2.4720+02	1.0533+01	1.00000	1.00222	0.96913	0.98878	1.04311	0.94792	
41	2.5560+02	1.0899+01	1.00000	1.00112	0.98511	0.99489	1.01997	0.97542	
42	2.6580+02	1.1050+01	1.00000	1.00028	0.99273	0.99739	1.00943	0.98898	
43	2.8440+02	1.1206+01	1.00000	1.00000	1.00000	1.00000	1.00000	1.00000	
44	3.0390+02	1.1457+01	1.00000	1.00062	1.01212	1.00441	0.99560	1.01949	
45	3.2330+02	1.1520+01	1.00000	1.00035	1.01455	1.00581	0.99285	1.02236	
46	3.4340+02	1.1520+01	1.00000	1.00035	1.01455	1.00581	0.98295	1.02336	
47	3.6270+02	1.1625+01	1.00000	1.00133	1.01940	1.00781	0.97740	1.03111	
48	3.8150+02	1.1520+01	1.00000	1.00035	1.01455	1.00581	0.98285	1.02336	
49	4.0090+02	1.1414+01	1.00000	1.00041	1.00970	1.00381	0.98836	1.01562	
50	4.2060+02	1.1362+01	1.00000	1.00019	1.00727	1.00280	0.99115	1.01176	
51	4.4010+02	1.1310+01	1.00000	0.99999	1.00485	1.00180	0.99395	1.00791	
52	4.5940+02	1.1362+01	1.00000	1.00000	1.00727	1.00280	0.99115	1.01176	
53	4.7820+02	1.1467+01	1.00000	1.00002	1.01212	1.00431	0.99550	1.01949	
54	4.9790+02	1.1520+01	1.00000	1.00003	1.01455	1.00581	0.99285	1.02336	
55	5.1740+02	1.1520+01	1.00000	1.00003	1.01455	1.00581	0.99285	1.02336	

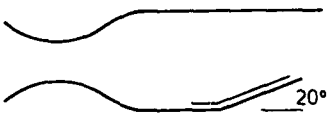
86030109

Spina/Smits

Turbulence Data

X = 1.5150E+00 UTAU = 2.1566E+01 RROW = 2.9951E-01 UINF = 5.6939E+02 MUEW = 1.6919E-05

I	Y	M	U	(RU) <sup>2</sup>	R U <sup>2</sup>	U <sup>2</sup>
			UINF	RW UT	RW UT2	UT2
1	3.9590E-3	1.8720E+0	8.2403E-1	5.3634E+0	3.2319E+0	1.8905E+0
2	5.4090E-3	1.9380E+0	8.3973E-1	5.2693E+0	2.7774E+0	1.5729E+0
3	6.8360E-3	2.0200E+0	8.5852E-1	5.6846E+0	2.8106E+0	1.5331E+0
4	8.2520E-3	2.1150E+0	8.7921E-1	6.3033E+0	2.9326E+0	1.5292E+0
5	9.6900E-3	2.1640E+0	8.861E-1	6.5000E+0	2.8661E+0	1.4586E+0
6	1.1150E-2	2.2650E+0	9.0840E-1	6.8143E+0	2.6535E+0	1.2879E+0
7	1.2610E-2	2.3130E+0	9.1690E-1	6.9445E+0	2.5390E+0	1.2037E+0
8	1.4050E-2	2.3840E+0	9.2930E-1	7.4305E+0	2.5796E+0	1.1823E+0
9	1.5490E-2	2.4450E+0	9.3899E-1	7.4575E+0	2.3486E+0	1.0454E+0
10	1.6970E-2	2.5140E+0	9.5109E-1	7.5930E+0	2.0992E+0	8.9534E-1
11	1.8410E-2	2.5980E+0	9.6229E-1	7.6967E+0	1.9477E+0	8.0684E-1
12	1.9840E-2	2.6740E+0	9.7298E-1	7.8333E+0	1.7810E+0	7.1138E-1
13	2.1290E-2	2.7010E+0	9.7578E-1	7.6278E+0	1.6152E+0	6.3610E-1
14	2.2750E-2	2.7660E+0	9.8418E-1	7.1903E+0	1.2937E+0	4.9416E-1
15	2.4200E-2	2.7920E+0	9.8658E-1	6.5870E+0	1.0407E+0	3.9216E-1
16	2.5650E-2	2.8460E+0	9.9298E-1	6.1341E+0	8.2877E-1	3.0448E-1
17	2.7100E-2	2.8720E+0	9.9598E-1	5.4925E+0	6.3826E-1	2.3171E-1
18	2.8530E-2	2.8890E+0	9.9807E-1	4.5396E+0	4.2464E-1	1.5297E-1
19	2.9990E-2	2.9150E+0	1.0017E+0	3.6517E+0	2.6406E-1	9.4069E-2
20	3.1470E-2	2.9260E+0	1.0037E+0	2.7574E+0	1.4831E-1	5.2664E-2
21	3.2910E-2	2.9290E+0	1.0037E+0	2.0988E+0	8.6427E-2	3.0264E-2
22	3.4360E-2	2.9290E+0	1.0037E+0	1.6473E+0	5.2646E-2	1.8657E-2
23	3.5830E-2	2.9400E+0	1.0057E+0	1.2948E+0	3.2024E-2	1.1308E-2
24	3.7270E-2	2.9360E+0	1.0047E+0	1.1161E+0	2.3930E-2	8.4572E-3
25	3.8740E-2	2.9250E+0	1.0027E+0	9.8275E-1	1.8830E-2	6.6751E-3
26	4.0220E-2	2.9150E+0	1.0017E+0	9.2306E-1	1.6888E-2	6.0190E-3
27	4.1660E-2	2.9090E+0	1.0007E+0	1.1653E+0	2.7090E-2	9.6673E-3
28	4.3140E-2	2.9040E+0	9.9967E-1	9.5219E-1	1.8235E-2	6.5202E-3

	$M(\infty): 2.84$ $R \text{ Theta} \times 10^{-3}: 78$ $TW/TR: 1.1$	8701
		CCF
Blowdown tunnel with symmetrical contoured nozzle. Max. running time "several minutes", normally 60 seconds. $W = H = 203 \text{ mm}$ . $L$ up to $2.7 \text{ m}$ . $PO: 0.69 \text{ MN/m}^2$ . $TO: 265 \text{ K} (\pm 6\%)$ . Air. $Re/\text{m} \times 10^{-6}: 63$ .		
SMITS A.J., MUCK K.C., 1987. Experimental study of three shock wave/ turbulent boundary layer interactions. J. Fluid. Mech. <u>182</u> , 291-314. <u>And:</u> Muck et al. (1983/1984), Settles et al. (1979), Selig et al. (1987); K.C. Muck and A.J. Smits, data tapes and private communications.		

- 1 The mean flow for these tests is described in CAT7904T, q.v.. This entry is concerned only with the turbulence measurements in the four compression-corner flows. The 8, 16, and 20 degree cases were studied by Muck et al. (1983/4), to which has been added recent data for the 24 degree case (Selig et al. (1987)).

- 8 The profiles were measured along a line  $12.7 \text{ mm}$  off the centreline so as not to disturb the flow at adjacent static tapings. The positions at which profiles were measured are given in table 1, together with their relationship to the mean flow data of CAT7904T. For two of the 8° profiles neighbouring profiles have been used where no exact match was available. Near the corner itself, the directions of the profile normals do not match for 0105-0106, 0302-3, 0503-6 and 0603. For the upstream profiles ( $X = -0.0508$ ) we assume one of many suitable sets of mean data has been used.

Turbulence measurements were made with both normal and inclined hot-wire probes supported from the tunnel roof opposite the test surface. The copper plated, soft soldered, sensor wires ( $d = 5 \mu\text{m}$ , active length about  $0.8 \text{ mm}$ ) were slightly slackened to avoid strain-gauging. The inclined wires were set at about  $60^\circ$  to the mean-flow direction. The support prongs were about  $2-3 \text{ mm}$  long and mounted in a cylindrical holder ( $d = 2.5-4 \text{ mm}$ ) the front of which formed a wedge with  $30^\circ$  included angle. The wires were operated in the constant-temperature mode, using a DISA 55M10 anemometer. The system frequency response was typically 10 to 120 kHz. The techniques are described in Smits et al. (1983) and Smits & Muck (1984). The authors warn that HWP data (inclined wires only, Smits PC) for mean flow Mach numbers below 1.2 (resolved normal to the wire) may be of dubious quality as a result of calibration difficulties in the transonic regime.

- 9 The authors have interpolated the original mean flow data to the measuring positions of the hot-wire probes, and incorporated no profile corrections, though it is not certain whether the original Pitot profiles were corrected for shear. The mean-flow data are therefore, in essence, the same for the two sets of profiles for each turning angle. The 13 profiles are presented incorporating the assumptions and reduction procedures of the authors. The wall data are also those presented with the profiles in their interpolated form, which describe a boundary layer subjected to the shock-wave structure resulting from compression corners turning the flow 8, 16, 20 and 24 degrees.

- 8 DATA: 87010101-0703. Mean flow data from CAT7904T. Normal and inclined wire turbulence profiles, distribution given in table 1.

15 Editors' comments:

The measurements described here, with the associated mean flow data of CAT7904T, form part of a continuing study of the effect of "extra strain rates" on turbulent boundary layers. Other experiments in which the same disturbance, i.e. pressure change, is applied to the same incoming boundary layer, but at different rates and in different ways, are described in CAT8401T/8702T and CAT8601T. Thus the "8° change" is accomplished here by a corner with zero radius of curvature, while in CAT8401/8702 it is caused by curved ramps with radius 254 and 1270 mm and in CAT8601 by a reflected wave structure matching the pressure gradient of CAT840102. The "16° change" is caused by corners with zero radius here, and radii of 1270 and 350 mm in CAT8401/8702. Directly comparable compression corner flows were studied by Debiève (CAT8301T) and Ardouneau (CAT8402T), the latter using a LDV to give turbulence data which may be compared with this entry (Fig. 11.2.19). Fluctuation data are also reported by Kuntz et al. (1987) and, using an axisymmetric configuration, Brown et al. (1987).

The skin- friction velocities used here for scaling are those derived from Preston-tube readings, using the Hopkins & Keener 1966 calibration with Settles' fictitious edge state. The value of these is discussed in connection with the mean-flow data. Edge states as reported in this entry do not affect the data in any way, and the editors have often, for convenience, taken the last point, or our estimate of the shock position. This last often shows up quite clearly in the hot-wire data, but with a systematic error when compared to static pressure data. We are not in a position to suggest which might be the more reliable.

The mean-flow data are shown in figures 10.3.8-12, and the turbulence data in 11.2.19, 23-25 & 11.3.7-9. Results from the normal wire studies should be little if at all affected by the problem of probe orientation, but data from the oblique wire can not be relied on when the probe is not closely aligned with the local flow. The mean-flow data are also susceptible to alignment errors, mainly through the effect on the static probe. (Taylor, 1984, reports an error of 30% at 10° incidence.) This is discussed in connection with CAT7904T above. Any mean flow or oblique wire data taken at  $X > 0$  and for Y-values outside the shock is likely to be seriously in error. For the 16° and 24° cases it seems that Settles took measures to deal with this, assuming free-stream static pressure in the outer part of the layer. For the other cases the data are as received from the authors and will require careful assessment before use, as no attempt has been made to correct the data.

In the separated flow cases there are substantial fluctuations in the shock position (see Ch. 8 and 9.3.1 above) and these may contribute a "non-turbulent" proportion to the fluctuation signals. The turbulence profiles do not go very close to the wall, so that the mean flow data given with them should not be used to determine integral values, which would be seriously in error. The integral quantities etc., where appropriate, should be taken from the mean-flow tables of CAT7904.

The Muck et al. (1983/4) papers contain a full assessment of the experimental errors. The possible error in  $(\bar{q} u'^2)$  is stated (Smits et al., 1983; Smits & Muck, 1984) as -10% to +19%, and in  $(\bar{q} u'v'/\rho_w u_\tau)$  as -32% to +12%. These estimates are for the upstream profiles and have been reassessed recently by Smits & Dussauge in chapter 5. These may seem to indicate large errors, but should rather be considered a sign of honesty in assessing measurements of this inherent difficulty.

Table 1: Relationship of hot-wire profiles to mean flow data.

X-value	Normal Wire Profile 8701	Traverse inclination degrees	Mean Flow Profile 7904	Traverse inclination degrees	Inclined Wire Profile 8701	Traverse inclination degrees
Turning angle 8 degrees						
-0.0508	0101	0	-	-	0201	0
-0.0254	0102	0	0101	0	-	-
-0.0152	0103	0	0102	0	-	-
-0.0051	0104	8	0103	0	-	-
-0.0025	0105	8	0104	0	-	-
0.0	0106	8	0201	8	-	-
0.0051	0107	8	0202	8	-	-
0.0102	0108	8	0203	8	-	-
0.0152	0109	8	0204	8	-	-
0.0203	0110	8	0205	8	0202	8
0.0254	0111	8	0206	8	-	-
0.0305	0112	0	0207	8	0203	8
0.0356	0113	8	0208	8	-	-
0.0457	0114	8	0209	8	-	-
0.0559	0115	8	0210	8	-	-
0.0660	0116	8	0211	8	0204	8
0.0762	0117	8	0212	8	-	-
0.0864	0118	8	0213	8	-	-
0.0965	0119	8	0214	8	-	-
0.1016	-	-	(Authors used 0215)	-	0205	8
0.1067	0120	8	0215	8	-	-
0.1168	0121	8	0216	8	-	-
0.1270	0122	8	0217	8	-	-
0.1524	0123	8	(Authors used $X = 0.1372$ ) (Not in CAT7904)	-	0206	8

8701			7904			8701		
Turning angle 16 degrees								
-0.0508	0301	0	-	-		0401	0	
-0.508	-	-	-	-		0402	0	
-0.0127	0302	16	0302	0		-	-	
-0.0063	0303	16	0303	0		-	-	
0.0	0304	16	0305	16		-	-	
0.0063	0305	16	0307	16		-	-	
0.0127	0306	16	0309	16		0403	16	
0.0191	0307	16	0310	16		-	-	
0.0254	0308	16	0311	16		0404	16	
0.0381	0309	16	0312	16		-	-	
0.0508	0310	16	0313	16		0405	16	
0.0762	0311	16	0314	16		0406	16	
0.1016	0312	16	0315	16		0407	16	
0.1397	0313	16	0317	16		0408	16	

Turning angle 20 degrees								
-0.0508	0501	0	-	-	-	0601	0	
-0.0508	0502	0	-	-	-	0602	0	
-0.0063	0503	20	0405	5.5	-	-	-	
0.0	0504	20	0406	5.5	-	-	-	
0.0039	0505	20	0407	5.5	-	-	-	
0.0127	0506	20	0408	5.5	0603	20		
0.0254	0507	20	0411	20	0604	20		
0.0414	0508	20	0412	20	0605	20		
0.0571	0509	20	0413	20	0606	20		
0.0762	0510	20	0414	20	0607	20		
0.0952	0511	20	0415	20	0608	20		
0.1143	-	-	0416	20	0609	20		

Turning angle 24 degrees								
0.0305	0701	24	0506	24	-	-	-	
0.0610	0702	24	0507	24	-	-	-	
0.1016	0703	24	0508	24	-	-	-	

87010204

Muck/Spina/Smits

Turbulence Data

X = 6.6000E-02 UTAU = 1.9528E+01 RHOW = 4.7466E-01 UINF = 5.8456E+02 MUEW = 1.7889E-05

I	Y	M	U	(RU)'V'	-R U'V'	U'V'
			UINF	RW UT2	RW UT2	UT2
1	1.9800E-3	1.4200E+0	6.9351E-1	-2.2832E+0	1.2643E+0	-9.2792E-1
2	3.2100E-3	1.4910E+0	7.1524E-1	-2.9822E+0	1.5784E+0	-1.1149E+0
3	4.6590E-3	1.6120E+0	7.5090E-1	-3.6045E+0	1.7677E+0	-1.1758E+0
4	6.0900E-3	1.6880E+0	7.7584E-1	-4.8656E+0	2.2744E+0	-1.4758E+0
5	7.5490E-3	1.7750E+0	7.9968E-1	-5.3629E+0	2.3734E+0	-1.4813E+0
6	8.9750E-3	1.8770E+0	8.2612E-1	-6.3456E+0	2.6341E+0	-1.5669E+0
7	1.0410E-2	1.9700E+0	8.4906E-1	-6.4720E+0	2.5351E+0	-1.4438E+0
8	1.1860E-2	2.0580E+0	8.6949E-1	-5.9096E+0	2.1929E+0	-1.1991E+0
9	1.3300E-2	2.1320E+0	8.8572E-1	-4.9330E+0	1.7502E+0	-9.2585E-1
10	1.4760E-2	2.2290E+0	9.0485E-1	-3.8450E+0	1.2873E+0	-6.5071E-1
11	1.6200E-2	2.2960E+0	9.1767E-1	-4.0422E+0	1.3001E+0	-6.3691E-1
12	1.7620E-2	2.3760E+0	9.3319E-1	-3.0506E+0	9.3627E-1	-4.4380E-1
13	1.9030E-2	2.4390E+0	9.4351E-1	-2.1216E+0	6.2801E-1	-2.8974E-1
14	2.0490E-2	2.4830E+0	9.4872E-1	-1.7158E+0	4.9507E-1	-2.2326E-1
15	2.1930E-2	2.5000E+0	9.5052E-1	-1.1268E+0	3.2209E-1	-1.4411E-1
16	2.3390E-2	2.5210E+0	9.5413E-1	-2.2403E-1	6.3223E-2	-2.8087E-2
17	2.4830E-2	2.5390E+0	9.5593E-1	-7.5205E-2	2.1011E-2	-9.3024E-3
18	2.6290E-2	2.6110E+0	9.6595E-1	1.6966E-1	-4.5532E-2	2.1070E-2
19	2.7750E-2	2.6890E+0	9.7656E-1	6.3595E+0	-1.6337E+0	9.3921E-1

87010306

Muck/Spina/Smits

Turbulence Data

X = 1.2700E-02 UTAU = 1.2303E+01 RHOW = 7.0624E-01 UINF = 5.6388E+02 MUEW = 1.6323E-05

I	Y	M	U UINF	(RU)' RW UT	R U'2 RW UT2	U'2 UT2
1	1.5000E-3	9.7070E-1	5.0736E-1	8.2030E+0	3.2405E+1	2.7236E+1
2	2.5800E-3	1.1320E+0	5.7375E-1	1.0245E+1	4.0299E+1	3.2230E+1
3	3.9800E-3	1.3040E+0	6.3819E-1	1.1495E+1	3.9046E+1	2.9439E+1
4	5.3800E-3	1.4500E+0	6.8881E-1	1.1830E+1	3.2906E+1	2.3630E+1
5	6.7800E-3	1.5740E+0	7.2852E-1	1.1102E+1	2.3836E+1	1.6445E+1
6	8.2000E-3	1.7800E+0	7.8703E-1	1.0389E+1	1.6072E+1	1.1088E+1
7	9.3400E-3	2.0040E+0	8.4359E-1	9.7688E+0	1.1814E+1	8.9916E+0
8	1.0760E-2	2.2450E+0	8.9401E-1	9.1293E+0	8.9971E+0	8.0520E+0
9	1.2160E-2	2.3880E+0	9.2029E-1	6.7802E+0	4.5462E+0	4.4317E+0
10	1.3540E-2	2.4790E+0	9.3470E-1	5.9831E+0	3.1628E+0	3.0685E+0
11	1.4960E-2	2.5480E+0	9.4482E-1	5.9616E+0	2.8470E+0	2.7153E+0
12	1.6390E-2	2.6050E+0	9.5212E-1	5.8745E+0	2.5287E+0	2.3537E+0
13	1.7820E-2	2.6700E+0	9.6244E-1	5.6451E+0	2.1054E+0	1.9051E+0
14	1.9170E-2	2.6950E+0	9.6449E-1	4.9243E+0	1.5340E+0	1.3678E+0
15	2.0520E-2	2.7290E+0	9.6760E-1	4.4507E+0	1.1859E+0	1.0388E+0
16	2.1470E-2	2.7630E+0	9.7188E-1	4.2528E+0	1.0248E+0	8.8314E-1
17	2.2830E-2	2.7920E+0	9.7539E-1	3.4454E+0	6.4233E-1	5.4598E-1
18	2.3330E-2	2.8000E+0	9.7636E-1	3.4994E+0	6.5461E-1	5.5448E-1
19	2.3900E-2	2.8090E+0	9.7734E-1	3.0130E+0	4.7843E-1	4.0350E-1
20	2.4300E-2	2.8090E+0	9.7734E-1	2.6806E+0	3.7843E-1	3.1903E-1
21	2.5690E-2	2.8100E+0	9.7636E-1	2.0135E+0	2.1260E-1	1.7874E-1
22	2.7130E-2	2.8200E+0	9.7636E-1	1.4718E+0	1.1160E-1	9.3175E-2
23	2.8550E-2	2.8260E+0	9.7636E-1	1.1670E+0	6.9395E-2	5.7691E-2
24	2.9990E-2	2.8300E+0	9.7734E-1	8.9039E-1	4.0174E-2	3.367E-2
25	3.1430E-2	2.8340E+0	9.7831E-1	7.8953E-1	3.1427E-2	2.6076E-2
26	3.2860E-2	2.8370E+0	9.7928E-1	7.5620E-1	2.8721E-2	2.3831E-2

87010403

Muck/Spina/Smits

Turbulence Data

X = 1.2700E-02 UTAU = 1.2778E+01 RHOW = 6.5472E-01 UINF = 5.7389E+02 MUEW = 1.7333E-05

I	Y	M	U UINF	(RU)'V' RW UT2	-R U'V' RW UT2	U'V' UT2
1	2.0000E-3	1.0450E+0	5.4974E-1	-4.7087E+0	3.2775E+0	-2.7042E+0
2	3.3210E-3	1.2330E+0	6.2567E-1	-6.2940E+0	3.9140E+0	-3.0362E+0
3	4.7580E-3	1.3930E+0	6.8382E-1	-6.1739E+0	3.4755E+0	-2.5354E+0
4	6.2110E-3	1.5210E+0	7.2705E-1	-7.4456E+0	3.8664E+0	-2.7137E+0
5	7.6530E-3	1.6780E+0	7.7466E-1	-1.0525E+1	4.9514E+0	-3.4124E+0
6	9.1020E-3	1.9520E+0	8.4861E-1	-5.9654E+0	2.3629E+0	-1.7446E+0
7	1.0560E-2	2.2200E+0	9.0795E-1	8.3604E+0	-2.8140E+0	2.4693E+0
8	1.1990E-2	2.3740E+0	9.3727E-1	-1.9137E+0	5.8810E-1	-5.7288E-1
9	1.3420E-2	2.4730E+0	9.5327E-1	-5.3024E+0	1.5385E+0	-1.4967E+0
10	1.4860E-2	2.5400E+0	9.6341E-1	-4.8042E+0	1.3413E+0	-1.2843E+0
11	1.6330E-2	2.6010E+0	9.7176E-1	-4.4165E+0	1.1915E+0	-1.1120E+0
12	1.7790E-2	2.6690E+0	9.8259E-1	-3.8532E+0	1.0008E+0	-9.0695E-1
13	1.9250E-2	2.6980E+0	9.8507E-1	-2.9618E+0	7.5724E-1	-6.7510E-1
14	2.0700E-2	2.7330E+0	9.8855E-1	-2.2965E+0	5.7582E-1	-5.0365E-1
15	2.2190E-2	2.7800E+0	9.9491E-1	-1.8782E+0	4.5906E-1	-3.9334E-1
16	2.3640E-2	2.8050E+0	9.9790E-1	-1.1719E+0	2.8265E-1	-2.3943E-1
17	2.5100E-2	2.8090E+0	9.9690E-1	-7.3683E-1	1.7728E-1	-1.4933E-1
18	2.6420E-2	2.8150E+0	9.9690E-1	-3.7002E-1	8.8729E-2	-7.4413E-2
19	2.7820E-2	2.8240E+0	9.9690E-1	-1.7347E-1	4.1420E-2	-3.4540E-2
20	2.9210E-2	2.8280E+0	9.9790E-1	-1.5392E-1	3.6659E-2	-3.0532E-2
21	3.0540E-2	2.8310E+0	9.9790E-1	-9.0978E-2	2.1625E-2	-1.7961E-2
22	3.1860E-2	2.8350E+0	9.9889E-1	-7.6709E-2	1.8202E-2	-1.5115E-2
23	3.3120E-2	2.8370E+0	9.9888E-1	-6.8653E-2	1.6270E-2	-1.3516E-2
24	3.4360E-2	2.8370E+0	9.9888E-1	-7.0254E-2	1.6651E-2	-1.3832E-2
25	3.5710E-2	2.8370E+0	9.9888E-1	-7.0569E-2	1.6726E-2	-1.3895E-2
26	3.7050E-2	2.8360E+0	9.9888E-1	-6.3313E-2	1.5017E-2	-1.2489E-2
27	3.8310E-2	2.8340E+0	9.9889E-1	-5.5196E-2	1.3105E-2	-1.0890E-2

87010308

Muck/Spina/Smits

Turbulence Data

X = 2.5400E-02 UTAU = 1.4343E+01 RHO = 7.1602E-01 UINF = 5.6388E+02 MUEW = 1.7104E-05

I	Y	M	U UINF	(RU)' RW UT	R U'2 RW UT2	U'2 UT2
1	1.3000E-3	9.8980E-1	5.3136E-1	6.1589E+0	1.7000E+1	1.3567E+1
2	1.8100E-3	1.0490E+0	5.5671E-1	6.7745E+0	1.9062E+1	1.5027E+1
3	3.2000E-3	1.1680E+0	6.0520E-1	9.2646E+0	3.0085E+1	2.2893E+1
4	4.6200E-3	1.2960E+0	6.5339E-1	1.0996E+1	3.4778E+1	2.5258E+1
5	6.0400E-3	1.4330E+0	7.0308E-1	1.2102E+1	3.3850E+1	2.3386E+1
6	7.4400E-3	1.5390E+0	7.3844E-1	1.0831E+1	2.2718E+1	1.5010E+1
7	8.8400E-3	1.6390E+0	7.6990E-1	1.0472E+1	1.7918E+1	1.1342E+1
8	1.0220E-2	1.7550E+0	8.0346E-1	9.6152E+0	1.2423E+1	7.4930E+0
9	1.1650E-2	1.8630E+0	8.3271E-1	9.9256E+0	1.1003E+1	6.3253E+0
10	1.3080E-2	1.9290E+0	8.4884E-1	9.7625E+0	9.5675E+0	5.3766E+0
11	1.4520E-2	1.8990E+0	8.3922E-1	1.0672E+1	1.2825E+1	7.7874E+0
12	1.5940E-2	2.0540E+0	8.7429E-1	6.0897E+0	4.2053E+0	3.1236E+0
13	1.7370E-2	2.4530E+0	9.5173E-1	4.1853E+0	1.4137E+0	1.2150E+0
14	1.8810E-2	2.6890E+0	9.8919E-1	3.3944E+0	7.4321E-1	6.7088E-1
15	2.0240E-2	2.7700E+0	9.9991E-1	2.6703E+0	4.2344E-1	3.8525E-1
16	2.1650E-2	2.7900E+0	1.0028E+0	2.1133E+0	2.5847E-1	2.3439E-1
17	2.2940E-2	2.8070E+0	1.0048E+0	1.6417E+0	1.5217E-1	1.3731E-1
18	2.4160E-2	2.8150E+0	1.0048E+0	1.2454E+0	8.6599E-2	7.7901E-2
19	2.5520E-2	2.8160E+0	1.0048E+0	8.0453E-1	3.6069E-2	3.2428E-2
20	2.6890E-2	2.8160E+0	1.0038E+0	7.3986E-1	3.0430E-2	2.7301E-2
21	2.8260E-2	2.8160E+0	1.0028E+0	6.7812E-1	2.5538E-2	2.2879E-2
22	2.9250E-2	2.8160E+0	1.0028E+0	6.2667E-1	2.1809E-2	1.9538E-2
23	3.0630E-2	2.8160E+0	1.0028E+0	5.9231E-1	1.9462E-2	1.7424E-2
24	3.2000E-2	2.8180E+0	1.0038E+0	5.6099E-1	1.7447E-2	1.5636E-2

87010404

Muck/Spina/Smits

Turbulence Data

X = 2.5400E-02 UTAU = 1.4776E+01 RHO = 6.7470E-01 UINF = 5.7389E+02 MUEW = 1.7919E-05

I	Y	M	U UINF	(RU)' V' RW UT2	-R U'V' RW UT2	U'V' UT2
1	2.0000E-3	1.0690E+0	5.7178E-1	-3.0638E+0	2.1027E+0	-1.6497E+0
2	3.3770E-3	1.1830E+0	6.1810E-1	-4.0905E+0	2.6229E+0	-1.9838E+0
3	4.8280E-3	1.3260E+0	6.7273E-1	-5.2799E+0	3.0994E+0	-2.2244E+0
4	6.2710E-3	1.4590E+0	7.2017E-1	-6.9080E+0	3.7324E+0	-2.5491E+0
5	7.7170E-3	1.5570E+0	7.5301E-1	-7.6966E+0	3.9070E+0	-2.5611E+0
6	9.1680E-3	1.6630E+0	7.8616E-1	-8.6415E+0	4.1035E+0	-2.5705E+0
7	1.0610E-2	1.7740E+0	8.1829E-1	-1.0091E+1	4.4672E+0	-2.6688E+0
8	1.2070E-2	1.8670E+0	8.4373E-1	-8.7877E+0	3.6706E+0	-2.1092E+0
9	1.3540E-2	1.9230E+0	8.5691E-1	9.7733E+0	-3.9434E+0	2.2299E+0
10	1.4970E-2	1.9090E+0	8.5123E-1	1.2545E+1	-5.1057E+0	3.2902E+0
11	1.6390E-2	2.1950E+0	9.1428E-1	-1.8631E+0	6.3644E-1	-5.0226E-1
12	1.7840E-2	2.5380E+0	9.7682E-1	-1.9323E+0	5.4022E-1	-4.7286E-1
13	1.9330E-2	2.7360E+0	1.0075E+0	-1.4006E+0	3.5069E-1	-3.1853E-1
14	2.0800E-2	2.7770E+0	1.0124E+0	-7.4598E-1	1.8262E-1	-1.6575E-1
15	2.2260E-2	2.8020E+0	1.0167E+0	-4.6594E-1	1.1252E-1	-1.0147E-1
16	2.3720E-2	2.8120E+0	1.0167E+0	-2.8149E-1	6.7609E-2	-6.0857E-2
17	2.5210E-2	2.8160E+0	1.0167E+0	-1.8309E-1	4.3890E-2	-3.9433E-2
18	2.6680E-2	2.8160E+0	1.0167E+0	-9.9754E-2	2.3919E-2	-2.1486E-2
19	2.8120E-2	2.8160E+0	1.0146E+0	-5.2162E-2	1.2503E-2	-1.1186E-2
20	2.9600E-2	2.8160E+0	1.0146E+0	-4.5844E-2	1.0988E-2	-9.8306E-3
21	3.1080E-2	2.8160E+0	1.0146E+0	-3.0236E-2	7.2484E-3	-6.4854E-3
22	3.2560E-2	2.8190E+0	1.0156E+0	-4.1754E-2	9.9913E-3	-8.9368E-3
23	3.4040E-2	2.8220E+0	1.0167E+0	-2.7435E-2	6.5553E-3	-5.8643E-3



87010310

Muck/Spina/Smits

Turbulence Data

X = 5.0800E-02 UTAU = 1.5553E+01 RHOW = 8.1568E-01 UINF = 5.6388E+02 MUEW = 1.6794E-05

I	Y	M	U UINF	(RU)' RW UT	R U'2 RW UT2	U'2 UT2
1	1.6500E-3	1.1380E+0	5.8575E-1	6.0028E+0	1.3662E+1	1.0860E+1
2	2.7700E-3	1.2090E+0	6.1496E-1	7.4925E+0	1.9379E+1	1.5241E+1
3	4.1900E-3	1.3050E+0	6.4961E-1	8.8549E+0	2.3317E+1	1.7706E+1
4	5.6160E-3	1.4030E+0	6.8427E-1	9.6847E+0	2.3765E+1	1.7350E+1
5	7.0500E-3	1.5050E+0	7.1813E-1	1.1413E+1	2.7989E+1	1.9666E+1
6	8.4700E-3	1.6390E+0	7.6001E-1	1.1754E+1	2.3657E+1	1.5694E+1
7	9.8890E-3	1.7570E+0	7.9328E-1	1.1653E+1	1.9039E+1	1.2011E+1
8	1.1340E-2	1.8540E+0	8.1962E-1	1.0670E+1	1.3512E+1	8.1619E+0
9	1.2780E-2	1.9480E+0	8.4328E-1	9.6663E+0	9.4287E+0	5.4515E+0
10	1.4180E-2	2.0290E+0	8.6189E-1	8.2977E+0	6.0214E+0	3.3425E+0
11	1.5630E-2	2.0980E+0	8.7615E-1	6.9131E+0	3.7169E+0	2.0000E+0
12	1.7060E-2	2.1510E+0	8.8437E-1	4.9940E+0	1.7627E+0	9.2044E-1
13	1.8500E-2	2.1750E+0	8.8843E-1	3.3583E+0	7.7108E-1	4.0122E-1
14	1.9930E-2	2.2340E+0	8.9922E-1	2.1884E+0	3.0718E-1	1.6114E-1
15	2.1370E-2	2.4040E+0	9.3130E-1	5.4592E+0	1.8102E+0	1.1044E+0
16	2.2780E-2	2.4900E+0	9.4566E-1	6.6317E+0	3.3502E+0	2.3389E+0
17	2.4240E-2	2.7030E+0	9.7774E-1	6.6662E-1	3.0026E-2	2.8852E-2
18	2.5690E-2	2.7960E+0	9.9110E-1	4.8031E-1	1.4354E-2	1.4100E-2
D 19	2.7130E-2	2.8210E+0	9.9407E-1	4.9140E-1	1.4748E-2	1.4613E-2

87010405

Muck/Spina/Smits

Turbulence Data

X = 5.0800E-02 UTAU = 1.6026E+01 RHOW = 7.6818E-01 UINF = 5.7389E+02 MUEW = 1.7606E-05

I	Y	M	U UINF	(RU)' RW UT2	-R U'V' RW UT2	U'V' UT2
1	2.0000E-3	1.1510E+0	5.9988E-1	-1.7874E+0	1.1680E+0	-9.3120E-1
2	3.2740E-3	1.2410E+0	6.3407E-1	-2.3969E+0	1.4830E+0	-1.1487E+0
3	4.7200E-3	1.3390E+0	6.7058E-1	-3.5178E+0	2.0479E+0	-1.5361E+0
4	6.1460E-3	1.4240E+0	6.9996E-1	-4.9852E+0	2.7527E+0	-1.9979E+0
5	7.5870E-3	1.5570E+0	7.4418E-1	-6.2287E+0	3.1629E+0	-2.1766E+0
6	9.0250E-3	1.6900E+0	7.8419E-1	-7.9179E+0	3.6966E+0	-2.3996E+0
7	1.0470E-2	1.7870E+0	8.1207E-1	-8.7609E+0	3.8487E+0	-2.3991E+0
8	1.1940E-2	1.9070E+0	8.4396E-1	-1.0020E+1	4.0823E+0	-2.4094E+0
9	1.3380E-2	1.9800E+0	8.6181E-1	-8.9501E+0	3.4861E+0	-1.9858E+0
10	1.4810E-2	2.0630E+0	8.8026E-1	-6.3197E+0	2.3385E+0	-1.2788E+0
11	1.6230E-2	2.1130E+0	8.8969E-1	-3.9196E+0	1.4069E+0	-7.5162E-1
12	1.7700E-2	2.1660E+0	8.9791E-1	-2.3664E+0	8.2256E-1	-4.2730E-1
13	1.9160E-2	2.1880E+0	9.0263E-1	-7.1665E-1	2.4580E-1	-1.2861E-1
14	2.0630E-2	2.3120E+0	9.2619E-1	7.2439E+0	-2.3073E+0	1.2771E+0
15	2.2070E-2	2.5030E+0	9.6019E-1	1.4572E+1	-4.1556E+0	3.0005E+0
16	2.3490E-2	2.5750E+0	9.7092E-1	1.3542E-1	-3.7088E-2	3.4330E-2
17	2.4890E-2	2.7680E+0	9.9970E-1	-4.0736E-2	1.0022E-2	-9.7743E-3
D 18	2.6290E-2	2.8090E+0	1.0048E+0	-4.7050E-2	1.1321E-2	-1.1177E-2

87010313

Muck/Spina/Smits

Turbulence Data

X = 1.3970E-01 UTAU = 1.9258E+01 RHOW = 7.6175E-01 UINF = 5.6388E+02 MUEW = 1.7020E-05

I	Y	M	U UINF	(RU)' RW UT	R U'2 RW UT2	U'2 UT2
1	1.3000E-3	1.3410E+0	6.6439E-1	1.0112E+0	2.6218E-1	1.7946E-1
2	1.5300E-3	1.3580E+0	6.7059E-1	3.0127E+0	2.2718E+0	1.5487E+0
3	1.8900E-3	1.3800E+0	6.7919E-1	5.1858E+0	6.5279E+0	4.4335E+0
4	2.2700E-3	1.4030E+0	6.8789E-1	6.3039E+0	9.3233E+0	6.3003E+0
5	2.6400E-3	1.4270E+0	6.9608E-1	6.4839E+0	9.5234E+0	6.3974E+0
6	3.0000E-3	1.4500E+0	7.0398E-1	6.7392E+0	9.8934E+0	6.5816E+0
7	3.9700E-3	1.4950E+0	7.1888E-1	7.3867E+0	1.1041E+1	7.2175E+0
8	5.1800E-3	1.5500E+0	7.3577E-1	7.8395E+0	1.1392E+1	7.3101E+0
9	6.6800E-3	1.5910E+0	7.4827E-1	8.1118E+0	1.1496E+1	7.3157E+0
10	8.1600E-3	1.6580E+0	7.6776E-1	8.9550E+0	1.2521E+1	7.7575E+0
11	9.6900E-3	1.7210E+0	7.8636E-1	9.4619E+0	1.2597E+1	7.6235E+0
12	1.1190E-2	1.8010E+0	8.0885E-1	1.0005E+1	1.2331E+1	7.2245E+0
13	1.2700E-2	1.8890E+0	8.3214E-1	1.0837E+1	1.2417E+1	6.9876E+0
14	1.4220E-2	1.9670E+0	8.5084E-1	1.0453E+1	1.0055E+1	5.4351E+0
15	1.5730E-2	2.0370E+0	8.6663E-1	1.0367E+1	8.7466E+0	4.5602E+0
16	1.7270E-2	2.1080E+0	8.8203E-1	1.0334E+1	7.6861E+0	3.8726E+0
17	1.8790E-2	2.1620E+0	8.9372E-1	8.3140E+0	4.5312E+0	2.2249E+0
18	2.0320E-2	2.1770E+0	8.9562E-1	6.9026E+0	3.0306E+0	1.4703E+0
19	2.1850E-2	2.1930E+0	8.9762E-1	5.3310E+0	1.7520E+0	8.4000E-1
20	2.3410E-2	2.1930E+0	8.9822E-1	4.0989E+0	1.0349E+0	4.9582E-1
21	2.4930E-2	2.1900E+0	8.9512E-1	2.4234E+0	3.6159E-1	1.7242E-1
22	2.6490E-2	2.1930E+0	8.9592E-1	1.4331E+0	1.2568E-1	5.9795E-2
23	2.7980E-2	2.1830E+0	8.9292E-1	8.8165E-1	4.8101E-2	2.2866E-2
24	2.7840E-2	2.1840E+0	8.9302E-1	9.9206E-1	6.0830E-2	2.8908E-2
25	2.7870E-2	2.1830E+0	8.9292E-1	8.1490E-1	4.1044E-2	1.9502E-2
26	2.7890E-2	2.1830E+0	8.9292E-1	8.2854E-1	4.2448E-2	2.0172E-2

87010408

Muck/Spina/Smits

Turbulence Data

X = 1.3970E-01 UTAU = 1.9707E+01 RHOW = 7.2744E-01 UINF = 5.7389E+02 MUEW = 1.7648E-05

I	Y	M	U UINF	(RU)'V' RW UT2	-R U'V' RW UT2	U'V' UT2
1	1.6200E-3	1.3630E+0	6.7653E-1	-6.5641E-1	3.7641E-1	-2.5642E-1
2	3.0640E-3	1.4550E+0	7.0930E-1	-1.1637E+0	6.3019E-1	-4.1869E-1
3	4.5230E-3	1.5060E+0	7.2649E-1	-1.7978E+0	9.4211E-1	-6.1456E-1
4	5.9780E-3	1.5440E+0	7.3735E-1	-2.5840E+0	1.3230E+0	-8.5623E-1
5	7.4180E-3	1.6290E+0	7.6369E-1	-3.7850E+0	1.8360E+0	-1.5000E+0
6	8.8480E-3	1.6850E+0	7.8027E-1	-3.9069E+0	1.8294E+0	-1.1230E+0
7	1.0300E-2	1.7500E+0	7.9867E-1	-4.3978E+0	1.9764E+0	-1.1820E+0
8	1.1780E-2	1.8420E+0	8.2430E-1	-4.4070E+0	1.8692E+0	-1.0747E+0
9	1.3250E-2	1.9070E+0	8.4139E-1	-4.3038E+0	1.7535E+0	-9.7922E-1
10	1.4710E-2	1.9930E+0	8.6150E-1	-5.2543E+0	2.0295E+0	-1.0826E+0
11	1.6180E-2	2.0570E+0	8.7587E-1	-5.0945E+0	1.8929E+0	-9.7785E-1
12	1.7660E-2	2.1260E+0	8.9095E-1	-3.2441E+0	1.1551E+0	-5.7719E-1
13	1.9130E-2	2.1660E+0	8.9939E-1	-2.0362E+0	7.0749E-1	-3.4657E-1
14	2.0590E-2	2.1820E+0	9.0161E-1	-1.8172E+0	6.2564E-1	-3.0285E-1
15	2.2060E-2	2.1930E+0	9.0221E-1	-7.9480E-1	2.7190E-1	-1.3026E-1
16	2.3550E-2	2.1930E+0	9.0301E-1	-2.6613E-1	9.0996E-2	-4.3602E-2
17	2.5010E-2	2.1890E+0	8.9980E-1	-7.1402E-2	2.4487E-2	-1.1680E-2
18	2.6490E-2	2.1930E+0	9.0090E-1	1.3517E-2	-4.6252E-3	2.2012E-3
19	2.7980E-2	2.1830E+0	8.9789E-1	1.4636E-2	-5.0349E-3	2.3944E-3
20	2.9430E-2	2.1840E+0	8.9829E-1	-5.6308E-3	1.9366E-3	-9.1837E-4
21	3.0930E-2	2.1830E+0	8.9829E-1	-1.9541E-3	6.7277E-4	-3.1924E-4
22	3.2440E-2	2.1860E+0	8.9869E-1	-1.4445E-3	4.9609E-4	-2.3425E-4
23	3.3900E-2	2.1930E+0	8.9909E-1	-1.0247E-3	3.5061E-4	-1.6501E-4

87010506 Muck/Spina/Smits Turbulence Data

X = 1.2700E-02 UTAU = 7.9006E+00 RHOW = 7.3374E-01 UINF = 5.7133E+02 MUEW = 1.7391E-05

I	Y	M	U UINF	(RU)' RW UT	R U'2 RW UT2	U'2 UT2
1	2.0000E-3	6.8390E-1	3.7986E-1	9.6536E+0	6.5904E+1	6.2187E+1
2	3.2590E-3	8.7690E-1	4.7300E-1	1.3188E+1	9.9501E+1	9.0325E+1
3	4.6950E-3	1.0750E+0	5.6022E-1	1.7714E+1	1.3697E+2	1.1681E+2
4	6.1360E-3	1.2510E+0	6.3054E-1	2.1913E+1	1.6098E+2	1.2914E+2
5	7.5630E-3	1.4070E+0	6.8615E-1	2.3901E+1	1.4907E+2	1.1261E+2
6	9.0230E-3	1.5700E+0	7.3899E-1	2.3304E+1	1.0865E+2	7.7165E+1
7	1.0480E-2	1.7170E+0	7.8294E-1	2.0193E+1	6.4614E+1	4.3789E+1
8	1.1920E-2	1.8400E+0	8.1632E-1	1.8190E+1	4.3283E+1	2.8304E+1
9	1.3360E-2	1.9860E+0	8.5307E-1	1.6950E+1	3.0188E+1	1.9074E+1
10	1.4780E-2	2.1450E+0	8.8912E-1	1.7267E+1	2.5489E+1	1.5974E+1
11	1.6250E-2	2.3580E+0	9.3050E-1	1.9064E+1	2.5864E+1	1.7500E+1
D 12	1.7700E-2	2.6600E+0	9.7979E-1	1.1648E+1	8.4146E+0	7.0634E+0

87010603 Muck/Spina/Smits Turbulence Data

X = 1.2700E-02 UTAU = 7.8623E+00 RHOW = 7.4091E-01 UINF = 5.7456E+02 MUEW = 1.7259E-05

I	Y	M	U UINF	(RU)'V' RW UT2	-R U'V' RW UT2	U'V' UT2
1	2.0000E-3	6.8390E-1	3.7592E-1	-5.9680E+0	5.0272E+0	-4.7425E+0
2	3.3800E-3	8.8320E-1	4.7093E-1	-1.3292E+1	1.0134E+1	-9.2014E+0
3	4.8120E-3	1.0980E+0	5.6408E-1	-2.8736E+1	1.9384E+1	-1.6483E+1
4	6.2520E-3	1.2630E+0	6.2869E-1	-3.6421E+1	2.2228E+1	-1.7764E+1
5	7.6850E-3	1.4270E+0	6.8558E-1	-3.9573E+1	2.1822E+1	-1.6361E+1
6	9.1310E-3	1.5840E+0	7.3553E-1	-5.0789E+1	2.5354E+1	-1.7941E+1
7	1.0580E-2	1.7320E+0	7.7912E-1	-5.2284E+1	2.3775E+1	-1.6024E+1
8	1.2010E-2	1.8510E+0	8.1079E-1	-4.4541E+1	1.8794E+1	-1.2252E+1
9	1.3430E-2	1.9970E+0	8.4686E-1	-4.0293E+1	1.5527E+1	-9.7893E+0
10	1.4850E-2	2.1570E+0	8.8244E-1	-1.3464E+1	4.7059E+0	-2.9534E+0
11	1.6320E-2	2.3540E+0	9.2007E-1	4.1519E+1	-1.2904E+1	8.7522E+0
D 12	1.7770E-2	2.6780E+0	9.7226E-1	4.0179E+0	-1.0386E+0	8.8344E-1

87010507 Muck/Spina/Smits Turbulence Data

X = 2.5400E-02 UTAU = 1.0859E+01 RHOW = 8.3300E-01 UINF = 5.7133E+02 MUEW = 1.7347E-05

I	Y	M	U UINF	(RU)' RW UT	R U'2 RW UT2	U'2 UT2
1	2.0000E-3	7.6800E-1	4.2081E-1	7.8711E+0	3.8778E+1	3.4786E+1
2	3.2420E-3	8.7700E-1	4.7153E-1	9.0752E+0	4.5996E+1	4.0765E+1
3	4.6920E-3	1.0530E+0	5.4869E-1	1.2333E+1	6.7447E+1	5.7041E+1
4	6.1520E-3	1.2310E+0	6.1976E-1	1.5228E+1	7.8960E+1	6.2864E+1
5	7.5920E-3	1.3970E+0	6.8011E-1	1.7098E+1	7.6440E+1	5.7162E+1
6	9.0220E-3	1.5540E+0	7.3172E-1	1.8396E+1	6.8421E+1	4.8113E+1
7	1.0450E-2	1.6810E+0	7.7045E-1	1.7878E+1	5.2296E+1	3.4969E+1
8	1.1930E-2	1.8470E+0	8.1606E-1	1.5753E+1	3.0931E+1	1.9450E+1
9	1.3380E-2	1.9610E+0	8.4358E-1	1.4303E+1	2.1299E+1	1.2922E+1
10	1.4860E-2	2.0830E+0	8.7169E-1	1.1998E+1	1.2690E+1	7.5917E+0
D 11	1.6310E-2	2.1860E+0	8.9332E-1	1.0106E+1	8.0936E+0	4.9464E+0
12	1.7790E-2	2.1800E+0	8.8948E-1	1.2869E+1	1.5228E+1	1.0721E+1
13	1.9240E-2	2.2300E+0	8.9784E-1	9.5822E+0	9.8435E+0	8.5895E+0

87010604

Muck/Spina/Smits

Turbulence Data

X = 2.5400E-02 UTAU = 1.0942E+01 RHOW = 8.2031E-01 UINF = 5.7456E+02 MUEW = 1.7557E-05

I	Y	M	U UINF	(RU)'V' RW UT2	-R U'V' RW UT2	U'V' UT2
1	2.0000E-3	7.6800E-1	4.2187E-1	-5.2635E+0	4.2589E+0	-3.8254E+0
2	3.4400E-3	8.9400E-1	4.8031E-1	-9.5135E+0	7.2089E+0	-6.3668E+0
3	4.8910E-3	1.0610E+0	5.5333E-1	-1.3684E+1	9.4343E+0	-7.9906E+0
4	6.3320E-3	1.2430E+0	6.2596E-1	-1.6077E+1	9.9327E+0	-7.8958E+0
5	7.7600E-3	1.4020E+0	6.8331E-1	-2.9247E+1	1.6377E+1	-1.2254E+1
6	9.1730E-3	1.5620E+0	7.3603E-1	-2.6516E+1	1.3424E+1	-9.4143E+0
7	1.0610E-2	1.6980E+0	7.7722E-1	-2.4356E+1	1.1313E+1	-7.5263E+0
8	1.2080E-2	1.8570E+0	8.2088E-1	-2.6007E+1	1.0929E+1	-6.8573E+0
9	1.3540E-2	1.9810E+0	8.5054E-1	-2.3257E+1	9.0505E+0	-5.4650E+0
10	1.4980E-2	2.0900E+0	8.7547E-1	-1.3739E+1	5.0007E+0	-2.9944E+0
D 11	1.6440E-2	2.1890E+0	8.9577E-1	7.0824E+0	-2.4287E+0	1.4968E+0
12	1.7920E-2	2.1850E+0	8.9262E-1	4.8459E+1	-1.6655E+1	1.1959E+1
13	1.9370E-2	2.2420E+0	9.0228E-1	1.6286E+1	-5.4103E+0	4.8011E+0

87010508

Muck/Spina/Smits

Turbulence Data

X = 4.1400E-02 UTAU = 1.2067E+01 RHOW = 9.1264E-01 UINF = 5.7133E+02 MUEW = 1.7311E-05

I	Y	M	U UINF	(RU)' RW UT	R U'2 RW UT2	U'2 UT2
1	2.0000E-3	8.4220E-1	4.5784E-1	6.9912E+0	2.6529E+1	2.2093E+1
2	3.2900E-3	9.3740E-1	5.0053E-1	8.7377E+0	3.7560E+1	3.1151E+1
3	4.7000E-3	1.0490E+0	5.4915E-1	1.0343E+1	4.5986E+1	3.1124E+1
4	6.1800E-3	1.1690E+0	5.9737E-1	1.2928E+1	6.0744E+1	4.7987E+1
5	7.6400E-3	1.3440E+0	6.6368E-1	1.4135E+1	5.5726E+1	4.1637E+1
6	9.1000E-3	1.4670E+0	7.0608E-1	1.6136E+1	5.9664E+1	4.2656E+1
7	1.0560E-2	1.6390E+0	7.6003E-1	1.7043E+1	5.0009E+1	3.3355E+1
8	1.2040E-2	1.7490E+0	7.9195E-1	1.5376E+1	3.3833E+1	2.1566E+1
9	1.3510E-2	1.8940E+0	8.3119E-1	1.3141E+1	1.9316E+1	1.1568E+1
10	1.4970E-2	1.9730E+0	8.5026E-1	1.0565E+1	1.0974E+1	6.3849E+0
11	1.6430E-2	2.0860E+0	8.7477E-1	7.9040E+0	5.1089E+0	2.8457E+0
12	1.7900E-2	2.1250E+0	8.8119E-1	5.3723E+0	2.2485E+0	1.2532E+0
13	1.9380E-2	2.1910E+0	8.9374E-1	4.1510E+0	1.2678E+0	7.2372E-1
D 14	2.0860E-2	2.3810E+0	9.3030E-1	1.4271E+1	1.3773E+1	9.0967E+0
15	2.2320E-2	2.5750E+0	9.6242E-1	7.9628E+0	5.0602E+0	4.9602E+0

87010605

Muck/Spina/Smits

Turbulence Data

X = 4.1400E-02 UTAU = 1.2140E+01 RHOW = 9.0174E-01 UINF = 5.7456E+02 MUEW = 1.7475E-05

I	Y	M	U UINF	(RU)'V' RW UT2	-R U'V' RW UT2	U'V' UT2
1	2.0000E-3	8.4220E-1	4.5793E-1	-4.7235E+0	3.6795E+0	-3.0625E+0
2	3.4120E-3	9.4810E-1	5.0537E-1	-6.6091E+0	4.8608E+0	-4.0240E+0
3	4.8440E-3	1.0500E+0	5.4975E-1	-9.8321E+0	6.8212E+0	-5.5747E+0
4	6.2770E-3	1.1750E+0	5.9957E-1	-1.4601E+1	9.4061E+0	-7.4175E+0
5	7.7320E-3	1.3580E+0	6.6866E-1	-1.8814E+1	1.0833E+1	-8.0498E+0
6	9.1570E-3	1.4720E+0	7.0760E-1	-1.7913E+1	9.6009E+0	-6.8524E+0
7	1.0600E-2	1.6400E+0	7.6048E-1	-2.0465E+1	9.8592E+0	-6.5716E+0
8	1.2030E-2	1.7470E+0	7.9162E-1	-1.9864E+1	8.9425E+0	-5.7016E+0
9	1.3480E-2	1.8910E+0	8.3066E-1	-1.7605E+1	7.2425E+0	-4.3413E+0
10	1.4950E-2	1.9730E+0	8.5033E-1	-1.3253E+1	5.1847E+0	-3.0173E+0
11	1.6390E-2	2.0850E+0	8.7484E-1	-5.2385E+0	1.9132E+0	-1.0656E+0
12	1.7810E-2	2.1210E+0	8.8057E-1	-8.9226E-1	3.1862E-1	-1.7750E-1
13	1.9220E-2	2.1810E+0	8.9204E-1	9.9056E+0	-3.4127E+0	1.9392E+0
D 14	2.0700E-2	2.3640E+0	9.2752E-1	8.0325E+1	-2.4833E+1	1.5871E+1
15	2.2150E-2	2.6010E+0	9.6686E-1	8.8730E+0	-2.3944E+0	2.1986E+0

87010511

Muck/Spina/Smits

Turbulence Data

X = 9.5200E-02 UTAU = 1.6135E+01 RHOW = 9.7944E-01 UINF = 5.7133E+02 MUZW = 1.7552E-05

I	Y	M	U UINF	(RU)' RW UT	R U'2 RW UT2	U'2 UT2
1	2.0000E-3	1.0820E+0	5.6568E-1	6.1476E+0	1.4882E+1	1.1530E+1
2	3.4100E-3	1.1590E+0	5.9754E-1	7.1520E+0	1.8523E+1	1.4406E+1
3	4.8800E-3	1.2160E+0	6.1935E-1	7.6985E+0	1.9935E+1	1.5395E+1
4	6.3600E-3	1.2890E+0	6.4623E-1	8.3574E+0	2.1203E+1	1.6122E+1
5	7.8300E-3	1.3630E+0	6.7302E-1	9.6121E+0	2.5153E+1	1.8758E+1
6	9.2800E-3	1.4600E+0	7.0638E-1	1.0780E+1	2.7172E+1	1.9625E+1
7	1.0750E-2	1.5570E+0	7.3764E-1	1.1422E+1	2.5826E+1	1.7853E+1
8	1.2220E-2	1.6780E+0	7.7488E-1	1.2677E+1	2.5903E+1	1.6999E+1
9	1.3700E-2	1.7830E+0	8.0545E-1	1.1312E+1	1.7199E+1	1.0745E+1
10	1.5170E-2	1.8750E+0	8.3094E-1	1.1331E+1	1.4661E+1	8.7521E+0
11	1.6650E-2	1.9460E+0	8.4767E-1	9.1777E+0	8.4494E+0	4.8468E+0
12	1.8110E-2	1.9950E+0	8.5803E-1	6.8482E+0	4.2793E+0	2.3750E+0
D 13	1.9610E-2	2.0100E+0	8.6072E-1	5.5193E+0	2.6951E+0	1.4778E+0
14	2.1110E-2	2.0150E+0	8.6171E-1	3.2023E+0	8.9645E-1	4.8858E-1
15	2.2570E-2	2.0090E+0	8.5912E-1	2.0942E+0	3.8612E-1	2.1044E-1
16	2.4080E-2	2.0080E+0	8.5753E-1	1.3933E+0	1.7088E-1	9.3027E-2
17	2.5570E-2	2.0020E+0	8.5524E-1	1.0070E+0	9.0153E-2	4.9182E-2
18	2.7050E-2	2.0020E+0	8.5574E-1	1.0776E+0	1.0410E-1	5.7254E-2
19	2.8560E-2	2.0020E+0	8.5584E-1	9.9210E-1	8.8884E-2	4.9250E-2
20	3.0060E-2	1.9950E+0	8.5424E-1	1.0083E+0	9.3474E-2	5.2297E-2
21	3.1550E-2	2.0090E+0	8.5743E-1	1.0267E+0	9.5581E-2	5.3646E-2
22	3.3080E-2	2.0240E+0	8.6062E-1	1.0115E+0	9.1433E-2	5.1511E-2
23	3.4590E-2	2.0340E+0	8.6271E-1	9.7217E-1	8.3942E-2	4.7609E-2
24	3.6100E-2	2.1040E+0	8.7814E-1	3.9543E+0	1.3227E+0	7.7945E-1
25	3.7620E-2	2.3280E+0	9.2444E-1	4.9760E+0	2.5263E+0	2.3615E+0
26	3.9150E-2	3.1680E+0	1.0465E+0	3.6420E-1	8.3666E-3	1.2420E-2


87010608

Muck/Spina/Smits

Turbulence Data

X = 9.5200E-02 UTAU = 1.6194E+01 RHOW = 9.7239E-01 UINF = 5.7456E+02 MUZW = 1.7651E-05

I	Y	M	U UINF	(RU)'V' RW UT2	-R U'V' RW UT2	U'V' UT2
1	2.0000E-3	1.0820E+0	5.6458E-1	-8.1021E-1	5.5171E-1	-4.2734E-1
2	3.4430E-3	1.1600E+0	5.9708E-1	-1.7077E+0	1.1100E+0	-8.6435E-1
3	4.8240E-3	1.2140E+0	6.1755E-1	-2.2774E+0	1.4322E+0	-1.1056E+0
4	6.2040E-3	1.2790E+0	6.4140E-1	-4.2045E+0	2.5412E+0	-1.9384E+0
5	7.6640E-3	1.3510E+0	6.6774E-1	-6.7496E+0	3.9006E+0	-2.9209E+0
6	9.1240E-3	1.4480E+0	7.0123E-1	-8.7417E+0	4.7547E+0	-3.4509E+0
7	1.0570E-2	1.5400E+0	7.3104E-1	-1.0914E+1	5.5999E+0	-3.9006E+0
8	1.2010E-2	1.6620E+0	7.6851E-1	-1.3680E+1	6.4992E+0	-4.2988E+0
9	1.3440E-2	1.7620E+0	7.9793E-1	-1.5850E+1	7.0696E+0	-4.4579E+0
10	1.4920E-2	1.8580E+0	8.2476E-1	-1.2484E+1	5.2446E+0	-3.1580E+0
11	1.6390E-2	1.9360E+0	8.4354E-1	-1.2554E+1	5.0239E+0	-2.9004E+0
12	1.7860E-2	1.9920E+0	8.5596E-1	-1.1550E+1	4.4634E+0	-2.4856E+0
D 13	1.9320E-2	2.0090E+0	8.5875E-1	-6.4845E+0	2.4805E+0	-1.3619E+0
14	2.0810E-2	2.0160E+0	8.6044E-1	-3.5809E+0	1.3638E+0	-7.4363E-1
15	2.2290E-2	2.0090E+0	8.5765E-1	-1.5267E+0	5.8393E-1	-3.1825E-1
16	2.3760E-2	2.0090E+0	8.5626E-1	-3.7648E-1	1.4400E-1	-7.8405E-2
17	2.5230E-2	2.0020E+0	8.5338E-1	-7.6637E-2	2.9439E-2	-1.6034E-2
18	2.6700E-2	2.0020E+0	8.5398E-1	1.1619E-1	-4.4634E-2	2.4521E-2
19	2.8170E-2	2.0020E+0	8.5417E-1	1.5193E-1	-5.8371E-2	3.2284E-2
20	2.9660E-2	1.9980E+0	8.5328E-1	1.9056E-1	-7.3367E-2	4.0933E-2
21	3.1130E-2	2.0060E+0	8.5507E-1	2.2355E-1	-8.5659E-2	4.7998E-2
22	3.2610E-2	2.0160E+0	8.5726E-1	2.3050E-1	-8.7766E-2	4.9456E-2
23	3.4100E-2	2.0300E+0	8.6024E-1	2.7357E-1	-1.0329E-1	5.8315E-2

	M: 2.9	8702
	R Theta $\times 10^{-3}$ : 90	CSF
TW/TR: 1.1		
Blowdown tunnel with symmetrical contoured nozzle. Max. running time "several minutes", normally 60 seconds. W = H = 203 mm. L up to 2.7 m. PO: 0.69 MN/m <sup>2</sup> . TO: 250 - 310 K. Air. Re/m $\times 10^{-6}$ : 63.		
JAYARAM M., TAYLOR M.W., SMITS A.J., 1987. The response of a compressible turbulent boundary layer to short regions of concave surface curvature. J. Fluid Mech. <u>175</u> , 343-362. And: Jayaram et al, (1985), Donovan & Smits (1987), Taylor, M.W., CAT8401T. A.J.Smits, data tapes and private communications.		

- 1 The mean flow for these tests is described in CAT8401T, q.v.. This entry is concerned only with the turbulence measurements on three of the four curved ramps, corresponding to CAT8401T series 01, 02 and 04. The data for the first two series, obtained by Jayaram et al., has been supplemented by the recent data of Donovan & Smits (1987) for series 04.
- 8 The data were measured along a line 12.7 mm off the centreline. Probes were supported from the tunnel roof opposite the test surface. The traverses were made normal to the surface at the profile station. The copper-plated, soft-soldered, sensor wires ( $d = 5 \mu\text{m}$ , active length about 0.8 mm) were slightly slackened to avoid strain-gauging. The inclined wires were set at about 60° to the mean-flow direction. The support prongs were about 2 mm long and mounted in a cylindrical holder ( $d = 2.5\text{--}4 \text{ mm}$ ) the front of which formed a wedge with 30° included angle. The wires were operated in the constant-temperature mode, using a DISA 55M10 anemometer. The system frequency response was typically 10 Hz - 120 kHz. The techniques are described in Smits et al. (1983) and Smits & Muck (1984). The authors warn that HWP data (inclined wires only, Smits PC) for mean flow Mach numbers below 1.2 may be of dubious quality as a result of calibration difficulties in the transonic range.
- 13 Five series of turbulence profiles are given. Series 870201/02 are inclined-wire profiles corresponding to the mean flow series CAT840101/02. Series 870203/04 are normal-wire profiles again for 840101/02. There are no turbulence data corresponding to 840103. Series 870205 gives three normal-wire profiles for the mean flow of 840104. The last two digits of the profile numbers are the same for CAT8401T and CAT8702T, save that 870501 was measured upstream of 840401, at  $X = -0.0635 \text{ m}$ . There are no turbulence profiles for 84010101/2, 84010201/2/12 otherwise there are both normal and inclined-wire profiles for both series. For 840104, the three profiles correspond to 840401/07/11.
- 9 The authors have interpolated the mean-flow data to the Y-values of the hot-wire probes, and incorporated no profile corrections. The editors have selected a D-state on the basis of the total pressure profiles. Otherwise the profiles are presented incorporating the assumptions and data-reduction procedures of the authors. The wall data are also those presented with the profiles, which describe boundary layers subjected to distributed simple-wave compression caused by concave curved surfaces.
- 8 DATA: 87020101-0503. Mean flow from CAT8401T. Normal and inclined-wire turbulence profiles. NX = 9, 14, 9, 14, 3.
- 15 Editors' comments.  
 These results are the first to become available in which reasonably complete coverage of the turbulent structure of a simple wave APG flow is presented. They form part of a systematic series studying the effect of "extra strain rates" on supersonic turbulent boundary layers. Other closely related experiments are Fernando & Smits (CAT8601T), in which the longitudinal pressure gradient of CAT 840102/ 870202/04 was reproduced on a straight wall by a reflected wave structure, and Settles (CAT7904T - mean flow), Smits & Muck (CAT8701T - turbulence) whose studies of compression-corner flows include 8° and 16° cases giving the same turning as for 870201-04/05 (see "Editors' comments" for CAT8701T). Other comparable studies are those of Sturek & Danberg, CAT7101, and Laderman, CAT7803S.

The turbulence profiles do not go very close to the wall, so that the mean-flow data given with them should not be used to determine integral values, which would be seriously in error. The integral thicknesses etc. should be taken from the mean-flow data of CAT8401T.

The flow just outside the boundary layer is shock-free so that a rational assessment of the edge-state is possible from the P0 profile. The data are discussed in 10.2 and 11.2/3 while mean flow and turbulence profiles are given in figures (10.2.2-7, 11.2.11-16, 11.3.2-5).

Table 1: Relationship of hot-wire profiles to mean flow

Note: The final two digits of the profile serial numbers are the same for the hot-wire profiles and the related mean flow data.

870201, 870203 with 840101 at X =		870202, 870204 with 840102 at X =		870205 with 840104 at X =	
03	-0.0127	03	-0.0127	01	-0.0254
04	0	04	0	07	0.1524
05	0.0127	05	0.0127	11	0.254
06	0.0254	06	0.0254		
07	0.0508	07	0.0508		
08	0.0762	08	0.0762		
09	0.1143	09	0.1016		
10	0.1524	10	0.1270		
11	0.1778	11	0.1524		
		13	0.2032		
		14	0.2286		
		15	0.2540		
		16	0.2794		
		17	0.3175		

87020105 Jayaram/Formica/Smits Turbulence Data  
 X = 1.2700E-02 UTAU = 2.0226E+01 RHOW = 3.3220E-01 UINF = 5.8705E+02 HUEW = 1.7662E-05

I	Y	M	U UINF	(RU)'V' RV UT2	-R U'V' RV UT2	U'V' UT2
1	3.3000E-3	1.7430E+0	7.8747E-1	-3.9254E+0	1.7721E+0	-1.1414E+0
2	4.5110E-3	1.8110E+0	8.0511E-1	-4.0308E+0	1.7440E+0	-1.1068E+0
3	5.9430E-3	1.9100E+0	8.2862E-1	-3.8667E+0	1.5724E+0	-9.6883E-1
4	7.3860E-3	2.0020E+0	8.5053E-1	-3.3813E+0	1.2983E+0	-7.8248E-1
5	8.8360E-3	2.1270E+0	8.7842E-1	-3.1526E+0	1.1216E+0	-6.5263E-1
6	1.0260E-2	2.2130E+0	8.9506E-1	-3.1341E+0	1.0588E+0	-6.0348E-1
7	1.1700E-2	2.3340E+0	9.1797E-1	-2.9496E+0	9.2758E-1	-5.1055E-1
8	1.3120E-2	2.4020E+0	9.3013E-1	-2.2869E+0	6.9125E-1	-3.7052E-1
9	1.4570E-2	2.4540E+0	9.3760E-1	-2.1545E+0	6.3216E-1	-3.2984E-1
10	1.6020E-2	2.5390E+0	9.5075E-1	-2.0641E+0	5.7686E-1	-2.8921E-1
11	1.7440E-2	2.5940E+0	9.5891E-1	-1.4344E+0	3.8866E-1	-1.8986E-1
12	1.8810E-2	2.6870E+0	9.7266E-1	-1.3755E+0	3.5374E-1	-1.6569E-1
13	2.0210E-2	2.7290E+0	9.7734E-1	-8.6357E-1	2.1708E-1	-9.9538E-2
14	2.1670E-2	2.7760E+0	9.8292E-1	-6.8104E-1	1.6681E-1	-7.4756E-2
15	2.3130E-2	2.8270E+0	9.8880E-1	-1.8191E-1	-4.3359E-2	1.8969E-2
16	2.4580E-2	2.8340E+0	9.8880E-1	-1.9641E-1	4.6643E-2	-2.0303E-2
17	2.6020E-2	2.8570E+0	9.9069E-1	7.5385E-3	-1.7676E-3	7.5975E-4
18	2.7430E-2	2.8700E+0	9.9199E-1	6.5092E-2	-1.5156E-2	6.4718E-3
19	2.8810E-2	2.8840E+0	9.9398E-1	8.5769E-2	-1.9820E-2	8.4146E-3
20	3.0260E-2	2.8820E+0	9.9388E-1	4.8259E-2	-1.1165E-2	4.7457E-3
21	3.1640E-2	2.8840E+0	9.9398E-1	9.5899E-3	-2.2161E-3	9.4050E-4
22	3.3030E-2	2.8700E+0	9.9259E-1	2.4738E-2	-5.7572E-3	2.4609E-3
23	3.4430E-2	2.8750E+0	9.9278E-1	6.9389E-3	-1.6109E-3	6.8641E-4

87020107 Jayaram/Formica/Smits Turbulence Data  
 X = 5.0800E-02 UTAU = 1.9050E+01 RHOW = 4.4833E-01 UINF = 5.8705E+02 HUEW = 1.7696E-05

I	Y	M	U UINF	(RU)'V' RV UT2	-R U'V' RV UT2	U'V' UT2
1	1.4200E-3	1.2920E+0	6.4002E-1	-2.0054E+0	1.2025E+0	-8.8846E-1
2	2.6610E-3	1.4290E+0	6.8892E-1	-2.0351E+0	1.1202E+0	-7.8692E-1
3	4.0340E-3	1.5640E+0	7.3184E-1	-3.7689E+0	1.9059E+0	-1.2659E+0
4	5.3830E-3	1.6620E+0	7.6311E-1	-5.1511E+0	2.4470E+0	-1.5738E+0
5	6.6580E-3	1.7740E+0	7.9278E-1	-6.3479E+0	2.8099E+0	-1.7183E+0
6	7.8720E-3	1.8690E+0	8.1788E-1	-7.3421E+0	3.0623E+0	-1.8040E+0
7	9.2420E-3	1.9480E+0	8.3759E-1	-6.5728E+0	2.6111E+0	-1.4890E+0
8	1.0590E-2	2.0560E+0	8.6090E-1	-6.9216E+0	2.5717E+0	-1.3985E+0
9	1.1950E-2	2.1320E+0	8.7703E-1	-6.8696E+0	2.4376E+0	-1.3060E+0
10	1.3320E-2	2.3050E+0	9.1119E-1	-6.3179E+0	2.0210E+0	-1.0447E+0
11	1.4670E-2	2.3970E+0	9.2702E-1	-5.0798E+0	1.5402E+0	-7.9796E-1
12	1.5980E-2	2.4680E+0	9.3917E-1	-4.2990E+0	1.2513E+0	-6.5727E-1
13	1.7350E-2	2.5500E+0	9.5132E-1	-2.2130E+0	6.1436E-1	-3.2615E-1
14	1.8630E-2	2.5970E+0	9.5819E-1	-1.1971E+0	3.2390E-1	-1.7690E-1
15	1.9970E-2	2.6460E+0	9.6496E-1	-9.3760E-1	2.4675E-1	-1.3909E-1
16	2.1250E-2	2.7230E+0	9.7482E-1	-7.0920E-1	1.7891E-1	-1.0269E-1
17	2.2570E-2	2.8230E+0	9.8846E-1	-3.5674E-1	8.5165E-2	-4.9640E-2
18	2.3810E-2	2.8870E+0	9.9583E-1	-1.4347E-1	3.1116E-2	-1.9475E-2
19	2.5180E-2	2.8900E+0	9.9474E-1	-1.7450E-1	4.0216E-2	-2.3670E-2
20	2.6470E-2	2.8940E+0	9.9543E-1	-1.0216E-1	2.3492E-2	-1.3813E-2
21	2.7870E-2	2.9000E+0	9.9583E-1	-3.1155E-2	7.1376E-3	-4.1813E-3
22	2.9120E-2	2.9090E+0	9.9683E-1	-2.0738E-2	4.7284E-3	-2.7582E-3
23	3.0420E-2	2.9000E+0	9.9583E-1	1.9715E-3	-4.5154E-4	2.6444E-4
24	3.1710E-2	2.9000E+0	9.9583E-1	2.7928E-3	-6.3992E-4	3.7481E-4
25	3.2940E-2	2.9000E+0	9.9583E-1	3.5033E-3	-8.0258E-4	4.7011E-4

87020109 Jayaram/Formica/Smits Turbulence Data  
 X = 1.1430E-01 UTAU = 1.9565E+01 RHOW = 4.9818E-01 UINF = 5.8705E+02 HUEW = 1.7620E-05

I	Y	M	U UINF	(RU)'V' RV UT2	-R U'V' RV UT2	U'V' UT2
1	1.4200E-3	1.3780E+0	6.7008E-1	-2.4533E+0	1.3946E+0	-1.0122E+0
2	2.7010E-3	1.4650E+0	6.9899E-1	-2.1457E+0	1.1548E+0	-8.0585E-1
3	4.0740E-3	1.5130E+0	7.1568E-1	-3.1931E+0	1.6670E+0	-1.1454E+0
4	5.3660E-3	1.6080E+0	7.4528E-1	-5.0713E+0	2.4924E+0	-1.6577E+0
5	6.7360E-3	1.7030E+0	7.7002E-1	-5.2578E+0	2.4344E+0	-1.5502E+0
6	8.1060E-3	1.7680E+0	7.8890E-1	-5.9676E+0	2.6516E+0	-1.6479E+0
7	9.4560E-3	1.8640E+0	8.1393E-1	-7.1169E+0	2.9780E+0	-1.7762E+0
8	1.0810E-2	1.9370E+0	8.3092E-1	-6.9924E+0	2.7959E+0	-1.6093E+0
9	1.2160E-2	2.0520E+0	8.5685E-1	-7.3721E+0	2.7460E+0	-1.4925E+0
10	1.3400E-2	2.1270E+0	8.7304E-1	-6.7369E+0	2.3980E+0	-1.2633E+0
11	1.4780E-2	2.2010E+0	8.8745E-1	-6.7470E+0	2.2969E+0	-1.1685E+0
12	1.6160E-2	2.2700E+0	9.0036E-1	-6.3568E+0	2.0770E+0	-1.0247E+0
13	1.7530E-2	2.3420E+0	9.1357E-1	-5.0688E+0	1.5874E+0	-7.5892E-1
14	1.8930E-2	2.4090E+0	9.2500E-1	-3.5715E+0	1.0756E+0	-4.9993E-1
15	2.0160E-2	2.4470E+0	9.3016E-1	-2.2137E+0	6.5170E-1	-2.9857E-1
16	2.1470E-2	2.4930E+0	9.3702E-1	-1.6942E+0	4.8594E-1	-2.1872E-1
17	2.2830E-2	2.5000E+0	9.3692E-1	-6.5568E-1	1.8734E-1	-8.4246E-2
18	2.4150E-2	2.5170E+0	9.3910E-1	-2.9064E-1	8.2272E-2	-3.6905E-2
19	2.5550E-2	2.5300E+0	9.3950E-1	-1.3800E-1	3.8762E-2	-1.7308E-2
20	2.6930E-2	2.5230E+0	9.3851E-1	-4.5419E-2	1.2805E-2	-5.7634E-3
21	2.8320E-2	2.5380E+0	9.4109E-1	4.2275E-3	-1.1819E-3	5.3255E-4
22	2.9710E-2	2.5300E+0	9.4050E-1	2.5979E-3	-7.2966E-4	3.3303E-4



87020305 Jayaram/Formica/Smits Turbulence Data

X = 1.2700E-02 UTAU = 2.0436E+01 RHOW = 3.2541E-01 UINF = 5.9160E+02 HUEW = 1.7948E-05

I	Y	M	U UINF	(RU)' RW UT	R U'2 RW UT2	U'2 UT2
1	5.2000E-3	1.8640E+0	8.1890E-1	5.1275E+0	3.1713E+0	1.9720E+0
2	6.5300E-3	1.9680E+0	8.4464E-1	5.0592E+0	2.6352E+0	1.5945E+0
3	8.0400E-3	2.0460E+0	8.6220E-1	5.0366E+0	2.3313E+0	1.3887E+0
4	9.6200E-3	2.1840E+0	8.9194E-1	5.2658E+0	2.0651E+0	1.1827E+0
5	1.1120E-2	2.2610E+0	9.0541E-1	5.6811E+0	2.1500E+0	1.2112E+0
6	1.2630E-2	2.3820E+0	9.2875E-1	5.7750E+0	1.8442E+0	9.9686E-1
7	1.4210E-2	2.4410E+0	9.3714E-1	5.8363E+0	1.7027E+0	8.9275E-1
8	1.5810E-2	2.5320E+0	9.5140E-1	6.0309E+0	1.5628E+0	7.8436E-1
9	1.7400E-2	2.5900E+0	9.5999E-1	6.3159E+0	1.5579E+0	7.6089E-1
10	1.8970E-2	2.6940E+0	9.7495E-1	6.3935E+0	1.3517E+0	6.2954E-1
11	2.0540E-2	2.7380E+0	9.8004E-1	6.1585E+0	1.1686E+0	5.3246E-1
12	2.2120E-2	2.7940E+0	9.8671E-1	5.9643E+0	1.0020E+0	4.4436E-1
13	2.3720E-2	2.8300E+0	9.9042E-1	5.6159E+0	8.3812E-1	3.6499E-1
14	2.5340E-2	2.8430E+0	9.9142E-1	4.9669E+0	6.4161E-1	2.7743E-1
15	2.6920E-2	2.8680E+0	9.9311E-1	4.4394E+0	4.9192E-1	2.0978E-1
16	2.8530E-2	2.8780E+0	9.9501E-1	3.0819E+0	2.3350E-1	9.9232E-2
17	3.0160E-2	2.8810E+0	9.9541E-1	2.2726E+0	1.2640E-1	5.3641E-2
18	3.1760E-2	2.8830E+0	9.9551E-1	1.8119E+0	8.0187E-2	3.4002E-2
19	3.3260E-2	2.8720E+0	9.9451E-1	1.3974E+0	4.8475E-2	2.0664E-2
20	3.4790E-2	2.8720E+0	9.9361E-1	1.2169E+0	3.6753E-2	1.5646E-2
21	3.6340E-2	2.8700E+0	9.9381E-1	8.1174E-1	1.6398E-2	6.9916E-3
22	3.7860E-2	2.8700E+0	9.9412E-1	7.4406E-1	1.3787E-2	5.8819E-3
23	3.9400E-2	2.8700E+0	9.9371E-1	7.6323E-1	1.4492E-2	6.1776E-3

87020307 Jayaram/Formica/Smits Turbulence Data

X = 5.0800E-02 UTAU = 1.9205E+01 RHOW = 4.4112E-01 UINF = 5.9160E+02 HUEW = 1.7921E-05

I	Y	M	U UINF	(RU)' RW UT	R U'2 RW UT2	U'2 UT2
1	2.7400E-3	1.4380E+0	6.9314E-1	5.8676E+0	8.0294E+0	5.6303E+0
2	4.1100E-3	1.5670E+0	7.3257E-1	6.3245E+0	7.4912E+0	4.9609E+0
3	5.6100E-3	1.6850E+0	7.6950E-1	6.1705E+0	5.8895E+0	3.7444E+0
4	7.1000E-3	1.8090E+0	8.0156E-1	6.4384E+0	5.1982E+0	3.1319E+0
5	8.6100E-3	1.9200E+0	8.3053E-1	6.3799E+0	4.2340E+0	2.4382E+0
6	1.0100E-2	2.0100E+0	8.5045E-1	6.9151E+0	4.2593E+0	2.3526E+0
7	1.1610E-2	2.1500E+0	8.8101E-1	7.1402E+0	3.6359E+0	1.9113E+0
8	1.3130E-2	2.2830E+0	9.0660E-1	7.3460E+0	3.2242E+0	1.6706E+0
9	1.4510E-2	2.3870E+0	9.2512E-1	7.0666E+0	2.5260E+0	1.3587E+0
10	1.6120E-2	2.4720E+0	9.3975E-1	6.6281E+0	2.1241E+0	1.1179E+0
11	1.7640E-2	2.5620E+0	9.5289E-1	6.1722E+0	1.6791E+0	8.9435E-1
12	1.9140E-2	2.6070E+0	9.5937E-1	5.1798E+0	1.1650E+0	6.4471E-1
13	2.0710E-2	2.6880E+0	9.7022E-1	4.1063E+0	6.8584E-1	3.9016E-1
14	2.2280E-2	2.8050E+0	9.8615E-1	3.3731E+0	4.1330E-1	2.3937E-1
15	2.3880E-2	2.8900E+0	9.9660E-1	2.6162E+0	2.2993E-1	1.3515E-1
16	2.5500E-2	2.8900E+0	9.9471E-1	1.9785E+0	1.3144E-1	7.7270E-2
17	2.7090E-2	2.9000E+0	9.9561E-1	1.4805E+0	7.2466E-2	4.2392E-2
18	2.8610E-2	2.9060E+0	9.9660E-1	1.0399E+0	3.5460E-2	2.0706E-2
19	3.0160E-2	2.9000E+0	9.9561E-1	9.4644E-1	2.9605E-2	1.7316E-2
20	3.1680E-2	2.9000E+0	9.9561E-1	6.0139E-1	1.1957E-2	6.9941E-3
21	3.3120E-2	2.9000E+0	9.9561E-1	5.8257E-1	1.1223E-2	6.5643E-3
22	3.4640E-2	2.9000E+0	9.9561E-1	5.4580E-1	9.8457E-3	5.7592E-3
23	3.6160E-2	2.9000E+0	9.9561E-1	5.3747E-1	9.5443E-3	5.5823E-3
24	3.7710E-2	2.9000E+0	9.9561E-1	5.3847E-1	9.5885E-3	5.6087E-3
25	3.9250E-2	2.9000E+0	9.9561E-1	5.5743E-1	1.0266E-2	6.0037E-3

87020309 Jayaram/Formica/Smits Turbulence Data

X = 1.1430E-01 UTAU = 1.9686E+01 RHOW = 4.9207E-01 UINF = 5.9160E+02 HUEW = 1.7791E-05

I	Y	M	U UINF	(RU)' RW UT	R U'2 RW UT2	U'2 UT2
1	2.4300E-3	1.4450E+0	6.9167E-1	5.7675E+0	7.7224E+0	5.4437E+0
2	3.8150E-3	1.5000E+0	7.1070E-1	6.0602E+0	7.7884E+0	5.3688E+0
3	5.3330E-3	1.6070E+0	7.4311E-1	6.5760E+0	7.7291E+0	5.1366E+0
4	6.8640E-3	1.7110E+0	7.7077E-1	6.7422E+0	6.7825E+0	4.2991E+0
5	8.3600E-3	1.8290E+0	8.0357E-1	7.4949E+0	6.8877E+0	4.1655E+0
6	9.9130E-3	1.8710E+0	8.1256E-1	7.5001E+0	6.3847E+0	3.7684E+0
7	1.1410E-2	1.9790E+0	8.3876E-1	7.8361E+0	5.7968E+0	3.2631E+0
8	1.2930E-2	2.1120E+0	8.6899E-1	8.3112E+0	5.2116E+0	2.7674E+0
9	1.4530E-2	2.1870E+0	8.8277E-1	8.2919E+0	4.5509E+0	2.3267E+0
10	1.6150E-2	2.2690E+0	8.9823E-1	8.0023E+0	3.6933E+0	1.8201E+0
11	1.7740E-2	2.3510E+0	9.1320E-1	7.6660E+0	2.9665E+0	1.4114E+0
12	1.9260E-2	2.4270E+0	9.2599E-1	7.1414E+0	2.2748E+0	1.0477E+0
13	2.0800E-2	2.4740E+0	9.3204E-1	5.9586E+0	1.4738E+0	6.6715E-1
14	2.2320E-2	2.5000E+0	9.3511E-1	5.0481E+0	1.0170E+0	4.5652E-1
15	2.3850E-2	2.5100E+0	9.3650E-1	3.3699E+0	4.4848E-1	2.0165E-1
16	2.5370E-2	2.5300E+0	9.3759E-1	2.6084E+0	2.6024E-1	1.1599E-1
17	2.6920E-2	2.5230E+0	9.3640E-1	1.8259E+0	1.2962E-1	5.8274E-2
18	2.8450E-2	2.5400E+0	9.3937E-1	9.7308E-1	3.6178E-2	1.6289E-2
19	2.9900E-2	2.5300E+0	9.3818E-1	8.5829E-1	2.8856E-2	1.3169E-2

87020501

Jayaram/Formica/Smits

Turbulence Data

X = -6.3500E-02 UTAU = 2.2657E+01 RHO = 2.8617E-01 UINF = 5.8099E+02 MUEW = 1.7482E-05

I	Y	M	U UINF	(RU)' RW UT	R U'2 RW UT2	U'2 UT2
1	1.9800E-3	1.6430E+0	7.6070E-1	5.9004E+0	5.8962E+0	3.8888E+0
2	2.7470E-3	1.7370E+0	7.8766E-1	5.1453E+0	3.8099E+0	2.4050E+0
3	3.6930E-3	1.8210E+0	8.1045E-1	5.3769E+0	3.5801E+0	2.1656E+0
4	4.5460E-3	1.8960E+0	8.2945E-1	5.6597E+0	3.5280E+0	2.0869E+0
5	5.1350E-3	1.9470E+0	8.4179E-1	5.7644E+0	3.3790E+0	1.9664E+0
6	5.5080E-3	1.9750E+0	8.4836E-1	5.7528E+0	3.2174E+0	1.8542E+0
7	6.1640E-3	2.0130E+0	8.5712E-1	5.6888E+0	2.9535E+0	1.6763E+0
8	6.5940E-3	2.0400E+0	8.6328E-1	5.9582E+0	3.0971E+0	1.7387E+0
9	7.4520E-3	2.0890E+0	8.7373E-1	6.0331E+0	2.9230E+0	1.6044E+0
10	7.8870E-3	2.1170E+0	8.7980E-1	6.1653E+0	2.9068E+0	1.5753E+0
11	8.3310E-3	2.1470E+0	8.8607E-1	6.2422E+0	2.8386E+0	1.5199E+0
12	9.3270E-3	2.2100E+0	8.9901E-1	6.5035E+0	2.7775E+0	1.4493E+0
13	1.0130E-2	2.2530E+0	9.0697E-1	6.5832E+0	2.6501E+0	1.3566E+0
14	1.1000E-2	2.2980E+0	9.1542E-1	6.9048E+0	2.7003E+0	1.3523E+0
15	1.1810E-2	2.3400E+0	9.2289E-1	7.0026E+0	2.5890E+0	1.2714E+0
16	1.2510E-2	2.3780E+0	9.2935E-1	7.3012E+0	2.6447E+0	1.2767E+0
17	1.3390E-2	2.4280E+0	9.3791E-1	7.5213E+0	2.5783E+0	1.2136E+0
18	1.4400E-2	2.4760E+0	9.4587E-1	7.6083E+0	2.4328E+0	1.1184E+0
19	1.5350E-2	2.5140E+0	9.5154E-1	7.5864E+0	2.2730E+0	1.0264E+0
20	1.6370E-2	2.5680E+0	9.5990E-1	7.8024E+0	2.2012E+0	9.6943E-1
21	1.7390E-2	2.6230E+0	9.6796E-1	7.8953E+0	2.0630E+0	8.8658E-1
22	1.8400E-2	2.6700E+0	9.7443E-1	7.8582E+0	1.9014E+0	8.0169E-1
23	1.9350E-2	2.7160E+0	9.8070E-1	7.5290E+0	1.6279E+0	6.7480E-1
24	2.0290E-2	2.7550E+0	9.8577E-1	7.3745E+0	1.4746E+0	6.0302E-1
25	2.1300E-2	2.7920E+0	9.9015E-1	6.7243E+0	1.1611E+0	4.6868E-1
26	2.2330E-2	2.8270E+0	9.9413E-1	6.4468E+0	1.0146E+0	4.0442E-1
27	2.3280E-2	2.8520E+0	9.9702E-1	5.2277E+0	6.4331E-1	2.5434E-1
28	2.4300E-2	2.8720E+0	9.9901E-1	4.9794E+0	5.6682E-1	2.2247E-1
29	2.5310E-2	2.8840E+0	1.0000E+0	4.0715E+0	3.7327E-1	1.4611E-1
30	2.6320E-2	2.8910E+0	1.0000E+0	3.7138E+0	3.0792E-1	1.2047E-1
D 31	2.7480E-2	2.8990E+0	1.0000E+0	2.5041E+0	1.3741E-1	5.3244E-2
32	2.8490E-2	2.9070E+0	1.0010E+0	1.7852E+0	6.9322E-2	2.6882E-2
33	2.9500E-2	2.9080E+0	1.0010E+0	1.5898E+0	5.5138E-2	2.1473E-2

87020507

Jayaram/Formica/Smits

Turbulence Data

X = 1.5240E-01 UTAU = 1.8402E+01 RHO = 8.1092E-01 UINF = 5.8099E+02 MUEW = 1.7764E-05

I	Y	M	U UINF	(RU)' RW UT	R U'2 RW UT2	U'2 UT2
1	5.9500E-3	1.4990E+0	7.1647E-1	9.3149E+0	1.9085E+1	1.3621E+1
2	6.8290E-3	1.5420E+0	7.2996E-1	9.8870E+0	2.0162E+1	1.4240E+1
3	7.9020E-3	1.5950E+0	7.4594E-1	1.0360E+1	2.0330E+1	1.4105E+1
4	9.0010E-3	1.6590E+0	7.6502E-1	1.0678E+1	1.9441E+1	1.3179E+1
5	1.0090E-2	1.7280E+0	7.8460E-1	1.1471E+1	2.0002E+1	1.3187E+1
6	1.1200E-2	1.8040E+0	8.0498E-1	1.1191E+1	1.6736E+1	1.0684E+1
7	1.2270E-2	1.8910E+0	8.2706E-1	1.1914E+1	1.6380E+1	1.0078E+1
8	1.3350E-2	1.9650E+0	8.4494E-1	1.0912E+1	1.2112E+1	7.2162E+0
9	1.4450E-2	2.0380E+0	8.6182E-1	9.8586E+0	8.7442E+0	5.0464E+0
10	1.5540E-2	2.0930E+0	8.7371E-1	1.0072E+1	8.3042E+0	4.6737E+0
11	1.6640E-2	2.1440E+0	8.8420E-1	8.4814E+0	5.4157E+0	2.9840E+0
12	1.7650E-2	2.1730E+0	8.8980E-1	6.9160E+0	3.4323E+0	1.8697E+0
D 13	1.8650E-2	2.1980E+0	8.9439E-1	5.8288E+0	2.3456E+0	1.2671E+0
14	1.9680E-2	2.2130E+0	8.9679E-1	4.0215E+0	1.0895E+0	5.8490E-1
15	2.0720E-2	2.2230E+0	8.9829E-1	3.0638E+0	6.2329E-1	3.3389E-1
16	2.1800E-2	2.2270E+0	8.9849E-1	2.3509E+0	3.6542E-1	1.9587E-1
17	2.2880E-2	2.2310E+0	8.9869E-1	1.6565E+0	1.8056E-1	9.6769E-2
18	2.3840E-2	2.2340E+0	8.9889E-1	1.4357E+0	1.3535E-1	7.2690E-2
19	2.4850E-2	2.2350E+0	8.9839E-1	7.0988E-1	3.3125E-2	1.7828E-2

87020511

Jayaram/Formica/Smits

Turbulence Data

X = 2.5400E-01 UTAU = 2.0336E+01 RHO = 8.3301E-01 UINF = 5.8099E+02 MUZW = 1.7905E-05

I	Y	M	U UINF	(RU)' RW UT	R U'2 RW UT2	U'2 UT2
1	1.1900E-3	1.3490E+0	6.7158E-1	1.0659E+1	3.1309E+1	2.3236E+1
2	2.1000E-3	1.4730E+0	7.1496E-1	6.7965E+0	1.0476E+1	7.4681E+0
3	3.2020E-3	1.5350E+0	7.3509E-1	6.0308E+0	7.4702E+0	5.2131E+0
4	4.3020E-3	1.5650E+0	7.4405E-1	6.3117E+0	7.7976E+0	5.3861E+0
5	5.3810E-3	1.5990E+0	7.5421E-1	6.3939E+0	7.6562E+0	5.2789E+0
6	6.4670E-3	1.6200E+0	7.6015E-1	6.5313E+0	7.7827E+0	5.3671E+0
7	7.5860E-3	1.6600E+0	7.7183E-1	6.6220E+0	7.5148E+0	5.1248E+0
8	8.6790E-3	1.6800E+0	7.7747E-1	6.7000E+0	7.4627E+0	5.0618E+0
9	9.7750E-3	1.7160E+0	7.8723E-1	7.1920E+0	8.0952E+0	5.4123E+0
10	1.0840E-2	1.7470E+0	7.9538E-1	7.2790E+0	7.8794E+0	5.2049E+0
11	1.1930E-2	1.7900E+0	8.0686E-1	7.4448E+0	7.6636E+0	4.9735E+0
12	1.3000E-2	1.8230E+0	8.1531E-1	7.3191E+0	7.1554E+0	4.6774E+0
13	1.4090E-2	1.8710E+0	8.2749E-1	6.5310E+0	6.1205E+0	4.5661E+0
14	1.5200E-2	1.9190E+0	8.3907E-1	5.7307E+0	5.0334E+0	4.2615E+0
15	1.6270E-2	1.9660E+0	8.5014E-1	5.1356E+0	4.2879E+0	4.0862E+0
16	1.7370E-2	2.0030E+0	8.5849E-1	4.0807E+0	2.8951E+0	3.0938E+0
17	1.8450E-2	2.0470E+0	8.6826E-1	3.5978E+0	2.3512E+0	2.7720E+0
18	1.9540E-2	2.0710E+0	8.7309E-1	3.3320E+0	2.1607E+0	2.8129E+0
19	2.0650E-2	2.1090E+0	8.8084E-1	2.8154E+0	1.5297E+0	2.0702E+0
20	2.1740E-2	2.1250E+0	8.8386E-1	2.1247E+0	8.8169E-1	1.2312E+0
21	2.2840E-2	2.1410E+0	8.8688E-1	1.8124E+0	6.0758E-1	8.2046E-1
22	2.3930E-2	2.1580E+0	8.8960E-1	1.6831E+0	5.0535E-1	6.7176E-1
23	2.5000E-2	2.1620E+0	8.8980E-1	1.2211E+0	2.6190E-1	3.4443E-1
24	2.6070E-2	2.1650E+0	8.8990E-1	9.1950E-1	1.4739E-1	1.9313E-1
25	2.7150E-2	2.1650E+0	8.8929E-1	6.2369E-1	6.7946E-2	8.9206E-2
26	2.8260E-2	2.1650E+0	8.8859E-1	6.6694E-1	7.7604E-2	1.0176E-1
27	2.9350E-2	2.1650E+0	8.8788E-1	4.6647E-1	3.7961E-2	4.9770E-2
28	3.0450E-2	2.1610E+0	8.8688E-1	3.9573E-1	2.7559E-2	3.6279E-2
29	3.1540E-2	2.1570E+0	8.8587E-1	3.2891E-1	1.9174E-2	2.5288E-2
30	3.2630E-2	2.1530E+0	8.8507E-1	2.4158E-1	1.0424E-2	1.3791E-2

## 13. REFERENCES FOR CHAPTERS 1 AND 9 TO 12

H.H. Fernholz

- Abbis J.B., East L.F., Nash C.R. et al., 1976, A study of the interaction of a normal shock-wave and a turbulent boundary layer using a laser anemometer. RAE Tr-75 141.
- Ackeret J., Feldmann F., Rott N., 1946, Untersuchungen an Verdichtungsstößen und Grenzschichten in schnell bewegten Gasen. Inst. f. Aerodynamik ETH Zürich.
- Allen J.M., 1973, Evaluation of Preston-tube calibration equations in supersonic flow. AIAA J. 11, 1461-1463 and NASA TN D-7190.
- Allen J.M., 1977, Re-evaluation of compressible flow Preston-tube calibrations. NASA TM X-3488 and J. Fluid Engrg. 99, 197.
- Ardonceanu P., 1981, Etude de l'interaction onde de choc couche limite supersonique. Thèse Université de Poitiers.
- Ardonceanu P.L., 1984, The structure of turbulence in a supersonic shock-wave boundary-layer interaction. AIAA J. 22, 1264-1262.
- Bradshaw P., 1973, Effects of streamline curvature on turbulent flow. AGARDograph-AG-169.
- Bradshaw P., 1974, The effect of mean compression or dilatation on the turbulence structure of supersonic boundary layers. J. Fluid Mech. 63, 449-464.
- Bradshaw P., Unsworth K., 1973, A note on Preston tube calibrations in compressible flow. Imperial College London, Aero Rep. 73-07.
- Bradshaw P., Unsworth K., 1974, Comment on "Evaluation of Preston-tube calibration equations in supersonic flow". AIAA J. 12, 1293-1296.
- Brown J.D., Brown J.L., Kussoy M.I., Holt M., Horstmann C.C., 1987, Two component LDV investigation of three-dimensional shock/ turbulent boundary layer interactions. AIAA Paper 87-0553.
- Brown K.C., Joubert P.N., 1969, The measurement of skin friction in turbulent boundary layers with adverse pressure gradient. J. Fluid Mech. 35, 737-758.
- Chew Y.T., 1978, Two-parameter skin friction formula for adiabatic compressible flow. AIAA J. 16, 186-188.
- Chew Y.T., Squire L.C., 1979, The boundary layer development downstream of a shock interaction at an expansion corner. Aero. Res. Council. R+M 3839, London.
- Copy C., Reisz J., 1980, Analyse expérimentale d'une interaction choc-couche limite turbulente à Mach 1.30 (décollement naissant). ONERA Rapport Technique No 42/7078 AY 014, No 44/7078 AY014 and No 59/7078 AN (1983).
- Debiève J.F., 1983, Etude d'une interaction turbulence onde de choc. Thèse Université d'Aix Marseille II.
- Debiève J.F., Gouin H., Gaviglio J., 1981, Momentum and temperature fluxes in a shock wave-turbulence interaction. Proc. ICHMT/IUTAM Symp. on the Structure of Turbulence and Heat and Mass Transfer, Dubrovnik.
- Délery J.M., 1983, Experimental investigation of turbulence properties in transonic shock boundary layer interactions. AIAA J. 21, 180-185 and ONERA TP 1983-157.
- Délery J.M., 1985, Shock wave/ turbulent boundary-layer interaction and its control. Progr. Aerospace Scie. 22, 209-280.
- Délery J.M. (Editor), 1986, Turbulent shear-layer/ shock-wave interactions. IUTAM Symp. Palaiseau, Springer Verlag Berlin.
- Délery J.M., Marvin J.G., 1986, Shock-wave boundary layer interactions. AGARDograph-AG-280.
- Délery J.M., Copy C., Reisz J., 1980, Analyse au vélocimètre laser bidirectionnel d'une interaction choc-couche limite turbulente avec décollement étendu. ONERA Rapport Technique No 37/7078 AY 014.

- Dolling D.S., Murphy M.T., 1983, Understeadiness of the separation shock-wave structure in a supersonic compression ramp flowfield. *AIAA J.* 21, 1628-1634.
- Donovan J.F., 1988, The structure of a supersonic turbulent boundary layer subjected to concave surface curvature. Ph.D. thesis. Princeton University. Dept. Mech. & Aerospace Engineering.
- Donovan J.F., Smits A.J., 1987, A preliminary investigation of large-scale organized motions in a supersonic turbulent boundary layer on a curved surface. *AIAA-87-1285*.
- Dussauge J.P., 1981, Evolution de transferts turbulents dans une détente rapide en écoulement supersonique. Thèse d'Etat, Univ. d'Aix Marseille II.
- Dussauge J.P., 1985, Expansion/ turbulent boundary layer interaction - recapitulation of experimental data. IMST U.A. C.R.N.S. No 130.
- Dussauge J.P., Gaviglio J., 1987, The rapid expansion of a supersonic turbulent flow: role of bulk dilatation. *J. Fluid. Mech.* 174, 81-112.
- East L.F., 1976, The application of a Laser anemometer to the investigation of shock-wave boundary layer interactions. *AGARD/ CP-193*.
- Fenter F.W., Stalmach D.J., 1957, The measurement of local turbulent skin friction at supersonic speeds by means of surface impact pressure probes. Rep. No DRL-392, CM-878.
- Fernando E.M., 1988, The effects of an adverse pressure gradient on a flat plate supersonic turbulent boundary layer. Ph.D. thesis. Princeton University. Dept. Mech. & Aerospace Engineering.
- Fernando E.M., Smits A.J., 1986, A data compilation for a supersonic turbulent boundary layer under conditions of an adverse pressure gradient. *MAE Rep.* 1746, Princeton Univ.
- Fernando E.M., Smits A.J., 1987, The effects of an adverse pressure gradient on the behaviour of a flat plate supersonic turbulent boundary layer. *AIAA Paper* 87-1286.
- Fernholz H.H., 1971, Ein halbempirisches Gesetz für die Wandreibung in kompressiblen turbulenten Grenzschichten bei isothermer und adiabater Wand. *ZAMM* 51, T 146-T 147. Since there are two misprints in the original paper the corrected relationships are given here:
- $$\ln (y/\Delta^*)_p \approx -0.404 \ln Re_{\delta_2} + 0.37$$
- $$u_1/U_\delta \approx (0.006501 M_\delta - 0.0296725) \ln \left( \frac{Re_{\delta_2}}{57.84} \right) + 0.705$$
- Fernholz H.H., Finley P.J., 1976, A critical compilation of compressible turbulent boundary layer data. *AGARDograph-AG-223*.
- Fernholz H.H., Finley P.J., 1980, A critical commentary on mean flow data for two-dimensional compressible turbulent boundary layers. *AGARDograph-AG-253*.
- Fernholz H.H., Finley P.J., 1981, A further compilation of compressible boundary layer data with a survey of turbulence data. *AGARDograph-AG-263*.
- Fernholz H.H., Finley P.J., 1983, On the breakdown of the Crocco temperature-velocity relationship and the law of the wall in compressible two-dimensional turbulent boundary layers. *Proc. IUTAM Symp. Marseille (Ed. Dumas). Springer Verlag Berlin*.
- Frei D., Thomann H., 1980, Direct measurement of skin friction in a turbulent boundary layer with a strong adverse pressure gradient. *J. Fluid. Mech.* 101, 79-95.
- Gaviglio J., 1971, Sur la détermination des sensibilités anémothermomètres à fil chaud en écoulement supersonique. *C.R. Acad. Sci. Paris, A* 273, 634-637.
- Gaviglio J., 1978, Sur les méthodes de l'anémothermométrie par fil chaud des écoulements turbulents compressibles de gaz. *J. Méc.* 2 (4), 449-498.
- Green J.E., 1971, Interactions between shock waves and turbulent boundary layers. *Progress in Aeronautical Sciences Vol. II (Ed. D. Küchemann. Pergamon Press)*.
- Hankey W.L., 1967, Prediction of incipient separation in shock boundary layer interactions. *AIAA J.* 5, 355-356.

- Hankey W.L., Holden M.S., 1975, Two-dimensional shock wave boundary-layer interactions in high speed flows. AGARDograph-AQ-203.
- Head M.R., Vasanta Ram V., 1971, Simplified presentation of Preston-tube calibration. The Aeronaut. Quart. XXII. 296-300.
- Hirt F., Thomann K., 1986, Measurements of wall shear stress in turbulent boundary layers subject to strong pressure gradients. J. Fluids Mech. 171, 547-563.
- Hopkins E.J., Keener E.R., 1966, Study of surface Pitots for measuring turbulent skin friction at supersonic Mach numbers - adiabatic wall. NASA TN D 3478, (CAT 6601).
- Jayaram M., Formica J.P., Smits A.J., 1985, Compilation of turbulence data for two concavely curved walls at Mach 2.9. MAE Rep. 1711, Princeton Univ.
- Jayaram M., Taylor M.W., Smits A.J., 1987, The response of a compressible turbulent boundary layer to short regions of concave surface curvature. J. Fluid Mech. 175, 343-362 and MAE Rep. 1737 (1986).
- Johnson D.R., King L.S., 1985, A mathematically simple turbulence closure model for attached and separated turbulent boundary layers. AIAA J. 23, 1684-1692.
- Klebanoff P.S., 1955, Characteristics of turbulence in a boundary layer with zero pressure gradient. NACA Rep. 1247.
- Kline S.J. et. al. (Eds) 1982, Proceedings of the 1980-81 AFOSR-HTTM Stanford Conference on Complex Turbulent Flows. Stanford University, Stanford, California.
- Kooi J.W., 1978, Influence of the free-stream Mach number on transonic shock-wave/ boundary-layer interactions. NLR MP-78013 U.
- Kuntz D.W., Amatucci V.A., Addy A.L., 1987, The turbulent boundary layer properties downstream of the shock wave/ boundary layer interaction. AIAA J. 25, 668-675.
- Kussoy M.I., Horstmann C.C., Acharya M., 1978, An experimental documentation of pressure gradient and Reynolds number effects on compressible turbulent boundary layers. NASA TM 78488, (CAT7802 S).
- Ladermann A.J., 1978, Pressure gradient effects on supersonic boundary layer turbulence. Ford Aerospace & Communications Corp. Aeronutronics Div. Rep. No U-6467. Newport Beach (Cat7803S).
- Lewis J.E., Gran R.L., Kubota T., 1972, An experiment on the adiabatic compressible turbulent boundary layer in adverse and favourable pressure gradient. J. Fluid Mech. 51, 657-672 (Cat7201).
- Liu X., 1985, Shock/ boundary-layer interaction on curved surfaces at transonic speeds. Ph.D. dissertation. Cambridge University, Engineering Department.
- Liu X., Squire L.C., 1985, An experimental investigation of shock/ boundary layer interaction on curved surfaces at transonic speeds (a data report). Cambridge University Engineering Department.
- Liu X., Squire L.C., 1985, An investigation of shock/ boundary layer interactions on curved surfaces at transonic speeds. Private communication and 1988 J. Fluid Mech. 187, 467-486.
- Morkovin M.V., 1956, Fluctuations and hot-wire anemometry in compressible flows. AGARDograph No 24.
- Morkovin M.V., Phinney R.E., 1958, Extended applications of hot-wire anemometry to high speed turbulent boundary layers. Dept. Aeronaut. The Johns Hopkins Univ. ASTIA AD-158-279.
- Muck K.C., Hayakawa K., Smits A.J., 1983, Compilation of turbulence data for a 16° compression corner at Mach 2.9. Princeton Univ. MAE Rep. 1619.
- Muck K.C., Hayakawa K., Smits A.J., 1983, Compilation of turbulence data for a 20° compression corner at Mach 2.9. Princeton Univ. MAE Rep. 1620.
- Muck K.C., Spina E.F., Smits A.J., 1984, Compilation of turbulence data for an 8° compression corner at Mach 2.9. Princeton Univ. MAE Rep. 1642.

- Patel V.C., 1965, Calibration of the Preston tube and limitations on its use in pressure gradients. *J. Fluid Mech.* 23, 185-208.
- Peake D.J., Brakman G., Romeskie J.M., 1971, Comparisons between some high Reynolds number turbulent boundary layer experiments at Mach 4 and various recent calculation procedures. *Nat. Res. Council of Canada and AGARD CP-93-71 Paper II* (Cat 7102).
- Reda D.C., Murphy J.D., 1973, Shock wave/ turbulent boundary-layer interactions in rectangular channels. *AIAA J.* 11, 139-140.
- Reisz J., 1981, Analyse expérimentale d'une interaction choc-couche limite turbulente à Mach 1.45. ONERA Rapport Technique No 44/7078 AY 014.
- Reisz J., 1983, Analyse expérimentale d'une interaction choc-couche limite turbulente à Mach 1.26. ONERA Rapport Technique No 59/7078 AN.
- Rotta J.C., 1959, Über den Einfluß der Machschen Zahl und des Wärmeübergangs auf das Wandgesetz turbulenter Strömungen. *ZfW* 7, 264-274.
- Schofield W.H., 1985, Turbulent boundary-layer development in an adverse pressure gradient after an interaction with a normal shock wave. *J. Fluid Mech.* 154, 43-62.
- Seddon J., 1960, The flow produced by interaction of a turbulent boundary layer with a normal shock wave of strength sufficient to cause separation. *R+M* 3502 London.
- Selig M.S., 1988, Unsteadiness of shock wave/ turbulent boundary-layer interactions with dynamic control. M.Sc. Thesis. Princeton University.
- Selig M.S., Andreopoulos J., Muck K.C., Dussauge J.P. and Smits A.J., 1987, Simultaneous wall-pressure and mass-flux measurements downstream of a shock wave/ turbulent boundary layer interaction. *AIAA Paper 87-0550*. To appear in *AIAA J.* 1988.
- Settles G.S., 1975, An experimental study of compressible turbulent boundary layer separation at high Reynolds numbers. Ph.D. Thesis Princeton Univ.
- Settles G.S., Vas I.E., Bogdonoff S.M., 1976, Details of a shock separated turbulent boundary layer at a compression corner. *AIAA J.* 14, 1709-1716.
- Settles G.S., Fitzpatrick T.J., Bogdonoff S.M., 1979, Detailed study of attached and separated compression corner flow fields in high Reynolds number supersonic flow. *AIAA J.* 17, 579-585.
- Settles G.S., Gilbert R.B., Bogdonoff S.M., 1980, Data compilation for shock wave turbulent boundary layer interaction experiments on 2-D compression corners. Princeton Univ. MAE Rep. 1489.
- Smits A.J., Hayakawa K., Muck K.C., 1983, Constant temperature hot-wire anemometer practice in supersonic flows. *Exp. in Fluids* 1, 83-92.
- Smits A.J., Muck K.C., 1984, Constant temperature hot-wire anemometer practice in supersonic flows. *Exp. in Fluids* 2, 33-41.
- Smits A.J., Muck K.C., 1987, Experimental study of three shock wave/ turbulent boundary layer interactions. *J. Fluid Mech.* 182, 291-314.
- Sommer S.C., Short B.J., 1955, Free-flight measurements of turbulent boundary layer skin friction in the presence of severe aerodynamic heating and Mach number from 2.8 to 7. *NACA TN - 3391* and *J. Aeronaut. Sci.* 23 (1956).
- Spina E.F., 1988, Organized structures in a supersonic turbulent boundary layer. Ph.D. thesis, Princeton University. Dept. Mech. & Aerospace Engineering.
- Spina E.F., Smits A.J., 1987, Organized structures in a supersonic turbulent boundary layer. *J. Fluid Mech.* 182, 85-109 and MAE Rep. 1736, Univ. Princeton (1986).
- Sturek W.B., Danberg J.E., 1971, Supersonic turbulent boundary layer in an adverse pressure gradient. Univ. Delaware TR No 141 (Cat 7101).
- Taylor M.W., 1984, A supersonic turbulent boundary layer on concavely curved surfaces. MAE Rep. 1684, Princeton Univ.

- Taylor M.W., Smits A.J., 1984, The effects of a short region of concave curvature on a supersonic turbulent boundary layer. AIAA Paper 84- 0169.
- Thomas C.D., 1974, Compressible turbulent boundary layers with combined air injection and pressure gradient. ARC R+M 3779 and Ph.D. Thesis Cambridge 1973 (Cat 7401).
- Townsend A.A., 1976, The structure of turbulent shear flow. Second Ed. Cambridge University Press.
- Vas I.E., Settles G.S., Bogdonoff S.M., 1976, An experimental study of the compressible turbulent boundary layer over a wide range of Reynolds number. Princeton University Report (CAT7601).
- Vas I.E., 1972, Flow field measurements using a total temperature probe at hypersonic speeds. AIAA J. 10, 317-323.
- Yanta W.J., Brott D.L., Lee R.L., 1969, An experimental investigation of the Preston tube including effects of heat transfer, compressibility and favourable pressure gradient. AIAA Paper 69-648.
- Zwarts F., 1970, Compressible turbulent boundary layers. Ph.D. Thesis, Mc Gill Univ. Dept. Mech. Eng. (Cat 7007).



# REPORT DOCUMENTATION PAGE

<b>1. Recipient's Reference</b>	<b>2. Originator's Reference</b>	<b>3. Further Reference</b>	<b>4. Security Classification of Document</b>								
	AGARD-AG-315	ISBN 92-838-0506-9	UNCLASSIFIED								
<b>5. Originator</b>	Advisory Group for Aerospace Research and Development North Atlantic Treaty Organization 7 rue Ancelle, 92200 Neuilly sur Seine, France										
<b>6. Title</b>	A SURVEY OF MEASUREMENTS AND MEASURING TECHNIQUES IN RAPIDLY DISTORTED COMPRESSIBLE TURBULENT BOUNDARY LAYERS										
<b>7. Presented at</b>											
<b>8. Author(s)/Editor(s)</b>	H.H. Fernholz, J.P. Dussauge, P.J. Finley, A.J. Smit Edited by E. Reshotko		<b>9. Date</b> May 1989								
<b>10. Author's/Editor's Address</b>	See Flyleaf		<b>11. Pages</b> 250								
<b>12. Distribution Statement</b>	This document is distributed in accordance with AGARD policies and regulations, which are outlined on the Outside Back Covers of all AGARD publications.										
<b>13. Keywords/Descriptors</b>	<table border="0"> <tr> <td>Turbulent boundary layer</td> <td>Pressure measurement</td> </tr> <tr> <td>Compressible flow</td> <td>Determination of stress</td> </tr> <tr> <td>Supersonic flow</td> <td>Shock waves</td> </tr> <tr> <td>Velocity measurement</td> <td></td> </tr> </table>			Turbulent boundary layer	Pressure measurement	Compressible flow	Determination of stress	Supersonic flow	Shock waves	Velocity measurement	
Turbulent boundary layer	Pressure measurement										
Compressible flow	Determination of stress										
Supersonic flow	Shock waves										
Velocity measurement											
<b>14. Abstract</b>	<p>This AGARDograph presents a wide range of recent work on compressible turbulent boundary layers. Special attention has been paid to flows with rapid changes in pressure including flows with shock waves, curved walls and expansions. Recent developments in the theory and experimental practice for these flows are presented. The application of rapid distortion theory to flows traversing expansion and shock waves is reviewed. This is followed by an account of experiments in progress aimed at elucidating the large scale structures present in supersonic boundary layers. The current status of the techniques of Laser-Doppler and Hot Wire anemometry in supersonic flow is discussed, and a new interferometric technique for the determination of wall-stress is described. The use of small pressure transducers to deduce information about the structure of zero pressure-gradient and severely perturbed boundary layers is investigated. Finally there is an extension of the review and data presentation of AGARDographs 223, 253 and 263 to cover some of the experiments dealing with rapidly distorted boundary layers.</p> <p>This AGARDograph has been produced at the request of the Fluid Dynamics Panel of AGARD.</p>										

<p>AGARDograph No. 315 Advisory Group for Aerospace Research and Development, NATO</p> <p>A SURVEY OF MEASUREMENTS AND MEASURING TECHNIQUES IN RAPIDLY DISTORTED COMPRESSIBLE TURBULENT BOUNDARY LAYERS</p> <p>by H.H.Fernholz, J.P.Dussauge, P.J.Finley and A.J.Smits</p> <p>Edited by E.Reshotko</p> <p>Published May 1989</p> <p>250 pages</p> <p>This AGARDograph presents a wide range of recent work on compressible turbulent boundary layers. Special attention has been paid to flows with rapid changes in</p> <p>P.T.O.</p>	<p>AGARD-AG-315</p> <p>Turbulent boundary layer Compressible flow Supersonic flow Velocity measurement Pressure measurement Determination of stress Shock waves</p>	<p>AGARDograph No. 315 Advisory Group for Aerospace Research and Development, NATO</p> <p>A SURVEY OF MEASUREMENTS AND MEASURING TECHNIQUES IN RAPIDLY DISTORTED COMPRESSIBLE TURBULENT BOUNDARY LAYERS</p> <p>by H.H.Fernholz, J.P.Dussauge, P.J.Finley and A.J.Smits</p> <p>Edited by E.Reshotko</p> <p>Published May 1989</p> <p>250 pages</p> <p>This AGARDograph presents a wide range of recent work on compressible turbulent boundary layers. Special attention has been paid to flows with rapid changes in</p> <p>P.T.O.</p>	<p>AGARD-AG-315</p> <p>Turbulent boundary layer Compressible flow Supersonic flow Velocity measurement Pressure measurement Determination of stress Shock waves</p>
<p>AGARDograph No. 315 Advisory Group for Aerospace Research and Development, NATO</p> <p>A SURVEY OF MEASUREMENTS AND MEASURING TECHNIQUES IN RAPIDLY DISTORTED COMPRESSIBLE TURBULENT BOUNDARY LAYERS</p> <p>by H.H.Fernholz, J.P.Dussauge, P.J.Finley and A.J.Smits</p> <p>Edited by E.Reshotko</p> <p>Published May 1989</p> <p>250 pages</p> <p>This AGARDograph presents a wide range of recent work on compressible turbulent boundary layers. Special attention has been paid to flows with rapid changes in</p> <p>P.T.O.</p>	<p>AGARD-AG-315</p> <p>Turbulent boundary layer Compressible flow Supersonic flow Velocity measurement Pressure measurement Determination of stress Shock waves</p>	<p>AGARDograph No. 315 Advisory Group for Aerospace Research and Development, NATO</p> <p>A SURVEY OF MEASUREMENTS AND MEASURING TECHNIQUES IN RAPIDLY DISTORTED COMPRESSIBLE TURBULENT BOUNDARY LAYERS</p> <p>by H.H.Fernholz, J.P.Dussauge, P.J.Finley and A.J.Smits</p> <p>Edited by E.Reshotko</p> <p>Published May 1989</p> <p>250 pages</p> <p>This AGARDograph presents a wide range of recent work on compressible turbulent boundary layers. Special attention has been paid to flows with rapid changes in</p> <p>P.T.O.</p>	<p>AGARD-AG-315</p> <p>Turbulent boundary layer Compressible flow Supersonic flow Velocity measurement Pressure measurement Determination of stress Shock waves</p>

<p>pressure including flows with shock waves, curved walls and expansions. Recent developments in the theory and experimental practice for these flows are presented. The application of rapid distortion theory to flows traversing expansions and shock waves is reviewed. This is followed by an account of experiments in progress aimed at elucidating the large scale structures present in supersonic boundary layers. The current status of the techniques of Laser-Doppler and Hot Wire anemometry in supersonic flow is discussed, and a new interferometric technique for the determination of wall-stress is described. The use of small pressure transducers to deduce information about the structure of zero pressure-gradient and severely perturbed boundary layers is investigated. Finally there is an extension of the review and data presentation of AGARDographs 223, 253 and 263 to cover some of the experiments dealing with rapidly distorted boundary layers.</p> <p>This AGARDograph has been produced at the request of the Fluid Dynamics Panel of AGARD.</p> <p>ISBN 92-835-0506-9</p>	<p>pressure including flows with shock waves, curved walls and expansions. Recent developments in the theory and experimental practice for these flows are presented. The application of rapid distortion theory to flows traversing expansions and shock waves is reviewed. This is followed by an account of experiments in progress aimed at elucidating the large scale structures present in supersonic boundary layers. The current status of the techniques of Laser-Doppler and Hot Wire anemometry in supersonic flow is discussed, and a new interferometric technique for the determination of wall-stress is described. The use of small pressure transducers to deduce information about the structure of zero pressure-gradient and severely perturbed boundary layers is investigated. Finally there is an extension of the review and data presentation of AGARDographs 223, 253 and 263 to cover some of the experiments dealing with rapidly distorted boundary layers.</p> <p>This AGARDograph has been produced at the request of the Fluid Dynamics Panel of AGARD.</p> <p>ISBN 92-835-0506-9</p>
<p>pressure including flows with shock waves, curved walls and expansions. Recent developments in the theory and experimental practice for these flows are presented. The application of rapid distortion theory to flows traversing expansions and shock waves is reviewed. This is followed by an account of experiments in progress aimed at elucidating the large scale structures present in supersonic boundary layers. The current status of the techniques of Laser-Doppler and Hot Wire anemometry in supersonic flow is discussed, and a new interferometric technique for the determination of wall-stress is described. The use of small pressure transducers to deduce information about the structure of zero pressure-gradient and severely perturbed boundary layers is investigated. Finally there is an extension of the review and data presentation of AGARDographs 223, 253 and 263 to cover some of the experiments dealing with rapidly distorted boundary layers.</p> <p>This AGARDograph has been produced at the request of the Fluid Dynamics Panel of AGARD.</p> <p>ISBN 92-835-0506-9</p>	<p>pressure including flows with shock waves, curved walls and expansions. Recent developments in the theory and experimental practice for these flows are presented. The application of rapid distortion theory to flows traversing expansions and shock waves is reviewed. This is followed by an account of experiments in progress aimed at elucidating the large scale structures present in supersonic boundary layers. The current status of the techniques of Laser-Doppler and Hot Wire anemometry in supersonic flow is discussed, and a new interferometric technique for the determination of wall-stress is described. The use of small pressure transducers to deduce information about the structure of zero pressure-gradient and severely perturbed boundary layers is investigated. Finally there is an extension of the review and data presentation of AGARDographs 223, 253 and 263 to cover some of the experiments dealing with rapidly distorted boundary layers.</p> <p>This AGARDograph has been produced at the request of the Fluid Dynamics Panel of AGARD.</p> <p>ISBN 92-835-0506-9</p>

**AGARD**  
**NATO OTAN**  
 7 rue Ancelle - 92200 NEUILLY-SUR-SEINE  
 FRANCE

Telephone (1)47.28.57.00 - Telex 910 178

**DISTRIBUTION OF UNCLASSIFIED  
 AGARD PUBLICATIONS**

AGARD does NOT hold stocks of AGARD publications at the above address for general distribution. Initial distribution of AGARD publications is made to AGARD Member Nations through the following National Distribution Centres. Further copies are sometimes available from these Centres, but if not may be purchased in Microfilm or Photocopy form from the Purchase Agencies listed below.

**NATIONAL DISTRIBUTION CENTRES**

**BELGIUM**

Coordonnateur AGARD - VSL  
 Etat-Major de la Force Aérienne  
 Quartier Reine Elisabeth  
 Rue d'Evere, 1140 Bruxelles

**CANADA**

Director Scientific Information Services  
 Dept of National Defence  
 Ottawa, Ontario K1A 0K2

**DENMARK**

Danish Defence  
 Ved Idraetspal  
 2100 Copenhagen

**FRANCE**

O.N.E.R.A. (C  
 29 Avenue de  
 92320 Châtill

**GERMANY**

Fachinformat  
 Physik, Math  
 Karlsruhe  
 D-7514 Egge

**GREECE**

Hellenic Air  
 Aircraft Supp  
 Department  
 Holargos, At

**ICELAND**

Director of A  
 c/o Flugrad  
 Reyjavik

**ITALY**

Aeronautica Militare  
 Ufficio del Delegato Nazionale all'AGARD  
 3 Piazzale Adenauer  
 00144 Roma/EUR

**LUXEMBOURG**

See Belgium

**NETHERLANDS**

Netherlands Delegation to AGARD  
 National Aerospace Laboratory, NLR  
 P.O. Box 126  
 2600 AC Delft

**NORWAY**

Norwegian Defence Research Establishment  
 Arm: Biblioteket



National Aeronautics and  
 Space Administration

Washington, D.C.  
 20546

**SPECIAL FOURTH CLASS MAIL  
 BOOK**

Postage and Fees Paid  
 National Aeronautics and  
 Space Administration  
 NASA-451

Official Business  
 Penalty for Private Use \$300



L1 001 AGARDAG315890725S002672D  
 DEPT OF DEFENSE  
 DEFENSE TECHNICAL INFORMATION CENTER  
 DTIC-FDAC  
 CAMERON STATION BLDG 5  
 ALEXANDRIA VA 223046145

Glasgow G2 8EA

**UNITED STATES**

National Aeronautics and Space Administration (NASA)  
 Langley Research Center  
 M/S 180  
 Hampton, Virginia 23665

**THE UNITED STATES NATIONAL DISTRIBUTION CENTRE (NASA) DOES NOT HOLD  
 STOCKS OF AGARD PUBLICATIONS, AND APPLICATIONS FOR COPIES SHOULD BE MADE  
 DIRECT TO THE NATIONAL TECHNICAL INFORMATION SERVICE (NTIS) AT THE ADDRESS BELOW.**

**PURCHASE AGENCIES**

National Technical  
 Information Service (NTIS)  
 5285 Port Royal Road  
 Springfield  
 Virginia 22161, USA

ESA/Information Retrieval Service  
 European Space Agency  
 10, rue Mario Nikis  
 75015 Paris, France

The British Library  
 Document Supply Centre  
 Boston Spa, Wetherby  
 West Yorkshire LS23 7BQ  
 England

Requests for microfiche or photocopies of AGARD documents should include the AGARD serial number, title, author or editor, and publication date. Requests to NTIS should include the NASA accession report number. Full bibliographical references and abstracts of AGARD publications are given in the following journals:

Scientific and Technical Aerospace Reports (STAR)  
 published by NASA Scientific and Technical  
 Information Branch  
 NASA Headquarters (MIT-40)  
 Washington D.C. 20546, USA

Government Reports Announcements (GRA)  
 published by the National Technical  
 Information Service, Springfield  
 Virginia 22161, USA

Printed by Specialised Printing Services Limited  
 40 Chigwell Lane, Loughton, Essex IG10 3TZ

ISBN 92-835-0506-9